

MICROCOPY RESOLUTION TEST CHART
NATIONAL BUREAU OF STANDARDS-1963-A

**PROCEEDINGS OF THE TWELFTH
NAVY SYMPOSIUM ON AEROBALLISTICS**

VOLUME I

12-13-14 MAY 1981

**HELD AT THE DAVID TAYLOR NAVAL SHIP R&D CENTER
BETHESDA, MARYLAND**

**SPONSORED BY THE
NAVAL AIR SYSTEMS COMMAND**

APPROVED FOR PUBLIC RELEASE: DISTRIBUTION UNLIMITED

TABLE OF CONTENTS

	PAGE
Foreword	ii
Welcome To The David Taylor Naval Ship R&D Center	v
Greetings and Remarks To Symposium Attendees	vi
Papers Presented	x
Authors	xvi
Attendees	xix
Navy Aeroballistics Committee	xxiv
NAC Panels And Panel Chairman For 1981	xxiv
Past NAC Chairmen	xxiv
U.S. Navy Symposiums On Aeroballistics	xxv
Paper Selection Committee	xxvi
Acknowledgments	xxvii

Accession for
DTIC GRA&I
DTIC TAB
Unannounced
Justification _____

By _____
Distribution/ _____
Availability Codes _____
Dist _____

A

DTIC
COPY
INSPECTED
2

12th Navy Symposium on Aeroballistics

Vol. I

FOREWORD



S. de los Santos
Chairman
Navy Aeroballistics Committee

It is a great pleasure and privilege for me, on behalf of the Navy Aeroballistics Committee to welcome you to the 12th U.S. Navy Symposium on Aeroballistics.

This Symposium is being held for the purpose of presenting the results of recent work associated with aeroballistics. As indicated in the program included in your registration package, the balance of our Symposium will consist of 45 papers presented in 5 technical sessions. A banquet, preceded by cocktails will be held this evening at the Kenwood Club, and for those who are interested, there will be a Center Facility tour on Thursday afternoon. The first four sessions of the Symposium are unclassified. For security reasons, all classified papers will be presented in the fifth session on Thursday. The Proceedings will include the unclassified papers in Volumes I and II and the classified papers in Volume III.

The papers accepted for presentation come from the NAC Activity Members, Air Force, NASA, The Universities, and Industry. To round out the program, we have invited several prominent speakers to share with us their knowledge and experience that would be of interest in aeroballistics. These speakers include Jack Nielsen of Nielsen Engineering & Research, Inc. who will review missile aerodynamics; Art Maddox of NWC, now visiting Professor at the Naval Academy, who will review store separation; G.C. Paynter of Boeing Military who will give us the current status of inlet flow prediction methods; J.W. Stultz of McDonnell Douglas who will speak on heating methods used to determine structural temperatures; and W. Ballhaus of NASA Ames who will talk on the numerical aerodynamic simulator. Our after dinner speaker will be Col. John Boyd (USAF, retired) who will talk on energy maneuverability.

This is the second time around for DTNSRDC to host a Navy Aeroballistic Symposium, and, perhaps, it would be appropriate here to share with you some observations. The first Center hosting (Sixth Symposium) was held at Fort McNair in 1963 for lack of an auditorium facility at the Center. It is recalled that 28 40-minute papers were presented by the participants (Navy, Air Force, Army, NASA, Universities, and Industry). Since then, the committee decided to limit the presentation time without limiting the length of the written manuscripts. It comes as no surprise then that for the same duration, more papers could be presented without loss of essential detail. Accordingly, the last 5 symposia have averaged 45 papers.

Although the number of papers has remained the same, the contributions of various activities have changed considerably. Since 1975, for instance, there has been a 50-percent reduction in Navy contributions; this has been offset by a several-fold increase from the universities. The decline in Navy participation is not surprising. It is the result of DOD's policy (promulgated in 1975) of seeking constant growth in its program to strengthen and revitalize its research base and ties with the external research community — a policy that resulted in increasing external research funding while maintaining reduced levels of research at the inhouse laboratories! Data indicate that the services, particularly the Air Force, took a beating (70-percent decline in inhouse research funds).

Laboratory heads and other knowledgeable individuals have expressed concern for this state of affairs. Allowing the laboratories to remain at the current level of research performance could, if it hasn't already, erode their long-term ability to perform those functions which are basic to supporting their missions.

A recent General Accounting Office (GAO) study recognized the predicament of the laboratories and has requested DOD to give the same careful consideration to the research base represented by the inhouse laboratories as has been given the needs of the external research community. How DOD will respond to this GAO recommendation is not yet known, but the feeling is that it would be better to accomplish the true increase in inhouse research by an overall increase in research funding rather than through a corresponding reduction of the planned growth in extramural research.

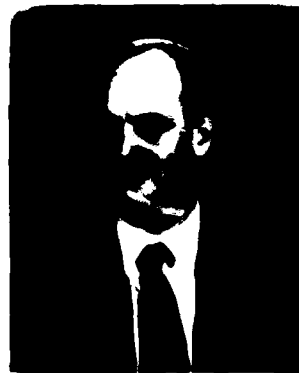
Already we seem pressed for time. The scheduling shown in the program was based on the cafeteria renovation being completed in April and having lunch on station. Unfortunately, the scheduled completion date has slipped, and now we'll have to go off station for lunch — some think this to be a blessing in disguise. I have accordingly requested each speaker to streamline their presentation or take no more time than has been allotted them.

Again, welcome and I hope you have a very profitable and enjoyable Symposium.

WELCOME TO THE DAVID TAYLOR NAVAL SHIP R&D CENTER



B.F. TIBBITTS
*Captain, USN
Commander
David Taylor Naval Ship R&D Center*



DR. ALAN POWELL
*Technical Director
David Taylor Naval Ship R&D Center*

On behalf of the David Taylor Naval Ship R&D Center, we are pleased to welcome you to the Twelfth U.S. Navy Symposium on Aeroballistics.

The Navy Aeroballistics Committee, established jointly by the Naval Air Systems Command and the Naval Sea Systems Command, has prepared an excellent program covering diverse technical disciplines. It should be noted that the NAC Symposium brings together speakers and guests with special competence in these technical disciplines from the Navy, Air Force, Army, and other government agencies, universities and from industry. It is our objective to provide the proper atmosphere for you to assure a productive and pleasant Symposium.

PRECEDING PAGE BLANK-NOT FILMED

GREETINGS AND REMARKS TO SYMPOSIUM ATTENDEES



R.J. MILLER
Captain, USN
Assistant Commander for
Research and Technology
Naval Air Systems Command

Good morning ladies and gentlemen. I wish to welcome you on behalf of the Commander of the Naval Air Systems Command, Vice Admiral E.R. Seymour. I understand that you as a group participating in this Twelfth Navy Symposium on Aeroballistics constitute a broad representation from the aerospace industry, government laboratories, and academia. It is very gratifying to see such open cooperation for exchange of ideas within this community.

It is well to note that such cooperation was high in the minds of those people who were responsible for organizing what is today known as the Navy Aeroballistics Committee, the group responsible for this meeting. As some of you know, this committee has been in continuous operation since its first meeting was held on 1 February 1949. Even in our bureaucratic society you must admit this is a long time for any committee to remain in existence. The earliest record we have that such an organization was considered is in the form of a letter from the Office of the Chief of Ordnance, War Department, to the Secretary of War dated 15 July 1940. The subject of this letter was "Appointments as Members of Ordnance Ballistic Advisory Committee." It is worth reading this short letter to you to show, at least by the caliber of the people being considered, the importance of the subject of ballistics.

12th Navy Symposium on Aeroballistics

Vol. I

It is requested that authority be granted . . . for the appointment of the following members of the Ordnance Ballistics Advisory Committee, at the rate of \$10.00 per diem when employed, for a period not to exceed thirty (30) days each fiscal year, in each case for duty at Aberdeen Proving Ground, Maryland:

Dr. H.L. Dryden,	Chief Mech. & Sound Division National Bureau of Standards, Washington, D.C.
Dr. A.W. Hull,	Research Laboratory General Electric Company, Schenectady, New York
Prof. I.I. Rabi,	Columbia University New York
Prof. Harold Clayton Urey,	Columbia University, New York
Prof. J. von Neuman,	Institute for Advanced Study, Princeton, New Jersey
Dr. Bernard Lewis,	Bureau of Mines Washington, D.C.
Prof. Henry N. Russell,	Princeton University, Princeton, New Jersey
Prof. T. von Karman,	California Institute of Technology, Pasadena, California

While this letter was endorsed by order of the Secretary of War on July 23, 1940, there is no further mention of such a committee until 1945. The letter does indicate by the caliber of the people considered the importance attached to ballistics. Planning which was begun in 1945 led to the first meeting of the Bureau of Ordnance Committee on Aerodynamics (BCA) on 1 February 1949. Under various name changes this committee has functioned continuously and is now the Navy Aeroballistics Committee.

A review of the program for this meeting shows a very diverse program, and I am sure you will find the next three days rewarding. Thank You.

12th Navy Symposium on Aeroballistics

Vol. I



DR. JULES BELLASCHI
*Deputy Director for
Surface Warfare Systems Group
Naval Sea Systems Command*

The following describes the content of the opening remarks made by Dr. J.J. Bellaschi at the 12th Navy Symposium on Aeroballistics.

Dr. Bellaschi opened his remarks with a welcome on behalf of the Naval Sea Systems Command and voiced his appreciation to all the attendees of the symposium.

A reorganization within the Naval Sea Systems Command, which occurred since the 11th Navy Symposium on Aeroballistics placed the management of Research and Exploratory Development Technology pertaining to weapons that fly through the air (missiles, rockets, and projectiles) in the Research and Technology Office (NAVSEA-62R) of the Surface Warfare Systems Directorate (NAVSEA-62) within the Combat Systems Directorate (NAVSEA-06).

The functional responsibilities of the Surface Warfare Systems Group are to:

- Provide life cycle engineering/management of surface warfare systems including ammunition, gun and missile systems, surveillance radar, and small arms.
- Develop command policies and procedures for weapon packaging and handling systems.
- Manage research and technology programs related to surface warfare systems.
- Provide surface warfare systems design and integration support to combat system managers and ship design managers.
- Provide single point managers for assigned field activities.

The programs in Advanced and Engineering Development that SEA-62 is responsible for are SEAFIRE, Guided Projectile, Vertical Launcher, Rolling Airframe Missile, Penguin Evaluation, manufacturing technology, new 5-inch projectile, TERRIER and TARTAR improvements, Close-In Weapon System, STANDARD MISSILE improvements, radar improvements, and NATO SEASPARROW. The programs in production are the MK 75/76-mm gun, MK 45/5-inch gun, MK-13 and 26 missile launchers, SPS-67, 49 and 52C Radar, Integrated Automatic Detection and Tracking, SPA-25 and 26 radars, MK-86 and 92 fire control, HARPOON surface ship system, and the Hifrag projectile.

The Exploratory Development Program for surface-launched weapons and the planning process used to derive that program were described. The "Surface-Launched Weaponry Task Area Objectives" (TAO) document was referenced. The TAO is a document that begins with Navy missions, derives weapon system design concepts needed to carry out the missions and the technology needs required to develop the design concepts. The technology program is derived from the technology needs. The technology needs identified in the TAO document which relate to aeroballistics include optimum airframe (weight, cost, drag, maneuverability), maneuver mode (bank-to-turn versus skid-to-turn), radome damage, aerodynamic heating, structural design, radome/body joint, inlet/body design, aerodynamic data base, low time constant (quick response), fast actuator, high-angle-of-attack aerodynamics, roll/yaw coupling, non-linear coupled aerodynamics, maneuverability at high altitudes, projectile obturator band design, low-drag projectiles, submunition dispersion, improved gun accuracy, aerodynamic prediction methodology, and guidance sensor-window technology.

Dr. Bellaschi also described how aeroballistics technology is an important contribution to weapon speed, maneuverability, response and control, intercept performance, and effectiveness against low radar cross-section targets.

Dr. Bellaschi was pleased to see that the aeroballistics technical community from government, industry and universities was so well represented at this symposium. He ended with the following quote from Theodore Roosevelt:

"The credit belongs to the man who is actually in the arena, whose face is marred by dust and sweat and blood, who strives valiantly, who errs and comes short again and again, who knows the great enthusiasms, the great devotion, and spends himself in a worthy cause, and if he fails, at least fails while daring greatly, so that he'll never be with those cold and timid souls who know neither victory nor defeat."

12th Navy Symposium on Aeroballistics

Vol. I

PAPERS PRESENTED

VOLUME I

	PAGE
1. Missile Aerodynamics — Dim Past and Indefinite Future DR. JACK N. NIELSEN* <i>Nielsen Engineering & Research Inc.</i>	I-1
2. Aerodynamics of Tactical Weapons to Mach Number 8 and Angle of Attack 180 Degrees L. DEVAN L.A. MASON F.G. MOORE <i>Naval Surface Weapons Center, Dahlgren Laboratory</i>	I-39
3. An Inviscid Computational Method for Tactical Missile Configurations A.B. WARDLAW, JR. J.M. SOLOMON F.P. BALTAKIS L.B. HACKERMAN <i>Naval Surface Weapons Center, White Oak Laboratory</i>	I-73
4. Status Report on Triservice Data Base Extension of PROGRAM MISSILE M.J. HEMSCH J.N. NIELSEN <i>Nielsen Engineering & Research, Inc.</i>	I-107
5. Wind Tunnel Test of an Integrated Rocket-Ramjet Missile W.J. RUNCIMAN R. BAUER <i>Boeing Aerospace Company, The Raytheon Company</i> (Paper Withdrawn)	Withdrawn
6. Theoretical and Experimental Supersonic Lateral-Directional Stability Characteristics M. LAMB W.C. SAWYER J.L. THOMAS <i>NASA Langley Research Center</i>	I-117
7. Aerodynamics of a Rolling Airframe Missile L.E. TISSERAND <i>The Johns Hopkins University, Applied Physics Laboratory</i>	I-125
8. Approximate Method for Predicting Supersonic Normal Force Coefficient of Very-Low-Aspect-Ratio Lifting Surfaces E.F. LUCERO <i>The Johns Hopkins University, Applied Physics Laboratory</i>	I-149

*Invited Speaker

12th Navy Symposium on Aeroballistics

Vol. I

PAGE

9. Supersonic Aerodynamics of a Class of Cone-Derived Waveriders M.L. RASMUSSEN D.C. DANIEL <i>Air Force Armament Laboratory, Eglin AFB</i> M.C. JISCHKE <i>University of Oklahoma</i>	1-181
10. Determination of Aerodynamic Characteristics of Ballistic Projectiles at Transonic Speeds S.S. STAHARA <i>Nielsen Engineering & Research, Inc.</i>	1-199
11. Store Separation -- A Review DR. ARTHUR MADDOX* <i>U.S. Naval Academy</i>	1-239
12. Study of Flow Fields and Store Forces in Close Proximity to a Triple Ejection Rack at Transonic Speeds F.K. GOODWIN J.N. NIELSEN <i>Nielsen Engineering & Research, Inc.</i>	1-251
13. Recent Experimental Efforts in Store Separation at DTNSRDC K.A. PHILLIPS <i>David Taylor Naval Ship R&D Center</i>	1-295
14. Computer Program for Simulating the Six-Degree-of-Freedom Motion of Missile Debris Fragments M.J. HEMSCH <i>Nielsen Engineering & Research, Inc.</i>	1-313
15. An Influence Function Method for Predicting Aerodynamic Characteristics during Weapon Separation R. MEYER A. CENKO <i>Grumman Aerospace Corporation</i> S. YAROS <i>NASA Langley Research Center</i>	1-331
16. Submissile Aerodynamics During Dispensing T.E. LUNDY W.F. BRADDOCK L.R. UTREJA <i>Lockheed-Huntsville R&E Center</i>	1-347

*Invited Speaker

12th Navy Symposium on Aeroballistics

Vol. I

	PAGE
17. Gun Launch Dynamics of the Navy 5-Inch Guided Projectile G. FOTIEO <i>Martin Marietta Aerospace, Orlando</i>	I-371
18. Dynamics of Subsonic Tracer Projectiles J.H. CUADROS <i>General Dynamics, Pomona Division</i> G.L. WINCHENBACH B.F. LUCAS <i>Air Force Armament Laboratory, Eglin AFB</i>	I-377
19. Thrust Augmentation for Tomahawk Cruise Missile B.F. NORTH I.K. KIM <i>General Dynamics, Convair Division</i>	I-395
20. Drag Characteristics and Suitability of Three-Foot Long Parachute Decelerators C.T. CALIANNO <i>Naval Air Development Center</i>	I-417

VOLUME II

21. Current Status of Inlet Flow Prediction Methods DR. G.C. PAYNTER* <i>Boeing Military Aircraft Company</i>	II-1
23. Rotational Flow in a Curved-Wall Diffuser Designed by Using the Inverse Method of Solution of Potential Flow Theory T. YANG F. NTONE <i>Clemson University</i>	II-37
24. Aerodynamic Characteristics of a Series of Airbreathing Missile Configurations C. HAYES <i>NASA Langley Research Center</i>	II-53
25. Parabolized Navair-Stokes Predictions for Three-Dimensional Viscous Supersonic Flows S. SWAMINATHAN M.D. KIM R.A. THOMPSON C.H. LEWIS <i>Virginia Polytechnic Institute and State University</i>	II-63

*Invited Speaker

12th Navy Symposium on Aeroballistics

Vol. I

PAGE

26. Results of a Government and Industry Survey of the Heating Methods Used to Determine Missile Structural Temperatures
DR. J. WARREN STULTZ*
McDonnell Douglas, St. Louis
D.B. PAUL
Air Force Wright Aeronautical Laboratories, Wright-Patterson AFB II-95
27. Supersonic Combustor Insulation Ablation Analysis and Tests
R.W. NEWMAN
H.G. FOX
The Johns Hopkins University, Applied Physics Laboratory II-101
28. Numerical Aerodynamic Simulator
DR. WILLIAM F. BALLHAUS, JR.*
NASA Ames Research Center II-129
29. Computation of Three-Dimensional Viscous Flow over Blunt Lifting Bodies at High Angle of Attack
K.Y. SZEMA
C.H. LEWIS
Virginia Polytechnic Institute and State University II-165
30. Computation of Hypersonic Laminar Viscous Flow over a Body with Mass Transfer and/or Spin at Angle of Attack
M.D. KIM
C.H. LEWIS
Virginia Polytechnic Institute and State University II-191
31. Three-Dimensional Viscous Shock-Layer Analysis of Laminar or Turbulent Flows in Chemical Equilibrium
R.R. THAREJA
K.Y. SZEMA
C.H. LEWIS
Virginia Polytechnic Institute and State University
B. DENYSYK
EG&G/Dahlgren II-241
32. Further Development of the Streamline Method for Determination of Three-Dimensional Flow Separation
T.C. TAI
David Taylor Naval Ship R&D Center II-281

*Invited Speaker

12th Navy Symposium on Aeroballistics

Vol. I

	PAGE
33. Comparison of Numerical Results and Measured Data for Smooth and Indented Nosetips T. HSIEH <i>Naval Surface Weapons Center, White Oak Laboratory</i>	II-297
35. Structural and Electrical Performance Considerations in the Design of Multiband Radomes G. DAILEY R.C. MALLALIEU <i>The Johns Hopkins University, Applied Physics Laboratory</i>	II-309
36. Structural Considerations for the Recovery of Air-to-Air Missiles A.A. ANDERSON <i>Pacific Missile Test Center</i>	II-331

**VOLUME III
(CLASSIFIED PAPERS)**

	PAGE
22. Preliminary Inlet Design Studies for a Hypersonic Wide-Area Defense Missile M.D. GRIFFIN J.R. STEVENS J.L. KEIRSEY <i>The Johns Hopkins University, Applied Physics Laboratory</i>	III-1
34. Aerodynamic Characteristics of Biconic Configurations at Mach 14 N.E. SCAGGS D.S. GILLIES <i>Air Force Wright Aeronautical Laboratories, Wright-Patterson AFB</i>	III-21
37. Structural Comparisons of Tandem- and Integral-Rocket Boosters for a Hypersonic Wide-Area-Defense Missile R.M. RIVELLO <i>The Johns Hopkins University, Applied Physics Laboratory</i>	III-47
38. Application of Metal Matrix Composites to Tactical Missiles C.M. STANDARD R.C. VAN SICLEN <i>Vought Corporation</i>	III-71
39. A Comparison of Flow Field Prediction Methods as Applied to the ASALM Configuration G.L. BURKE <i>Air Force Wright Aeronautical Laboratories, Wright Patterson AFB</i>	III-103

12th Navy Symposium on Aeroballistics

Vol. I

PAGE

40. Standard Missile Aerodynamics—Comparison of Recent Flight Test Results
with Predictions Based on Ground Tests
E.T. MARLEY
The Johns Hopkins University, Applied Physics Laboratory III-171
41. Lift and Controllability of Two Tail-Control Missile Configurations Differing in
Wing Planform
G.A. BARNES
The Johns Hopkins University, Applied Physics Laboratory III-187
(Proceedings Only)
42. Advanced Flight Control Concepts for Airbreathing Missile Applications
T.R. PEPITONE
P.R. TABBERT
Naval Surface Weapons Center, Dahlgren Laboratory III-199
43. Aerodynamic Studies of Two Candidate Air-to-Air Ramjet Powered Missiles
R.E. MEEKER
L.W. STRUTZ
Naval Weapons Center III-235
44. Stand-Off Jammer Suppressor (SOJS) Candidate Airframe Evaluation
S.R. HARDY
Naval Surface Weapons Center III-275
45. A Handbook of Experimental Data for the Effects of Inlet Systems on Airbreathing
Missiles External Aerodynamics
O.J. McMILLAN
S.C. PERKINS, JR.
Nielsen Engineering & Research, Inc. III-311

AUTHORS

	Paper	Volume	Page
ANDERSON, ARVID A.	36	II	II-331
BALLHAUS, WILLIAM S., Jr.	28	II	II-129
BALTAKIS, FRANK P.	3	I	I-73
BARNES, G.A.	41	III	III-187
BAUER, RALPH L.	5	I	Withdrawn
BRADDOCK, WILLIAM F.	16	I	I-347
BURKE, GERALD L.	39	III	III-103
CALIANNO, CARL T.	20	I	I-417
CENKO, ALEXIS	15	I	I-331
CUADROS, JAIME H.	18	I	I-377
DAILEY, G.	35	II	II-309
DANIEL, DONALD C.	9	I	I-181
DENYSYK, BO	31	II	II-241
DEVAN, LEROY	2	I	I-39
FOTIEO, GEORGE	17	I	I-371
FOX, HAROLD G.	27	II	II-101
GILLIES, D.S.	34	III	III-21
GOODWIN, FREDERICK K.	12	I	I-251
GRIFFIN, MICHAEL D.	22	III	III-1
HACKERMAN, L.B.	3	I	I-73
HARDY, SAMUEL R.	44	III	III-275
HAYES, CLYDE	24	II	II-53
HEMSCH, MICHAEL J.	4, 14	I	I-107, 313
HSIEH, CARL T.	33	II	II-297
JISCHKE, MARTIN C.	9	I	I-181
KEIRSEY, JAMES L.	22	III	III-1
KIM, IN-KUN	19	I	I-395
KIM, MOO DO	25, 30	II	II-63, 191

AUTHORS

	Paper	Volume	Page
LAMB, MILTON	6	I	I-117
LEWIS, CLARK H.	25, 29, 30, 31	II	II-63, 165, 191, 241
LUCAS, BILLY F.	18	I	I-377
LUCERO, EDDIE F.	8	I	I-149
LUNDY, THOMAS E.	16	I	I-347
MADDOX, ARTHUR R.	11	I	I-239
MALLALIEU, R.C.	35	II	II-309
MARLEY, E.T.	40	III	III-171
MASON, L.A.	2	I	I-39
McMILLAN, O.J.	45	III	III-311
MEEKER, RICHARD E.	43	III	III-235
MEYER, RUDOLPH	15	I	I-331
MOORE, F.G.	2	I	I-39
NEWMAN, ROBB W.	27	II	II-101
NIELSEN, JACK N.	1, 4, 12	I	I-1, 107, 251
NORTH, B.F.	19	I	I-395
NTONE, FRANCOIS	23	II	II-37
PAYNTER, G.C.	21	II	II-1
PEPITONE, THOMAS R.	42	III	III-199
PERKINS, S.C., Jr.	45	III	III-311
PHILLIPS, KENNETH A.	13	I	I-295
RASMUSSEN, MAURICE L.	9	I	I-181
RIVELLO, ROBERT M.	37	III	III-47
RUNCIMAN, WILLIAM J.	5	I	Withdrawn
SAWYER, WALLACE C.	6	I	I-117
SCAGGS, NORMAN E.	34	III	III-21
SOLOMON, JAY M.	3	I	I-73

AUTHORS

	Paper	Volume	Page
STAHARA, STEPHEN S.	10	I	I-199
STANDARD, CHARLES M.	38	III	III-71
STEVENS, JAMES R.	22	III	III-1
STRUTZ, LARRY W.	43	III	III-235
STULTZ, J. WARREN	26	II	II-95
SWAMINATHAN, S.	25	II	II-63
SZEMA, K.Y.	29, 31	II	II-165, 241
TABBERT, PAUL R.	42	III	III-199
TAI, TSZE C.	32	II	II-281
THAREJA, RAJIV R.	31	II	II-241
THOMAS, JAMES L.	6	I	I-117
THOMPSON, R.A.	25	II	II-63
TISSERAND, L.E.	7	I	I-125
UTREJA, LAJPAT R.	16	I	I-347
VAN SICLEN, ROBERT C.	38	III	III-71
WARDLAW, ANDREW B., Jr.	3	I	I-73
WINCHENBACH, GERALD L.	18	I	I-377
YANG, TAH-TEH	23	II	II-37
YAROS, STEVE F.	15	I	I-331

ATTENDEES

NAME	AFFILIATION
ANDERSON, Arvid A.	Pacific Missile Test Center
BAKER, William B.	CALSPAN
BALLHAUS, William F.	NASA Ames Research Center
BALTAKIS, F.P.	NSWC, White Oak Laboratory
BELLASCHI, Jules J.	NAVSEA
BENARD, Irvin J.	United Technologies Corporation
BOYD, John	Air Force (Retired)
BRADDOCK, Bill F.	Lockheed Missiles & Space Company
BURKE, Gerald L.	AF Wright Aeronautical Laboratories
CALIANNI, Carl T.	Naval Air Development Center
CARTER, Stephen K.	Naval Weapons Center
CAYWOOD, William C.	JHU/APL
CENKO, Alexis	Grumman Aerospace Corporation
CHALK, Joseph B.	Naval Intelligence Support Center
CLANCY, Tom M.	DTNSRDC
CLARK, W.H.	Naval Weapons Center
COBB, Kenneth K.	Air Force Armament Laboratory
CRONVICH, L.L.	JHU/APL
CUADROS, Jaime H.	General Dynamics Pomona Division
DAILEY, George	JHU/APL
DE LOS SANTOS, S.	DTNSRDC
DEVAN, Leroy	NSWC, Dahlgren Laboratory
DRIFTMYER, Richard T.	NSWC, White Oak Laboratory
ESTES, Robert H.	Naval Weapons Center
FORTUNATO, Enrico	NSWC, White Oak Laboratory
FOTIEO, George	Martin Marietta Aerospace
FRIEDMAN, Eugene M.	U.S. Army ARRADCOM

12th Navy Symposium on Aeroballistics

Vol. I

NAME	AFFILIATION
GILBERT, Lee N.	Naval Weapons Center
GLEASON, Larry L.	Naval Weapons Center
HACKERMAN, Louis B.	NSWC, White Oak Laboratory
HALL, Darryl W.	Science Applications, Inc.
HARDY, Samuel R.	NSWC, Dahlgren Laboratory
HAYES, Clyde	NASA Langley Research Center
HEMSCH, Michael J.	Nielsen Engineering & Research, Inc.
HOPPS, Jack C.	Honeywell, Minneapolis
HSIEH, Tsuying	NSWC, White Oak Laboratory
HUDGINS, Henry E.	U.S. Army ARRADCOM
JOHNSON, Arne (LCDR, USN)	DTNSRDC
JOHNSON, Lloyd	NSWC, Dahlgren Laboratory
KANURI, Ravi	General Electric Company
KAUTZ, Frederick A.	Central Intelligence Agency
KIM, Moo Do	Virginia Polytechnic Institute
KRAUSE, David L.	Naval Ordnance Station
KREMZIER, Emil J.	The Marquardt Company
KRUMINS, M.V.	NSWC, White Oak Laboratory
LAMB, Milton	NASA Langley Research Center
LARSEN, Kenneth A.	Pacific Missile Test Center
LEHMAN, Larry O.	Naval Air Development Center
LESLIE, David L.	General Dynamics, Pomona Division
LEWIS, Clark H.	Virginia Polytechnic Institute
LOEZOS, Stavros	Naval Air Systems Command
LUCERO, Eddie F.	JHU/APL
MacALLISTER, Leonard C.	Ballistic Research Laboratory
MADDOX, Arthur R.	U.S. Naval Academy
MAGUIRE, Bill	DTNSRDC
MARLEY, Edward T.	JHU/APL

12th Navy Symposium on Aeroballistics

Vol. I

NAME	AFFILIATION
MARSHALL, James R.	Hughes Aircraft Company
MASON, Lawrence A.	NSWC, Dahlgren Laboratory
MATTHEWS, R.K.	CALSPAN
McKAY, D.W.	Eglin AFB
McMILLAN, Oden J.	Nielsen Engineering & Research, Inc.
MEYER, Rudolph C.	Grumman Aerospace Corporation
MILLER, Robert A.	Rockwell International Corporation
MILLER, Richard J. (CAPT, USN)	Naval Air Systems Command
MOORE, Frank G.	NSWC, Dahlgren Laboratory
MORRIS, George W.	Lockheed Missiles & Space Company
NEWMAN, Robb W.	JHU/APL
NIELSEN, Jack N.	Nielsen Engineering & Research, Inc.
NORTH, Bob F.	General Dynamics Convair Division
OHRENBERGER, John T.	TRW, California
OSTROWSKI, Paul P.	Naval Ordnance Station
PAPADOPOULOS, James	MBD Advanced Technology Center
PASIUK, Lionel	Naval Sea Systems Command
PAYNTER, Gerald C.	The Boeing Company, Seattle
PEPITONE, Thomas R.	NSWC, Dahlgren Laboratory
PHILLIPS, Kenneth A.	DTNSRDC
POLLIN, Irvin	Harry Diamond Laboratories
POPHAM, Edgar R.	McDonnell Douglas Corporation
POWELL, Alan	DTNSRDC Technical Director
PRILLMAN, Floyd W.	Vought Corporation
RACHNER, Jerome E.	Rockwell International Corporation
RAGSDALE, W.C.	NSWC, White Oak Laboratory
RASMUSSEN, Maurice L.	University of Oklahoma
RIVELLO, Robert M.	JHU/APL
RUTLEDGE, Walter H.	NSWC, Dahlgren Laboratory

12th Navy Symposium on Aeroballistics

Vol. I

NAME	AFFILIATION
RYAN, Bertha	Naval Weapons Center
SCAGGS, Norman E.	AF Wright Aeronautical Laboratories
SCHINDEL, Leon H.	NSWC, White Oak Laboratory
SCHMIDT, L.V.	Naval Post Graduate School
SEARS, Edward S.	Air Force Armament Laboratory
SIMPERS, Glen	Naval Ordnance Station
SMITH, Lloyd H.	Naval Weapons Center
SMITH, Renard E.	Naval Weapons Center
SMITH, Stephen D.	McDonnell Douglas Astronautics
SMITHEY, W.J.H. (CAPT, USN)	Pacific Missile Test Center
SOLIS, Ricardo	NSWC, Dahlgren Laboratory
SOLOMON, Jay M.	NSWC, White Oak Laboratory
STAHARA, Stephen S.	Nielsen Engineering & Research, Inc.
STANDARD, Charles M.	Vought Corporation
STEVENS, J.R.	JHU/APL
STRUTZ, Larry W.	Naval Weapons Center
STULTZ, J. Warren	McDonnell Douglas Corporation
STUREK, Walter B.	U.S. Army Ballistic Research Lab
SUN, John	Hughes Aircraft Company
SWAMINATHAN, S.	Virginia Polytechnic Institute
SZEMA, K.Y.	Virginia Polytechnic Institute
TAI, Tsze C.	DTNSRDC
TAYLOR, Robert M.	DTNSRDC
THAREJA, Rajiv R.	Virginia Polytechnic Institute
TIBBITTS, B.F. (CAPT, USN)	Commander, DTNSRDC
TISSERAND, Lawrence E.	JHU/APL
TESSITORE, Frank A.	Grumman Aerospace Corporation
UTREJA, Lajpat Rai	Lockheed Missiles & Space Company
VAN AKEN, Ray W.	Naval Weapons Center

12th Navy Symposium on Aeroballistics

Vol. I

NAME	AFFILIATION
VAN TUYL, Andrew H.	NSWC, White Oak Laboratory
VOLZ, William C.	NAVAIR
WARDLAW, Andrew B.	NSWC, White Oak Laboratory
WASICKO, Richard J.	NASA, Washington, D.C.
WAUGH, Charles E.	Martin Marietta Corporation
WECKESSER, Louis B.	JHU/APL
WEISEL, John S.	NSWC, Dahlgren Laboratory
WERBACK, Bill	Naval Weapons Center
XERIKOS, James	McDonnell Douglas Astronautics
YANG, Tah-Teh	Clemson University
ZARLINGO, Frederick C.	Naval Weapons Center
ZIEN, Tse-Fou	NSWC, White Oak Laboratory

NAVY AEROBALLISTICS COMMITTEE

MEMBERS AND ALTERNATE MEMBERS FOR 1981

S. de los Santos, Chairman (DTNSRDC)	A.E. Johnson
L.L. Cronvich (JHU/APL)	E.T. Marley
C. de Crescente (NADC)	E.J. McQuillen
L.H. Schindel (NSWC)	F.G. Moore
W.J.H. Smithey (PMTC)	W.L. Miller
R.W. Van Aken (NWC)	L. Smith

ASSOCIATES

- L. Pasiuk, Executive Secretary (NAVSEASYSKOM)
- W.E. Volz (NAVAIRSYSKOM)
- G.S. Pick (NAVSEASYSKOM)
- F.S. Pierce (NAVAIRSYSKOM)

**NAC PANELS AND PANEL CHAIRMAN
FOR 1981**

Air Inlets and Diffusers	T.C. Tai (DTNSRDC)
Gas Dynamics	W.H. Clark (NWC)
Heat Transfer	T.F. Zien (NSWC)
Launch Dynamics	K. Okauchi (NWC)
Missile Stability & Performance	T.R. Pepitone (NSWC)
Structures & Aeroelasticity	A.A. Anderson (PMTC)

PAST NAC CHAIRMEN

Feb 1949 - Nov 1949	CDR H.M. Mott-Smith (BuOrd)
Dec 1949 - Oct 1950	CDR L.G. Pooler (BuOrd)
Oct 1950 - Feb 1953	CDR L.G. Pooler (NOL)
Mar 1953 - Jul 1953	A.I. Moskovits (Acting) (BuOrd)
Sep 1953 - Jul 1955	E.A. Bonney (JHU/APL)
Aug 1955 - Aug 1957	H.H. Kurtzweg (NOL)
Sep 1957 - Jul 1959	W.R. Haseltine (NWC)
Aug 1959 - Jul 1961	R.A. Niemann (NSWC/DL)
Jul 1961 - Jan 1963	R.E. Wilson (NOL)
Jan 1963 - Jan 1965	S.T. de los Santos (DTNSRDC)
Jan 1965 - Jan 1967	R.H. Peterson (NMC)
Jan 1967 - Jan 1969	W.A. Kemper (NSWC/DL)

PAST NAC CHAIRMEN

Jan 1969 - Jan 1971	L.L. Cronvich (JHU/APL)
Jan 1971 - Jan 1973	W.R. Haseltine (NWC)
Jan 1973 - Jan 1975	R.E. Wilson (NSWC/WOL)
Jan 1975 - Jan 1976	S.T. de los Santos (DTNSRDC)
Jan 1976 - Jan 1977	J.W. Rom (PMTC)
Jan 1977 - Jan 1978	W.A. Langen (NADC)
Jan 1978 - Jan 1979	R.W. Van Aken (NWC)
Jan 1979 - Jan 1980	L.L. Cronvich (JHU/APL)
Jan 1980 - Jan 1981	L.H. Schindel (NSWC)
Jan 1981 -	S.T. de los Santos (DTNSRDC)

U.S. NAVY SYMPOSIUM ON AEROBALLISTICS

FIRST SYMPOSIUM – NOVEMBER 1950

Hosted by Defense Research Laboratory
Held at University of Texas, Austin, Texas

SECOND SYMPOSIUM – MAY 1952

Hosted by Naval Weapons Center
Held by Huntington Hotel, Pasadena, Calif.

THIRD SYMPOSIUM – OCTOBER 1954

Hosted by The Johns Hopkins University, Applied Physics Laboratory
Held at The Johns Hopkins University, Applied Physics Laboratory
Silver Spring (Howard County Location), Md.

FOURTH SYMPOSIUM – NOVEMBER 1957

Hosted by Naval Weapons Laboratory
Held at Department of Commerce Auditorium, Washington, D.C.

FIFTH SYMPOSIUM – OCTOBER 1961

Hosted by Naval Ordnance Laboratory
Held at Naval Ordnance Laboratory, White Oak, Md.

SIXTH SYMPOSIUM – OCTOBER-NOVEMBER 1963

Hosted by Naval Ship Research & Development Center
Held at National War College Fort McNair, Washington, D.C.

SEVENTH SYMPOSIUM – JUNE 1966

Hosted by Naval Missile Center
Held at Naval Missile Center, Point Mugu, Calif.

12th Navy Symposium on Aeroballistics

Vol. I

U.S. NAVY SYMPOSIUM ON AEROBALLISTICS

EIGHTH SYMPOSIUM – MAY 1969

Hosted by Naval Weapons Center
Held at NWC Corona Laboratories, Corona, Calif.

NINTH SYMPOSIUM – MAY 1972

Hosted by The Johns Hopkins University, Applied Physics Laboratory
Held at The Johns Hopkins University, Applied Physics Laboratory
Silver Spring (Howard County Location), Md.

TENTH SYMPOSIUM – JULY 1975

Hosted by Naval Surface Weapons Center, Dahlgren, Virginia
Held at Sheraton Fredericksburg Motor Inn, Fredericksburg, Va.

ELEVENTH SYMPOSIUM – AUGUST 1978

Hosted by Naval Air Development Center, Warminster, Pa.
Held at Hilton Northeast Philadelphia, Trevose, Pa.

TWELFTH SYMPOSIUM – MAY 1981

Hosted by David Taylor Naval Ship Research & Development Center
Held at David Taylor Naval Ship Research & Development Center, Carderock, Md.

PAPER SELECTION COMMITTEE

S. de los Santos, Chairman DTNSRDC
R.W. Van Aken NWC
A.A. Anderson PMTC
G. Seidel NADC
T.R. Pepitone NSWC
L. Weckesser JHU/APL
T.C. Tai DTNSRDC
K. Phillips DTNSRDC
W. Clark NWC

ACKNOWLEDGMENTS

The helpful efforts and cooperation of the following individuals in preparing for the Twelfth Navy Symposium on Aeroballistics are acknowledged:

C.A. Applegate
C.C. Burdette
J.R. Hatley
A.E. Johnson
T.D. Jones

C.A. Mueller
K.A. Phillips
T.C. Tai
R.M. Taylor

Thanks,

S. de los Santos

S. DE LOS SANTOS

Chairman

Twelfth Navy Symposium on Aeroballistics

MISSILE AERODYNAMICS - DIM PAST

AND INDEFINITE FUTURE

Jack N. Nielsen
Nielsen Engineering & Research, Inc., Mountain View, California

ABSTRACT

The present paper covers two distinctly different subjects. The first subject is the efforts of the U.S. Navy and the U.S. Army to develop aerial torpedos during World War I. The Navy team had such prominent engineers as Elmer and Lawrence Sperry and Glenn Curtis. The Army team included Charles F. Kettering and Orville Wright. Despite these eminent personalities, a successful aerial torpedo was not developed for use in World War I.

The second subject area covered in the paper is suggestions for future work in missile aerodynamics. High angle of attack aerodynamics, engine-airframe integration and autopilot-airframe integration are covered. In addition the future of asymmetric vortices, external stores, and computational fluid dynamics are discussed.

INTRODUCTION

It is a privilege to be an invited speaker to the Twelfth U.S. Navy Aeroballistics Symposium. I was pleased when my old friend, Dr. de los Santos, called me and invited me to the Symposium. I was, of course, delighted particularly since this presented an opportunity to choose my material at will. The title of the talk "Missile Aerodynamics - Dim Past and Indefinite Future" is accurate. I chose not to repeat the Wright Brothers Lecture. Rather I am taking this opportunity to divest myself of a number of preprints of the lecture. Anyone who would like a copy should help himself.

The first matter I should like to cover is the efforts of the Navy to develop a flying torpedo during World War I. It is an interesting history. In my Wright Brothers Lecture, I said a number of things about the efforts of the U.S. Army to develop an aerial torpedo in World War I, but gave only brief mention to the U.S. Navy. I now have the opportunity to remedy that shortcoming. At the same time I will expand on the efforts of the U.S. Army. You may want to take sides on the question, "Who invented the first successful guided missile in the United States?" So much for the dim past.

The other general area I would like to address is the never-never land of the indefinite future. I will discuss and make suggestions for future research in a number of areas of missile aerodynamics.

2. U.S. NAVY MISSILE DEVELOPMENT IN THE WORLD WAR I PERIOD

2.1 INTRODUCTORY REMARKS

The history of the development of the aerial torpedo by the U.S. Navy during World War I is of interest involving, as it did, such engineers as Elmer and Lawrence Sperry, Glen Curtiss, and Carl Norden. The interest of the U.S. Navy followed naturally from the successful automatically controlled underwater torpedo to the aerial torpedo, or flying bomb, as it was variously called. The basic requirement it was envisioned to fulfill was to increase the range of artillery. The history of the development of pilotless aircraft and guided missiles to about 1948 has been summarized by RADM. D. S. Fahrney, USN (ret.) in reference 2.1, and much of the material contained herein has been obtained from this source. I am indebted to Dr. William J. Armstrong, Historian of NAVAIR, for a copy of this document. Its interest, in my view, is such that it should be published as a book. Additional material has been taken from references 2.2 to 2.6.

2.2 BEGINNING OF AERIAL TORPEDO PROJECT

On October 7, 1915 the U.S. Navy set up the Naval Consulting Board to advise the Secretary and Navy Department on matters of scientific and technical natures. A committee of the board was formed on "Aeronautics, including Aero Motors." Among the seven members of the committee were Elmer Sperry and Peter Cooper Hewitt. Hewitt was interested in a flying bomb prior to the creation of the Board and approached Sperry concerning such a device. Sperry had designed successful gyro systems for the automatic control of torpedos over a number of years. Sperry agreed to carry out some experiments if Hewitt supplied the necessary funds, estimated to be about \$3,000. These funds went fast and Sperry supplied much more of his own money. To obtain more backing they decided to put on a demonstration for the U.S. Navy.

On September 12, 1916 Lawrence Sperry, son of Elmer Sperry, demonstrated no-pilot automatic control of a hydroplane to Lt. Wilkinson. The pilot took the hydroplane off the water and turned it over to automatic control. The plane thereupon climbed to a predetermined altitude and flew at this altitude a predetermined distance maintaining a given heading the whole time. Lt. Wilkinson recommended that the U.S. Army develop the flying bomb since they were useful for deployment against large targets on land rather than ships on water because of their perceived inaccuracy. However, on April 14, 1917 the Naval Consulting Board recommended to the Secretary of the Navy that \$50,000 be made available "to carry on experimental work on the subject aerial torpedos in the nature of automatically controlled airplanes or aerial machines carrying high explosives capable of being initially directed and thereafter automatically managed." Strictly speaking, they were talking about pilotless aircraft.

The next action was for the Secretary of the Navy to set up another committee to make a recommendation on the recommendation. The review committee reported favorably and on May 22, 1917 the Sperry project was approved. The Sperry company received a contract for 6 sets of automatic control gear for aerial bombs at \$3,900 apiece. The plan was to install these in N-9 type seaplanes and conduct flight tests.

2.3 FLIGHT TESTS WITH N-9 SEAPLANES

Amityville, Long Island was selected as the site for flight testing the N-9 seaplanes with Sperry automatic controls. In this operation the pilot always takes the plane off before turning the plane over to automatic control. A period of ground testing preceded the flight testing which started in September 1917. Successful flight was made on September 5, 1917, one plane made a run on a target eight miles away with little error in course but 12½-percent error in range. During these tests significant gyro drifts were noted. Elmer Sperry tried to convince the U.S. Navy of the importance of radio control for correcting errors in targeting, but he never succeeded during the entire project, thus delaying the first application of command-updated inertial guidance.

It is of interest that the Chief Signal Officer of the Army witnessed a successful test on November 21, 1917. Later the U.S. Army developed its own aerial torpedo with Charles F. Kettering and Orville Wright on the team.

2.4 PROCUREMENT OF PILOTLESS AIRCRAFT

In the opinion of Elmer Sperry, the top speed of the N-9 was too low, and a special design was needed for the aerial torpedo. By increasing top speed, errors due to gyro drift could be reduced. It was necessary to be able to launch the bird without a pilot, and this specialized problem needed to be worked out.

Sperry had for years worked with the Glenn H. Curtis Company on aeroplane stabilization. He contacted Glenn Curtis concerning the design and manufacture of a pilotless aircraft to act as a flying bomb. A specification was written for such an aircraft by Glenn Curtis as follows:

Payload: 1000 lb of explosive
Empty weight: 500 lbs
Take off: catapult launch
Top speed: 90 mph
Range: 50 miles
Provide for special control equipment
Engine: Should be as light as possible compatible with its duties

The Curtis cost estimate for producing these flying bombs with engines was a minimum of \$6,000 apiece and a maximum of \$10,000 apiece. A best effort to achieve delivery in 30 days was promised. A contract was signed and the delivery was made within 30 days. A sketch of the Curtis flying bomb is shown in Figure 2.1.

2.5 LAUNCHING OF THE CURTIS FLYING BOMB

The first launching device tried was a downward sloping wire, with tip wires to hold the wings level. Tests of this device were unsuccessful. Next it was decided to try a launching device which might work aboard ship. Such a device might consist of a launching car on tracks, and a device to give an initial impulse to the car. The device was built but the first tests in December 1917 and January 1918 were unsuccessful. The flying bomb was observed to be tail heavy. It was realized that the flying bomb must first be a

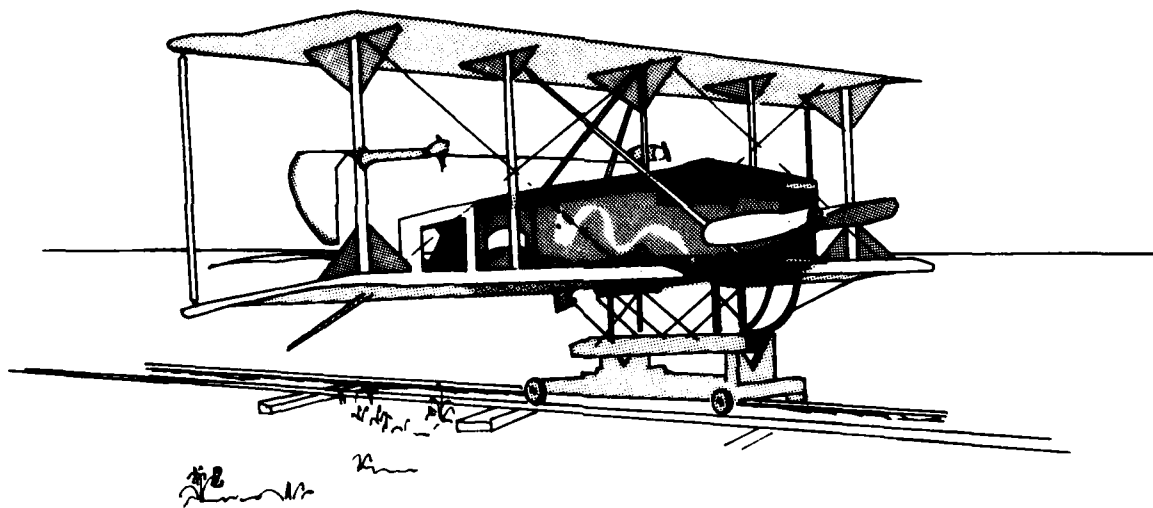


Figure 2.1 - Curtiss Flying Bomb.

practical flying machine before it could be demonstrated with automatic control.

In an attempt to correct the stability and control of the flying bomb, a seat to accommodate a pilot was put into the explosive bay. Ski runners were put on the plane and take-offs and landing were practiced by Lawrence Sperry on a bay of ice. He cracked up the plane several times and luckily escaped serious injury.

On March 6, 1918 a successful launch of the flying bomb was made from the track which satisfied all the test objectives. The machine launched successfully, and flew in a straight line climbing steadily. The distance gear cut the throttle at the prescribed distance, 1,000 yards, and the machine spiraled into the water. This flight is said by Admiral Fahrney (ref. 2.1) to be the "first successful flight of an automatic missile in the U.S. and possibly the world."

Another flying bomb on April 7, 1918 was launched successfully but crashed after takeoff. Hereafter the Navy decided to do further work to improve the aerodynamics of the flying bomb as well as its launching.

2.6 SUBSEQUENT HISTORY OF CURTIS FLYING BOMB

Lawrence Sperry entered the Navy Reserve on active duty on January 1, 1918 but became ill and entered the Naval Hospital on March 19, 1918. He was found physically unfit for flying and discharged from active duty subsequently. He formed the Lawrence Sperry Aircraft Co. and started vigorously to solve the flight characteristics of the bomb under automatic control. A special Marmon automobile was used to mount the flying bomb for high-speed ground testing, thus predating sled testing at NWC and Holloman Air Force Base. After some useful experimentation with the flying bomb attached to the automobile, it was decided to put the automobile on railroad tracks and try launching in this mode. The tests were unsuccessful.

At this time the Navy decided to retain Carl L. Norden to design a fly-wheel type of catapult which he successfully accomplished. Tested on a flying bomb, the launching was successful but the flight of the bird thereafter was erratic. The test of another flying bomb was also successful in launch but not in flight.

At this point the Navy decided to launch N-9 seaplanes with the Norden catapult to further test the Sperry control system. At least one successful test was made. It became apparent that if the N-9 had been used on the flying bomb, the project would have reached a successful stage of development much earlier. Elmer Sperry concluded "I feel that we have gone a long way towards completing the development of an extremely significant engine of war, it being nothing short of the coming gun..."

By this time (September 1918) Cdr. McCormick, in charge of the flying bomb development, concluded that future work should be directed to improvements of the automatic pilot and a new design of the flying bomb airplane.

2.7 POST WAR EPILOGUE

The Navy asked Norden to review the design of the Sperry automatic pilot and make recommendations for further work. Specifications for a new flying bomb plane were approved by the Navy and a contract for five planes awarded to the Witteman-Lewis Company. Norden got the contract for design and fabrication of the automatic control gear for the Witteman-Lewis machine. Both Sperry and Curtis were now out of the picture. At the same time plans were made for the Navy to direct the project at the Naval Proving Ground, Dahlgren, Virginia.

The flight tests of the Witteman-Lewis machine in the summer of 1919 by Navy pilots revealed the machine to be too tail heavy with insufficient aileron. The design of the airframe was changed, and flight testing was resumed in the spring of 1920. On August 18, 1920 with the pilotless version, the plane released from the catapult went smoothly, but stalled 150 yards out. Norden stated "No plane has ever been flown under automatic control successfully without previous adjustment after trial flights by a competent pilot," (Reference 2.1). The Navy accepted this and the "pilotless" aircraft were flown by pilots and tuned prior to pilotless launch from the catapult. On October 25, 1920 the next launching was "perfect." The airplane flew in circles all over the sky before it ran out of gas, spun, and crashed. On April 25, 1921 the next launching was also perfect. However, the plane climbed a short distance, but settled into the water and upset due to the fixed landing gear.

The Bureau was losing interest fast.

"The Bureau is not impressed with the practicability of this aerial torpedo (F.B.) for use against vessels, even when they are in Fleet formation, because of the difficulty of controlling the height within sufficient limits to permit a torpedo to be flown at low altitudes, such as would be required for use against a vessel. It is believed they may, however, be of use as aerial targets by installing controls in condemned planes - the question of radio control has been under consideration and is believed to be feasible. The original intention for use of the 'F.B.' was for the distant bombardment from sea of large areas, such as naval stations, fleet anchorages, and fortified towns. It is still believed that this use can be realized with fair success. The tactical value of such a use is, however, believed to be doubtful. Its greatest value for us is probably for use in control of surveyed planes used as targets. In designing the Bureau Controls, allowance was made for possible future fitting of a radio control, which is considered to be quite feasible." This essentially ended the flying torpedo, but the ideas of radio control of airplanes lived on.

3. U.S. ARMY MISSILE DEVELOPMENT IN WORLD WAR I

3.1 THE ARMY GETS UNDERWAY

It is of interest to review the efforts of the U.S. Army to develop an aerial torpedo during World War I. Major General O. Squier had witnessed a flight test of the U.S. Navy's aerial torpedo in Amityville on November 21, 1917. He was so impressed that he got the U.S. Army to start its own project. The principal idea was to get innovative weapons to take to the war in Europe since "wars are won largely by new instrumentalities." Mr. Charles F. Kettering

became Director of the Army's Flying Bomb Project. Mr. Kettering, who with others, had acquired the Dayton Wright Co., enlisted Orville Wright as his aerodynamic consultant. A pair of consultants and manufacturers were obtained for power plants and controls. The Army's aerial torpedo was variously known as an automatic flying machine, automatic carrier, Bug, and Flying Bomb.

3.2 SPECIFICATIONS

Mr. Kettering laid down a number of points for the Army's aerial torpedo:

- (1) Simplicity
- (2) Easiness of manufacture
- (3) Easily assembled in the field
- (4) Economy of shipping space
- (5) Ease of launching
- (6) Reliability
- (7) Load carrying aspects
- (8) Accuracy

As a result of these points certain specifications were developed:

Total weight: 520 lbs
Biplane wings:
 span: 15 ft
 chord: 30 ins
 dihedral: 10°
Take-off speed: 55 mph
Engine: 4 cylinder, V90°, 2 cycle, 37 HP at 2150 RPM
Altitude control: aneroid barometer
Direction control: Air valve sensing apparatus on gyroscope
Distance control: Air log (propeller revolution count)
Material:
 Fuselage: Plywood, paste board
 Wings: Muslin, brown paper, dope
 Tail surfaces: Paste board

Every effort was made to use materials not needed by the aircraft industry. It was estimated that the total cost including explosive came to about \$1.00 per pound.

In contrast to the Navy design, the automatic controls were in the design stage whereas the Navy designs were completed and had been tested in N-9 airplanes.

A sketch of the Kettering "Bug" is shown in Figure 3.1.

3.3 FLIGHT TESTING

The flight tests were started in September 1918. However, numerous changes in design and much testing preceded the flight tests. It should be pointed out that no piloted versions of the flying torpedo were used to test or adjust the automatic controls prior to flight testing. Launch was from a rail-mounted cart powered by the aerial torpedo.

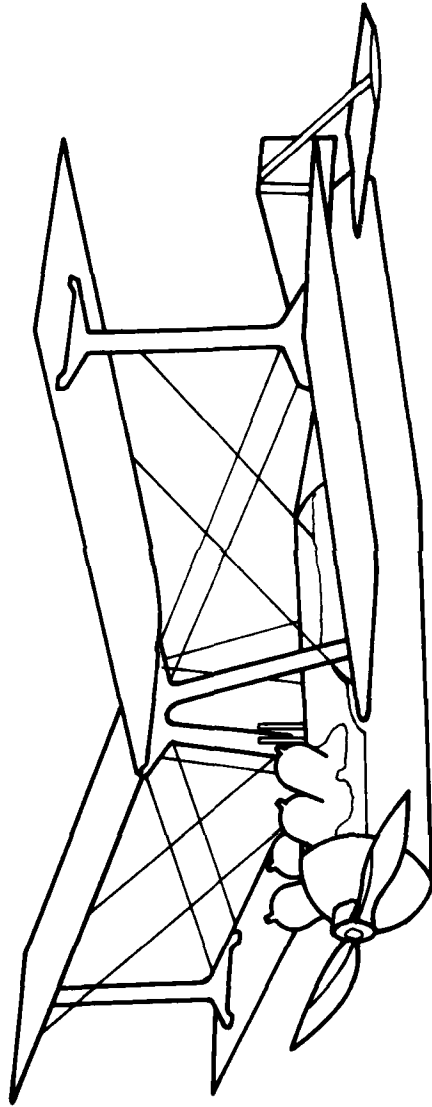


Figure 3.1 - Kettering Aerial Torpedo.

The first flight test put the flying torpedo through a hair-raising series of aerobatics before crashing at the end of an Immelman turn. In the second flight a different series of aerobatics occurred, but the ship corrected itself and flew away. A tendency of the planes to fly in a wide circle as a result of propeller torque was noted.

The status of the flight tests was such that on October 5, 1918, General Squier in a memorandum to the Chief of Staff wrote "The Chief Signal Officer believes that the development of this new weapon, which has now demonstrated its practicability, marks an epoch in the evolution of artillery for war purposes of the first magnitude, and comparable, for instance, with the invention of gunpowder in the fourteenth century. The development is not known to our overseas Forces, nor to the Forces of our allies. It comes as a distinct product of American genius, as applied to our present methods of warfare."

This optimism was on firmer ground when on October 22, 1918 the first perfect test of the aerial torpedo occurred. The altitude was set at 200 feet and the range for 500 yards. The impact was almost exactly on target.

3.4 POST-WAR DEVELOPMENTS

The Army had a number of aerial torpedos made and was preparing to transfer flight operations to the former Navy site at Amityville, Long Island when World War I came to an end. At this point 25 aerial torpedos plus parts were put into storage at McCook Field.

A series of flight tests under Army cognizance of 14 aerial torpedos at Carlstrom Field, Florida were generally unsatisfactory. All the know-how obtained at Dayton was not transferred to the Army test units. As a result of these tests recommendations were made to (1) develop means for launching regardless of wind direction, (2) develop self-propelled launching cars on a catapult, and (3) make improvements in controls, gyroscopes, and engines.

On December 30, 1919 the Adjutant General directed the Air Service to continue the development of the automatic carriers.

In March 1920, plans were laid down for the development of the flying torpedo. They covered three aspects:

- (a) Perfection of the automatic controls
- (b) Specification of control means
- (c) Testing of controls in a piloted aircraft

The firm of Lawrence Sperry Aircraft was given contracts in the first few months of 1920 to construct automatic controls and six "Messenger" airplanes, and to carry out tests under full automatic control. The first flight tests with a standard L-1 airplane with pilot in September 1920 to April 1921 proved out launching and distance control, but the gyroscopes gave problems due to precision, poor bearings, and installation difficulties. Further flight tests with a new gyro were made, but the problems of maintaining a predetermined course was still unsolved because of wind changes and gyro difficulties. At this point the contractor requested permission to use radio control to correct deviations from a predetermined course. Tests were made using radio control up into 1926, initiating more or less successful application of command updated inertial guidance. However, the hand writing was on the wall.

On June 7, 1926 the Chief of the Engineering Division, Major John F. Curry, wrote to the Chief of Air Service expressing the views of his Division "that no torpedo development can be successful if it depends on a system of stabilization alone, but that, in addition, radio control is absolutely necessary. The gyroscopically controlled aerial torpedo, equipped with radio, is necessarily very expensive. A project has been initiated to cover the study of the aerial torpedo as an automatically stable airplane equipped with radio control. --- Due to the shortage of experimental funds, the aerial torpedo development has had to give way to other and more necessary developments. --- Due to other more urgent projects, the allotment of personnel and money is not sufficient to complete the aerial torpedo projects during the coming fiscal year."

This wrote "finis" to the aerial torpedo development until World War II urged the reopening of the development. Little was accomplished before all development was greatly curtailed in the lean years following the stock market crash in 1929.

I am indebted to Mr. Carl Tusch of the AFSC Liaison Offices at Ames Research Center and the Air Force Museum for supplying historical material on the Army aerial torpedo project. Also I wish to thank the Albert F. Simpson Historical Research Center of Maxwell AFB who provided additional material.

At this point I would like to skip over sixty or more years from the dim past to the indefinite future and make some prognostications concerning the future of missile aerodynamics.

4. HIGH ANGLE OF ATTACK AERODYNAMICS

4.1 AREAS OF IMPORTANCE

High angle of attack aerodynamics has been an area of interest among missile aerodynamists for a number of years. The subject embraces a number of areas, some of which are discussed in the following sections. Here we will only treat the subject broadly since specific aspects of the subject will be subsequently discussed. For purposes of discussion let us consider high angles of attack to be those over about 20 degrees.

The general interest in high angle of attack aerodynamics stems from the fact that missiles use higher and higher angles of attack in the search for increased maneuverability. Some particular applications of past and present interest include the bomber defense missile (SRBDM), short-range air-to-air (Agile and ILAAT), and AAW missiles which must turn over quickly from vertical launch. Another application is the high altitude missile which may be unpowered at extreme range and yet be required to have a maneuver capability of two- or three-fold over an evasive target. Also a tumbling missile or missile fragment is another particular application.

4.2 SPECIAL PROBLEMS OF IMPORTANCE

A few special problem areas in high angle of attack aerodynamics are now discussed. First there is the question of air inlets at high angles of attack. It is hard to design an efficient air inlet for a large angle of attack range

(and appears feasible only for bank-to-turn missiles.) Another problem is that aerodynamic controls suffer severe losses of effectiveness at high combined angles of pitch and deflection (Reference 4.1). These losses make it difficult to trim the airframe at high angle of attack thus limiting maneuverability.

There is a severe loss of favorable wing-body interference at high angles of attack and Mach numbers as shown in Figure 4.1. The factor K_W is the ratio of the normal force on the fins mounted on the body to that of the wing alone at the same angle of attack. In this figure a value of K_W greater than unity indicates favorable interference whereas a number less than unity indicates unfavorable interference. The unfavorable effects can be very large at high angles of attack and Mach numbers.

Another problem about which very little is known is nonlinear afterbody effects at high angles of attack. The body section between the missile nose or canards and its empennage can shed vortices at high angles of attack which cause large nonlinearities and greatly reduce tail effectiveness in stabilized missiles.

The above problems represent areas in which additional research is needed.

4.3 PREDICTION METHODS FOR HIGH INCIDENCE

The term "prediction methods" is meant to cover both computational fluid mechanics and engineering prediction methods. The discussion is confined to methods for predicting static forces and moments. The former will be treated in a subsequent section, and the latter will now be discussed with regards to the transonic, supersonic, and hypersonic speed regimes.

Engineering prediction methods for the high angle of attack transonic regime are almost entirely data-base methods (Reference 4.2), which permit little extrapolation out of the test range. This subject is worthy of attention for both transonic and subsonic speeds.

At supersonic speeds there are several methods such as References 4.3 to 4.5. These methods use data bases sometimes combined with rational modeling. In this approach a skeletal but systematic data base is obtained covering a range of the parameters of interest such as angle of attack, roll angle, Mach number, fin aspect ratio, etc. A theoretical model of the flow over the missile is made, and rational mathematical techniques are used to interpolate and extrapolate from the data base. While several high incidence supersonic engineering design methods exist, they cover different configuration spaces with some overlap. The effects of roll angle are generally not included. The effects of aerodynamic controls is an area needing much attention. Force and moment prediction methods for missiles with noncircular bodies and with inlets also need more attention in view of the current interest in bank-to-turn missiles.

For high supersonic and hypersonic speeds the principal methods are based on Newtonian theory, shock-expansion theory, or derivatives of these approaches. While for certain simple configurations these methods give good results, no suitable general method exists which applies to more complicated configurations and at the same time handles vortex effects. A need for such a method exists.

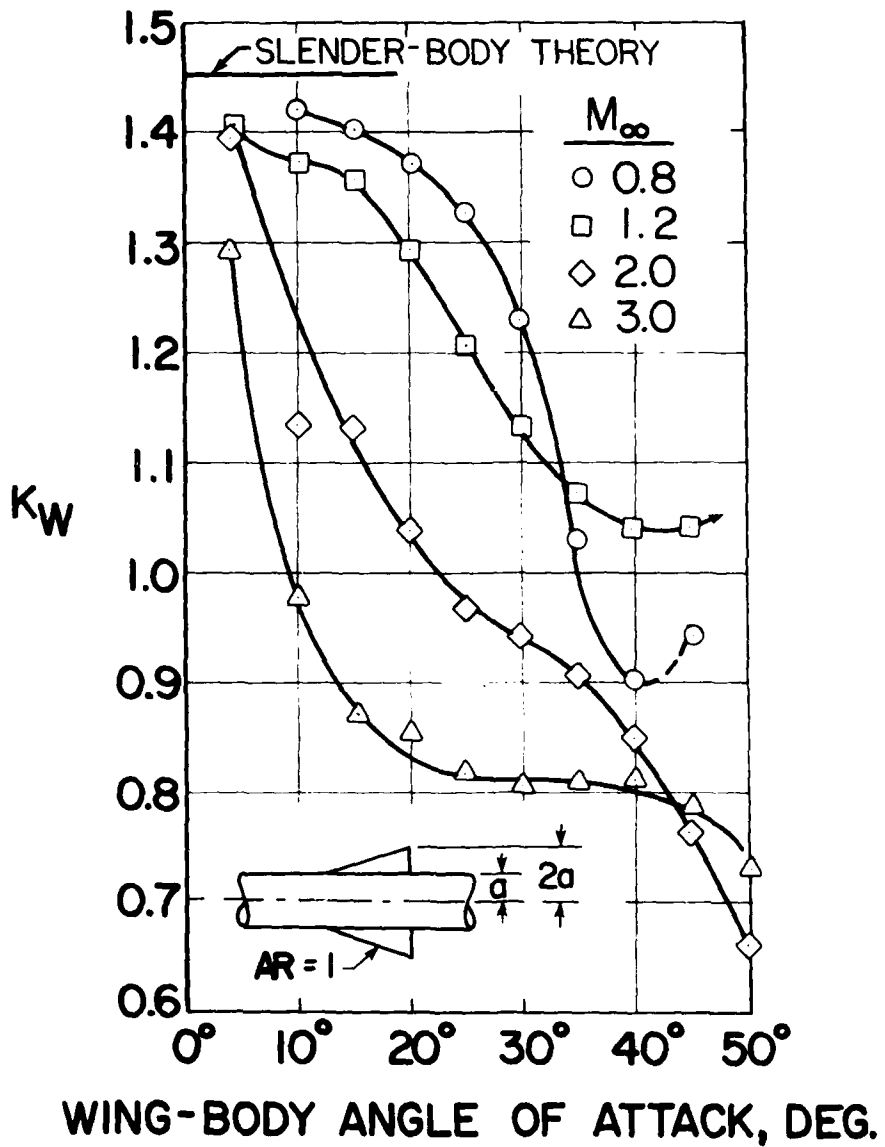


Figure 4.1 - Effect of Angle of Attack and Mach Number on Wing-Body Interference.

4.4 HIGH ANGLE OF ATTACK WIND-TUNNEL TESTING

The need for high α data is not only to obtain design data for particular missiles but it also includes the requirements for high quality data for testing aerodynamic theories and systematic data for rational modeling methods. In the area of data for checking theory there is a requirement for coordinated flow-field measurements, pressure distribution data, and flow visualization.

One of the primary difficulties that makes high angle of attack testing difficult at all speeds is the need to design model supports which will stand the high loads involved and at the same time will minimize the effect of support interference on the quantities being measured. There is much room for ingenuity in the design of such support systems.

A particular speed range of difficulty for high α testing is the transonic range not only because of the well-known wall interference but also because of support interference. The simple case of a body of revolution shows quite different characteristics at high α depending on whether it is supported by a strut or by a sting. An example of this effect is shown in Figure 4.2 as taken from Reference 4.6. It appears that the strut interferes with asymmetric vortex formation. Further experiments are required to develop high α interference-free support systems at transonic speeds.

5. INTEGRATION OF ENGINES AND AIRFRAMES

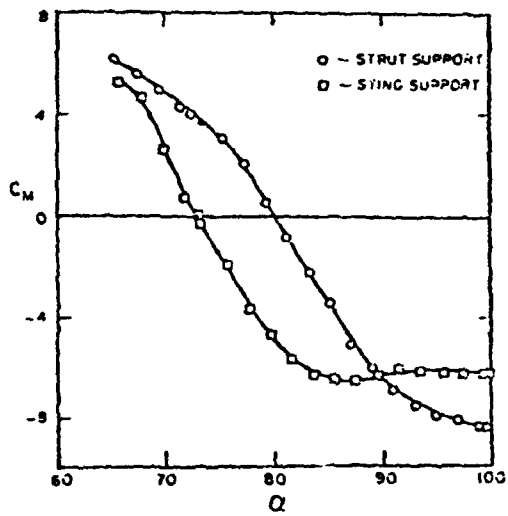
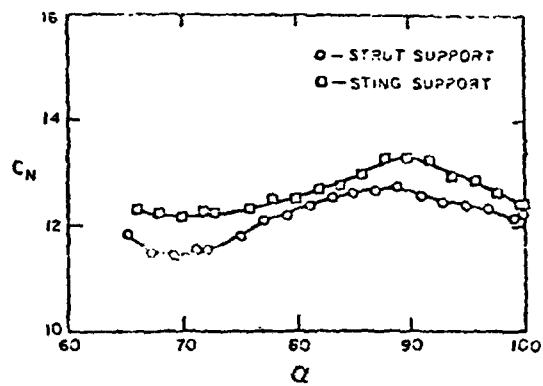
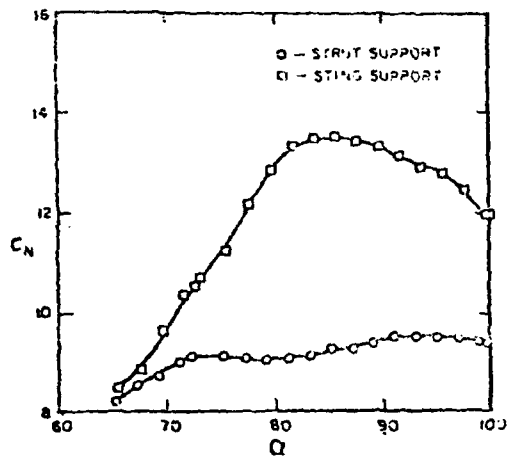
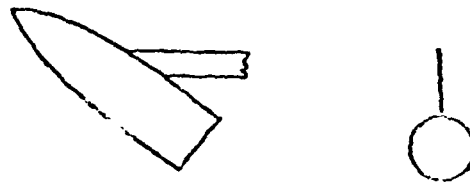
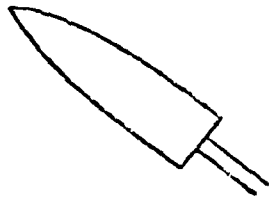
5.1 Preliminary Observations

The problems of engine-airframe integration are most important for air-breathing missiles, and these comments apply to such missiles. Included in this area are the effect of the airframe on the airflow into the inlet, and the interference of the inlet on the external airflow about the missile. Both effects are important. Generally missiles utilizing air-breathing engines will not be allowed to roll continuously because of the difficulty of maintaining efficient inlet operation under these conditions. Exceptions probably exist. We will address the question of the state of the art concerning CFD methods for inlet design, data available for design methods, and engineering design methods. Suggestions for future work in these areas are also considered.

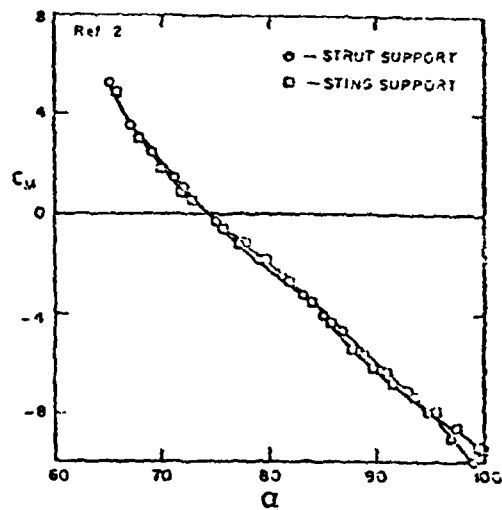
5.2 COMPUTATIONAL FLUID DYNAMICS (CFD) METHODS

The principal CFD methods available for studying airframe/inlet interference are based on the Navier-Stokes equations, the Euler equations, or on paneling procedures. With regard to Navier-Stokes methods no complete solutions seem to have been carried out for the three-dimensional case. For the subcritical case not even a two-dimensional calculation is available for realistic geometries. The difficulties lie in the lack of powerful enough computing machines and in turbulence modeling, especially in association with boundary-layer shock-wave interaction. Those difficulties will eventually be overcome. Until then other methods must be used in design.

Euler codes have been applied to supercritical inlets with some degree of success. Their applications to subcritical inlet problems are not yet fully demonstrated. The basic problems with the Euler equations for internal flows



$M_{\infty} = 0.6.$



$M_{\infty} = 0.9.$

Figure 4.2 - Effect of Support Type on Normal Force and Pitching Moment of Ogive Cylinder at High Angle of Attack and Transonic Speed.

is that boundary-layer, shock-wave interaction causes the internal waves to be in different positions from those predicted for an inviscid fluid as given by the Euler equations. The possibility of using an Euler code together with an embedded boundary-layer analysis appears to be a practical approach which should be attempted to provide a basis for design tools. It is possible to account for body vortices and fin vorticity with Euler codes so that the effect of these quantities on the quality of the flow entering the inlet can be predicted. Also the effect of the inlet on the external flow should be amenable to treatment by Euler codes.

It is possible to treat the effects of variable inlet mass flow with panel methods as has been demonstrated by Dillenius (Reference 8.7). However, a careful comparison between experiment and theory for such an approach has not been made. One would expect to be able to calculate the effect of the inlet on the external aerodynamics by such an approach. It seems worthwhile to determine the accuracy and limitations of panel methods in this connection because of their potential economy.

5.3 STATUS OF THE DATA BASE

Much data exist on engine-airframe integration as a result of testing many specific designs. However, the data are generally not systematic nor consistent with respect to definitions of quantities or terminology. The data on the effects of the inlet system on the external aerodynamics of air-breathing missiles are being assembled into a data handbook. Dr. O. J. McMillan will cover this subject in the last paper of this Symposium.

5.4 ENGINEERING PREDICTION METHODS

The state of the art with regards to engineering prediction methods leaves a great deal to be desired. Existing methods which fulfill the requirement of being cheap suffer from lack of accuracy. In fact, a general method of good accuracy does not exist.

A simple approach to remedying the present unsatisfactory state of the art probably does not exist. It will probably involve a thorough evaluation of the accuracy of present methods to determine their inadequacies, the definition of problem areas where deficiencies exist, and overcoming the deficiencies by systematic experimental tests and the use of rational modeling and computational fluid dynamics.

6. AUTOPILOT-AIRFRAME INTEGRATION

6.1 BACKGROUND

The principal limitations to maneuverability of missiles which are aerodynamically controlled are due to the autopilot. These limitations are often associated with the inability of the autopilot to cope with the cross-coupling of the aerodynamic control functions, largely between yaw and roll. Often the limitations are associated with the variation in the magnitude of the direct control derivatives with angle of attack and roll angle.

6.2 PROBLEMS IN CURRENT PRACTICE

There are a number of factors in current practice which are not conducive to proper autopilot-airframe integration. Frequently the autopilot designer sees the aerodynamics as given or measured, and complicates the autopilot design in an effort to control a missile in the presence of severe aerodynamic nonlinearity. In many companies the aerodynamic and system control groups are separate, and the engineering manager does not exercise the necessary direction to see that cross fertilization occurs. In order to do this, he must have a good knowledge of each discipline. Part of the problem is that undergraduate schools stress linear control theory, leaving nonlinear control theory as an elective course. Yet, as von Kármán said, "It is a nonlinear world in which we live."

Another part of the problem is due to the fact that good engineering methods for predicting control cross-coupling derivatives are lacking. If the aerodynamicist and autopilot designers work together, it seems that better missile maneuverability can be achieved at lower cost; also, the success of efforts to adjust autopilot gains based upon state estimation is enhanced by close coordination. What then can be done to improve the present practice?

6.3 RECOMMENDATIONS

The first step in the process should be to make sure that the aerodynamicist and autopilot designers work together before the airframe design is frozen so that some control can still be exercised over its nonlinearities. Perhaps jointly they could establish specifications for the airframe, allowing for nonlinearities (many of the known classes of airframe nonlinearities are described in Reference 6.1). To accomplish this step will require better aerodynamic methods in some cases for predicting control cross-coupling among other nonlinearities. In many cases the airframe aerodynamics will still need to be determined experimentally, but the test model should be a better approximation to the final design by applying missile aerodynamic prediction methods first. It seems quite feasible that the integrated problem of airframe-autopilot design will become a subject of fundamental research and development to see how a coordinated design effort can synergistically enhance the final product.

7. ASYMMETRIC VORTEX PROBLEMS

7.1 BACKGROUND

Asymmetric vortices are known to form on the leeward side of a body of revolution if the angle of attack is increased beyond a certain limiting value that depends on a number of parameters, the most important of which is probably body fineness ratio. The unexpected phenomenon, first reported by Cooper et al. (Reference 7.1) in 1952 has been termed "phantom yaw." The onset of vortex asymmetry is usually accompanied by large side forces and yawing moments which are undesirable from the standpoints of both stability and control. The precise cause of vortex asymmetry is not clear, but it appears to be associated with a neutrally stable condition of a symmetrical vortex pair depending on its strength and geometric configuration. Then a disturbance can cause it to take

one or another of several asymmetric positions. Slight body geometric asymmetries or wind-tunnel flow disturbances can trigger it one way or the other.

An oversimplified, but useful, diagram which shows the general occurrence of asymmetric vortices is shown in Figure 7.1. Here the $\alpha - M_\infty$ diagram is divided into three regions by the line $\alpha = 25^\circ$ and $M_c = M_\infty \cos \alpha = 0.5$. A typical angle of attack for the onset of asymmetric vortices for a body of moderate fineness ratio is 25° . It is also known that if the crossflow Mach number, M_c , is greater than about 0.5 to 0.6 (Reference 7.2) that the leeward flow changes character. The relatively concentrated vortex pair is now replaced by two large symmetrical elliptical regions of rotational flow, and an asymmetric vortex pair does not occur. It is thus seen that asymmetric vortices are of no significance above the transonic speed range for moderate fineness ratios.

7.2 PARAMETERS AFFECTING PHANTOM YAW

A number of parameters are known to influence phantom yaw. A good survey is contained in Reference 7.3. Increases in body fineness ratio cause the onset of vortex asymmetry at lower angles of attack. Rolling the missile can cause changes in side forces and yawing moments of different magnitudes and sign in a repeatable manner depending on body roughness (departures from circularity). Nose bluntness seems to inhibit asymmetric vortices.

7.3 CONTROLLING OR HARNESSING PHANTOM YAW

While changes in basic geometry to reduce phantom yaw effects are of interest, it is of even greater interest to control or harness phantom yaw by the use of novel ideas. One idea in this category is a rotating nose. Rotating the nose causes an asymmetric vortex pattern to switch as shown in Figure 7.2 taken from Reference 7.2. Increasing the rate of spin may reduce the amplitude of the side force which is oscillatory, not random. I am indebted to Dr. Gary Chapman of NASA/Ames Research Center for these data. Further data are contained in Reference 7.3. If the nose spin rate is above the bandwidth of the autopilot, then the effect of phantom yaw is eliminated.

Another novel idea for harnessing phantom yaw is due to Mr. T. Canning (Reference 7.4) from work performed under an AFATL sponsored experimental study of support interference on the loads on bodies of revolution at transonic speed and high angles of attack. The next two figures (Figures 7.3 and 7.4) show plots of $C_N \cos \alpha$ versus C_Y for an ogive-cylinder at different roll angles of the body. The body had a small piece of tape on the nose at a fixed azimuthal angle. The variations of C_N and C_Y with roll angle were irregular but repeatable. However, paired values of C_N and C_Y formed smooth curves as shown. Note that vortex asymmetry increases both normal force and side force.

Now the maximum resultant force in a plane normal to the free-stream direction is given by $(C_Y^2 + C_N^2 \cos^2 \alpha)^{1/2}$. The radius vector from the origin (Figures 7.3 and 7.4) is the value of the maximum force coefficient and its direction is about 30° from the leeward meridian. The nose strip is generally between the leeward meridian and the direction of the maximum resultant force. The data show that resultant forces as much as 35 percent greater than for

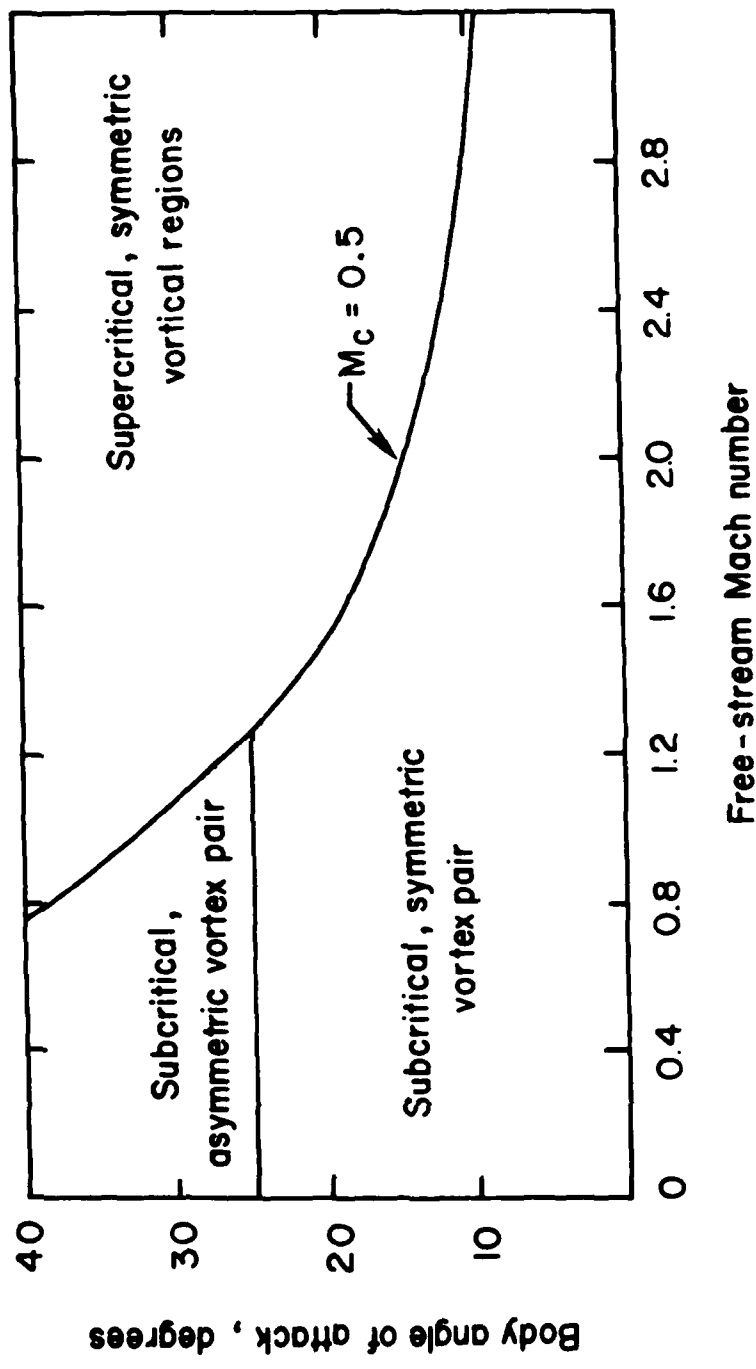


Figure 7.1 - Approximate Regions for Various Types of Body Vortices.

$M_\infty = 0.6$

$\alpha = 60^\circ$

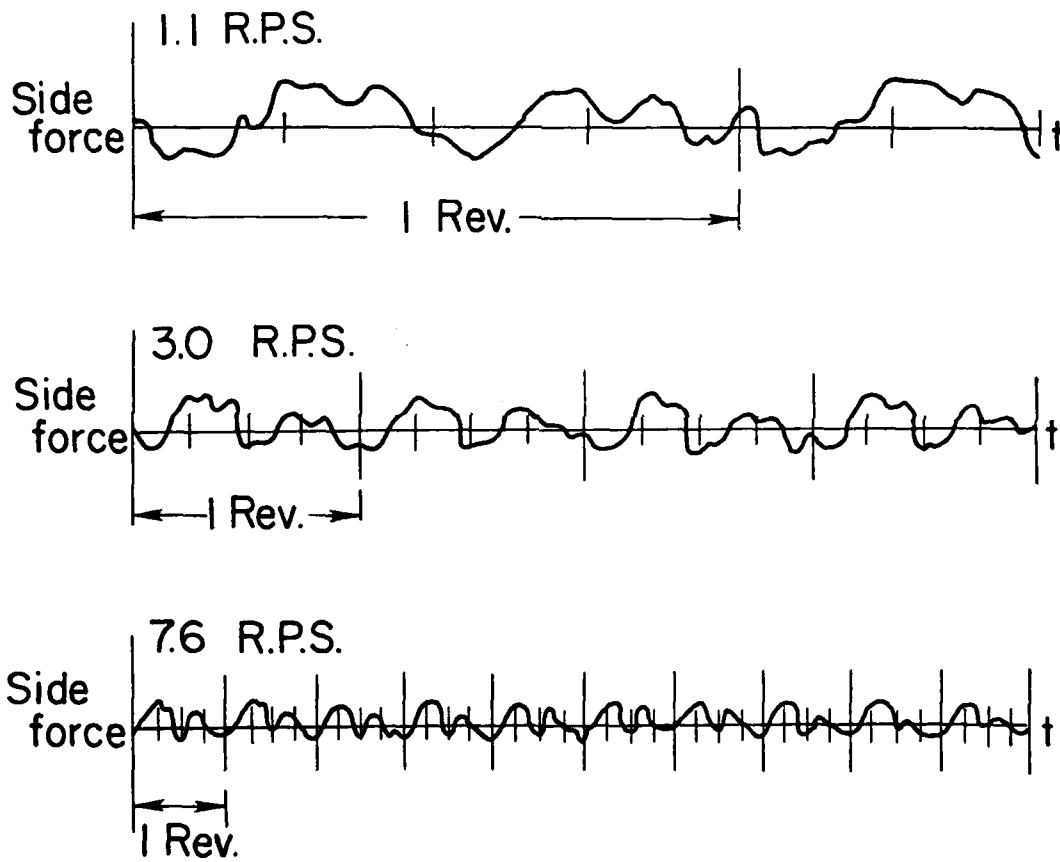


Figure 7.2 - Effect of Spin Rate on Side Forces of
10° Half Angle Cone.

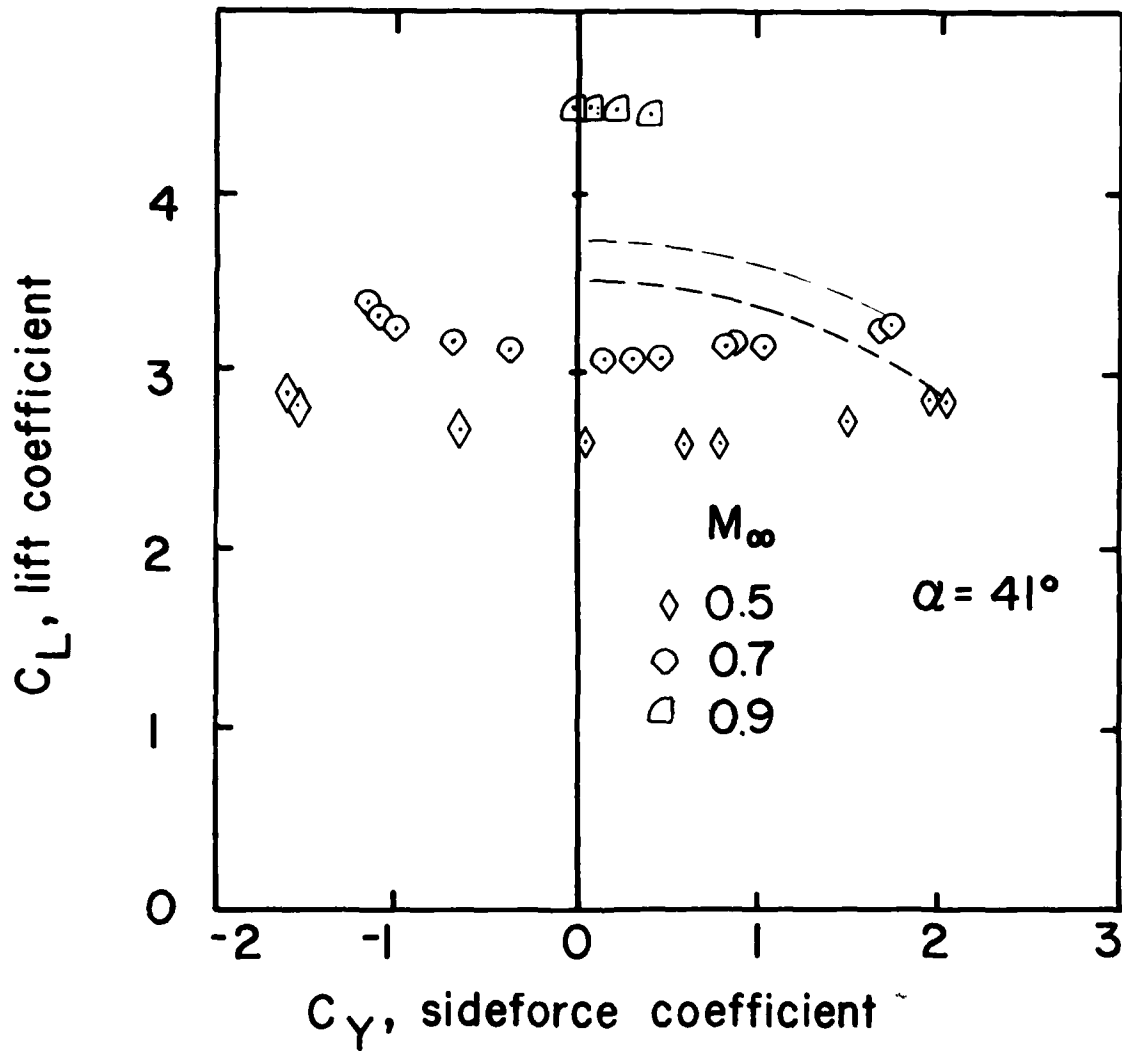


Figure 7.3 - Total Force Available for Maneuvering at Various Roll Positions of a Fineness Ratio 7.5 Ogive-Cylinder; Effect of Mach Number.

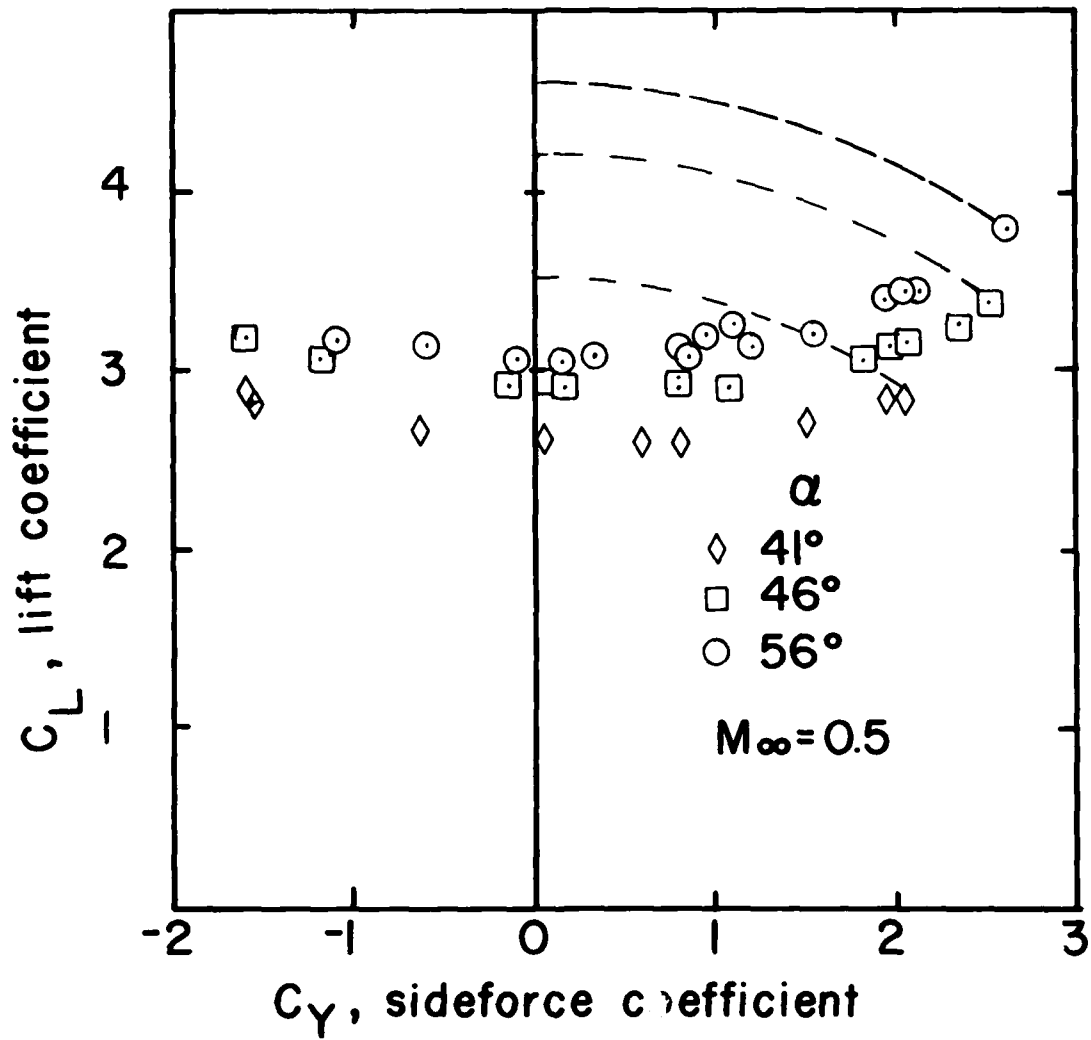


Figure 7.4 - Total Force Available for Maneuvering at Various Roll Positions of a Fineness Ratio 7.5 Ogive Cylinder; Effect of Angle of Attack.

symmetrical vortices can be obtained by harnessing phantom yaw. The gain decreases as the Mach number and angle of attack increase.

For a missile that must pull high accelerations in a transonic turn, it is possible to control phantom yaw by use of roll control and a nose strip and at the same time get greater maneuverability. The design of an actual system to achieve this is an interesting problem.

8. EXTERNAL STORES - LAUNCH DYNAMICS

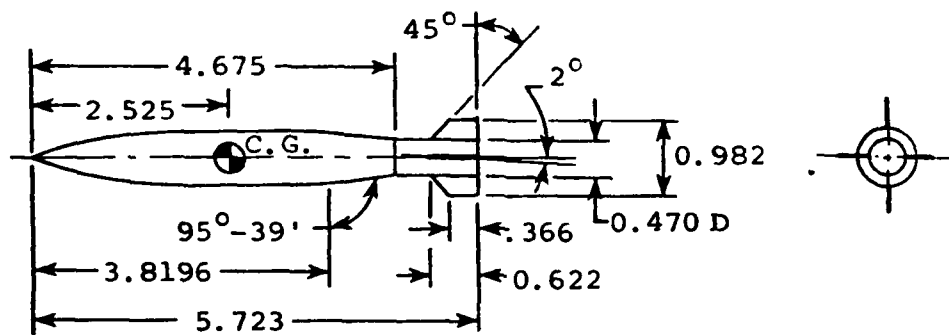
8.1 BACKGROUND

In recent years the addition to certain aircraft of many missiles externally mounted on racks and pylons has resulted in large drag penalties to aircraft optimized for minimum drag without external stores. In fact, missile installations have turned otherwise supersonic aircraft into subsonic ones so that the next generation of combat aircraft were designed with this danger in mind. Up to now the clean separation of external stores from aircraft and the performance penalties due to hanging external stores on aircraft have been investigated principally in expensive wind tunnel and flight tests. The large number of combinations and permutations of aircraft and stores requires extensive testing. For a number of years the power of large-scale computers has been brought to bear on these problems. It is probable that computer analysis of these problems can profitably be greatly expanded.

I am looking forward to what Professor Maddox has to say on the subject in his invited lecture, as well as the other speakers in the external store session. I would now like to make a few remarks about store separation at subsonic, transonic, and supersonic speeds and suggest problems of interest in each speed range.

8.2 SUBSONIC SPEEDS

Much analytical work has been done to develop codes for predicting store separation from fighter-bomber aircraft at subsonic speeds. A particular code developed by Fred Goodwin (Reference 8.1) under Air Force Flight Dynamics Laboratory sponsorship is well known. One of the comparatively recent developments has been the discovery that store loads for an attached store versus one just off the rack can differ markedly. This fact has emerged in wind-tunnel tests by Dix (Reference 8.2) and flight tests at Patuxent River by Maddox (Reference 8.3). These tests stimulated careful wind-tunnel tests (Reference 8.4) to investigate the causes of this phenomenon for stores mounted on a TER rack. Figure 8.1 shows the finned stores tested on the TER rack under a model of the F-4 airplane. Figure 8.2 shows the normal force on the lower finned store of the TER rack in the attached position and for positions beneath the rack. What is of interest is the rapid change in normal-force coefficient for a store displacement of less than a tenth of its diameter. The significance of the results are that special methods are required to predict attached loads. The methods which are adequate for predicting loads for store separation purposes may not be adequate for attached loads. More work is needed in this area.



ALL DIMENSIONS IN INCHES

Figure 8.1 - Store Model Used in TER Force and Moments Tests; S_{MF}

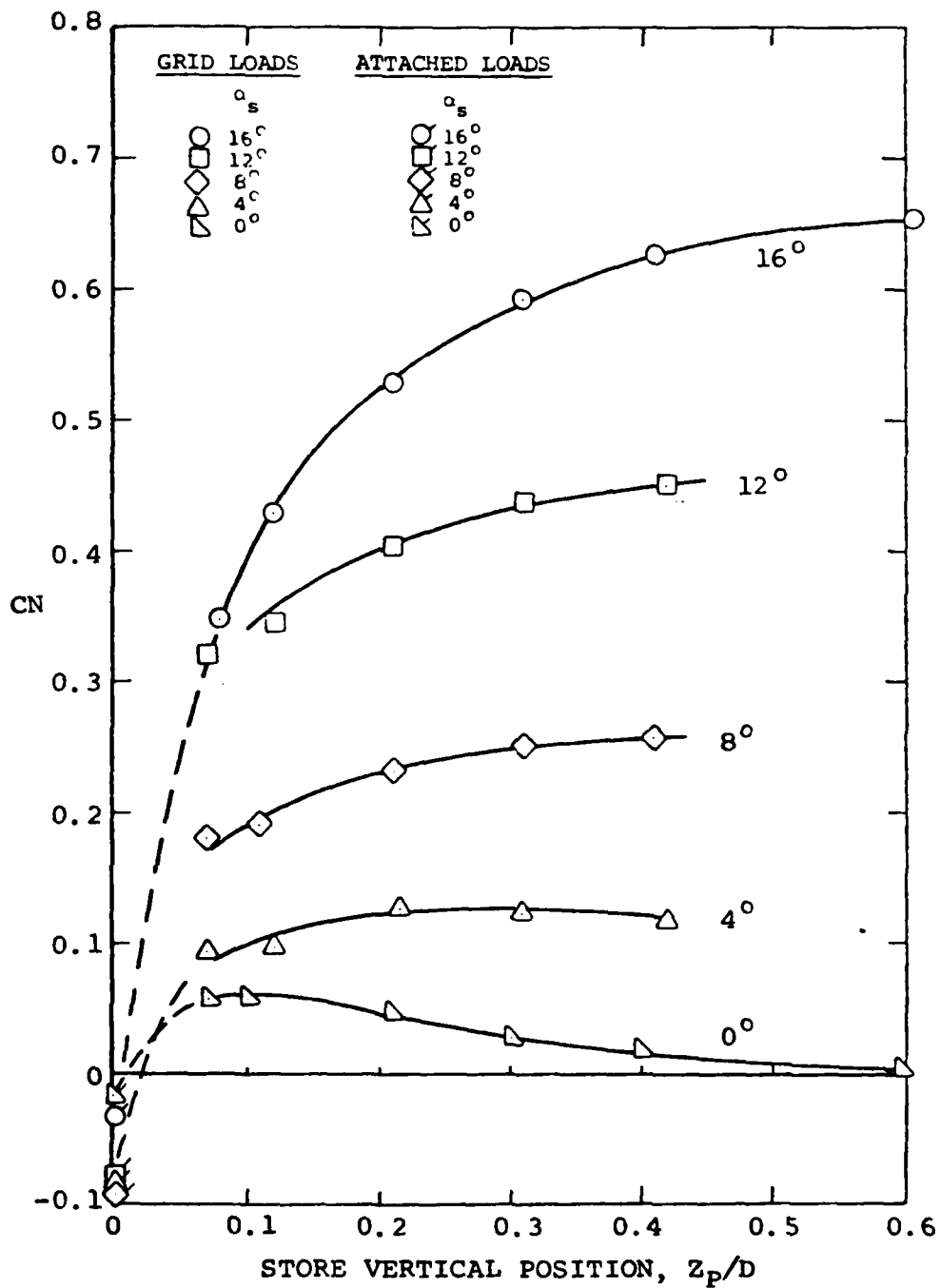


Figure 8.2 - Comparison of Attached and Grid Normal-Force Coefficients at $M = 0.6$ in Combination With Wing-Body Pylon and TER Rack; Bottom Store.

8.2 TRANSONIC SPEEDS

I would like to make a few general remarks about store separation at transonic speeds. A transonic method has been developed for determining flow fields at store locations (Reference 8.5). This method builds on the subsonic method mentioned in the previous section. Figure 8.3 shows a wing-body-pylon combination under which flow angles were measured in the 4-Foot Transonic Tunnel at Tullahoma. Figure 8.4 shows a comparison between theory and data for the flow angles just below the rack mounted under the wing for $\alpha = 5^\circ$ and $M = 0.95$. What is remarkable is that the linear theory, shown by the dashed line, fits the data so well at this condition. The effect of compressibility on the downwash angle is small as shown, but the effect on sidewash is larger than measured. At higher angles of attack, transonic effects may be more significant.

Figure 8.5 shows a pressure distribution store which was used to determine normal-force axial loading distributions. Loadings for this store directly below the pylon ($Z/D = 2$) are shown in Figure 8.6 taken from Reference 8.6 for $\alpha = 0$ and $\alpha = 5^\circ$. The ability of the linear theory to predict the flow field is better than for calculating loads. Better ways of calculating loads on stores embedded in transonic flow fields are needed.

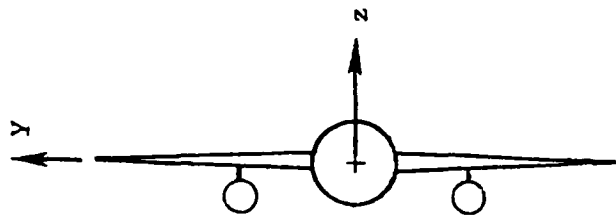
8.4 SUPERSONIC CASES

The delivery of missiles at supersonic speeds has received some attention, and a computer program to compute supersonic store trajectories (Reference 8.7) has been written. Supersonic store separation done with linear methods is not adequate for obtaining store forces and moments during separation. One reason is that the positions of shock waves differs from those for Mach waves as used in linear theory. The difference in position for a wave intersecting a store can introduce significant error with the linear theory calculations of forces and moment. Nonlinear corrections to linear theory are now used in Reference 8.7. Further work in the area of supersonic store separation is needed to understand all the problems involved.

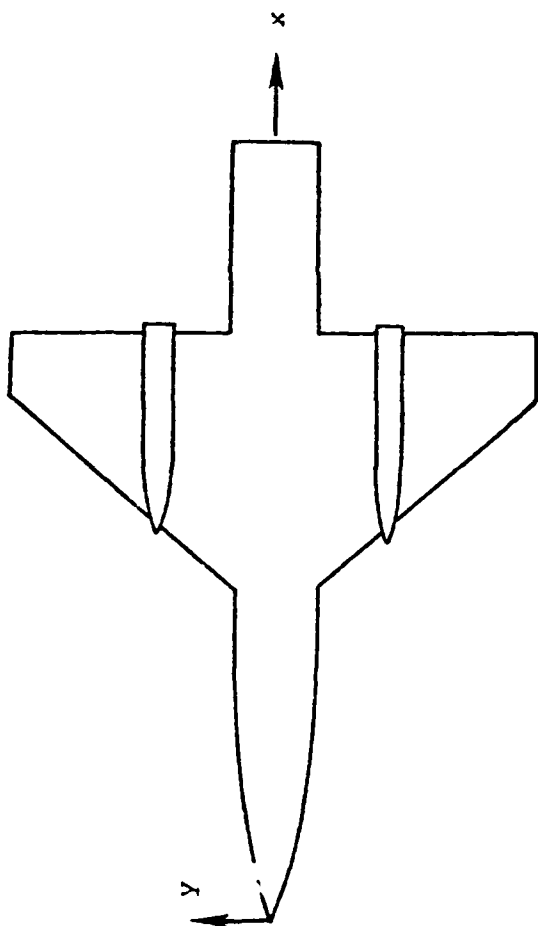
One supersonic problem of particular importance is that of the excessive drag of stores externally mounted on racks. Novel ideas like conformal carriage promise greatly to reduce supersonic store drag. Further progress in this general area is needed with the general theme of designing the stores and airframes as an integral unit.

8.5 CONCLUDING REMARKS

With regards to fruitful areas for further analytical studies and computer programs; we can broadly conclude that attached loads need further attention for all speeds. Higher angles of attack need attention for both subsonic and transonic speeds in accordance with current air combat tactics. For subsonic speeds nonlinear wing characteristics must be accounted for, and for transonic speeds the usual transonic nonlinearities must be taken into account. Supersonic store separation involves nonlinearities also despite the fact supersonic linear theory is well established.



(c) REAR VIEW



(a) BOTTOM VIEW



(b) SIDE VIEW

Figure 8.3 - Wing-Body/Pylon/Store Model Configuration for
AEDC 4T Tunnel Test Program.

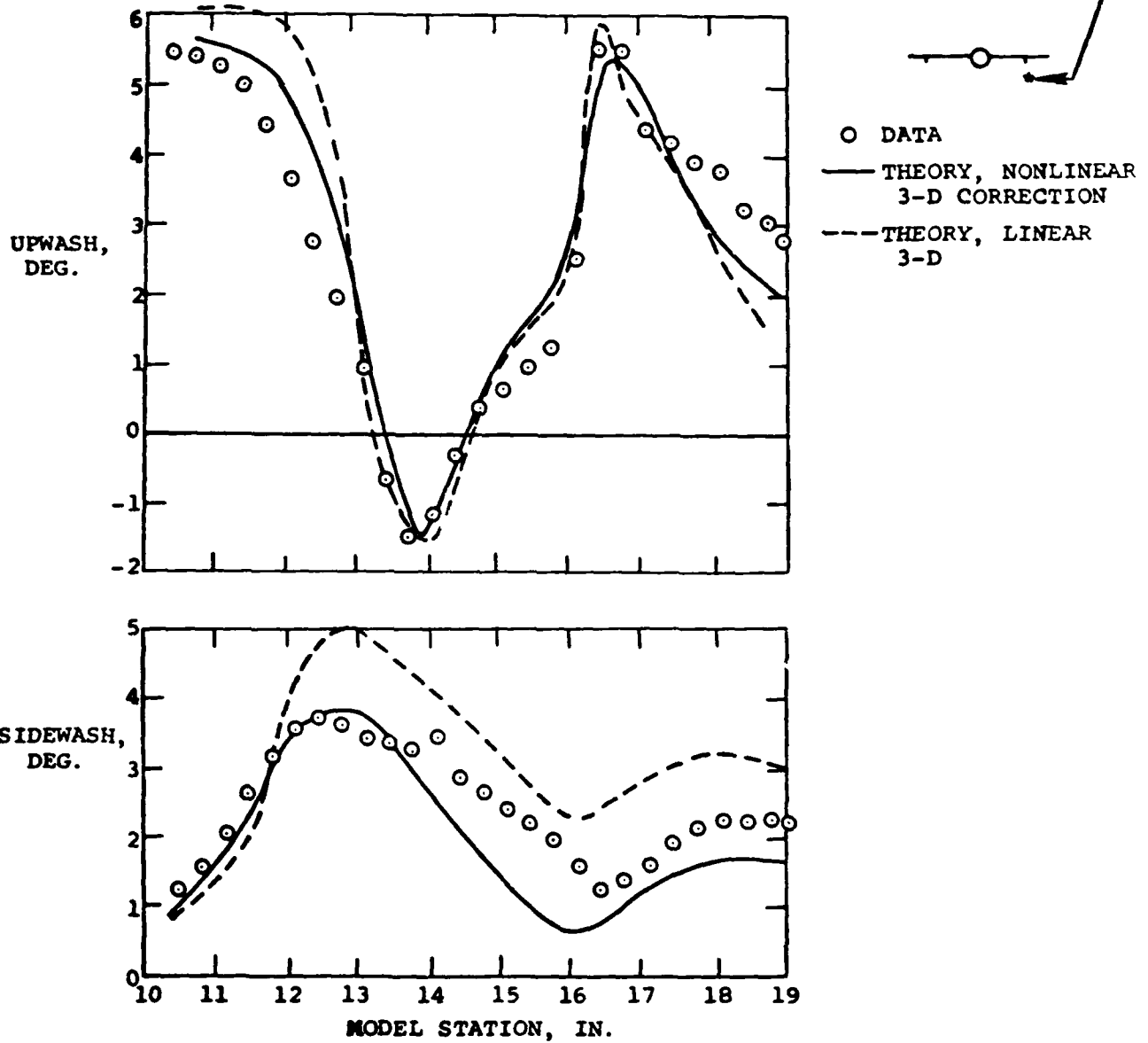
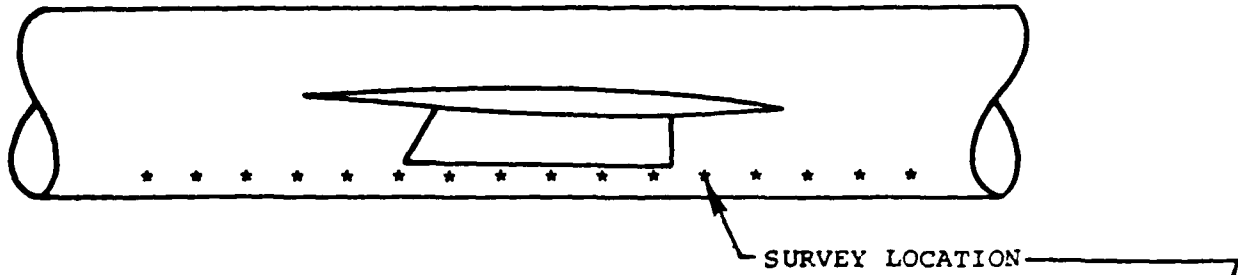


Figure 8.4 - Comparison of Theoretical and Experimental Results for Local Upwash and Sidewash Angles Directly Under the Wing Pylon for Flow Past a Scaled F-14 Wing/Body/Pylon Model at $M_\infty = 0.95$ and $\alpha = 5^\circ$.

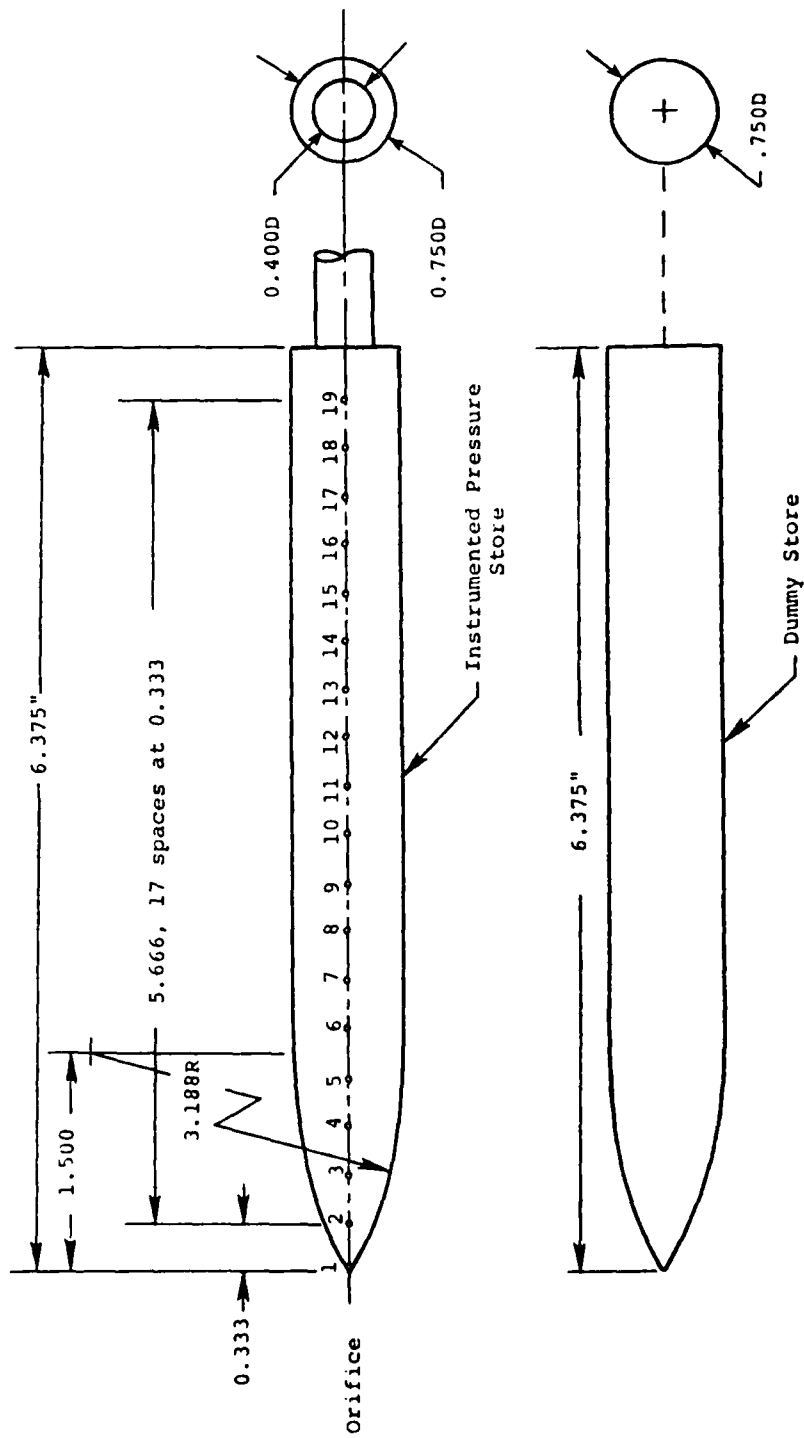


Figure 8.5 - Instrumented and Dummy Store Geometric Details.

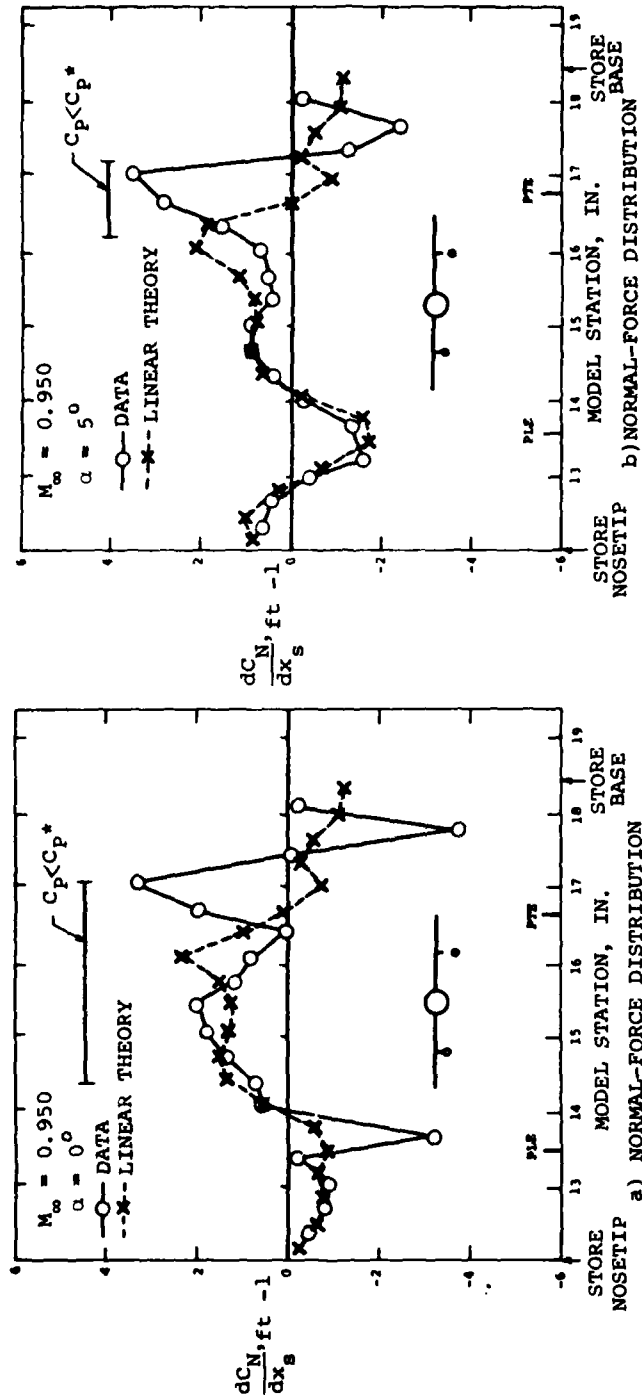


Figure 8.6 - Comparison of Store Theoretical and Experimental Normal-Force Loadings Based on Paneling Method Flow Fields for Store Separated From Wing Pylon at $M_\infty = 0.950$ and $\alpha = 0^\circ, 5^\circ$.

One recommendation I have made for a number of years and I would like to repeat it. Since large numbers of aircraft and stores are used in different combinations, it would be useful to compile a data bank of aerodynamic models of those components to use with the subsonic store trajectory program. Such a data bank would eliminate duplication and make it possible to run trajectories with much less effort since the principal effort is usually devoted to modeling airplanes and stores.

9. EXPLOITATION OF LARGE-SCALE COMPUTERS

9.1 INTRODUCTORY REMARKS

The application of large-scale computers to missiles has lagged its application to airplanes for reasons which are not clear to me but which may have to do with aerodynamic efficiency. However, there is increasing emphasis in this area for missiles, an emphasis which will probably increase with the growing interest in airbreathing propulsion. While large-scale computers are not likely to be the principal tool of preliminary design for some time, they provide several important services at the present time. They provide benchmark cases for evaluating the accuracy of more approximate methods. They can also be used to develop data bases for use in approximate methods. They are also useful in verifying final designs. With further improvements in computer capability and reduction in cost, their application will greatly increase.

9.2 LEVELS OF SOPHISTICATION IN COMPUTER PROGRAMS

At least four levels of sophistication can be differentiated in computer programs of interest in missile aerodynamics.

- (a) Engineering prediction codes
- (b) Potential flow codes, linear and nonlinear
- (c) Euler codes
- (d) Navier-Stokes codes

After some preliminary remarks about the first two methods, we consider the last two in greater detail.

Engineering prediction methods as referred to here are approximated methods which are based on engineering assumptions and/or data bases. These programs generally do not need large-scale computers, although extensive data bases can be put into core if they are available.

Potential flow codes of the linear type are typified by panel programs for complete configurations (such as Reference 9.1) and for nonlinear potential flow by the Bailey-Ballhaus program, Reference 9.2. For nonlinear programs the present computer capability is taxed for complete configurations and, bigger machines will probably be needed for multi-finned missiles. Their limitations to low angles of attack can be partially overcome by incorporating vortex models into them as in DEMON2 (Reference 9.3). Potential methods break down when strong shock waves are present. Although research is underway to partially alleviate this problem, Euler and Navier-Stokes codes are really required.

9.3 NAVIER-STOKES CODES

It is generally acknowledged that present computer capacity is too limited to solve the flow about complex three-dimensional configurations with Navier-Stokes codes. In the particular cases where a calculation has been made for a body, the computer costs have been prohibitive for preliminary design use. However, if progress in computer development in the future keeps pace with that of the past, it is only a matter of time before the problems of computer capacity and cost will be overcome. I presume the invited lecture of Dr. Ballhaus on the future plans of Ames Research Center, NASA, will contain some interesting material on this subject.

Another limitation in the use of Navier-Stokes codes at the present time is the lack of understanding of turbulence modeling. It turns out that many problems in missile aerodynamics are dependent only on turbulent convection, not turbulent diffusion, so that there is some relief from this limitation. However, when larger machines are available it will be possible to create turbulent models of the required accuracy through an approach called large-scale eddy simulation (Reference 9.4). In large-scale eddy simulation, the unsteady Navier-Stokes equations (filtered) are solved to follow the motion of the eddies down to the smallest scale that can be handled within the capacity of the machine. Smaller eddies are modeled by some universal law. The hope is that large eddies, whose statistics depend on the geometry in question, can all be treated within the capacity of the computer, and the effects of small eddies which follow universal laws can be modeled. For low Reynolds numbers and periodic boundary conditions, predictions by this technique have shown good agreement with experiment. The use of larger computers will permit solutions for higher Reynolds number.

For use with the time-averaged Navier-Stokes equations, eddy viscosity models are usually used. It turns out that there are many classes of flow with different eddy viscosity models. In my Wright Brothers paper I have suggested that NASA create a national data bank of eddy viscosity models.

9.4 EULER CODES

The Euler equations can be used where vorticity convection is important but vorticity diffusion is not. Many missile aerodynamic problems fall within this realm. In these cases the Euler equations will require less computer time than the Navier-Stokes solutions, not only because the viscous terms are not present, but because a fine mesh to resolve the boundary layer is not required.

The problems of the appropriate boundary conditions to use with the Euler equations is still very much an open question. It is through the boundary conditions that the vorticity is shed from the solid boundaries into the flow field. By using a Kutta condition at a subsonic edge it has been possible (Reference 9.5) to discharge vorticity into the flow. Figure 9.1 illustrates the calculated flow field. Also by inputting a separation line location and appropriate boundary condition, it has been possible to calculate flows with primary vortex separation on a body of revolution (Reference 9.6). Figure 9.2 compares vortex strengths calculated by this method with the data of Oberkampf. Much of missile aerodynamics can be predicted with a supersonic marching code for which the calculation times are matters of minutes. However, if the

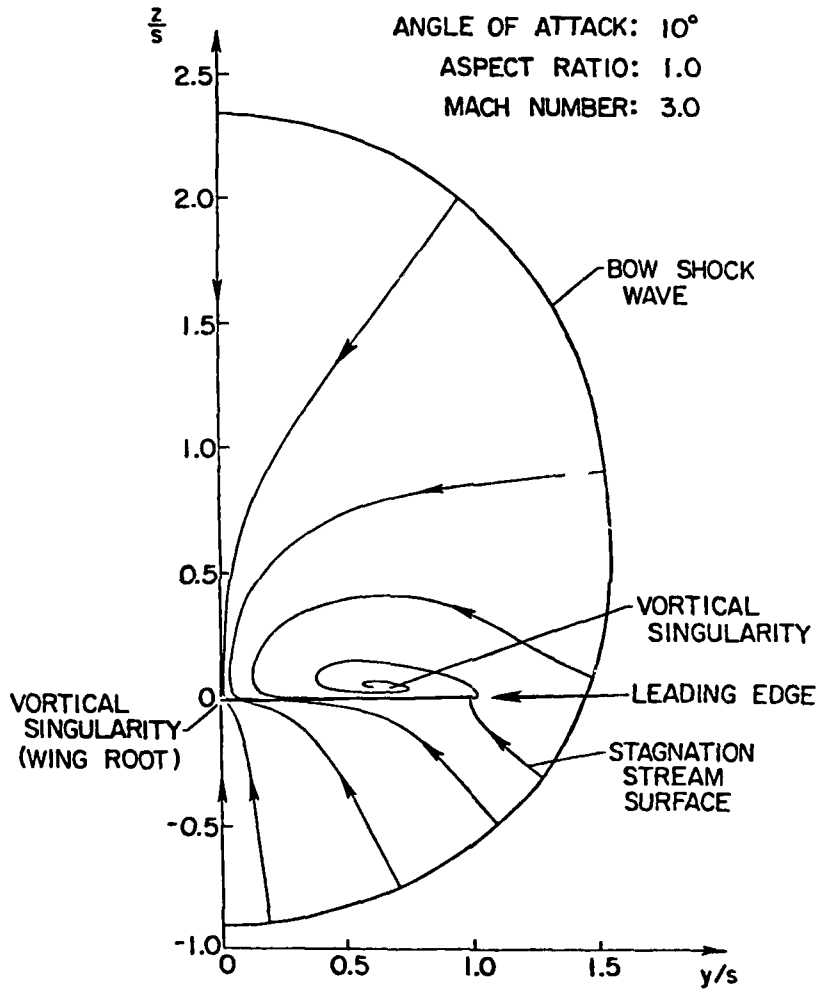


Figure 9.1 - Projection of Streamlines on Crossflow Plane as
 Determined from Euler Code with Kutta Condition at
 Leading Edge of Delta Wing.

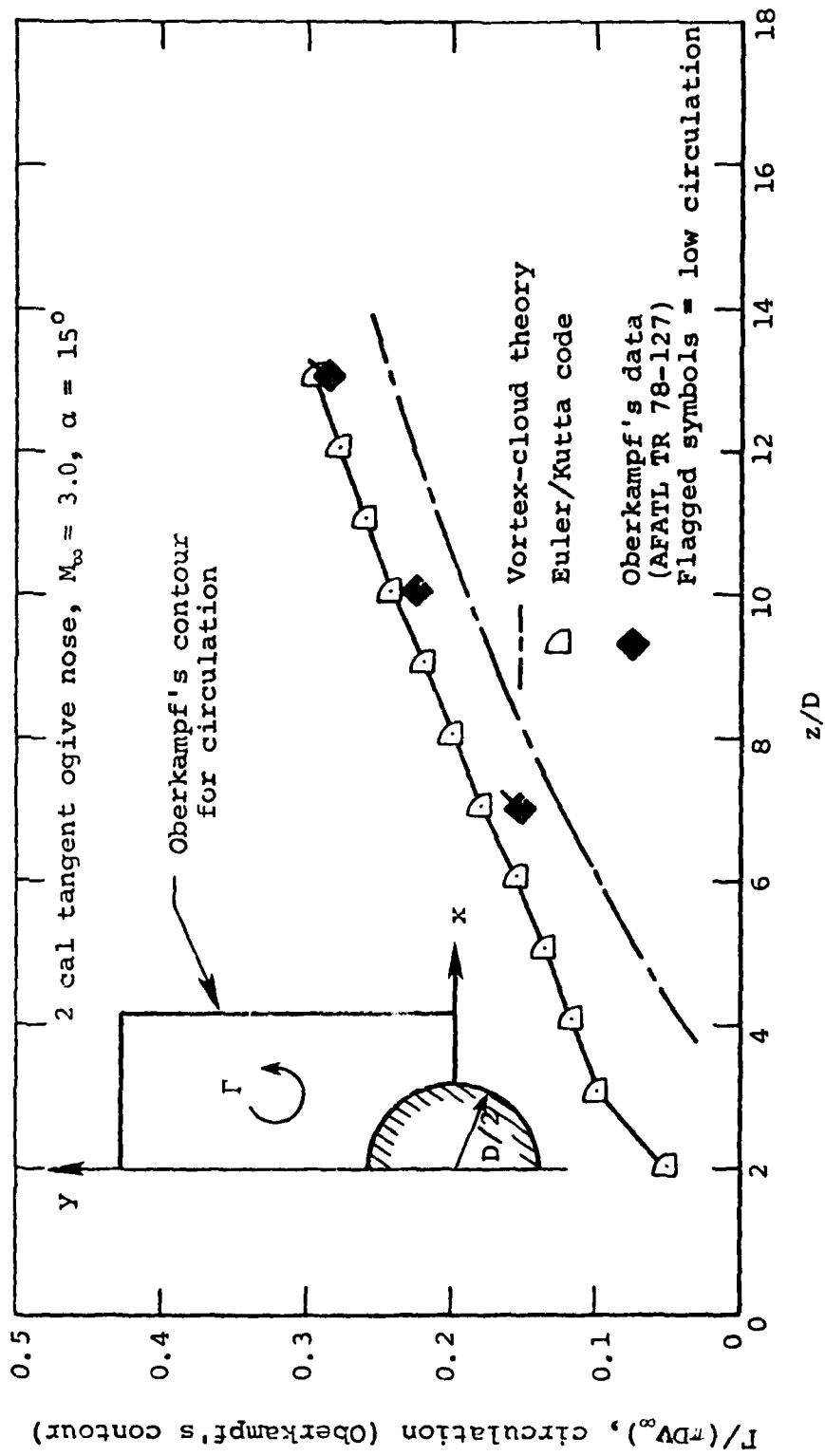


Figure 9.2 - Comparison of Circulation for Euler/Kutta Code, Vortex-Cloud Theory, and Experimental Data.

axial Mach number is subsonic, existing methods of solving Euler equations take much time. Mathematical techniques for overcoming this problem are of considerable interest.

Existing application of Euler equations to missile aerodynamics include bodies alone (Reference 9.6), wings alone (Reference 9.5), and wing-body combinations (References 9.5 and 9.7). In addition, the Euler equations have been applied to missile inlets (Reference 9.8).

I cannot conclude a discussion of large-scale computers without addressing the question of the future role of the wind tunnel versus the computer. Much controversy has surrounded the subject since the thought-provoking paper of Chapman, Mark, and Pirtle (Reference 9.9). In their paper they state: "When a sufficiently advanced computer becomes available, we believe it will displace the wind tunnel as the principal facility for providing aerodynamic flow simulation." There is no doubt in my mind that many measurements now made in the wind tunnel can be calculated just as well on large computers, and that more of the conventional wind-tunnel problems will be tractable on computers in the future. The rate at which this will happen can be argued. However, the above quote does not imply that the wind tunnel will be superseded by the computer. Indeed, it can be argued that the requirements for wind tunnels will be increased. The wind tunnel can reproduce fluid mechanical phenomena for which the physics is not understood and hence which cannot be put into a computer. Also wind tunnels and computers can be used to verify the results of one another. Wind tunnels and computers can reinforce each other in other synergistic ways in such applications as "smart" wind tunnels and conditional sampling. The requirements for both will thus continue and, in my view, will increase.

REFERENCES

- 1.1 Nielsen, Jack N.: Wright Brothers Lectureship in Aeronautics. Missile Aerodynamics - Past, Present, Future. Journal of Spacecraft, Vol. 17, No. 3, May-June 1980, pp. 165-176.
- 2.1 Rear Admiral Delmar S. Fahrney: Missiles. An unpublished manuscript on the history of guided missiles in the custody of the historian, Naval Air Systems Command, Washington, D.C.
- 2.2 Hughes, Thomas Parke: Elmer Sperry, Inventor and Engineer. The John Hopkins Press, 1971.
- 2.3 Charles L. Keller: The First Guided Missile Program: The Aerial Torpedo. Sperry Engineering Review, March 1961.
- 2.4 Rear Admiral Delmar S. Fahrney and Robert Strobell: America's First Pilotless Aircraft. Aero Digest LXIX, 1954.
- 2.5 Lee Pearson: Developing the Flying Bomb. Naval Aviation News, May 1968.
- 2.6 Lawrence Sperry: Patent No. 1,418,605, Aerial Torpedo. Issued July 6, 1922, Filed December 22, 1916 (138,485).

REFERENCES (Continued)

- 4.1 Smith, C. A. and Nielsen, J. N.: Nonlinear Characteristics of All-Movable Controls. Paper in AGARD Conference Proceedings No. CP262, Aerodynamic Characteristics of Controls.
- 4.2 Baker, W. O., Jr.: An Aerodynamic Coefficient Prediction Technique for Slender Bodies with Low-Aspect-Ratio Fins at Transonic Mach Numbers and Angles of Attack to 180°. Ph.D. Dissertation, University of Tennessee, August 1976.
- 4.3 Aiello, G. and Bateman, M. C.: Aerodynamic Stability Technology for Maneuverable Missiles. Vol. I - Configuration Aerodynamic Characteristics. AFFDL-TR-76-55, March 1979.
- 4.4 Nielsen, J. N., Hensch, M. J., and Smith, C. A.: A Preliminary Method for Calculating the Aerodynamic Characteristics of Cruciform Missiles to High Angles of Attack Including Effects of Roll Angle and Control Deflections. Report ONR-CR215-226-4F, November 1, 1977.
- 4.5 Jorgensen, L. H.: Prediction of Static Aerodynamic Characteristics of Slender Bodies Alone and with Lifting Surfaces to Very High Angles of Attack. NASA TR R-474, September 1977.
- 4.6 Dietz, W. E., Jr. and Altstatt, M. C.: Experimental Investigation of Support Interferences on an Ogive Cylinder at High Incidence. AIAA Paper No. 78-165, presented at AIAA 16th Aerospace Sciences Meeting, Huntsville, Alabama, January 16-18, 1978.
- 6.1 Nielsen, J. N.: Nonlinearities in Missile Aerodynamics. AIAA Paper No. 78-20, presented at the AIAA 16th Aerospace Sciences Meeting, Huntsville, Alabama, January 16-18, 1978.
- 7.1 Cooper, M., Gapcynski, J. P., and Hasel, L. E.: A Pressure-Distribution Investigation of a Fineness-Ratio - 12.2 Parabolic Body of Revolution (NACA RM-10) at $M = 1.59$ and Angles of Attack to 36°. NACA RM L52G14a, October 1952.
- 7.2 Chapman, G. T., Keener, E. R., and Malcolm, G. N.: Asymmetric Aerodynamic Forces on Aircraft Forebodies at High Angles of Attack - Some Design Guides. AGARD CP-199, Meeting on Stall-Spin Problems of Military Aircraft, November 1976.
- 7.3 Fidler, J. E.: Active Control of Asymmetric Vortex Effects. AIAA Paper No. 80-182, AIAA 18th Aerospace Sciences Meeting, Pasadena, California, January 14-16, 1980.
- 7.4 Canning, T. N. and Nielsen, J. N.: Experimental Study of the Influence of Supports on Aerodynamic Loads on an Ogive Cylinder at High Angles of Attack. AIAA Paper No. 81-0007, AIAA 19th Aerospace Sciences Meeting, St. Louis, MO, January 12-15, 1981.

REFERENCES (Continued)

- 8.1 Dillenius, M. F. E., Goodwin, F. K., and Nielsen, J. N.: Extension of the Method for Predicting Six-Degree-of-Freedom Store Separation Trajectories at Speeds up to the Critical Speed to Include a Fuselage with Noncircular Cross Section. Vol. I - Theoretical Methods and Comparisons with Experiment. Vol. II - Users Manual for the Computer Program. AFFDL-TR-74-130, Vols. I and II, Nov. 1974.
- 8.2 Dix, R. E.: Comparison of Two Methods Used to Measure Aerodynamic Loads Acting on Captive Store Models in Wind-Tunnel Tests. AEDC-TR-76-122, September 1976.
- 8.3 Maddox, A. R., Dix, R. E., and Mattasits, G. R.: In-Flight Measurements of Captive Loads on a Store as Compared with Wind Tunnel and Mathematical Simulations. NWC TP 6026, April 1978.
- 8.4 Goodwin, F. K. and Nielsen, J. N.: Experimental and Theoretical Study of Flow Fields and Store Forces in Close Proximity to a Triple Ejection Rack at Transonic Speeds. NWC TP 6210, June 1980.
- 8.5 Crisalli, A. J., Stahara, S. S., Nielsen, J. N., and Spreiter, J. R.: The Development of Rapid Predictive Methods for Three-Dimensional Transonic Flow Fields About Fighter Bomber Aircraft. Part I, AFOSR-TR-1281, July 1979.
- 8.6 Crisalli, A. J., Stahara, S. S., and Hensch, M. J.: The Rapid Prediction of Aircraft Store Loading Distributions at Transonic Speeds. Part II. AFOSR-TR-79-1282, October 1979.
- 8.7 Goodwin, F. K., Dillenius, M. F. E., and Mullen, J., Jr.: Prediction of Supersonic Store Separation Characteristics Including Fuselage and Stores of Noncircular Cross Section. Vol. I - Theoretical Methods and Comparisons with Experiment. Vol. II - Users Manual for the Computer Program. Vol. III - Appendices A and B, Details of Program I. Vol. IV - Appendices C and D, Details of Program II. AFWAL-TR-80-3032, Vols. I through IV, November 1980.
- 9.1 Ehlers, F. E., Epton, M. A., Johnson, F. T., Magnus, A. E., and Rubbert, P. E.: An Improved Higher Order Panel Method for Linearized Supersonic Flow. AIAA Paper No. 78-15, presented at AIAA 16th Aerospace Sciences Meeting, Huntsville, AL, January 16-18, 1978.
- 9.2 Bailey, F. R. and Ballhaus, W. F.: Comparisons of Computed and Experimental Pressures for Transonic Flows About Isolated Wings and Wing-Fuselage Configurations. Aerodynamic Analysis Requiring Advanced Computers. NASA SP-347, Part II, March 1975, pp. 1213-1231.
- 9.3 Dillenius, M. F. E. and Nielsen, J. N.: Computer Programs for Calculating Pressure Distributions Including Vortex Effects on Supersonic Monoplane or Cruciform Wing-Body-Tail Combinations with Round or Elliptical Bodies. NASA CR-3122, April 1979.

REFERENCES (Concluded)

- 9.4 Ferziger, J. H. and Leslie, D. C.: Large Eddy Simulation - A Predictive Approach to Turbulent Flow Computation. AIAA Paper No. 79-147. AIAA Computational Fluid Dynamics Conference, Williamsburg, VA, July 23-25, 1979, Collection of Technical Papers, pp. 234-246.
- 9.5 Klopfer, G. H. and Nielsen, J. N.: Basic Studies of Wing-Body Interference at High Angles of Attack and Supersonic Speed. ONR-CR215-263-1, October 1979.
- 9.6 Klopfer, G. H. and Nielsen, J. N.: Basic Studies of Body Vortices at High Angles of Attack and Supersonic Speeds. NEAR TR 226, October 1980.
- 9.7 Wardlaw, A. B., Jr., Solomon, J. M., and Baltakis, F. P.: Supersonic Inviscid Flow Field Computations of Missile Type Bodies. AIAA Paper No. 80-0271, presented at AIAA 18th Aerospace Sciences Meeting, Pasadena, CA, January 14-16, 1980.
- 9.8 Biringen, S. and McMillan, O. J.: An Implicit Method for the Calculation of Inlet Flow Fields. NEAR TR 232, December 1980 (To be published as a NASA CR).
- 9.9 Chapman, D. R., Mark, H., and Pirtle, M. W.: Computers vs. Wind Tunnels for Aerodynamic Flow Simulation. Astro. and Aero., Vol. 13, April 1975, pp. 22-30,35.

RECEIVED DISTRICT ATTORNEY



AERODYNAMICS OF TACTICAL WEAPONS

TO MACH NUMBER 8 AND ANGLE-OF-ATTACK OF 180° (U)

L. Devan
L. A. Mason
F. G. Moore

Naval Surface Weapons Center, Dahlgren, Virginia

ABSTRACT

The NSWC Aeroprediction Code has been extensively applied to the prediction of static and dynamic aerodynamics of missile configurations. Major extensions have recently been made to the code to extend its capability to $0 \leq M_\infty \leq 8$ and $0^\circ \leq \alpha \leq 180^\circ$ and also to improve the transonic inviscid body alone static aerodynamic predictions and the dynamic derivative predictions for all Mach numbers. The theoretical basis for the code extensions are outlined and previous methods are briefly reviewed. The code is evaluated through comparisons of computational examples with experiment for body alone, body-tail and body-tail-canard configurations. The speed and accuracy of the code are ideal for use in preliminary design. Examples of design applications to specific tactical weapon configurations are presented.

INTRODUCTION

A continuous need exists for estimating the aerodynamic characteristics of a wide variety of tactical missile and projectile configurations, especially in the preliminary or conceptual design phase. To meet this need, the Navy (in cooperation with the Army) undertook the development of a rapid, inexpensive, easy to use Aerodynamic Prediction Code in 1971. The code was developed so as to handle fairly general wing-body-tail configurations and hence have direct application to a high percentage of tactical weapon designs. Preliminary versions of the code were published in 1972, 1975, and 1977. The changing mission requirements for both current and future weapons has dictated, however, the need to revise and extend the capabilities of the 1977 version of the Aeroprediction Code, which was limited to $M_\infty \leq 3.0$ and small angles-of-attack ($\alpha \leq 15^\circ$), to higher Mach numbers and angles-of-attack.

The objective of the current effort, which is nearing completion, is to extend the 1977 version of the Aeroprediction Code to $M_\infty = 8$ and $\alpha = 180^\circ$. In addition, modification of some of the existing methods due to advances in the state-of-the-art and computer program optimization is desirable.

The general approach of the code development has been to combine existing and newly developed computational methods into a single computer program. The basic method is that of component superposition where the body-alone, lifting-surface-alone and interference contributions are added to obtain total configuration aerodynamics. The code development has occurred in four increments. The first three of these increments were previously reported, and led to the development of a code capable of determining the aerodynamic coefficients for axisymmetric, non air-breathing configurations with up to two sets of lifting surfaces for low angles-of-attack and Mach numbers to 3.0. The results of the fourth increment, required to meet the stated objective, is the subject of this paper. Program plans for this effort and some early results were presented at the 11th Naval Symposium on Ballistics. The theories used, outlined briefly here, are discussed in more detail elsewhere.^{5,6} The resulting code has computational times, required for the estimate of static and dynamic aerodynamic coefficients for a body-tail-canard configuration for one freestream condition, that are in CPU seconds on a CDC 6700 computer as opposed to minutes or hours often required for more detailed physical and numerical models. The accuracy obtained, however, is compatible with that required for preliminary or intermediate design estimates.

Numerous computations for a variety of configurations have been attempted on the Extended Aeroprediction Code and the results compared with available data. Representative comparisons with experiment used in evaluating the code and sample applications illustrating the use of the code to achieve improved performance will be discussed in a later section.

CONFIGURATIONAL GEOMETRY AND FREESTREAM CONDITIONS

The most complex configuration considered is illustrated in Figure 1. The body may be pointed, spherically blunted or truncated. The remainder of the body may consist of one or two piecewise continuous nose sections, a constant crosssection afterbody, and a boattail or flare. The wing or canard fins have a trapezoidal planform with a biconvex or modified double-wedge crosssection and sharp o. spherically blunted leading and trailing edges. Tip edges are assumed parallel to the freestream at zero angle-of-attack. Fin crosssections are piecewise similar with span. No camber, twist, dihedral, or airfoil distortion is considered. Lifting surface sets are planar or cruciform. Horizontal, all-movable control deflections in the plus position are considered. Canard/wing and tail fin sets are aligned.

For various Mach number and angle-of-attack regions there are geometric restrictions. These will be elaborated upon in later sections.

Freestream condition description consists of Mach number, Reynolds number per foot per Mach number, and angle-of-attack. Roll orientation is considered at higher angles-of-attack only. Inlet and exhaust plume effects are not considered.

SUMMARY OF ANALYSIS METHODS

The analysis methods will be discussed in general terms. For more detailed theoretical discussions and derivations of the individual methods, the reader is referred to reports currently published as well as those in publication (References 2-7, 9).

BODY-ALONE STATIC METHODS

The body-alone low angle-of-attack static prediction methods²⁻⁵ are summarized in Figure 2. The transonic nose pressure drag and body inviscid normal force methods were modified under contract to NEAR, Inc., with additional modifications accomplished in-house. The second-order shock-expansion extension work was accomplished under contract by Professor F. DeJarnette of North Carolina State University.

The transonic/subsonic nose wave drag prediction assumes that the nose, boattail, and base are aerodynamically isolated. This assumes the existence of a minimum length afterbody. The nose shape is assumed to be a spherically blunted tangent ogive or a spherically blunted cone. To obtain results for a more general nose shape, linear interpolations between the tangent ogive and the cone pressure drag predictions are made using the initial body slope at the sphere-nose junction and the nose-afterbody slope. Thus, for a zero shoulder slope, the tangent ogive value is computed and for equal values of initial and final slope values, the cone value is computed. The tangent ogive pressure drag prediction is based upon interpolation in a table of values of Mach number, M_∞ ; nose length, L_N ; and nose spherical radius, R_N . Ranges of values are $.8 < M_\infty < 1.2$, $.75 < L_N < 5.0$ calibers, and $0 < R_N < .5$ calibers. The majority of the pressure drag data was generated by solving the Euler equations by an unsteady implicit time asymptotic method. A portion of the data was generated by solution of the full potential equation by the method of South and Jameson. Below $M_\infty = .8$ the pressure drag is decayed quadratically to zero at $M_\infty = .5$. The cone pressure drag is obtained from a blend of integrated pressure data and Taylor-Maccoll solutions. The pressure drag is obtained as an interpolation in a table of values of M_∞ versus cone angle, δ (bluntness is neglected). Ranges of values are $.5 < M_\infty < 1.2$, $0 < \delta < 20^\circ$. Below $M_\infty = .5$ an asymptotic value is assumed. The boattail wave drag is based upon small disturbance solutions assuming a long afterbody for $1.05 < M_\infty < 1.2$. Below $M_\infty = 1.05$ the boattail drag is decayed linearly to zero at $M_\infty = .95$.

The transonic/subsonic normal force prediction is for $0 < M_\infty < 1.2$. The new transonic normal force prediction is based on a combination interpolation and least squares curve fit in Mach number and geometric parameters. The nose is a blunted tangent ogive. Other body parameters are afterbody length, boattail angle, and boattail length. Parameter limits are $0 < R_N < .5$ calibers, $1.5 < L_N < 5.0$ calibers, $0 < L_A$ (afterbody length) < 5.0 calibers, $0 < L_B$ (boattail length) < 2.0 calibers, and $0 \leq \theta_B \leq 10^\circ$ for the conical boattail angle. Values of $C_{N\alpha}$ and $C_{M\alpha}$ (about the nose) are obtained by solving the Euler equations at 1° by an unsteady implicit time asymptotic method at $M_\infty = .75, .90, .95$ and 1.2 . Currently prediction values at $M_\infty = .6$ are given by the earlier model and at $M_\infty = 1.2$ by a low supersonic Mach number potential model. Interpolation provides a solution for $.6 < M_\infty < 1.2$. Below $M_\infty = .6$, the earlier model was used. Currently the new algorithm is an input choice to the program since neither method is particularly satisfactory over the full range of conditions.

The small disturbance potential solutions for the low supersonic range are applicable from $1.2 < M_\infty < M_0$; M_0 , a program input, is chosen between 2 and 3.5 depending on nose shape and whether or not lifting surfaces are also present. A high supersonic prediction method is used for $M_\infty > M_0$. The method used is a modified version of the second-order shock-expansion method which predicts inviscid static coefficients with good accuracy for bodies with short afterbodies and a flare. The wave drag predicted is adequate for nose-afterbody

configurations but is poorer for bodies with a boattail. The normal force prediction is fair for nose-afterbody configurations, and again is poorer for bodies with negative slopes. The pitching moment prediction in general is poorer not only for the higher Mach numbers but is a weakness of all of the methods available over the entire Mach number range.

LIFTING SURFACE AND INTERFERENCE STATIC METHODS

Lifting surface and interference methods are summarized in Figure 3. The high supersonic methods were developed by Professor F. DeJarnette.

Above $M_{\infty} = M_c$, a shock-expansion strip estimate is used. First the angle between the local surface normal and the free stream velocity is found. A local oblique shock value is used for compression angles and a local Prandtl-Meyer value is used for expansion angles. The pressure distribution is independent of span since similarity of crosssection is assumed. For a blunt leading edge a modified Newtonian distribution is assumed. As Mach number and aspect ratio increase the wing-alone prediction improves. However, interference effects are neglected.

The methods used at lower Mach numbers were previously documented.³ For the symmetric low supersonic drag problem no swept forward trailing edge is permitted. This is a numerical method restriction rather than a physical restriction. For the low supersonic lift problem no subsonic trailing edge is allowed. In addition, the zone of influence must not include the opposite tip edge of a two fin planform. For the drag problem, the trailing edge sweep angle is cut off at 0° . For the lifting problem the Mach number is kept just above or at the critical Mach number.

METHODS FOR COMPUTING DYNAMIC DERIVATIVES

Methods for computing dynamic derivatives are summarized in Figure 4.

For the fourth increment in the code development process, improvements and extensions were made in the pitch and roll damping prediction method.

Dr. L. Ericsson of Lockheed Missiles and Space Company, under contract to NSWC, was responsible for developing a method to improve the prediction of pitch damping for small angles of attack. In the low supersonic region the method is restricted by the slender wing-body analysis. It is assumed that the slender-wing body analysis is usable to $M_{\infty} = 2$. At this condition the aspect ratio of the tail is restricted to less than 2.3. The current theory is restricted to body-tail configurations. For the body-alone prediction, when the LMSC model deviates too greatly from the older, empirical G.E. SPINNER code prediction, the SPINNER prediction is selected. Currently the use of the LMSC algorithm is a code input option. For body-canard-tail configurations only the body-alone prediction is utilized.

For the earlier methods used in the code the same restrictions on Mach number, which prevent trailing edge subsonic conditions or the opposite side edge lying in the zone of influence, which were made for the lifting surface-alone normal force problem, again apply. For the lifting surface-body problem

the planform considered is that obtained by extending the leading and trailing edges to the body centerline.

Improvements were also made in the method of computing the transonic empirical roll and pitch damping for configurations with lifting surfaces. At high Mach numbers above $M_\infty = M_L$, a strip method, based on the static normal force strip loading, is used to predict roll and pitch damping for configurations with lifting surfaces. Thus, two methods are available for predicting pitch damping for the entire Mach number regime.

HIGH ANGLE-OF-ATTACK STATIC AERODYNAMICS

The method used in the code is a direct adaption of the empirical methodology of Reference 7. Restrictions of this code are:

- (1) Mach number: .8 to 3.0.
- (2) Angle-of-attack: 0° to 180° for isolated components (plus position) and 0° to 45° for body-tail combinations and roll angles 0° to 180° .
- (3) Tail: Trapezoidal plan form, edge parallel to body centerline
 - (a) Leading edge sweep angle: 0 to 70 degrees
 - (b) Taper ratio: 0 to 1.
 - (c) Aspect ratio (two fins): .5 to 2.0.
 - (d) No control deflection
 - (e) Tail trailing edge: sweep zero and parallel to body base.
- (4) Nose length (pointed tangent ogive): 1.5 to 3.5 calibers.
- (5) Cylindrical afterbody 6 to 18 calibers long.
- (6) Total span to diameter ratio (two fins): 1 to $3 \frac{1}{3}$.

Body alone and body-tail normal force and X_{cp} are predicted as a function of Mach number, roll angle, and angle of attack. In addition, the roll moment is also predicted.

ANALYSIS EVALUATION AND SAMPLE COMPUTATIONS FOR NEW CODE ELEMENTS

This section will present examples illustrating both the strengths and the weaknesses of the new methods adapted and integrated into the NSWC code. The reader should remember that all of the new methods met our accuracy requirements in general over the range of applicability although in some individual cases shown, the accuracy was poorer.

An illustration of the capability of the new High Mach number routine is given in Figures 5-7. Here the body alone static aerodynamic predictions of

the current routine are compared to integrated pressure data and the small disturbance potential codes^{1,8} for a blunted, tangent ogive nose, 6.0 caliber afterbody configuration. Above $M_\infty = 1.5$, the comparison of the High Mach prediction with data is quite good for the forebody drag, C_{AF} (wave drag plus friction drag) while the normal force, $C_{N\alpha}$, and center-of-pressure, X_{cp} , predictions are shown to degrade somewhat. In general, the predictions improve with increasing nose length and Mach number (although this was not shown for this case due to a lack of data). In Figure 8, comparisons are shown for a NASA flared body. Small modifications were necessary to the body geometry to make it compatible with the input requirements of the computer code. As a result, the agreement in general is only fair except for $C_{N\alpha}$ at the higher Mach numbers where the agreement is good. In general, the $C_{N\alpha}$ prediction will be poorer for bodies with negative slopes (i.e. boattails). It is also shown that X_{cp} is rather poorly predicted by all three computational methods.

In Figures 9 and 10 are shown comparisons of the shock-expansion strip theory for wings with the low Mach number small disturbance estimates. For larger aspect ratios and higher Mach numbers (smaller zones of influence) the comparison is improved. No interference is considered for $M_\infty > M_l$. However, the $C_{N\alpha}$ prediction is generally on the high side which partially compensates for this omission. In these examples Λ_l is the leading edge sweep, A_w is the aspect ratio and λ_w is the taper ratio. The wing crosssection is that of a symmetric diamond.

Figures 11 and 12 illustrate applications of the code to body-canard-tail and body-wing configurations. Data for the TMX-1751 configuration include the contributions of body strakes (not shown in the sketch). These strakes were not included in the model, due to limits on the number of lifting surfaces and the small aspect ratio, which partially accounts for the $C_{N\alpha}$ and X_{cp} differences. The comparison is good for the TMX-187 configuration with the flared afterbody.

Figures 13-16 illustrate the capabilities of the adapted Martin High angle-of-attack empirical algorithm. The slope and magnitude of the C_N predictions compare quite well. However, the X_{cp} and C_l predictions are of the right order of magnitude only, except at fairly high angles-of-attack where the predictions improve markedly for the lower Mach numbers.

As previously indicated, the modified LMSC dynamic derivatives model occasionally experiences a total breakaway from the data for body alone configurations. This problem is illustrated in Figure 17 for the Army-Navy Spinner configuration. As a result, the current combined code compares the LMSC model predictions with the G.E. SPINNER code prediction. If the deviation is large, as in this case, the SPINNER prediction is selected. In Figure 18, the relative capabilities of the older pitch damping prediction method, the LMSC model and the strip theory are shown for the Basic Finner configuration. The strip theory is seen to be quite adequate at the higher Mach numbers for predicting both the pitch damping and the roll damping coefficient, C_{lp} (see Figure 19). The overall agreement of the new method for all Mach numbers is considered to be good.

The relative improvement in the transonic predictions is illustrated in Figures 20-23. In Figure 20, the computed transonic nose wave drag for the M-117 Bomb is compared with data. For this case, the NEAR algorithm is shown to improve the estimate somewhat. The experimental pressure data, however, was

somewhat sparse for an accurate numerical integration. The improvement is much more obvious in Figure 21 which shows a comparison of the NEAR algorithm prediction and older theory with data for blunted tangent ogive-cylinders with 6.0 caliber afterbodies. However, there is no apparent improvement in the prediction for $C_{N\alpha}$ and X_{CP} in the transonic flow regime as shown in Figures 22 and 23. Neither method seems to be particularly outstanding. (A more thorough evaluation is present in Reference 5.)

SPECIAL CODE FEATURES

The Aeroprediction Code which applies the methodology previously indicated in Figures 2-4 and the High Angle-of-Attack algorithm, has been updated to include the new methodology presented. (Details of the earlier version of the code are available in Reference 9). In addition to the new computational methods, other elements of the code have been corrected and improved. For example, the data input and output have been extensively changed to simplify and clarify those aspects of the program and to optimize the code for the user. For example, the wing or tail input data consists of the minimum required for the computations and yet allows considerable detail to be given. The body-along geometry is described by the number of points on the body surface for each piecewise continuous segment, a single logic variable, and body surface coordinates. The description is basically independent of Mach number with only minor exceptions. The program has been segmented in order to minimize the storage required for loading. Currently, the code requires 160K octal central memory or less. For more universal use, all FORTRAN statements will be standard ANSI format or machine independent. For missile design, the output has been expanded to include the pitching moment coefficient components about the given moment center and the normal force/pitching moment dependencies on angle-of-attack and control deflections. Thus, for the entire configuration, the normal force coefficient for a given Mach number can be described as

$$C_N = \alpha (C_{N\alpha} + C_{N\alpha\alpha} \alpha) + C_{N\delta_t} \delta_t + C_{N\delta_c} \delta_c$$

where δ_c and δ_t are the canard and tail control deflections, respectively, and $C_{N\alpha\alpha}$ is the body viscous crossflow term. The expression is similar for the moment coefficient. Utilizing these outputs one can obtain the hinge moments and other coefficients needed for a linear aerodynamic performance analysis of a missile configuration.

APPLICATIONS TO DESIGN

The Aerodynamic Prediction Code has been extensively applied to the design of both conventional and unconventional tactical weapons. To conserve space, only a few specific examples are shown here which hopefully will provide some indication of the code's flexibility. Many more examples will be given in the design manual to be published later this year (Reference 6).

PROJECTILE PERFORMANCE OPTIMIZATION

The objective of this study was to optimize the performance of a full-bore, axisymmetric projectile to obtain the minimum time-of-flight and highest terminal velocity at a given range with no degradation in accuracy. This was to be accomplished by optimizing the shape to minimize the total drag, through determination of the best weight to obtain the optimum ballistic coefficient and by judicious selection of the center-of-gravity location. An optimization scheme developed by Hagar, et al.¹⁰ (which has since been upgraded by Moga¹¹) indicated that for a five caliber body, the minimum drag profile would be similar to that shown in the top corner of Figure 24. Methods to quickly predict the aerodynamics of this profile are more limited than one might at first suppose, particularly with respect to the two-third power law nose contour and the 1.8 caliber boattail. For instance, the range of applicability of the DATCOM is for boattail lengths greater than 2.0 calibers and tangent or conical nose shapes. The G.E. SPINNER code includes data for some secant ogive nose shapes which can closely approximate the two-third power law nose but is limited to boattail lengths of less than 1.0 calibers. The small afterbody length (approximately .05 calibers) also restricted the use of additional methods and data. The Aeroprediction Code was utilized to obtain the static aerodynamic coefficients for this configuration so initial estimates of its stability could be made. Using these initial estimates, the design was fabricated and successfully flown in the 30 MM caliber size. Comparisons of the theory with the ballistic range data later obtained for the design are given in Figure 24. Good agreement was obtained in each case. As a result, the predicted values could then be used to conduct a stability analysis throughout the trajectory with greater confidence. Use of the Aeroprediction Code therefore allowed the designer to eliminate expensive wind tunnel tests and the bulk of ballistic range tests, even though extensive changes in the design were made, and demonstrate the benefits of the proposed design. The improvements in this case were substantial as shown in Table I below.

Table 1. Benefits of the 30 MM Optimal Projectile*

	<u>30 MM</u> <u>Standard</u>	<u>30 MM</u> <u>Optimal</u>	<u>Improvement</u>
Range (KM)	3.0	3.0	---
Average C_D	.36	.22	39%
Time-of-Flight (sec)	5.70	3.86	32%
Terminal Velocity (FPS)	967	1559	61%
Accuracy (rad. std. dev., mts)	.6	.65	---

* Computer generated trajectory based on experimental drag data.

STRUCTURAL ANALYSIS

An example of application toward structural design was presented at the

11th Navy Symposium on aeroballistics.¹ As indicated in the previous paper, the Aeroprediction Code was modified to compute the total sectional normal force coefficients along the body as a function of Mach number and angle-of-attack. The results were then used in the structural analysis. The results of the analysis, repeated here in Figure 25, indicate that structural failure of the two configurations examined could occur during maneuvering flight due to the large aerodynamic bending moment. Flight tests confirmed the prediction and the design was successfully modified.

MISSILE CONTROL DESIGN

The use of the code in preliminary missile design was recently illustrated for the Advance Point Defense System (APODS) missile concept. The guided APODS missile is currently an 18.0 caliber design with a 2.0 caliber Van Kármán ogive radome, a 16.0 caliber afterbody and four cruciform tail fins for control (see Figure 26). In order to obtain an estimate of its performance capabilities and determine the optimum control gains, the Aeroprediction Code was utilized to provide the static aerodynamics at angle-of-attack and the moment contributions relative to the center-of-gravity. The estimated static and dynamic aerodynamic coefficients for the APODS missile are given in Figure 27. These results were fed into the computer guidance model. A sample trajectory and the tail control autopilot response are shown in Figures 28 and 29, respectively. Results such as these can then guide the design in modifying the configuration or the control gains to maximize performance.

SUMMARY

An Extended Aerodynamic Prediction Code for rapid, approximate estimates of the static and dynamic coefficients for guided and unguided tactical weapons has been developed. The range of applicability of the code is $0 < M_{\infty} < 6.0$ (up to $M_{\infty} = 8.0$ for certain body alone cases) and $0^{\circ} < \alpha < 45^{\circ}$ (up to $\alpha = 180^{\circ}$ for computing the drag on certain body alone configurations). A large number of configurations can be accurately modeled on the program. Final verification of the predictions is nearing completion. The code, accompanied by a Design Manual and a User's Guide, is scheduled for release in the fourth quarter of FY81.

REFERENCES

1. J. Sun, L. Devan, N. J. Moga, and F. G. Moore, "Aerodynamic Prediction for Tactical Weapons," presented at the 11th Naval Symposium on Aeroballistics, 22-24 August 1978, Philadelphia, PA, Proceedings, Vol. I, pp 1-31.
2. F. G. Moore, Body Alone Aerodynamics of Guided and Unguided Projectiles at Subsonic, Transonic, and Supersonic Mach Numbers, NWL TR-2796, November 1972.
3. F. G. Moore, Aerodynamics of Guided and Unguided Weapons Part I - Theory and Application, NWL TR-3018, December 1973.
4. F. G. Moore and R. C. Swanson, Jr., Aerodynamics of Tactical Weapons to Mach Number 3 and Angle-of-Attack 15° : Part I - Theory and Application, NSWC/DL TR-3584, February 1977.
5. L. Devan, Aerodynamics of Tactical Weapons to Mach Number 8 and Angle-of-Attack 180° , NSWC TR 80-346, October 1980.
6. L. Devan, L. Mason, D. McMillan, and F. Moore, Aerodynamic Design Manual for Tactical Weapons, NSWC Report in Progress, 1981.
7. G. F. Aiello, Aerodynamic Methodology (Bodies with Tails at Arbitrary Roll Angles, Transonic and Supersonic), Martin Marietta Corp., OR 14, 145, Orlando, FL, April 1976.
8. L. Devan, "An Improved Second-Order Theory of Inviscid Supersonic Flow Past Bodies of Revolution," Paper 80-0030, presented at the AIAA 18th Aerospace Sciences Meeting, Pasadena, CA, January 1980.
9. R. C. Swanson, Jr., and F. G. Moore, Aerodynamics to Mach Number 3 and Angle of Attack 15° , Part II - Computer Program and Usage, NSWC/DL TR-3600, March 1977.
10. W. W. Hager, F. R. DeJarnette, and F. G. Moore, Optimal Projectile Shapes for Minimum Total Drag, NSWC TR-3597, Dahlgren, VA, May 1977.
11. N. J. Moga, Optimal Bodies for Minimum Total Drag at Supersonic Speeds, NSWC TR-80-208, Dahlgren, VA, May 1980.

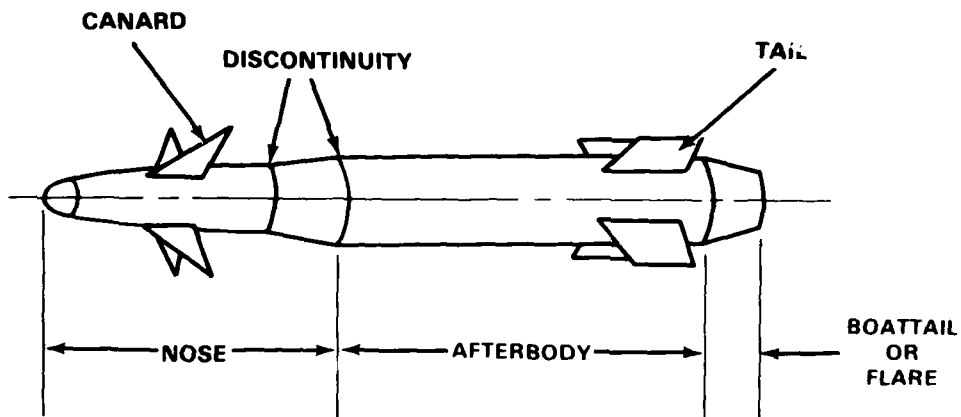


Figure 1. Configuration Geometry

COMPONENT \ MACH NUMBER REGION	SUBSONIC	TRANSONIC	LOW SUPERSONIC	HIGH SUPERSONIC
NOSE WAVE DRAG	-	EULER PLUS EMPIRICAL	SECOND-ORDER VAN DYKE PLUS MODIFIED NEWTONIAN	SECOND-ORDER SHOCK-EXPANSION PLUS MODIFIED NEWTONIAN
BOATTAIL WAVE DRAG	-	WU AND AOYOMA	SECOND-ORDER VAN DYKE	SECOND-ORDER SHOCK-EXPANSION
SKIN FRICTION DRAG	VAN DRIEST II			
BASE DRAG	EMPIRICAL			
INVISCID LIFT AND PITCHING MOMENT	EMPIRICAL	EULER OR WU AND AOYOMA PLUS EMPIRICAL	TSIEN FIRST-ORDER CROSSFLOW	SECOND-ORDER SHOCK-EXPANSION
VISCOUS LIFT AND PITCHING MOMENT	ALLEN AND PERKINS CROSSFLOW			

Figure 2. New Methods for Computing Body-Alone Aerodynamics

COMPONENT	MACH NUMBER REGION	SUBSONIC	TRANSONIC	LOW SUPERSONIC	HIGH SUPERSONIC
INVISCID LIFT AND PITCHING MOMENT		LIFTING SURFACE THEORY	EMPIRICAL	LINEAR THEORY	SHOCK EXPANSION STRIP THEORY
WING-BODY INTERFERENCE		SLENDER BODY THEORY AND EMPIRICAL		LINEAR THEORY, SLENDER BODY THEORY AND EMPIRICAL	—
WING-TAIL INTERFERENCE		LINE VORTEX THEORY			—
WAVE DRAG		—	EMPIRICAL	LINEAR THEORY + MODIFIED NEWTONIAN	SHOCK EXPANSION + MODIFIED NEWTONIAN STRIP THEORY
SKIN FRICTION DRAG		VAN DRIEST			
TRAILING EDGE SEPARATION DRAG		EMPIRICAL			
BODY BASE PRESSURE DRAG CAUSED BY TAIL FINS		EMPIRICAL			

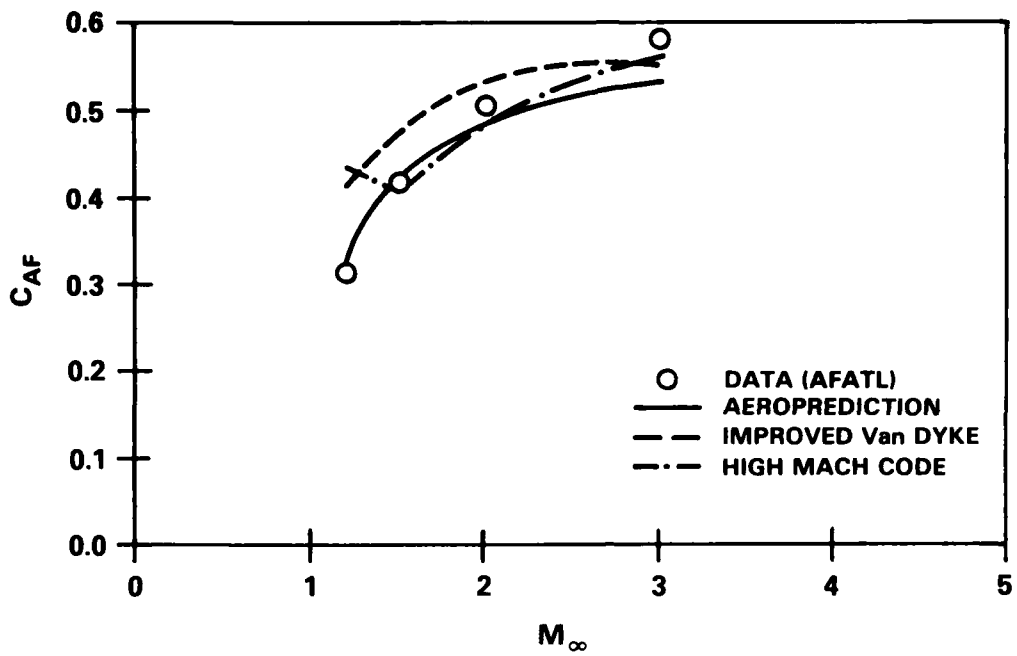
Figure 3. New Methods for Computing Wing-Alone and Interference Aerodynamics

COMPONENT	MACH NUMBER REGION	SUBSONIC	TRANSONIC	LOW SUPERSONIC	HIGH SUPERSONIC
BODY-ALONE PITCH DAMPING MOMENT		EMPIRICAL			
		(OR) MODIFIED SLENDER-BODY THEORY	(OR) LINEAR INTERPOLATION	(OR) EMBEDDED NEWTONIAN THEORY	
WING AND INTERFERENCE ROLL DAMPING		LIFTING SURFACE THEORY	EMPIRICAL	LINEAR THIN-WING THEORY	STRIP THEORY
BODY-ALONE MAGNUS MOMENT		EMPIRICAL			
WING AND INTERFERENCE MAGNUS MOMENT		ASSUMED ZERO			
BODY-ALONE ROLL DAMPING MOMENT		EMPIRICAL			
WING AND INTERFERENCE PITCH DAMPING MOMENT		SLENDER-WING THEORY	SUPERSONIC SLENDER-WING THEORY	EMBEDDED NEWTONIAN STRIP THEORY	
		(OR) LIFTING SURFACE THEORY	(OR) EMPIRICAL	(OR) LINEAR THIN-WING THEORY	(OR) STRIP THEORY

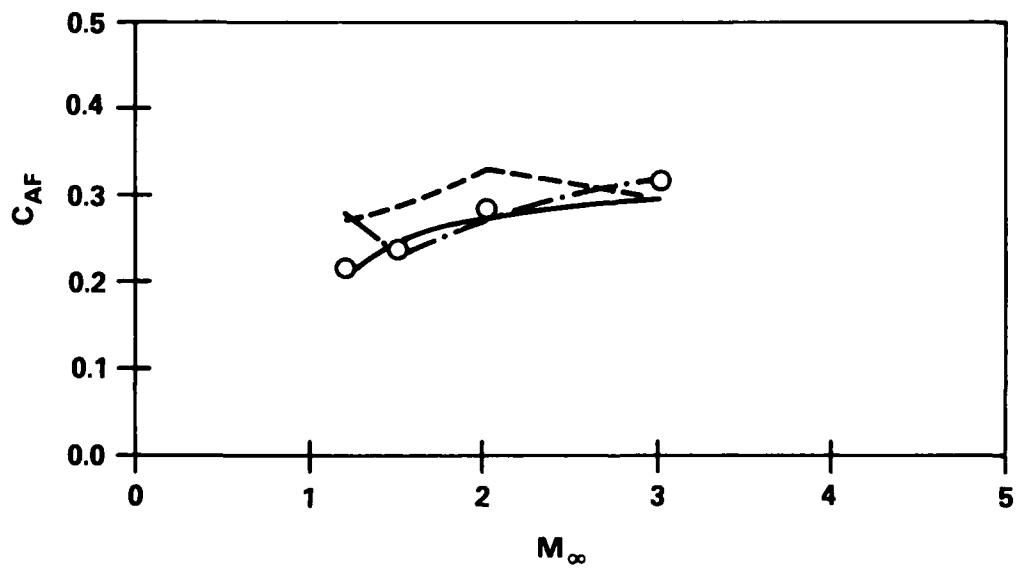
* INPUT OPTION. MACH DIVISION POINTS ARE AT $M_{\infty} = 1$ AND $M_{\infty} = \bar{M}^*$. \bar{M}^* IS VARIABLE, BUT $\bar{M}^* \geq 1.5$.

** INPUT OPTION. MACH DIVISIONS AT $M_{\infty} = 1$ AND A MACH NUMBER DEPENDENT ON ASPECT RATIO. $M_{\infty} = \sqrt{1 + (A_w/4)^2}$.

Figure 4. New Methods for Computing Dynamic Derivatives

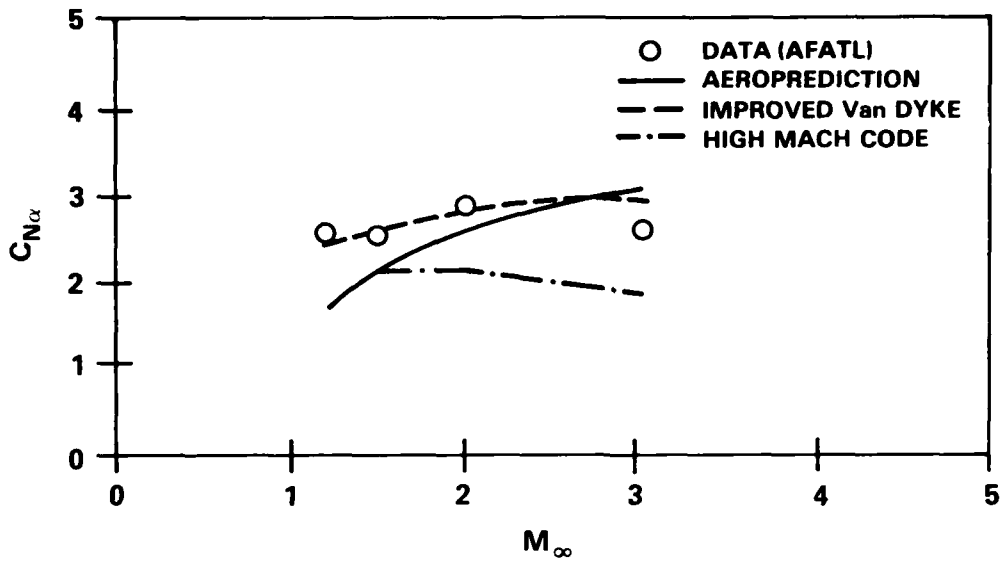


(a) $L_N = 1.859$, $R_N = 0.375$, $\alpha = 0$

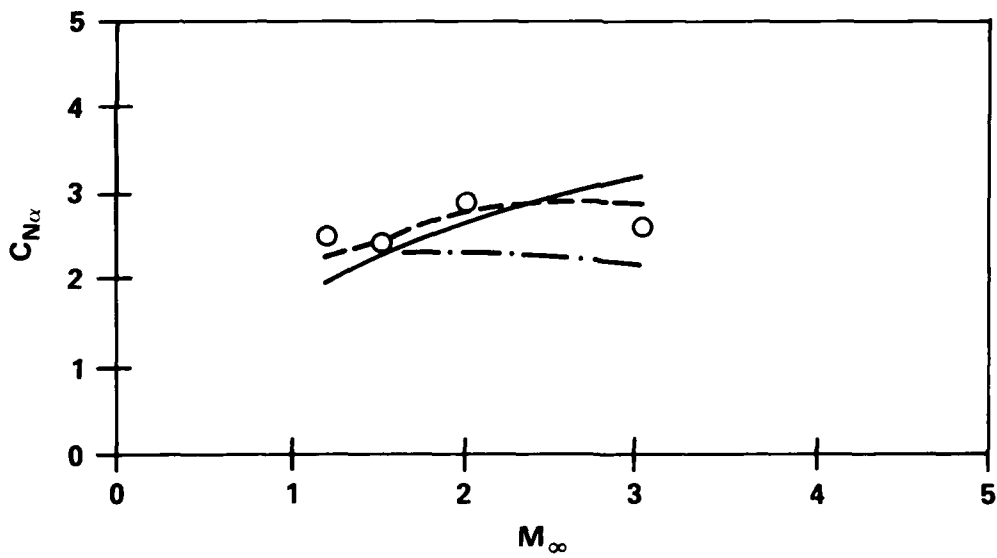


(b) $L_N = 2.357$, $R_N = 0.250$, $\alpha = 0$

Figure 5. Blunted Tangent Ogive-Forebody Axial Force

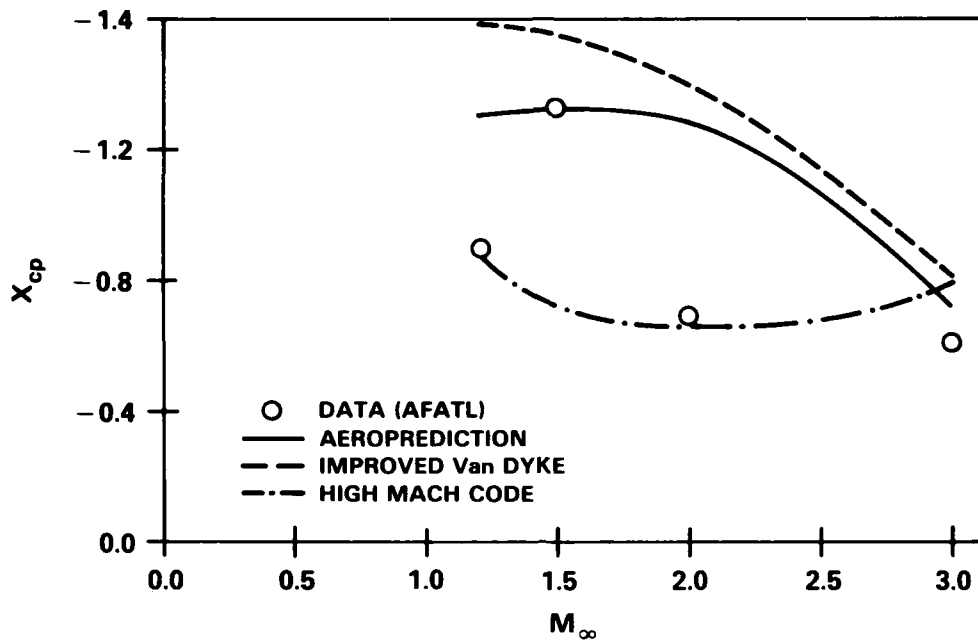


(a) $L_N = 1.859$, $R_N = 0.375$, $\alpha = 0$

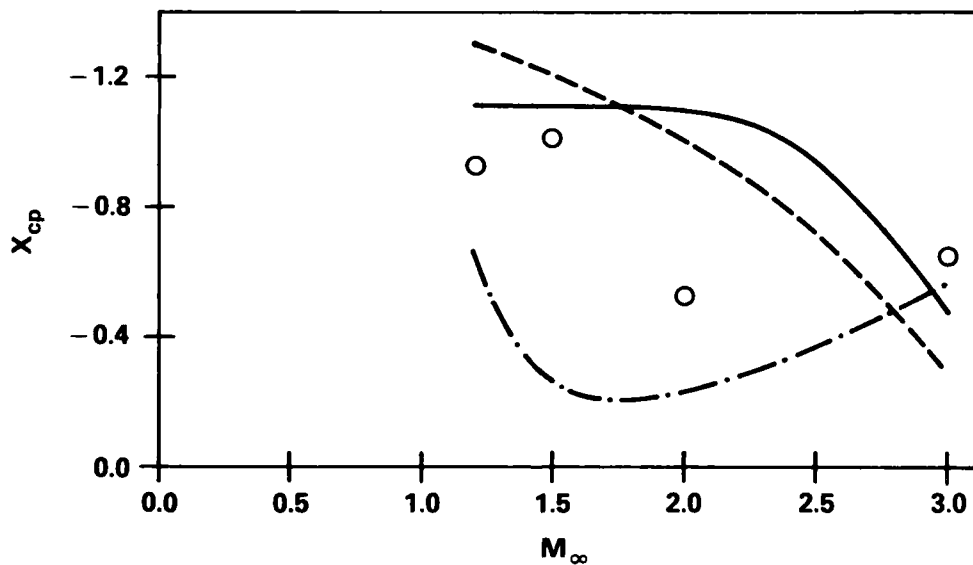


(b) $L_N = 2.357$, $R_N = 0.250$, $\alpha = 0$

Figure 6. Blunted Tangent Ogive-Cylinder, $C_{N\alpha}$



(a) $L_N = 2.357$, $R_N = 0.250$, $\alpha = 0$



(b) $L_N = 1.859$, $R_N = 0.375$, $\alpha = 0$

Figure 7. Blunted Tangent Ogive-Cylinder, X_{cp} (From Body-Nose Junction)

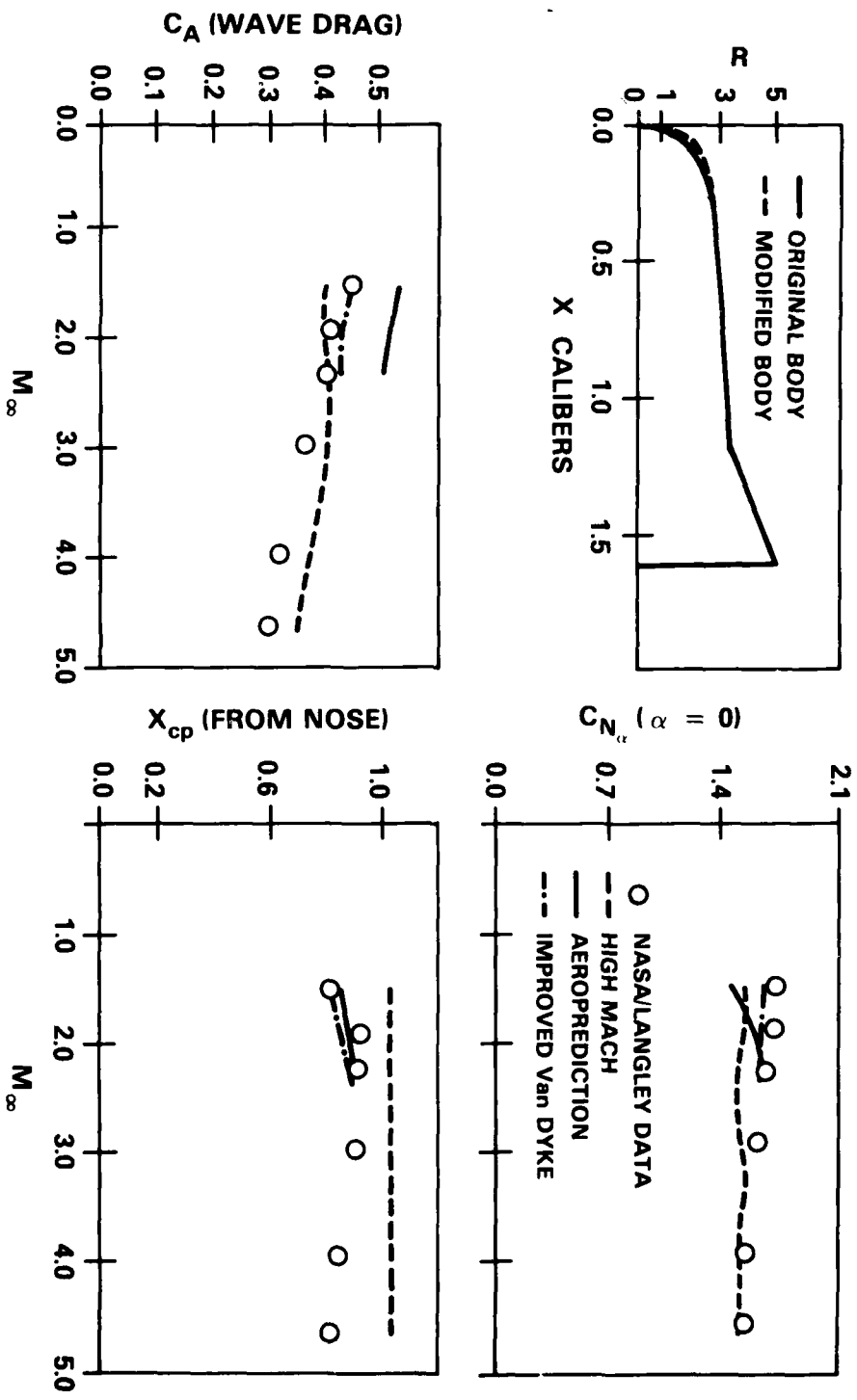
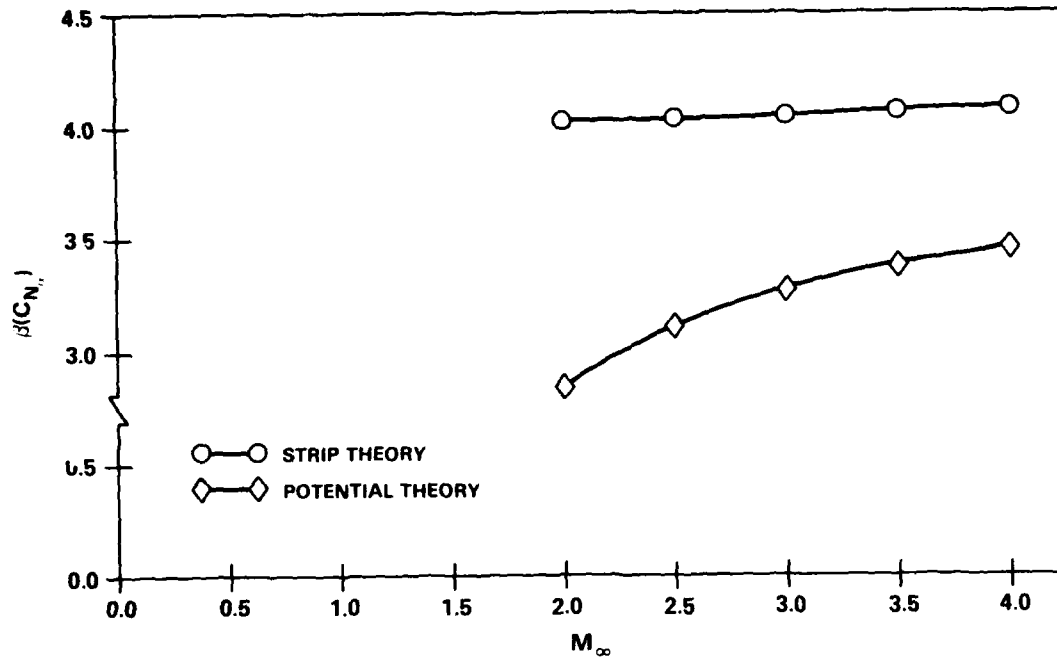
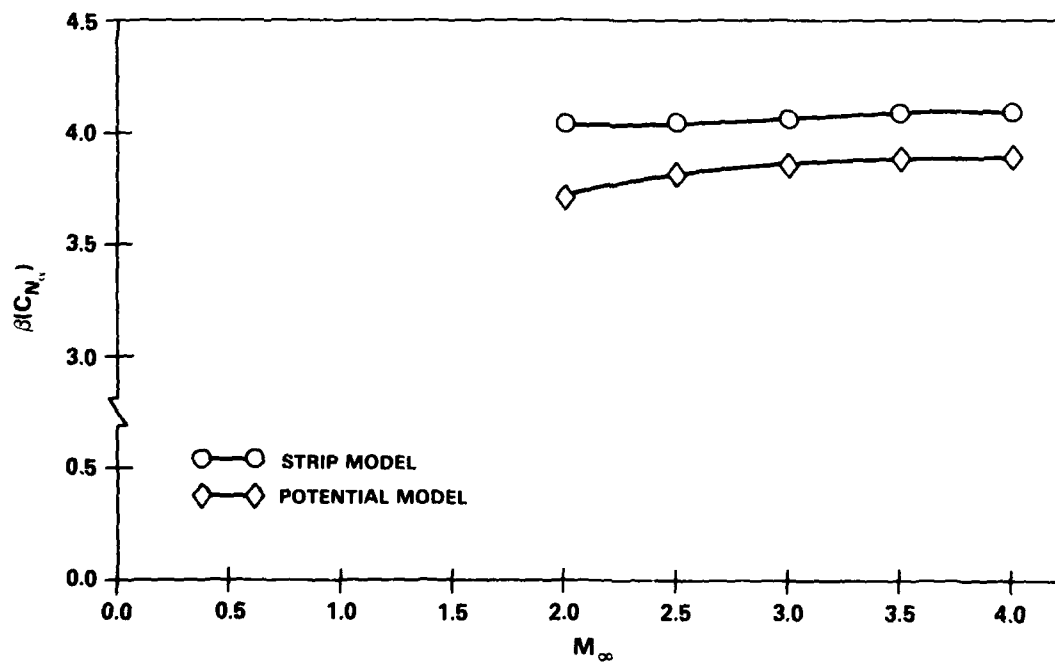


Figure 8. NASA Flared-Body Data Comparison

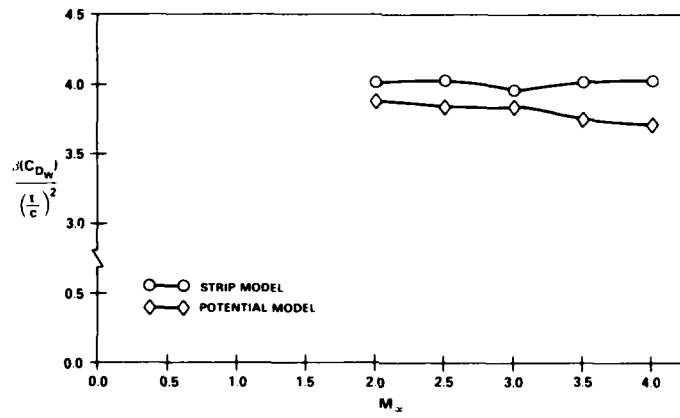


(a) $\lambda_W = 0.99, A_W = 1, \alpha_1 = 1^\circ$

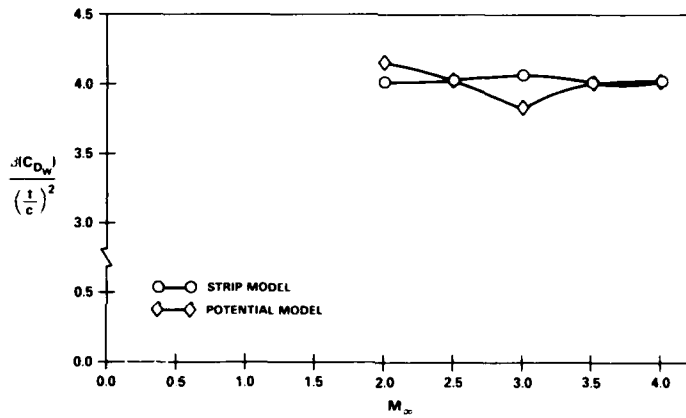


(b) $\lambda_W = 1/3, A_W = 2, \alpha_1 = 45^\circ$

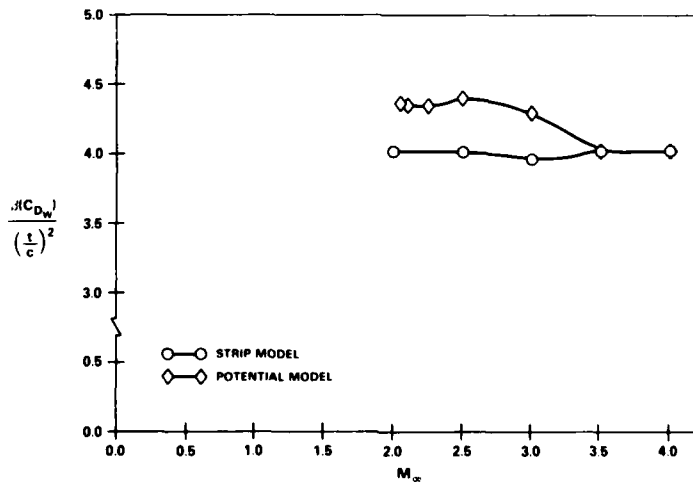
Figure 9. C_{N_α} Comparison for a Wing



(a) $\lambda_W = 0.99$, $A_W = 1$, $\lambda_1 = 1$



(b) $\lambda_W = 1/3$, $A_W = 2$, $\lambda_1 = 45$



(c) $\lambda_W = 0.40$, $A_W = 1$, $\lambda_1 = 60$

Figure 10. C_{Dw} Comparison for a Wing

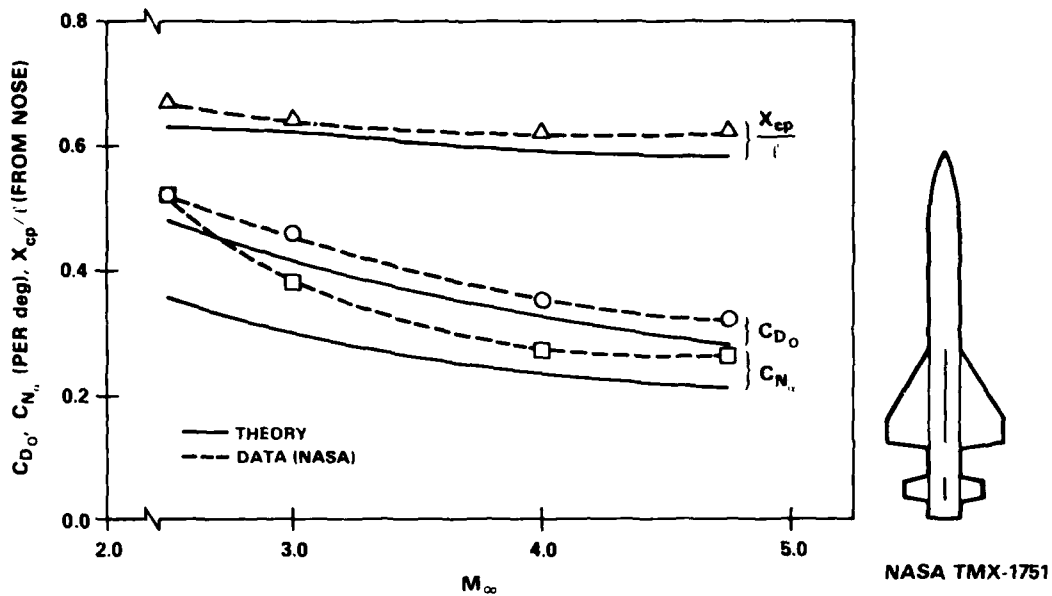
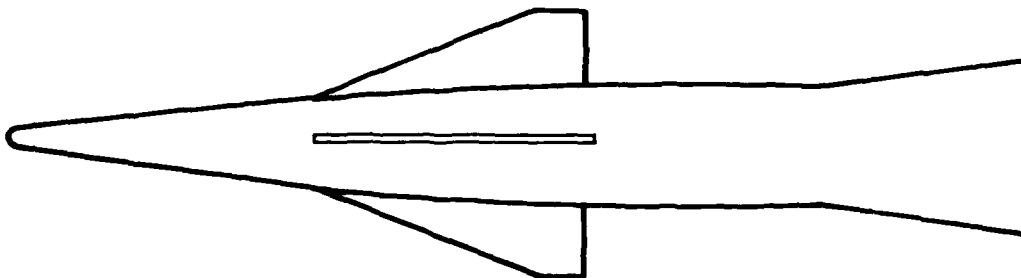


Figure 11. Comparison of Static Aerodynamics for Finned Body at High Mach Numbers ($\alpha = 0^\circ$)



	C_{D0}	$C_{N\alpha}$ (PER rad)	X_{cp}/l (FROM NOSE)
THEORY	0.39	8.4	0.63
DATA (NASA)	0.36	7.7	0.59

Figure 12. Aerodynamics for TMX-187 ($M_\infty = 4.65$, $\alpha = 0^\circ$)

DIMENSIONS IN INCHES

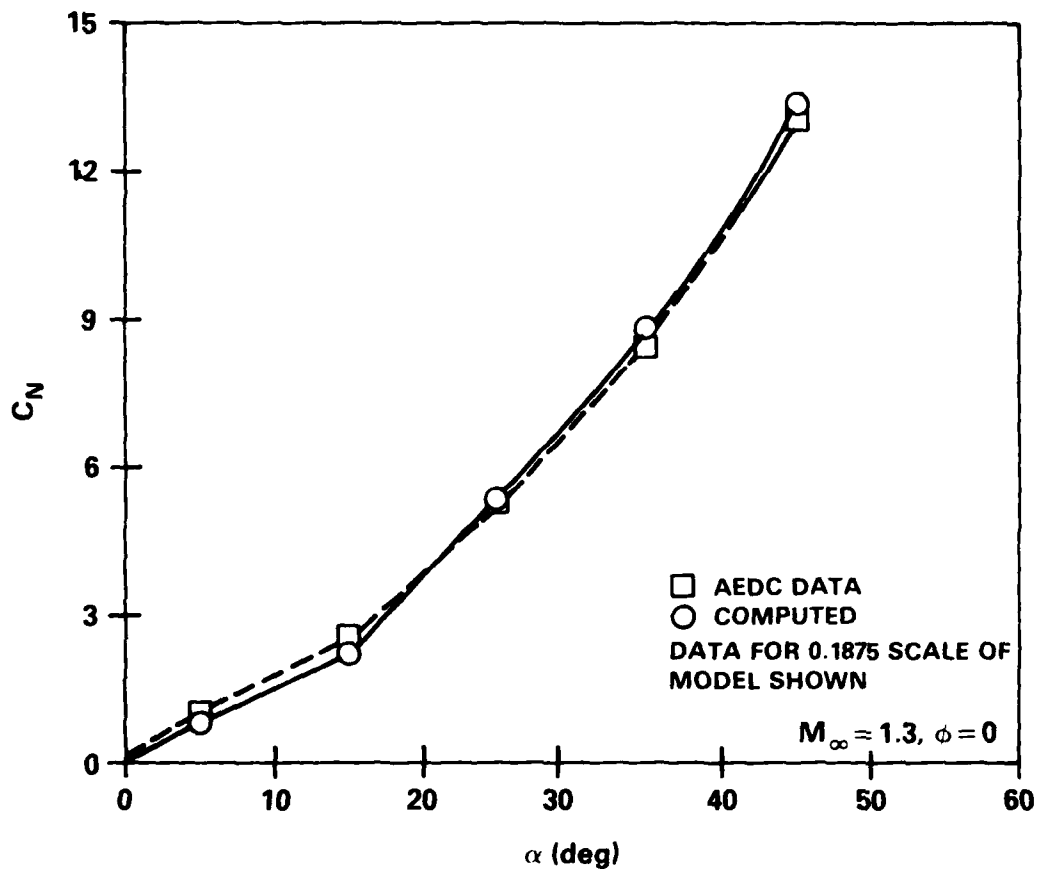
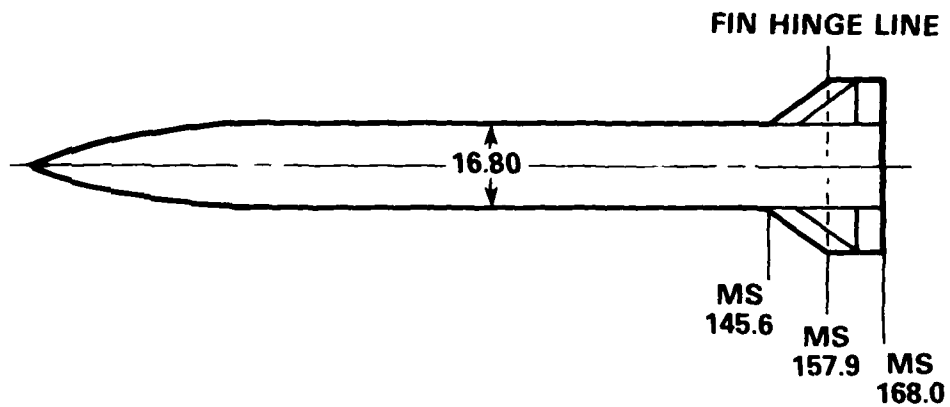


Figure 13. C_N Comparison for Air Slew Demonstrator

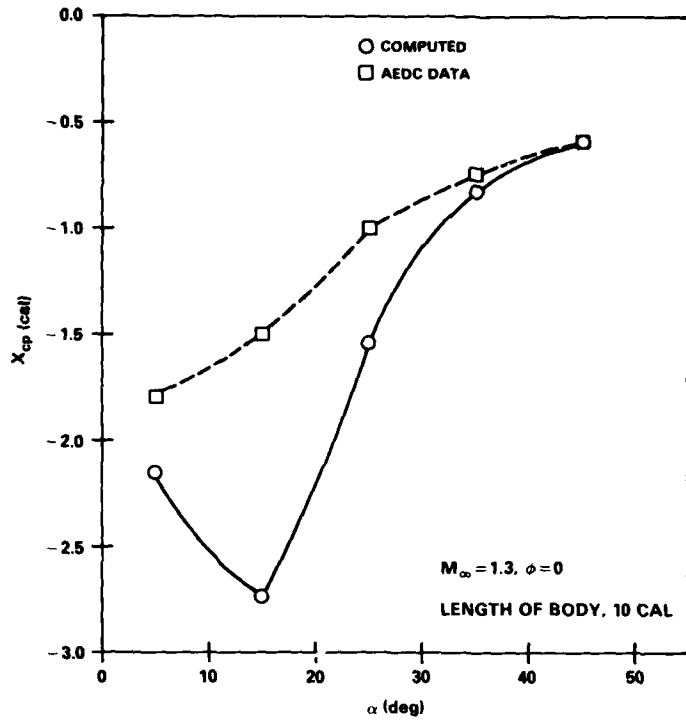


Figure 14. X_{cp} Comparison for Air Slew Demonstrator Forward of Body Midpoint

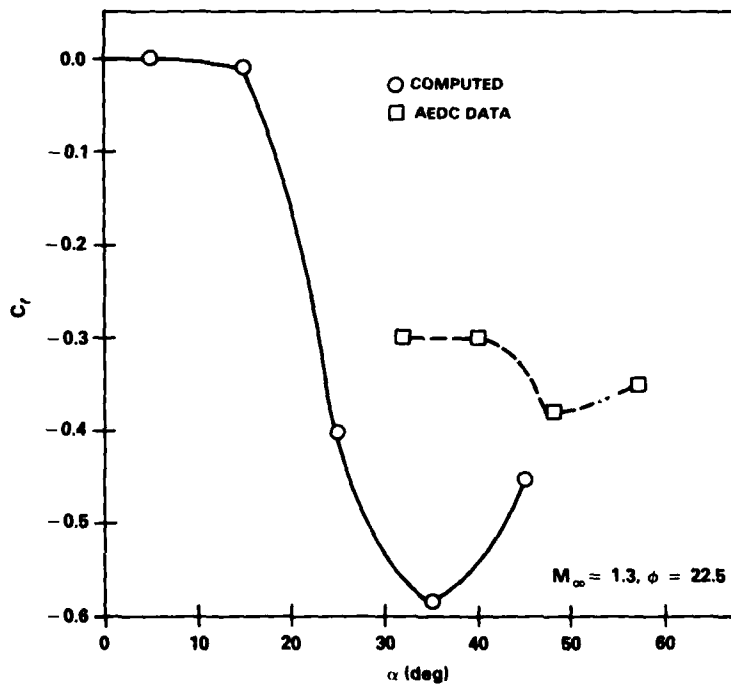
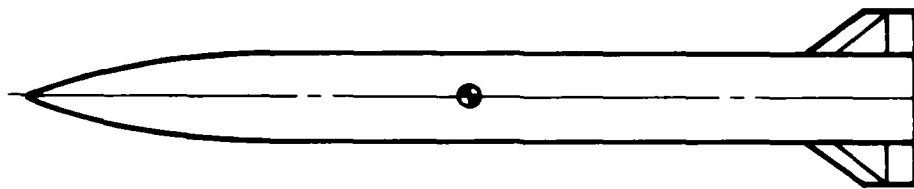


Figure 15. C_l Comparison for Air Slew Demonstrator



$D = 0.15 \text{ ft}$

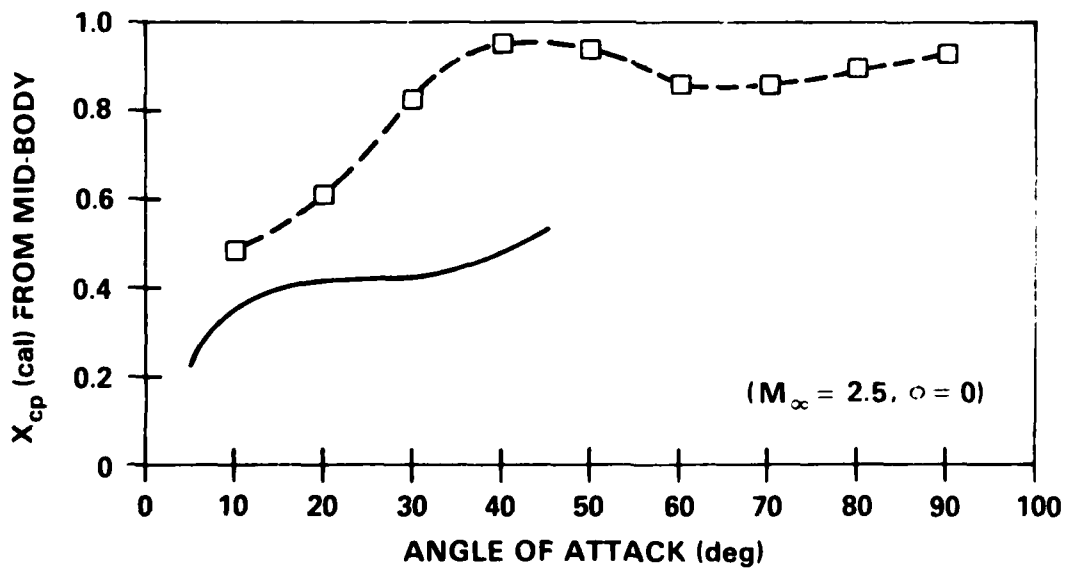
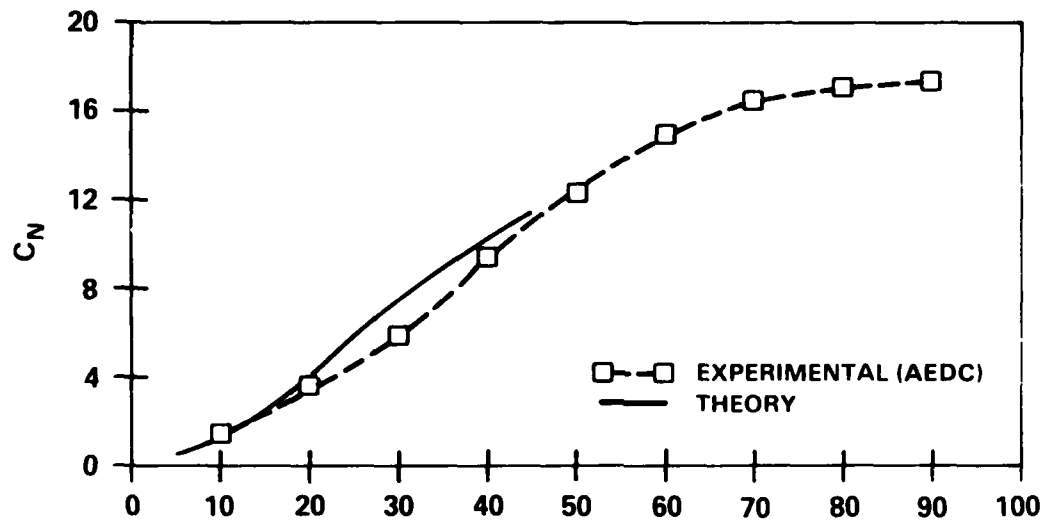


Figure 16. Modified Basic Finner Aerodynamic Comparison

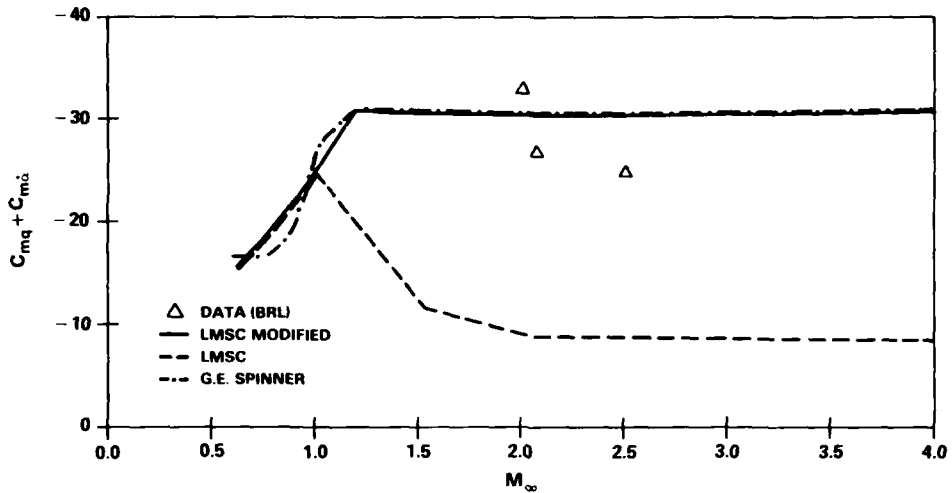
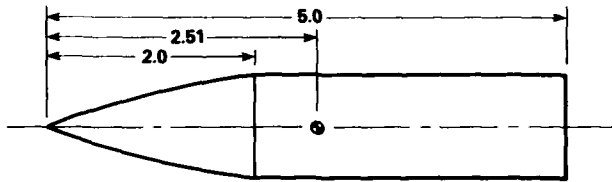


Figure 17. Army-Navy Spinner Pitch Damping Comparison

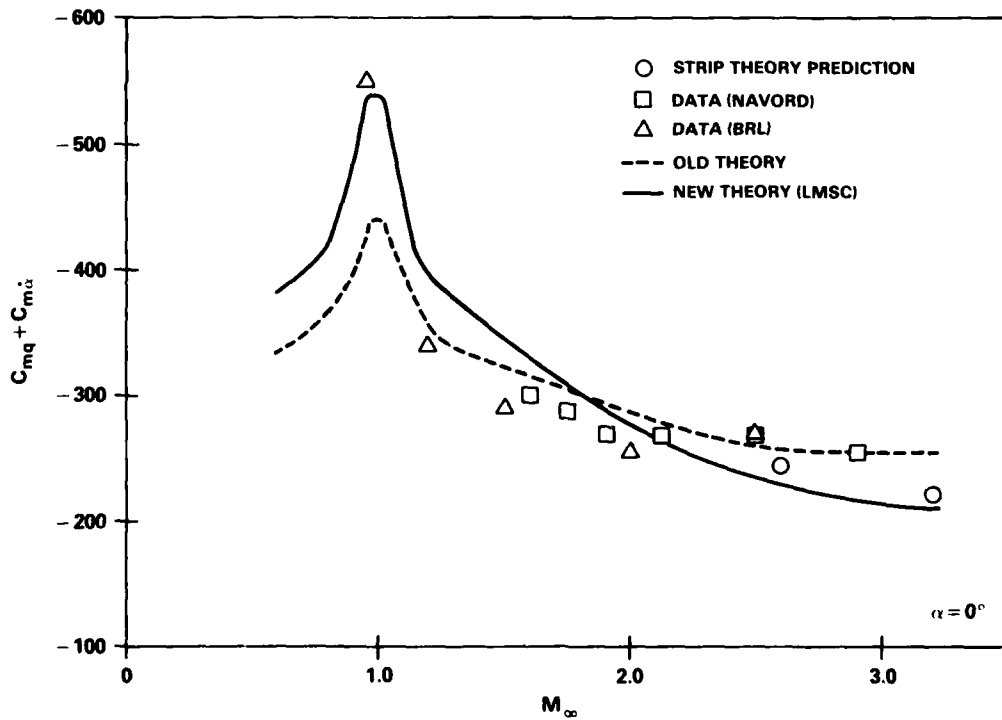


Figure 18. Basic Finner Pitch Damping Comparison

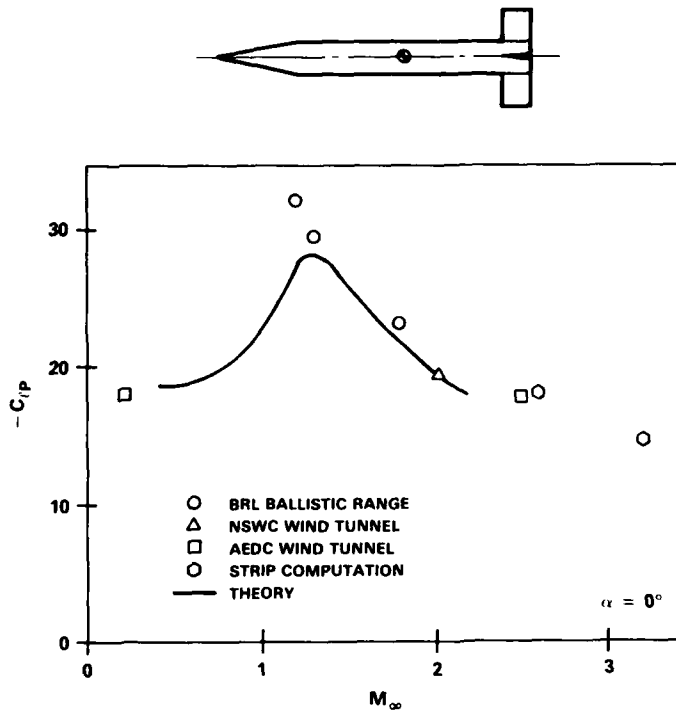


Figure 19. C_{lp} Comparison for Army-Navy Basic Finner

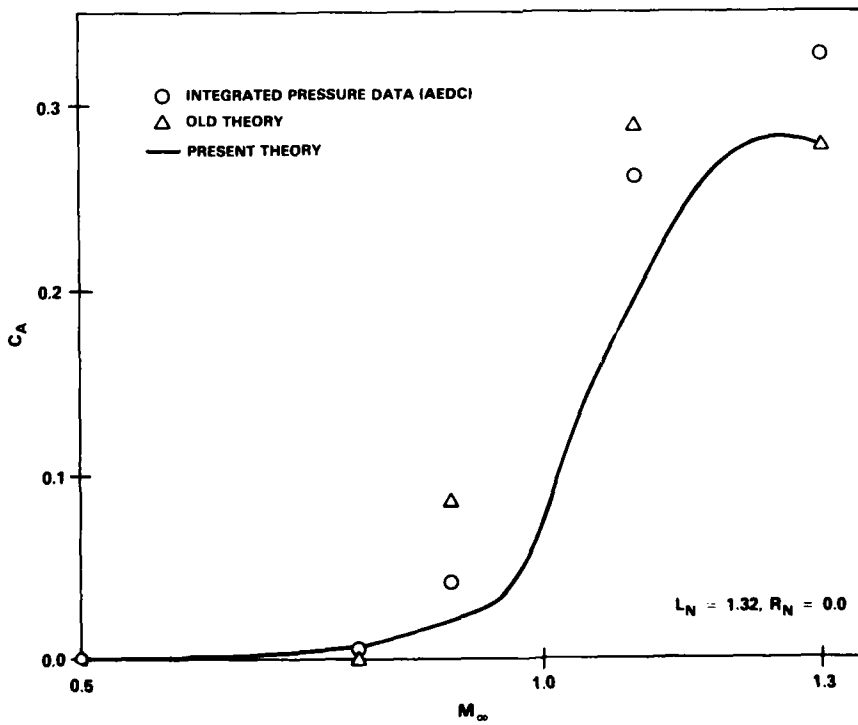


Figure 20. M-117 Bomb Nose Wave Drag Comparison

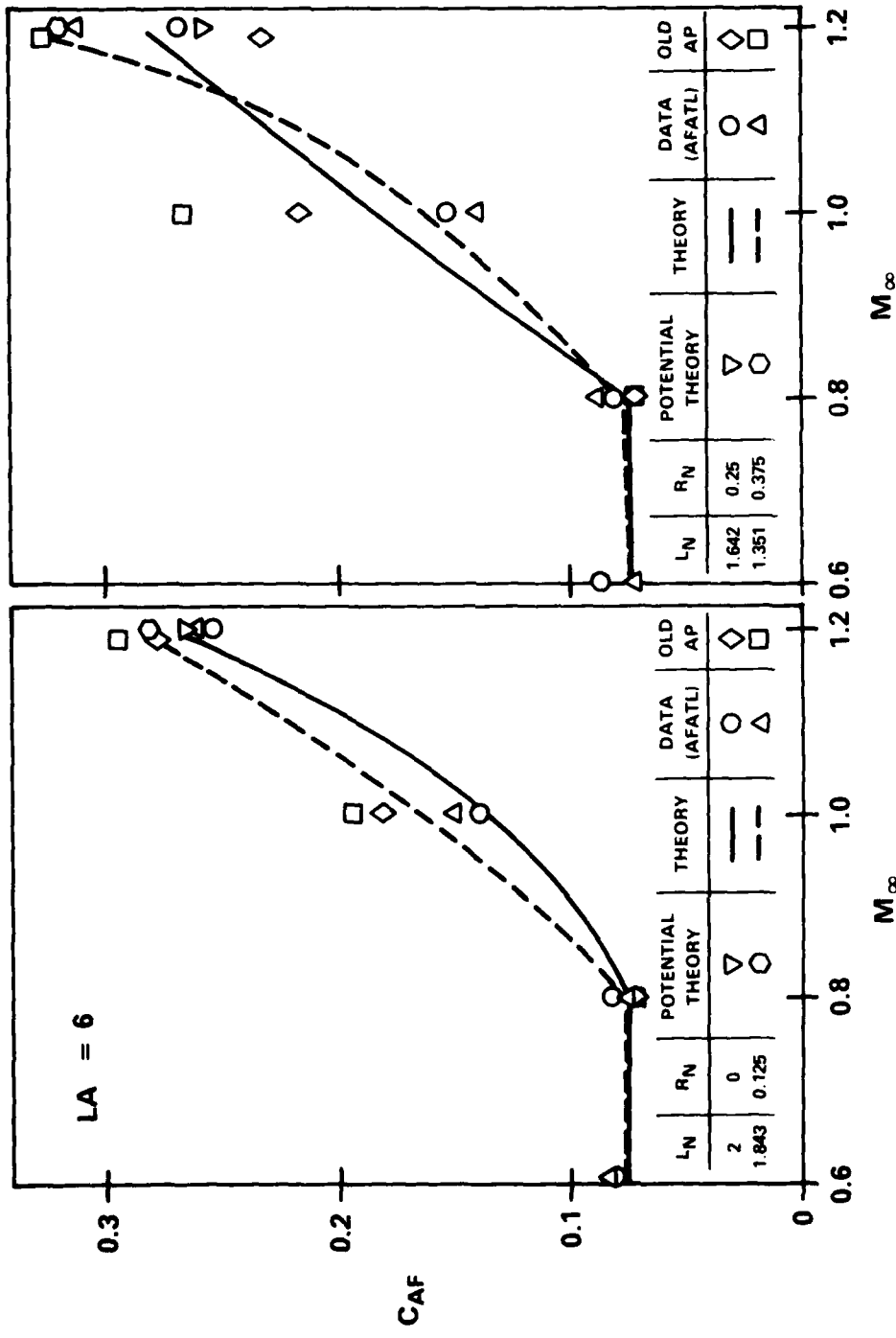


Figure 21. C_{AF} Comparison for Blunted Tangent Ogive-Cylinders

TRANSONIC $C_{N\alpha}$ AND X_{cp}

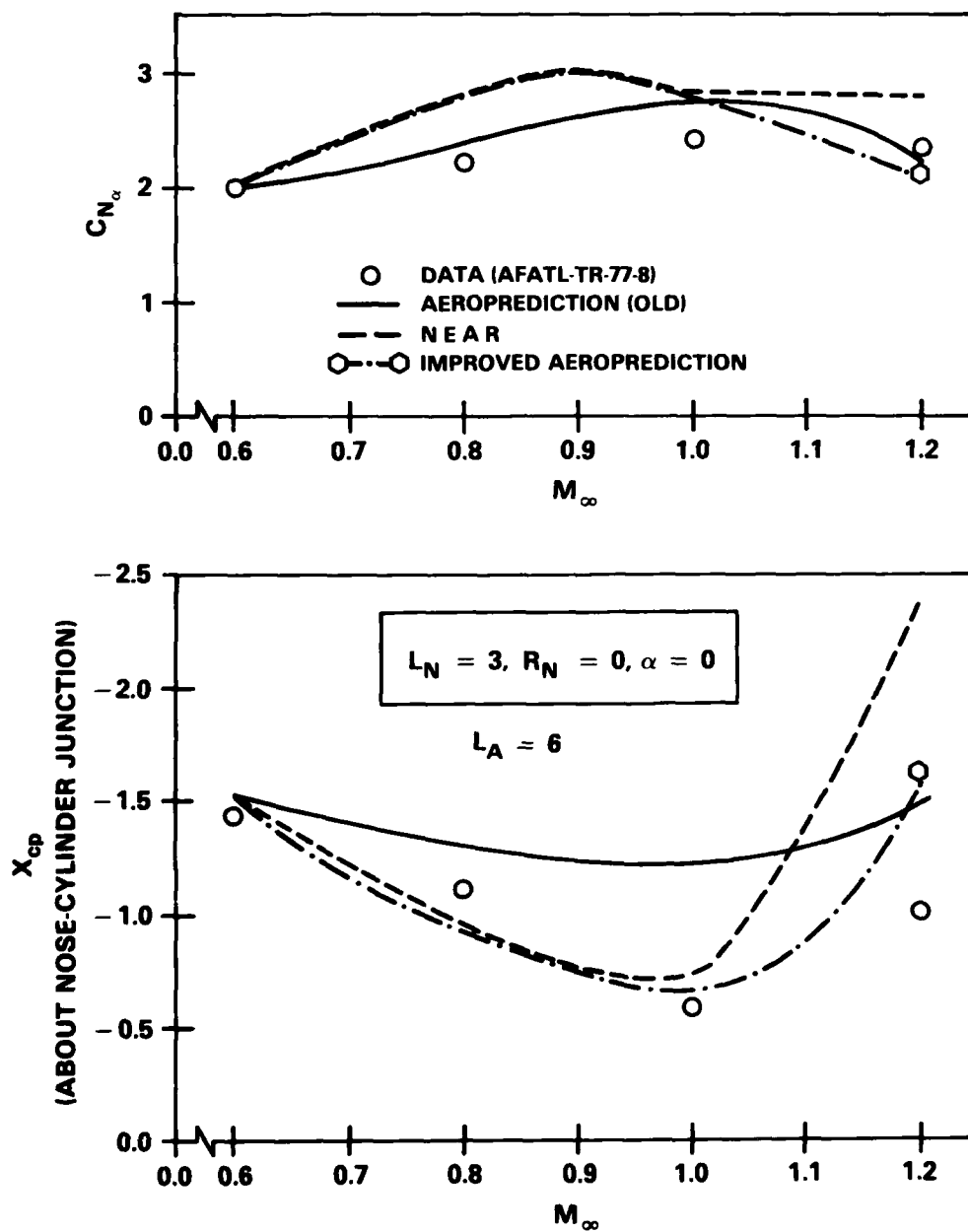


Figure 22. $C_{N\alpha}$ and X_{cp} Comparison for Blunted Tangent Ogive-Cylinders

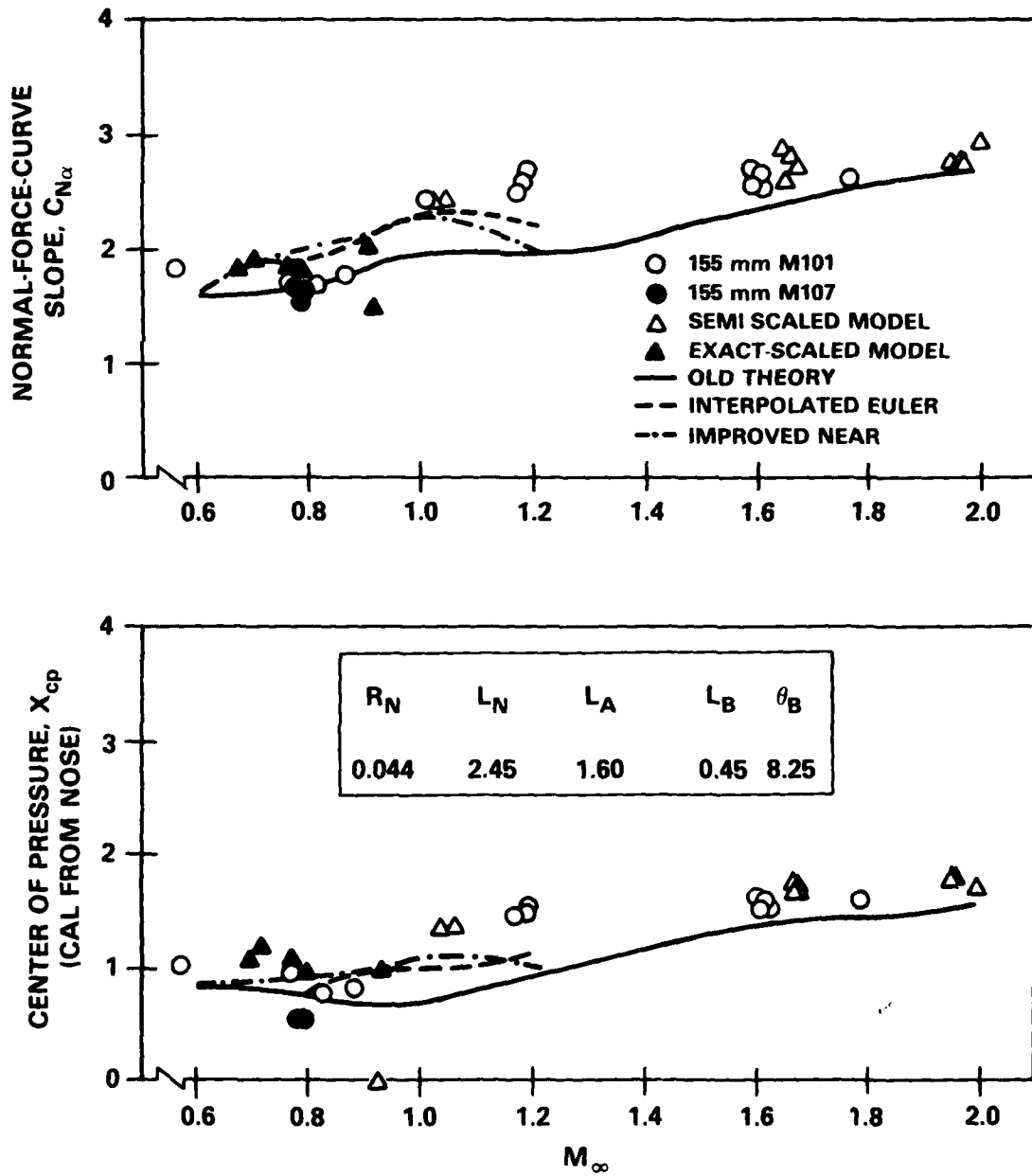


Figure 23. Comparison of Theory and Test Data for 155 mm Projectile

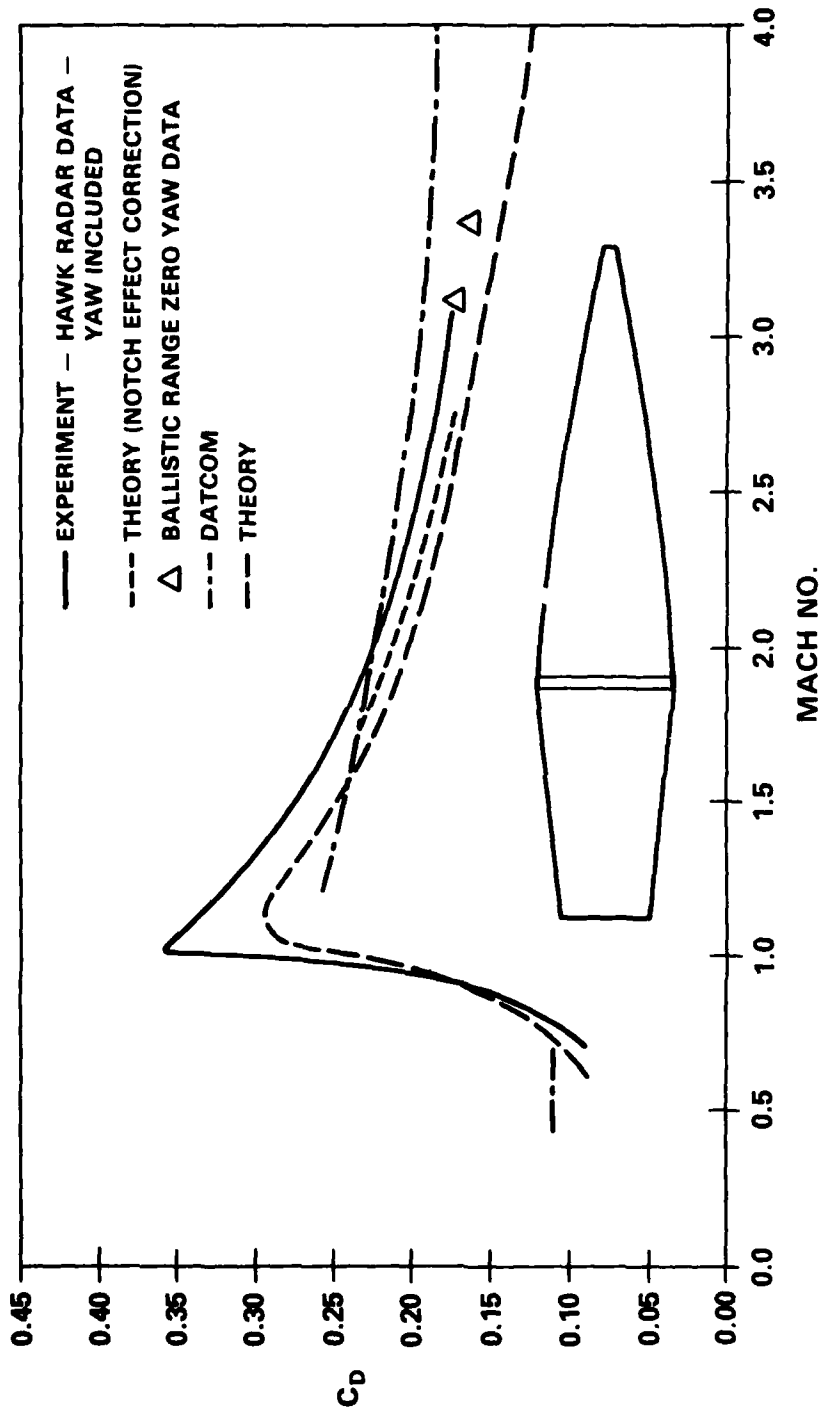


Figure 24. Static Aerodynamics for 30 mm Air Defense Projectile
Using the Aeroprediction Code

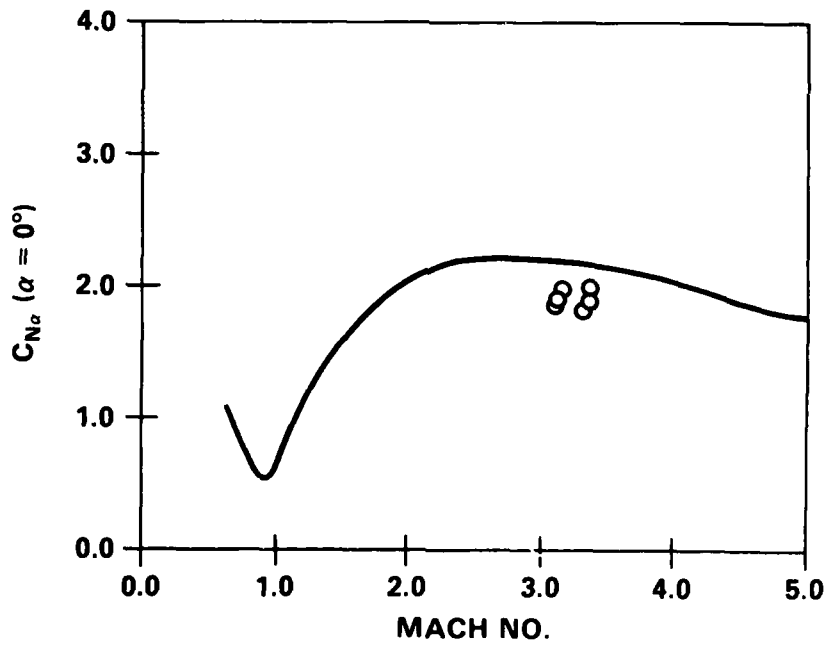
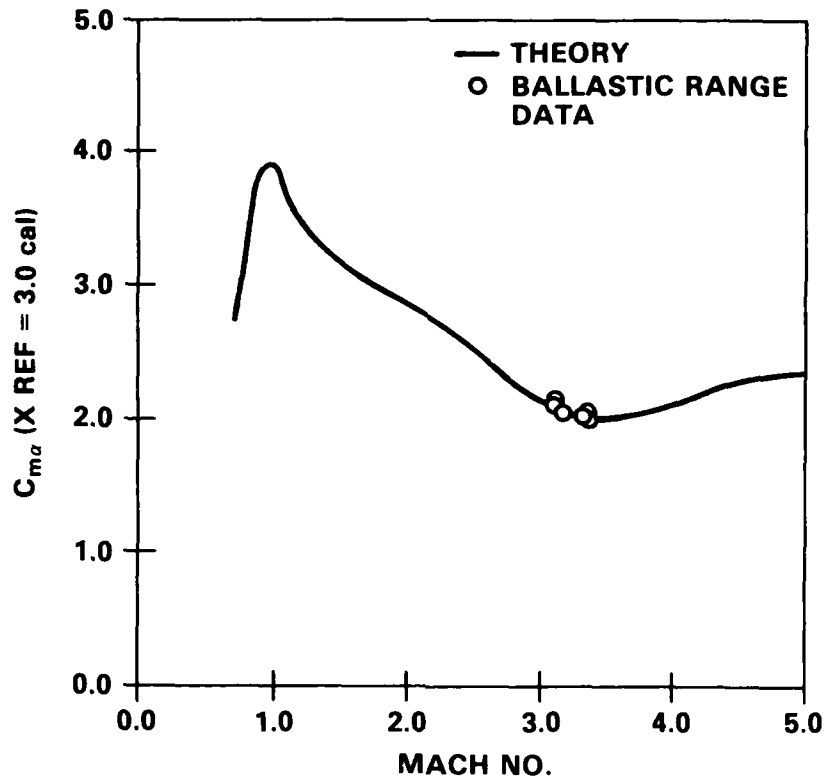


Figure 24 (cont.). Static Aerodynamics for 30 mm Air Defense Projectile Using the Aeroprediction Code

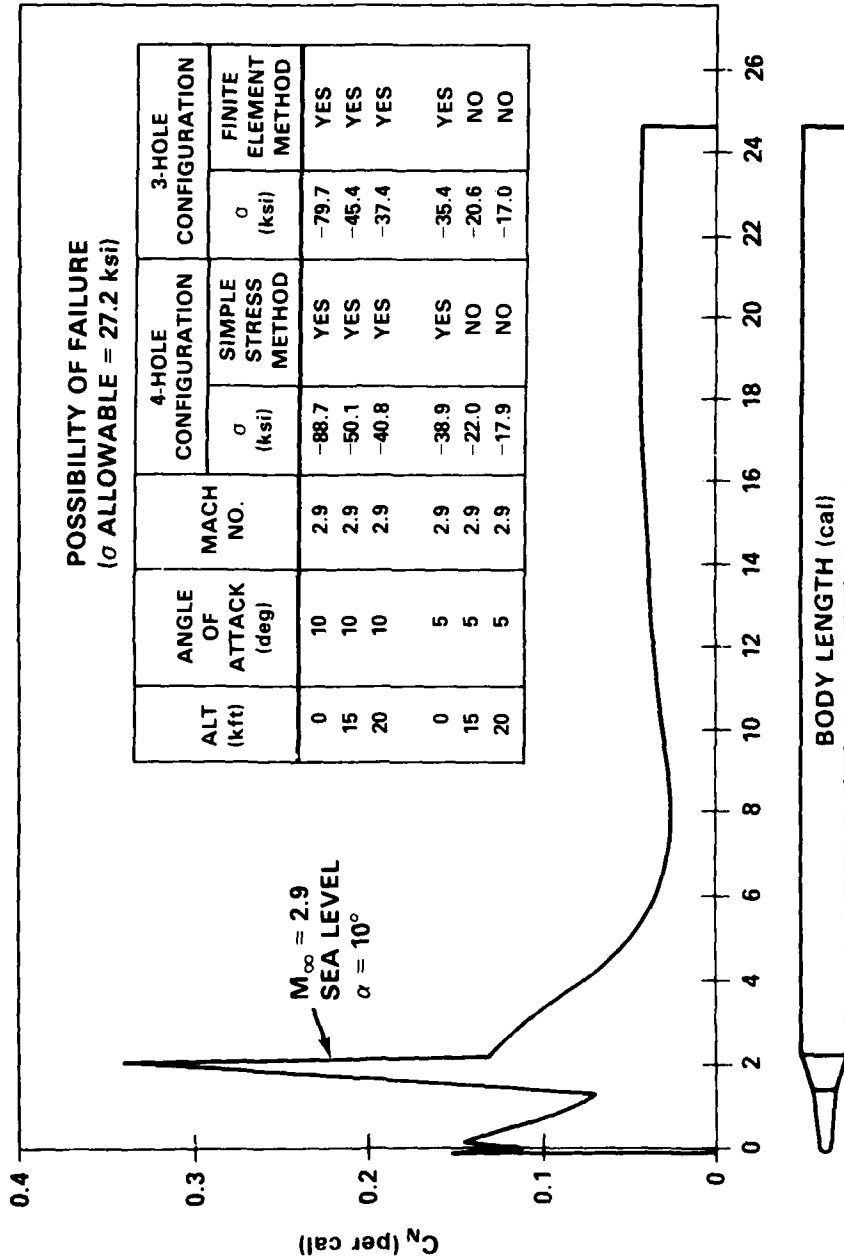
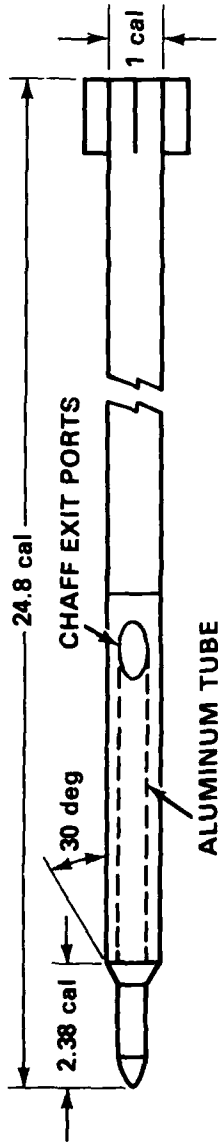


Figure 25. Structural Integrity Study Using the Aeroprediction Code



28 25



MILITARY STANDARD 1917-1950
NATIONAL BUREAU OF STANDARDS

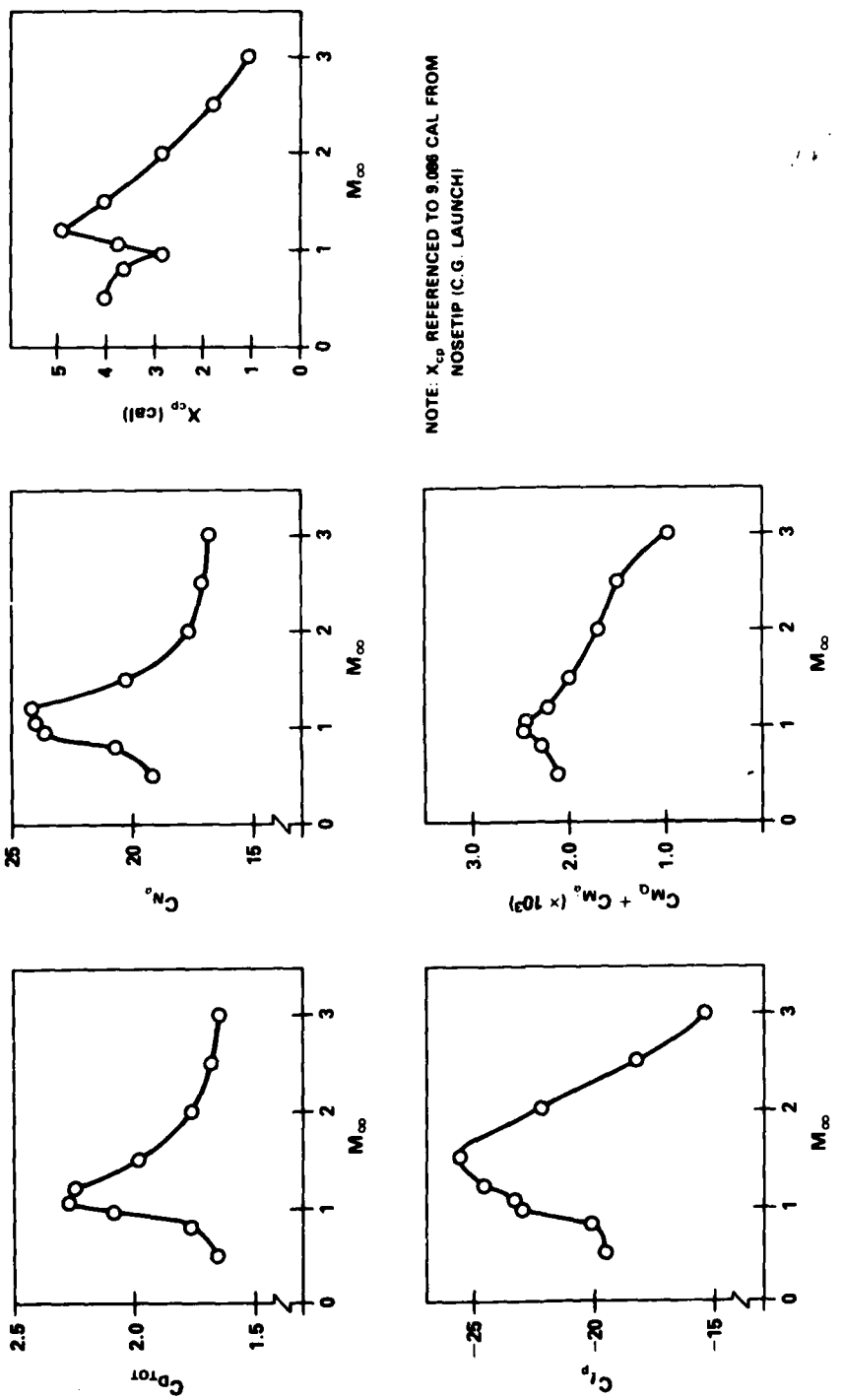


Figure 27. APODS Predicted Aerodynamics Using Aeroprediction Code ($\alpha = 15^\circ$)

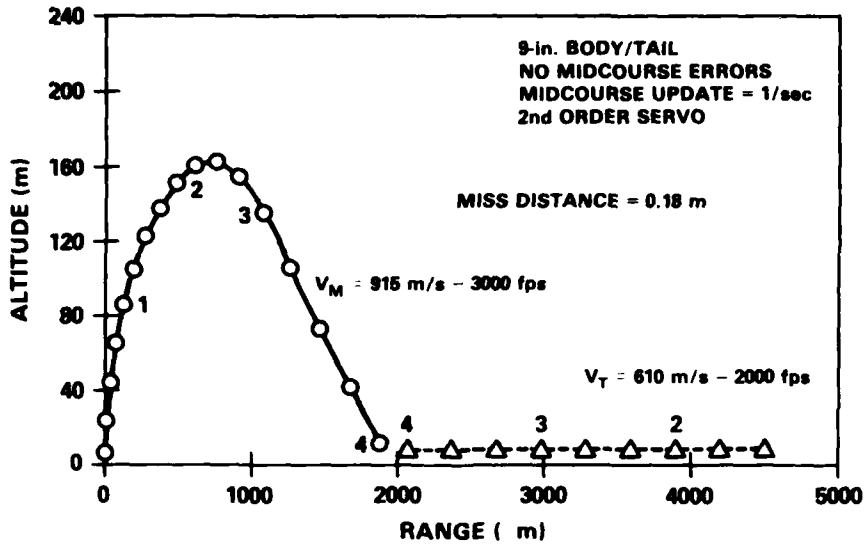


Figure 28. Sample APODS Performance Trajectory

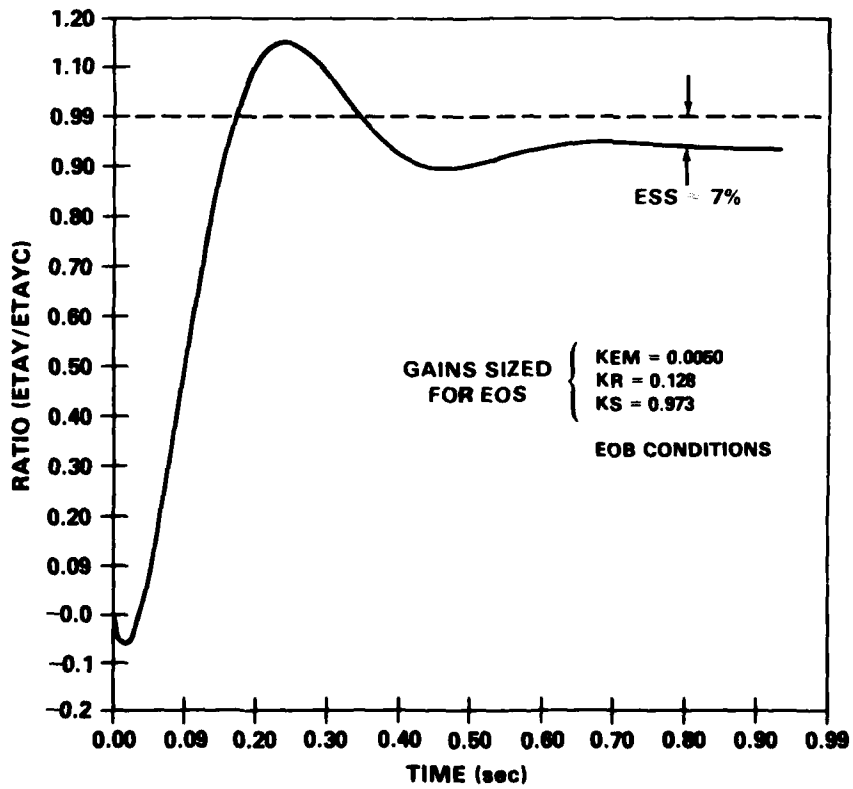


Figure 29. Sample APODS Tail Control Autopilot Response

AN INVISCID COMPUTATIONAL METHOD FOR TACTICAL
MISSILE CONFIGURATIONS

A. B. Wardlaw, Jr., J. M. Solomon, F. P. Baltakis and L. B. Hackerman
Naval Surface Weapons Center, Silver Spring, Maryland 20910

Abstract

A finite difference method suitable for design calculations of finned bodies is described. Efficient numerical calculations are achieved using a thin fin approximation which neglects fin thickness but retains a correct description of the fin surface slope. The resulting algorithm is suitable for treating relatively thin, straight fins with sharp edges. Methods for treating the fin leading and trailing edges are described which are dependent on the Mach number of the flow normal to the edge. The computed surface pressures are compared to experimental measurements taken on cruciform configurations with supersonic leading and trailing edges and to a swept wing body with detached leading edge shocks. Calculated forces and moments on body-wing-tail configuration with subsonic leading edges are compared to experiment also. Body alone configurations are studied using a Kutta condition to generate a lee-side vortex.

1. Introduction

A practicable means of predicting the nonlinear, inviscid, supersonic shock layer on missile configurations is to numerically solve the steady, three-dimensional inviscid equations using an efficient finite difference method. Several computer programs are currently available for this purpose, e.g. Refs. 1-7. Although these supersonic flow field codes can be applied to relatively arbitrary body shapes, their application to practical wing-body-tail configurations presents some serious computational problems. Existing codes treat the complete fin-body cross section as a single entity. Thus when cylindrical coordinates, as shown in Fig. 1, are used a large number of ϕ mesh

planes are needed to adequately resolve the fin. When several fins are present at the same axial station, the number of grid points needed becomes prohibitively large for practical design calculations. The number of grid points can be substantially reduced by mapping the fin body cross-section into a more "rounded" figure. The existing methods utilizing this approach are based on conformal mapping techniques developed by Moretti^{2,8} (see Refs. 3,6). The mappings however are complicated even for the case of a single smooth fin or wing and often tend to cluster large numbers of mesh points near wing tips. This reduces the permissible marching step and increases computational time.

The primary focus of the present study is the development of a more efficient numerical technique for treating finned bodies. To achieve this, the approach used here departs from the basic computational strategy used in Refs. 1-7 when fin surfaces are present. Instead of considering the cross-sectional body-fin geometry as a single entity, the present approach considers the body alone (i.e., the body with all fin surfaces removed) and the fin geometry separately. The computational grid is generated using normalizing transformations^{1,4,5,7} applied to the body alone configuration. The fin surfaces are allowed to extend into the computational region and can be adequately resolved within a relatively coarse computational grid. In order to treat the complex flow in the immediate vicinity of fin leading and trailing edges, appropriate local analyses are built into the program which depend strongly on the local Mach number of the flow component normal to the edge. These local analyses can range from locally exact, when the edge is sharp and the normal velocity component is sufficiently supersonic, to ad hoc or semi-empirical in other situations.

Within this framework, various approaches for numerically treating general fin surface shapes are possible. One approach would be to introduce extra

computational points to represent the fin surfaces which would float within the basic grid. This would complicate the application of the boundary conditions on the fin surfaces. Another approach, would be to subdivide the flow domain into several sub-regions each containing the flow between adjacent fin surfaces. Relatively simple transformations would be applied separately in each sub-region to map adjacent fin surfaces onto constant computational coordinate planes.

Relatively coarse meshes could be used in each sub-region and the computations in the various sub-regions could be linked in a manner suggested by Hindman, et al.⁹ Both the above mentioned approaches are in principle capable of handling general fin surface geometries.

To simplify the development for the present study, the analysis is restricted to relatively thin fins with sharp edges which lie approximately along constant ϕ planes (cf., Fig. 1). A thin fin approximation is employed which neglects the fin thickness but retains the actual fin surface slopes. For an important class of body-fin configurations, the thin fin approximation allows the direct use of the basic grid generated for the body alone shape (see Sec. 2) without the introduction of floating points to describe the fin surface or additional mappings. To verify the thin fin approximation and the versatility of the computational method presented here (see Secs. 2 and 3), comparisons are made of computed and measured surface pressure distributions for body alone, body-wing and body-wing-tail configurations. A representative sampling of these is presented in Sec. 4.

2. Notation and Preliminaries

The numerical methods for treating fin body combinations presented here differ from existing supersonic inviscid flow field codes¹⁻⁷ only in the treatment of fin surfaces. In the present work, the procedures for treating

fin surfaces, which appear in Sec. 3, will be described and implemented within the context of the algorithm described in Refs. 7 and 9. However, this fin treatment can be adapted in a straightforward manner to other existing supersonic inviscid flow codes which have the capability of treating internal shock waves either by "tracking" or "capturing".

A body oriented cylindrical coordinate system (r, ϕ, z) depicted in Fig. 1 is used in this study. Standard notation will be used; viz., ρ is the density, p the pressure, h the enthalpy, a the sound speed, γ the ratio of specific heats, and \vec{q} the velocity vector with components (u, v, w) as indicated in Fig. 1. It is assumed that for $z \geq z_0$, $w > a$ everywhere. For computational purposes, attention is restricted to the region $z \geq z_0$ between the body alone, expressed by $r=b(\phi, z)$ and the bow shock wave, expressed by $r=c(\phi, z)$. This region is mapped into the computational region $Z \geq z_0$, $0 \leq X \leq 1$, $0 \leq Y \leq 1$ by the standard normalizing transformations ^{1,4,5,7}

$$Z = z, X = (r-b)/(s-b), Y = \phi/\phi_0 \quad (1)$$

where ϕ_0 is the ϕ value of a symmetry plane if one exists and 2π otherwise.

Every computational plane $Z = \text{constant}$ is covered by a grid with uniform ΔX and ΔY . As will be described in Sec. 3, the fin cross-section is represented by the thin fin approximation as double valued grid points lying along portions of certain $Y = \text{constant}$ grid lines; cf., Fig. 2.

The algorithm for advancing the unknown flow field quantities from $Z = Z^k$ to the next axial station $Z = Z^{k+\Delta Z}$ depends on the location of the individual mesh points in the shock layer. These are divided into the following four types: interior, body surface, shock, and fin surface point. The numerical procedures used to treat the first three types of points are essentially the same as those given in Refs. 7 and 9. The only difference is that the inviscid, weak conservation equations have been recast to simplify the source term. For

interior points the MacCormack predictor-corrector scheme is applied directly to the associated conservation form of these equations in the X, Y, Z space. The points on the body and bow shock surfaces are treated using predictor-corrector methods applied to certain characteristic compatibility relations for each surface along with the appropriate flow boundary conditions. See Refs. 7, 10 and 11 for complete details.

3. Computational Procedure for Fin Surfaces

The Thin Fin Approximation

The thin fin approximation is applicable to fins with surfaces that lie close to a constant ϕ plane, say $\phi = \phi_f$, which is defined as the fin plane. The fin geometry is assumed to be represented by two surfaces, the upper and lower surfaces, each described independently by relations of the form

$$\phi = \phi_f + \sigma(r, z). \quad (2)$$

In the cross-section $Z = \text{const.}$, the actual fin surfaces will lie within the computational mesh as shown in Fig. 2. The thin fin approximation assumes that $|\sigma|$ is small and thus places the fin surfaces along the fin plane corresponding to $Y = Y_f$ in each $Z = \text{constant}$ plane. Although the fin is approximated by a zero thickness plane lying on $\phi = \phi_f$, the correct description of the fin surface slope is retained. Only the fin surface slopes and their r and z derivatives are required. The derivatives of σ , correct to $O(|\sigma|)$, are given by

$$\begin{aligned} r\sigma_r &= \tan \theta, \quad r\sigma_z = \tan \nu, \\ r\sigma_{rr} &= \sec^2 \theta (\theta_r - \sigma_r) - \sigma_r \\ r\sigma_{zz} &= \sec^2 \theta \nu_z - \sigma_r \tan^2 \nu, \quad r\sigma_{rz} = \sec^2 \theta (\theta_z - \sigma_z) \end{aligned}$$

Here θ and ν are the angles between the fin surface tangency plane and the fin plane in the r and z directions, respectively. Within the restriction that $|\sigma|$ be "small", the thin fin approximation can be applied to arbitrary fin geometries including surfaces with discontinuous slopes and fins with "small"

deflections, camber, and variations in dihedral.

The Numerical Procedure For Fin Surfaces

The numerical algorithm for treating fins by the thin fin approximation requires that the computational mesh be chosen so that each fin plane is coincident with a computational mesh plane, $Y = Y_f$. Two sets of computational points are carried on the $Y = Y_f$ plane to describe the flow properties on the upper and lower surfaces, (cf., Fig 2). As the calculation is marched down the length of the body, fin surfaces are encountered on $Y = Y_f$. Thus a point at some X may at one axial location be an interior flow field point and in the next axial step move onto the fin. The interior point is split into two points corresponding to the upper and lower fin surfaces. The fin points thus created are referred to as leading edge points. For a fixed X , a pair of points which are on the fin at one axial step can in the next step move off the fin and become a single interior flow field point. Such a point will be referred to as a trailing edge point. The flow variables at leading and trailing edge points are determined from an appropriate local analysis which is described in the following subsections. The adjustment for the presence of a leading or trailing edge is made immediately after the completion of the step in which the edge is encountered. The values of the flow variables prior to the adjustment are termed "upstream" while the adjusted values are termed "downstream".

All points on the fin surfaces not designated leading or trailing edge points are advanced using certain characteristic compatibility relations and the tangent flow boundary condition as described in Ref. 11. These relations are evaluated numerically within the framework of the thin fin approximation by placing all fin surface flow quantities on the fin plane and making all evaluations at the fin plane. The juncture of the fin and the body is assumed

to be a sharp corner where the flow velocity is directed along the corner. This condition and special characteristic relations¹¹ are used to advance the points along the juncture. Discontinuities in the fin surface slope are explicitly treated using essentially the same techniques as those for treating discontinuities in the body surface slopes given in Refs. 7 and 10 with appropriate modifications to account for the form of (2) defining the fin surface.

Leading Edge Points

The downstream flow properties at leading edge points are determined by a local analysis based on the computed flow upstream of the edge and the prescribed local fin geometry. Using this information, the Mach number normal to the leading edge, M_n , is determined. If $M_n > 1$ an attached shock or expansion fan occurs in most cases which permits a local analysis (see, e. g. Chapter XI, of Ref. 12). The velocity component tangent to the edge, is unaffected by the edge and all other downstream flow quantities are determined by turning the normal flow component using either an oblique shock or a Prandtl-Meyer expansion. A similar procedure for the case of an attached oblique shock has also been used in Ref. 6. In Ref. 6, the leading edge shocks are "tracked" downstream of the edge whereas in the present work these shocks are "captured" using the conservative and dissipative properties of the interior point scheme without additional numerical smoothing.

At leading edges where a compression turn is required, the condition $M_n > 1$ does not guarantee the existence of an attached oblique shock. For sufficiently large turning angle, δ , a detached shock wave will be present and a purely local analysis is, at best, an approximation. However, it has been possible to formulate empirical rules for determining reasonable leading edge

conditions. This procedure predicts an effective shock angle which is used to turn the normal flow component and assigns the streamline direction at the leading edge. When a detached shock occurs, the upper and lower fin surfaces are treated independently of one another. If one surface permits either an attached shock or a Prandtl Meyer expansion this procedure is applied as described above. Such an approach is suggested by the experimental data of Ref. 13. When the upstream flow crosses the edge with $M_n < 1$, the flow at the leading edge is free of shock waves. On an expansion surface the flow is accelerated to sonic velocity and then turned into the plane of the wing using a Prandtl-Mayer expansion. A compression surface is treated by isentropically compressing the flow to an empirically determined Mach number and specifying a streamline direction.

On highly swept wings, which form strong leeside vortices, M_n is usually small (i.e. $M_n \ll 1$) or negative. On such configuration the streamlines flow outwards at wing tip, and leading edge pressure and density values are set equal to those at the adjacent wing point while the resulting velocity vector is directed along the wing tip.

For the leading edge points at the fin-body juncture a special procedure is required. The flow in the vicinity of these points features a complicated shock interaction pattern which probably cannot be resolved within the relatively coarse mesh used in the present calculations. Accordingly, a simple heuristic procedure is used to determine the flow variables immediately downstream of the leading edge corners. The upstream velocity vector on the body lies in the body tangency plane which also contains the corner direction. The flow downstream of the leading edge corner is obtained by rotating the velocity vector within the body tangency plane and aligning it with the corner using either the oblique shock or the Prandtl-Meyer turning relations.

The technique of applying a local analysis at the leading edge is employed to improve the quality and robustness of the solution near the leading edge and thus to enhance the use of coarse grids. At a sufficiently large number of steps away from the edge, the influence of the conditions employed at a leading edge will disappear and all treatments result in similar flow fields. In certain situations it is difficult to determine reasonable leading edge conditions. Accordingly, the strategy of marching directly across the leading edge without applying a leading edge adjustment has been used. This approach works well as long as the pressure rise at the leading edge is restricted to less than a factor of two.

Trailing Edge Points

At a trailing edge the two points on $Y = Y_f$, representing the upper and lower fin surfaces, are coalesced into a single interior flow field point. A local analysis is used to determine the flow downstream of the edge from the computed flow on each fin surface upstream of the edge and the given local fin geometry.

One approach, described in Ref. 11, consists of turning the normal flow component from both surfaces, using an oblique shock and Prandtl-Meyer expansion, onto a plane containing the trailing edge. The orientation of this plane is iteratively determined by requiring that pressure on both surfaces be equal. The conditions on both sides of this plane are then averaged to produce the conditions at the coalesced interior flow field point. Such a procedure can be applied only where M_n is sufficiently large to assure the existence of the necessary oblique shocks. In practice it has been found that averaging the upper and lower surface at the trailing edge without using the iterative process to determine pressure does not change computed results significantly. This shorter process is currently used whenever the trailing edge is supersonic. At subsonic trailing edges an averaging process is used

but the interior flow point on the fin plane and adjacent to trailing edge point is included in the average.

Special Differencing Procedures

Special treatment is provided for advancing the outermost grid point on the fin surfaces, at say $X = X_\ell$, and the adjacent interior flow point, $X_{\ell+1} = X_\ell + \Delta X$. The MacCormack scheme for advancing the interior flow point, $X_{\ell+1}$, must be modified since there are two sets of flow values at X_ℓ corresponding to the upper and lower fin surfaces. The present procedure is to advance the flow variables at $X_{\ell+1}$ by the basic interior point scheme using the flow values at X_ℓ corresponding to the upper surface and then repeating the calculation at $X_{\ell+1}$ using the lower surface values at X_ℓ . The two values of the conservation vector, U , are then averaged at the end of the predictor and corrector step to obtain the final value of U at $X_{\ell+1}$. The outermost fin points are advanced using the interior flow values at $X_{\ell+1}$.

An alternate strategy is to use one sided differences to advance the interior point at $X_{\ell+1}$. If this option is used the outermost fin point is also advanced without wing information at $X_{\ell+1}$. Differences in the X direction which would normally be formed using properties at X_ℓ and $X_{\ell+1}$ are set to zero. This option is used in most cases which use a local analysis at the leading edge.

Special Y differencing procedures are also applied downstream of leading edges which feature attached shock waves. It has been found in example calculation on two dimensional rectangular fins that the standard procedure for advancing the fin surface points predicts inaccurate surface pressures immediately downstream of such discontinuities. In this region, the Y differences used to advance the fin surface flow variables must be taken across the oblique shock generated by the leading edge and these Y differences will be unrealistic for a few steps following the formation of a leading edge

point. To circumvent this problem, the Y differences used in the fin surface calculation are multiplied by a factor which is zero at the leading edge and increases to unity after a few steps. The selection of the number of steps for which the Y derivatives are damped is based on the values of the Y derivative at the leading edge and on an estimate of the number of steps required for the shock to move out to the adjacent row of points.

In a number of the examples to be discussed, calculations will feature large body or tip vortex. When such cases are run on fine grids it is necessary to add dissipation to the interior flow, body and wing surfaces. This is accomplished using a Shuman filter with a density switch.¹⁶

4. Numerical Results

The results computed with the present code are presented in this section and compared with the experimental data. The investigated cases consist of body alone, body-wing, body-tail and body-wing-tail configurations. The wing and tail surfaces have sharp leading and trailing edges which feature normal velocity components that range from subsonic to supersonic. All computations assume a perfect gas with $\gamma = 1.4$. The computations are started near the body vertex using a numerically generated conical flow field (see ref. 11).

Inviscid calculations for the body alone configuration at high incidence produce a leeside crossflow shock which is not present in the experimental flow field. A more realistic leeside flow field can be generated by applying an additional boundary condition, or Kutta condition, near the experimentally observed separation point. This destroys the crossflow shock and produces a leeside recirculation region or a vortex which is in agreement with experimental observations. In the current study the separation point is specified as a function of distance along the body. The separation location generally falls between two surface grid points and both of these points are specially treated.

The basic presumption in specifying properties at these points is that the velocity at the separation point should be oriented along the separation line and that pressure and density should vary smoothly across the separation line. The resulting flow field is illustrated in Fig. 3 and is qualitatively similar to the results of Oberkampf¹⁵, which are also shown. Similar numerical results have been obtained by Klopfer and Nielsen¹⁶ although their method of specifying the Kutta condition differs from that outlined above.

A comparison of calculated and measured surface pressures is given in Fig. 4 using the experimental data of Perkins and Jorgensen.¹⁷ Pressure profiles have been computed with and without use of the Kutta condition. Clearly, application of the Kutta condition improves the agreement between calculation and experiment.

In Ref. 18 a tangent ogive body, equipped with tail fins of several different planforms, is tested in supersonic flow. Numerical results have been compared to experimentally measured surface pressures taken at Mach 3.7 for configurations featuring clipped delta and cranked tail fins. Both types of fins feature surface slope discontinuities at various locations along the surface. The freestream Mach number is sufficiently large to allow an attached shock solution at the fin leading edge in almost all cases. Calculated and measured surface pressures are compared for the cranked delta wing in Fig. 5 and are in reasonable agreement. The scatter in the experimental data is a result of plotting experimental measurements from several different runs. On fin surfaces, which feature strong leading edge shocks, the leading edge pressure is over-predicted at the root and the calculated pressure jumps, occurring at the various surface discontinuities, also tend to be greater than experimental values. The thick corner boundary layer and the complex leading edge shock-body boundary interaction, presumably, have a large influence on the corner and

account for much of this discrepancy. Another area of disagreement occurs along the tip. Here predicted and measured pressures are of similar value, but the experimental pressure profile features a negative slope, while the numerical pressure distribution is almost constant. It is not clear whether this discrepancy is due to viscous phenomena. On fin surfaces which have a weak leading edge shock (or expansion) the predicted and measured fin tip pressure profiles are in good agreement. Also, the leading edge pressure at the corner is close to the experimental value. Over the entire span, calculated pressures on the trailing edge panel tend to be less than measured, probably reflecting the existence of a very thick boundary layer or separation.

Wind tunnel tests on the swept wing configurations of Ref. 19 (see Fig. 6) offer an opportunity to compare calculation with experiment for cases where detached shock waves are predicted to occur. Calculations have been compared to experiment at the Mach numbers of 2.96, 3.95 and 4.5, and at angles of attack of 0° , $+2^\circ$, $+4^\circ$ and $+6^\circ$. (Here positive and negative incidence refers to the windward and leeward wing surfaces respectively). The body-wing geometry, and sample results are shown in Fig 6&7. These indicate that the current computations accurately reflect changes in Mach number and angle of attack.

The data of Ref. 19 also include pressure measurements along a pitch plane body meridian. At positive incidences the instrumented ray is on the windward side of the body while at negative incidences it is on the lee-side. These measurements are compared to numerical results at an incidence of 6° , 0° and -6° in Fig. 8 for a Mach number of 2.96. At $\alpha = 6^\circ$ the body alone data are in good agreement. The influence of the wing on the body causes an increase in the experimentally measured pressure. This increase is

correctly reflected by the calculations, but the peak predicted values are located approximately one caliber downstream of the measured ones. At an incidence of 0° , the same trend is visible but the lagging appears to be somewhat less. When the angle of attack is changed to -6° , the presence of the wing causes a decrease in body pressure. In this case, the body alone calculation does not agree well with experiment, presumably due to viscous effects. The body features a decreasing diameter near the base which undoubtedly results in changes in the effective body shape due to boundary layer thickening or separation. The calculated flow field features a crossflow shock near the base which produces an increase in the leeward meridian pressure profile. The numerical results for the body-wing configuration are much closer to experiment and feature the correct downward change in the body surface pressure. The predicted onset of the wing influence on the leeward meridian body pressure does not appear to lag the experimentally measured one.

On Fig. 9 additional comparisons are shown of computed and measured surface pressures for a delta planform wing-body configuration for which detached leading edge shock is predicted. The configuration features a 6-percent thick, double-wedge wing at Mach 2.86 at an angle of incidence of 8.6° . Experimental measurements²⁰ were available along several span-wise locations and are in agreement with present computations.

Normal force and moment prediction for an airplane type configuration is illustrated on Fig. 10. The computations were performed at Mach 2 at angle of incidence of 10° and are in good agreement with experiment.²¹ The influence of the tail is also predicted correctly. The wing and tail surfaces of this configuration were essentially flat and had attached leading and trailing edge shocks.

On Fig. 11 computed normal force and center of pressure coefficients are compared with experiment²² for an ogive-cylinder body with a cruciform type wing and tail surfaces. Three wing planforms, yielding different leading edge sweep angles, are included along with deflected and undeflected tail surfaces. The comparison is made at Mach 2.86 at incidences of 6° and 12° , providing subsonic leading edge conditions for all three wing planforms.

The computed normal force and center of pressure values are in reasonable agreement with experiment for all three wing planforms. Variation in wing aspect ratio produces a monotonic change in the computed normal force coefficient. This is contrary to experimental results in which the minimum value is yielded by a wing with an intermediate aspect ratio. Presumably, the non-linearity in experimental results is due to the influence of the leeside vortex which is not modeled with sufficient accuracy in the computations.

The computed crossflow velocities for the wing of the minimum aspect ratio is qualitatively illustrated on Fig. 12. No experimental data were available for comparison.

6. Concluding Remarks

A numerical method has been developed which predicts the inviscid supersonic flow field about finned configurations of engineering interest. The computational requirements are generally modest. For example, the wing-body and cruciform body-tail cases, examined in the preceding sections, nominally required 3 and 7 minutes respectively of CPU time on a CDC 6500. The present study differs from previous methods by treating the fin and body geometries separately. At present, a thin fin approximation is employed which limits the applicability of the computational procedure to relatively slender fins with sharp leading edges. The fins must approximately lie along planes which intersect at a line inside the missile body. With this formulation it is possible to treat a wide variety

of configurations of engineering interest which can feature an arbitrary number of fins and tails containing small deflection, camber or variation in dihedral. By appropriate modeling at wing tips and at estimated body separation points, it appears feasible to simulate flow field vortices.

Acknowledgement

This work was jointly supported by the Naval Sea Systems Command and the Naval Air Systems Command. The authors would also like to acknowledge the enthusiastic support of Frank Moore of the Naval Surface Weapons Center, Dahlgren, VA., throughout the course of this investigation.

REFERENCES

1. Thomas, P. D., Vinokur, M., Bastianon, R., and Conti, R. J., "Numerical Solution for Three-Dimensional Inviscid Supersonic Flow," AIAA J., Vol. 10, No. 7, 1972, pp. 887-894.
2. Moretti, G., Grossman, B., and Marconi, F., "A Complete Numerical Technique for the Calculation of Three-Dimensional Inviscid Supersonic Flows," AIAA Paper 72-192, San Diego, Calif., 1972.
3. Marconi, F. and Salas, M., "Computation of Three Dimensional Flows About Aircraft Configurations," Computers and Fluids, Vol. 1, 1973, pp. 185-195.
4. Kutler, P., Reinhardt, W. A., and Warming, R. F., "Multishocked, Three-Dimensional Supersonic Flowfields with Real Gas Effects," AIAA J., Vol. 11, No. 5, 1973, pp. 657-664.
5. Kyriss, C. L. and Harris, T. B., "A Three-Dimensional Flow Field Computer Program for Maneuvering and Ballistic Re-entry Vehicles," Tenth USN Sym. on Aeroballistics, July, 1975.
6. Marconi, F., Salas, M., and Yaeger, L., "Development of a Computer Code for Calculating the Steady Super/Hypersonic Inviscid Flow Around Real Configurations, Vol. I-Computational Techniques", NASA CR 2675, April, 1976.
7. Solomon, J. M., Ciment, M., Ferguson, R. E., Bell, J. B., "Inviscid Flowfield Calculations for Reentry Vehicles with Control Surfaces," AIAA J., Vol. 15, No. 12, 1977, pp. 1742-1749.
8. Moretti, G., "Conformal Mappings for Computation of Steady, Three-Dimensional, Supersonic Flows," Numerical/Lab. Computer Methods in Fluid Dynamics, ASME, 13, 1976.

9. Hindman, R. S., Kutler, P., Anderson, D., "A Two-Dimensional Unsteady Euler-Equation Solver for Flow Regions with Arbitrary Boundaries," AIAA Paper 1465, Williamsburg, VA., 1979.
10. Solomon, J. M., Ciment, M., Ferguson, R. E., Bell, J. B., and Wardlaw, A. B., "A Program for Computing Steady Inviscid Three-Dimensional Supersonic Flow on Reentry Vehicles, Vol. 1: Analysis and Programming," Naval Surface Weapons Center/White Oak, Silver Spring, MD., NSWC/WOL TR 77-28, Feb. 1977.
11. Wardlaw, A. B., Solomon, J. M., and Baltakis, F. P., "Supersonic Inviscid Flowfield Computations of Missile Type Bodies", AIAA Paper 80-0271, Pasadena, Calif., Jan. 1980.
12. Landau, L. D. and Lifshitz, E. M., Fluid Mechanics, Pergamon Press (Addison-Wesley), 1959.
13. Ferri, A., "Supersonic Flows with Shock Waves," in General Theory of High Speed Aerodynamics, High Speed Aerodynamics and Jet Propulsion, Vol. 7, Ed.: W. R. Sears, Princeton University Press, 1954.
14. Harten, A. and Zwas, G. "Switched Numerical Shuman Filters for Shock Calculations" Journal of Engineering Mathematics, 6, 2, April. 1972, pp. 207-216.
15. Oberkampf, W. L. and Bartel, T. J., "Supersonic Flow Measurements in the Body Vortex Wake of an Ogive Cylinder" AFATL-TR-78-127, November 1978.
16. Klopfer, G. H. and Nielsen, J. N. "Euler Solutions of the Body Vortices of Tangent Ogive Cylinders at High Angles of Attack and Supersonic Speeds" AIAA Paper 81-0361.
17. Perkins, E. W. and Jorgensen, L. H. "Comparison of Experimental and Theoretical Normal Force Distributions (Including Reynolds Number Effects) on an Ogive Cylinder Body at Mach Number 1.98", NACA TN 3716, May 1956.

18. Lamb, M., Sawyer, W. C. Wassum, D. L., Babb, C. D., "Pressure Distributions on Three Different Cruciform Aft-Tail Control Surfaces of a Wingless Missile at Mach 1.60, 2.36 and 3.70," Vol. II and III, NASA TM 80097, August 1979.
19. Jackson, C. M., Jr. and Sawyer, W. C., "A Method for Calculating the Aerodynamic Loading on Wing-Body Combinations at Small Angles of Attack in Supersonic Flow," NASA TN D-6441, 1971.
20. Jernell, L. S., "Comparisons of Theoretical and Experimental Pressure Distributions over a Wing-Body Model at Supersonic Speeds," NASA TN D-6480, Sept. 1971.
21. Jorgensen, L. H. and Nelson, E. R., "Experimental Aerodynamic Characteristics for Slender Bodies with Thin Wings and Tail," NASA TMX-3310, March 1976.
22. Spearman, M. L. and Sawyer, W. C., "Longitudinal Aerodynamic Characteristics at Mach Numbers from 1.6 to 2.86 for a Fixed-Span Missile With Three Wing Planforms" NASA TM 74088, Nov. 1977.

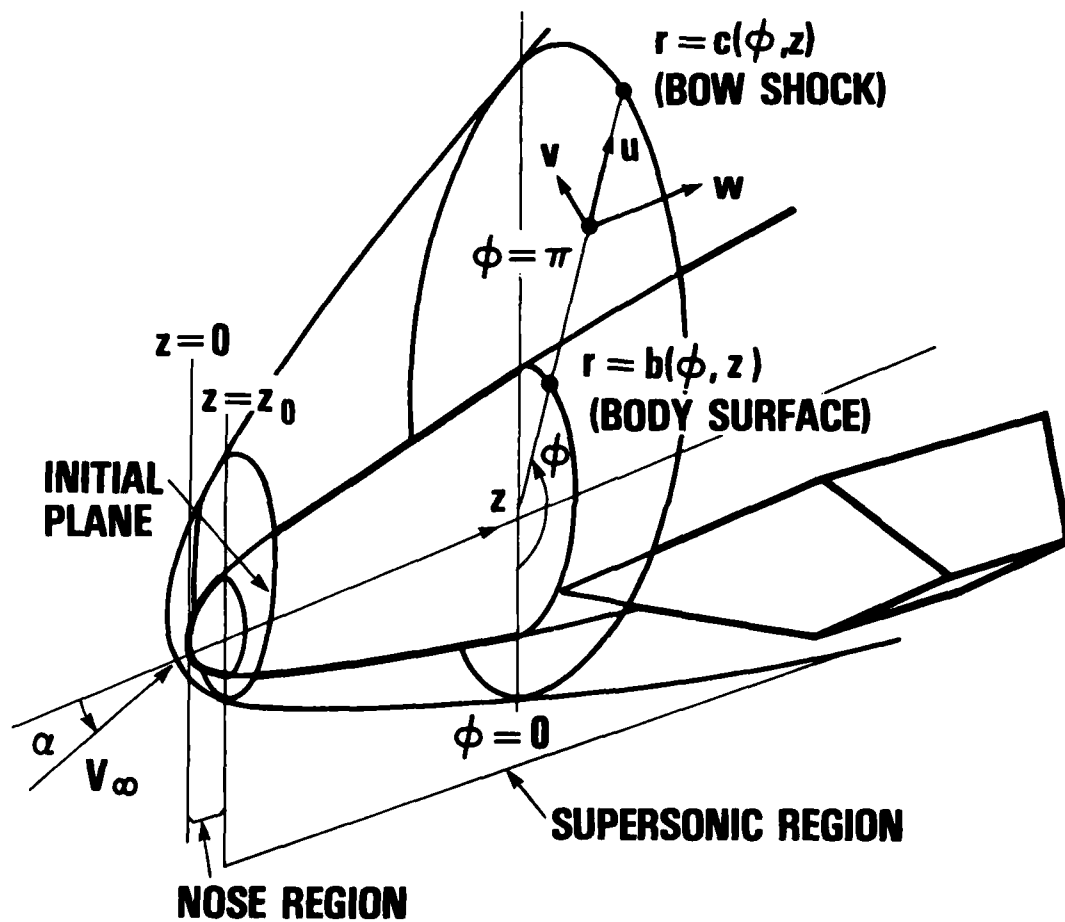


Figure 1. Cylindrical coordinate system used for inviscid flow calculation.

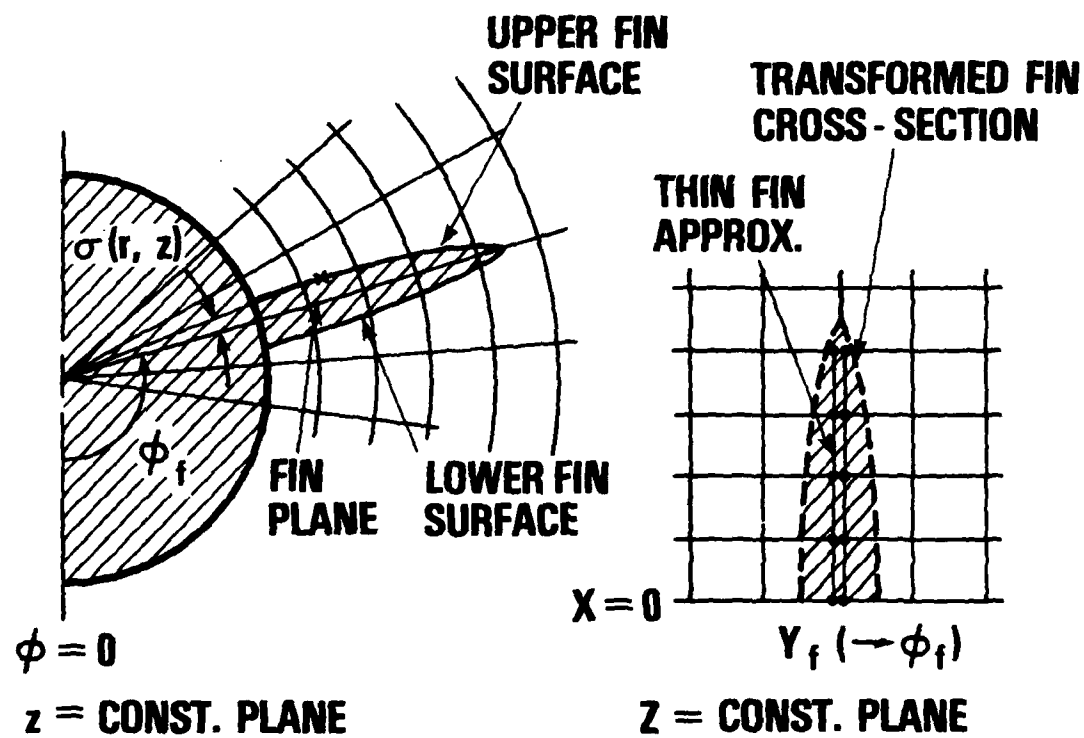
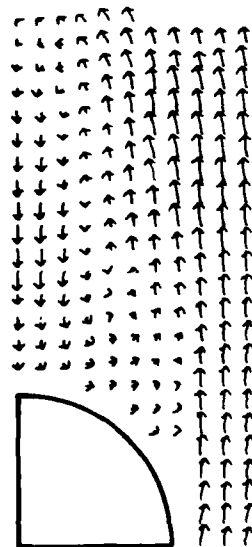


Figure 2. Cross-section view of the thin fin approximation.



COMPUTED



EXPERIMENTAL

Figure 3. Calculated and measured crossflow fields on a tangent ogive at Mach 3., $RE_D = 1.7(10^6)$, $\alpha = 15^\circ$.

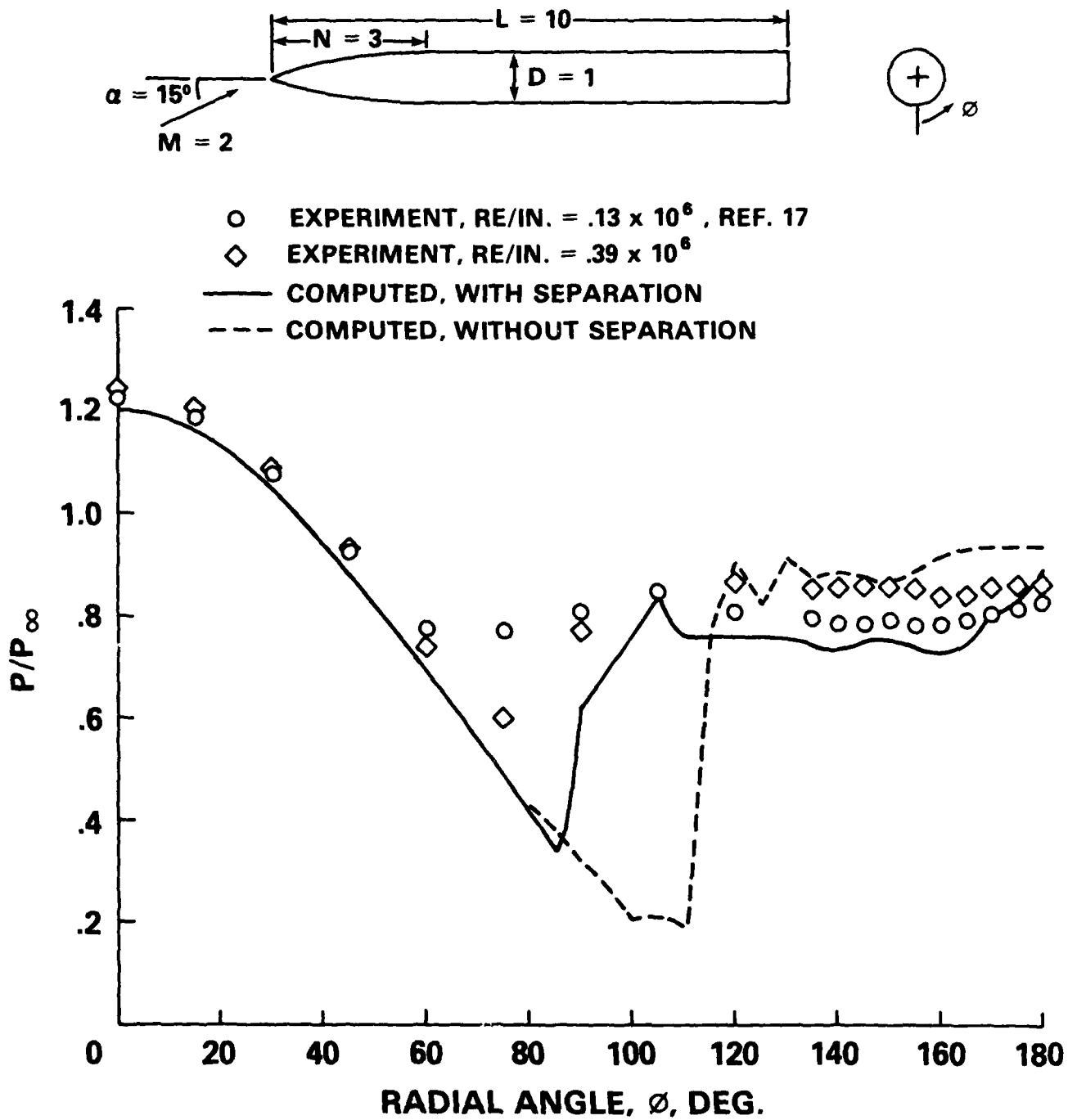


Figure 4. Calculated and measured surface pressures on a tangent ogive at Mach 2.

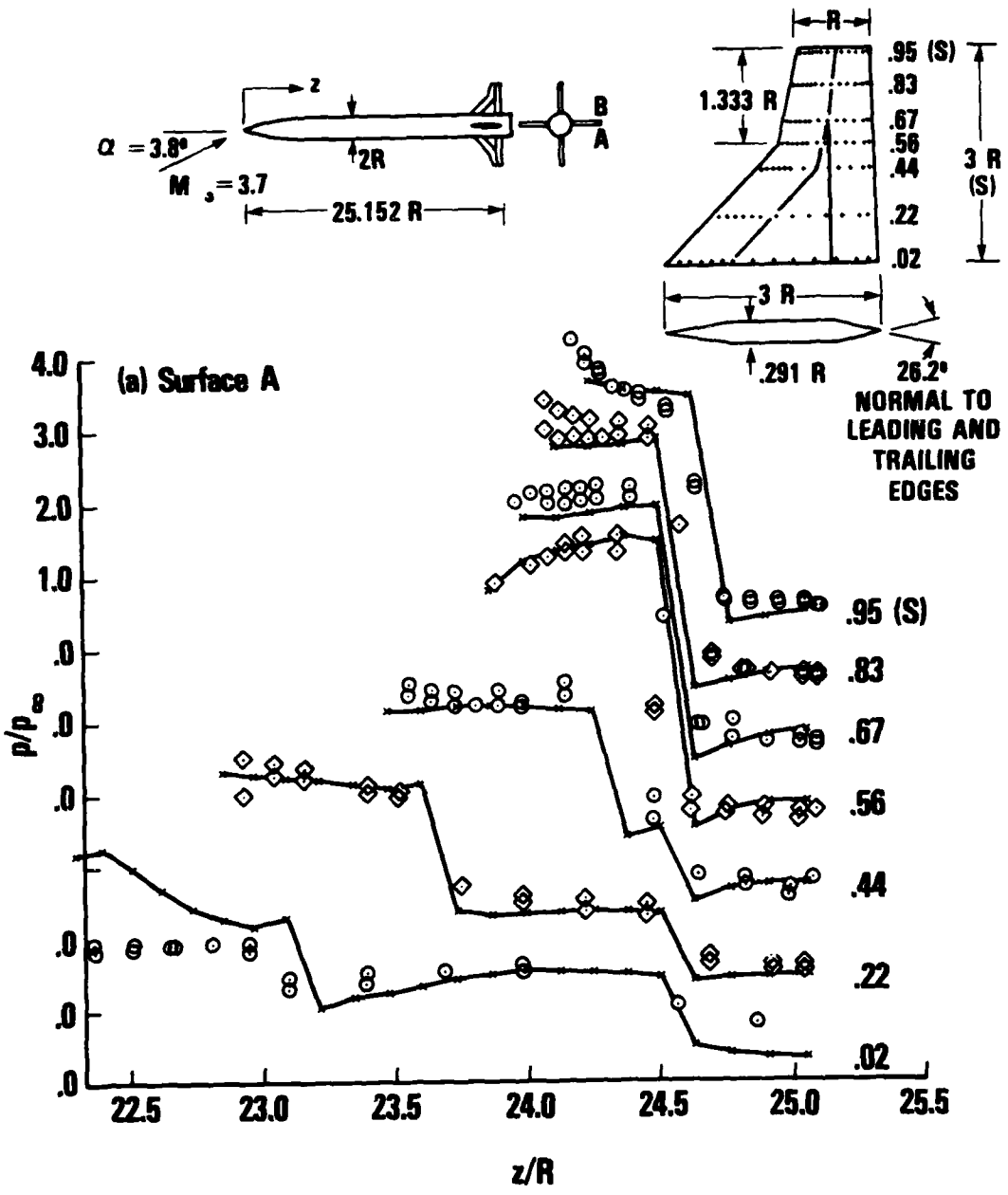


Figure 5. Comparison of computed and measured fin surface pressures on the cranked tail configuration at Mach 3.7, at $\alpha = 3.8^\circ$.

a. Surface A

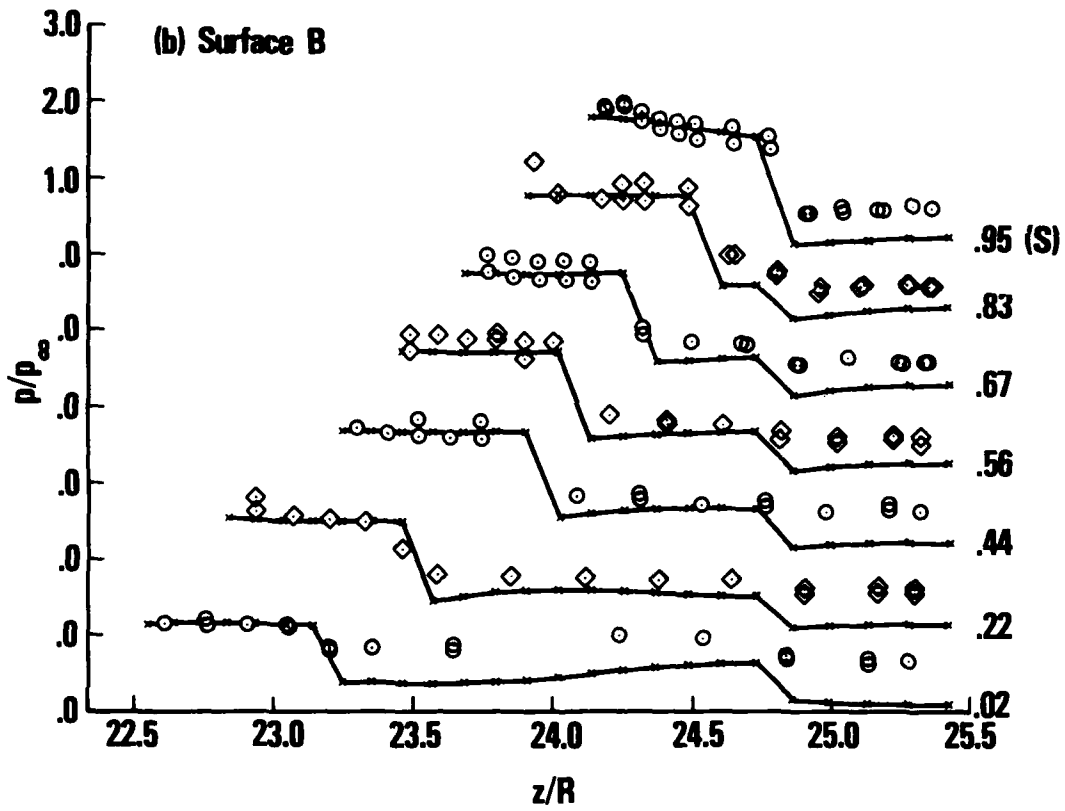


Figure 5. (Continued)

b. Surface B

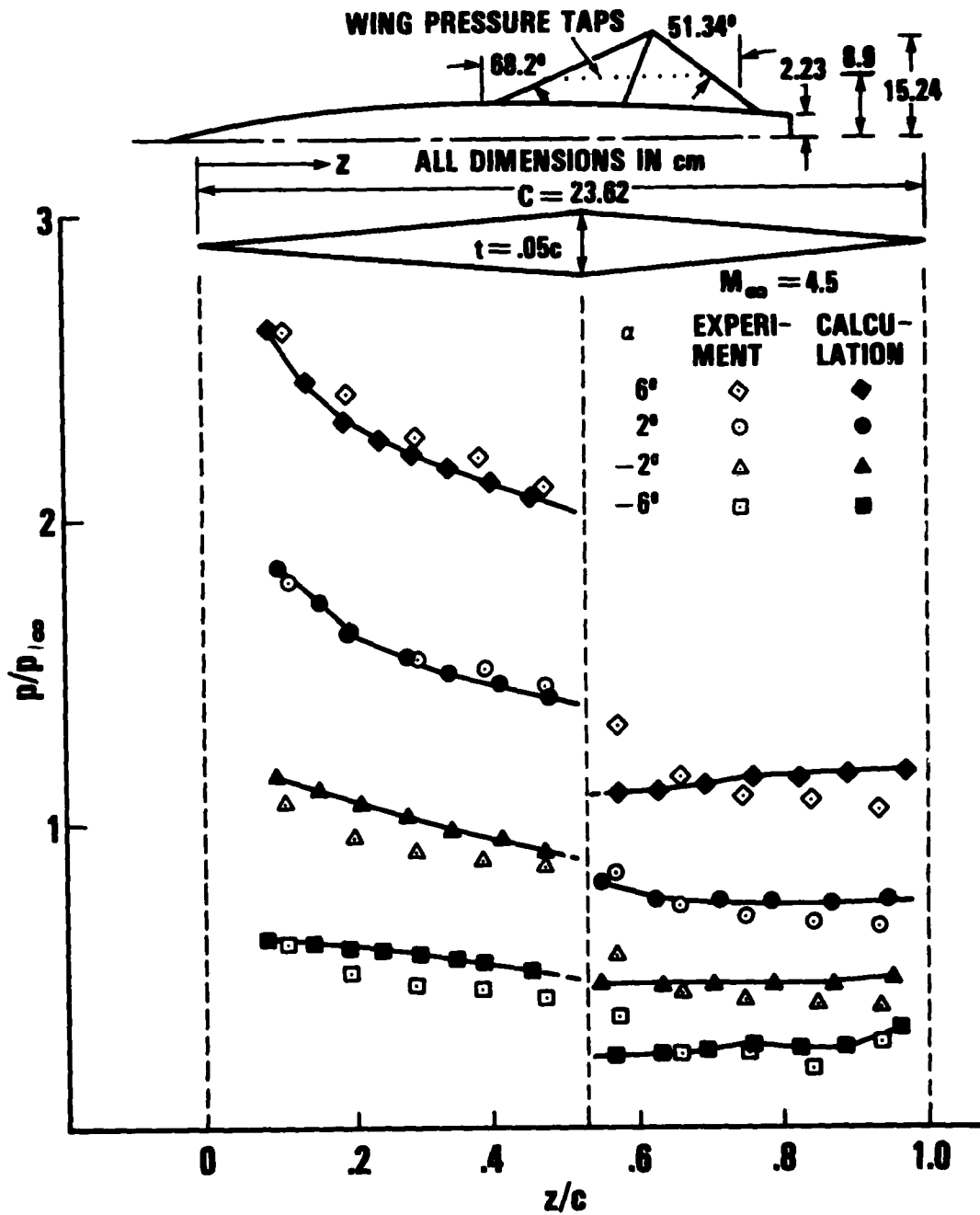


Figure 6. Comparison of computed and measured fin surface pressure as a function of incidence at Mach 4.5.

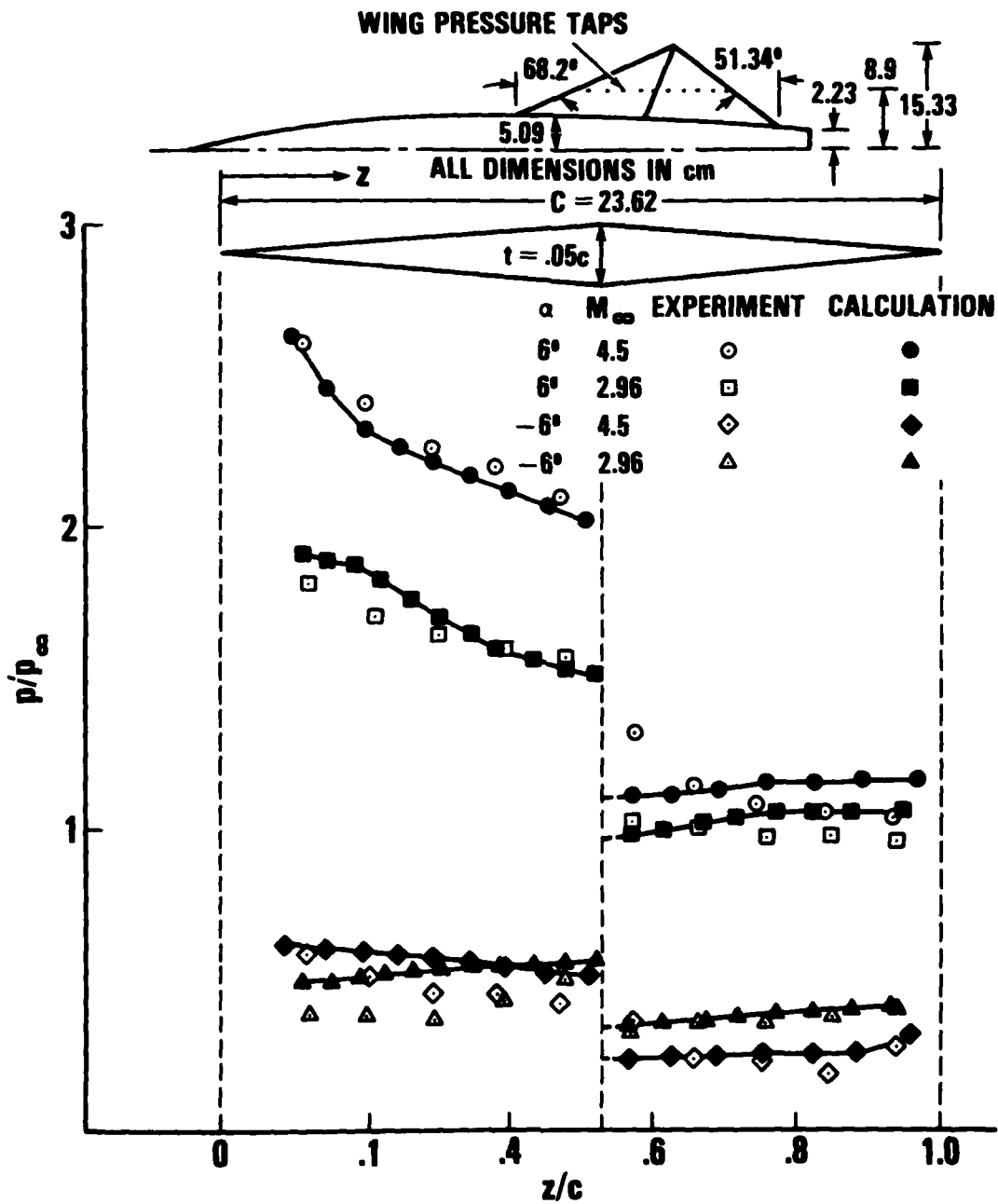


Figure 7. Comparison of computed and measured fin surface pressures at varying Mach numbers at $\alpha = \pm 6^\circ$.

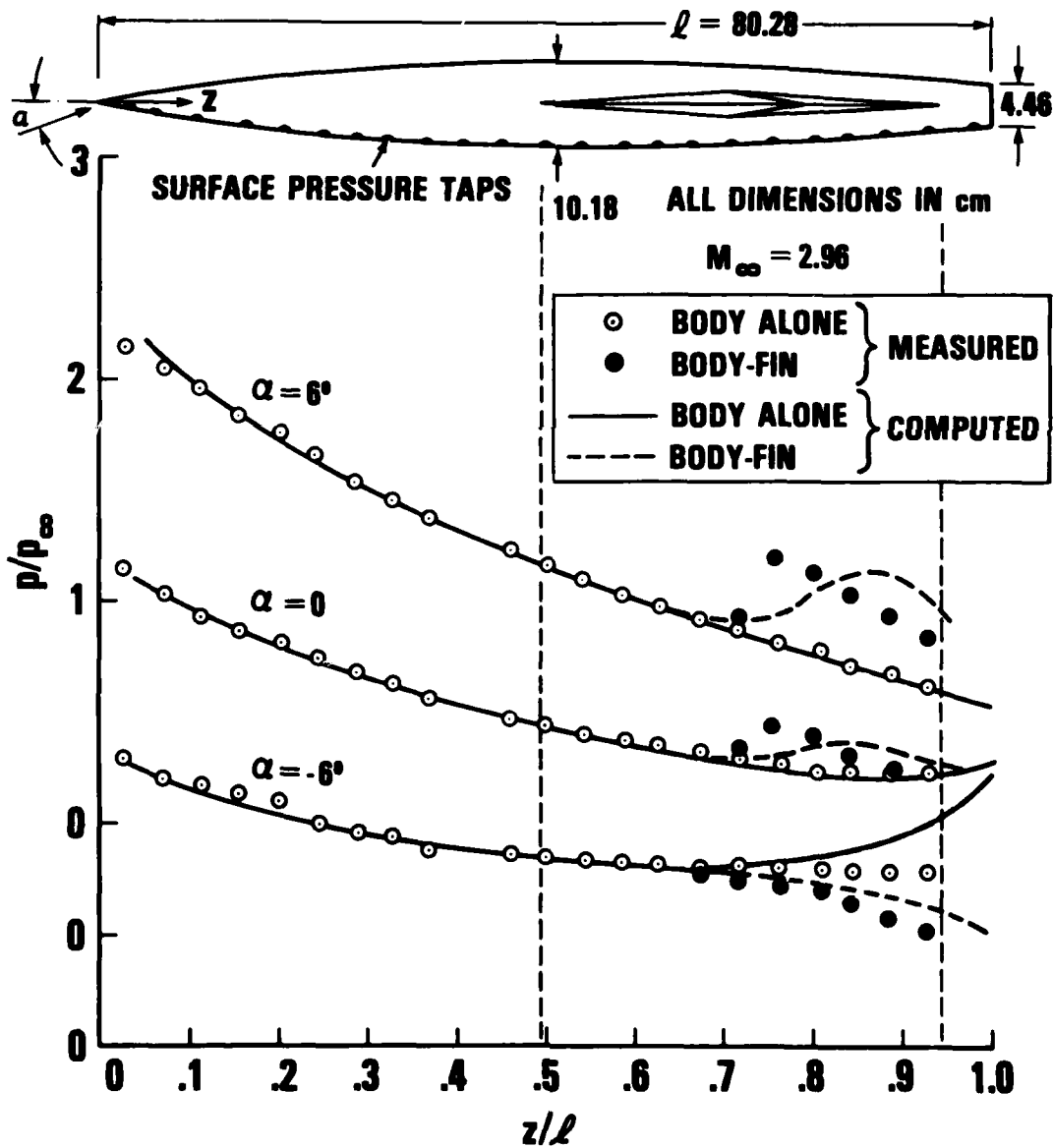


Figure 8. Calculated and measured body surface pressures with and without fins on the windward and leeward meridian at Mach 2.96.

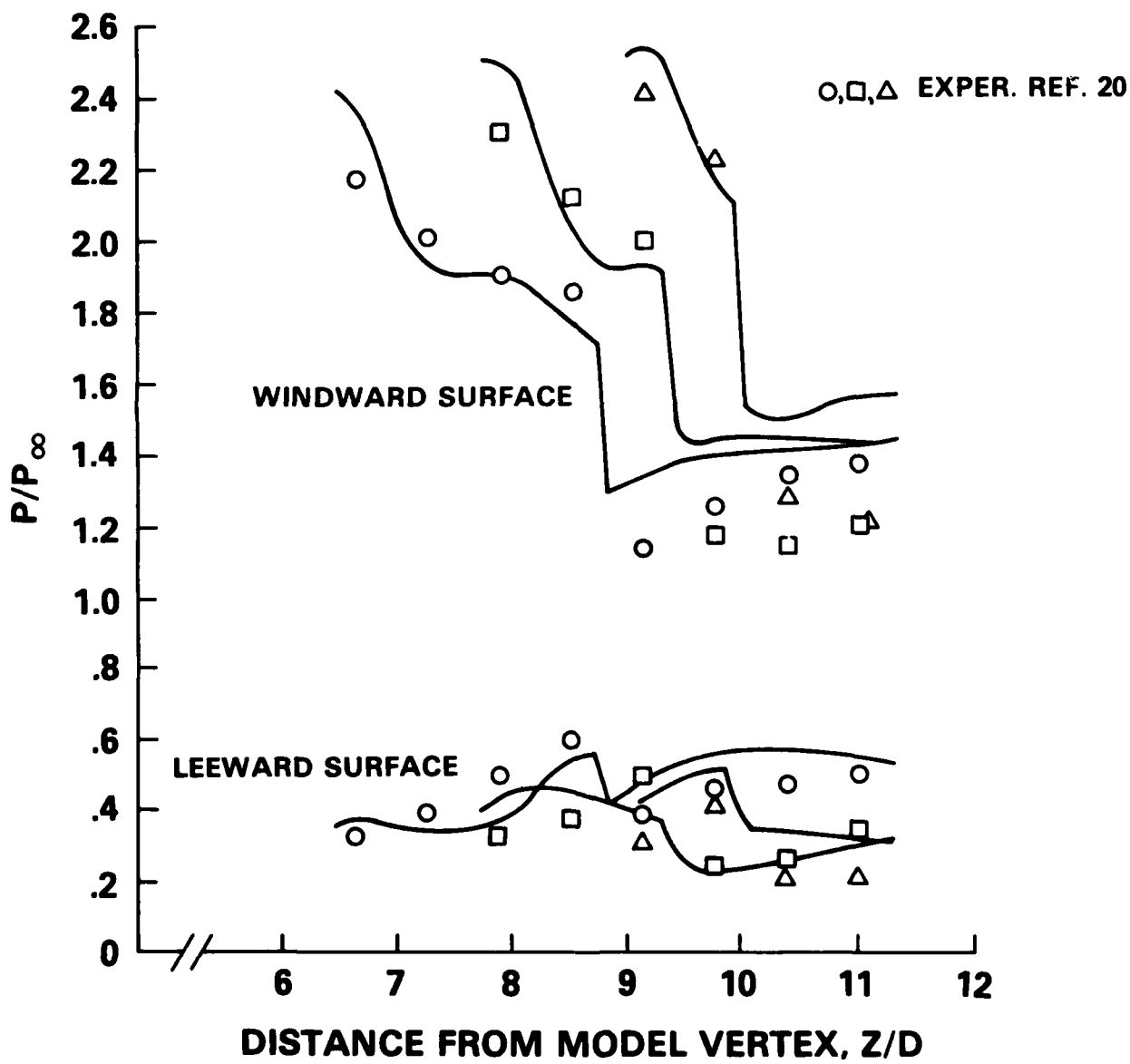
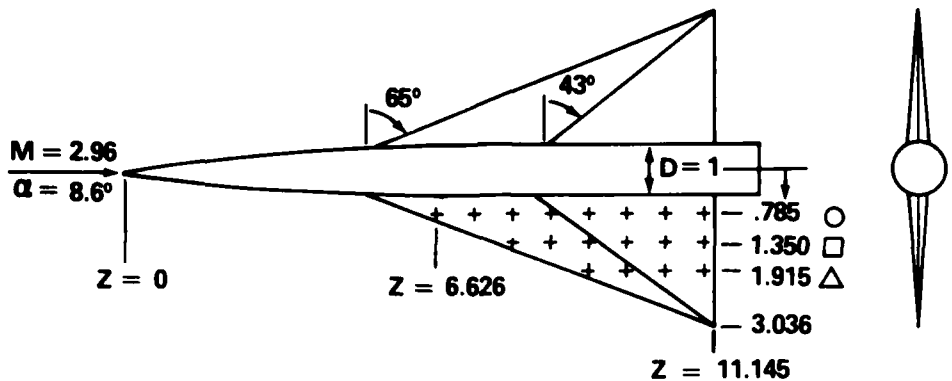
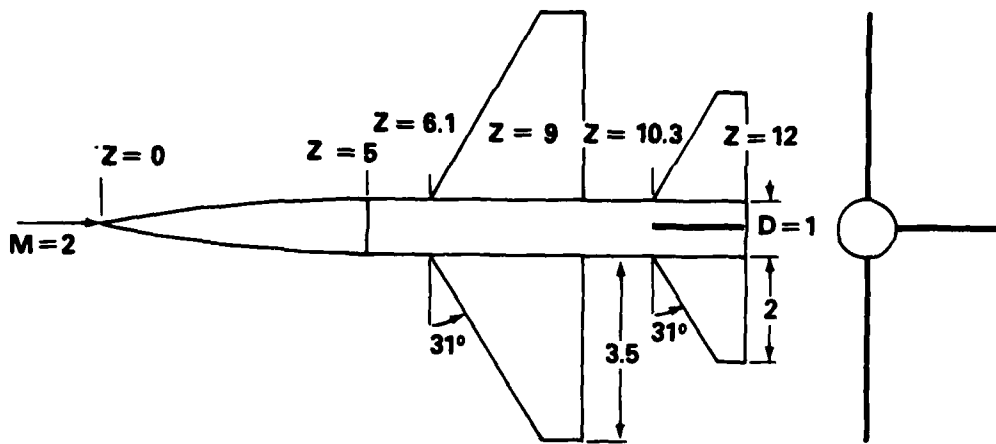


Figure 9. Comparison of computed and measured surface pressures at Mach 2.96 at $\alpha = 8.6$.



- BODY - WING
 - ◇ BODY - WING - TAIL
 - ◆ COMPUTED
- } EXPERIMENT, REF. 21

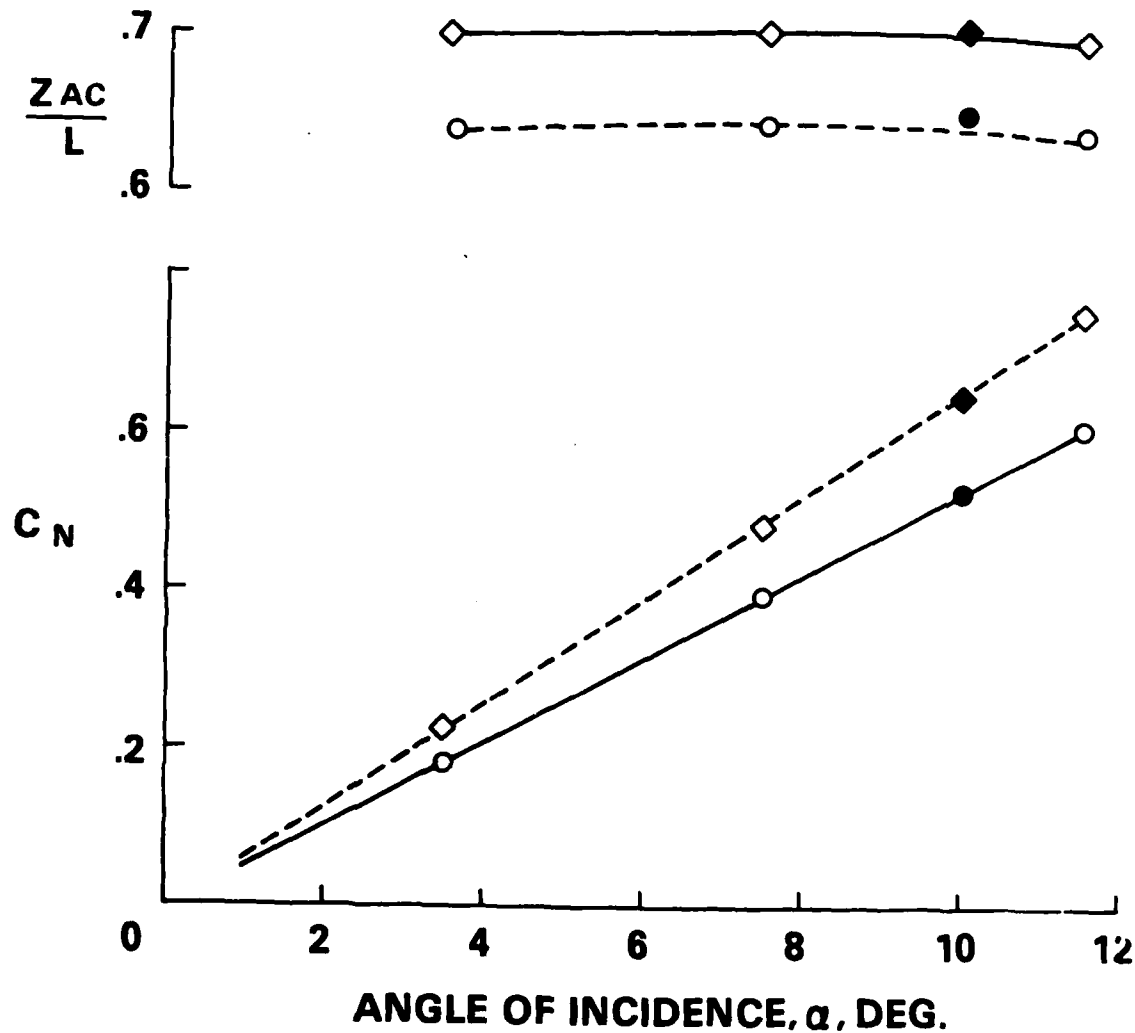


Figure 10. Measured and calculated normal force and center of pressure on a body-wing and body-wing-tail configurations at Mach 2.0.

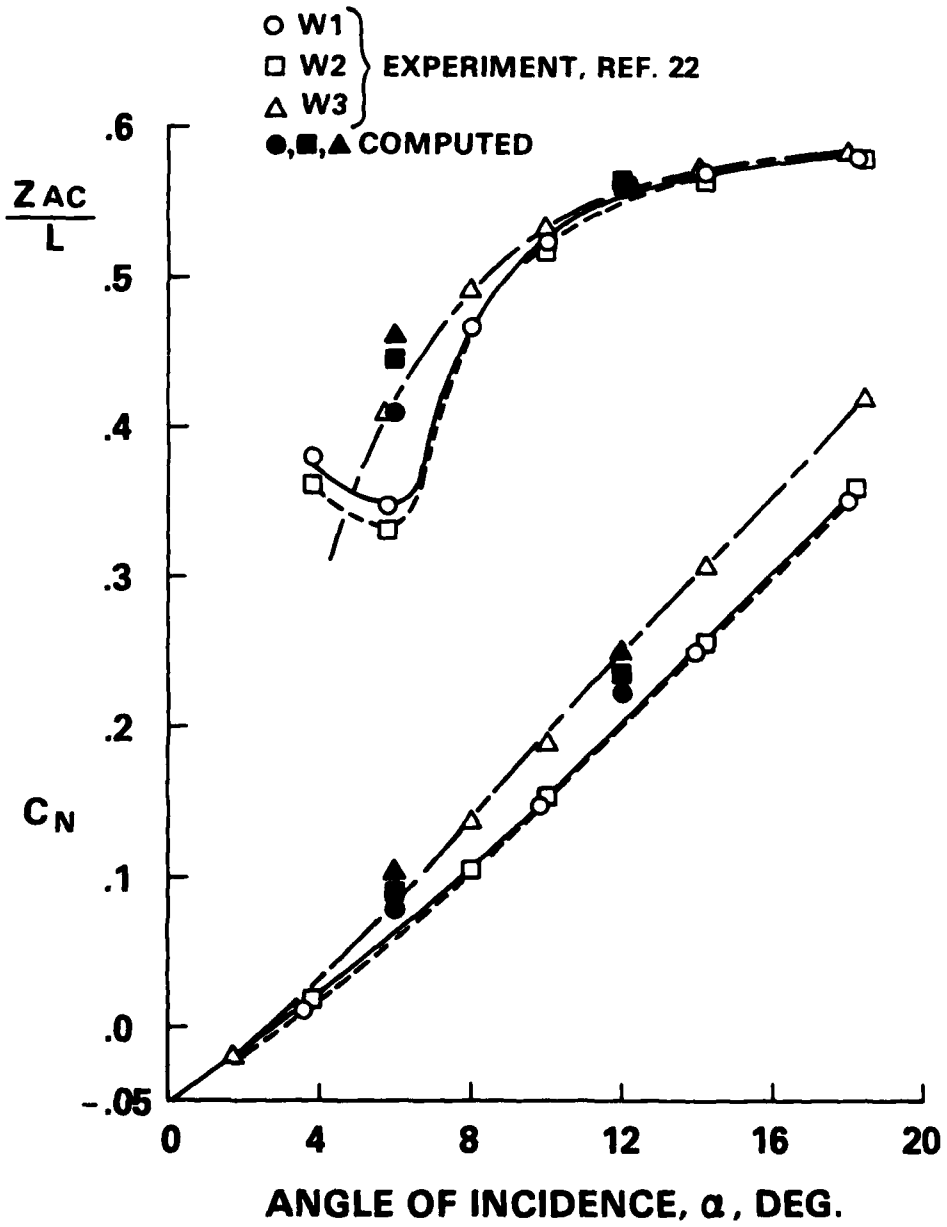
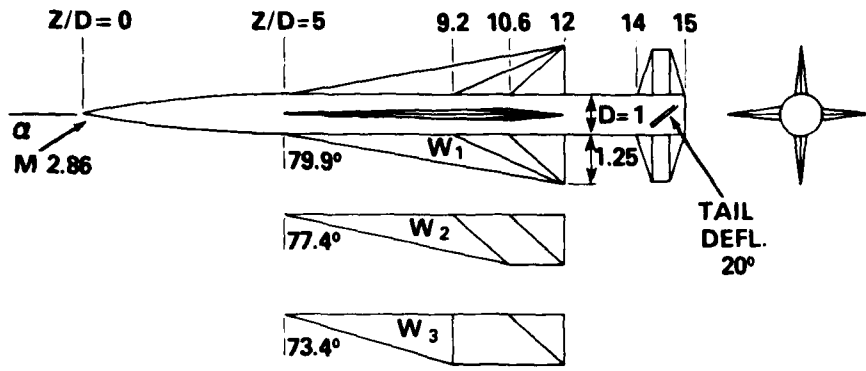


Figure 11. (Continued)

b. Tail deflected 20° ($\delta_T = -20^\circ$).

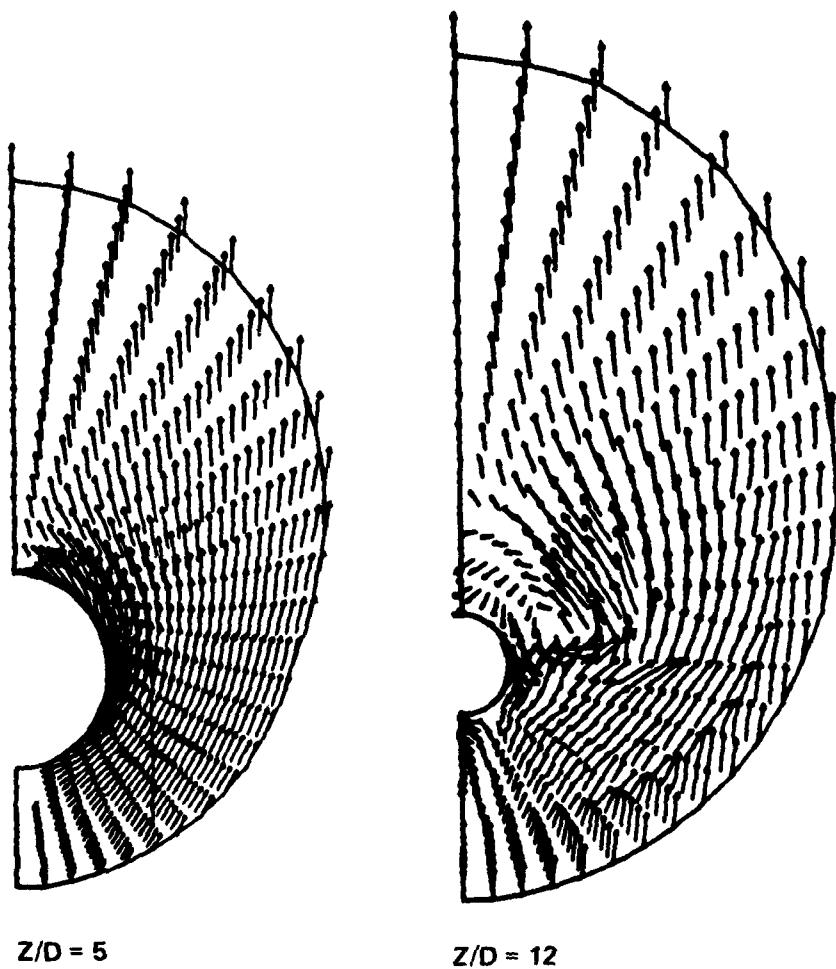
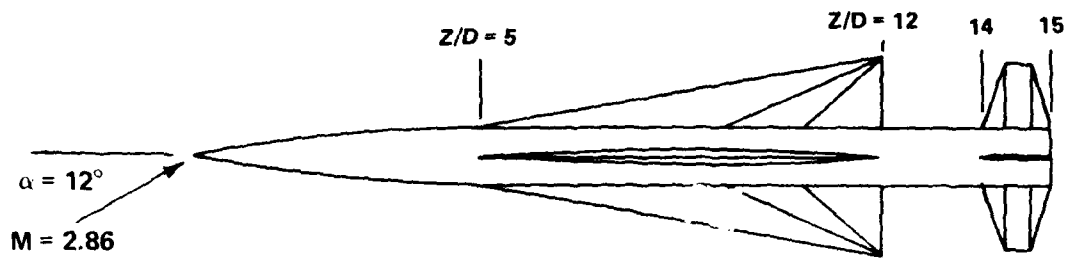
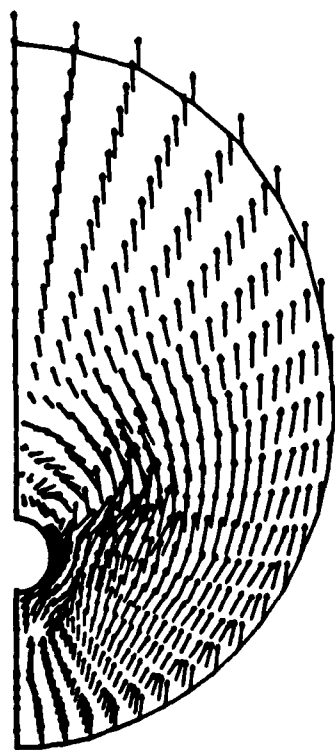
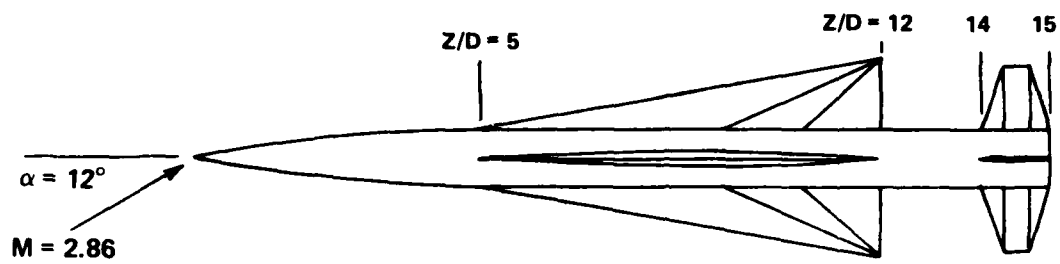
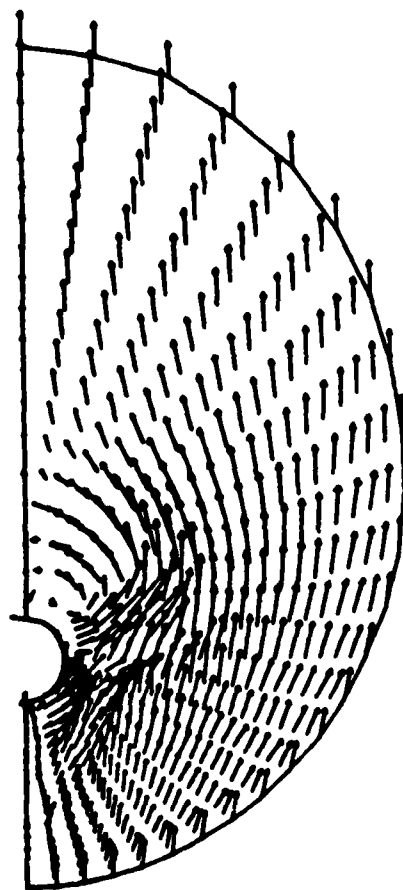


Figure 12. Calculated crossflow fields for the wing-body-tail configurations at several axial stations.

a. $Z/D = 5$ and $Z/D = 12$



Z/D 14



Z/D = 15

Figure 12. (Continued)

b. $Z/D = 14$ and $Z/D = 15$

STATUS REPORT ON TRISERVICE DATA BASE EXTENSION
OF PROGRAM MISSILE

Michael J. Hemsch and Jack N. Nielsen
Nielsen Engineering & Research, Inc., Mountain View, California

ABSTRACT

A status report is given on the development of PROGRAM MISSILE^{1,2}, which is a comprehensive aerodynamic prediction code capable of computing the longitudinal and lateral stability and control characteristics of cruciform body-tail and canard (wing)-body-tail tactical missiles. The methodology used is described and the planned data base extension is outlined. The rational modeling concepts used to extend the fin-body data base to general body-tail and canard-body-tail missiles are presented.

INTRODUCTION

Despite considerable progress in recent years, there still exists a need for general reliable predictive methods for the forces and moments acting on missiles for use in design studies over the entire speed range from subsonic to hypersonic flow, particularly for high angles of attack. The approaches to predictive methodology which seem most applicable to this task include: (1) data base, (2) rational modeling, (3) paneling methods, and (4) computational fluid dynamics.

There is little question that computational fluid dynamics (CFD), which involves numerical solutions of the basic flow equations will become more important in the future. However, there are considerable obstacles to be overcome before such powerful techniques will be available for design studies. Computers are not big, fast, or cheap enough and will not be for many years. Turbulence modeling has not reached the stage where it can be confidently applied to general flow problems. Hence, although this work will and should be continued, the designer must cast around for other means to satisfy his needs.

In the data-base approach to predictive methods development, correlations or other means of rationally assembling experimental data are used to produce predictive techniques. In these, the ranges of geometry and flow parameters are systematically investigated in order to give the best possible foundation for correlation and interpolation work. The data-base approach has the considerable advantage that all of the flow phenomena affecting vehicle performance are accounted for, whether or not the details are specifically recognized on a physical basis. However, the approach is limited to the geometry and flow ranges of the data. This means that while interpolation is a fairly certain process, extrapolation is not. Thus, in order to have wide generality, the data base itself has to be very wide and

this can involve much testing. For a generalized missile with forward and aft lifting surfaces, the cost would be prohibitive.

The idea of rational modeling is to conceptualize the primary phenomena affecting vehicle behavior (vortices, wakes, attached flow) and to stimulate these with flow models based on classical potential and viscous fluid-dynamic theory. This approach is less configuration and flow parameter limited than the data-base approach, and it does permit extrapolation. However, the main disadvantage is that not all of the flow phenomena affecting vehicle behavior may be properly recognized or understood. Hence, the modeling of phenomena may be imprecise and not even complete. It is only necessary to consider, for example, a vapor-screen photograph of the flow around a complex missile configuration and compare this with the classical fluid-dynamic models available to recognize the difficulties inherent in rational modeling.

For high angle-of-attack aerodynamics, we suggest that the best approach to method development is a combination of data base and rational modeling. In such an approach the rational modeling predictions are modified empirically or semiempirically by comparing them with and matching them to the data. This should, given better accounting of the phenomena affecting vehicle behavior, result in better precision. What is particularly important is that the applicability of the data base can be extended orders of magnitude beyond its original configuration space by rational modeling. Inputs from experimental data ensure that the shortcomings of the rational models will be supplemented by the systematic experimental data. Of course, the use of experimental data to modify a predictive technique is not new. What is new here is the emphasis on the combination of a powerful systematic data base generated over extensive ranges of geometry and flow parameters, coupled with the rational modeling. This is the approach which has been used to produce PROGRAM MISSILE. The following section briefly describes the combination of data base and rational modeling used in PROGRAM MISSILE. The concluding section outlines the planned TRISERVICE effort to extend the available data base.

DESCRIPTION OF THE PRESENT METHOD

GENERAL CONSIDERATIONS

A typical configuration considered is shown in Figure 1 in a flow at an angle of attack. Also shown is the general vortex flow field produced by such a configuration. The configuration consists of the following components:

1. Forebody section - up to the first set of lifting surfaces,
2. Canard or wing section - over the length of the root chord of the first set of lifting surfaces,
3. Afterbody section - between the first and second set of lifting surfaces,

4. Tail section - behind the root-chord leading edge of the rear set of lifting surfaces.

Although the method was designed specifically for configurations such as the one shown in Figure 1, the computational procedures are such that it will accommodate less geometrically-complex configurations as well, such as a body-alone or a body-tail design.

Determination of the loads (forces and moments) on the various components of a missile at an arbitrary combination of angle of attack, roll angle, and control surface deflection in a flow field requires accurate modeling of several aerodynamic effects. These effects include that due to angle of attack (i.e., potential lift), interference among the various components, such as panel-panel interference, viscosity, and the loading induced by the external vortex field. This vorticity originates in the boundary layer of both the body and the fins. At higher angles of attack these various effects result in the loads on the missile exhibiting strong nonlinear behavior. Recent comprehensive reviews of this nonlinear behavior are given in References 3 and 4.

FOREBODY SECTION

PROGRAM MISSILE is restricted to bodies with circular cross sections. Furthermore, it is assumed that the flow over the forebody is symmetrical about the plane formed by the body axis and the wind velocity vector. Thus, the program is not likely to be accurate for very long forebodies at high angles of attack in subsonic flow.

The normal force and pitching-moment on the forebody are found using a slightly modified version of Allen's crossflow theory together with Jorgensen's compilation of crossflow drag coefficients⁵. The vorticity shed by the forebody is modeled by two symmetrical Rankine vortices with large solid-body cores. The locations and strengths of the vortices at the leading edge of the first finned section are obtained from a table. The table is composed of available data for angles of attack less than 20° and computer generated results using vortex cloud theory⁶ for angles of attack greater than 20°. Boundary conditions for the computer program were modified heuristically to account for the effects of compressibility on the vortex strengths^{1,3}.

FINNED SECTION (CANARD, WING OR TAIL)

Calculation of fin loads by PROGRAM MISSILE for arbitrary roll angles, fin deflection and vorticity fields depends on five things:

1. a model of vorticity field; i.e., the forebody model of the previous section or the afterbody model of the next section;
2. a method for computing the average angle of attack, $(\Delta\alpha_{eq})_{v_i}$, induced on the fins by the vorticity field;
3. a data base for fin-body combinations with no vortices present for $a/s_m = 0.5$;
4. a wing-alone data base;

5. an addition theorem to account for the effects of vortices and $a/s_m \neq 0.5$.

We will restrict the discussion to the computation of fin normal force. The methods used to compute body force and center of pressure and fin center of pressure are described in detail in Reference 1 and 7.

Vortex Effects

The vorticity field at each cross section of the finned section is assumed to be the same as that at the leading edge of the fin root chord (beginning of the section). Various vapor-screen studies and limited vortex tracking computations indicate that this is a reasonable assumption for the distributed vortex field typical of missiles. We plan to check this assumption further using a new Euler code which is capable of representing distributed vortex fields accurately^{8,9}. The average angle of attack induced on the fins by the computed vorticity field is obtained by reverse flow theory^{1,10}.

Data Base

The present PROGRAM MISSILE data base for a fin-body combination with $a/s_m = 0.5$ was developed from body-tail data obtained by J. E. Fidler¹¹ and supplied to us by Dr. Donald Spring of the Army Missile Command. The parameters of the data base are given in a later section. Vortex effects were removed from the data base using the models described above. The method used in PROGRAM MISSILE to account for vortex effects and $a/s_m \neq 0.5$ (addition theorem) requires a wing-alone data base. Such a data base which would be complementary to the Fidler data base was not available. However, sufficient systematic data were available to guide construction of the necessary base by interpolation and extrapolation.

Addition Theorem

The method used in PROGRAM MISSILE to account for vortex effects and $a/s_m \neq 0.5$ is based on wing-alone data and the idea of an equivalent angle of attack. The notion is to determine the coefficient of normal force acting on the fin in the presence of a body, $\hat{C}_{NF_i(B)}$, with $a/s_m = 0.5$ and no vortices present for the body angle of attack, α_c , and the fin roll angle, ϕ_i , of interest. As shown in Figure 2, this value of $\hat{C}_{NF_i(B)}$ is used to determine an equivalent wing-alone angle of attack, $\alpha_{eq,p}$. A change in the equivalent angle of attack is computed and added to $\alpha_{eq,p}$. Then the wing-alone curve is used to obtain the desired fin normal force coefficient, $C_{NF_i(B)}$.

AFTERBODY SECTION

The flow over the afterbody section is computed in two different ways depending upon the version of PROGRAM MISSILE used. In both versions the trailing vorticity from each fin is assumed to be fully rolled up into one or two Rankine vortices depending upon the spanwise location of the center of pressure. In MISSILE1, the afterbody vorticity is modeled as two asymmetric Rankine vortices whose positions are computed by slender-body tracking. The positions of the fin vortices and forebody vortices (if present) are computed

at the same time. The mutual interactions of all of the vortices are accounted for. The method used to determine the changing strengths of the afterbody vortices is a heuristic one based on crossflow drag theory and the vortex impulse theorem⁷.

In MISSILE2, the afterbody vorticity is modeled by dividing the afterbody into axial segments and allowing each segment to shed a Rankine vortex on each side of the body. The strengths and positions of the newly shed vortices are determined from the computed pressure and velocity distributions on the body. This "vortex cloud" method, while requiring greater computing time, does allow the program to represent the afterbody wake more closely when asymmetric conditions are present.

PLANNED EXTENSION

PARAMETER RANGE

There are two parts to the planned extension of the PROGRAM MISSILE data base: (1) the wing-alone and fin-on-body parameter range will be extended in aspect ratio and Mach number, and (2) a comprehensive data base will be obtained for fin deflection. The present and planned parameter range is shown in Figure 3. The wing-alone data base is being obtained under separate contract.* The angle of attack range for the TRISERVICE tests will be 0-45° and the fin deflection range will be -40° to +40°. All the fins will be clipped delta planforms with the taper ratio ranging from 0 to 1. The fin deflection tests will be confined to the $1 \leq AR \leq 4$ range.

An important aspect of the tests will be the determination of hinge moments. To make the data systematic with respect to airfoil section effects and to make it easier to model the fins, double wedge airfoils with constant thickness to chord ratio over the planform will be used. The control fins will have the same thickness to chord ratio of 0.06.

MODEL AND WIND TUNNELS

The model to be used is an advanced remote control rig developed by NASA/LRC and MICRO CRAFT, Inc. It is capable of remote roll with the sting held fixed and each of four fins can be deflected independently. Two sets of fins can be mounted and the deflecting fins can be positioned in three different locations corresponding to canard, wing or tail control. For the planned tests, only the tail position will be used to generate the data base. In addition to the main balance, each fin will have its own three-component balance.

In order to cover the entire Mach number range, testing will be conducted in the NASA/LRC Unitary Wind Tunnel, section 2, for $M_\infty = 2-4.5$ and in

*The wing-alone work is being coordinated by the Army Research Office under direction of Dr. Robert Singleton. Other sponsors are NAVAIR, NASA/Ames Research Center, NASA/Langley Research Center, and the Army Missile Command.

The NASA/ARC 6- by 6-Foot Supersonic Wind Tunnel for $M_\infty = 0.6-2$. Testing is expected to begin in early September, 1981.

DATA HANDLING

The data base to be obtained will consist of approximately one million words. This is too large a data base to be stored in core. Hence, we plan to store the data base on tape together with the source code for PROGRAM MISSILE. When a new user wishes to use the code, he would obtain a copy of that tape and store the source code and data base on disk files. When he wishes to use the code for a particular configuration, a preprocessor would be used to interpolate in the data base and construct only those tables needed for the computation. Then the main program would use those tables to compute the aerodynamic characteristics of that configuration.

ACKNOWLEDGMENTS

The authors would like to thank NAVAIR, the Office of Naval Research, the Army Missile Command, the Air Force Armament Test Laboratory, the Air Force Wright Aeronautical Laboratory, NASA/Ames Research Center, and NASA/Langley Research Center for sponsoring this project. In particular, we would like to thank Mr. William C. Volz of NAVAIR and Dr. Robert Whitehead of ONR for coordinating the effort.

SYMBOLS

a	body radius
AR	aspect ratio
$C_{N_{F_i}(B)}$	normal-force coefficient for fin i
$\hat{C}_{N_{F_i}(B)}$	normal-force coefficient for fin i if $a/s_m = 0.5$, no vortices are present and no fins are deflected
C_{N_W}	normal-force coefficient for wing-alone
M_∞	free-stream Mach number
s_m	semispan of fin on body
α	wing-alone angle of attack
α_c	included angle of attack, angle between body axis and free-stream velocity vector
α_{eq}	equivalent angle of attack
$\alpha_{eq,p}$	equivalent angle of attack corresponding to $\hat{C}_{N_{F_i}(B)}$
$\Delta\alpha_{eq}$	increment in equivalent angle of attack

- $(\Delta\alpha_{eq})_{v_i}$ increment in equivalent angle of attack due to presence of vortices
- δ_j angle of deflection of fin j
- ϕ_i bank angle of fin i, measured clockwise from right horizontal position

REFERENCES

1. Nielsen, J. N., Hensch, M. J., and Smith, C. A.: A Preliminary Method for Calculating the Aerodynamic Characteristics of Cruciform Missiles to High Angles of Attack Including Effects of Roll Angle and Control Deflections. Office of Naval Research Rept. ONR-CR215-226-4F, Nov. 1977.
2. Smith, C. A. and Nielsen, J. N.: Prediction of Aerodynamic Characteristics of Cruciform Missiles to High Angles of Attack Utilizing a Distributed Vortex Wake. Nielsen Engineering & Research, Rept. TR 208, Jan. 1980.
3. Nielsen, J. N.: Nonlinearities in Missile Aerodynamics. AIAA Paper No. 78-20, 1978.
4. Smith, C. A. and Nielsen, J. N.: Nonlinear Aerodynamics of All-Movable Controls. AGARD Symposium on Aerodynamic Characteristics of Controls, AGARD CP-262, May 1979.
5. Jorgensen, L. H.: Prediction of Static Aerodynamic Characteristics for Slender Bodies Alone and With Lifting Surfaces to Very High Angles of Attack. NASA TR R-474, Sept. 1977.
6. Mendenhall, M. R., Spangler, S. B., and Perkins, S. C., Jr.: Vortex Shedding from Circular and Noncircular Bodies at High Angles of Attack. AIAA Paper No. 79-0026, 1979.
7. Hensch, M. J., Smith, C. A., Nielsen, J. N., and Perkins, S. C., Jr.: Calculation of Component Forces and Moments of Arbitrarily Banked Cruciform Missiles with Control Deflections. Office of Naval Research Rept. ONR-CR215-226-3, Nov. 1976.
8. Klopfer, G. H. and Nielsen, J. N.: Euler Solutions for Wing and Wing-Body Combinations at Supersonic Speeds with Leading-Edge Separation. AIAA Paper No. 80-0126, 1980.
9. Klopfer, G. H. and Nielsen, J. N.: Euler Solutions of the Body Vortices of Tangent Ogive Cylinders at High Angles of Attack and Supersonic Speeds. AIAA Paper No. 81-0361, 1981.
10. Nielsen, J. N.: Missile Aerodynamics. McGraw-Hill Book Co., Inc., New York, NY, 1960.
11. Fidler, J. E.: Aerodynamic Methodology, Bodies with Tails at Arbitrary Roll Angle. Martin Marietta Rept. OR 13,375-1, Dec. 1974.

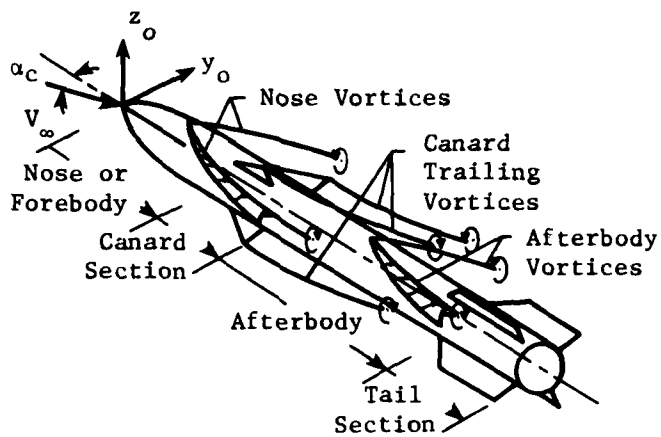


Figure 1 Banked canard-cruciform missile at angle of attack showing typical vortex field

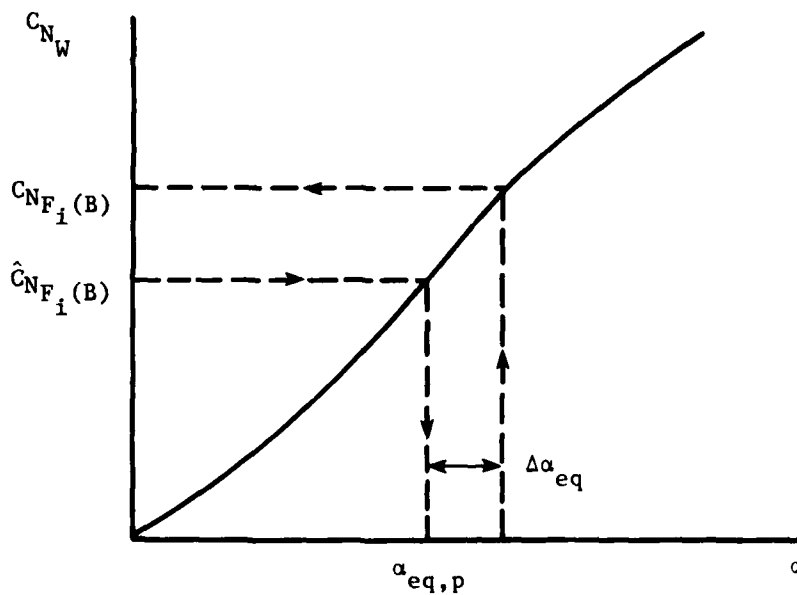
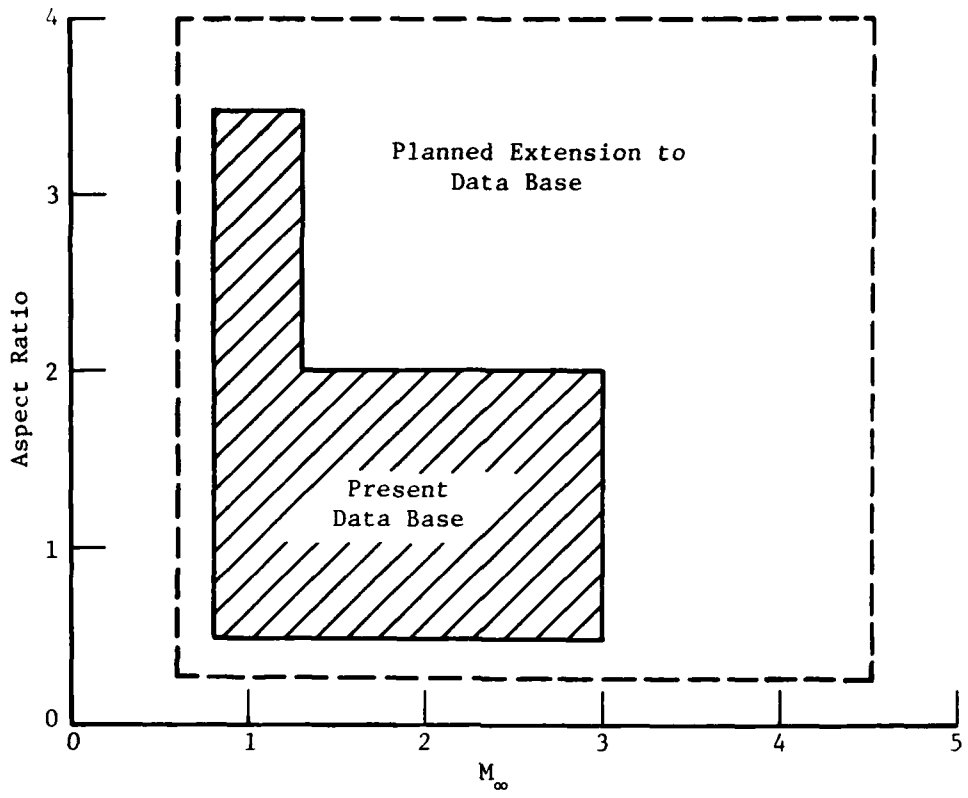


Figure 2 Illustration of equivalent angle of attack concept



(a) Aspect-ratio/Mach-number range

AR \ λ	0	1/2	1
1/4		X	
1/2	X	X	X
1		X	
2	X	X	X
4		X	

Wing Base (rows 1/4, 1/2, 1)
 Control Base (rows 2, 4)

(b) Aspect-ratio/taper-ratio range

Figure 3 Planned data base range for PROGRAM MISSILE

THEORETICAL AND EXPERIMENTAL SUPERSONIC LATERAL-DIRECTIONAL

STABILITY CHARACTERISTICS

Milton Lamb, Wallace C. Sawyer, and James L. Thomas
NASA Langley Research Center, Hampton, Virginia

ABSTRACT

A program has been initiated at NASA Langley Research Center to assess several methods for estimation of lateral-directional stability. As a basis for comparison, experimental data are presented for a simple wing-body vertical tail configuration. The methods for estimating the characteristics include a second-order shock expansion and panel method (MISLIFT), a slender body and "first-order" panel method (APAS), and a "higher-order" panel method for linearized supersonic flow (PAN AIR). The results show that PAN AIR provides accurate estimates of these characteristics at moderate angles of attack for complete configurations with either single or twin vertical tails. APAS will provide estimates for complete configurations at zero angle of attack. However, MISLIFT will only provide estimates for the simplest body-vertical tail configurations at zero angle of attack.

INTRODUCTION

Recent developments in analytical methods have resulted in computer codes for rapid accurate estimates of the aerodynamic characteristics of aircraft and missile configurations at supersonic speeds. Much attention has been given to the development and assessment of these methods for predicting the lift, drag, and pitching moment of complex configurations. Many of these methods have the capability of predicting the lateral-directional characteristics of aircraft and missiles, but their utility has not been evaluated by comparison with experiment.

A program has been initiated at NASA Langley Research Center to provide experimental data on simple wing-body-vertical tail configurations for the purpose of assessing lateral-directional stability estimates at supersonic speeds. This paper will present these data along with an assessment of several of the existing methods capable of estimating lateral-directional parameters. The methods include a second-order shock expansion and panel method¹, a slender body and "first order" panel method², and a "higher-order" panel method for linearized supersonic flow³.

SYMBOLS

The lateral-directional characteristics are referred to the body axis system. The moment reference center was located at 75.6 percent of the body length.

A maximum cross-sectional area of body

$C_{l\beta}$ effective dihedral parameter (roll stability), $\left(\frac{\Delta C_l}{\Delta\beta}\right)_{\beta = 0^\circ, 3^\circ}$, where

$$C_l = \frac{\text{rolling moment}}{qAd}$$

$C_{n\beta}$ directional-stability parameter, $\left(\frac{\Delta C_n}{\Delta\beta}\right)_{\beta = 0^\circ, 3^\circ}$, where

$$C_n = \frac{\text{yawing moment}}{qAd}$$

$C_{Y\beta}$ side-force parameter, $\left(\frac{\Delta C_Y}{\Delta\beta}\right)_{\beta = 0^\circ, 3^\circ}$, where $C_Y = \frac{\text{side force}}{qA}$

d maximum body diameter

l body length

M free-stream Mach number

q free-stream dynamic pressure

α angle of attack

β angle of sideslip

DISCUSSION

The configuration variables are shown in figure 1. The body had a fineness ratio of 11.67 consisting of a 3.5 caliber tangent ogive nose followed by a cylindrical section. The wings were 68° swept delta planforms with sharp leading and trailing edges. Vertical tail planforms are shown for both the single and twin configurations. The vertical tail series for the single vertical tail configuration incorporates leading- and trailing-edge sweep variations as well as taper ratio. The area of these vertical tails is constant and equal to 18 percent of the wing area. For the twin vertical configuration, two areas were used; one is identical to the single tail and the other is one-half that of the single tail. The twin verticals were investigated at lateral spacings of both 2 and 4 body diameters apart. Experimental investigations were conducted in the Langley Unitary Plan Wind Tunnel at Mach numbers from 1.60 to 2.86 for a Reynolds number of 8.2×10^6 per meter. The nominal angle-of-attack range was from -4° to 12° .

The features of computational methods used to predict the lateral-directional characteristics are discussed in figure 2. MISLIFT¹, developed at NASA Langley Research Center, is a second-order shock expansion and panel method. The contribution of the body is obtained from a second-order shock expansion theory, and the contribution of the vertical is obtained from a simple panel method. APAS², developed by Rockwell, is a slender body and first-order panel method. The body contribution is obtained from a slender body theory which concentrates the surface effects along the centerline of the body. The wing and vertical contributions are obtained from a first-order panel method. Skill is required in modeling the geometry even for the simple first-order methods. For example, it is important to align the edge of the wing panel with the vertical, otherwise erroneous estimates may be obtained. PAN AIR³, developed by Boeing for NASA Ames Research Center, is a higher-order panel method for linearized supersonic flow. As indicated in figure 2, the entire surface of the configuration is represented by panels. Proper use of PAN AIR requires careful attention to the way in which these panels are defined, especially in the area where configuration components join, such as wing-body or body-vertical junctions.

Figures 3 through 5 present comparisons of the experimental and predicted lateral-directional characteristics at $\alpha = 0^\circ$ for various configurations. The comparisons shown in figure 3 are for four body-vertical configurations. The agreement indicates that all three methods are able to predict the roll stability ($C_{l\beta}$) and the side force parameter ($C_{y\beta}$) quite well; however, only MISLIFT and PAN AIR predict the directional stability ($C_{n\beta}$) with any degree of success. In figure 4, comparisons are presented for body-wing and body-wing-vertical configurations. The code MISLIFT has not been compared because it can only estimate characteristics for surfaces in their planform plane. APAS and PAN AIR are capable of predicting the lateral-directional characteristics of a wing-body-vertical configuration at zero angle of attack. The agreement ranges from good to excellent for the PAN AIR code. Figure 5 presents a comparison of the theoretical methods with experiment for twin vertical tail configurations at zero angle of attack. The PAN AIR code prediction is in better agreement with experiment than the APAS code, especially for estimation of the directional stability of the configuration with small tails inboard.

Because of the limitations of the methods considered, only PAN AIR will provide estimates of the lateral-directional stability derivatives at angles of attack. Figures 6 and 7 present comparisons of the PAN AIR code predictions with experimental lateral-directional characteristics at angles of attack for Mach numbers 1.60 and 2.86. The agreement for the single and twin vertical tail configurations shown in figures 6 and 7 is excellent for moderate angles of attack. At higher angles of attack and Mach number, the body nose slopes violate linear theory assumption and the solution is invalid.

CONCLUDING REMARKS

A program has been initiated at NASA Langley Research Center to assess several methods for estimation of lateral-directional stability at supersonic speeds. The methods for estimating the characteristics include a second-order shock expansion and panel method (MISLIFT); a slender body and "first-order" panel method (APAS); and a "higher-order" panel method for linearized supersonic flow (PAN AIR). The results lead to the following concluding remarks:

- (1) PAN AIR provides accurate predictions at moderate angles of attack for complete configurations with either single or twin vertical tails.
- (2) APAS will provide fairly accurate predictions at zero angle of attack for complete configurations with either single or twin vertical tails.
- (3) MISLIFT will only provide estimates for the simplest body-vertical tail configurations at zero angle of attack.

REFERENCES

1. Jackson, Charlie M. Jr.; and Sawyer, Wallace C.: A Method for Calculating the Aerodynamic Loading of Wing-Body Combinations at Small Angles of Attack in Supersonic Flow. NASA TN D-6441, 1971.
2. Bonner, E.; Clever, W.; and Dunn, K.: Aerodynamic Preliminary Analysis System. Part I.- Theory. NASA CR-145284, 1978.
3. Ehlers, F. E.; Epton, M. A.; Johnson, F. T.; Magnus, A. E.; and Rubbert, P. E.: An Improved Higher-Order Panel Method for Linearized Supersonic Flow. AIAA Paper No. 78-0015, 1978.

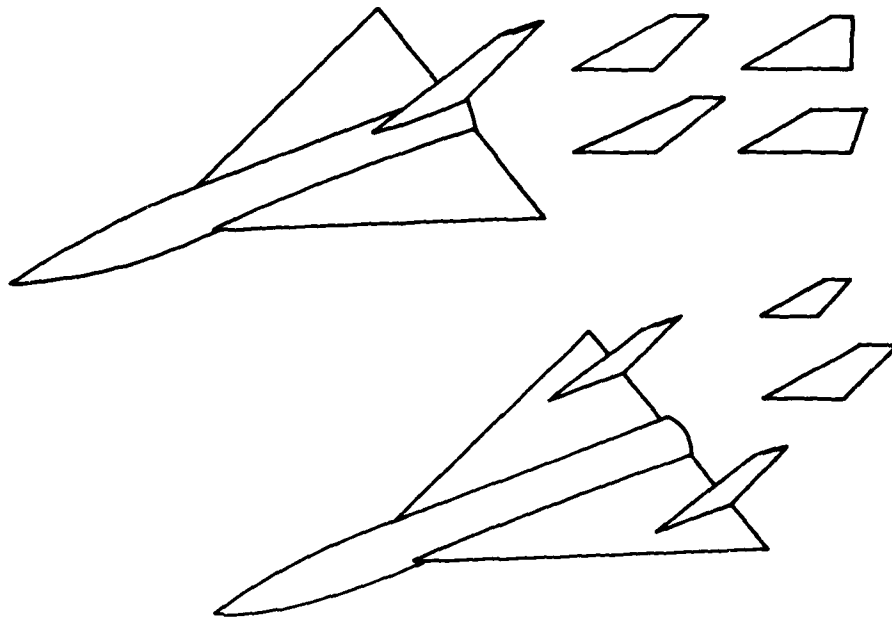
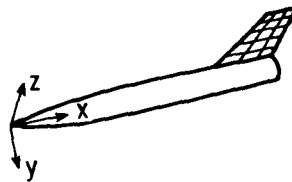
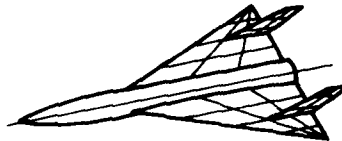


Figure 1. - Configuration variables.

- MISLIFT - A SECOND-ORDER SHOCK EXPANSION AND PANEL METHOD



- APAS - A SLENDER BODY AND "FIRST ORDER" PANEL METHOD



- PAN AIR - A "HIGHER ORDER" PANEL METHOD FOR LINEARIZED SUPERSONIC FLOW

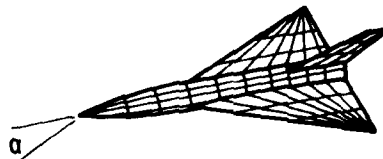


Figure 2. - Computational methods.

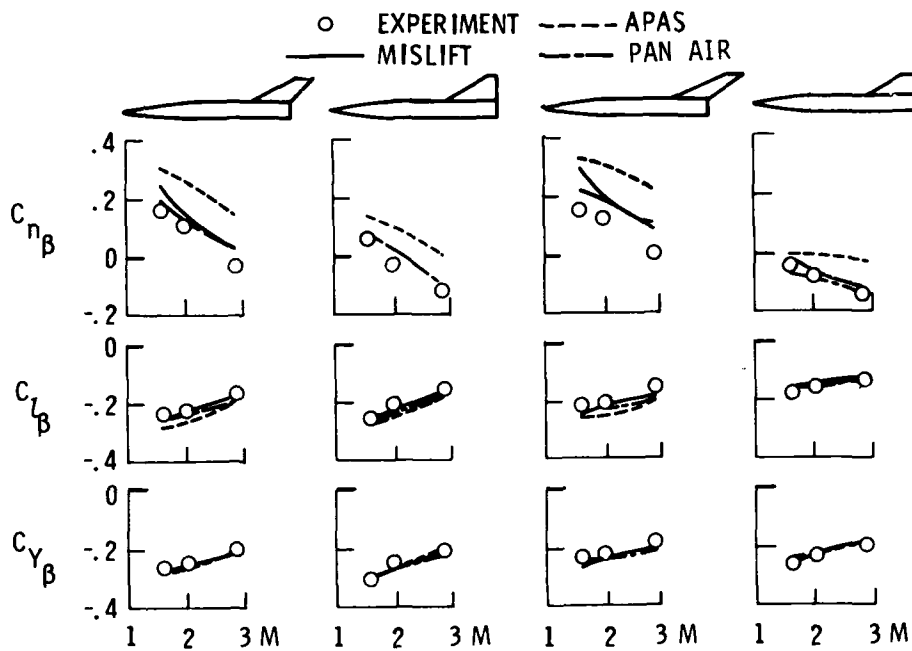


Figure 3. - Comparison of experimental and predicted lateral-directional characteristics. $\alpha = 0^\circ$; body-vertical.

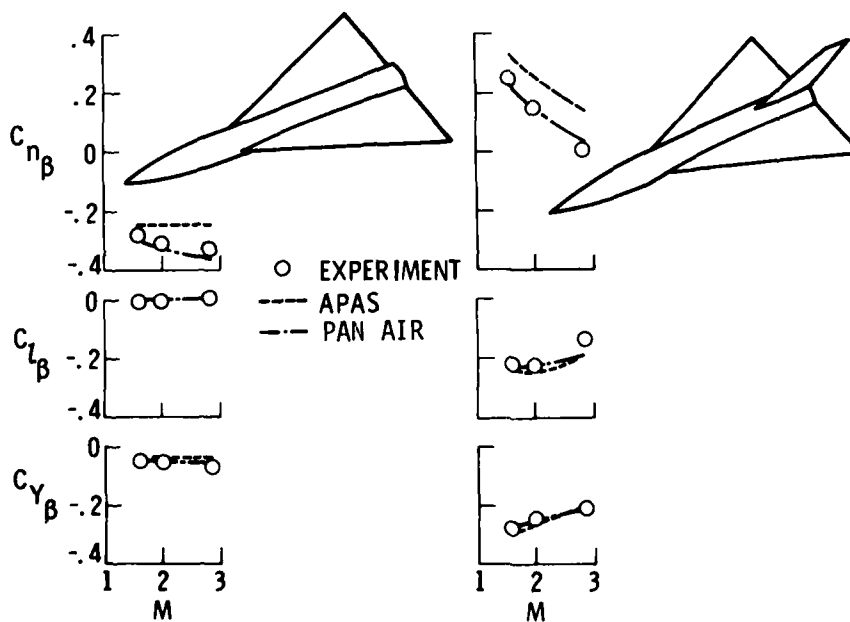


Figure 4. - Comparison of experimental and predicted lateral-directional characteristics. $\alpha = 0^\circ$; body-wing, body-wing-vertical.

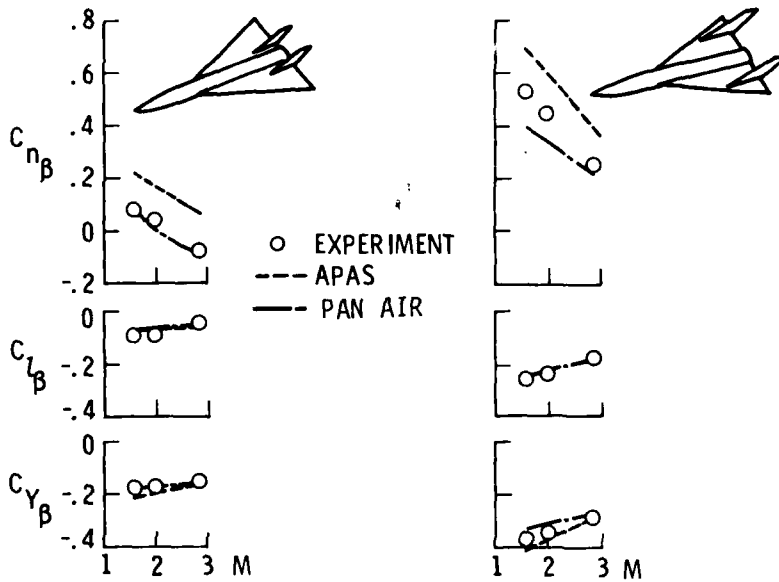


Figure 5. - Comparison of experimental and predicted lateral-directional characteristics. $\alpha = 0^\circ$; body-wing-twin verticals.

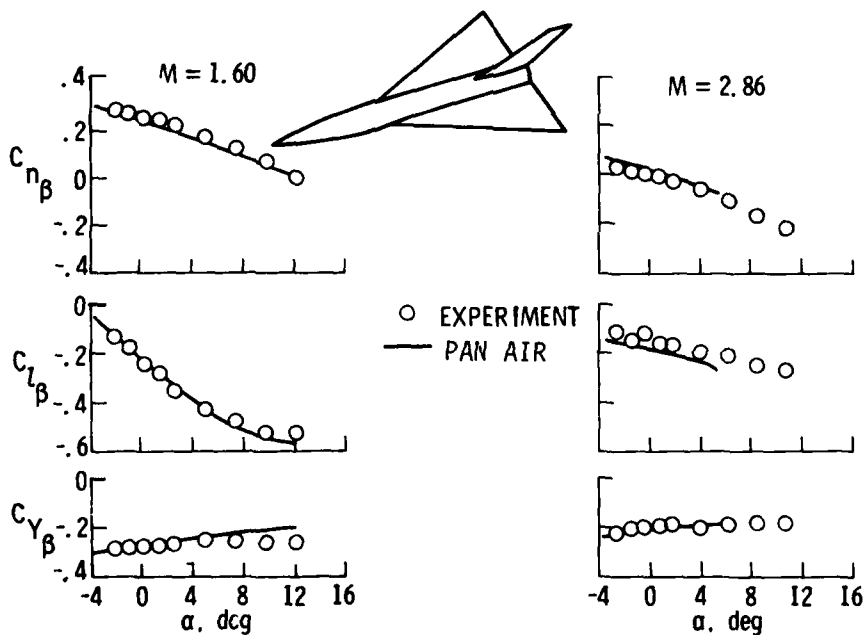


Figure 6. - Comparison of experimental and predicted lateral-directional characteristics. $\alpha \neq 0^\circ$; body-wing-vertical.

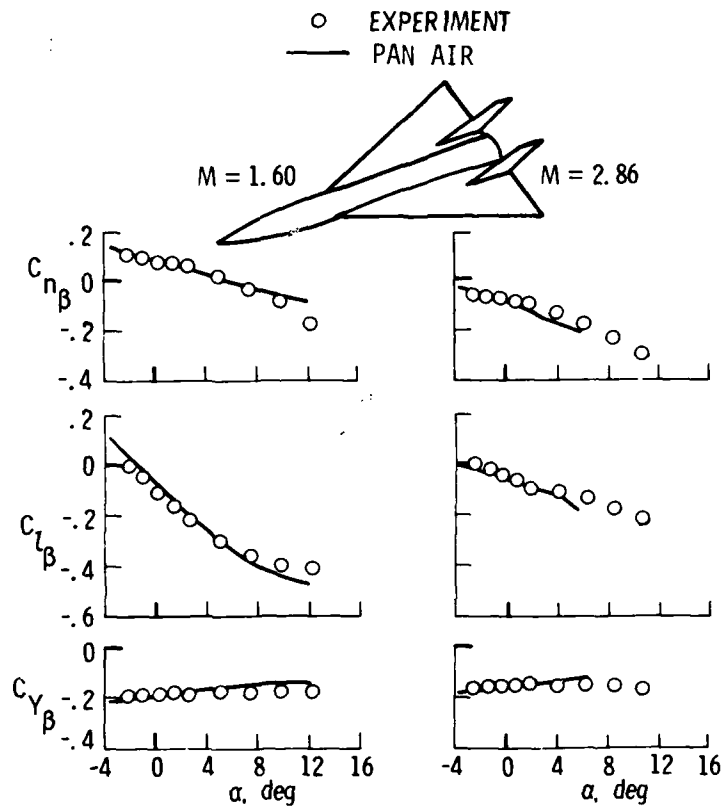


Figure 7. - Comparison of experimental and predicted lateral-directional characteristics. $\alpha \neq 0^\circ$; body-wing-twin verticals.

AERODYNAMICS OF A ROLLING AIRFRAME MISSILE*

L. E. Tisserand
The Johns Hopkins University/Applied Physics Laboratory
Laurel, Maryland

ABSTRACT

For guidance-related reasons, there is considerable interest in rolling missiles having single-plane steering capability. To aid the aerodynamic design of these airframes, a unique investigation into the aerodynamics of a rolling, steering missile has been carried out. It represents the first known attempt to measure in a wind tunnel the aerodynamic forces and moments that act on a spinning body-canard-tail configuration that exercises canard steering in phase with body roll position.

Measurements were made with the model spinning at steady-state roll rates ranging from 15 to 40 Hz over an angle-of-attack range up to about 16° .

This short, exploratory investigation has demonstrated that a better understanding and a more complete definition of the aerodynamics of rolling, steering vehicles can be developed by way of simulative wind-tunnel testing.

INTRODUCTION

In mid-December 1978, wind tunnel tests were conducted using the newly fabricated model of a Rolling Airframe Missile. The Applied Physics Laboratory planned¹ and conducted the testing for the Navy under APL sub-contract with the Vought Corporation, High Speed Wind Tunnel. General Dynamics, Pomona Division, designed and fabricated the test item.^{2,3,4}

The purpose of this wind-tunnel investigation was to gain a better understanding of the configuration's aerodynamic characteristics, under proper simulative conditions, that would lead to the development of better predictive capabilities. Prior to this effort, aerodynamic characteristics used in designing and evaluating rolling, steering missiles have been derived from wind tunnel data collected on nonspinning models and from the cumulative experiences gained from analyses of flight test data. Those aerodynamic descriptions of rolling airframes emphasize their longitudinal stability and control characteristics but ignore the likelihood of induced side forces and yawing moments.

*The work reported in this paper was supported by NAVSEA, PMS-404-50, under Contract N00017-72-C-4401, Task A3B0

This exploratory test was limited purposely to 35-hours of test time. It represents Phase One of a two-phase wind-tunnel investigation into the aerodynamics of the rolling, steering airframe. The objectives of this short test were to check out the test item, test procedures and data acquisition, and to probe the aerodynamics of the configuration under dynamic-flight conditions at a representative transonic and supersonic speed. It was proposed that, after an evaluation of all aspects of this test, a second tunnel entry would be made to fully document the aerodynamics of the configuration throughout its performance envelope, and to conduct configurational breakdown investigations appropriate to the identification and sizing of relevant aerodynamic causes and effects.

This first phase of the proposed test program was a success. The test data have been evaluated and the results documented.⁶

SYMBOLS AND NOMENCLATURE

The aerodynamic forces and moments presented herein are referred to an axes system of rectangular coordinates (x,y,z) that pitches with the missile but does not roll with the missile, and does not roll to the angular orientation for the occurrence of peak-steering deflection. The flight-path velocity vector is denoted by V with projections u, v, w on the x,y,z-axis respectively (v ≡ 0 for the axes system selected herein). The positive sense of the velocity components, force and moment coefficients, and steering-control deflection are shown on the next page. Definitions of symbols are:

$C_A, C_Y, C_N,$
 C_l, C_m, C_n

orthogonal set of aerodynamic force and moment coefficients:

$$C_A = -F_x/qS, C_Y = F_y/qS, C_N = -F_z/qS, C_l = M_x/qSd$$

$$C_m = M_y/qSd, C_n = M_z/qSd$$

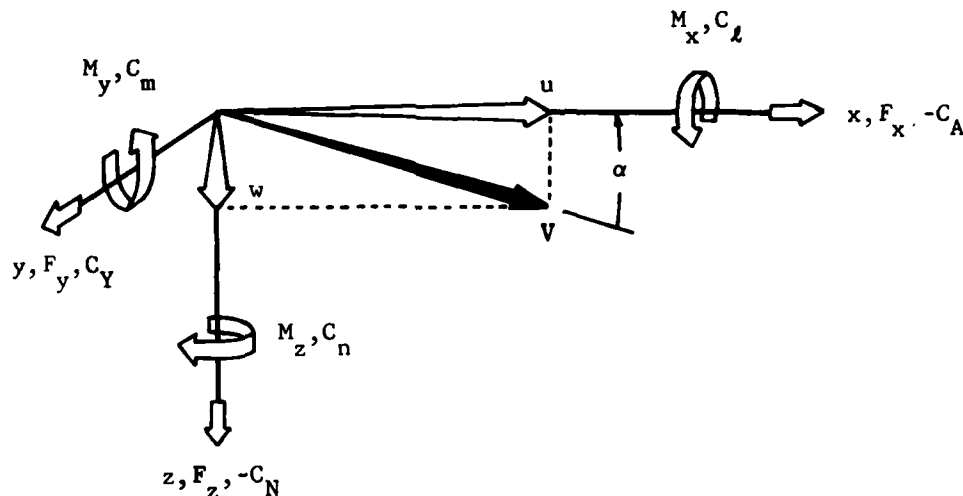
d reference length, body diameter (inches)

F_x, F_y, F_z
 M_x, M_y, M_z

projections of the total aerodynamic force (lbs) and total aerodynamic moment (in-lbs) onto the non-rolling x, y, z-axis respectively

i steering deflection amplitude, $i > 0$ increases α and $i < 0$ decreases α [an observer riding in the non-rolling axes system will see the instantaneous steering deflection vary as $i |\cos \theta|$; an observer riding in the rolling body-fixed axes system will see the instantaneous steering deflection vary as $i \cos \theta$]

- M Mach number
- MRC moment reference center located seven model diameters downstream of body nose tip
- q dynamic pressure (psf)
- S reference area, body cross-sectional area, $\pi d^2/4$ (sq. ft)



- XCP longitudinal center of pressure (used to indicate the resultant center-of-pressure location for the normal force coefficient where body station is given in model diameters measured downstream from nose tip)
- α total angle of attack (deg) measured between the total velocity vector (V) and the centerline of the missile (x-axis): $\alpha = \arctan (w/u)$
- \emptyset when $\emptyset = 0$, \emptyset is the aerodynamic roll angle (deg) measured from the angle-of-attack plane (defined by the total velocity vector and the centerline of the missile) to the centerline of the reference leeward canard; when $\emptyset \neq 0$, \emptyset is the steering-control direction defined as the angle (deg) measured from the angle-of-attack plane to the roll attitude for the occurrence of peak-steering deflection.
- $\dot{\emptyset}$ roll rate (Hz); $\dot{\emptyset} > 0$ is clockwise spin looking upstream

$\dot{\phi}/2V$	spin parameter (radians)
δ	differential deflection angles (deg) set on lifting panels
cw, ccw	clockwise, counterclockwise
ζ	nonzero value of C_Y at $\alpha = 0^\circ$
ξ	nonzero value of C_n at $\alpha = 0^\circ$
∂	partial differentiation as in $\partial C_Y / \partial \alpha$

TEST ITEM

The configuration tested is shown in Figure 1. The model is 42.408 inches long and its outer diameter is 1.925 inches. The nose section consists of a hemispheric nose stepped into a conical-transition section leading to the cylindrical body. Two hemispherically-tipped antennas are mounted on the transition section in line with the two fixed, rectangular-planform canards that are canted differentially ($\delta = -0.75^\circ$) for the intended purpose of supplementing aerodynamic rolling moment. The two steering canards have a delta planform with 45° leading-edge sweep. Provisions exist for testing steering-deflection amplitudes of 0° , $\pm 5^\circ$, $\pm 10^\circ$, $\pm 15^\circ$ or $\pm 20^\circ$. Four like tail panels are mounted on a cylindrical sleeve which is slip-fitted over, and fastened to, the cylindrical afterbody. The cruciform tail arrangement is interdigitated at 45° relative to the canard panels. Asymmetric wedging of the tail leading edges yields a camber effect, and small flap-type tabs at the trailing edges are deflected differentially ($\delta = -7.5^\circ$) to produce aerodynamic roll-driving moment. The base is flared.

A special sting support was designed and fabricated to be compatible with the model's large length-to-diameter ratio. Packaged inside the model are: (a) a five-component strain gauge balance to measure the orthogonal aerodynamic forces (less drag) and moments that act on the model, (b) a DC motor to provide roll torque supplemental to aerodynamic roll-driving moment, and (c) an interchangeable steering cam to produce mechanically sinusoidal deflection of the steering canards in phase with body roll position. The sting support, balance, motor casing, and cam are locked together as one unit that does not spin; the model is slip-fitted over, and fastened to, a spin-bearing case that is free to rotate. The roll rate of the model can be controlled remotely by regulating the power supply to the torque motor.

Pretests showed the model's mass asymmetry in roll is quite small, and the effects of motor-generated heat and magnetic fields on the performance of the balance are negligible. Resonant frequencies of the cantilevered model-balance-sting assembly are 12, 22 and 24 Hz.

TEST CONDITIONS

A dynamic variable to be duplicated in tunnel testing is the missile's spin parameter, $\dot{\theta}d/2V$, rather than the missile's roll rate, $\dot{\theta}$. Hence, to simulate properly the flight conditions associated with missile roll rates of 8 to 15 Hz, it is necessary for the 0.385-scale model to experience steady state roll rates of 15 to 30 Hz. Resonant frequencies within the simulative range of model roll rates would have been a serious problem had it not been for the ability to control the roll rate of the model remotely. Figure 2 shows, for Mach 1.2 and 2.5, the model roll rates tested and the equivalent missile roll rates (evaluated at sea level) determined from the equivalence of the spin parameter.

Measurements were taken under conditions of pitch and pause at the nominal angles of attack of -2° , 0° , 2° , 4° , 6° , . . . , 16° . The effects of data sampling rate, roll rate, Reynolds number, Mach number, and steering control (directed "in" and "out" of the angle-of-attack plane) on the configuration's rigid-body aerodynamics were examined.

RESULTS

A pretest calibration of the balance provided a measure of the basic, static accuracy of the instrument. The root-mean-square variations in the balance-measured forces and moments are shown in subsequent plots of coefficient data. Evaluation of all test results has shown the repeatability of balance measurements is excellent and the measurements satisfy principles of symmetry when required. These important data properties are used as justification to define some coefficient behavior to finer precision than the advertised accuracy of the balance.

Some pertinent results follow. Additional information and detail are given in the final report.⁵

EFFECTS OF ROLL RATE AND DATA SAMPLING RATE

Tests were made holding the model roll rate constant at -17, -30 or -40 Hz. At each pause, 48 data points were recorded at the rate of 240 data points per second. This yielded about 16 data points per one revolution of the model when $\dot{\theta} = -17$ Hz, 8 data points per revolution when $\dot{\theta} = -30$ Hz, and 6 data points per revolution when $\dot{\theta} = -40$ Hz. In the data reduction program, these 48 lines of coefficients were divided into four equal groups, and for each group, a mean value and standard deviation were computed for each coefficient. Hence, in the figures, four mean values could appear at each condition of pause; less than four plotted points indicates no significant difference in some of the coefficient's computed mean values.

Figures 3, 4 and 5 show, for Mach 2.51, the effect of roll rate on the aerodynamic forces and moments that act on the configuration. It is evident that normal force and pitching moment coefficients are not sensitive to the roll rates tested. The data allow smooth fairings without anomalies.

The induced side force and yawing moment coefficients, Figure 5, show a dependence on roll rate and angle of attack. Although these forces and moments induced out of the plane of maneuver are small compared to the normal force and its associated pitching moment, their appearance was not unexpected.¹ If these fairings of induced coefficients are shifted to a common origin, it is possible to combine the slopes for low angles of attack into second-order expressions of the form,

$$\frac{\partial^2 C_Y}{\partial \alpha \partial P} \quad \text{and} \quad \frac{\partial^2 C_n}{\partial \alpha \partial P} \quad \text{for } 0^\circ \leq \alpha < 4^\circ, \quad \text{where } P = \frac{\dot{\theta} d}{2V},$$

which are used commonly to describe the behavior of Magnus effects on bodies of revolution. It is not proposed that Magnus forces acting on the model's body are the only contributors to the configuration's induced side force and yawing moment characteristics.⁶

Tests were made to determine the effect of data sampling rate on aerodynamic output. Holding $\dot{\theta} = -30$ Hz, measurements were taken over the angle of attack range -2° to 16° using data sampling rates of 80, 240 and 320 data points per second respectively. Comparison of results obtained indicates no measurable effect of data sampling rate on the recorded aerodynamic forces or moments. One test run was made with the balance rolled to a different orientation relative to the angle-of-attack plane, and it is significant that the balance output (when resolved to the axes system adopted herein) duplicate the results for $\dot{\theta} = -30$ Hz presented in Figures 3, 4, and 5.

EFFECTS OF STEERING CONTROL DIRECTED IN THE ANGLE OF ATTACK PLANE

The results presented in this section are for conditions where peak-steering deflection occurs as the steering canards become normal to the angle-of-attack plane, i.e., $\dot{\theta} = 0^\circ$.

Longitudinal Stability and Control Characteristics and Induced Side Force and Yawing Moment Coefficients

Figures 6 and 7 show, for Mach 2.51, the effect of steering-deflection amplitude on the contributors to longitudinal stability and control. The variations of normal force and pitching moment coefficients with angle of attack and steering control show remarkably smooth and consistent behavior. Figure 8 shows the behavior of the induced side force and yawing moment characteristics. The fairings for zero incidence are the same as shown earlier and their nonzero intercepts with the ordinate are designated, for purposes of discussion, as Zeta (ζ_1) and Xi (ξ_1). At zero angle of attack, principles of symmetry require that the incremental force and incremental moment resulting from plus and minus steering deflection to be equal and opposite; this condition is satisfied if increments are measured from ζ_1 and ξ_1 respectively.

The test data should also image about zero angle of attack; i.e., C_Y ($\alpha = j, i = k$) $\equiv -C_Y$ ($\alpha = -j, i = -k$) and C_n ($\alpha = j, i = k$) $\equiv -C_n$ ($\alpha = -j, i = -k$). These conditions are satisfied (for the range of data taken) when the origins of the plots are shifted (without rotation) to ζ_1 and ξ_1 respectively.

Figures 9, 10 and 11 show, for Mach 1.19, the effects of angle of attack and steering-deflection amplitude on the force and moment coefficients. Measurements taken with a substantial increase in Reynolds number show no observable change in normal force coefficient and a 0.2-diameter upstream shift in longitudinal center of pressure throughout the angle-of-attack range tested. Due to the nature of transonic flowfields, it was expected that measurements taken at Mach 1.19 would indicate some abrupt changes in the components of the aerodynamic force and moment coefficients; however, it can be observed that the normal force and pitching moment fairings are without anomalies.

Tests were conducted with the direction of spin reversed. For the forces and moments induced out of the maneuver plane to be real and aerodynamic in origin, these coefficients must change sign when spin direction is reversed, and must image about the abscissa or a line parallel to the abscissa. In Run No. 45, the model was spun in the clockwise direction looking upstream. The tail-tabs settings were not reversed, nor was the differential cant on the rectangular canards; hence, the test setup for Run No. 45 is similar but not identical to that of No. 44. The torque motor was used to override the aerodynamic roll-driving moment, roll-damping moment and bearing friction, and as a result, the motor could not produce a steady-state roll rate larger than +15 Hz (cw). Nevertheless, comparisons of normal force and pitching moment coefficients (Figures 9 and 10) from Run No. 44 and 45 show good agreement. Figure 11 compares the measured side force and yawing moment coefficients when roll direction is reversed. The results show clearly that both side force and yawing moment reverse sign and exhibit elements of symmetry when viewed about new abscissas drawn through ζ_2 and ξ_2 . Since the magnitude of the roll rates differ, mirror images of the coefficient traces would not be expected.

Plans to interchange the model's tail assembly with an extra assembly preset to produce near identical test conditions for clockwise and counter-clockwise spin were not carried out due to an unexpected installation problem.

Transonic tests were made holding angle of attack constant (0° , 4° and 8°) while increasing Mach number from 0.6 to 1.10. Roll rate was -30 Hz. These Mach number sweeps provided some valuable information about the configuration's low-speed aerodynamics and were appropriate to this probing investigation. Measurements taken under conditions of pause yield smooth fairings for the normal and side force coefficients and for the pitching and yawing moment coefficients. It is significant that the side force and yawing moment coefficients obtained at $\alpha = 8^\circ$ with clockwise spin ($\dot{\phi} = +25 \rightarrow +12$ Hz as $M = 0.6 \rightarrow 1.1$) are opposite in sign to those obtained at $\alpha = 8^\circ$ with $\dot{\phi} = -30$ Hz, but their magnitudes differ (note that deflections on roll producing surfaces were not reversed).

Aerodynamic Roll Driving and Roll Damping Characteristics

It was planned to evaluate the aerodynamic roll-driving characteristics from nonspin test data. Under these conditions, measurements obtained from the balance roll gauge provide the summations of all roll moments resulting from differential deflection on the nonsteering canards (when installed), asymmetric wedging of tail leading edges, tail-tab deflections, and canard-to-tail interferences.

It was planned to evaluate roll-damping characteristics by solving the one-degree-of-freedom equation of motion in roll:

$$I\ddot{\theta} = C_{l_{aero}} qSd + C_{l_{(d/2V)}} \frac{\dot{\theta}d}{2V} qSd.$$

The roll-rate feedback loop in the motor controller maintained very accurately a constant roll rate during the data-recording intervals; therefore, steady-state conditions are satisfied. Motor current was recorded, and using a pre-test calibration curve of current versus torque, data reduction provided a printout of motor torque coefficient. There is, of course, friction in the spin-bearing case that acts always to oppose model rotation. The summation of torques that act on the model can be written as:

$$C_{l_{aero}} - C_{l_{friction}} + C_{l_{motor}} + C_{l_{(d/2V)}} \frac{\dot{\theta}d}{2V} = 0$$

or, with some approximation, as

$$C_{l_{aero}} - C_{l_{balance}} + C_{l_{(d/2V)}} \frac{\dot{\theta}d}{2V} = 0$$

where, because of motor losses, $|C_{l_{bal}}| \geq | -C_{l_{friction}} + C_{l_{motor}} |$.

The aerodynamic roll-driving coefficients were determined from angle-of-attack sweeps conducted at selected roll attitudes without spin. For given angles of attack, the rolling moment coefficients obtained at different roll angles with $i = 0^\circ$ were averaged, and these mean values were taken to be representative of the model's aerodynamic roll-driving moment ($C_{l_{aero}}$) when spinning.

Aerodynamic roll-damping coefficients calculated from the equation of motion in roll under steady-state conditions are presented in Figure 12 for Mach 2.51. These computed roll-damping derivatives show a decreasing trend for the increasing roll rates tested. Also, these roll-damping derivatives exhibit an apparent dependence on steering-deflection amplitude at low angles of attack.

The orderly dependence of the computed damping coefficients on steering deflection forces reconsideration of the assumption made in these calculations, namely, that the roll-driving coefficients determined from static test data when $i = 0^\circ$ are independent of spin parameter and steering-deflection amplitude. Perhaps roll-driving moment, or roll-damping moment, or both, depend on spin parameter and steering control.

Aerodynamic roll-driving and roll-damping coefficients deduced from test data collected in the transonic Mach sweeps with $i = 0^\circ$ are well behaved and exhibit expected trends.

CONFIGURATIONAL BREAKDOWN TESTS

Since this was an exploratory investigation, a few tests were made with some model components removed. With the rectangular-planform canards removed, tests with and without spin were carried out at Mach 1.19 and 2.51. A significant result obtained is that the rectangular canards, canted differentially to produce an increase in net roll-driving moment to offset their contribution to total roll-damping moment, induce a nulling increment of roll-reversal moment⁷ on the downstream tails. Tests made at Mach 1.19 with both the rectangular canards and tails removed give further insight into the configurational contributors to both pitch and yaw aerodynamics, and offer additional evidence that steering-deflection amplitude affects roll damping.

EFFECT OF STEERING CONTROL DIRECTED OUT OF THE ANGLE OF ATTACK PLANE

The flight vehicle will respond to guidance called-for maneuvers directed in or out of the instantaneous angle-of-attack plane by causing the steering deflection amplitude to occur in or out of the angle-of-attack plane. Tests were made to determine the effect on maneuver force and its associated moment characteristics due to steering-deflection amplitudes of 10° and 20° directed to roll attitudes of 0° , -22.5° and -45° . The brevity of the tunnel test limited this portion of the study to Mach 2.51.

Viewing collectively the results obtained, it is concluded that the effect of directing steering control out of the angle-of-attack plane can be approximated, for the conditions tested, by directing the control-force increments and control-moment increments obtained when $\theta = 0^\circ$ to the new steering direction, then resolving these increments back to the nonrolling axes system used herein. The accuracy of this procedure (exact at zero angle of attack) deteriorates somewhat as angle of attack increases.

Evaluation of the test data indicates that steering-control direction affects substantially the aerodynamic contributors to roll characteristics. It is deduced that steering control directed out of the angle-of-attack plane induces a net change in roll-driving moment somewhat like the roll moments induced by roll-stabilized missiles with vertical tails deflected to port or starboard. For the rolling airframe, however, the induced roll-moment increments (dependent on steering amplitude and direction) will increase or decrease the airframe's roll-driving moment (ccw) depending on whether nose-up steering control is directed to the starboard side or port side respectively.

CONCLUSIONS

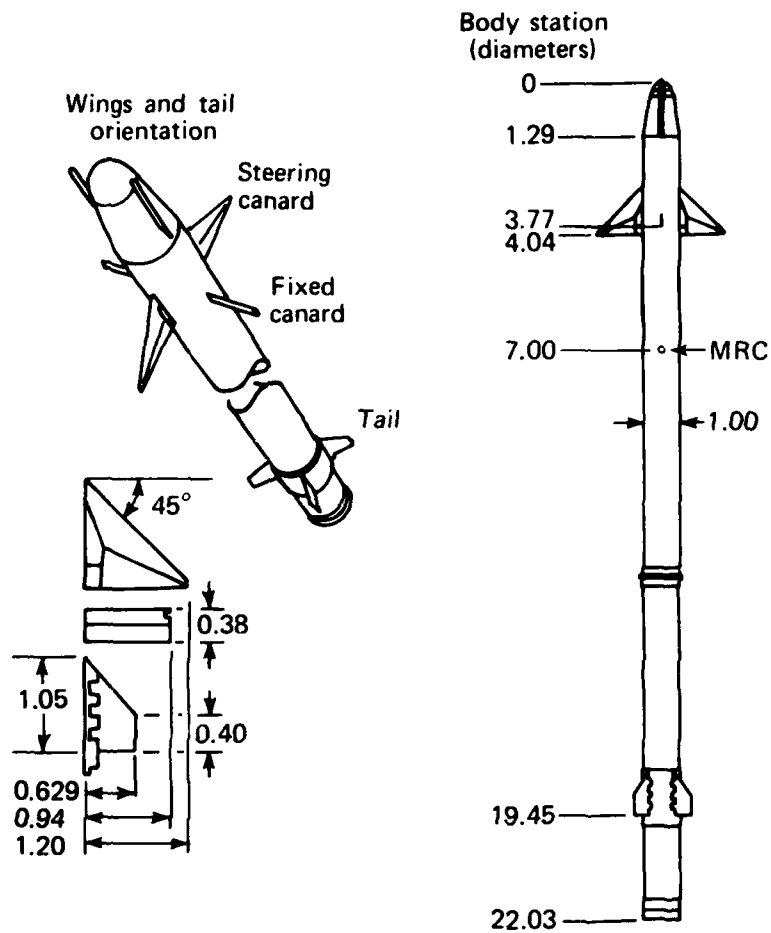
The normal force and pitching moment data provide smooth definitions of the configuration's longitudinal stability and control characteristics. These forces and moments are not sensitive to the values of spin parameters tested.

Small side forces and associated yawing moments, induced out of the plane of maneuver, show dependence on Mach number, angle of attack, steering-control amplitude and direction, and spin parameter. Before this test, aerodynamic descriptions of rolling, steering airframes omitted aerodynamics induced in the yaw plane because there were no systematic data from experiment on which to base predictions. The importance of these induced side forces and yawing moments to the airframe's flight behavior can be determined from dynamic-flight simulations.

Results show that steering control directed in or out of the angle-of-attack plane affect the aerodynamic contributors to roll characteristics.

REFERENCES

1. L. E. Tisserand, "Test Plan for Wind Tunnel Investigation of the 0.385-Scale ASMD Block I Rolling, Steering Airframe - Phase One (U)," (Unclassified), APL/JHU Internal Memorandum BFD-1-77-032, 30 November 1977.
2. H. Beutel, "ASMD Wind Tunnel Model Design (U)," (Unclassified), General Dynamics Pomona Division, Technical Memorandum 6-420-615, 14 November 1978.
3. F. Shum, "ASMD Wind Tunnel Model Controller (U)," (Unclassified), General Dynamics Pomona Division, Technical Memorandum 6-420-594, September 1978.
4. F. D. Fernandes, "Normal Force and Pitching Moment Coefficients for ASMD Block I with 3-Inch Body Spacer (U)," (Unclassified), General Dynamics, Pomona Division, Technical Design Information 6-332-101.53-59, 19 May 1977.
5. L. E. Tisserand, "Wind Tunnel Investigation by JHU/APL of the 0.385-Scale Block I Rolling Airframe Missile -- Results From Phase One Testing (U)," (Unclassified), APL/JHU Internal Memorandum BFD-1-79-012, 31 July 1979.
6. J. C. Uselton and J. B. Carmon, "A Study of the Magnus Effects on a Sounding Rocket at Supersonic Speeds," Journal of Spacecraft and Rockets, Vol. 8, No. 1, January 1971, pp. 28-34.
7. A. R. Eaton, Jr., "Experimental Investigations of Roll-Reversal Effects for Generalized Missile Configurations at Supersonic Velocities," Bumblebee Aerodynamics Symposium, 4-5 November 1948, pp. 237-265.



Note: Dimensions normalized with body diameter (1.92 in.)

Fig. 1 Sketch of external configuration.

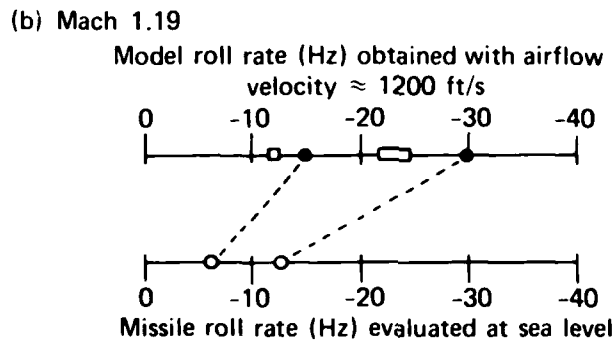
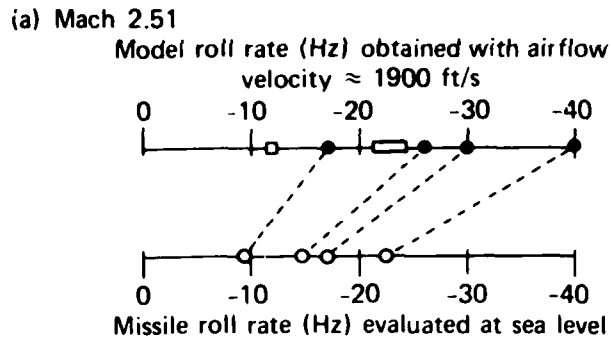


Fig. 2 Model roll rates tested and equivalent missile roll rates.

M = 2.51

Sym	Run No.	$\dot{\phi}$ (Hz)	$\dot{\phi}d/2V$ (rad)	Re x 10 ⁻⁶ (per ft)	i (deg)	Data sampling (pts/sec)
△	7	-17	-0.0046	8.8	0	240
○	5	-30	-0.0080	8.3	0	240
●	5	-9	-0.0024	8.3	0	240
□	6	-40	-0.0108	8.9	0	240

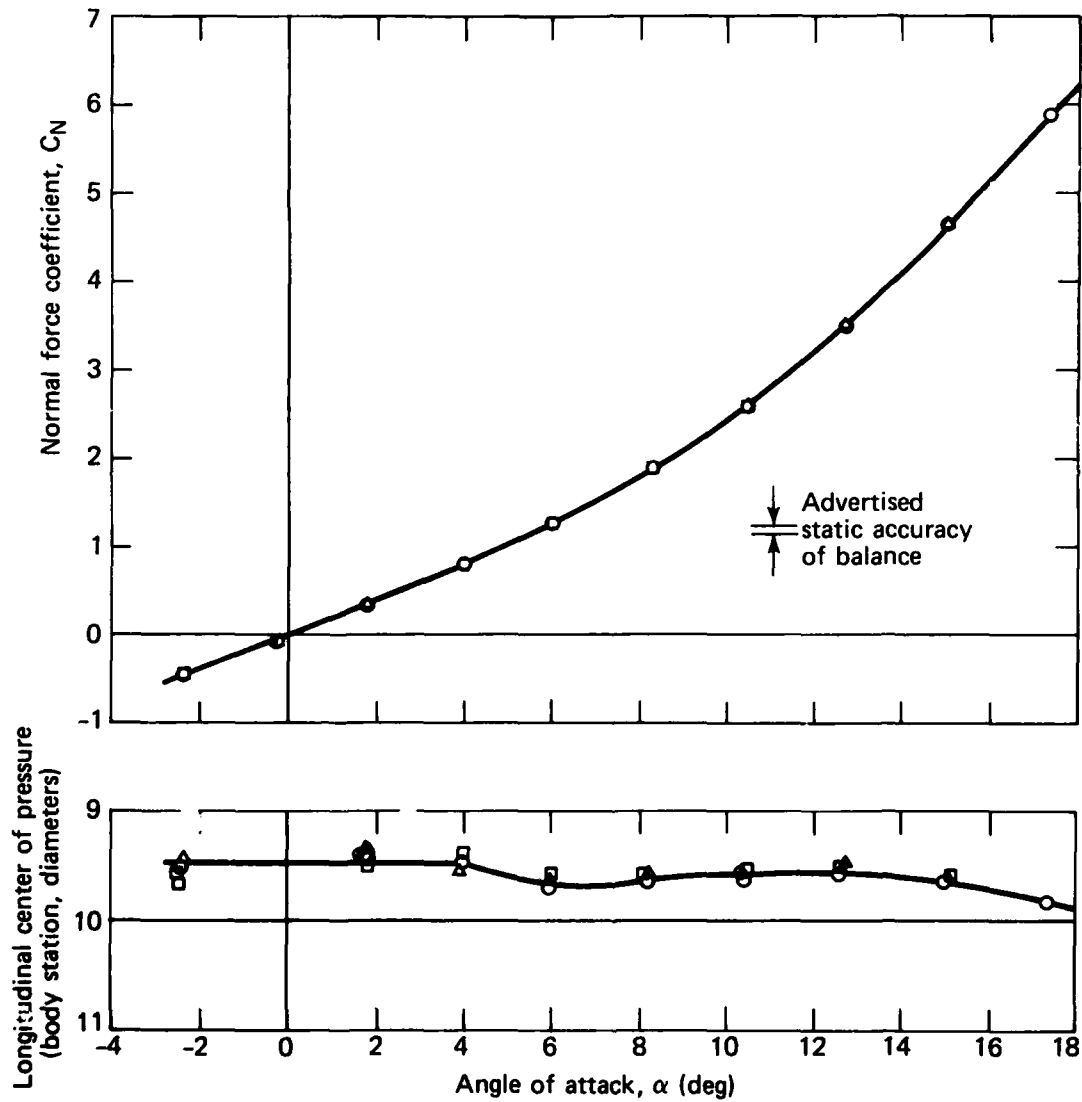


Fig. 3 Effect of roll rate on normal force coefficient and center of pressure travel.

M = 2.51

Sym	Run No.	$\dot{\phi}$ (Hz)	$\dot{\phi}d/2V$ (rad)	Re x 10 ⁻⁶ (per ft)	i (deg)	Data sampling (pts/sec)
△	7	-17	-0.0046	8.8	0	240
○	5	-30	-0.0080	8.3	0	240
●	5	-9	-0.0024	8.3	0	240
□	6	-40	-0.0108	8.9	0	240

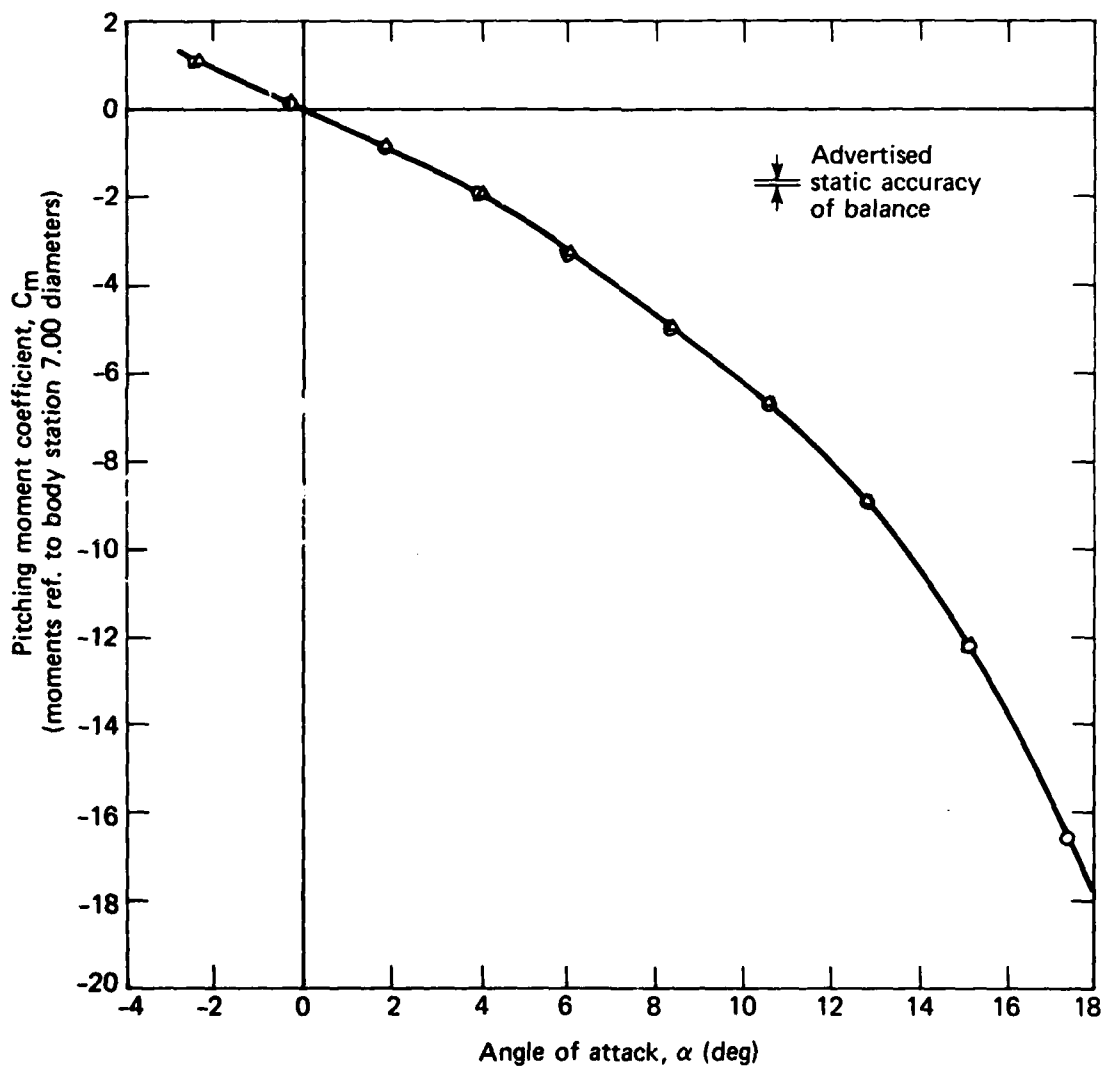


Fig. 4 Effect of roll rate on pitching moment coefficient.

M = 2.51

Sym	Run No.	$\dot{\phi}$ (Hz)	$\dot{\phi}d/2V$ (rad)	Re x 10 ⁻⁶ (per ft)	i (deg)	Data sampling (pts/sec)
△	7	-17	-0.0046	8.8	0	240
○	5	-30	-0.0080	8.3	0	240
●	5	-9	-0.0024	8.3	0	240
□	6	-40	-0.0108	8.9	0	240

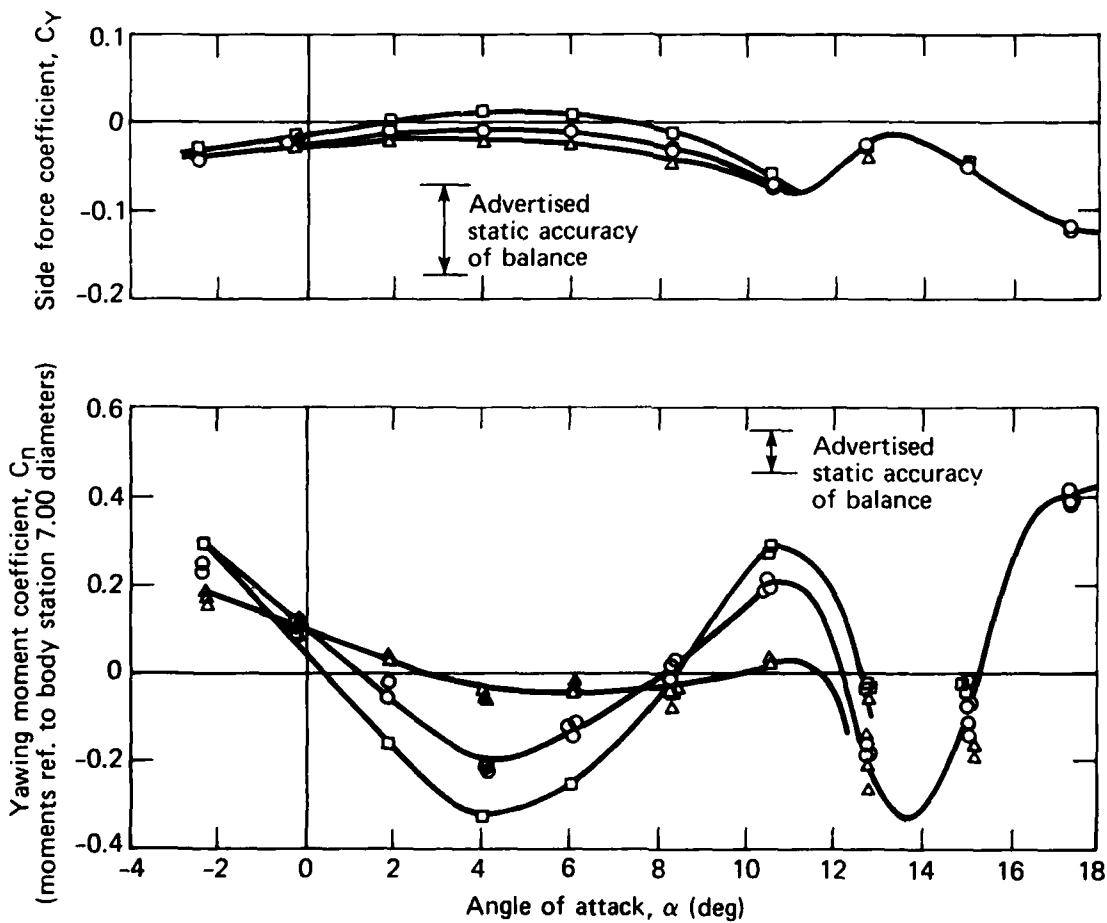


Fig. 5 Effect of roll rate on induced side force and yawing moment coefficients.

M = 2.51

Sym	Run No.	$\dot{\phi}$ (Hz)	$\dot{\phi}d/2V$ (rad)	Re x 10 ⁻⁶ (per ft)	i (deg)
□	14	-30	-0.0082	8.4	20
△	9	-30	-0.0081	8.5	10
○	5	-30	-0.0080	8.3	0
▽	13	-30	-0.0081	8.3	-10
◇	17	-30	-0.0081	8.5	-20

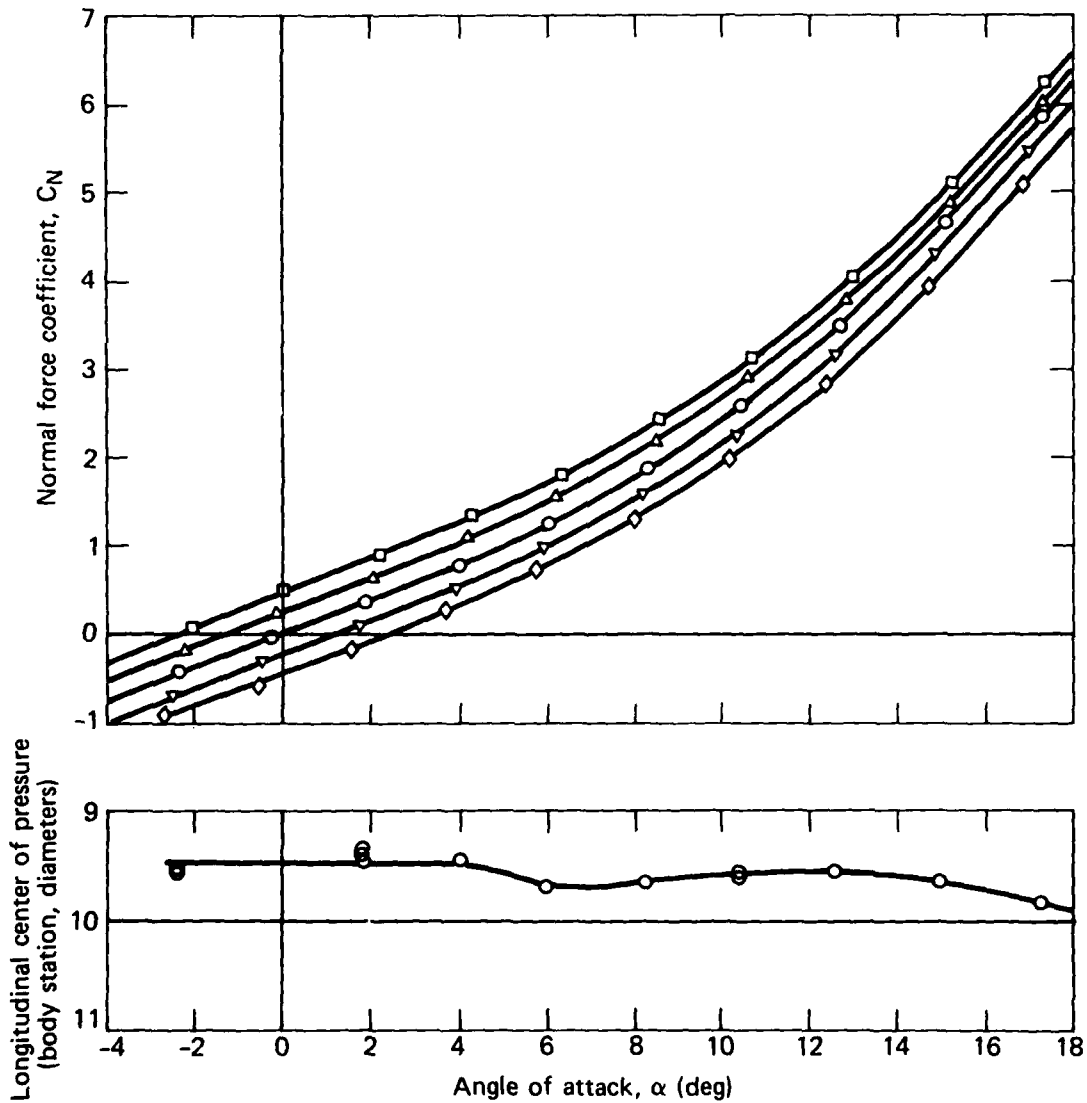


Fig. 6 Variation in normal force coefficient and center of pressure travel with angle of attack and steering deflection amplitude.

M = 2.51

Sym	Run No.	$\dot{\phi}$ (Hz)	$\dot{\phi}d/2V$ (rad)	$Re \times 10^{-6}$ (per ft)	i (deg)
□	14	-30	-0.0082	8.4	20
△	9	-30	-0.0081	8.5	10
○	5	-30	-0.0080	8.3	0
▽	13	-30	-0.0081	8.3	-10
◇	17	-30	-0.0081	8.5	-20

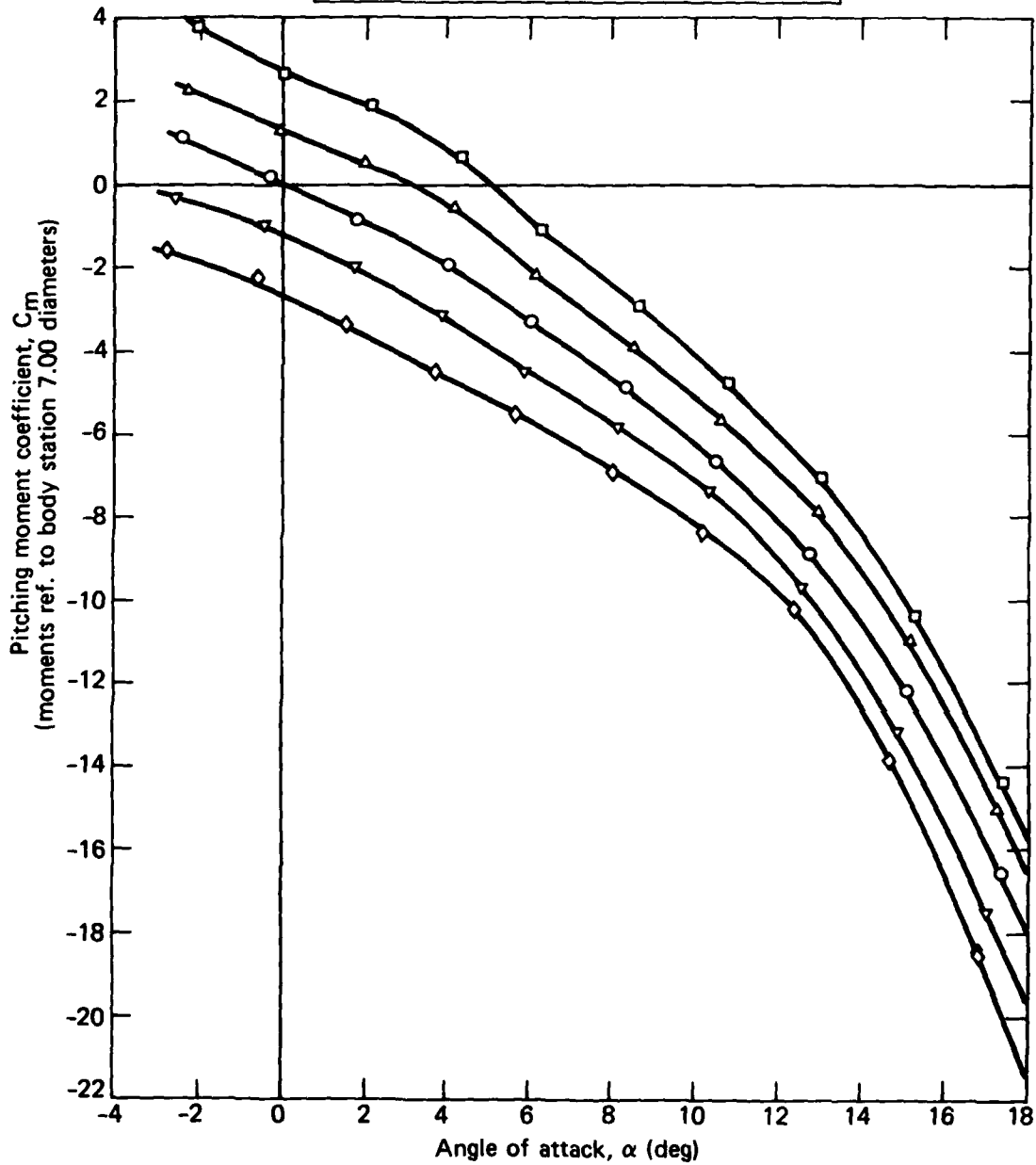


Fig. 7 Variation in pitching moment coefficient with angle of attack and steering deflection amplitude.

M = 2.51

Sym	Run No.	$\dot{\phi}$ (Hz)	$\dot{\phi}d/2V$ (rad)	Re x 10 ⁻⁶ (per ft)	i (deg)
□	14	-30	-0.0082	8.4	20
△	9	-30	-0.0081	8.5	10
○	5	-30	-0.0080	8.3	0
▽	13	-30	-0.0081	8.3	-10
◇	17	-30	-0.0081	8.5	-20

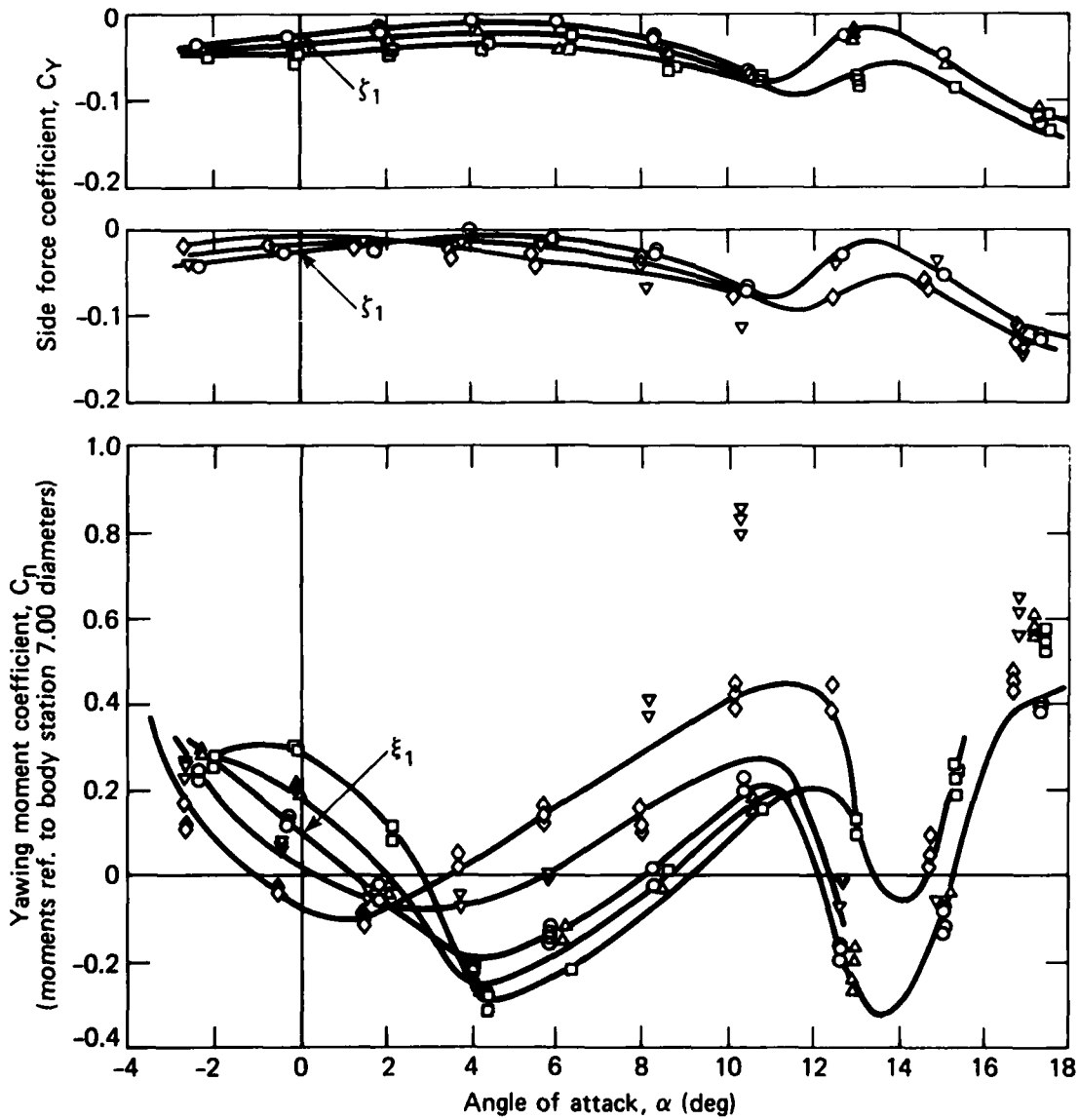


Fig. 8 Variation in induced side force and yawing moment coefficients with angle of attack and steering deflection amplitude.

M = 1.19

Sym	Run No.	$\dot{\phi}$ (Hz)	$\dot{\phi}d/2V$ (rad)	Re x 10 ⁻⁶ (per ft)	i (deg)
□	43	-30	-0.0127	7.2	20
○	44	-30	-0.0126	6.9	0
△	45	+15	+0.0062	6.8	0
◇	46	-30	-0.0124	12.2	0

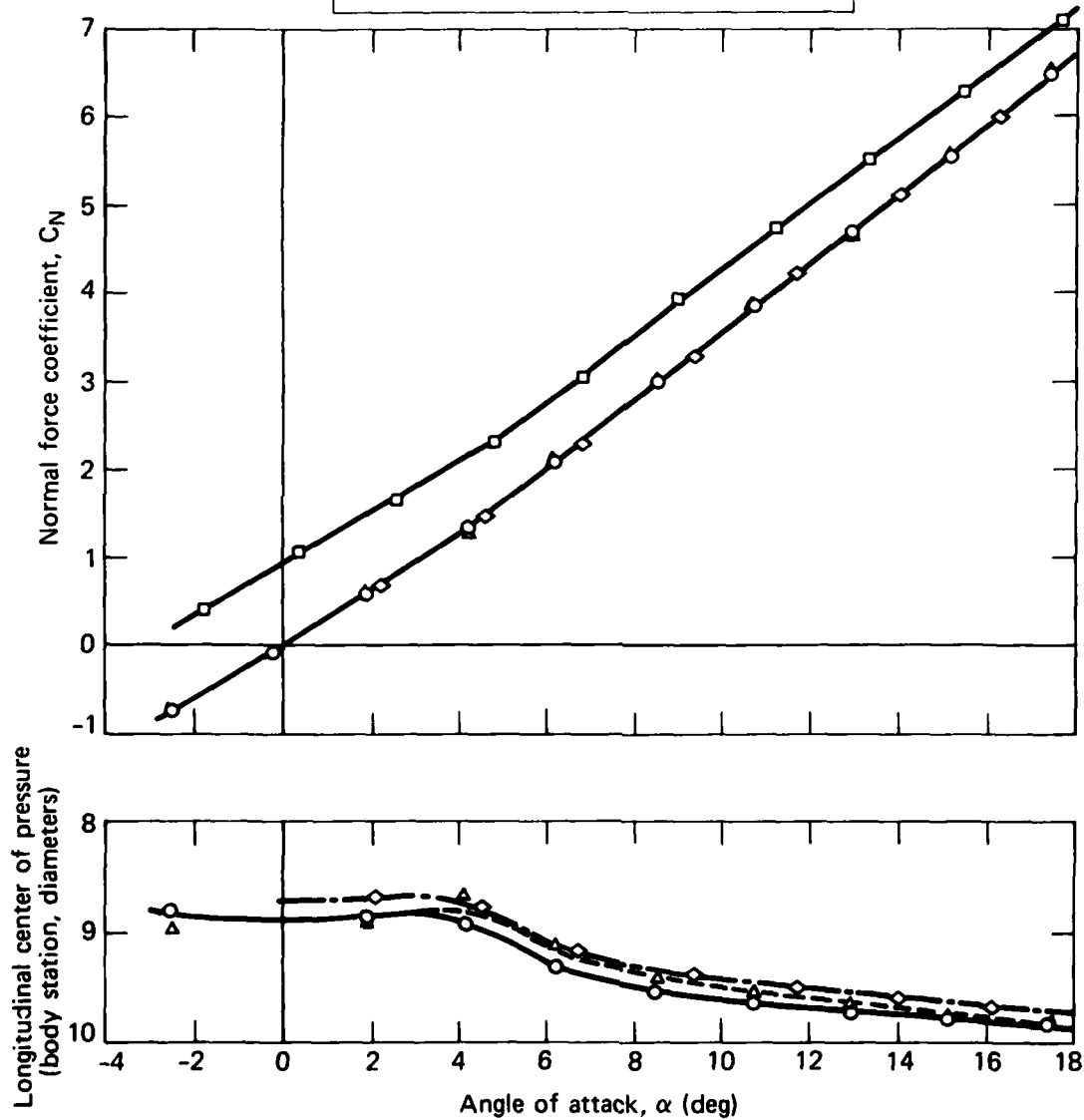


Fig. 9 Variation in normal force coefficient and center of pressure travel with angle of attack and steering deflection amplitude.

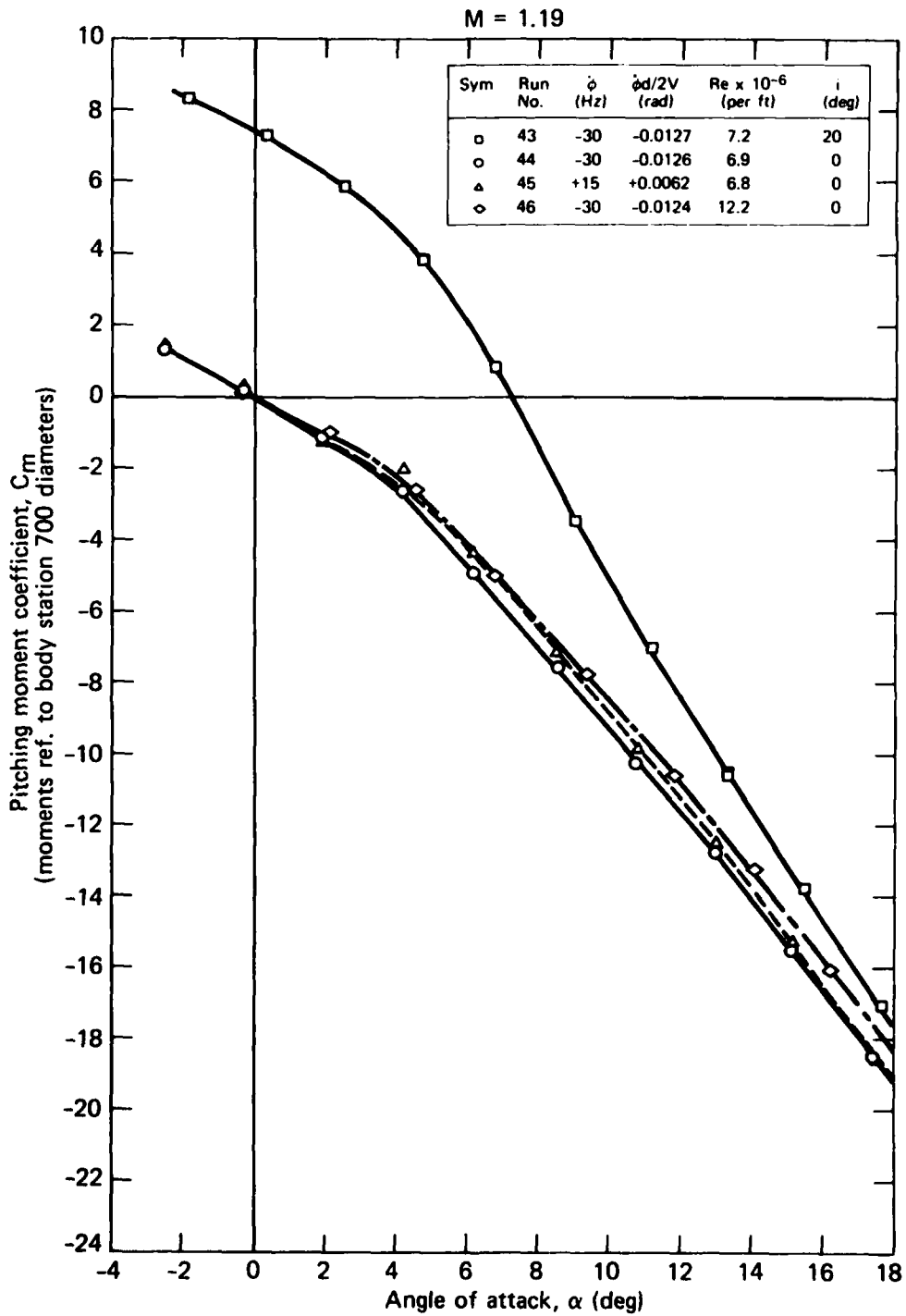


Fig. 10 Variation in pitching moment coefficient with angle of attack and steering deflection amplitude.

Sym	Run No.	ϕ (Hz)	$\phi d/2V$ (rad)	$Re \times 10^{-6}$ (per ft)	i (deg)
□	43	-30	-0.0127	7.2	20
○	44	-30	-0.0126	6.9	0
●	44	-18.5	-0.0070	6.9	0
▲	45	+15	+0.0062	6.8	0

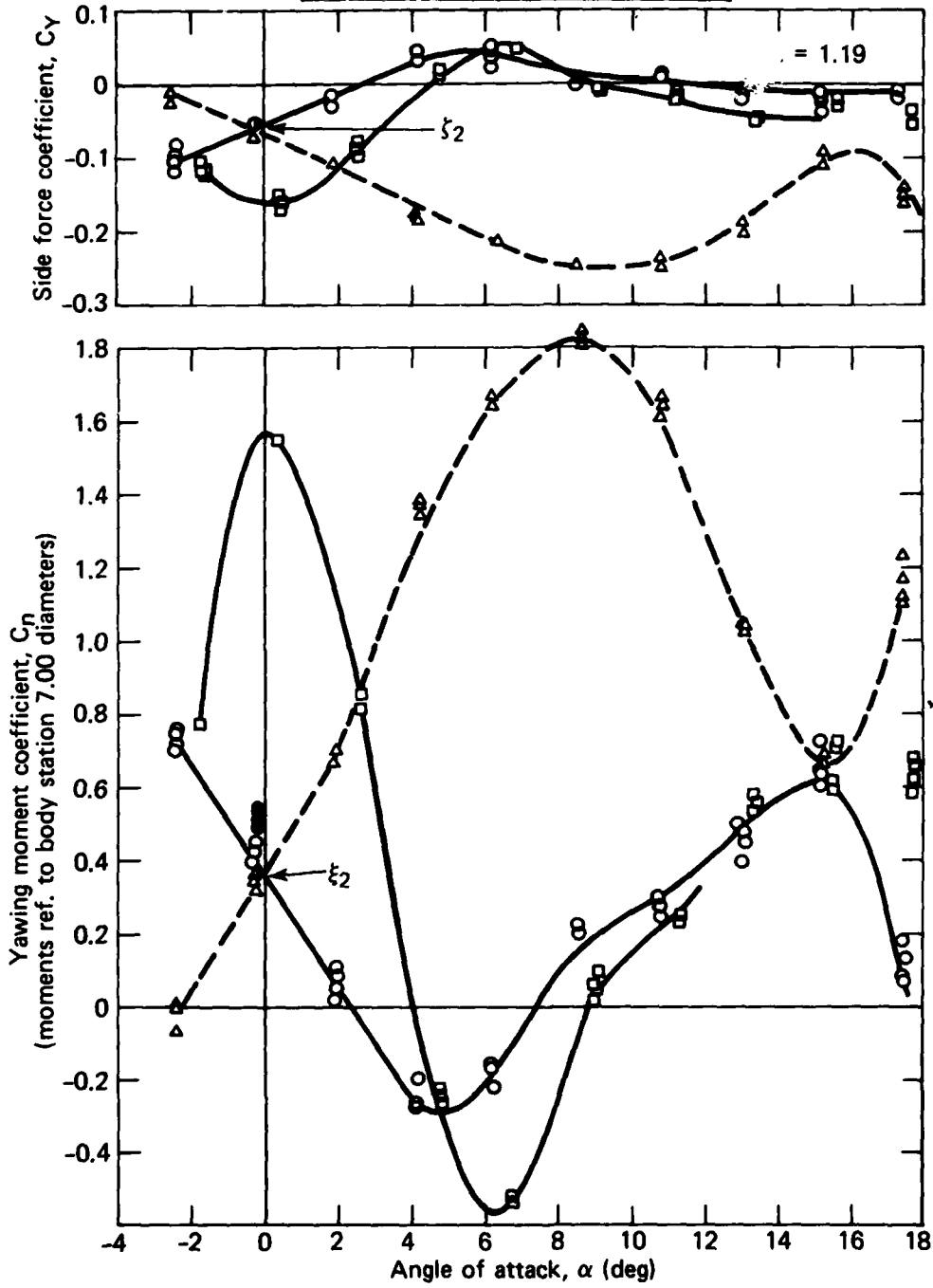
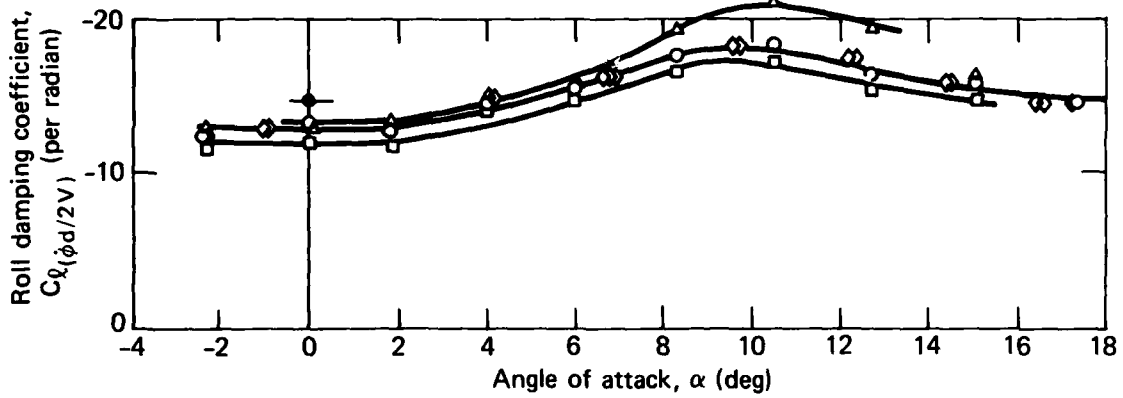


Fig. 11 Variation in induced side force and yawing moment coefficients with angle of attack and steering deflection amplitude.

M = 2.51

Sym	Run No.	$\dot{\phi}$ (Hz)	$\dot{\phi}d/2V$ (rad)	Re x 10 ⁻⁶ (per ft)	i (deg)
△	7	-17	-0.0046	8.8	0
○	5	-30	-0.0080	8.3	0
●	5	-9	-0.0024	8.3	0
◇	8	-30	-0.0080	8.6	0
□	6	-40	-0.0108	8.9	0



Sym	Run No.	$\dot{\phi}$ (Hz)	$\dot{\phi}d/2V$ (rad)	Re x 10 ⁻⁶ (per ft)	i (deg)
□	14	-30	-0.0082	8.4	20
△	9	-30	-0.0081	8.5	10
○	5	-30	-0.0080	8.3	0
▽	13	-30	-0.0081	8.3	-10
◇	17	-30	-0.0081	8.5	-20

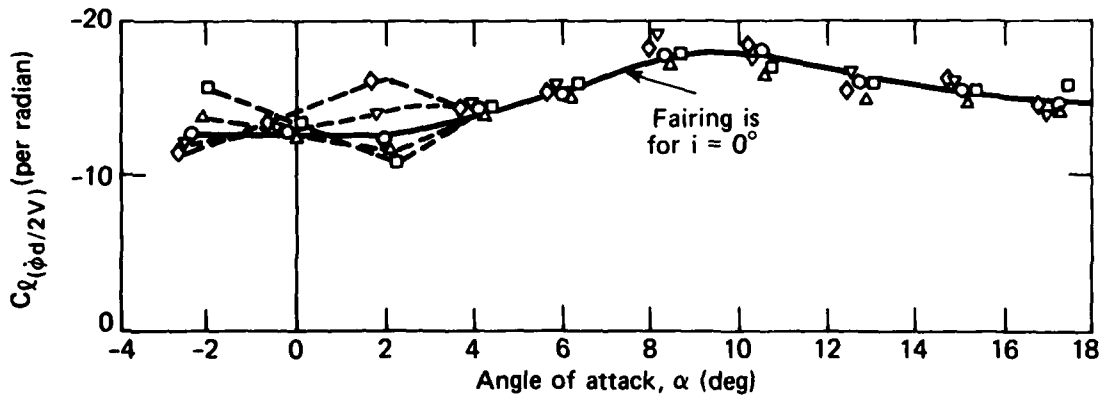


Fig. 12 Calculated roll damping characteristics.

APPROXIMATE METHOD FOR PREDICTING SUPERSONIC NORMAL
FORCE COEFFICIENT OF VERY-LOW-ASPECT-RATIO LIFTING SURFACES

E. F. Lucero
The Johns Hopkins University/Applied Physics Laboratory
Laurel, Maryland 20810

ABSTRACT

A simple, empirical method has been developed for predicting at supersonic speeds the normal force coefficient, C_N , (including carryover) of very-low-aspect ratio lifting surfaces mounted on bodies of revolution. Predicted values of C_N using this method are shown to be in good agreement with test data obtained on both thick and thin surfaces, at Mach numbers from about 2.5 to 7.7 and angles of attack to 24° .

SYMBOLS AND NOMENCLATURE

A_c, A_I, A_o	cross-sectional areas of the forebodies of the inlets, the inlets, and the freestream tube captured by the inlets of ramjet missiles, respectively	in^2
A.R.	aspect ratio = b^2/S_E or b^2/S_W	
b/2	exposed semi-span of a lifting surface mounted on a body of revolution	in
C_{D_c}	cross-flow drag coefficient	
C_N	normal force coefficient, normal force/qS	
C_{N_α}	$\partial C_N / \partial \alpha$	per rad
$\Delta C_{N_E}, \Delta C_{N_W}$	$C_{N_{BE}} - C_{N_B}; C_{N_{BW}} - C_{N_B}$ at $\theta = 0^\circ$	
C_r	root chord	in

Supported by NAVSEA 62R

d	reference diameter; diameter of body on which lifting surfaces are mounted	in
E	complete elliptic integral of second kind with modulus $(1 - \beta^2 \cot^2 \Lambda)^{\frac{1}{2}}$	
K_B, K_W	Morikawa's interference factors	
M	Mach number	
q	dynamic pressure	lbs/in ²
S	reference area, $\pi d^2/4$	in ²
S_E, S_W	total planform area of housings (wings)	in ²
t	average thickness of lifting surface	in
X	body station; X = 0 at nose tip of body	in
$X_{c.p.}$	center-of-pressure location	in
α	angle of attack; angle between the velocity vector and the longitudinal axis of the body	deg
β	$\sqrt{M^2 - 1}$	
γ	ratio of specific heats; $\gamma = 1.4$ used herein	
Λ	leading edge sweep angle for delta wings	deg
\emptyset	aerodynamic roll angle; at $\emptyset = 0^\circ$ the lifting surfaces are normal to the plane of α	deg

Subscripts

B	body alone
BE	body-housing combination
BW	body-wing combination
E	housing
I	refers to inlet forebody and internal lift as in ΔC_{N_I}
W	wing

INTRODUCTION

The requirement for compactness in U. S. Navy missile designs results frequently in configurations which incorporate thick lifting surfaces of very-low-aspect ratio. These surfaces are invariably thick, e.g., Figures 1 and 2, because they are used to house electronics and hydraulics or serve as ducts, as in the case of side-mounted inlets on ramjet missiles. Current requirements on missile speed have increased to regions where guidance for making aerodynamic estimates for these surfaces is not available, either from theory or experiment.

Empirical estimation of the normal force coefficient, C_N , and center-of-pressure location, $X_{c.p.}$, for these surfaces is difficult because the shapes are usually unique for each new missile design and, therefore, the limited test data available are invariably for shapes that are quite different from the proposed shape in a new missile design. Existing empirical methods¹ have been derived for a specific class of surfaces and apply to the lower end of the Mach number range of interest in this presentation.

Simple theoretical methods that have been used (with limited success) do not take into account the effects of Mach number. Those that do, are not applicable at the very low values of aspect ratio inherent to these types of surfaces. These concerns have been expressed for some time.^{2,3}

A need exists, therefore, for either an empirical data base for a more general class of low-aspect-ratio lifting surfaces or a simple predictive method that is adequate in preliminary design for predicting C_N and $X_{c.p.}$ of this class of surfaces in speed ranges from moderate supersonic to hypersonic.

A simple, empirical predictive method for estimating C_N for very-low-aspect ratio surfaces is presented herein. It is shown to provide estimates of C_N that are adequate for preliminary design for a variety of thicknesses and shapes and a wide range of Mach numbers ($M \approx 2.5$ to 7.7) and angles of attack (α to 24°).

OBJECTIVE

The objective of this study was to determine a simple method for estimating in preliminary design the aerodynamic normal force coefficient of very-low-aspect ratio lifting surfaces (and body-wing carryover) at moderate supersonic to hypersonic speeds and to moderate angles-of-attack.

METHODOLOGY

A. BACKGROUND

The method presented herein for predicting C_N of very-low-aspect-ratio lifting surfaces evolved from observations of the experimental lifting characteristics of thick surfaces such as those depicted by the housings on the wind tunnel model shown in Figure 1. This model is representative of an Integral Rocket-Ramjet (IRR) missile. It was tested by APL/JHU in order to compile aerodynamic design information for components of this class of configurations since empirical methods for predicting C_N and $X_{c.p.}$ for this type of configuration and combinations of components were not available. Hart's empirical curves¹ had been shown to provide good predictions for low-aspect-ratio surfaces at $M \lesssim 3.0$, but these curves had been derived mostly for wings that were primarily thin surfaces. The applicability of this method to thick surfaces and to higher Mach numbers was therefore not known.

Simple theoretical methods that account for the Mach number variation of ΔC_{N_W} noted from test data are not applicable at the very-low-aspect ratios of interest herein; those derived for aspect ratios approaching zero do not account for the Mach number effects. This is demonstrated in Figure 3 wherein the test values of ΔC_{N_W} of the IRR E_1 housings (ΔC_{N_E} minus internal momentum) are compared with two simple theoretical methods, viz: modified Newtonian theory,⁴ plus wing-body carryover, i.e.,

$$\Delta C_{N_W} = \frac{\gamma + 3}{\gamma + 1} \left(1 - \frac{2}{\gamma + 3} \frac{1}{M^2} \right) (K_W + K_B) \frac{S_E}{S} \sin^2 \alpha \quad (1)$$

and slender wing theory⁵ plus cross flow as recommended by Flax and Lawrence,³ i.e.,

$$\Delta C_{N_W} = \left[\frac{\pi A.R.}{2 \times 57.3} \alpha + C_{D_c} \sin^2 \alpha \right] (K_W + K_B) \frac{S_E}{S} \quad (2)$$

The value of $C_{D_c} = 1.0$ was used in these calculations following the recommendation of Flax and Lawrence for the case of rounded tips. This number, however, could be something other than 1.0 according to Hoerner.⁶ The Morikawa carryover factors⁷ were used in Equations 1 and 2, and are used throughout this analysis.

B. APPROACH

Test data obtained on both thick and thin wings in various APL/JHU aerodynamic research and exploratory development programs were the primary source of data for the development of the empirical method presented herein. Selected

NASA data were also used. Sketches of the housing and wing configurations used in the analysis are given in Figures 4, 5, and 6; the sources for the test data⁸⁻¹⁶ are noted in the figures for each configuration.

In all cases, the wing (or housing) data were obtained from tests conducted with cruciform wing-body and with body alone configurations. The wing-body was roll oriented at $\emptyset = 0^\circ$, i.e., one pair of wings in the angle-of-attack plane. The test data then are derived from $\Delta C_{N_W} = C_{N_{BW}} - C_{N_B}$ and thus wing-body carryover is included in the wing lift.

The general approach in deriving and evaluating the present method using the test data discussed above, is:

1. Values of $\beta C_{N_{\alpha_W}}$ were extracted from test data obtained on the wing configurations sketched in Figures 4, 5, and 6.
2. Correlation curves of $\beta C_{N_{\alpha_W}}$ were deduced from the test values as follows: $\beta C_{N_{\alpha_W}} = F(\beta A.R.)$ for rectangular wings,
 $\beta C_{N_{\alpha_W}} = F(\beta \cot \Lambda)$ for delta wings, and
 $\beta C_{N_{\alpha_W}} = \text{constant}$ for thick wings.

A comparison of the derived curves with appropriate linear and slender wing theories is given.

3. These empirically derived curves were then used to calculate the values of ΔC_{N_W} for the 29 Mach number-configurational combinations used in the analysis. Comparisons with test data are given to demonstrate the adequacy of the present method.

RESULTS

A. PROCEDURE FOR EXTRACTING $\beta C_{N_{\alpha_W}}$ FROM TEST DATA

Values of $\beta C_{N_{\alpha_W}}$ that provide a good representation of the test data in the range of angle of attack tested were derived by first linearizing ΔC_{N_W} vs α as demonstrated in Figure 7 and then extracting $C_{N_{\alpha_W}}$ from the linearized values

of ΔC_{N_W} as follows:

$$C_{N_{\alpha_W}} = \frac{(57.3) (S/S_W)}{K_W + K_B} \frac{\Delta C_{N_W}}{\alpha}, \text{ per rad.} \quad (3)$$

where $\Delta C_{N_W} = C_{N_{BW}} - C_{N_B}$ and this includes mutual body-wing carryover. The carryover factors K_W and K_B were obtained from Morikawa's charts, Reference 7; Morikawa's values of K_W for rectangular wings were used for the configurations that are nearly rectangular. In the linearization of ΔC_{N_W} vs α , more emphasis was given to obtaining a representation of ΔC_{N_W} at the moderate to higher values of α than at the lower values according to the objective of this investigation.

The E_1 , E_2 , and E_3 configurations of Figure 4 have flow through the inlet-duct system and thus ΔC_{N_E} for these configurations include internal lift. The lift attributed to the inlet forebody and internal momentum was subtracted from the total lift of these housings in order to obtain ΔC_{N_W} since we are only interested in the external lift. Thus, for these configurations,

$$\Delta C_{N_W} = \Delta C_{N_E} - \Delta C_{N_I} = \Delta C_{N_E} - 2 \left(\frac{A_O}{A_I} \frac{A_I}{S} + \frac{A_C}{S} \right) \sin \alpha \quad (4)$$

A value of $A_O/A_I = 1.0$ was used in these calculations since the internal shock was not expelled for the cases considered. A_I and A_C are the combined cross sectional areas of the inlets and inlet forebodies, respectively.

Finally, the derived slopes were expressed in the usual functional forms found in design charts, i.e.,

$$\beta C_{N_{\alpha_W}} = F(\beta \text{ A.R.})$$

for rectangular wings, and

$$\beta C_{N_{\alpha_W}} = F(\beta \cot \Lambda)$$

for delta wings.

B. CORRELATION CURVES OF $\beta C_{N\alpha_W}$

1. Nearly-Rectangular Wings

The "best fit" values of $\beta C_{N\alpha_W}$ deduced from the test data on the nearly-rectangular housings and wings of Figures 4 and 5 are plotted in Figure 8 as a function of $1/\beta$ A.R. For comparison, the values of $\beta C_{N\alpha_W}$ predicted from linear and slender wing theories, Reference 5, for rectangular wings, are also shown in Figure 8, i.e.,

$$\beta C_{N\alpha_W} = 4 \left(1 - \frac{1}{2\beta \text{ A.R.}} \right) \quad \beta \text{ A.R.} > 1$$

$$\beta C_{N\alpha_W} = \frac{4}{\pi} \left[\left(2 - \frac{1}{\beta \text{ A.R.}} \right) \sin^{-1} \beta \text{ A.R.} + (\beta \text{ A.R.} - 2) \cosh^{-1} \frac{1}{\beta \text{ A.R.}} \right. \\ \left. + \left(1 + \frac{1}{\beta \text{ A.R.}} \right) \sqrt{1 - (\beta \text{ A.R.})^2} \right] \quad \frac{1}{2} < \beta \text{ A.R.} < 1 \quad (5)$$

and,

$$\beta C_{N\alpha_W} = \frac{\pi}{2} (\beta \text{ A.R.}) \quad \beta \text{ A.R.} < 1/2 \\ \text{(Slender Wing)}$$

It is seen, from Figure 8, that the difference between experiment and theory (given by these simple methods) is very large for $\beta \text{ A.R.} \gtrsim 0.67$ [$(1/\beta \text{ A.R.}) \approx 1.5$].

Note that the theoretical values of $C_{N\alpha}$ are lift curve slopes at $\alpha = 0^\circ$ whereas the test values are the mean values of C_N/α obtained from the full range of α tested. For the test cases where C_N was linear with α ($M \gtrsim 3.0$), these two values should be the same. These theoretical methods are usually recommended in various handbooks and textbooks because of their success in predicting $C_{N\alpha_W}$ at low values of α . Their success has been demonstrated by

several investigators at the low values of α and at low supersonic Mach numbers. The inadequacy of these theoretical methods for predicting ΔC_{N_W}

without adding a non-linear term, such as cross-flow lift, was demonstrated by Flax and Lawrence³ in 1951. Cross-flow lift for wings is a concept, taken from cross-flow lift on cylinders, which attempts to account for the vortex lift. The cross-flow drag value used in determining cross-flow lift is basically an experimental value obtained for a limited class of wings.^{3,6} More recent approaches use the concept of leading-edge and side-edge suction^{17,18} to account for non-linear lift. As far as can be established from the literature this approach is not applicable to the wing geometries of interest in this study.

Returning to the discussion of Figure 8, it is noted that the test values of $\beta C_{N_{\alpha_w}}$ for thick housings is generally lower than those for the "thin"

wings. A separate R.M.S. curve for the thin wings demonstrates this. The value of $\beta C_{N_{\alpha_w}} = 4/3$ marked on the ordinate of Figure 8 will be shown later

to provide a reasonable agreement with the majority of test values of ΔC_{N_w} for the thick wings used in this study, 12 Mach number-configurational combinations. The solid points shown in Figure 8 are for test cases where $M \lesssim 3.0$. In this region ΔC_{N_w} is very non-linear with α at low values of α . For these cases, it will be shown later that Hart's empirical method¹ provides good predictions at the lower values of α and for some cases at all values of α tested.

2. Thin Delta Wings

A similar correlation plot of $\beta C_{N_{\alpha_w}}$ for the test data for delta wings

is given in Figure 9 and is compared with linear theory for these wings. In this case $\beta C_{N_{\alpha_w}}$ is given as a function of $\beta \cot \Lambda$ and plotted vs. $1/\beta \cot \Lambda$.

The disagreement with linear theory is obvious. Note specifically that the test values of $\beta C_{N_{\alpha_w}}$ do not tend to 4 at $\beta \cot \Lambda = 1$ as predicted

by linear theory but rather they tend to 4 at $\beta \cot \Lambda = \infty$ which is in agreement with predictions for rectangular wings.

3. Combined Correlation Curve for Very-Low-Aspect-Ratio Wings

A comparison of the R.M.S. curve of $\beta C_{N_{\alpha_w}} = F(1/\beta A.R.)$ for thin nearly-rectangular wings (Figure 8) with the R.M.S. curve of $\beta C_{N_{\alpha_w}} = F(1/\beta \cot \Lambda)$

for thin delta wings (Figure 9) shows that the two curves are essentially the same. Thus, one single curve is proposed for predicting $\beta C_{N_{\alpha_w}}$, for both thin rectangular (or nearly rectangular) and for delta wings.

The curve has the same functional form for $\beta C_{N_{\alpha_w}}$ as shown in Figure 10. For

the thick wings, $\beta C_{N_{\alpha_W}} = 4/3$ is proposed for $(1/\beta \text{ A.R.}) \gtrsim 1.5$. Data were not found for thick surfaces for the region $(1/\beta \text{ A.R.}) \lesssim 1.5$ to determine the trend of $\beta C_{N_{\alpha_W}}$ for this region. The effect of wing thickness for ratios, t/d , between 0.2 and 0.1 also is not known; the thick wings used in the analyses had $t/d \geq 0.2$; the average "thickness" for the thin wings used was $t/d \lesssim 0.1$.

In summary, the correlation curves of Figure 10 are proposed as a simple empirical method for obtaining $\beta C_{N_{\alpha_W}}$ for very-low-aspect ratio wings. Since in practice these surfaces are usually mounted on a body of revolution the mutual body-wing interference should also be accounted for. Morikawa's factors are recommended for accounting for this interference mainly because they were used in deriving $\beta C_{N_{\alpha_W}}$ from test data. The adequacy of the proposed method for providing good engineering estimates of $\Delta C_{N_W} = C_{N_{BW}} - C_{N_B}$ at $M \gtrsim 2.5$ and α to about 24° is demonstrated in the next section.

C. COMPARISON OF TEST VALUES OF ΔC_{N_W} WITH EMPIRICAL PREDICTIONS USING THE PRESENT METHOD

The predicted values of ΔC_{N_W} are derived from the empirical curves of Figure 10 as follows:

$$\Delta C_{N_W} = \frac{\beta C_{N_{\alpha_W}}}{57.3 \beta} (K_W + K_B) \frac{S_W}{S} \alpha \quad (6)$$

where $\beta C_{N_{\alpha_W}}$ is per radian and α is in degrees. These values are compared in Figures 11 to 22 with the test data obtained from $C_{N_{BW}} - C_{N_B}$ for the 29 Mach number-configurational combinations used in the analysis. Calculated values of ΔC_{N_W} using Hart's method¹ are also shown, for the cases where this method is applicable, to demonstrate the adequacy of this method.

1. Thick Wings

Calculated values of ΔC_{N_W} using the present method, given by Figure 10 and Equation 6, are compared with test data from the thick housings in Figures 11 through 15. Values of ΔC_{N_W} obtained from Hart's empirical correlation curves¹ are also shown. The comparisons show, in general, that the

present method with $\beta C_{N_{\alpha_w}} = 4/3$ gives a good to excellent representation of the test values of $\Delta C_{N_{\alpha_w}}$ to $\alpha = 24^\circ$, $M \gtrsim 2.5$, for the five housing configurations of Figure 4. The predictions of the present method are especially good at $M \gtrsim 3.0$ where $\Delta C_{N_{\alpha_w}}$ is nearly linear with α .

At $M \lesssim 3.0$, the data are very non-linear with α at low angles-of-attack and Hart's method gives a better prediction than the present method, see Figures 11 and 14. At the higher Mach numbers the present method provides a better prediction.

2. Thin Nearly-Rectangular Wings

The results of the evaluation of the present method for thin nearly-rectangular wings are given in Figures 16 through 19. The test data are for the configurations of Figure 5. The comparisons again show that the present method provides good predictions. Hart's method also gives good predictions in the region of applicability of his method, $\beta A.R. \lesssim 0.8$, but this method is not better than the present method.

3. Thin, Delta Wings

The present method provides excellent predictions for the test data for the delta wings of Figure 6, Figures 20, 21 and 22. Hart's method was not derived for delta wings and thus a comparison with this method is not made for these wings.

CONCLUSIONS

An empirical method is derived herein for estimating the normal force coefficient (plus wing-body carryover), $\Delta C_{N_{\alpha_w}}$, of nearly-rectangular thick and thin wings, and of thin delta wings, of very-low-aspect ratio. The method, in combination with Morikawa's interference factors, gives good predictions in the range of Mach numbers from 2.5 to 7.7 and angles of attack to 24° . For near-rectangular wings at $M \lesssim 3.0$, Hart's empirical correlation curves of Reference 1 are recommended for estimating $\Delta C_{N_{\alpha_w}}$.

REFERENCES

1. H. H. Hart, "An Aerodynamic Study of Very-Low-Aspect-Ratio, Nearly Rectangular Lifting Surfaces at Supersonic Speeds, APL/JHU CM-931, February 1958.
2. W. Hatalsky and P. H. Jackson, Jr., "Correlation of Theory and Experiment in the Supersonic Interference of Very Low Aspect Ratio Wings," Appendix II, Unclassified. Minutes of the Thirty-Sixth Regular Meeting, Bumblebee Aerodynamics Panel, June 1957, APL/JHU TG 14-33, August 1957, Confidential.
3. A. H. Flax and H. R. Lawrence, "The Aerodynamics of Low-Aspect-Ratio Wings and Wing-Body Combinations," Cornell Aeronautical Laboratory Report CAL-37, September 1951.
4. Robert Earl Oliver, An Experimental Investigation of Flow About Simple Blunt Bodies at a Nominal Mach Number of 5.8, Journal of the Aeronautical Sciences, February 1956.
5. Donovan and Lawrence, Editors, Aerodynamic Components of Aircraft at High Speeds, Volume VII, High Speed Aerodynamics and Jet Propulsion, Princeton University Press, 1957, Section A.14.
6. Hoerner and Borst, Fluid Dynamic Lift, page 17-7, published by Mrs. Liselotte A. Hoerner, 1975.
7. George Morikawa, "Supersonic Wing-Body Lift," Journal of the Aeronautical Sciences, Vol. 18, No. 4, April 1951.
8. E. F. Lucero, "Longitudinal Aerodynamics of the Configurational Components of the Integral Rocket-Ramjet (IRR) Configurations at Mach Numbers 2.0 to 4.5 and Angles of Attack to 24°," APL/JHU BFD-1-79-016, 25 September 1979.
9. General Dynamics/Convair High Speed Wind Tunnel Test Report HST 258-0, 3-5 May 1968.
10. General Dynamics/Convair High Speed Wind Tunnel Test Report HST 259-0, March 1968.
11. General Dynamics/Convair High Speed Wind Tunnel Test Report HST TR-009-0, July 1979.
12. E. F. Lucero, "Hypersonic Configuration Study, Part II: Body-Dorsal Configurations," APL/JHU BBA-2-71-021, 6 December 1971.
13. M. Leroy Spearman and Charles D. Trescott, Jr., "Effects of Wing Planform on the Static Aerodynamics of a Cruciform Wing-Body Missile for Mach Numbers up to 4.63," NASA TMX-1839, July 1969.

14. R. J. Vendemia, Jr., and M. P. Guthrie, "Effects of Variation of Lifting Surfaces' Leading and Trailing Edge Locations on Aerodynamic Normal Force, Pitching Moment, and Tail Characteristics of a Standardized Medium Range Type Missile at $M = 2.5$," APL/JHU BBA-SM-007-64, 8 May 1964.
15. APL/Navy Standard Missile Test Data Package: von Karman Gas Dynamics Facility, AEDC, U. S. Air Force, Tunnel A; Project No. V41A-N2A, Test Period: March 15-23, April 1-5, May 13-25, 1977.
16. General Dynamics/Convair High Speed Wind Tunnel Test Report HST-TAR-180-0, May 1966.
17. Edward C. Polhamus, "Predictions of Vortex-Lift Characteristics by a Leading-Edge Suction Analogy," Journal of Aircraft, Vol. 8, No. 4, April 1971.
18. John E. Lamar, "Prediction of Vortex Flow Characteristics of Wings at Subsonic and Supersonic Speeds," Journal of Aircraft, Vol. 13, No. 7, July 1976.



Fig. 1 Photo showing one type of very-low-aspect ratio, thick housings (with flow through) used in analysis.

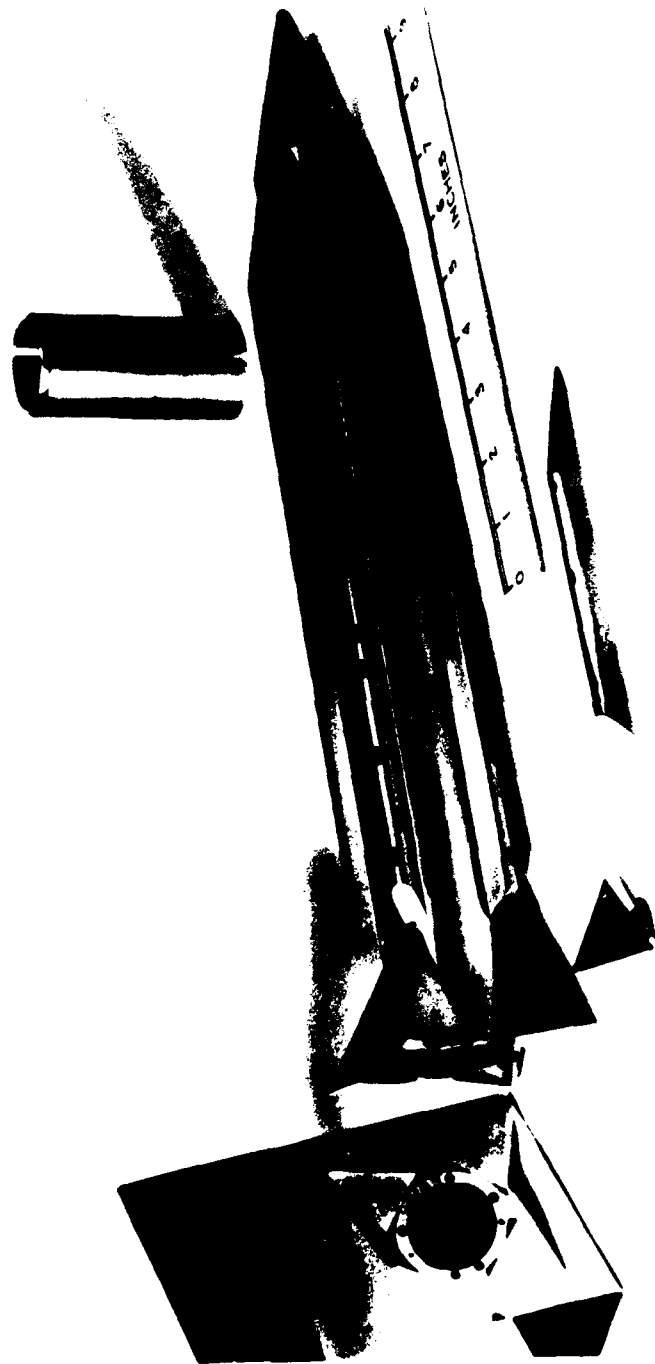


Fig. 2 Photo showing one type of very-low-aspect-ratio, thick wings used in analysis.

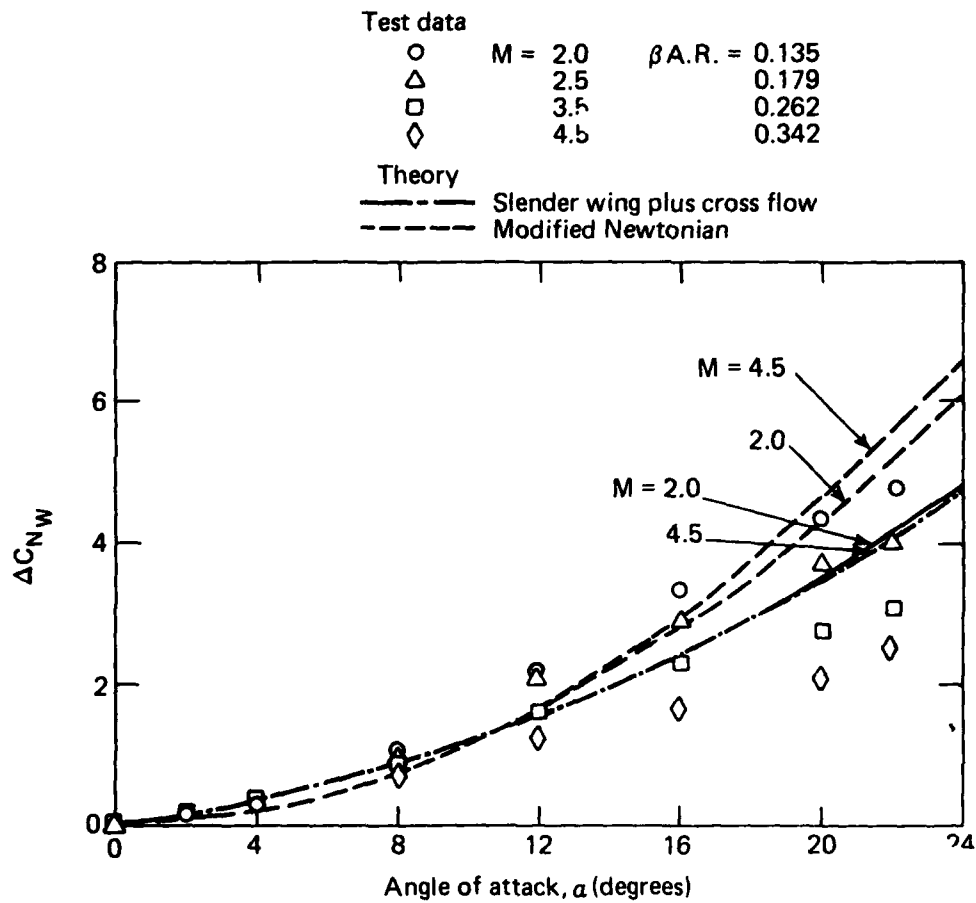
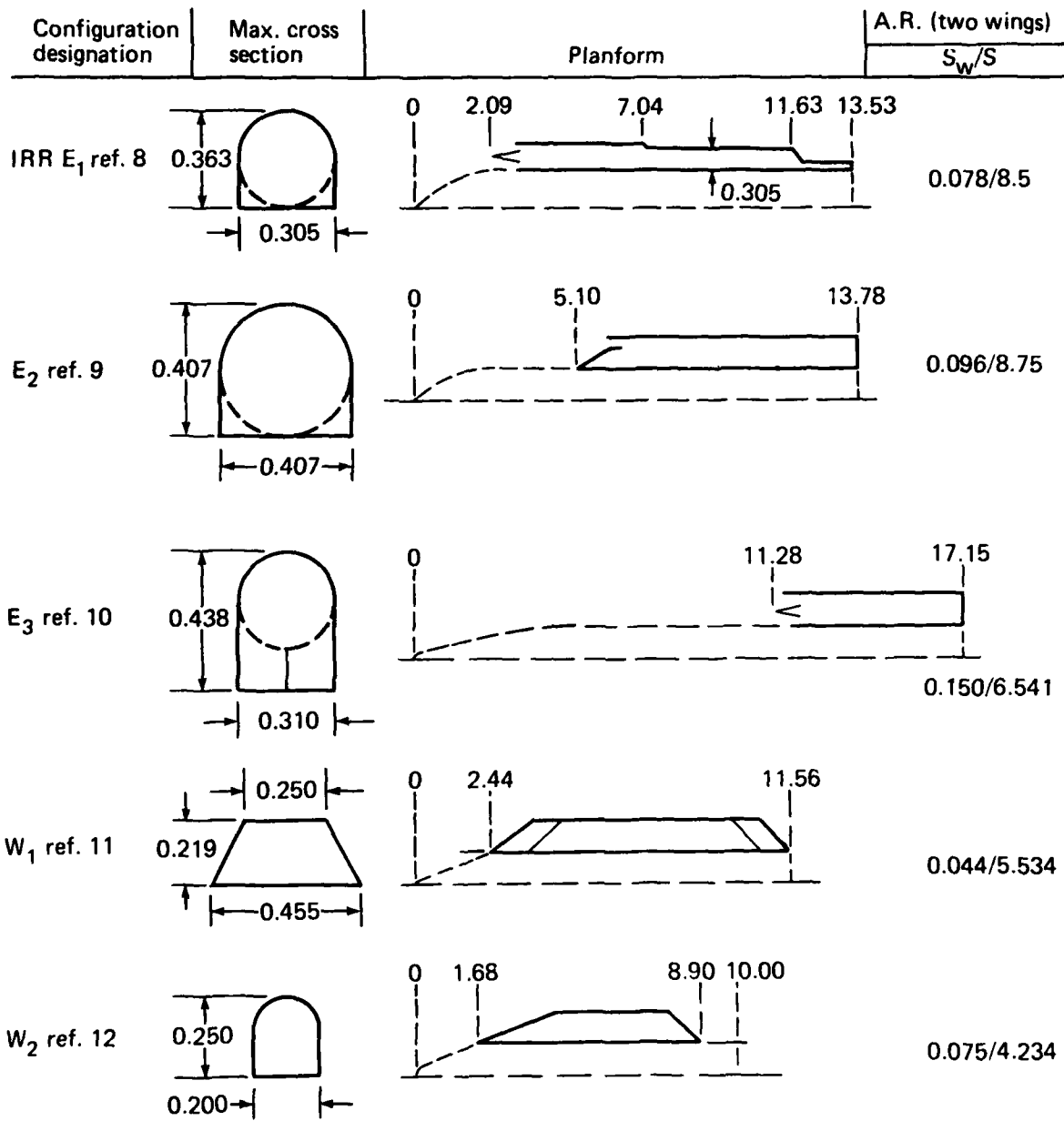
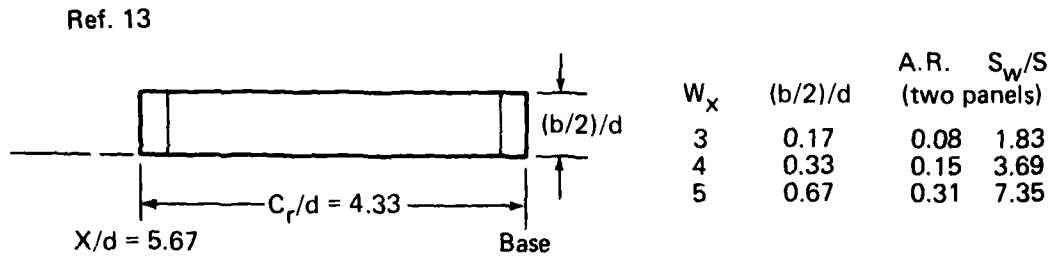


Fig. 3 Comparison of C_N data from IRR E_1 housing with two simple predictive methods. $\beta = 0^\circ$.



Dimensions in body diameters

Fig. 4 Sketches of low A.R. wings (housings) used in analysis.



W_6 (ref. 14): A.R. = 0.120; $S_w/S = 6.285$

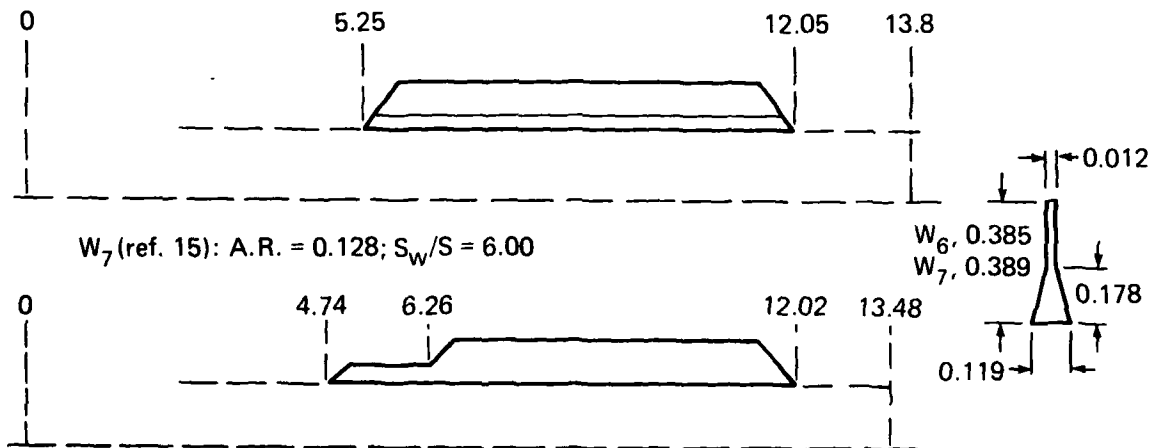
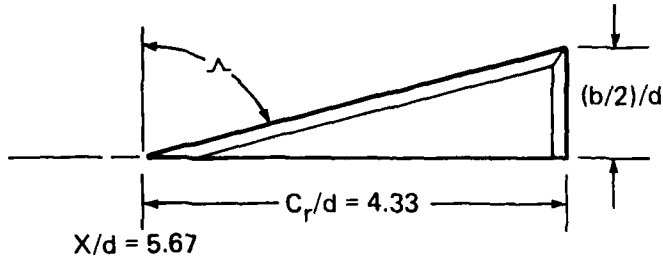


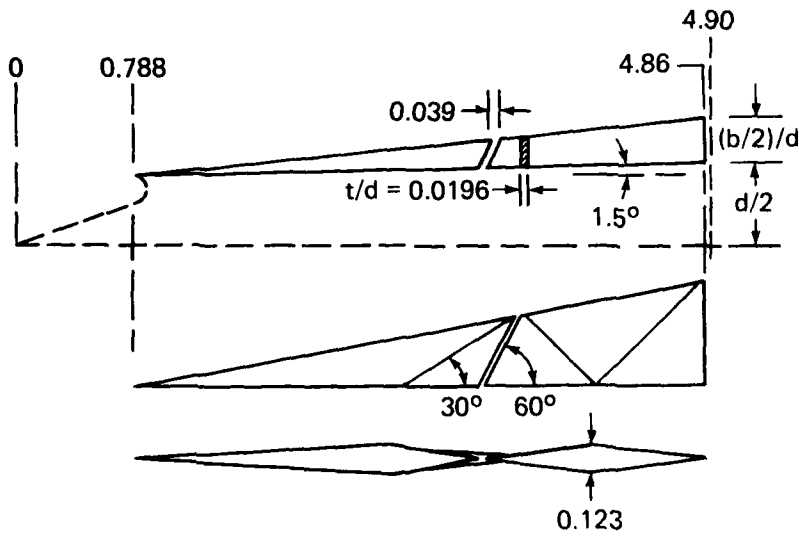
Fig. 5 Thin, low-aspect-ratio, nearly-rectangular wings.

Ref. 13



W_x	$b/2/d$	Λ	A.R.	S_w/S (two panels)
8	0.33	85.6°	0.31	1.83
9	0.67	81.3°	0.61	3.69
10	1.33	72.9°	1.23	7.35

Ref. 15



W_x	$(b/2)/d$	A.R.	S_w/S
11	0.088	0.088	0.453
12	0.206	0.204	1.057
13	0.706	0.710	3.61

Dimensions in body diameters

Fig. 6 Thin, low-aspect-ratio, delta wings.

Let ΔC_{N_W} be approximated, in range of a tested, by

$$\Delta C_{N_W} = C_{N_{a_W}} (K_W + K_B) (S_W/S) a / 57.3$$

Then,

$$\beta C_{N_{a_W}} = \frac{(\Delta C_{N_W} / a) (57.3 \beta)}{[(K_W + K_B) (S_W/S)]}$$

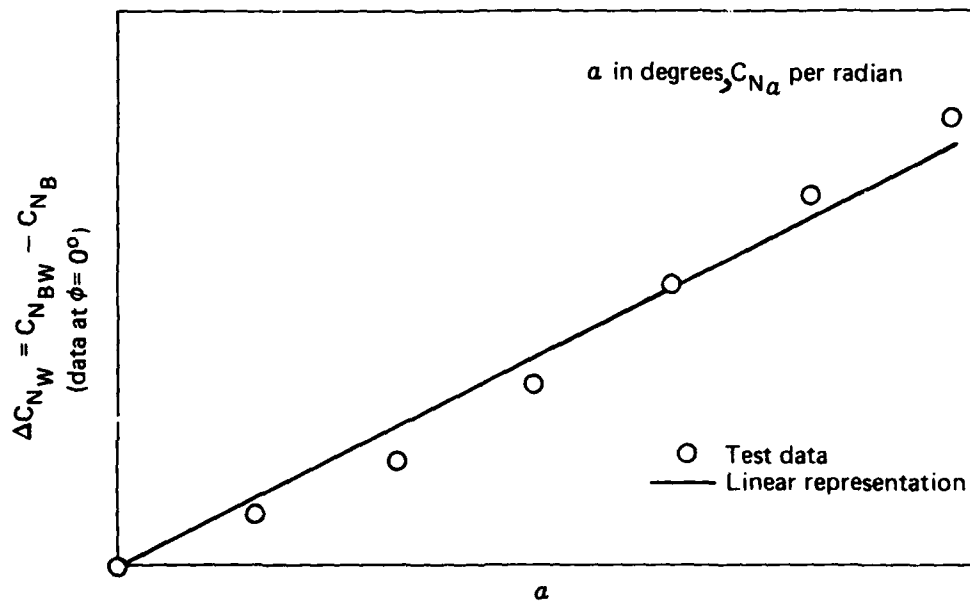


Fig. 7 Procedure used for linearization of test data to derive $\beta C_{N_{a_W}}$

AD-A111 763

NAVY AEROBALLISTICS ADVISORY COMMITTEE

F/G 20/4

PROCEEDINGS OF THE NAVY SYMPOSIUM ON AEROBALLISTICS (12TH) HELD--ETC(U)

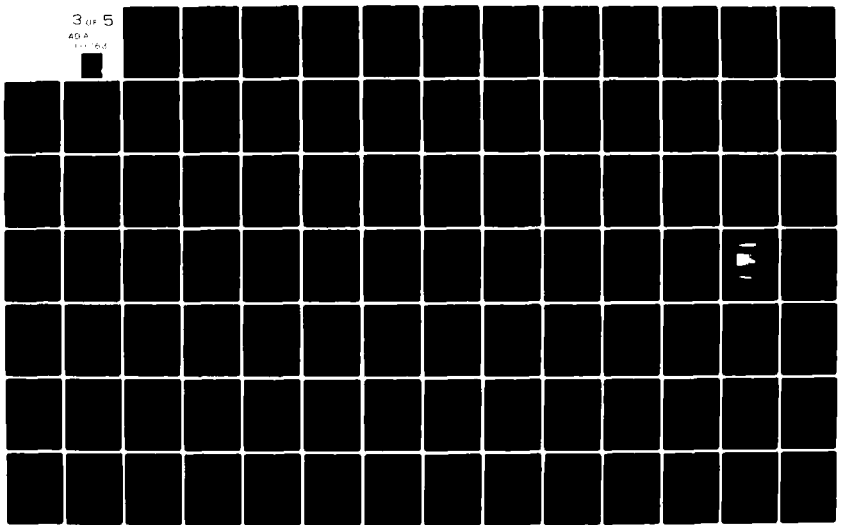
MAY 81

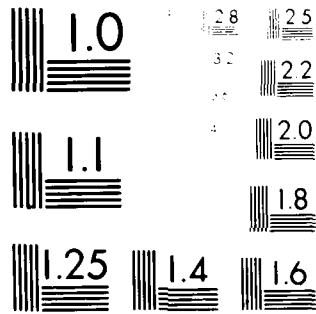
UNCLASSIFIED

NL

3 of 5

ADA
111 763





MICROCOPY RESOLUTION TEST CHART
 NATIONAL BUREAU OF STANDARDS-1963-A

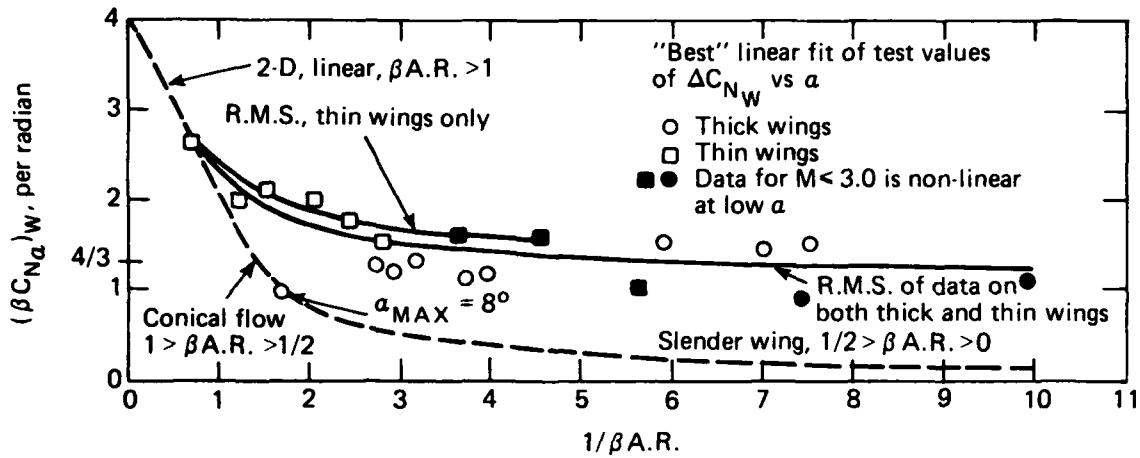


Fig. 8 Correlation of test data on nearly-rectangular wings with $\beta A.R.$

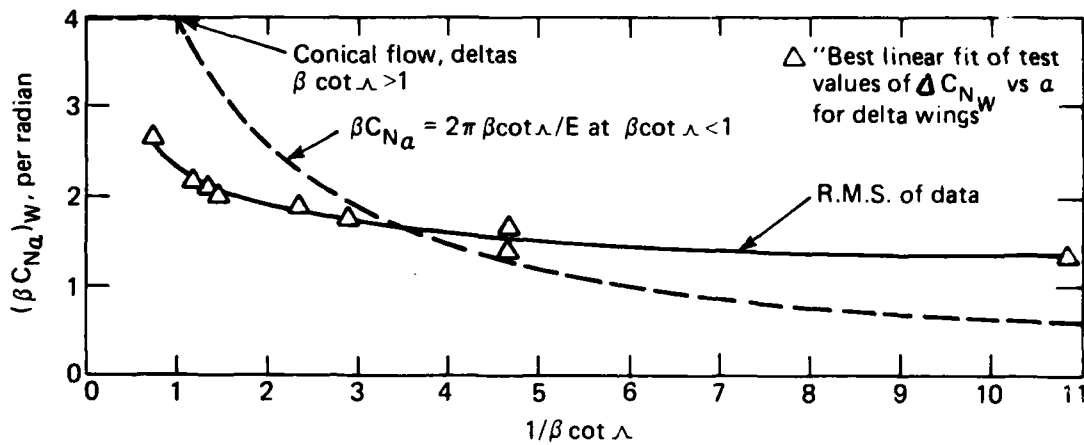


Fig. 9 Correlation of test data on thin delta wings with $\beta \cot \lambda$.

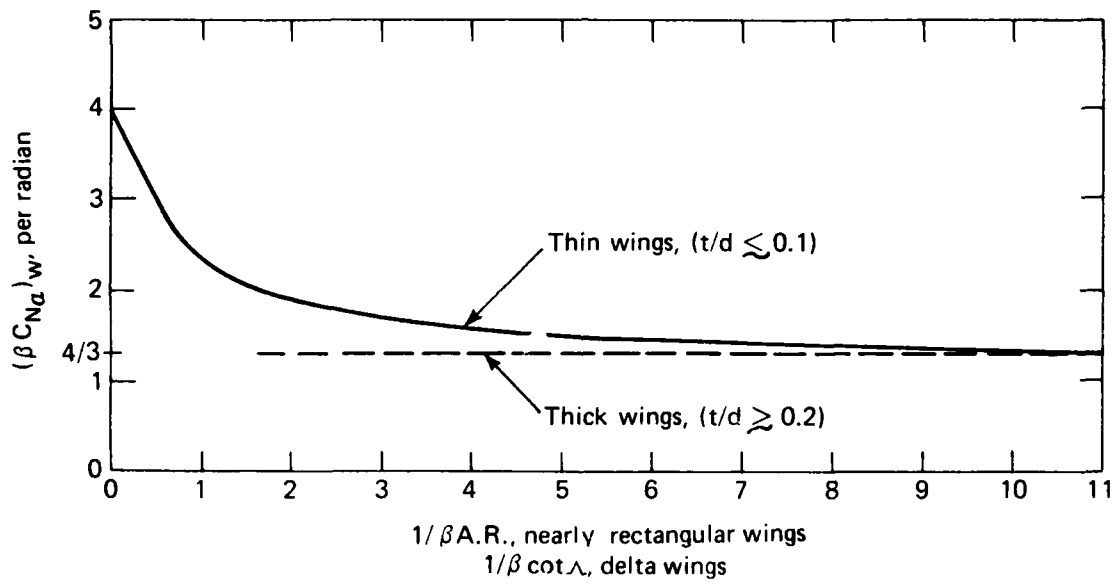


Fig. 10 Proposed design charts for $\beta C_{N\alpha}$ of low-aspect-ratio wings $M \leq 2.5$ $\phi = 0^\circ$.

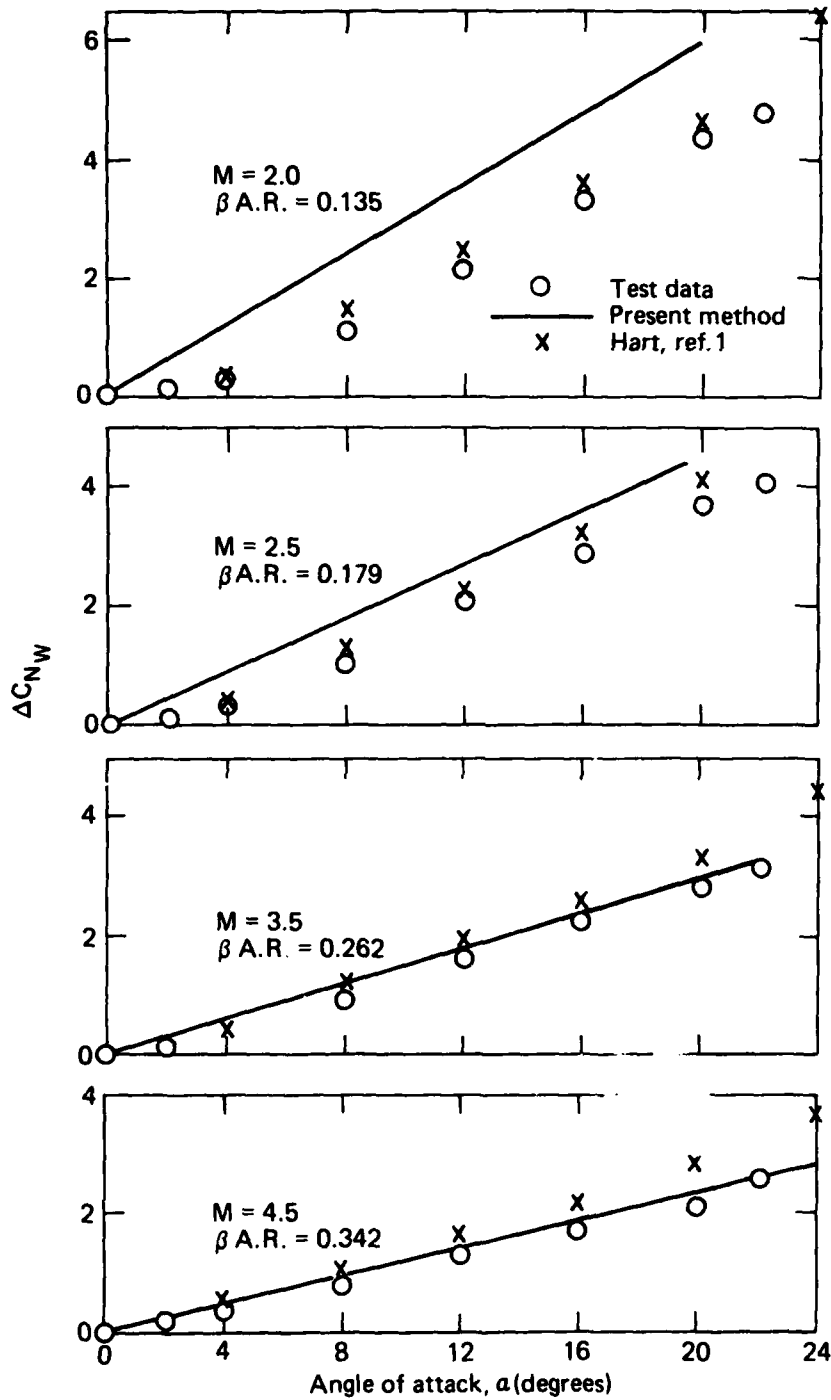


Fig. 11 Comparison of test and predicted values of ΔC_{N_W} of E_1 , $\phi = 0^\circ$, $t/d = 0.305$.

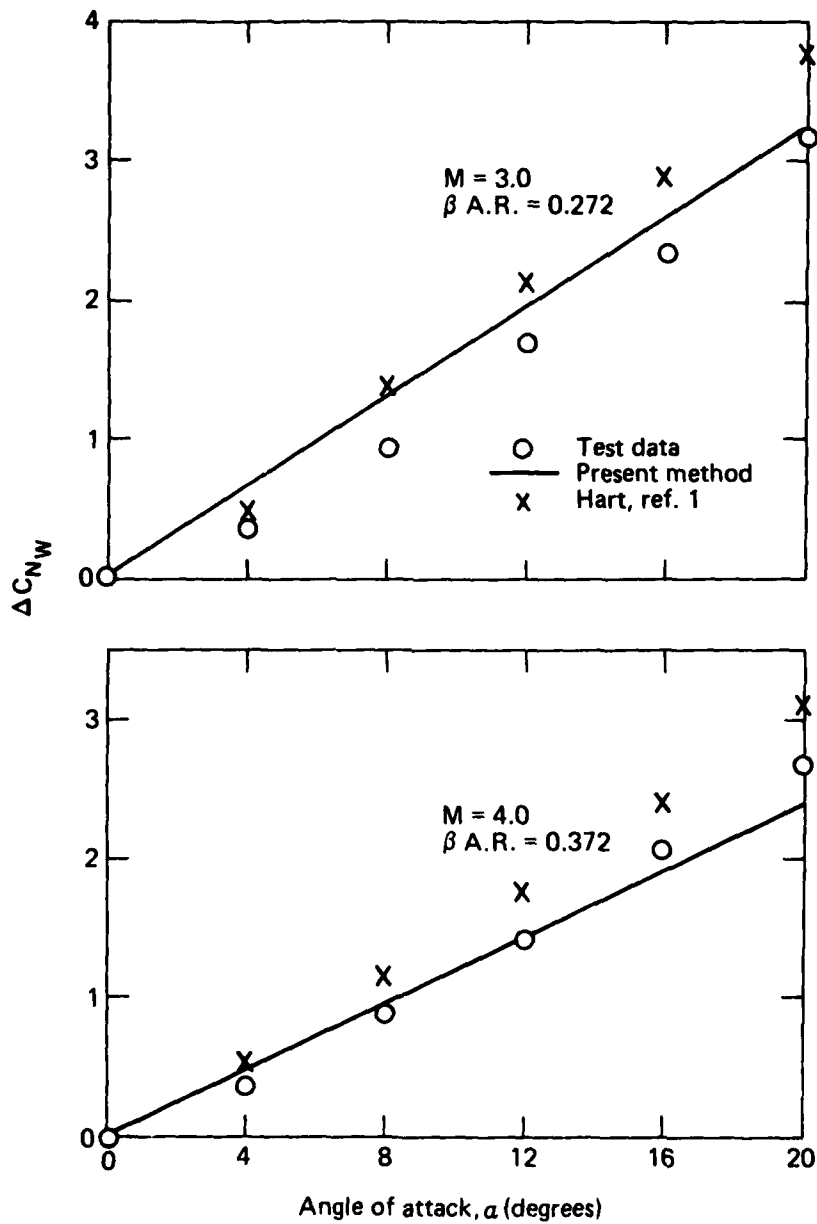


Fig. 12 Comparison of test and predicted values of ΔC_{NW} of E_2 , $\phi = 0^\circ$, $t/d = 0.407$.

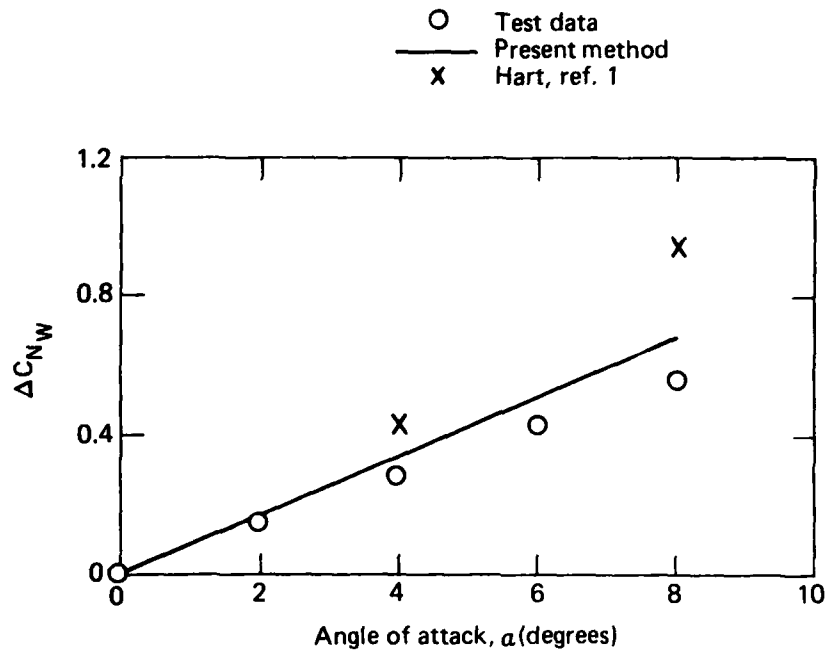


Fig. 13 Comparison of test and predicted values of ΔC_{N_W} of E_3 , $M = 4.17$; $\phi = 0^\circ$, $\beta A.R. = 0.607$, $t/d = 0.312$.

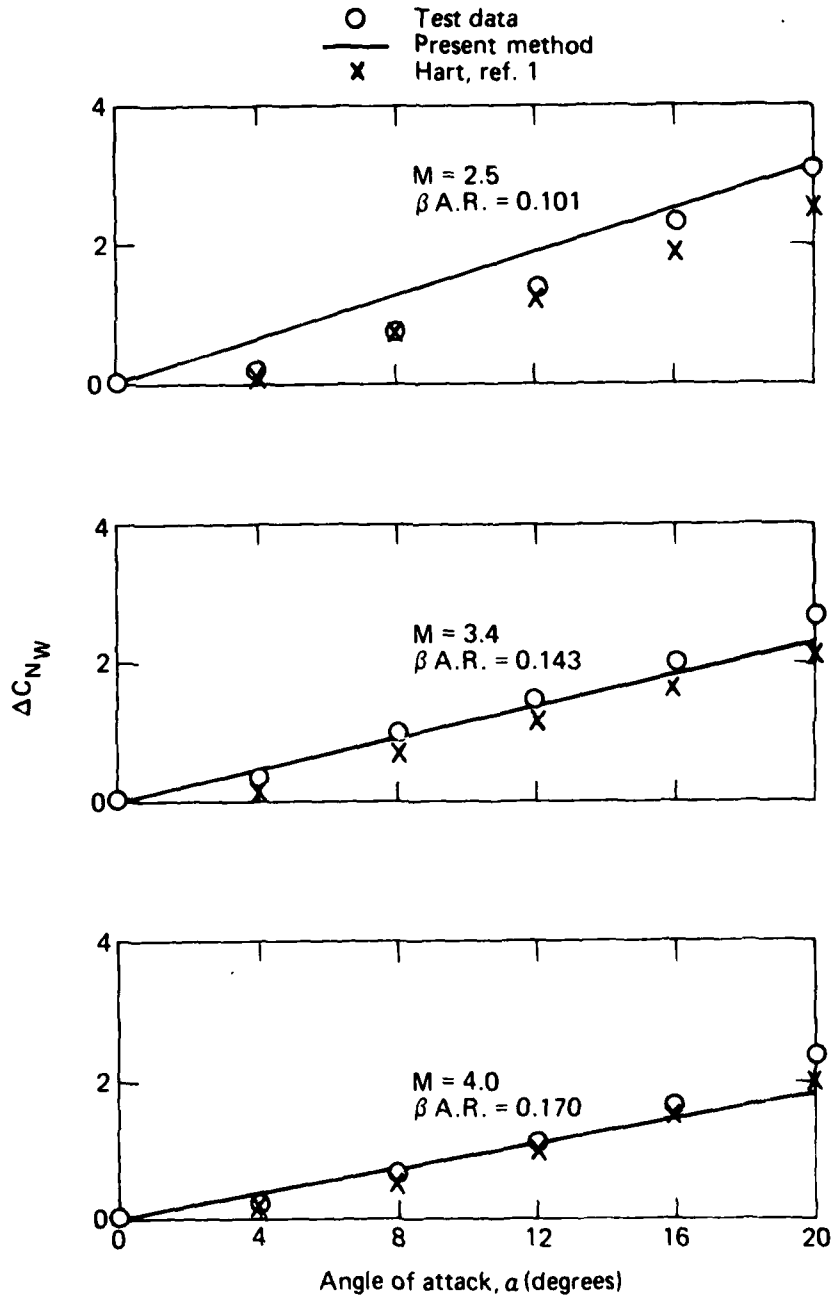


Fig. 14 Comparison of test and predicted values of ΔC_{NW} of W_1 , $\phi = 0^\circ$, $t/d = 0.352$ Ave.

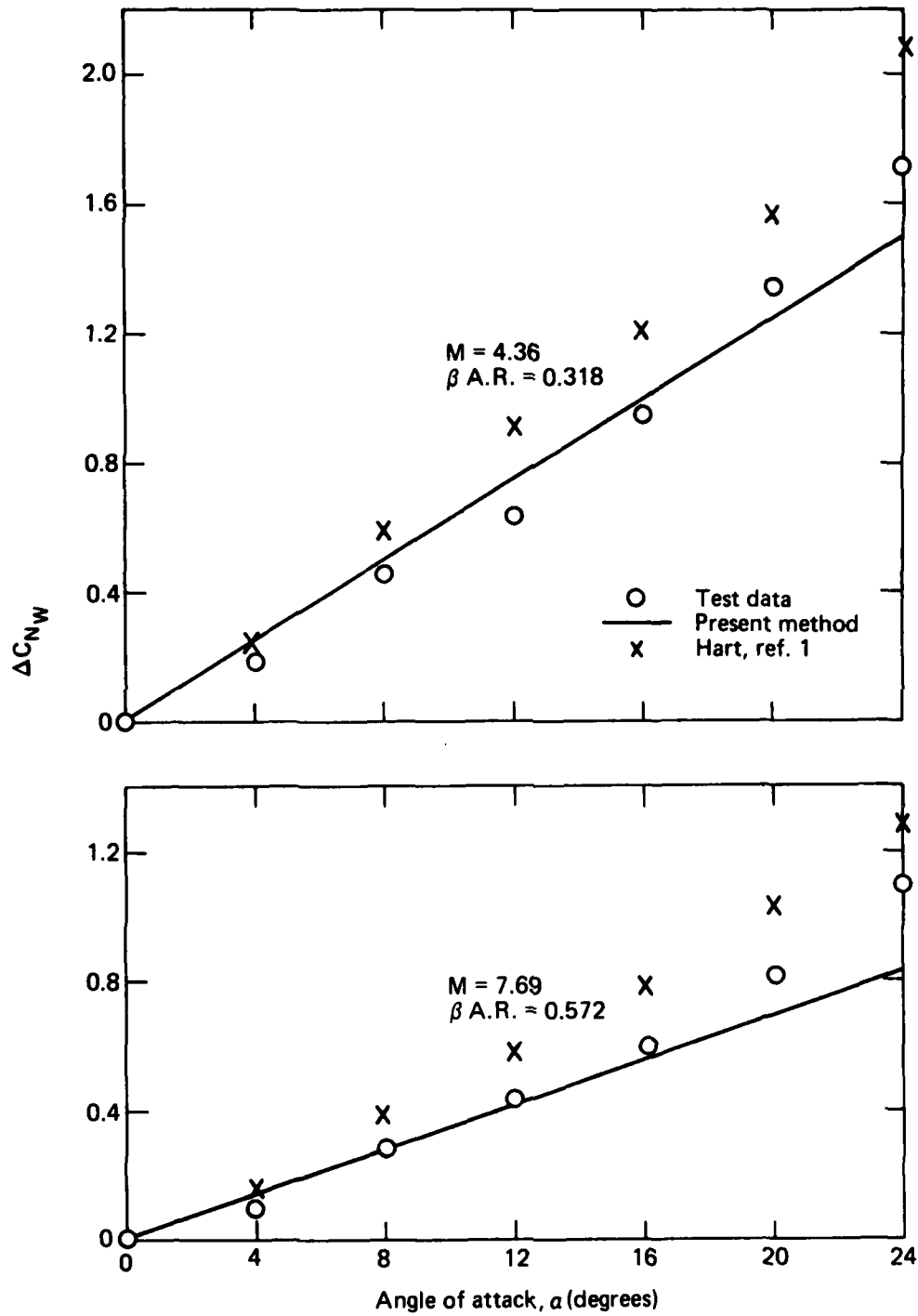


Fig. 15 Comparison of test and predicted values of ΔC_{N_W} of W_2 , $\phi = 0^\circ$, $t/d = 0.200$.

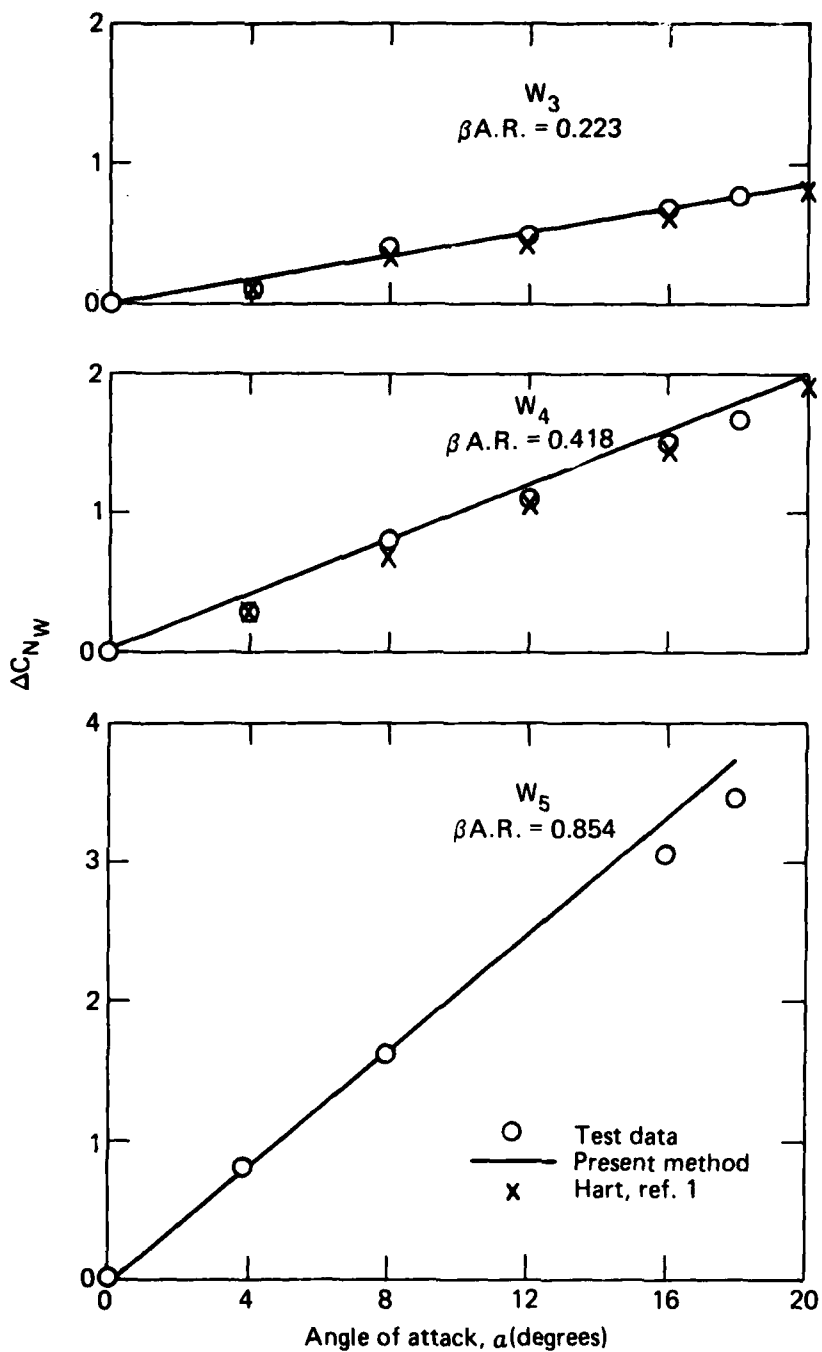


Fig. 16 Comparison of test and predicted values of $\Delta C_{N,W}$ for thin rectangular wings
 $M = 2.96$, $\phi = 0^\circ$.

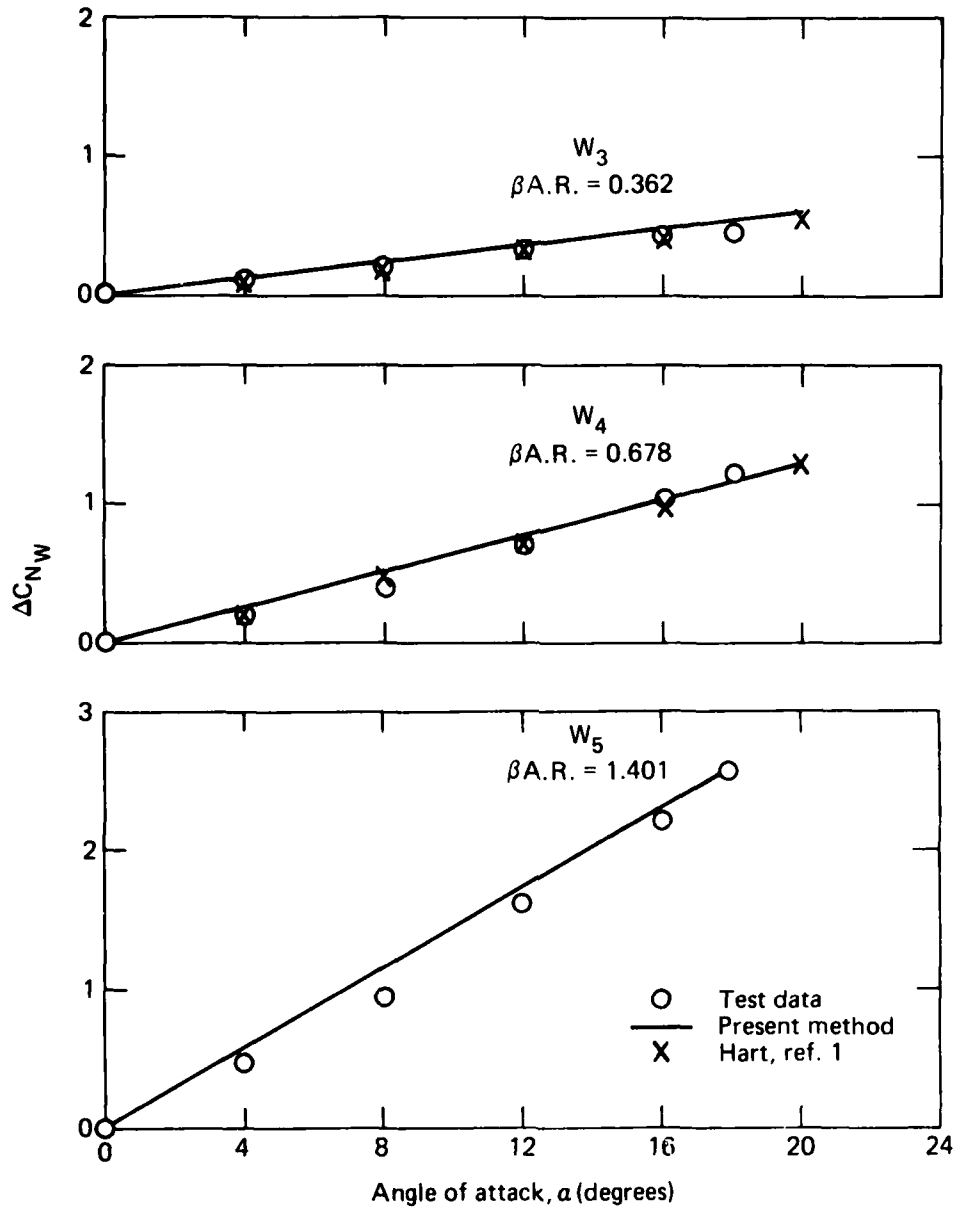


Fig. 17 Comparison of test and predicted values of ΔC_{N_W} for thin rectangular wings $M = 4.63$, $\phi = 0^\circ$.

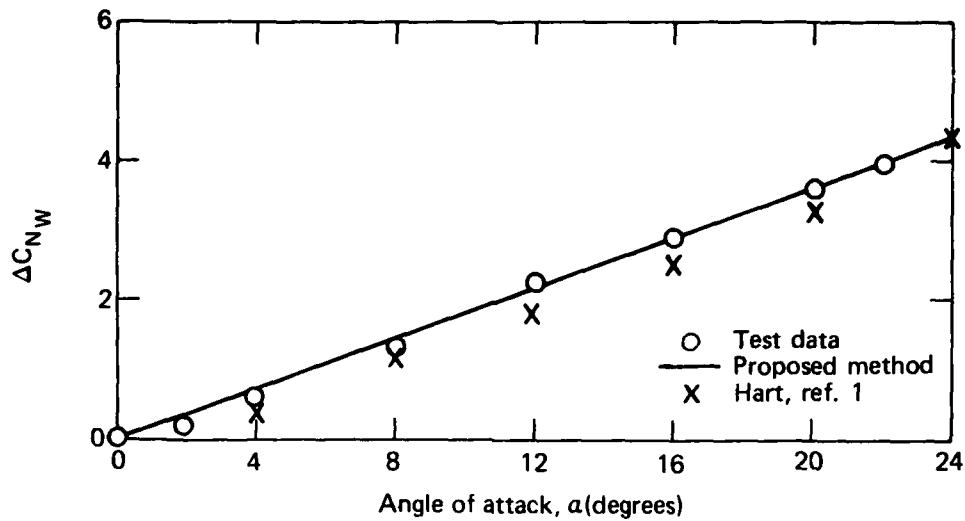


Fig. 18 Comparison of test and predicted values of ΔC_{N_W} for W_6 , $M = 2.5$, $\phi = 0^\circ$, $\beta A.R. = 0.275$.

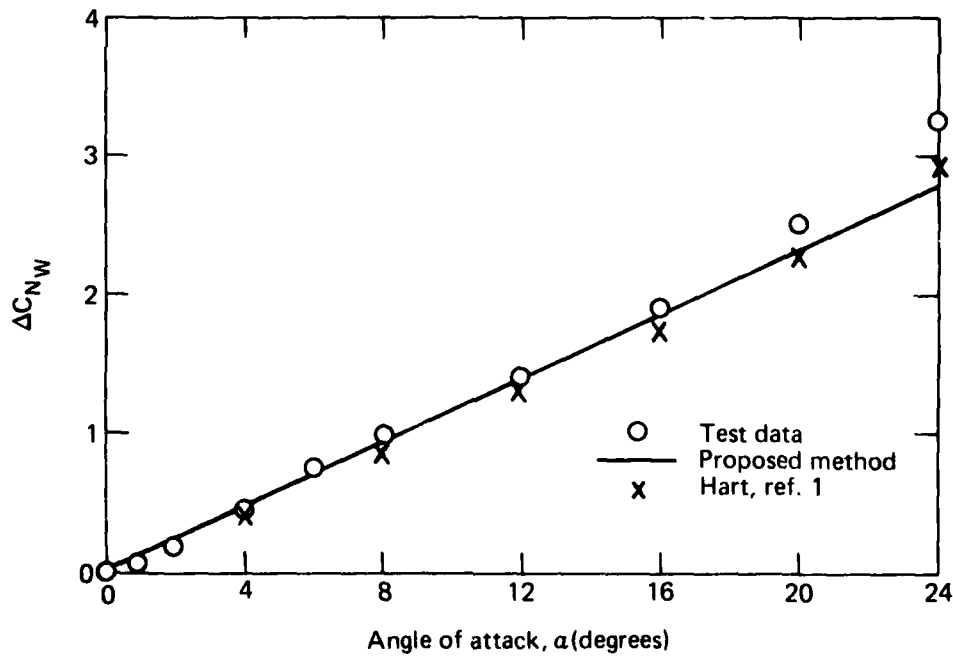


Fig. 19 Comparison of test and predicted values of ΔC_{N_W} for W_7 , $M = 4.02$, $\phi = 0^\circ$, $\beta A.R. = 0.498$.

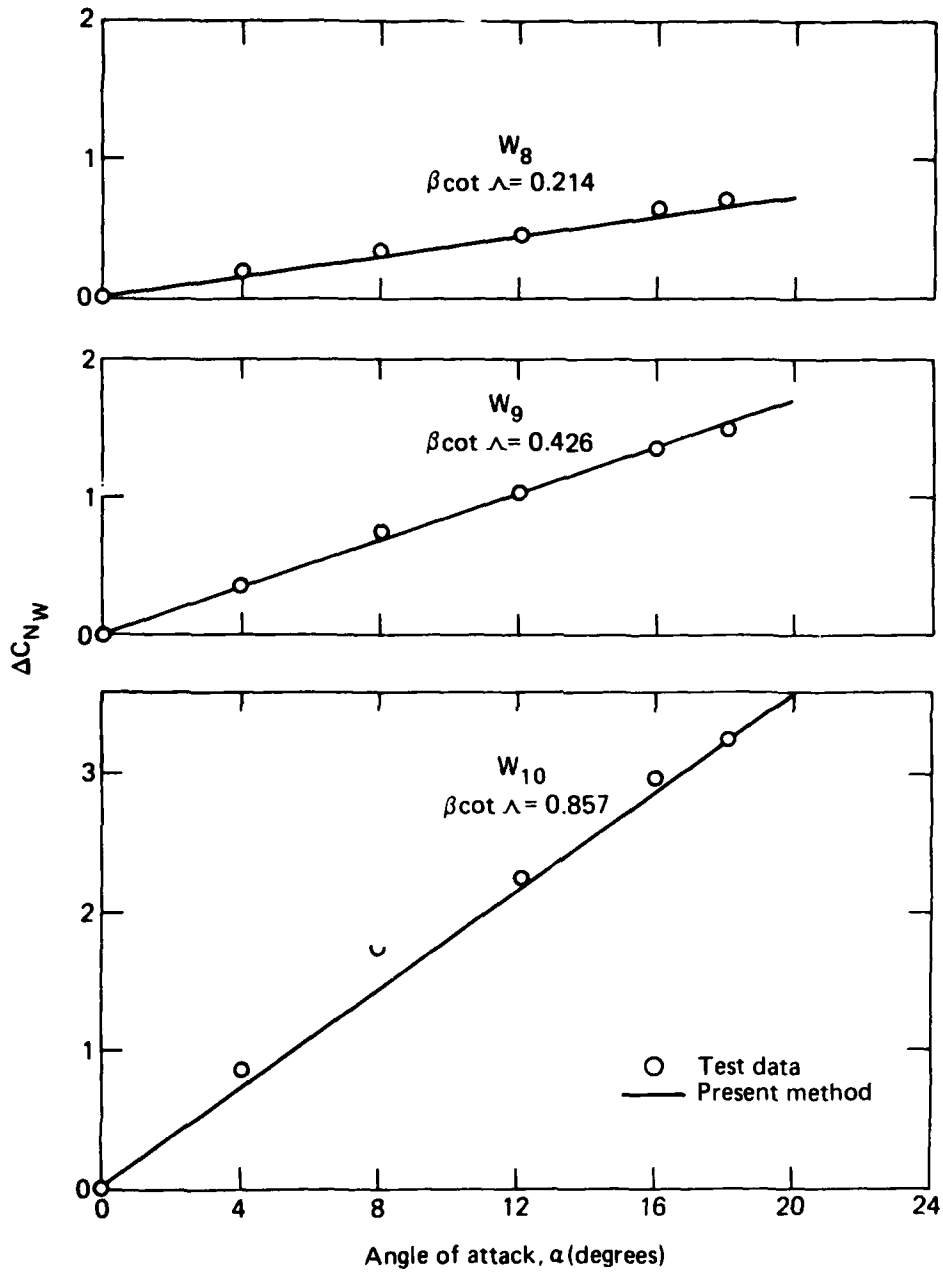


Fig. 20 Comparison of test and predicted values of ΔC_{N_W} for thin delta wings, $M = 2.96$, $\phi = 0^\circ$.

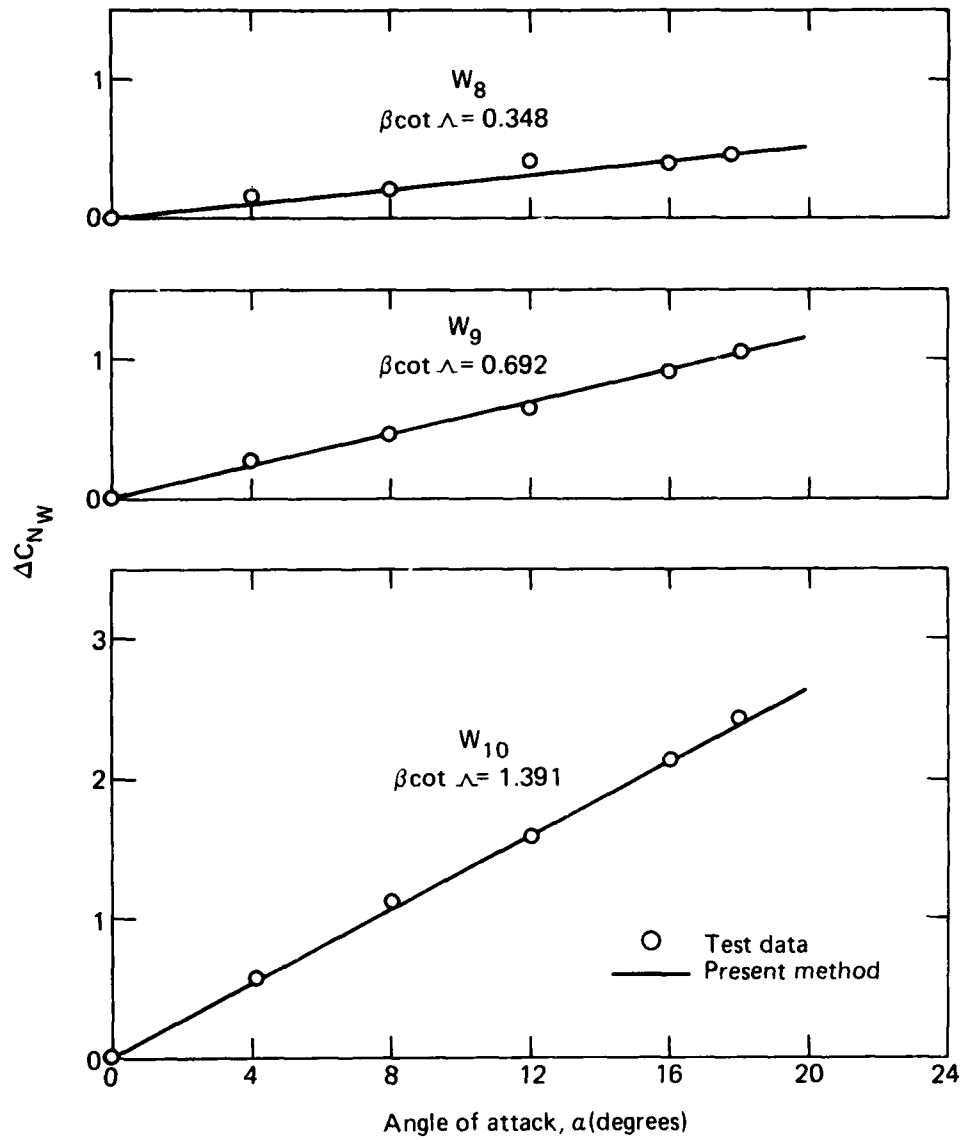


Fig. 21 Comparison of test and predicted values of ΔC_{N_W} for thin delta wings, $M = 4.63$, $\phi = 0^\circ$.

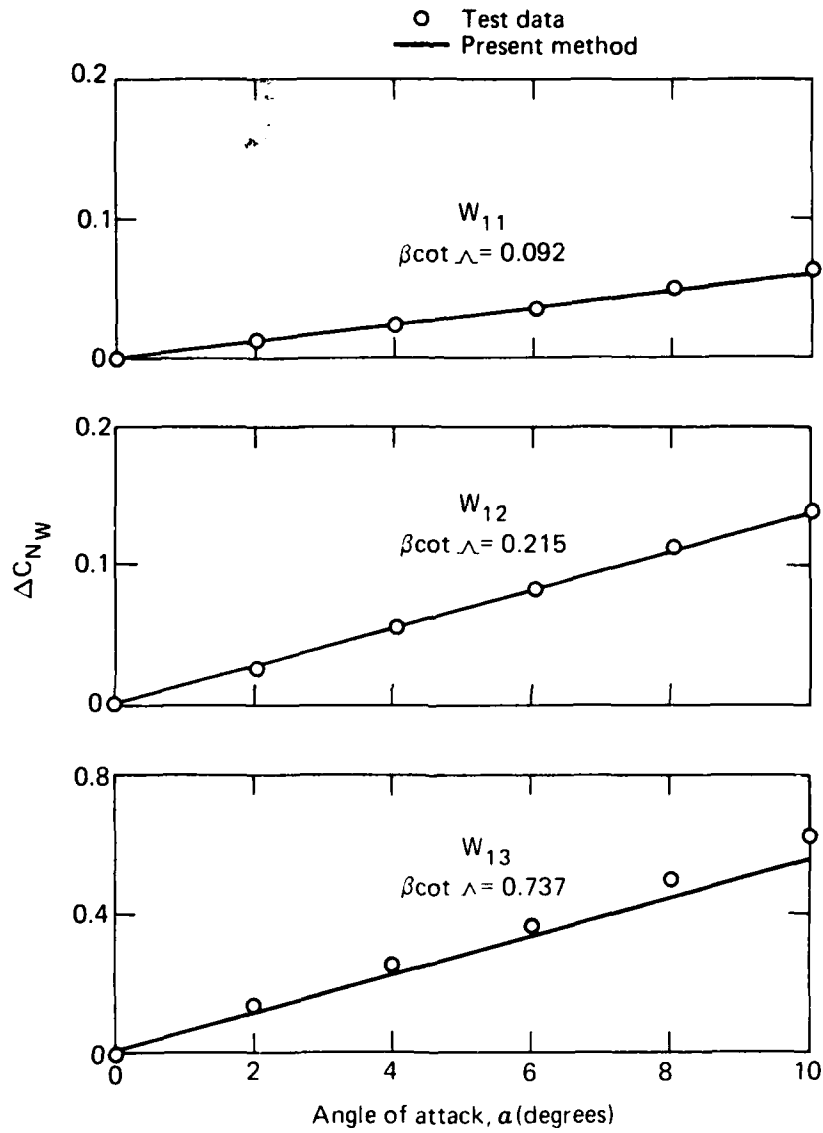


Fig. 22 Comparison of test and predicted values of ΔC_{N_W} of thin delta wings, $M = 4.37$, $\phi = 0^\circ$.

SUPERSONIC AERODYNAMICS OF A CLASS
OF CONE-DERIVED WAVERIDERS

Maurice L. Rasmussen
University of Oklahoma, Norman, Oklahoma, and
Air Force Armament Laboratory, Eglin AFB, Florida

Donald C. Daniel
Air Force Armament Laboratory, Eglin AFB, Florida

Martin C. Jischke
University of Oklahoma, Norman, Oklahoma

ABSTRACT

The aerodynamic properties of a new class of missile airframes that are derived from the known supersonic flow fields past inclined circular and elliptic cones are discussed. The theoretical foundations and initial force and moment data have been presented recently elsewhere. The present paper advances this knowledge in several ways. Force and moment data for two waverider configurations are presented for $M_\infty = 8$, extending the previous data taken in the range $M_\infty = 3$ to 5. Surface pressure data are also presented, and plans for future free-flight ballistic tests are discussed. The implications of the data and the underlying theory toward the design of highly maneuverable missiles with high lift and low drag, together with proposals for integrated vertical fins and blended inlets, are considered.

INTRODUCTION

Demanding performance and maneuverability requirements for future supersonic and hypersonic missiles will require high-lift, low-drag configurations with good control effectiveness. Non-circular airframe configurations that efficiently integrate volumetric storage, lifting capability, and propulsion components such that aerodynamic heating and radar cross-section are minimized and lift-to-drag ratios are maximized will be required. Discussions of such requirements are given by Giragosian,¹ Fleeman,² and Nielsen.³

A comprehensive research program that addresses many of these requirements is under way. This research is directed toward the study of lifting-body configurations operating at the high Mach numbers of interest. The theoretical analysis is based on small perturbations of axisymmetric flows past circular cones, the perturbations stemming from small angles of attack and small eccentricity of the cone cross section. By this means accurate approximate analytical results are obtained for shock shapes and the shock-layer structure. Since any stream surface can be utilized as a solid surface in an inviscid flow, lifting-body configurations are constructed when free-stream upper surfaces are selected to complement the lower conical-flow stream surfaces.

The resulting aerodynamic shapes are called cone-derived waveriders because they appear to ride on a conical shock wave attached beneath them. The generation of certain specific shapes and the properties of their shock-layer structures are discussed by Rasmussen.⁴ The generalization of this analysis for arbitrary small conical perturbations of a basic axisymmetric conical flow is given by Jischke.⁵ General design considerations relating to the aerodynamic performance of waverider configurations are discussed by Kuchemann.⁶

Experimental results for the forces and moments on two waverider configurations were presented recently⁷ for the Mach-number range 3 to 5, the on-design conditions being $M_\infty = 4$. Those results focused on a configurational comparison of the two waveriders with themselves and with a baseline elliptic cone. For this experimental range, the waverider models were observed to be efficient lift-producing configurations, producing maximum L/D ratios on the order of 2.5 times greater than for the comparative elliptic cone. The overall implications of these results suggest that the waverider configurations make strong contenders for future hypersonic missile and aircraft configurations.

In this paper further results describing the aerodynamics of these waverider configurations are presented. A comparison of the experimental pressure distribution with the theoretical prediction, for the on-design condition $M_\infty = 4$, will be shown. Additional force and moment results for the off-design condition $M_\infty = 8$ will also be presented. Plans for ballistic free-flight tests will be discussed briefly. In view of the promise of these waverider configurations, proposals for integrated vertical fins and blended inlets will be set forth within the framework of the underlying waverider blended-streamsurface philosophy.

DESCRIPTION OF EXPERIMENTS

Sketches of the waverider model configurations that were tested are shown in Figures 1(a) and 1(b) together with a table of the pertinent dimensions in inches. The configuration shown in 1(a) is referred to as the circular-cone waverider (CCWR) and the configuration in 1(b) as the elliptic-cone waverider (ECWR). The base area of the models is denoted by A_b . The position of the body-fixed (or sting) coordinate system, to which the six force and moment coefficients are referred, is also shown. These models were designed on the basis of the theory of Reference 4, and a more complete description of the surface shapes and shock shapes is given in Reference 7. The on-design Mach number is $M_\infty = 4$, for which the theoretical shock shapes are also shown in Figures 1(a) and 1(b).

Tests on the two waverider configurations were conducted in tunnels A and B of the von Karman Facility at the USAF Arnold Engineering Development Center. The tests in tunnel A were conducted over the angle-of-attack and angle-of-sideslip ranges of $\pm 20^\circ$ and at the Mach numbers 3.0, 3.5, 4.0, 4.5, and 5.0, and results for the forces and moments, Schlieren data, and oil-flow data were reported in Reference 7. Corresponding data for $M_\infty = 8$ were obtained in tunnel B. Descriptions of the tunnels and airflow calibration information can be found in Reference 8.

Besides the results described in Reference 7, surface pressure distribution data were obtained in tunnel A. A comprehensive description of these results will be presented in the future. In the present paper only the azimuthal pressure distributions at the on-design conditions ($M_\infty = 4$) will be presented so that a comparison with the related theory can be realized.

The data taken in tunnel B for the nominal Mach number $M_\infty = 8$ (the actual Mach number was $M_\infty = 7.93$) show the effects of strong Mach-number deviations from the on-design conditions. In these tests no measurements of pressure distribution were made. The unit Reynolds number, Re/L , for these tests was 2 million per foot. The corresponding test in tunnel A showed essentially no differences on the force and moment coefficients for the change of unit Reynolds number from 1 to 2 million per foot.

PRESSURE DISTRIBUTIONS

A comparison of theory and experiment for the pressure coefficient on the curved surface of the circular-cone waverider for the on-design conditions ($M_\infty = 4.02$, $\alpha = -3.76^\circ$, $\beta = 0^\circ$) is shown in Figure 2. A corresponding comparison for the elliptic-cone waverider is shown in Figure 3 ($M_\infty = 4.02$, $\alpha = \beta = 0$). The symmetry rays on the curved underneath compression surfaces are denoted by $\phi = 180^\circ$. The theoretical pressure distribution is determined by the perturbation theory described in Reference 7 or 9. The theory agrees with the data well, being most in error near $\phi = 180^\circ$, about 10% for the circular-cone waverider and 5% for the elliptic-cone waverider. For both waveriders the pressure first increases inward from the lip ($\phi = 90^\circ$ for the circular-cone waverider and $\phi = 110^\circ$ for the elliptic-cone waverider), reaches a maximum near the region where the delta winglet fairs into the body, and then decreases toward a minimum at the symmetry ray $\phi = 180^\circ$.

For both configurations it was found that the pressure distributions were conical, that is, the surface pressure on a given ray was constant. Further, the pressure coefficient on the upper flat surfaces was measured to be zero for the on-design condition, in accordance with theory. A comprehensive presentation of the pressure data for the off-design conditions will be forthcoming.

FORCE AND MOMENT COEFFICIENTS

Figures 4 to 11 show the Mach-number variations in the force and rolling-moment coefficients, in the Mach-number range 3 to 8, as either angle of attack or sideslip angle is varied in the range $\pm 20^\circ$. These results are for the forebody contribution only, that is, the contribution of the base pressure has been eliminated. Since $M_\infty = 4$ is the on-design Mach number, $M_\infty = 3$ is the off-design on the low side and $M_\infty = 8$ is the off-design on the high side. Variations in angle of attack or sideslip angle represent off-design conditions due to orientation.

The normal-force coefficients, $C_N \equiv -F/qA_b$, are shown in Figures 4 and 5 as functions of angle of attack for the circular-cone and elliptic-cone waveriders. For a given angle of attack, the absolute value of C_N decreases as M_∞ increases. This behavior continues the trend reported in Reference 7

for which $M_\infty = 5$ was the largest Mach number. For positive angles of attack the curves for a given Mach number are nearly linear with α up to $\alpha = 20^\circ$. The slopes of those curves yield $C_{N\alpha}$. Approximately, these are, per radian,

<u>CCWR</u>		<u>ECWR</u>	
M_∞	$C_{N\alpha}$	M_∞	$C_{N\alpha}$
3	3.76	3	6.03
4	3.31	4	5.63
8	3.14	8	4.94

As a basis for comparison of these values, the elliptic cone with 1.87 major-minor axis ratio tested in Reference 7 showed values of $C_{N\alpha}$ equal to 2.58 and 1.15 when the cross wind was perpendicular to the major and minor axes, respectively. Of course, $C_{N\alpha}$ for a slender circular cone has the small disturbance value 1.96 approximately. The waveriders, and especially the elliptic-cone waverider, thus produce large normal-force coefficients. The change for above-design Mach numbers is more gradual than for below-design Mach numbers.

The Mach-number effects are small for the axial-force coefficients, $C_A \equiv -F_x/qA_b$, and the drag coefficients, $C_D \equiv D/qA_b$. These results are shown in Figures 6 and 7 for the elliptic-cone waverider. Similar results exist for the circular-cone waverider, and the results for $M_\infty = 4$ can be found in Reference 7. The minimum value of C_D occurs near the angle of zero lift, which has a small, but non-negligible, variation with Mach number.

Variations in the L/D ratios with Mach number and angle of attack are shown in Figures 8 and 9 for the circular-cone and elliptic-cone waveriders. Near its maximum value, L/D decreases as M_∞ increases. This variation with Mach number is most pronounced near the maxima in the curves and is maintained, but to a lessening degree, as α increases. As α decreases from the maximum L/D condition, the variation with Mach number reverses character down to zero lift, the values of L/D increasing as M_∞ increases. As α further decreases such that the lift is negative, a maximum in the absolute value of L/D is reached which is nearly the same value as the maximum L/D value near the on-design condition. Thus the waveriders could fly upside down with the maximum L/D values being nearly the same as for the corresponding near on-design conditions, but the individual values of C_L and C_D would both be less than the near on-design conditions.

The theoretical on-design orientations (at $M_\infty = 4$) are $\alpha = -3.72^\circ$ for the circular-cone waverider and $\alpha = 0$ for the elliptic-cone waverider, and these are very close to the orientation that produces the maximum experimental L/D values. For $M_\infty = 8$, the maximum values of L/D are shifted slightly toward negative angles of attack, and the angles of zero lift become more negative also.

The body-fixed side-force coefficient, $C_y \equiv F_y/qA_b$, as a function of Mach number and sideslip angle, β , is shown in Figure 10 for both the circular-cone and elliptic-cone waveriders. The variation with M_∞ is very

small from $M_\infty = 3$ to 4, that is, near the on-design Mach number. As M_∞ increases from $M_\infty = 4$ to 8, however the value of C_y decreases significantly for a fixed negative value of β .

For sideslip conditions the flow near the leeward and windward lips of the waveriders is different depending on whether the Mach number is below or above the on-design value, which in this case is $M_\infty = 4$. For Mach numbers on-design and below, the shock wave is always detached from the leeward lip, becoming more so as the angle of sideslip increases. For Mach numbers above the on-design value, the shock wave at the leeward lip will remain attached at small sideslip angles and become detached as the sideslip becomes larger. On the other hand, at the windward lip for below-design Mach numbers the shock wave will be detached until a certain sideslip is obtained, and it will be attached as the sideslip further increases. For above-design Mach numbers, the shock wave will remain attached on the windward lip.

The pressure on the surface near the lips of the waveriders appears to be more affected by Mach-number variations than the remainder of the body surface. Since the winglets near the lip are relatively thin, the surface area projected in the direction of the axis is small, and hence the axial and drag coefficients show little variation with M_∞ . The variations of C_N and C_L are much more pronounced, however.

The pitching-moment and yawing-moment coefficients show the corresponding variations with Mach number as their counterpart force coefficients C_N and C_L . Their variations with α and β at $M_\infty = 4$ are shown in Reference 7. The variations of the rolling-moment coefficients, $C_l \equiv M_x / q A_b L$, with Mach number and sideslip angle are shown in Figure 11 for both waveriders. The curves for the circular-cone waverider are nearly linear with sideslip angle and show a small decrease as M_∞ changes from $M_\infty = 3$ to 4, and a much larger decrease as M_∞ changes further from $M_\infty = 4$ to 8. For the elliptic-cone waverider, the curves for $M_\infty = 3$ and 4 show some nonlinearity with sideslip angle, and for larger amounts of sideslip C_l decreases more as M_∞ increases from $M_\infty = 3$ to 4 than it does from $M_\infty = 4$ to 8. The rolling-moment coefficient is much larger for the circular-cone waverider, and it appears that both waveriders would tend to roll into a turn when $\alpha = 0$.

PLANNED BALLISTIC TESTS

Plans have been formed for ballistic free-flight tests of the elliptic-cone waverider at the Air Force Armament Laboratory Aeroballistic Research Facility. These tests are meant to determine static and dynamic stability characteristics of the elliptic-cone waverider and to observe its overall flight behavior. The model will be approximately $L = 2.5$ inches long and launched at about $M_\infty = 3$, which is the maximum speed available for this model at this facility. For a homogenous cone the center of mass occurs at 75% of its length from the vertex. For the elliptic-cone waverider, the forebody center of pressure is at approximately 68% of the length from the vertex in the pitching mode and 82% of the length of the cone in the yawing mode (based on the data of Reference 7). In order to obtain static stability, the model will be hollowed out by drilling into the base so that the center of mass is forward of the center of pressure.

CONSIDERATIONS ON THE DESIGN OF FINS AND INLETS

The cone-derived waveriders produce large lifting forces and L/D ratios which are favorable for missile maneuverability and range. The on-design conditions can be predicted well by the underlying, relatively simple, perturbation theory. This is very desirable as a design tool, yielding conceptual simplicity and allowing for ease of parametric studies. The experimental study shows that off-design effects resulting from Mach-number variation and orientation of the body produce flows that remain clean and essentially conical, without undesirable secondary flow or other effects. The data together with the theory show substantial promise for the design of practical new missile configurations. Toward these ends, it is useful to speculate on the design of control surfaces and blended-inlet configurations.

VERTICAL FINS

It is conceivable that control devices such as flaps and ailerons can be built into the trailing edges of either the flat upper surfaces or the curved lower surface of the waveriders. It is also possible that a vertical fin would be desirable or necessary for proper control. A fin that produces a known simple disturbance flow field can be designed. Reference 4 suggests a methodology for doing this by means of well-known caret-waverider configurations which are constructed from the known two-dimensional constant flow behind plane oblique shock waves. Two such caret-waverider vertical fins are shown attached to an elliptic-cone waverider in Figures 12(a) and 12(b). The fin in Figure 12(a) begins at the vertex of the elliptic-cone waverider, and the fin in Figure 12(b) begins at half the distance back on the body. For the purposes of illustration, these fins are shown thicker than probably desirable. The starting position of the fin and the thickness of the fin at its base (described by a wedge flow-disturbance angle) allow for versatility in the design of this family of fins. For on-design conditions, the shock produced by this fin is planar, and the flow behind it is uniform and known. Thus further flow disturbances produced by flaps on the trailing edge of the fin can be calculated. Experimental tests are being planned for a set of such fins attached to the elliptic-cone waverider.

INLETS

The geometrical surfaces of waveriders are constructed by utilizing the stream surfaces of known flow fields. In a sense, therefore, viscous effects ignored, these waverider surfaces are natural surfaces and the flow tends to move easily past them. This motion appears to be substantiated by the data presented herein and in Reference 7. In addition, the flow properties for the waverider configurations are known for the special on-design condition. It is useful to extend this concept to the design of exterior contours of inlets. The basic ideas can be formulated by constructing an idealized conical waverider with an inlet.

If $\vec{V}(\vec{r})$ is a known velocity field and $d\vec{r}$ is a differential line element, then the differential equation for a streamline element is given by $\vec{V} \times d\vec{r} = 0$. In spherical coordinates and for conical flow, this reduces to

$$\frac{dr}{u(\theta, \phi)} = \frac{rd\theta}{v(\theta, \phi)} = \frac{r \sin \theta d\phi}{w(\theta, \phi)}, \quad (1)$$

where u , v , and w are the known radial, polar, and azimuthal components of velocity. The last two members of Equation (1) are independent of r and integration thus yields the form

$$F_1(\theta, \phi) = C_1, \quad (2)$$

where C_1 is an arbitrary constant of integration. In the framework of perturbation theory, the lowest order of approximation of Equation (2) was used to generate the curved surfaces of the circular-cone and elliptic-cone waveriders.

The first two members of Equation (1) can be written as

$$\frac{dr}{r} = \frac{u(\theta, \phi)d\theta}{v(\theta, \phi)}. \quad (3)$$

When ϕ is eliminated in Equation (3) in favor of θ by means of Equation (2), then Equation (3) can be integrated in principle to the form

$$F_2(r, \theta; C_1) = C_2, \quad (4)$$

where C_2 is another arbitrary constant of integration. Equations (2) and (4) constitute two families of stream surfaces, and their intersections produce the streamlines, a specific value of C_1 and C_2 for each streamline.

Any arbitrary stream surface is described by $F(\vec{r}) = 0$, where

$$\vec{V} \cdot \nabla F = 0 \quad \text{on} \quad F = 0. \quad (5)$$

Equation (5) is a first-order equation for $F(\vec{r})$, and it has the characteristic equations (1). Thus any arbitrary function of the constants of integration C_1 and C_2 is a solution to Equation (5), that is,

$$F = F(C_1, C_2). \quad (6)$$

It follows that an arbitrary stream surface can be specified by setting one constant of integration to be an arbitrary function of the other:

$$C_2 = G(C_1). \quad (7)$$

Since the functional relations (2) and (4) are presumed known, any arbitrary stream surface can be developed by means of Equation (7).

These ideas can be developed simply for an idealized conical waverider, devised from the well-known axisymmetric flow past a circular cone. In this case, we have $u = u_0(\theta)$, $v = v_0(\theta)$, and $w = 0$. Equation (2) becomes simply

$$\phi = C_1, \quad (8)$$

that is, any plane through the axis of symmetry is a stream surface. It is also possible to integrate Equation (3) to the form

$$r [\rho_0(\theta)v_0(\theta)\sin\theta]^{\frac{1}{2}} = C_2, \quad (9)$$

where $\rho_0(\theta)$ is the density field of the axisymmetric cone flow. For hypersonic flow past slender cones,⁴ the density field is nearly a constant, and Equation (9) can be approximated by the form

$$r [\sin\theta]^{\frac{1}{2}} = C_2, \quad (10)$$

where δ is the semi-vertex angle of the cone. Setting $C_2 = 0$ yields $\theta = \delta$, which is the stream surface for the cone itself. Any arbitrary stream surface can be generated by the equation

$$r [\rho_0(\theta)v_0(\theta)\sin\theta]^{\frac{1}{2}} = G(\phi), \quad (11)$$

where $G(\phi)$ is an arbitrary function.

Figures 13(a), (b), and (c) show the development of an idealized conical waverider with an inlet. We arbitrarily construct the exterior contour of the inlet to be axisymmetric by choosing the function $G(\phi)$ to be a constant, so that Equation (9) or its approximation Equation (10) holds. Setting $C_2 = 0$ yields the surface of the cone itself. Another positive value of $C_2 = C_2^*$ yields an exterior stream surface shown in Figure 13(a). The flow in the cylinder in front of shock contained by this axisymmetric stream surface passes through an annular region embracing the basic-cone body, $\theta = \delta$. The thickness of this annular region goes to zero as r goes to infinity. An ideal axisymmetric inlet is constructed by treating the stream surface C_2^* as a solid surface starting at some arbitrary distance behind the shock, as shown in Figure 13(b). The flow in the original cylinder ahead of the shock thus passes through the annular region which is now the inlet. The flow outside the original cylinder passes around the inlet which is now the exterior of the body. In this idealized inviscid flow, the inlet has a sharp lip that allows the flow to pass around it without the formation of a shock, providing that the internal flow can be appropriately accommodated or completely swallowed. An idealized conical waverider configuration can now be constructed by using the family of stream surfaces $\phi = C_1$ to form delta winglets of infinitesimal thickness. Thus, a lower portion of Figure 13(b) is used to construct the idealized conical waverider in Figure 13(c).

A similar procedure can be used to construct inlets for the circular-cone and elliptic-cone waveriders shown in Figure 1. A study is now under way making use of perturbation methods in accordance with the original analysis.

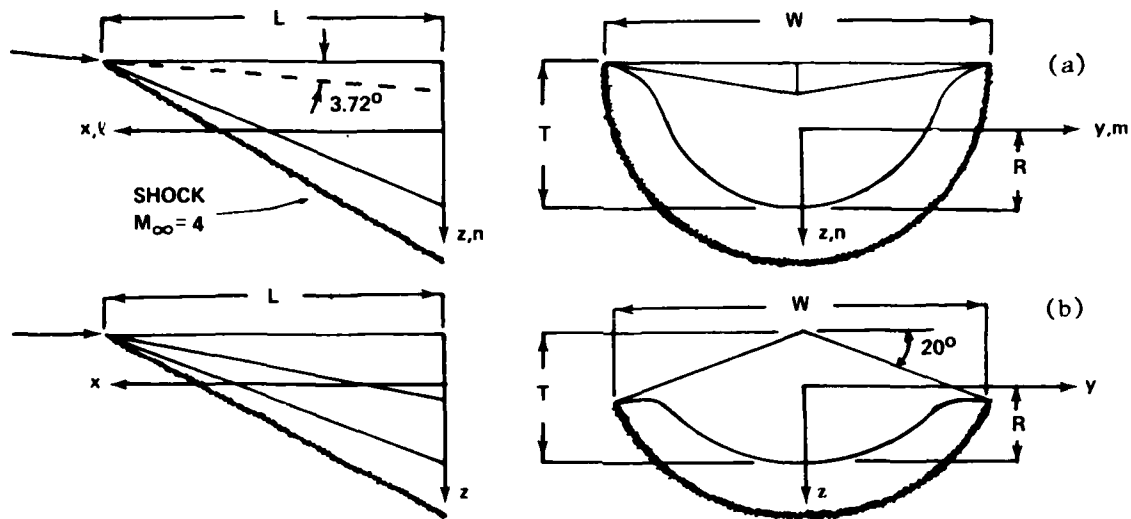
It is desired to shape the external boundary of the inlet so that it blends into the curved undersurface of the basic waverider. In this way sharp corners do not appear in the final contour of the waverider undersurface. Since no shock appears from the lip of the inlet in the ideal-flow on-design case, the inlet does not produce wave drag as it would in other arbitrary designs. Wind tunnel tests are being planned for an inlet added to the elliptic-cone waverider to ascertain the flow properties of on-design and off-design conditions in a real flow.

CONCLUDING REMARKS

The basic theory and supportative data base for the cone-derived waveriders discussed herein make these lifting-body configurations attractive for meeting the high-speed, high-performance requirements of present-day missile technology. Further studies on fins and inlets will add to the technology base of these novel configurations. In this connection other studies under way include contour optimization and boundary-layer development.

REFERENCES

1. Giragosian, P. A., "Critical Aerodynamic Technology Issues in Air-to-Air Missile Design," AIAA Paper 79-0089, presented at AIAA 17th Aerospace Sciences Meeting, New Orleans LA, January 1979.
2. Fleeman, E. L., "Aeromechanics Technologies for Tactical and Strategic Guided Missiles," presented at the AGARD FMP Meeting on Missile Systems Flight Mechanics, London, England, May 1979.
3. Nielsen, J. N., "Missile Aerodynamics - Past, Present, Future," AIAA Paper 79-1819 (Wright Brothers Lectureship in Aeronautics), presented at the AIAA Aircraft Systems and Technology Meeting, New York, August 1979.
4. Rasmussen, M. L., "Waverider Configurations Derived from Inclined Circular and Elliptic Cones," J. of Spacecraft and Rockets, Vol. 17, No. 6, Nov. - Dec. 1980, pp. 537-545.
5. Jischke, M. C., "Supersonic Flow Past Conical Bodies with Nearly Circular Cross Sections," AIAA Journal, Vol. 19, No. 2, February 1981, pp. 242-245.
6. Küchemann, D., The Aerodynamic Design of Aircraft, Pergamon Press, London, Chap. 8, 1978.
7. Rasmussen, M. L., Jischke, M. C., and Daniel, D. C., "Experimental Results for Forces and Moments on Cone-Derived Waveriders in the Mach-Number Range 3 to 5," AIAA Paper 81-0149, AIAA 19th Aerospace Sciences Meeting, St. Louis, January 1981.
8. Test Facilities Handbook (Eleventh Edition), "Von Karman Gas Dynamics Facility," Vol. 3, Arnold Engineering Development Center, Arnold Air Force Station, Tennessee, June 1979.
9. Rasmussen, M. L., and Lee, H. M., "Approximation for Hypersonic Flow Past a Slender Elliptic Cone," AIAA 17th Aerospace Sciences Meeting, New Orleans, January 1979.



Model Dimensions (inches)

	L	W	T	R	A_b in. ²
Circular-Cone Waverider	23.62	21.98	7.96	4.46	103.60
Elliptic-Cone Waverider	23.62	21.50	7.11	4.62	75.83

Figure 1. Model Configurations: (a) Circular-Cone Waverider (CCWR), (b) Elliptic-Cone Waverider (ECWR).

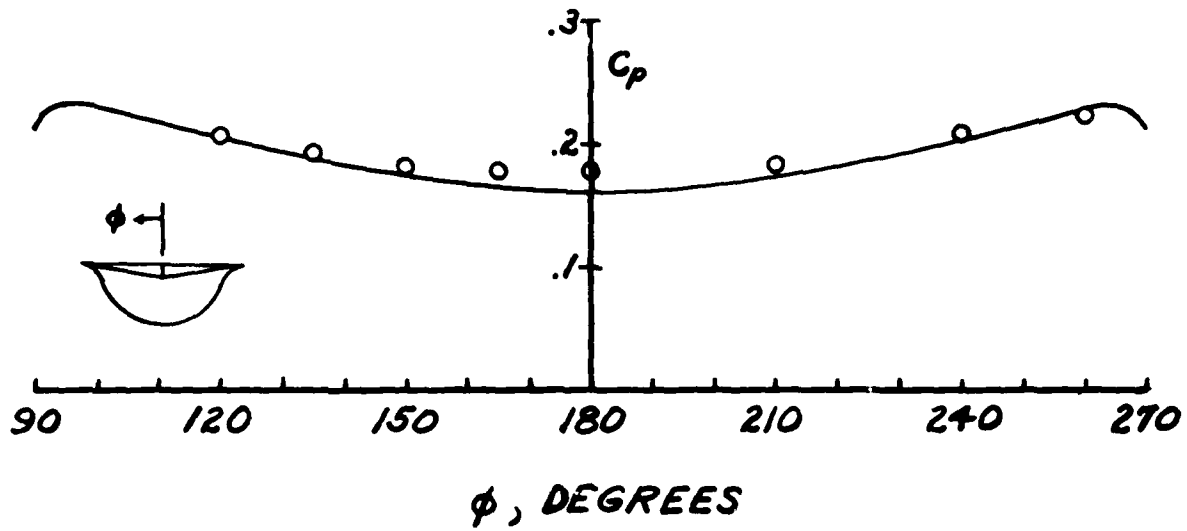


Figure 2. Comparison of Theory and Experiment of Under-surface Pressure Coefficient for Circular-Cone Waverider: On-design Conditions, $\alpha = -3.76^\circ$, $\beta = 0$, $M_\infty = 4.02$.

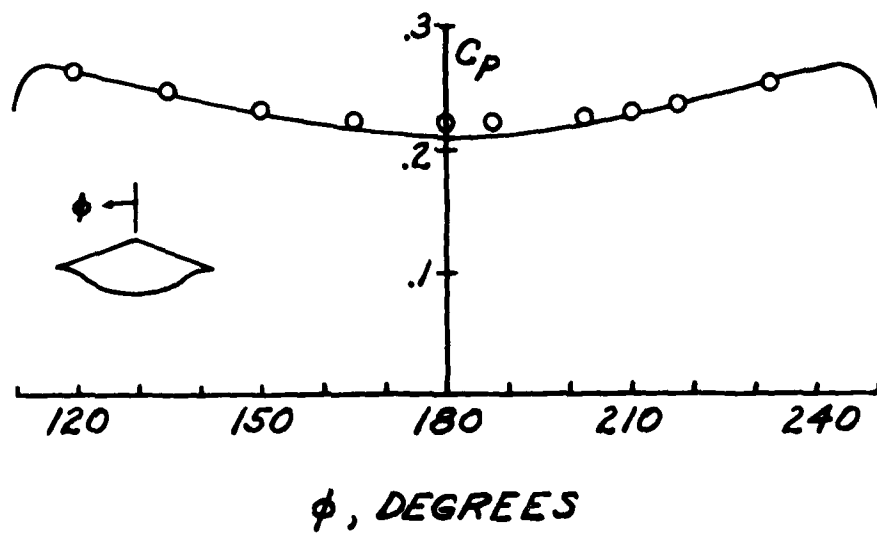


Figure 3. Comparison of Theory and Experiment of Under-surface Pressure Coefficient for Elliptic-Cone Waverider: On-design Conditions, $\alpha = \beta = 0$, $M_\infty = 4.02$.

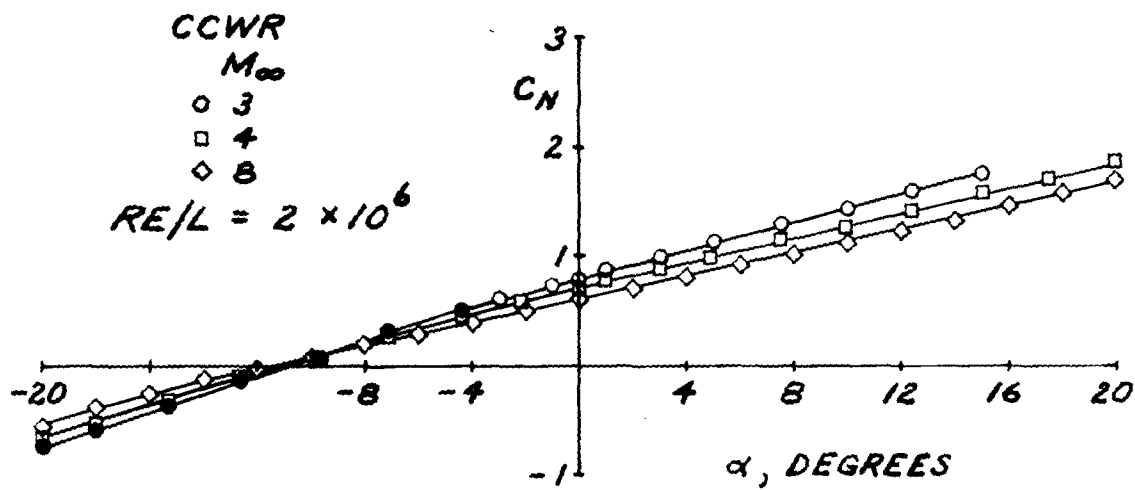


Figure 4. Normal-Force Coefficient versus Angle of Attack for Circular-Cone Waverider at Different Mach Numbers. Solid Symbols Represent $Re/L = 10^6$.

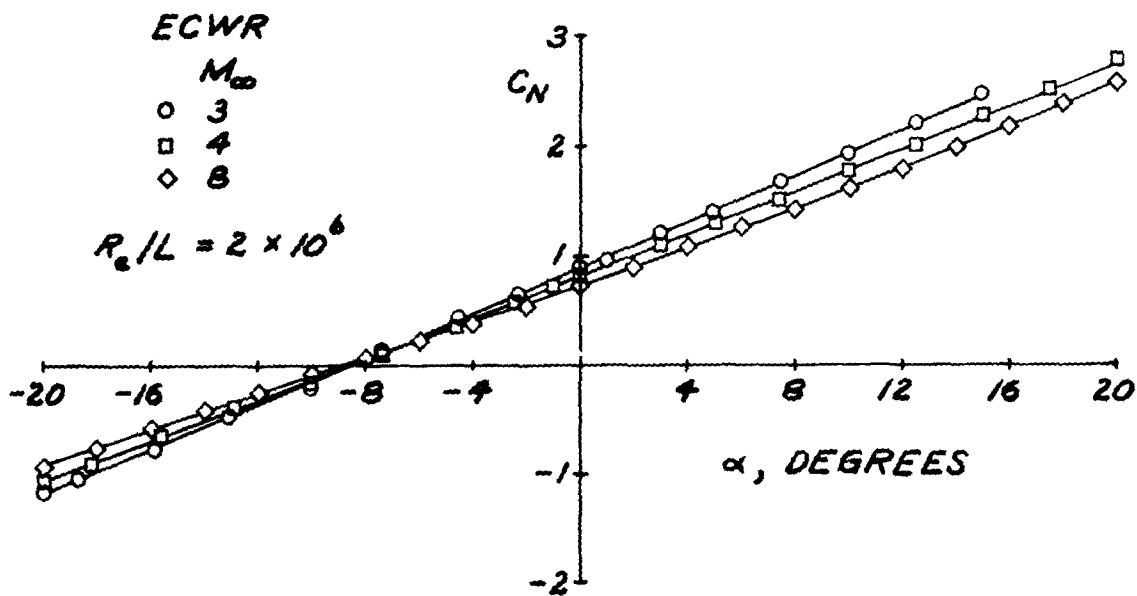


Figure 5. Normal-Force Coefficient versus Angle of Attack for Elliptic-Cone Waverider at Different Mach Numbers.

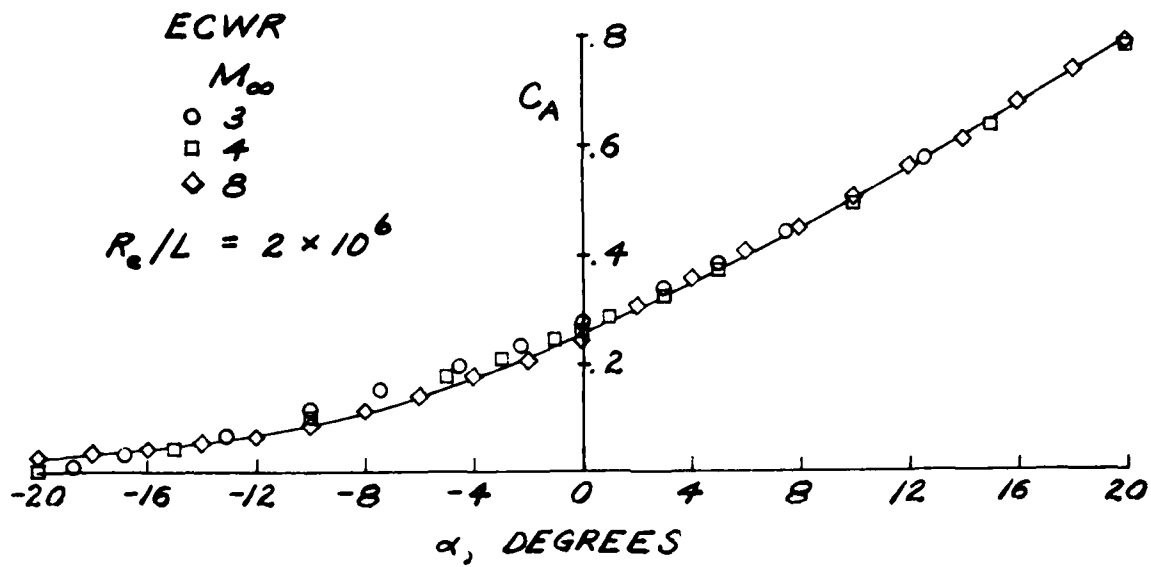


Figure 6. Axial-Force Coefficient versus Angle of Attack for Elliptic-Cone Waverider at Different Mach Numbers.

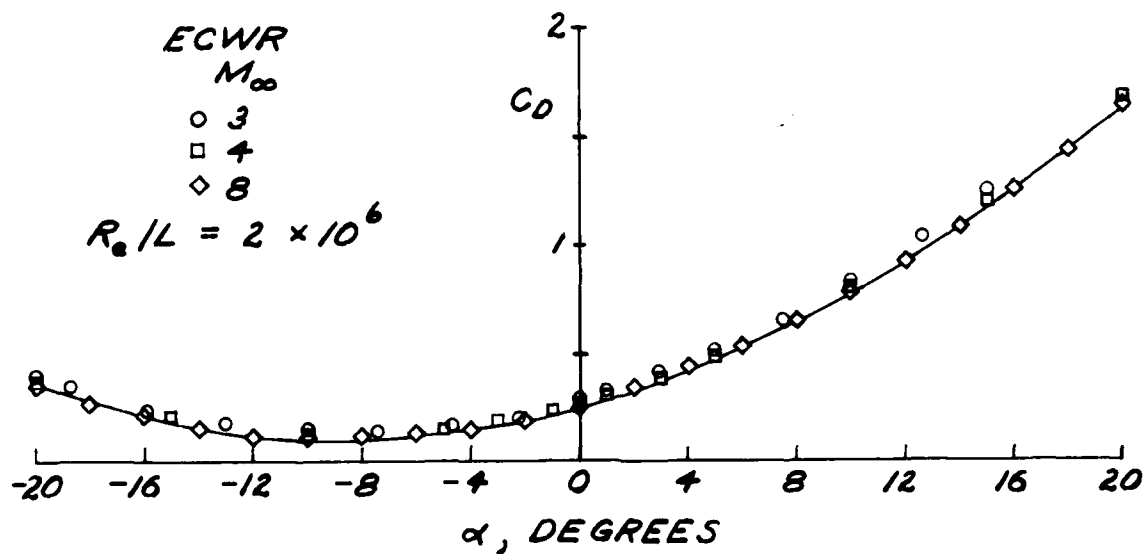


Figure 7. Drag Coefficient versus Angle of Attack for Elliptic-Cone Waverider at Different Mach Numbers.

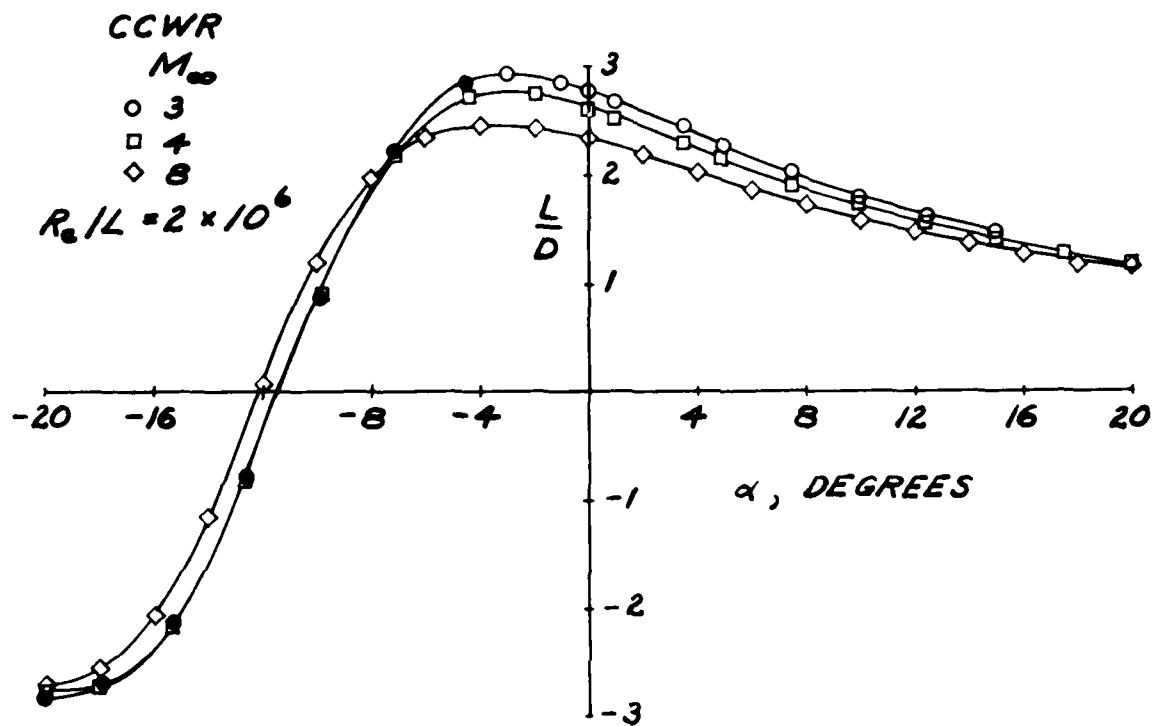


Figure 8. L/D Ratio versus Angle of Attack for Circular-Cone Waverider at Different Mach Numbers. Solid Symbols Represent $Re/L = 10^6$.

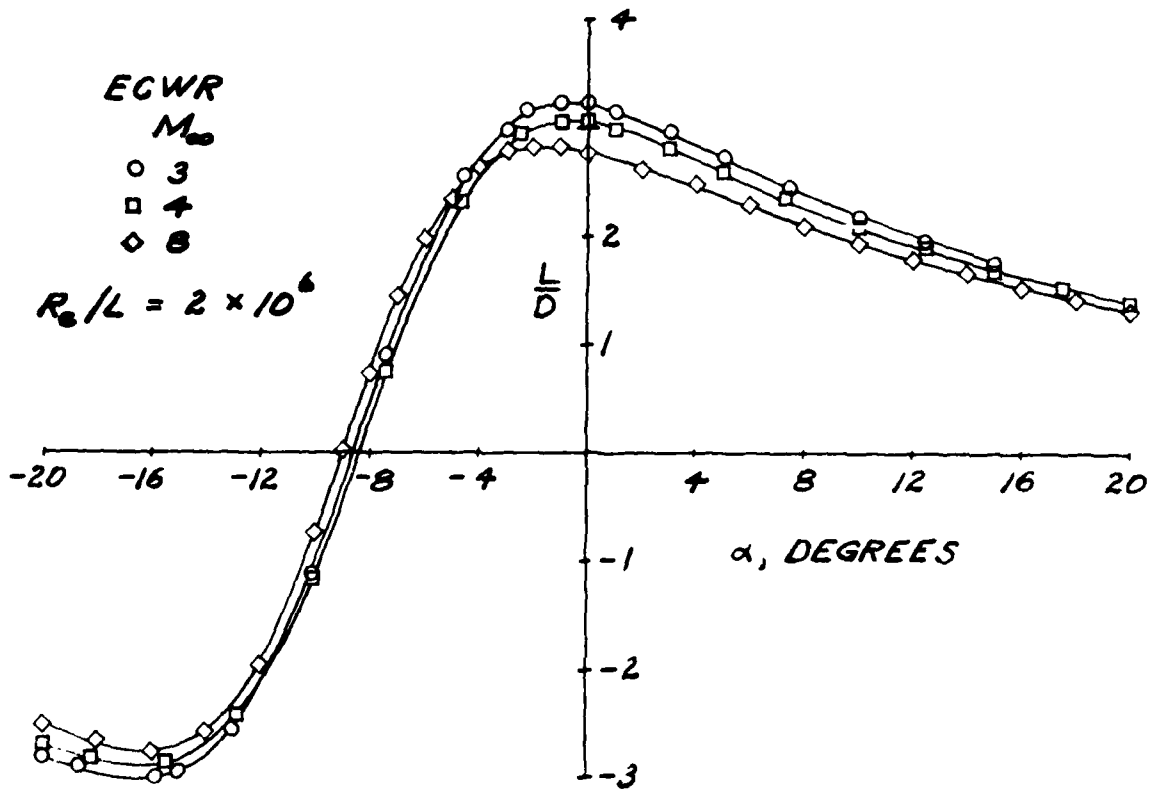


Figure 9. L/D Ratio versus Angle of Attack for Elliptic-Cone Waverider at Different Mach Numbers.

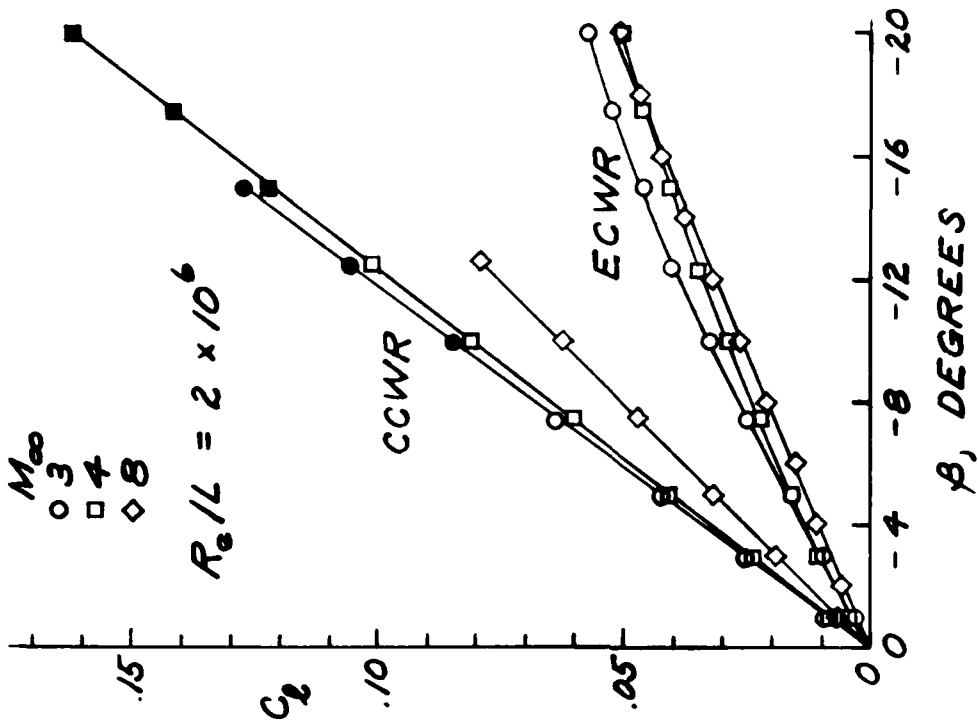


Figure 11. Rolling-Moment Coefficient versus Angle of Sideslip for Different Mach Numbers. Solid Symbols Represent $Re/L = 10^6$.

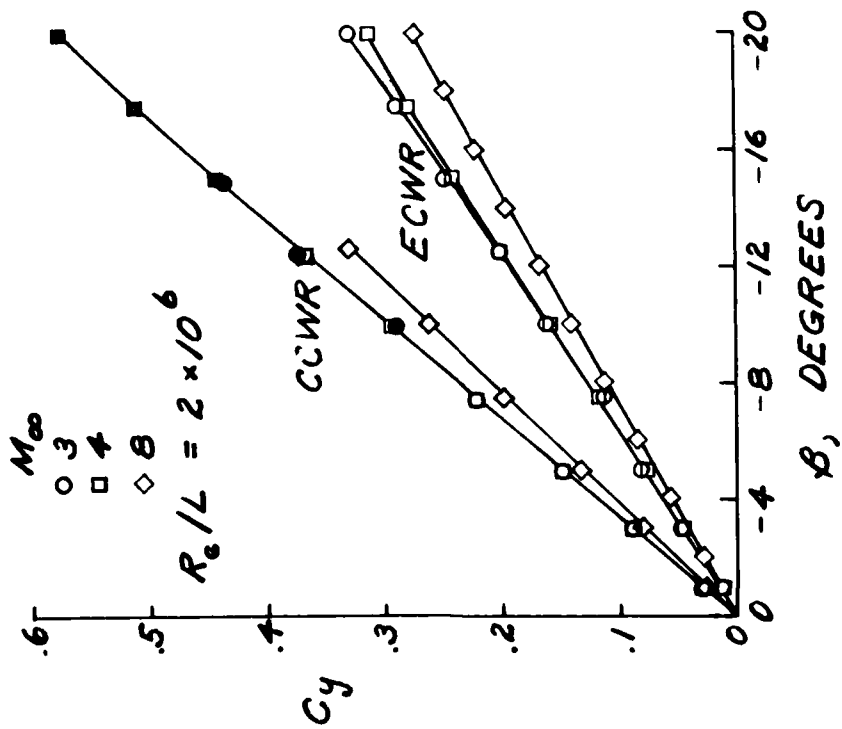


Figure 10. Side-Force Coefficient versus Angle of Sideslip for Different Mach Numbers. Solid Symbols Represent $Re/L = 10^6$.

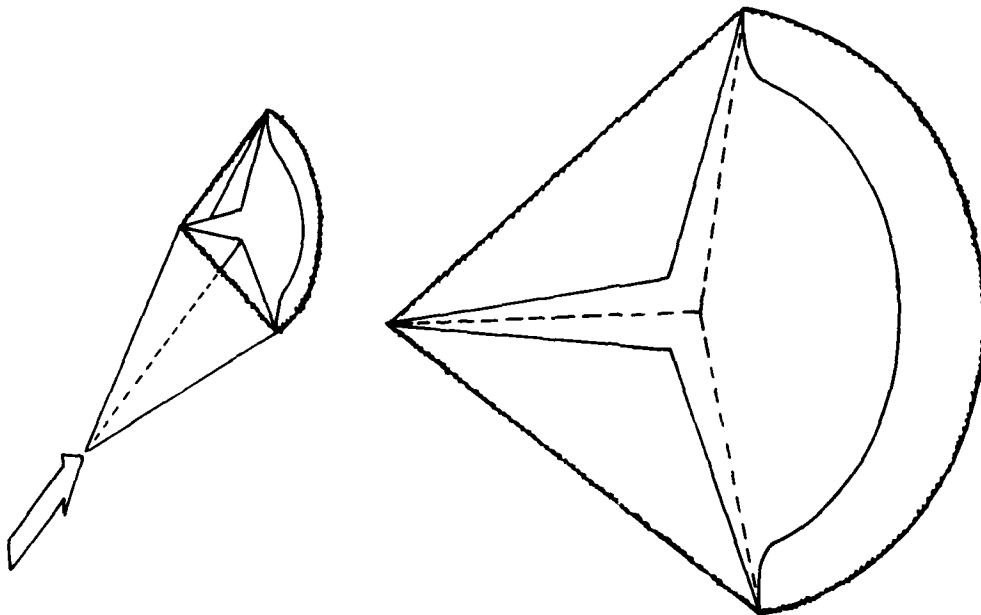


Figure 12(a) Vertical Fin Starting at Vertex of an Elliptic-Cone Waverider.

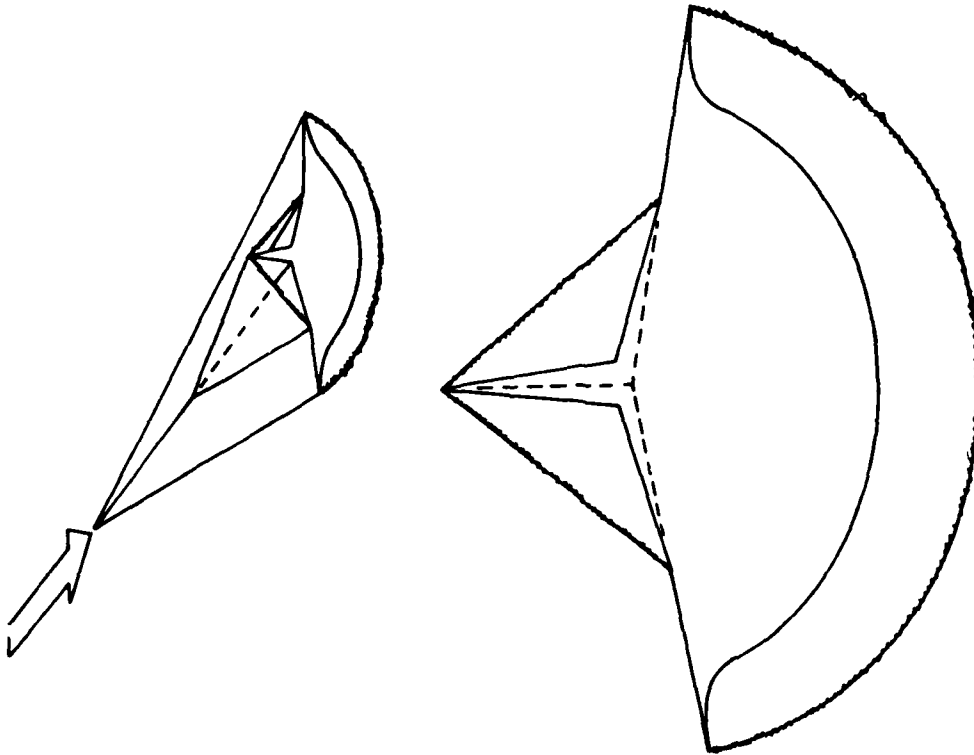


Figure 12(b). Vertical Fin Starting at Half Length of an Elliptic-Cone Waverider.

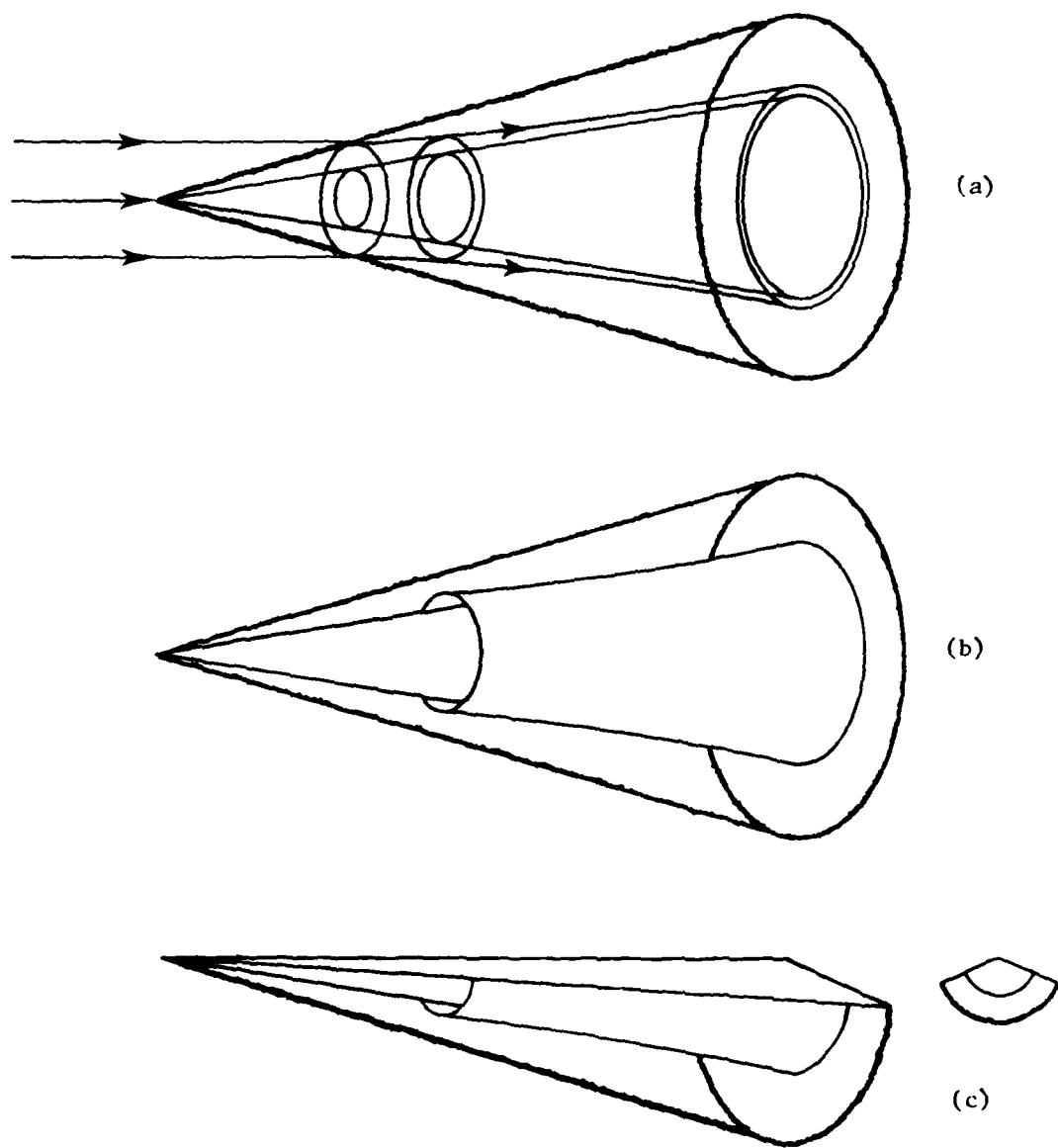


Figure 13. Construction of Axisymmetric Inlet on Idealized Conical Waverider: (a) Axisymmetric Stream Surfaces in Axisymmetric Flow Past a Circular Cone, (b) Axisymmetric Inlet on Circular Cone, (c) Axisymmetric Inlet on Idealized Conical Waverider.

DETERMINATION OF AERODYNAMIC CHARACTERISTICS
OF BALLISTIC PROJECTILES AT TRANSONIC SPEEDS

Stephen S. Stahara
Nielsen Engineering & Research, Inc., Mountain View, California

ABSTRACT

The development of a predictive method for determining the steady inviscid aerodynamic behavior of ballistic projectiles throughout the transonic range is reported. The development has been directed toward establishing the theoretical capability for predicting the static stability characteristics of both the standard conical boattail projectiles as well as a variety of new nonaxisymmetric boattail shapes under study by the U.S. Army. The theoretical procedure employs the classical transonic equivalence rule together with a new loading calculation method which is based on apparent mass concepts and makes use of the nonlinear equivalence rule flow solutions. Theoretical results for surface pressures, loadings, and static aerodynamic characteristics are presented throughout the transonic range for a variety of projectiles. Comparisons are made both with other theoretical methods as well as with experimental results and verify the accuracy of the procedure. Future extension and application of the overall procedure to missile stability and performance is suggested and discussed.

INTRODUCTION

Current projectiles used by the Army are generally slender, spin-stabilized bodies of revolution. The boattail configuration which has become the standard is a conical shape with a relatively shallow cone angle $\sim(5-10^\circ)$. The primary purpose of any boattail is to increase the projectile range by reducing drag from what it would be without boattailing and with the projectile afterbody a straight cylindrical shape (Fig. 1). While a drag reduction is effectively accomplished, mainly through the reduction in base area, a subsequent detrimental result of such a geometric change is the creation of a negative lift on the boattail. This tends to increase even further the destabilizing pitching moment, which already exists due to positive lift on the nose, and consequently acts to reduce additionally the gyroscopic stability of the projectile. At flight speeds within the transonic range, which usually occur near ballistic trajectory apex, the negative loading on the boattail is strongly augmented due to the appearance and movement of shock waves on the aft portion of the boattail. This results in a rapid peaking at flight Mach numbers just below one in the destabilizing pitching moment as well as a similar behavior in other aerodynamic characteristics. Insofar as the aerodynamic derivatives are concerned, this nonlinear behavior due to shock formation and motion is the dominant fluid dynamic characteristic of ballistic projectile flows in the transonic speed regime.

In this regard, and as noted previously,¹ the relative simplicity of basic projectile shapes - which typically consist of an ogive nose followed by a straight cylindrical section and a conical boattail - is deceptive. This is so because the locations where these sections join normally have discontinuities in surface slope and/or curvature; and it is precisely these discontinuities which induce the shock patterns and subsequent sensitive aerodynamic behavior in the transonic range.

In an effort to reduce the adverse transonic behavior of ballistic projectiles, the Army has recently investigated experimentally² a series of nonaxisymmetric boattail shapes. Some of these nonstandard shapes were found to improve significantly the projectile aerodynamic characteristics over those of the conical configuration. In particular, it was found that both increased gyroscopic and dynamic stability and decreased drag could be attained simultaneously, so that for the first time projectile designs were feasible which not only provide increased range over the standard boattail shapes but also improved stability.

The present work describes the development of a theoretical method for predicting the transonic static aerodynamic characteristics of these projectiles. The objective has been the enablement of a rational modeling of the aerodynamic effects of incorporating different axisymmetric and nonaxisymmetric boattail geometries into ballistic projectile design with a view toward optimizing the aerodynamic performance of these shapes. The theoretical analysis for determining the nonlinear three-dimensional projectile flow fields is based on the classical transonic equivalence rule (TER); and employs finite-difference successive line over-relaxation (SLOR) solutions of the axisymmetric transonic small-disturbance potential equation for the outer nonlinear flow region, and finite-element solutions of the cross flow Laplace equation to determine the nonaxisymmetric inner flow region.

A new loading calculation method which is based on apparent mass concepts and which makes use of nonlinear equivalence rule flow solutions is used to predict the static aerodynamic coefficients. Theoretical results for surface pressures, loadings and static aerodynamic coefficients are presented for a variety of projectiles with different boattail geometries at Mach numbers throughout the transonic range. Comparisons are made insofar as possible with both other theoretical methods and experimental results.

ANALYSIS

GENERAL

The most notable feature of transonic flow past typical ballistic projectiles is the formation and movement as a function of oncoming Mach number of a variety of shock waves both on the surface and in the flow field of these configurations. This is clearly evident in shadowgraphs such as those shown in Figure 2, which illustrate the characteristic shock formation and movement on such shapes as the Mach number increases beyond subcritical.

The result of the rapid formation and movement of shock waves on the aerodynamic characteristics of typical projectiles in the transonic regime is a sharp peaking in their behavior in the vicinity of $M_\infty = 1$. As indicated in the sketches in Figure 3, both the overturning pitching moment coefficient and drag strongly exhibit this behavior. With regard to pitching moment, the sketch in Figure 3 displaying a typical projectile shock pattern illustrates clearly why this occurs. At angle of attack, the shock positions on the windward surface are displaced farther aft than on the leeward side, resulting in a strong negative loading at those axial locations. Both shock strengths and negative loading are strongest by a considerable amount for the boattail shock. As the Mach number increases and the boattail shock moves further aft, both the strength of the negative loading and its moment arm from the center of mass of the projectile increase, and result in a peak pitching moment occurring just prior to the shock moving off the boattail. This inevitably occurs at a Mach number just below one. As the Mach number increases beyond that value, the destabilizing pitching moment decreases rapidly and usually smoothly, and then eventually plateaus as the Mach number increases further supersonically.

BASIC EQUATIONS AND BOUNDARY CONDITIONS

The coordinate system employed in the analysis is a body-fixed Cartesian system with origin at the nose of the configuration, and orientation such that the x axis is directed downstream and coincident with the longitudinal body axis, and the y axis to the right facing forward, and the z axis directed vertically upward, as illustrated in Figure 4. The oncoming free-stream may be inclined in pitch to the x axis at some arbitrary small angle, α , but sideslip has not been considered. The flow is assumed to be inviscid and steady, and the configurations sufficiently slender and smooth that the resulting flow field is irrotational and adequately treated by small-disturbance theory. Accordingly, a disturbance velocity potential ϕ can be defined by:³

$$\phi(x,y,z) = U_\infty \ell [x + \alpha z + \phi(x,y,z)] \quad (1)$$

where ϕ is the total velocity potential, U_∞ represents the freestream velocity, ℓ is the body length, and the coordinates (x,y,z) have been nondimensionalized by ℓ . The governing partial differential equation for ϕ , appropriate for the low-lift slender configurations considered, is given by:

$$(1-M_\infty^2)\phi_{xx} + \phi_{yy} + \phi_{zz} = \frac{\partial}{\partial x} \left[\frac{1}{2} M_\infty^2 (\gamma+1) \phi_x^2 \right] \quad (2)$$

We note that the quadratic terms $(\phi_y^2 + \phi_z^2)$, which usually appear^{4,5} within the bracket on the right-hand side to account for situations where the lift is significant, are of higher order and negligible for the thickness-dominated situations of interest here. For the body-fixed coordinate system shown in Figure 4, the expression for the pressure coefficient is given by:

$$C_p = \frac{p-p_\infty}{\rho_\infty U_\infty^2 / 2} = -2(\phi_x + \alpha \phi_z) - (\phi_y^2 + \phi_z^2) \quad (3)$$

In general, the boundary conditions to be satisfied consist of: (1) far-field conditions appropriate to the behavior of the flow far removed from the body in either a free-air flow or in a wind tunnel environment; (2) the body surface condition that the velocity component normal to the body surface be zero at the body; and (3) shock wave conditions to be applied at any shock surface appearing in the flow, such that the potential is continuous through the shock and the velocity components satisfy the small disturbance approximation to the Rankine-Hugoniot conditions at the location of the shock. These requirements lead for slender shapes to the following condition on ϕ for free-air flows:

$$\phi(\infty) = 0 \quad (4)$$

$$[n_1 + \alpha n_3] + n_2 \phi_y + n_3 \phi_z]_{\text{body}} = [(n_1 + \alpha n_3) + \phi_n]_{\text{body}} = 0 \quad (5)$$

$$[\phi]_{\text{shock}} = 0,$$

$$\left\{ [(1 - M_\infty^2) - M_\infty^2(\gamma + 1) \langle \phi_x \rangle] [\phi_x^2] + [\phi_y^2] + [\phi_z^2] \right\}_{\text{shock}} = 0 \quad (6)$$

where $n = i n_1 + j n_2 + k n_3$ is the unit normal to the body surface, (n_1, n_2, n_3) are the direction cosines of n with respect to the (x, y, z) axes and the symbols $[\]$ and $\langle \ \rangle$ signify the difference and the mean, respectively, of the enclosed quantity on the two sides of the shock surface.

TRANSONIC EQUIVALENCE RULE FOR THICKNESS DOMINATED FLOWS

The transonic equivalence rule (TER) was developed initially in the form, now known as the classical or thickness-dominated limit, by Oswatitsch^{6,7} for thin nonlifting wings, and extended later to moderately lifting wings⁸ and slender configurations of arbitrary cross section³. Subsequent extensions of the rule^{4,5,9} to include situations where the lift is significant both revealed its dependence on lift as well as clarified the classical limit and range of validity. In essence, the rule provides the basis for greatly simplifying the calculation of transonic flows past a special but aerodynamically important class of three-dimensional configurations. It accomplishes this by recognizing that the structure of transonic flows past slender shapes in the vicinity of $M_\infty \approx 1$ consists of two distinct but coupled domains whose governing equations and boundary conditions are significantly easier to solve than the original equations, Equations (2) and (4)-(6). For flows at low to moderate lift conditions, such as those typical for stable projectile flight, the solution domains consist of an inner region governing by a linear equation, the same as in slender-body theory, and an outer nonlinear region consisting of the axisymmetric flow about an "equivalent" nonlifting body of revolution having the same longitudinal distribution of cross-sectional area.

The theoretical essentials of the equivalence rule for thickness-dominated flows past slender configurations are illustrated in Figure 4, which displays the decomposition of the flow into its first-order inner and outer components, and the resulting uniformly valid composite solution; that is

$$\phi = \phi_{2,\alpha} + \phi_{2,t} + \phi_{2,\omega} - \phi_{2,B} + \phi_B \quad (7)$$

Here each component of ϕ has the meaning indicated in Figure 4. The first-order lift ($\phi_{2,\alpha}$), thickness ($\phi_{2,t}$), and rotation ($\phi_{2,\omega}$) inner solutions describe, respectively, the translating, expanding and rotating cross section in the y,z plane, and satisfy the two-dimensional Laplace equation

$$\phi_{2yy} + \phi_{2zz} = 0 \quad (8)$$

together with the no-flow boundary condition in the y,z plane at the body surface at each x station. The first-order outer solution, ϕ_B , satisfies the axisymmetric transonic small-disturbance equation:

$$(1 - M_\infty^2)(\phi_B)_{xx} + (\phi_B)_{rr} + (1/r)(\phi_B)_r = [M_\infty^2(\gamma + 1)(\phi_{B,x})^2/2]_x \quad (9)$$

subject to an inner boundary condition determined by the "equivalent" body singularity source distribution. This, in turn, is determined by the outer behavior ($\phi_{2,B}$) of the inner solution:

$$\lim_{r \rightarrow 0} [r(\phi_B)_r] = \lim_{r \rightarrow 0} r[\phi_{2,\alpha} + \phi_{2,t} + \phi_{2,\omega}] = r(\phi_{2,B})_r = S'(x)/2\pi \quad (10)$$

where $S(x)$ is the equivalent body cross-sectional area nondimensionalized by ξ^2 , and the effects of lift and rotation are recognized to be small in comparison to thickness effects, so that their contribution to the outer flow is of a higher order. Shock conditions appropriate to the outer flow are given by:

$$\begin{aligned} & \llbracket \phi_B \rrbracket_{\text{shock}} = 0, \\ & \left\{ r[1 - M_\infty^2 - M_\infty^2(\gamma + 1)\langle \phi_{B,x} \rangle] \llbracket \phi_{B,x}^2 \rrbracket + \llbracket (r\phi_{B,r})^2 \rrbracket \right\}_{\text{shock}} = 0 \end{aligned} \quad (11)$$

The final boundary condition for the outer problem relates to conditions representative of the flow far from the configuration. For free-air flows at infinity this is given by Equation (4). Appropriate asymptotic conditions for a bounded free-air domain or a tunnel environment are discussed in the following section.

Higher order TER solutions for thickness-dominated flows beyond the first-order terms indicated in Equations (7)-(11) can be determined systematically by the methods described in References 4 and 5. These consist of a doubly infinite coupled series of inner and outer solutions. In general, the higher order inner solutions satisfy a Poisson equation in the crossflow plane, with the right-hand side a known function of lower order inner solutions and satisfy a linear equation with nonconstant coefficients dependent on the first-order outer (ϕ_B) solution. For the results presented here, only the first-order components are employed.

OUTER FLOW SOLUTION

The method employed to determine the outer flow component, ϕ_B , satisfying Equations (9)-(11) is a finite-difference SLOR procedure using Murman-Cole type-dependent difference operators¹⁰⁻¹². To realize the calculation, we have

employed the following fully conservative form of Equation (9):

$$[\eta(K\bar{\phi}_x - \bar{\phi}_x/2)]_x + [\eta\bar{\phi}_\eta]_\eta = 0 \quad (12)$$

where

$$\bar{\phi}(x, \eta) = (1/\tau^2)\phi_B(x, r), \quad K = (1 - M_\infty^2)/(\tau \cdot M_\infty^2)(\gamma + 1), \quad \eta = \tau M_\infty \sqrt{\gamma + 1} r \quad (13)$$

and τ signifies the thickness ratio of the equivalent body. The finite-difference form of the equation actually solved is that suggested by Jameson¹³ in terms of a correction potential. Additionally, a pseudotime term of the form $-\epsilon(\Delta t/\Delta x)\phi_{Bxt}$ was added to enhance stability and speed convergence. The inner boundary condition, Equation (10), becomes

$$\lim_{\eta \rightarrow 0} (\eta\bar{\phi}_\eta) = \frac{\bar{S}(x)}{2\pi} \quad (14)$$

where $\bar{S}(x) = S(x)/\tau^2$.

For free-air flows, since the boundaries of the computational mesh employed are at a finite rather than infinite distance from the origin, a more accurate representation of the far-field potential which reflects its asymptotic behavior should be employed rather than Equation (4). These conditions depend, of course, upon the free-stream Mach number and are different for subsonic, sonic, and supersonic oncoming conditions. The appropriate boundary conditions employed on the computational domain at the upstream, lateral, and downstream boundaries are given in detail in Reference 14 and are summarized in Figure 5, where both the inner and outer conditions are provided.

Verification of the accuracy and versatility of the outer flow solution procedure has been made by extensive comparisons with data. These results are reported in Reference 14 and cover a variety of different body shapes at Mach numbers throughout and beyond the transonic range. The corresponding comparisons with data taken in conventional ventilated transonic tunnels indicated excellent agreement.

INNER FLOW SOLUTION

The determination of the inner flow problem consists of solving the crossflow Laplace Equation (8) for the three first-order inner components, $\phi_{2,\alpha}$, $\phi_{2,t}$ and $\phi_{2,\omega}$, corresponding to the vertical translation, expansion, and rotation, respectively, of the projectile cross section in the y, z plane. The component $\phi_{2,B}$ in Equation (7) represents the outer behavior of the inner solution, and for the thickness-dominated flows considered here is given analytically by [see Eq. (10)]

$$\phi_{2,B} = \frac{S'(x)}{2\pi} \eta n r \quad (15)$$

For the axisymmetric portion of the projectile, the three inner solutions can be determined analytically, and are

$$\psi_{2,x} = \frac{\alpha S(x)}{r} \cdot \frac{\sin \theta}{r} \quad (16)$$

$$\psi_{2,t} = \frac{S'(x)}{2r} \ln r \quad (17)$$

$$\psi_{2,r} = 0 \quad (18)$$

Along the nonaxisymmetric boattail, general analytic expressions cannot be given for typical cross-sectional shapes of interest to this study. Those shapes comprise a general class of contours formed by $N(N \geq 3)$ equal-length, flat-sided segments separated by N equal-angle circular arc segments, and are formed by cutting planes acting on the axisymmetric projectile boattail. Those cutting planes are inclined at a small angle to the main projectile axis, and result in flat surfaces being formed longitudinally on the boattail. In general, these cutting planes may also rotate about the projectile axis as they proceed downstream so as to provide twist to the cut surface and thereby prevent projectile despinning. Figure 6 provides an illustration of two such boattail shapes formed by employing three and four cutting planes. For these shapes, the basic axisymmetric boattail was cylindrical rather than conical, the cutting planes were not rotated, and the cutting plane angles and axial starting locations were chosen such that the cutting planes meet at the boattail end and result in an inscribed triangle and square, respectively.

The computational method employed to determine the inner flow solutions is a finite-element procedure. The procedure uses the Galerkin method of weighted residuals and employs isoparametric quadrilateral elements with quadratic shape functions of the serendipity type. The linear, symmetric matrix equations that result from discretization of the Laplace equation are solved directly using Gaussian elimination. The body surface boundary conditions for each of the three inner computational problems are summarized in Figure 7. In the computational procedure they are implemented via a Neumann (flux) condition. On the outer boundary of the finite element mesh, Neumann conditions are also employed for each of the component problems, as this was found to be much more convenient and of essentially equal accuracy as the corresponding Dirichlet conditions. A typical finite element mesh employed for these calculations is illustrated in Figure 8. That figure displays the mesh for a body formed by three cutting planes acting on a circular cross section such that a sectored triangular shape results in which the circular arc segments subtend 30° angles. The mesh shown consists of six rings extending radially outward from the body surface and having 12 quadrilateral elements per ring. The radial spacing of the rings is geometrical, and for the mesh illustrated here the spacing ratio was 1.4.

A series of numerical experiments were performed in order to examine inner solution accuracy as a function of mesh parameters, viz. number of rings, number of elements per ring, radial mesh spacing ratio, and outer boundary location. The results indicated that mesh configurations similar to that shown in Figure 8 were adequate with regard to both number of rings and elements per ring, provided that the outer boundary was located at approximately 8 body radii and that radial mesh spacing near the body surface

was slightly more compact than that shown in the figure. A geometric ratio of 2.0 was found to be satisfactory.

Figure 9 provides an indication of the typical accuracy of the finite-element solver when applied to one of the three component inner problems. Displayed are the surface velocity components for the contraction problem for the 30° sectored triangular cross section shown previously in Figure 8. The predicted velocities shown are adjusted to be relative to the local body surface, and thus should be entirely tangential to the local surface. The particular contraction problem solved here was for a unit contraction of the flat segments ($\phi_n = dF/dx = -1$) and with the circular arc segments stationary ($\phi_n = dR/dx = 0$). The surface velocity vectors are shown at the surface node point locations. As can be seen, the velocity vectors on both the flat and circular segments are indeed essentially tangential to the local surface. At the junctions of the flat and circular segments, two vectors are indicated since for those points a velocity vector can be predicted employing values of the potential associated either with the element lying on the circular segment or the adjacent element lying on the flat segment. Potential theory is in fact discontinuous at those locations; and although velocities exactly at those corner points are never used or required in any of the calculations performed here, it is nevertheless instructive to observe the behavior of the finite-element solver at those singular points. As is evident from the results shown in Figure 9, the solver provides both the correct trend (high magnitude) and direction (tangential to the surface) of the solution behavior at those locations. From additional numerical experiments involving both an examination of surface pressures in the vicinity of these points, as well as contour integrals of surface velocity and potential about the entire cross section (in order to determine apparent mass coefficients, see section following, we have verified that the finite-element solver is capable of adequately resolving the flow behavior in the vicinity of the corners and providing rapid and accurate solutions for all the inner problems for the geometries of interest here.

LOADING CALCULATIONS

The objective of the development and application of the TER procedure to ballistic projectiles was to provide the means for determining the 3-D transonic flow fields about these shapes and, subsequently, the surface pressures and the resultant steady aerodynamic forces and moments. Since the primary utility of the present predictive method to projectile applications, however, is in the accurate determination of those static aerodynamic characteristics, the calculation and subsequent integration of surface pressures predicted via the TER method over the entire projectile is an undesirable intermediate, computationally-expensive step. Consistent with the order of accuracy of the present flow solution, it is possible to formulate a procedure based on the TER solution and slender body theory which avoids that step and provides the axial loading distribution directly.

This procedure, known as the method of apparent masses¹⁵, relates the kinetic energy of the fluid per unit axial length to contour integrals involving various crossflow velocity potentials describing the translation, rotation, etc., of the cross section and their normal gradients on the local surface. These contour integrals are relatable to the apparent mass coeffi-

icients of the configuration cross section; and with those coefficients in hand, the determination of the lateral force and moment distributions is direct.

The utility of the apparent mass method is in the determination of stability derivatives, both static and dynamic, for slender configurations. The method has been successfully employed in the past in a wide number of aerodynamic applications¹⁶, particularly for missile configurations. A detailed formulation of the method for combined upwash, side-wash, and roll including derivations of all the important static and dynamic stability derivatives is provided in Reference 19. Such previous applications of the method have focused exclusively in the subsonic and supersonic regimes where the governing small-disturbance potential equations are linear. Since slender body theory is equally valid throughout the transonic regime as well, and in fact underlies the basis of TER method, application of the apparent mass method at transonic speeds is certainly feasible. However, a well-known result of the classical TER method³⁻⁸, and actually verified by experiment for certain classes of aerodynamic configurations³, is that the loading distributions and hence the lateral forces and moments are independent of oncoming Mach number. This, of course, is not the case for typical projectiles, as noted in Figure 3. The reason for this discrepancy lies not in an overall breakdown of the TER procedure, but rather in the failure to take into account locally the large axial gradients which occur in the vicinity of shock waves located on the body surface. These large gradients locally violate the moderate axial gradient hypothesis inherent in the apparent mass method.

Because of the deficiency of the procedure for applications at transonic speeds is associated primarily with the behavior of the axial velocity component in the vicinity of shock waves, we have postulated and successfully tested the following modification of the classical apparent mass method: (1) correct the axial velocity in the classical apparent mass formulation by replacing the free-stream velocity by the local axial velocity, and (2) apply a similar correction to the lateral velocities. Here, the axial perturbation velocity component to be added locally to the free-stream velocity can be considered as provided by the TER composite solution Equation (7). However, since the effect we are attempting to correct for is a transonic one due to nonlinear Mach number dependent variations in the vicinity of shock waves, and since the two-dimensional crossflow solutions contained in Equation (7) are independent of M_∞ , it is sufficient to consider the local axial velocity as augmented by the equivalent body perturbation axial velocity alone, viz.

$$V_x = 1 + \phi_{B_x} \quad (19)$$

In order to implement these ideas, consider the normal force loading distribution dC_N/dx for combined angle of attack, α , sideslip, β , and roll rate, p , of a typical ballistic projectile. (Although we have not considered sideslip in our derivations of the TER method, it would be a straightforward extension to do so.) The transonically corrected classical loading distribution¹⁶ is given by:

$$\frac{dC_N}{dx} = 2 \left\{ v_x \frac{\partial}{\partial x} [M_{12}v_1 + M_{22}v_2 + M_{23}p] - p[M_{11}v_1 + M_{12}v_2 + M_{13}p] \right\} \quad (20)$$

where

$$M_{ij} = - \oint_C \rho_i \frac{\partial \phi_j}{\partial n} \quad (21)$$

$$v_x = 1 + \epsilon_{B_x} \quad (22)$$

$$v_1 = f(1 + \epsilon_{B_x}) \quad (23)$$

$$v_2 = u(1 + \epsilon_{B_x}) \quad (24)$$

Here, the M_{ij} are apparent mass coefficients determined from the following inner flow solution representation (see Fig. 4)

$$\phi_2 = f\phi_1 + u\phi_2 + p\phi_3 + \phi_{2,t} \quad (25)$$

where ϕ_1, ϕ_2 represent crossflow potentials for unit horizontal and vertical translation, respectively, of the cross section, ϕ_3 represents the potential for unit angular velocity of the cross section about the longitudinal axis, v_1, v_2 , are the transonically corrected sidewash and upwash, and the normal force coefficient is defined by

$$C_N = Z / \frac{1}{2} \rho_\infty V_\infty^2 \pi R_{\max}^2 \quad (26)$$

Thus, for a projectile having a conical boattail for which the apparent mass coefficients are known analytically ($M_{11} = M_{22} = \pi R^2$, $M_{12} = M_{23} = M_{13} = 0$), at zero sidewash ($f = 0$) and roll rate ($p = 0$), the normal force loading distribution is given by

$$\frac{dC_N}{dx} = 2u(1 + \epsilon_{B_x}) \cdot \frac{d}{dx} \left[(1 + \epsilon_{B_x}) \cdot \left(\frac{R}{R_{\max}} \right)^2 \right] \quad (27)$$

Corresponding results for the static normal force and overturning pitching moment coefficients $C_{N_\alpha}, C_{m_\alpha}$ are found from

$$C_{N_\alpha} = \frac{\partial}{\partial \alpha} \int_0^1 \frac{dC_N}{dx} dx \quad (28)$$

$$C_{m_\alpha} = \frac{\partial}{\partial \alpha} \int_0^1 (x_{c_m} - x) \frac{dC_N}{dx} dx \quad (29)$$

where x_{cm} is the overturning moment center and the pitching moment is defined as positive nose-up.

In general, for the nonaxisymmetric cross sections such as those of interest here, the apparent mass coefficients cannot be determined analytically and must be found numerically. The finite-element solver described in the previous section provides a convenient means of readily determining these coefficients. Consequently, although both inner and outer TER solution procedures are necessary to determine the projectile loading distribution, viz. the finite-element inner solver to calculate the apparent mass coefficients of the projectile cross section, and the SLOR solver to calculate the axisymmetric nonlinear transonic flows past the equivalent body of revolution, the determination of the detailed surface pressures and their integration over the body surface is avoided.

In order to test the loading procedure, we have applied the method to a variety of different projectiles having both axisymmetric and nonaxisymmetric boattail geometries at Mach numbers throughout the transonic range. In the following section, we provide some typical results of such calculations, together with comparisons with other theoretical methods and data.

RESULTS

To examine the applicability of the transonic equivalence rule for determining transonic flows past ballistic projectiles, as well as to test the validity and accuracy of the proposed nonlinear loading procedure, we have applied these procedures to predict the surface pressures, loading distributions, and static aerodynamic coefficients of a variety of different projectiles at flow conditions throughout the transonic range. In the following sections, we provide some selected results typical of the projectile calculations that were performed. Comparisons with data and as far as possible with other theoretical methods are provided.

SURFACE PRESSURES

Insofar as the basic validity and range of accuracy of the TER method for predicting transonic flow fields past slender bodies are concerned, extensive comparisons of TER results with data have been made and are provided in Reference 17. In that study, experimental results and TER theory were compared for body surface pressures obtained in conventional transonic tunnels for a number of different axisymmetric and nonaxisymmetric shapes. The configurations included both smooth bodies as well as projectile-like discontinuous slope shapes. Those results, which also incorporated wind tunnel interference effects, provide the most extensive comparison of the classical equivalence rule with experiment. They indicate good agreement with data, including the region near shock waves, at oncoming Mach numbers throughout and beyond the transonic regime for low to moderate angles of attack.

Here, we provide some further results for specific projectile shapes. In Figure 10 we have exhibited TER results for the surface pressure coefficient on a secant ogive nose, straight cylindrical midbody, and 7° conical

boattail projectile at $M_\infty = 0.94$ and $\alpha = 4^\circ$. These results display typical axial and azimuthal surface pressure variations characteristic of transonic flows past standard ballistic projectile shapes. The most notable feature of the results in Figure 10 is the prominent expansion and compression spikes in the vicinity of the nose/midbody and midbody/boattail junctures; and are associated with the acceleration and deceleration of the flow in those regions where the surface geometry is discontinuous.

The TER results display the surface pressure along longitudinal rays at the windward, leeward, and midbody azimuthal positions. For this axisymmetric boattail projectile shape, the inner flow solutions are provided analytically everywhere by Equations (16)-(18). The outer flow equivalent body finite-difference solution used in these results employed an (x,r) mesh density of 140x40 points with 100 equally spaced points on the body. The r grid as well as the x grid ahead and behind the body were expanded using a grid ratio of 1.2:1. The x mesh extended 2 body lengths ahead of the nose and 2 body lengths behind the tail of the body, and the location of the first radial grid line was at $r = r/2$. The r mesh extended laterally to 5 body lengths. This grid was the standard one employed in determining all of the equivalent body solutions reported here.

Also shown in Figure 10 are Reklis's¹⁸ three-dimensional transonic small-disturbance results for pressures along the windward ray. The agreement between the two theoretical methods is quite good everywhere, with the only exception being some minor disagreement in the pressure spike regions near the nose/midbody and midbody/boattail junctions. At those locations, the TER results predict a slightly higher and earlier expansion. However, it is probable that even these slight discrepancies are attributable to different grid densities and/or boundary condition treatment in those locations rather than from the difference in the level-of-approximation of the two methods.

LOADING DISTRIBUTIONS

In order to check and verify the proposed loading calculation method for applications to ballistic projectiles, we have employed it to predict loadings on a number of different projectile shapes for which results from other theoretical methods are available. Figure 11 presents a comparison of results for the normal force distribution on an idealized 5.6 caliber length M549 projectile at $M_\infty = 0.95$ and $\alpha = 1^\circ$. For these comparisons, the geometry of the actual projectile shape has been simplified by considering the nose as sharp, by neglecting the rotating bands, and by simulating the afterbody wake geometry by extending the conical boattail beyond the actual projectile length.

In addition to the present method, results from the three-dimensional transonic small-disturbance (3-D TSD) procedure of Reklis¹, from three-dimensional Euler equations calculations¹⁹, and from slender body theory are provided in the figure. On the ogive nose, the present method and the Euler equation result compare quite closely, and are only moderately removed from the slender body result. However, the 3-D TSD results predict a noticeably higher loading. On the cylindrical midbody, the present method indicates a slight positive loading at points beyond the immediate vicinity of the ogive/midbody juncture; whereas, the Euler results predict a negative

loading over the majority of the cylindrical midbody, and the 3-D TSD results show essentially no loading at all. The slender body loading along that unchanging cylindrical cross section is, of course, zero.

As the discontinuity in surface slope at the midbody/boattail juncture is approached and passed, the present method displays first a large positive then negative loading spike corresponding to the rapid flow expansion and compression at the location. Downstream of that junction, the present theory displays another sharp spike, due to the boattail shock. Once beyond the boattail shock, the present method essentially provides the slender body result. Along the boattail, the corresponding 3-D TSD result displays no expansion spikes at the boattail junction. However, similar to the present theory, that result does indicate the same strong downward loading spike on the main boattail section due to the boattail shock, although that peak is displaced slightly rearward from the present theory prediction. With regard to the Euler equation prediction on the boattail, a positive loading is indicated just beyond the boattail juncture and then an increasing negative loading on the remainder of the boattail. In the calculation, the boattail was extended to $x/D = 6.5$ at which point for numerical convenience a spherical cap was added to close the body. That spherical cap, which was located sufficiently far downstream so as not to influence the solution on the actual projectile, locally induces a sharp discontinuous behavior which is to be disregarded. At first glance, the Euler result appears to be quite different from the present theory and the 3-D TSD result over the major portion of the boattail. That is in fact not the case since the Euler prediction was carried out on a much coarser computational grid than both the present method and the 3-D TSD calculation. That has resulted in a broad smearing of the boattail shock, and it is felt that increasing the grid density would result in good correspondence between the Euler result and the present method. In particular, we observe that as in the present result, a positive expansion loading exists in the Euler prediction near the boattail junction. Finally, with regard to the overall agreement evident from this comparison, we note that the present loading method is able to capture all of the critical features of the loading behavior for this typical projectile geometry as predicted by other more accurate but computationally far more expensive procedures.

In Figure 12, we present an additional loading comparison between the present method and Euler equation solutions¹⁹. These are intended to illustrate the loading behavior both as a function of Mach number throughout the transonic range and also for extremes of projectile geometry. That figure provides a comparison of the normal force distribution on a slender 12 caliber length projectile having a 5 caliber cylinder midbody, and 2 caliber 10° conical boattail. For the Euler calculations, a small spherical cap was added at the base of the projectile, while for the present method, the conical base was extended downstream. Results are displayed for $M_\infty = 0.75, 0.90, 0.95$ at $\alpha = 1^\circ$. As with the results of Figure 11, the present method and the Euler predictions are essentially identical on the ogive nose for all three Mach numbers. On the cylindrical midbody, the comparison is also quite good at all Mach numbers for points ahead of the vicinity of the midbody/boattail junction. Near that junction, as well as on the boattail, some disagreement occurs. At $M_\infty = 0.75$, both methods indicate first a rapid positive then negative loading near the boattail

junction, with the loading remaining negative but gradually recovering toward zero along the boattail. At $M_\infty = 0.90$, the present method essentially accentuates that behavior, while the Euler result indicates instead a rapid negative then positive loading near the boattail junction, and then an increasing negative loading along the boattail. This behavior of the Euler result is very similar to that in Figure 11, and reflects again a broad shock smearing due to grid coarseness.

Consequently, based on these and other related comparisons, we have concluded that the proposed transonically-corrected loading method is able to capture the primary nonlinear inviscid transonic effects which exist on typical ballistic projectiles.

STATIC AERODYNAMIC COEFFICIENTS FOR VARIOUS BOATTAIL PROJECTILES

The ultimate objective of the development of the TER solution procedure and the transonically modified loading method is in the prediction of the static aerodynamic coefficients of various boattail ballistic projectiles. In Figures 13-19 we provide results of the application of these procedures to a variety of different projectile shapes at conditions throughout the transonic regime.

Figure 13 exhibits a comparison of results from the present theory with 3-D TSD results and some limited data¹ for the variation of the overturning pitching moment coefficient C_{m_i} with oncoming Mach number M_∞ for an idealized M549 projectile having various conical boattail lengths. For both theoretical results, the actual nose was replaced by a sharp one of equal length, the rotating bands were neglected so that the cylindrical midbody was smooth, and the afterbody wake geometry was simulated by extending the conical boattail downstream. Three different boattail lengths on the basic projectile shape were considered, i.e., $l_{bt} = 0.579, 0.437, \text{ and } 0.242$, with the longest being that of the actual projectile. For the comparisons at $l_{bt} = 0.579$, indicated as solid lines, both theoretical methods display essentially identical variation with M_∞ and peak C_{m_i} value, but with the 3-D TSD results displaced forward in M_∞ by approximately 0.05. The range data indicate a slightly higher peak value, occurring at the same Mach number predicted by the present method.

The variation of the theoretical solutions for the two shorter boattails is noteworthy. Those results predict the occurrence of lower and earlier peaks in C_{m_i} with decreasing boattail length. This is consistent with both experimental findings and the fact that as the boattail length decreases the shock in that region will move off the boattail and into the wake at a lower Mach number. Additionally, there will exist a geometrically shorter moment arm for the negative loading created by the shock to act upon, thereby reducing the peak overturning moment. With regard to the comparisons between the two theoretical methods for the shorter boattail length, at $l_{bt} = 0.437$ the prediction of peak C_{m_i} is again quite close, with the present theory peak displaced rearward in M_∞ . At $l_{bt} = 0.242$, however, in addition to the rearward displacement of peak C_{m_i} values, the present method predicts a somewhat lower peak value as well. Without further details about the 3-D TSD results, it is difficult to identify precisely the cause of disagree-

ments. Clearly, however, both the variation trends and the general levels of the results are in quite reasonable agreement.

To examine the effect of various idealizations of projectile geometry that were made to facilitate some of these initial conditions, we have performed several parametric studies involving the independent variation of selected projectile geometry parameters. These have primarily involved investigating the idealizations of afterbody wake geometry and approximation of nose geometry, although a preliminary investigation of bore rider influence has also been made. Figure 14 provides the effect of different nose and afterbody wake geometry on the variation of $C_{m\alpha}$ with M_α for the idealized M549 projectile, for which results for the sharp nose, and conical wake geometry model were presented previously in Figure 13. The four theoretical results include the following geometry combinations: (i) sharp nose, cylindrical wake, (ii) sharp nose, conical wake, (iii) blunt nose, conical wake, and (iv) blunt nose with fuze, conical wake. Limited range data¹ are also presented for the actual projectile. We note that the difference between the cylindrical and conical wake model results in the largest change in $C_{m\alpha}$; with the continuous conical wake model most certainly being the more accurate simulation of the actual afterbody wake flow rather than the discontinuous cylindrical model. The shift in peak $C_{m\alpha}$ location and the change to a more peaky behavior in the vicinity of the maximum resulting from the change from cylindrical to conical wake model confirms this, and exhibits excellent agreement with the range data. The addition of the blunt nose to the conical wake model projectile results in an upward shift in magnitude of $C_{m\alpha}$, but no essential difference in trend from the sharp nose result, and continues to bring the theoretical prediction in closer accord with the data near the maximum. The final addition of the fuze geometry to the blunt nose results in a similar but smaller change. The importance of modeling as much as possible of the geometric detail of the actual projectile, however, is clear.

In Figure 15, we present a similar comparison of theoretical results and range data for $C_{m\alpha}$ versus M_α for a T388 projectile²⁰. That standard projectile has a 5.58 caliber overall length, 2.90 caliber ogive nose, and 0.59 caliber conical boattail with 7°37' boattail angle. Theoretical predictions are presented based on a (i) sharp nose, cylindrical wake, (ii) sharp nose, conical wake, and (iii) blunt nose, conical wake. As with the M549 projectile, the change from cylindrical to conical wake model brings the predicted results into almost exact agreement with the range data. Addition of the blunt nose in the theoretical calculation for this projectile results in a downward shift in $C_{m\alpha}$ level, opposite to that of the M549, and indicating the interdependence of these geometric changes.

In Figure 16, we provide the final comparison between the present theory and range data for a standard conical boattail projectile. That figure compares theoretical results with both range and tunnel data²¹ for an improved 5"/54 projectile. This projectile is 5.20 calibers in length, with a 2.75 caliber ogive nose, and 1 caliber conical boattail with 7.5° boattail angle. The theoretical calculations exhibited are based on a conical afterbody wake model and blunt nose with fuze geometry included. Exhibited in the figure is the $C_{m\alpha}$ versus M_α variation from $M_\alpha = 0.5$ to 2.0, demonstrating the capability of the method throughout and beyond the transonic regime.

We note that the theoretical results agree very well for both overall trend and location of the peak pitching moment, with the magnitude and the predicted result being slightly higher throughout the entire range than the data indicate.

For this projectile, we performed several additional calculations to determine whether wind tunnel interference effects were present in the data. Accordingly, we determined the TER equivalent body outer flow solution subject to both a solid and various porous wall boundary conditions. These calculations were performed at Mach numbers at and in the vicinity of the C_{m_α} peak. All of these calculations resulted in indiscernible changes from the free air result provided in Figure 16. We conclude that the discrepancy in C_{m_α} level is most likely due to the midbody waisting on the actual projectile²¹, which was not modeled in the theoretical calculations.

In the next three figures, Figures 17-19, we present results which demonstrate the capability of the present predictive method to treat a variety of different projectile boattail shapes, both axisymmetric and non-axisymmetric. Figure 17 presents the predicted variation of C_{m_α} with M_∞ for the four different boattail shape projectiles shown previously in Figures 1 and 6, plus an additional conical boattail projectile with shorter boattail ($l_b = 0.5$) length. All of these projectiles have a 5 caliber overall length and identical 2 caliber sharp ogive nose geometry. Consequently, the results presented illustrate, in a design sense, the effect on C_{m_α} of varying the boattail shape through a wide range of geometries. We note that the 1 caliber conical boattail projectile exhibits the highest C_{m_α} and thus is the worst choice from a stability design criterion. Decreasing the conical boattail length to 0.5 calibers improves the situation somewhat, but not significantly. The square boattail further improves the situation, but the triangular boattail, of these four shapes, provides the best result for minimum peak C_{m_α} . These results are in direct correspondence with the experimental results of Reference 2. Although the cylindrical boattail exhibits the lowest peak C_m , its high drag and consequent low range make it an undesirable candidate shape.

In Figure 18, we present the corresponding results for the normal force coefficient C_{N_α} for these same five shapes. We note the prediction that the longer conical boattail has the lowest lift of all the projectiles, due to the strong negative loading on the boattail section.

In Figure 19, we exhibit the surface pressure drag coefficient variation with M_∞ for these same projectiles. This calculated drag represents the wave drag of these various shapes. In order to determine the total inviscid drag, those results must be augmented by the base pressure drag. This could be done within the framework of the present computational procedure either from a correlation of base pressure drag and inviscid base pressure, or through a boundary layer/wake computation coupled to the inviscid flow prediction. The point of presenting these results is to indicate the means for a first-order approximation of the projectile drag is feasible with the present theoretical procedure.

Finally, we note the computational efficiency of the present method. A complete calculation (TER calculation plus loading determination) requires less than 30 seconds CPU time on a CDC 7600 for a typical projectile at a

specified M_∞ . As a typical example, regard to the theoretical predictions of $C_{m\alpha}$, $C_{N\alpha}$, and C_D provided in Figures 17 through 19 involving the 5 different boattail projectiles. The separate points on each of the curves indicate the individual calculations made and total 110 separate TER and loading solutions. Computational time for all of these cases was less than 30 minutes of CDC 7600 CPU time.

POTENTIAL APPLICATION TO MISSILES AT HIGH ANGLE OF ATTACK

In this section, we point out the potential utility of the concepts and procedures developed here to applications involving current missile configurations and requirements. In the current applications of the TER procedure to ballistic projectiles, attention was focused on the low to moderate lift situation (thickness-dominated flows). This was done because that lift range is the necessary operating regime for these shapes, since current ballistic projectiles are spin stabilized and have no means (no lifting surfaces) of recovering from a high angle of attack condition. For applications to present-design missiles, however, which often employ both canard and tail surfaces, the control situation is quite different and the operation requirements imposed usually require capability of operating at high angle of attack. Under such conditions, the primary nonlinear effects²² arise from compressibility effects and the various vortical flows (nose, canard, afterbody, and tail vortex systems) generated by different segments of the missile surface. At transonic conditions, both of these nonlinear effects can be treated by employing the lift-dominated limiting form the TER. Figure 20 provides an illustration of the application of the TER to such configurations at high angle of attack transonic conditions; together with the decomposition of the flow into its various inner and outer components. In that illustration, for clarity of presentation, we have omitted indicating the nose and afterbody vortices, and have only shown the canard trailing vortices. In the actual TER application and calculation, all of these vortical flows would be accounted for.

As shown in Figure 20, the various component problems in the inner region now consist of both vertical and horizontal translation of the cross section corresponding to upwash and sidewash, the crossflow vortical flow field consisting of all vortices generated upstream of a particular longitudinal station, and the familiar thickness problem, whereas the outer flow now consists of axial flow past both an equivalent source and doublet distribution in which the source distribution consists of the equivalent area source distribution augmented by additional source-like terms due to the axial and spanwise lift distribution⁵.

Although the outer problem is now three-dimensional, the TER provides a means for solution that is nevertheless significantly simpler than solving the full nonlinear three-dimensional flow problem past the actual configuration. In light of the success of the TER method for ballistic projectile applications, it is felt that the potential of the method for providing an accurate and computationally-efficient solution to the transonic high angle of attack slender missile problem is high.

CONCLUDING REMARKS

The development of a theoretical predictive method for determining the steady inviscid aerodynamic behavior of ballistic projectiles throughout the

transonic regime is described. The emphasis of the work was directed toward establishing the capability for investigating the now standard conical boattail projectiles as well as a variety of new shapes characteristic of the non-axisymmetric boattail projectiles under current study by the U.S. Army. The final objective is the development of a rational modeling procedure for the investigation of the transonic aerodynamic effects of incorporating different boattail and body geometries into ballistic projectile design, with a view toward optimizing the aerodynamic performance of these shapes, such as increasing range and/or payload while simultaneously avoiding stability problems.

The theoretical analysis is based on the transonic equivalence rule (TER) and includes a finite-difference SLOR procedure for determining the nonlinear axisymmetric outer (far field) flow about the "equivalent" body of revolution, and a two-dimensional finite-element solver for providing general solutions to the inner (near field) cross-flow problem for the arbitrary geometries characteristic of the new boattail projectiles. The ultimate utility of the predictive method is in the accurate determination of the static aerodynamic characteristics of these projectiles, specifically the lift and destabilizing pitching moment. Toward that end, a new nonlinear loading calculation procedure which incorporates transonic effects has been formulated and tested. The technique is based on apparent mass concepts and employs the finite-element inner crossflow solver to determine the appropriate apparent mass coefficients and uses the nonlinear outer TER solution for the axisymmetric flow about the equivalent body to account for nonlinear effects due to shock waves.

Results are presented for a wide variety of projectile shapes, having both axisymmetric and nonaxisymmetric boattail geometries, and demonstrates the ability of the procedure to predict successfully the observed range and tunnel variations of pitching moment and normal force throughout the transonic range. Additional calculations illustrating the separate effects of different geometry models to simulate the afterbody wake and nose bluntness including fuze geometries are presented.

ACKNOWLEDGEMENT

This research was supported by the U.S. Army Research Office under Contract DAAG29-77-C-0038 with Dr. Robert Singleton as Technical Monitor.

REFERENCES

1. Reklis, R. P., Sturek, W. V., and Bailey, F. R.: Computation of Transonic Flow Past Projectiles at Angle of Attack. AIAA Paper No. 78-1182, July 1978.
2. Platou, A. S.: Improved Projectile Boattail. AIAA Jour., Vol. 12, Dec. 1975, pp. 727-732.
3. Heaslet, M. A. and Spreiter, J. R.: Three-Dimensional Transonic Flow Theory Applied to Slender Wings and Bodies. NACA Rept. 1318, 1957.
4. Cheng, H. K. and Hafez, M. M.: Equivalence Rule and Transonic Flows Involving Lift. Dept. of Aero. Eng. Rept. USCAE 124, Univ. of Southern

California, School of Engineering, Apr. 1973.

5. Cheng, H. K. and Hafez, M. M.: Transonic Equivalence Rule: A Nonlinear Problem Involving Lift. J. of Fluid Mech., Vol. 72, 1975, pp. 161-188.
6. Oswatitsch, K.: Die Theoretischen Arbeiten über schallnahe Strömungen am Flugtechnischen Institut der Kungl. Techniska Högskolan, Stockholm. Eighth Inter'l Congress on Theoretical and Applied Mechanics, Istanbul, 1952, (1953) pp. 261-262.
7. Oswatitsch, K.: The Area Rule. Applied Mech. Reviews, Vol. 10, Dec. 1957, pp. 543-545.
8. Spreiter, J. R.: Theoretical and Experimental Analysis of Transonic Flow Fields. NACA-Univ. Conf. on Aerodynamics, Construction, and Propulsion II, "Aerodynamics," 1954, pp. 18-1 - 18-17.
9. Barnwell, R. W.: Transonic Flow About Lifting Configurations. AIAA Jour., Vol. 11, May 1973, pp. 764-766.
10. Bailey, F. R.: The Numerical Calculation of Transonic Flow about Slender Bodies of Revolution. NASA TND-6582, Dec. 1971.
11. Krupp, J. A. and Murman, E. M.: Computation of Transonic Flows Past Lifting Airfoils and Slender Bodies. AIAA Jour., Vol. 10, July 1972, pp. 880-886.
12. Murman, E. M.: Analysis of Embedded Shock Waves Calculated by Relaxation Methods. AIAA Jour., Vol. 12, May 1974, pp. 626-633.
13. Jameson, A.: Transonic Flow Calculations. VKI Lecture Series 87, Computational Fluid Dynamics, von Kármán Institute for Fluid Dynamics, Rhode-St. Genesse, Belgium, Mar. 1976.
14. Stahara, S. S. and Spreiter, J. R.: Transonic Wind Tunnel Interference Assessment-Axisymmetric Flows. AIAA Jour., Vol. 18, Jan. 1980, pp. 63-71.
15. Bryson, A. E., Jr.: Stability Derivatives for a Slender Missile with Application to a Wing-Body-Vertical Tail Configuration. J. Aeronaut. Sci., Vol. 20, No. 5, 1953, pp. 297-308.
16. Nielsen, J. N.: Missile Aerodynamics. McGraw-Hill, New York, 1960.
17. Stahara, S. S. and Spreiter, J. R.: Transonic Flows Past Nonaxisymmetric Slender Shapes - Classical Equivalence Rule Analysis. AIAA Jour., Vol. 17, No. 5, Mar. 1979, pp. 245-252.
18. Reklis, R. P., Danberg, J. E., and Ingu, G. R.: Boundary Layer Flows on Transonic Projectiles. AIAA Paper No. 79-1551, July 1979.
19. Klopfer, G. H. and Chaussee, D. S.: Numerical Solution of Three Dimensional Transonic Flows Around Axisymmetric Bodies at Angle of Attack. Nielsen Engineering & Research, Inc. TR 176, Feb. 1979.

20. Krial, K. S. and MacAllister, L. C.: Aerodynamic Properties of a Family of Shell of Similar Shape--105mm XM308E5, XM308E6, T388 and 155mm T387. BRL Memo Rept. No. 2023, Feb. 1970.
21. Ohlmeyer, E. J.: Dynamic Stability of the Improved 5"/54 Projectile. NWL Tech. Rept. TR-2871, Dec. 1972.
22. Nielsen, J. N.: Wright Brothers Lectureship in Aeronautics, Missile Aerodynamics - Past, Present, and Future. AIAA Paper No. 79-1819, Aug. 1979.

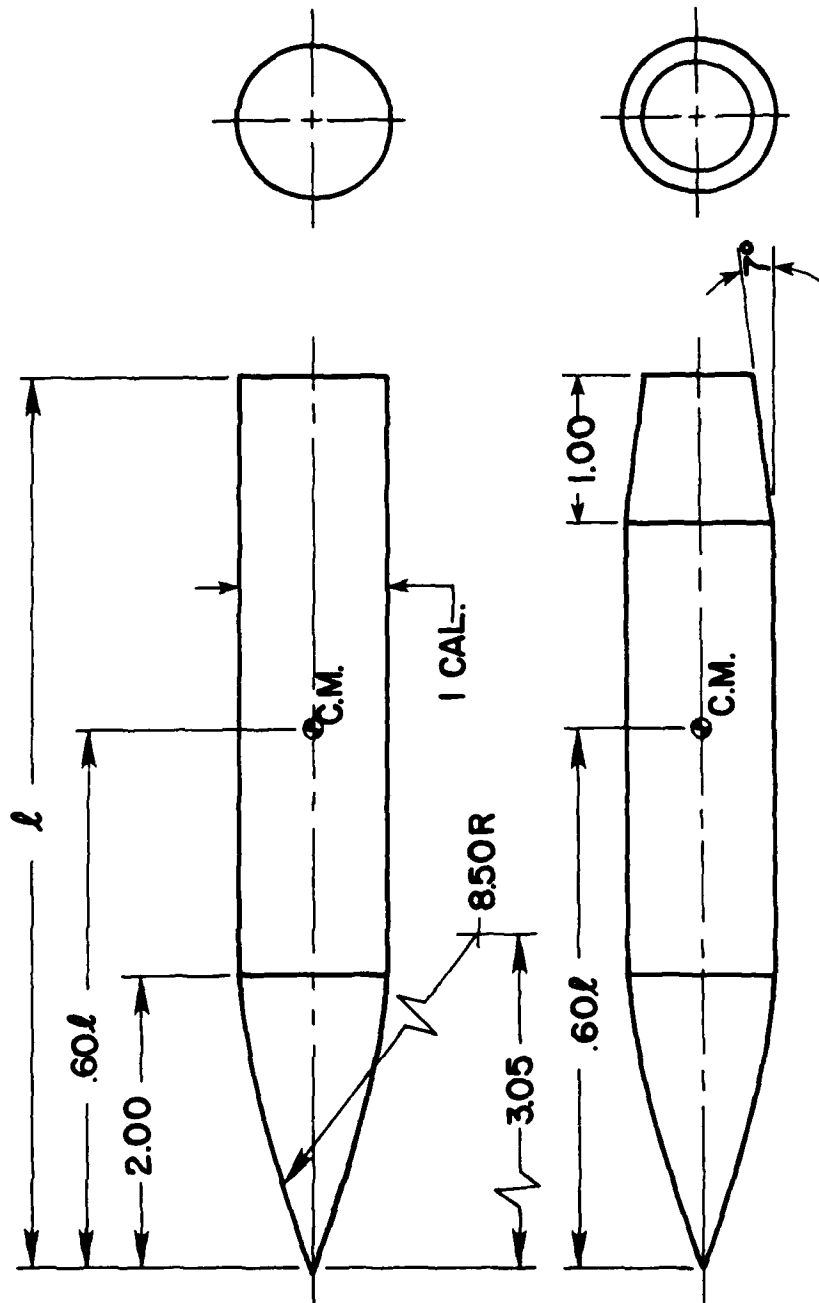
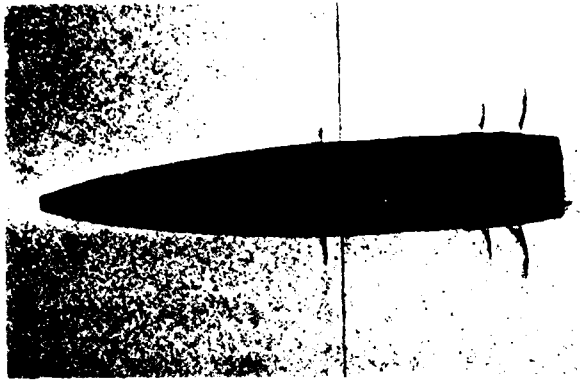
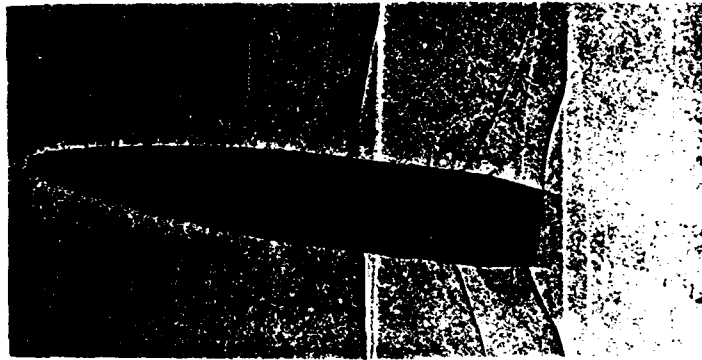


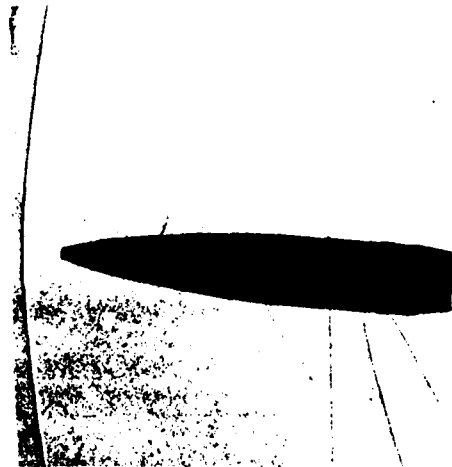
Figure 1 Illustration of typical ballistic projectiles having cylindrical and conical boattails; dimensions in calibers.



a. $M_{\infty} = 0.898$



b. $M_{\infty} = 0.957$



c. $M_{\infty} = 1.033$

Figure 2 Shadowgraphs of ballistic projectiles at various transonic Mach numbers illustrating characteristic shock formation and movement.

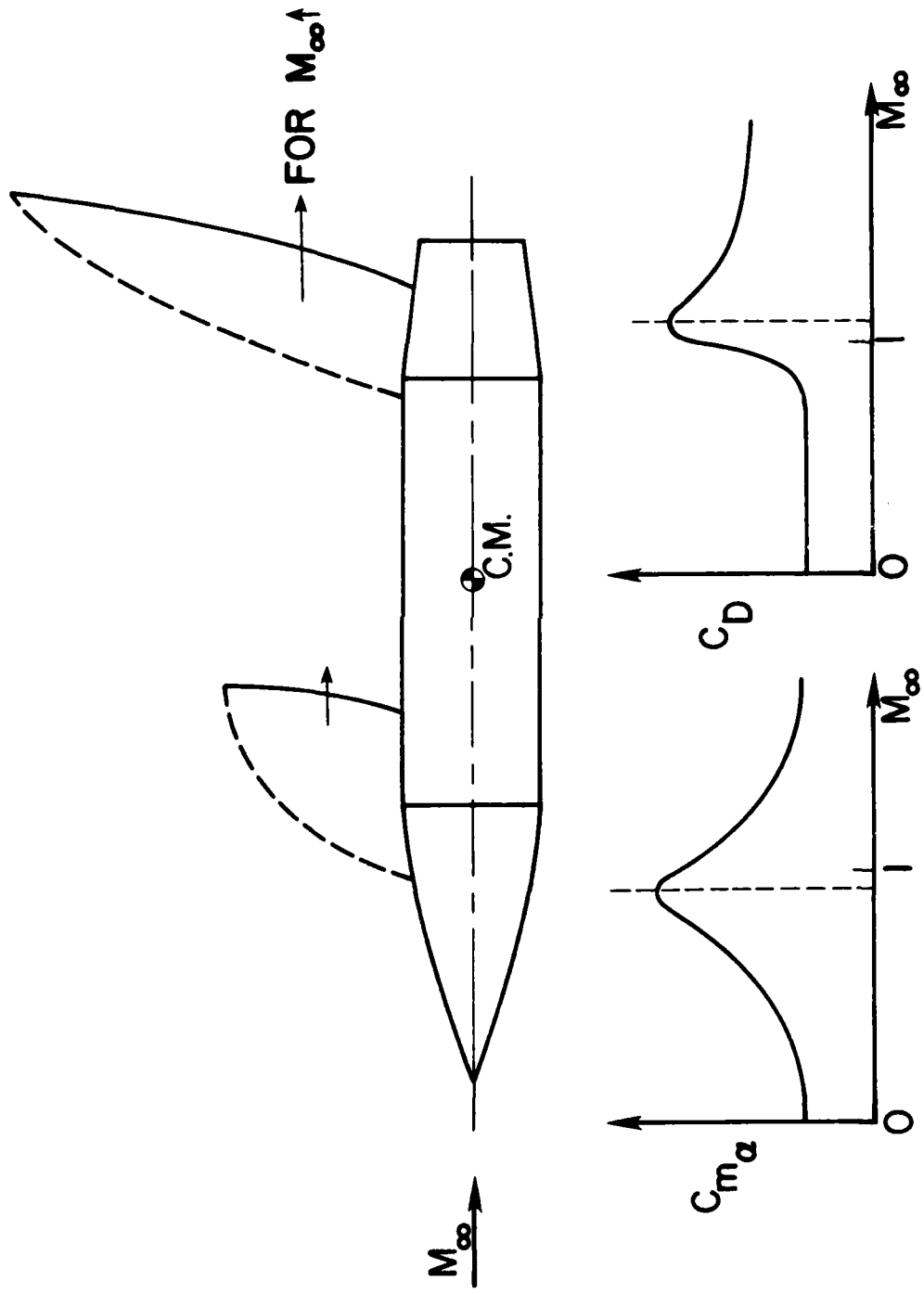


Figure 3 Variation of shock movement, destabilizing pitching moment, and drag with M_∞ on a typical ballistic projectile.

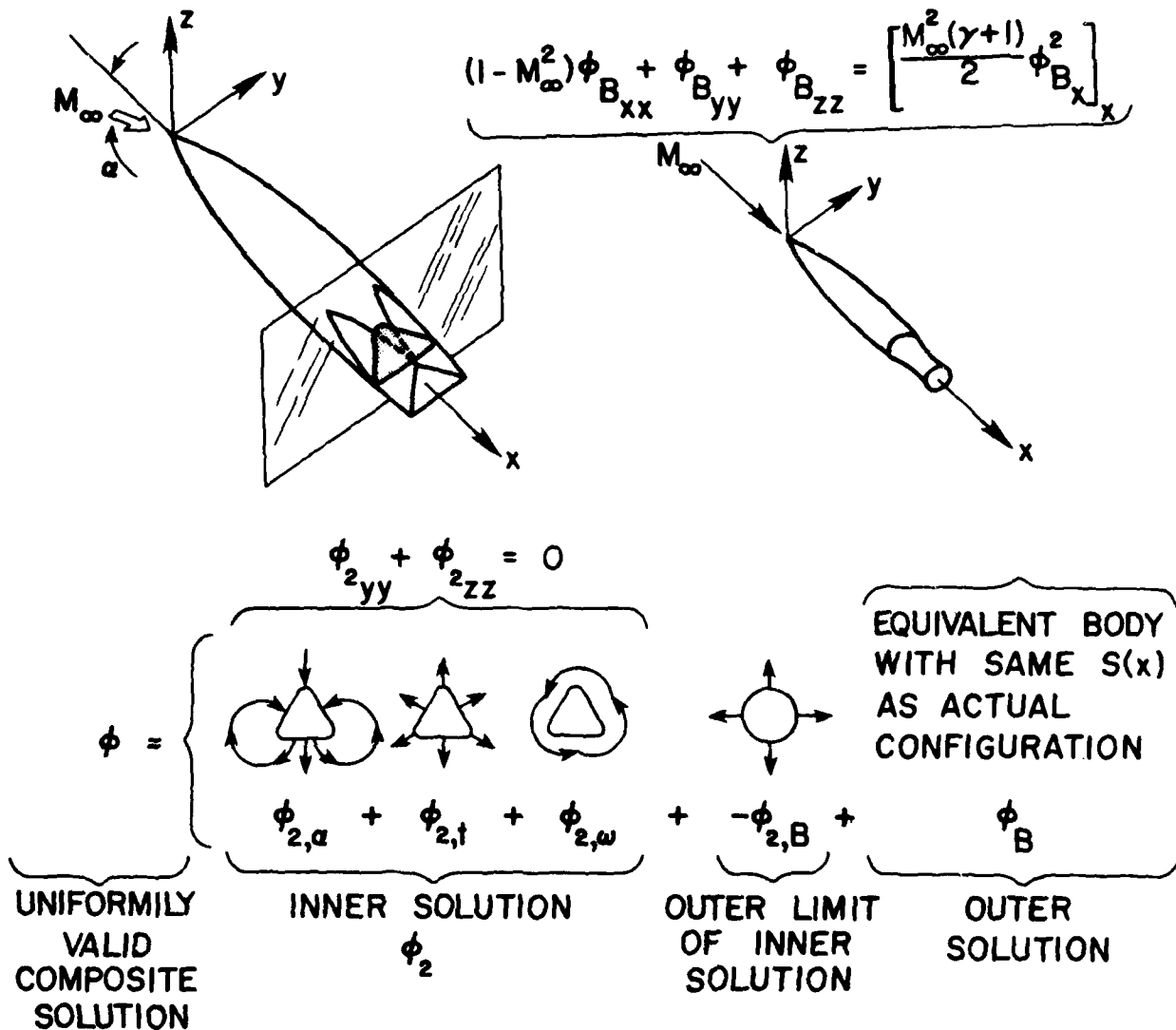


Figure 4 Illustration of the classical transonic equivalence rule for slender configurations

$$\bar{\phi} = -\frac{1}{P} \int_{x_1}^x \bar{\phi}_{\eta}(\xi, \eta_s) d\xi$$

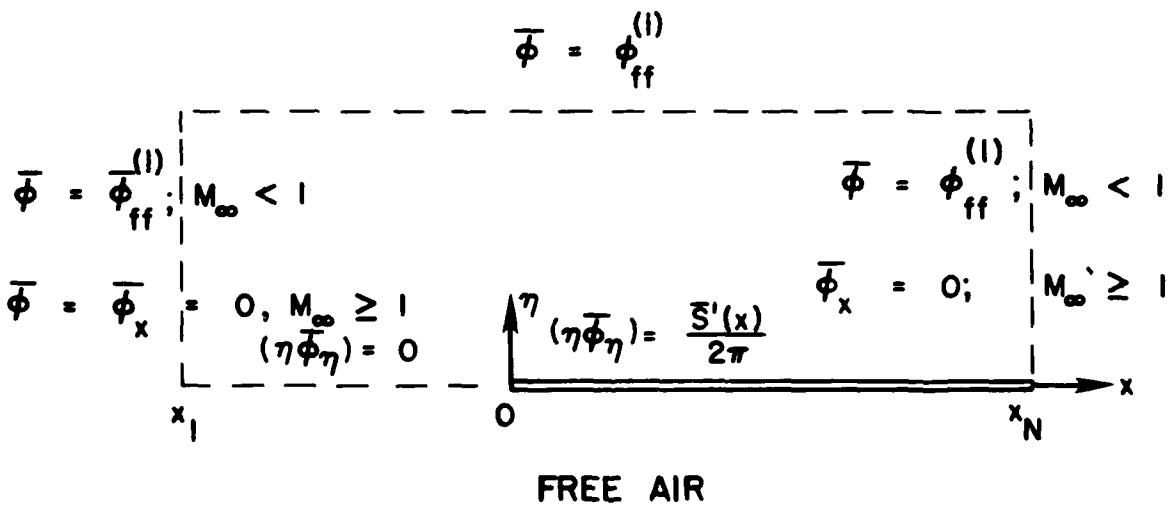
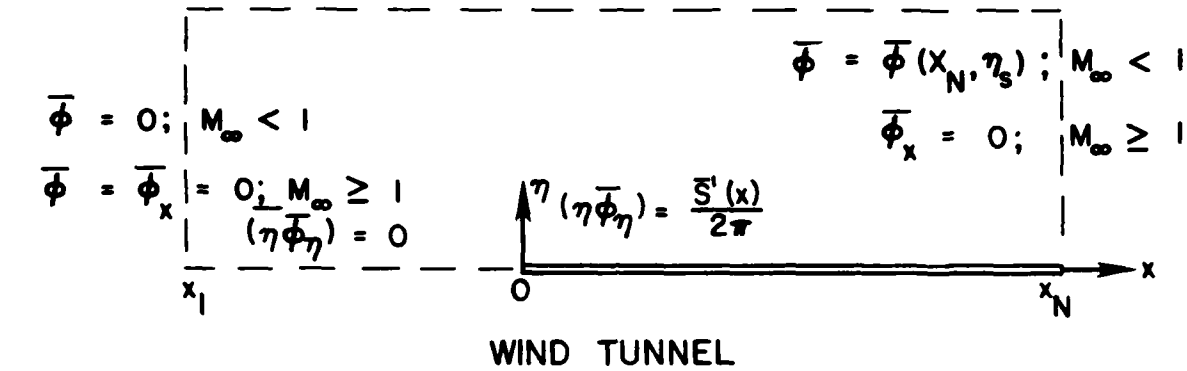


Figure 5 Summary of boundary conditions for outer flow computational problem.

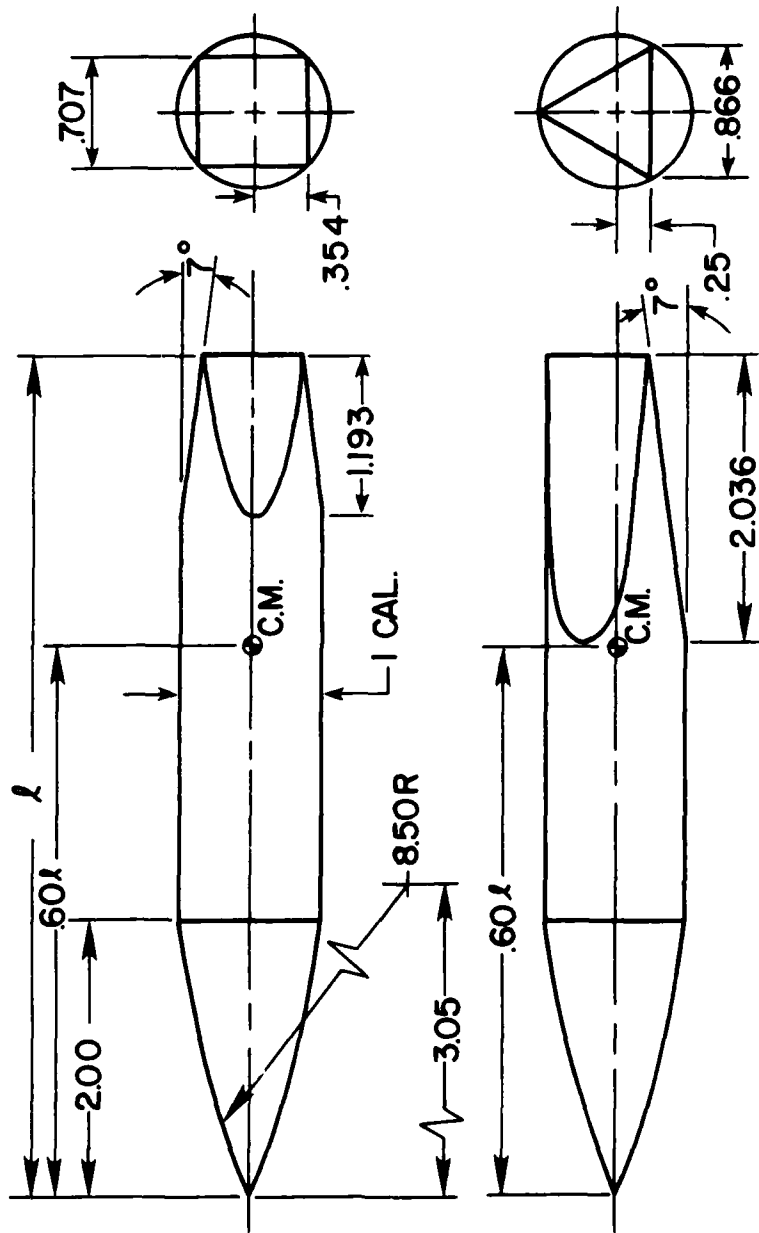
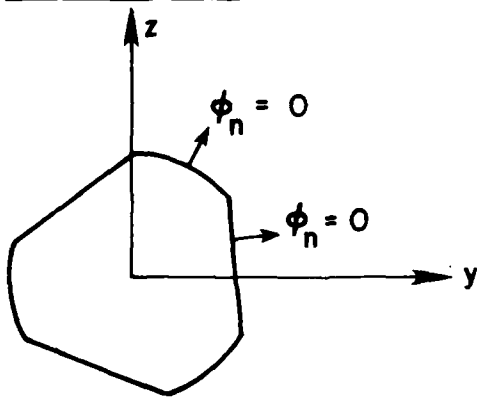


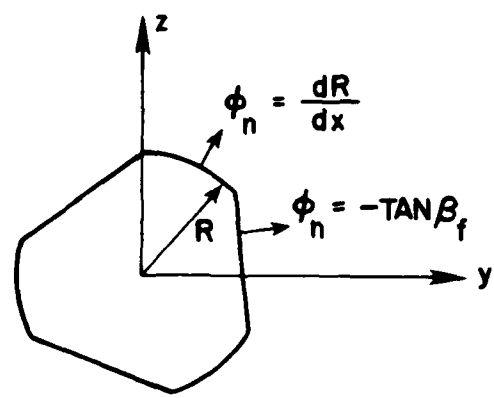
Figure 6 Ballistic projectiles having inscribed square and triangular boattail shapes formed by cutting planes acting on the cylindrical boattail section.

CROSSFLOW: $\phi_{2,q}$



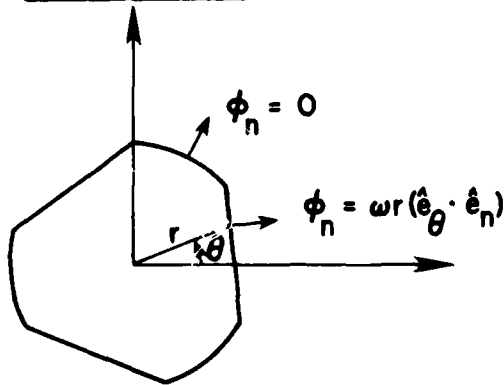
(A)

CONTRACTION: $\phi_{2,t}$



(B)

TWIST: $\phi_{2,\omega}$



(C)

Figure 7 Body surface boundary conditions for inner flow computational problem.

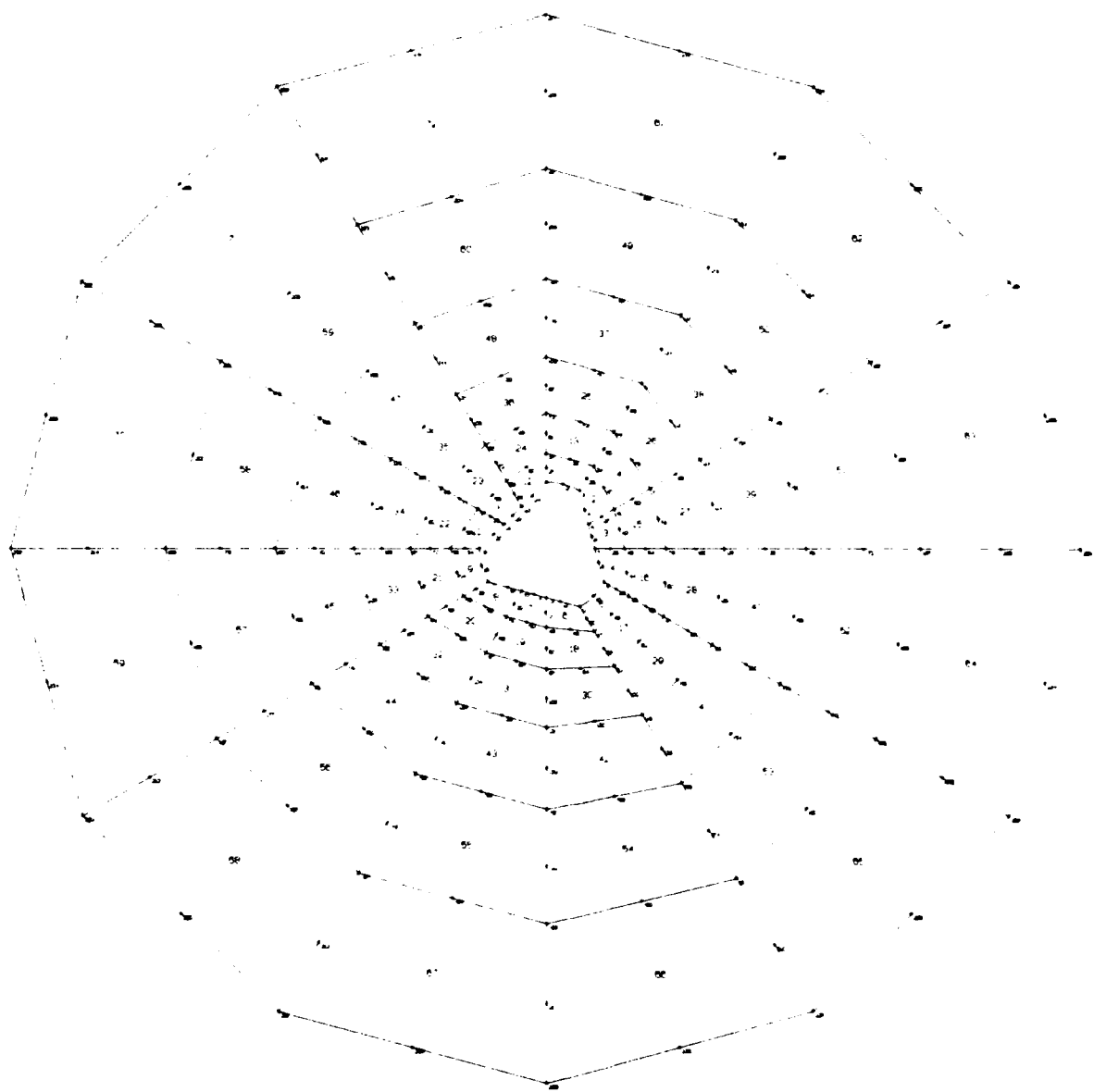


Figure 8 Illustration of typical finite-element mesh employed for inner problem.

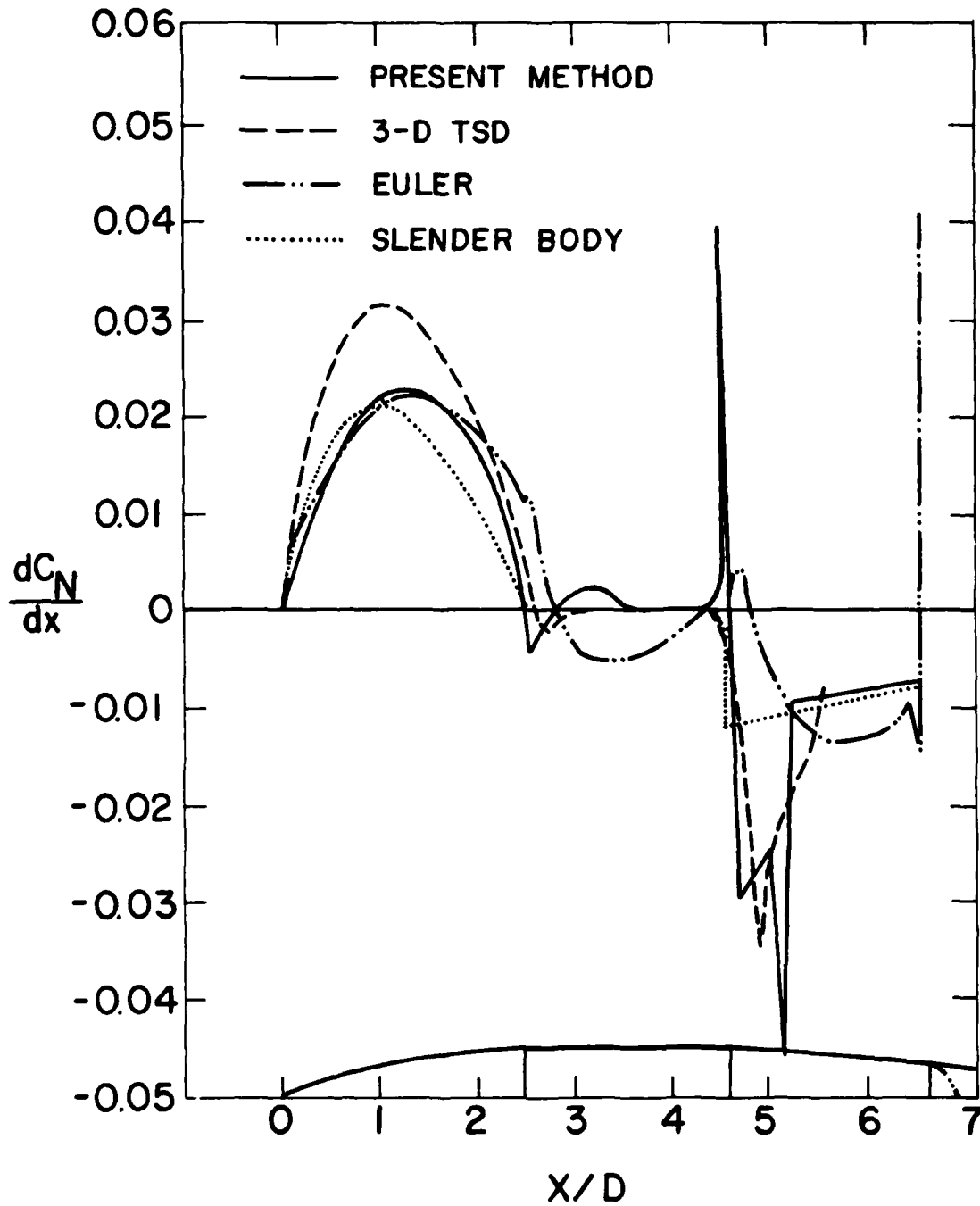


Figure 11 Comparison of present loading method with other theoretical methods for the normal force loading distribution on an idealized M549 projectile at $M_\infty = 0.95$, $\alpha = 1^\circ$.

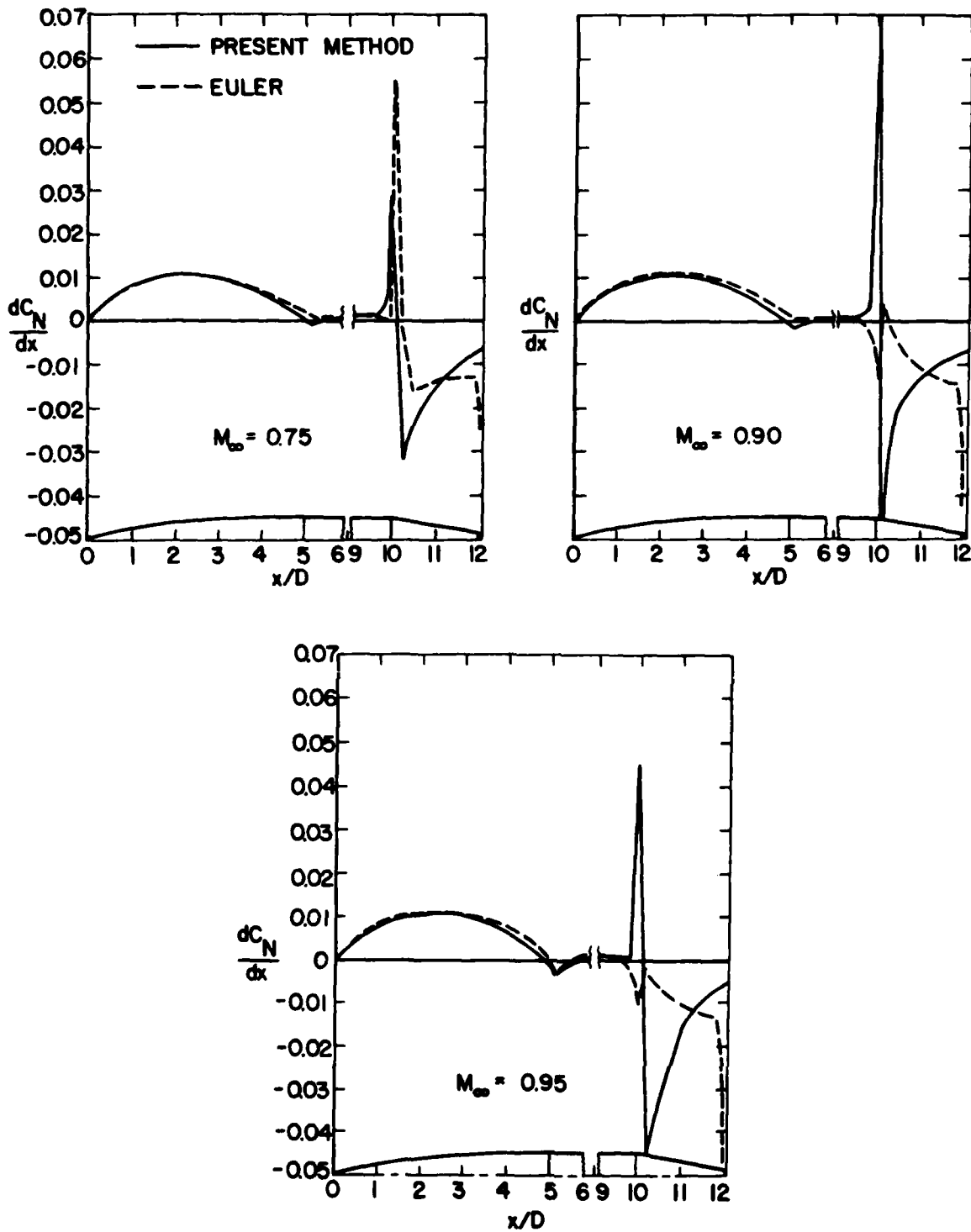


Figure 12 Comparison of present loading method with 3-D Euler equation results for the normal force loading distribution on a slender 12 caliber length projectile at various transonic Mach numbers.

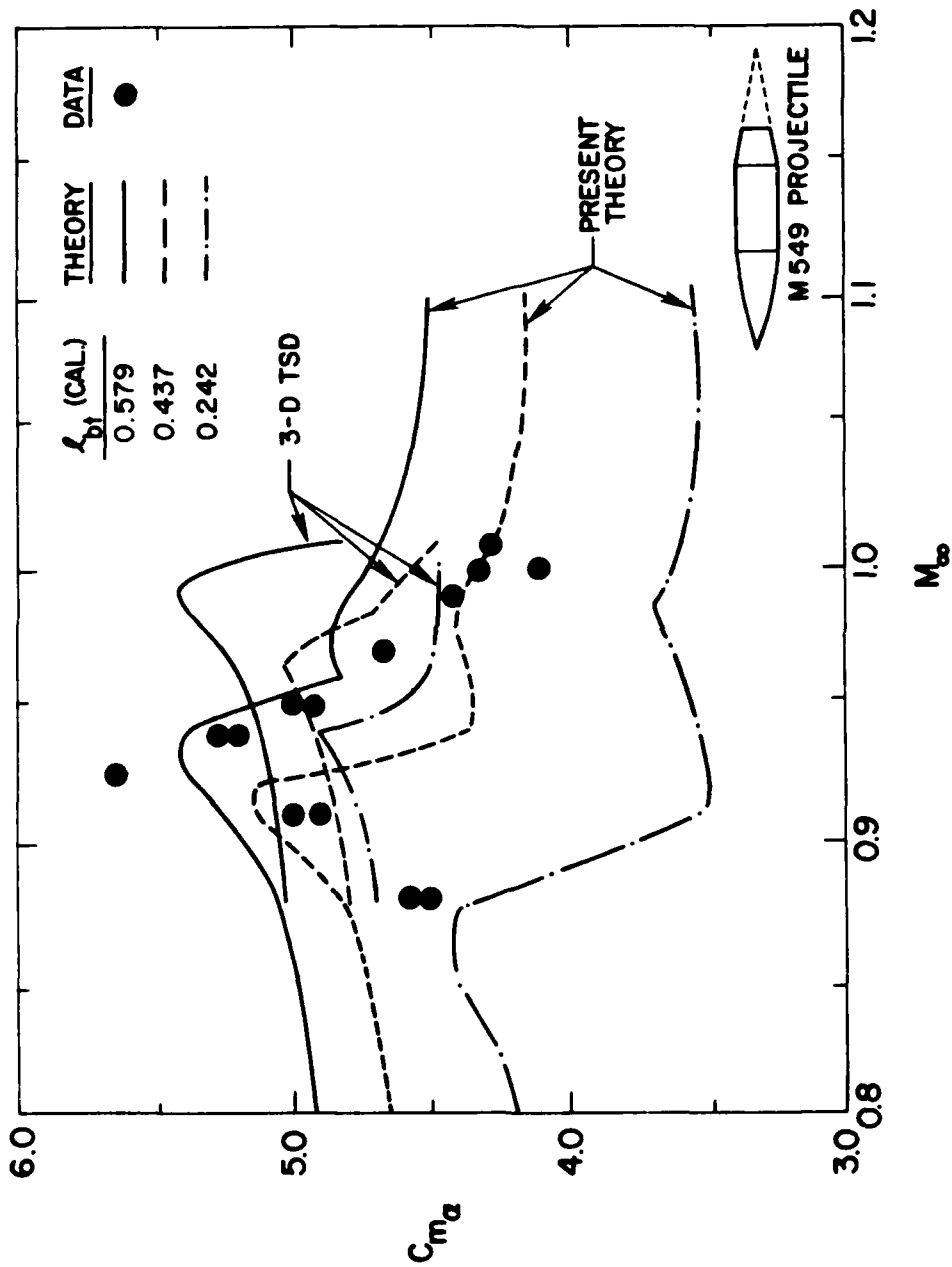


Figure 13 Comparison of present method with 3-D TSD results and data for the variation of destabilizing pitching moment $C_{m\alpha}$ with M_{bo} for a basic M549 projectile having various boattail lengths.

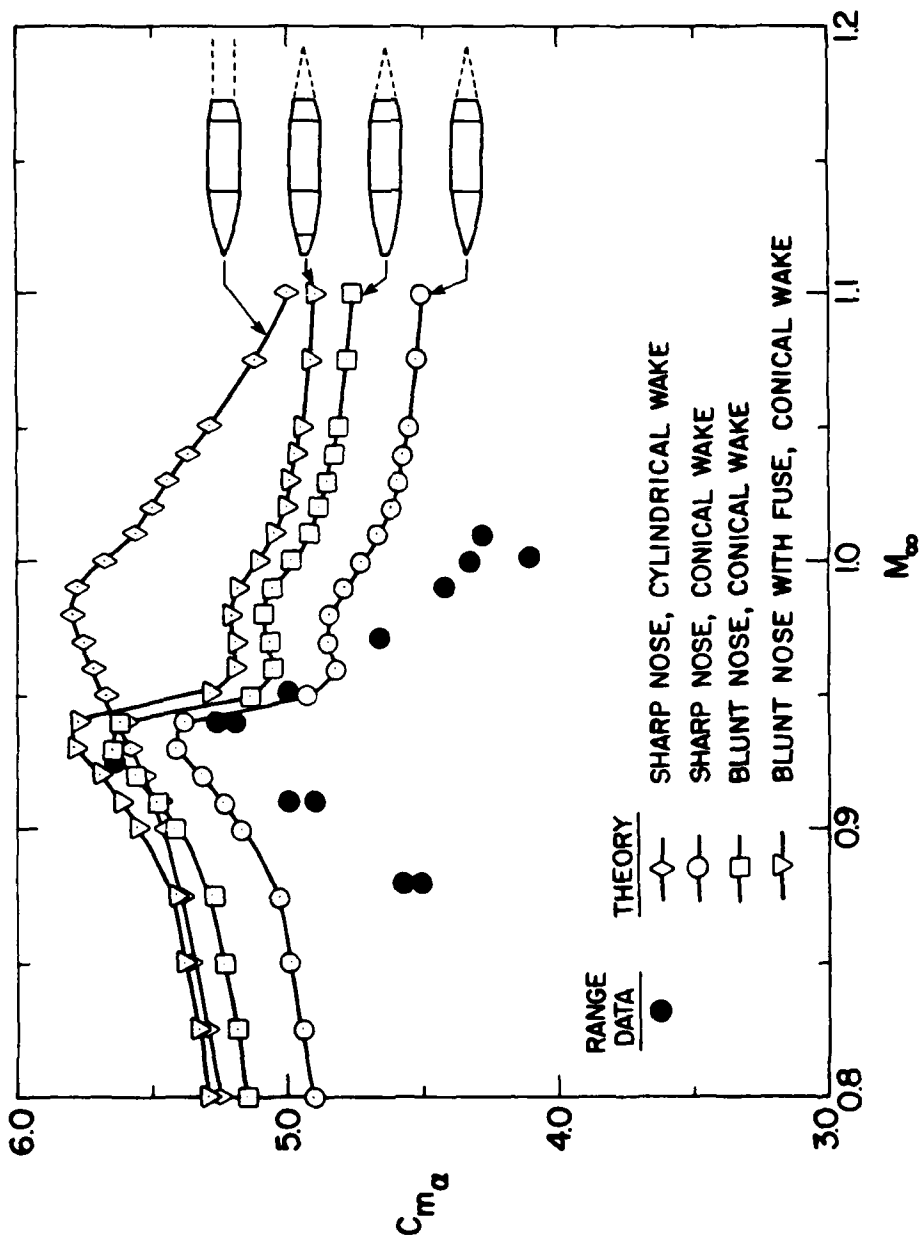


Figure 14 Effect of afterbody wake geometry and nose bluntness on variation of C_{m_α} with M_∞ for a M549 projectile.

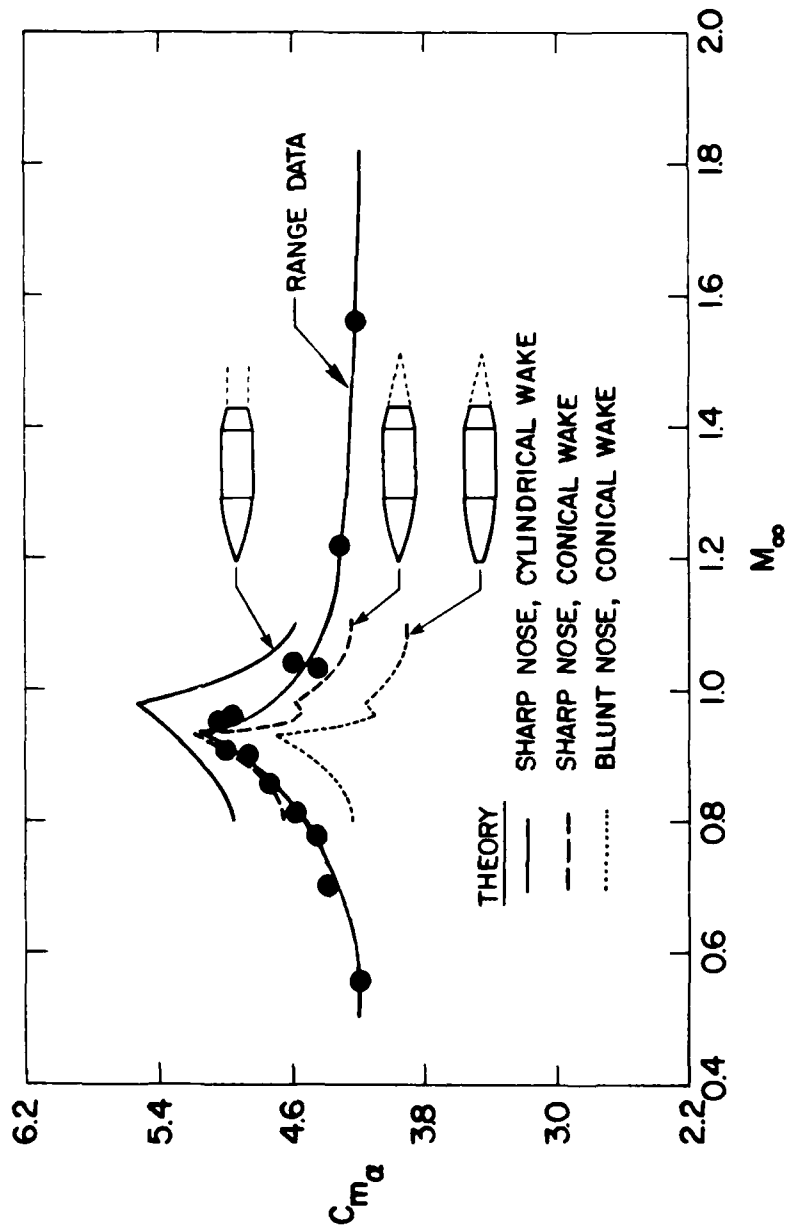


Figure 15 Comparison of theoretical results and data for the variation of $C_{m\alpha}$ versus M_∞ for a T388 projectile illustrating the effect of wake geometry and nose bluntness

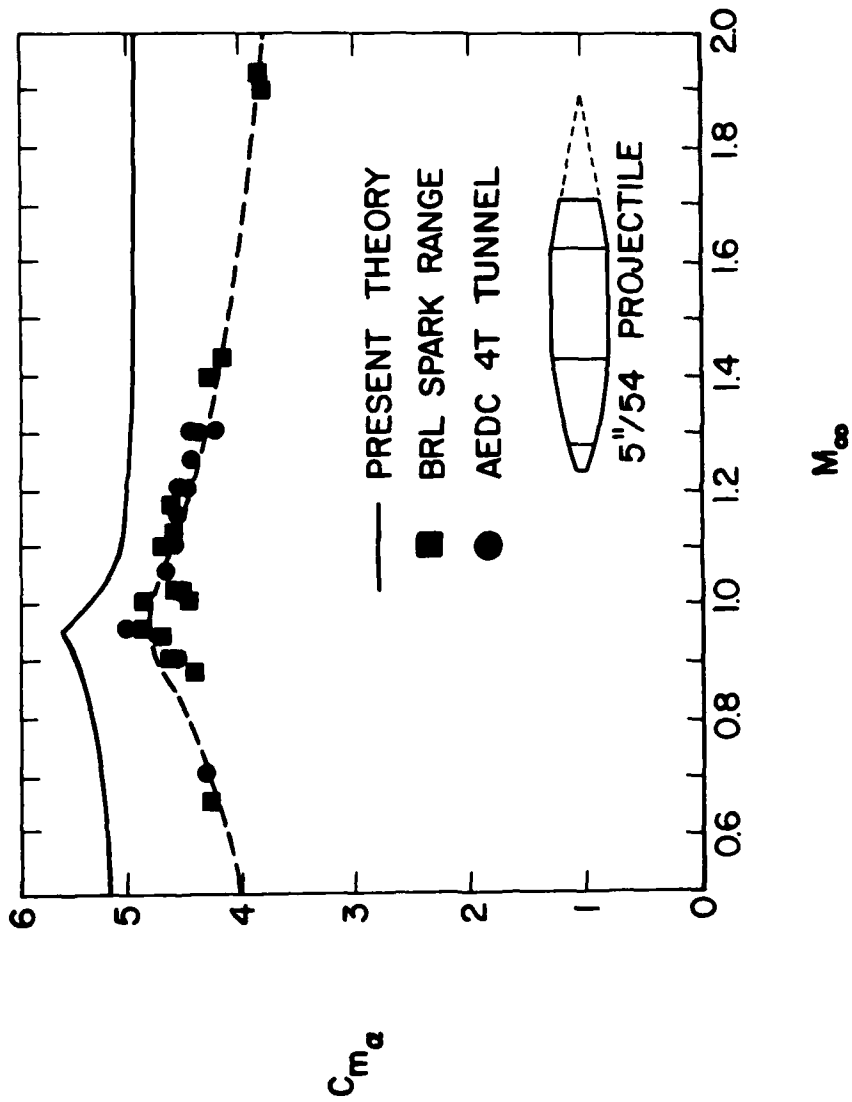


Figure 16 Comparison of theoretical results and data for the variation of $C_{m\alpha}$ versus M_∞ for the improved 5"/54 projectile.

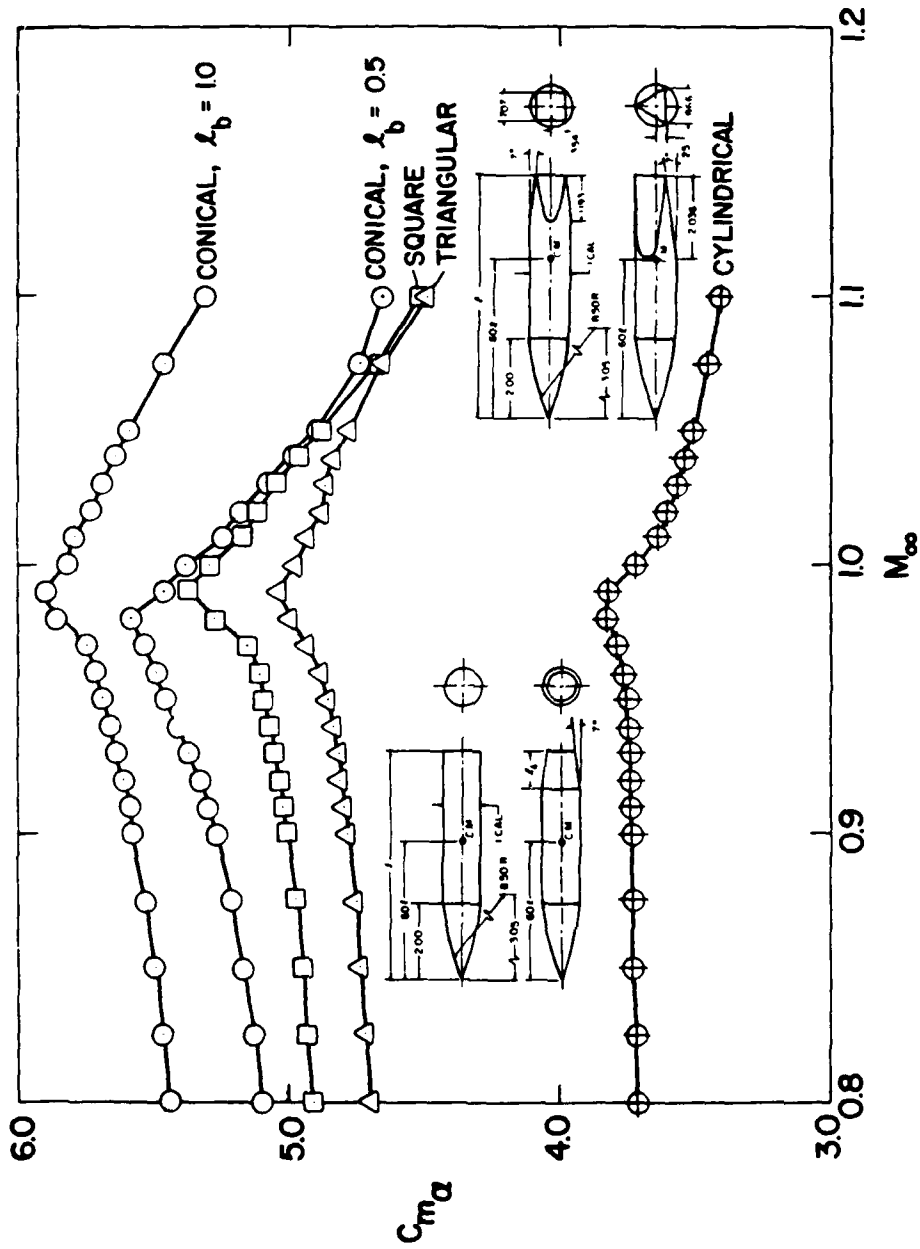


Figure 17 Effect of various boattail geometries on $C_{m\alpha}$ variation with M_∞ for a 5 caliber length, fixed nose geometry projectile.

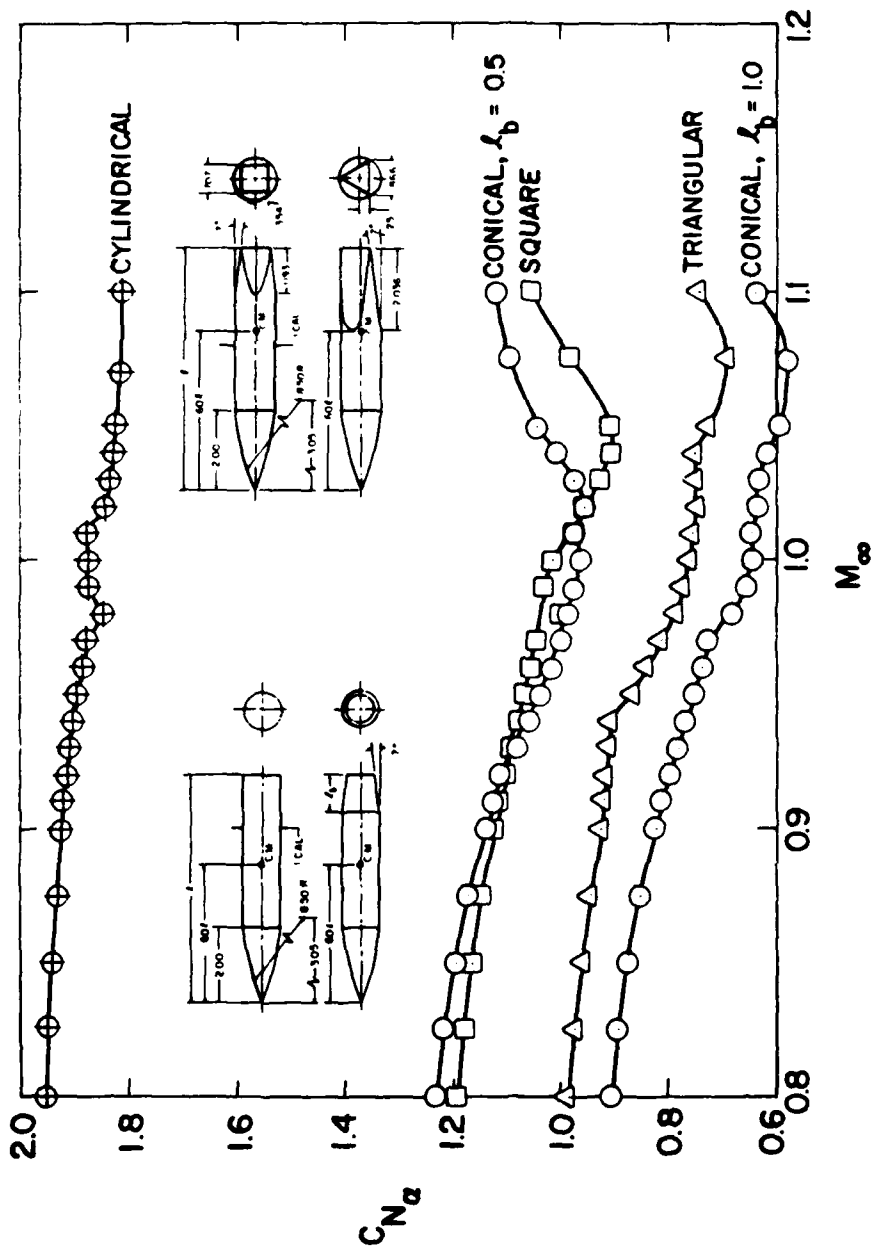


Figure 18 Effect of various boattail geometries on $C_{N\alpha}$ variation with M_∞ for a 5 caliber length, fixed nose geometry projectile.

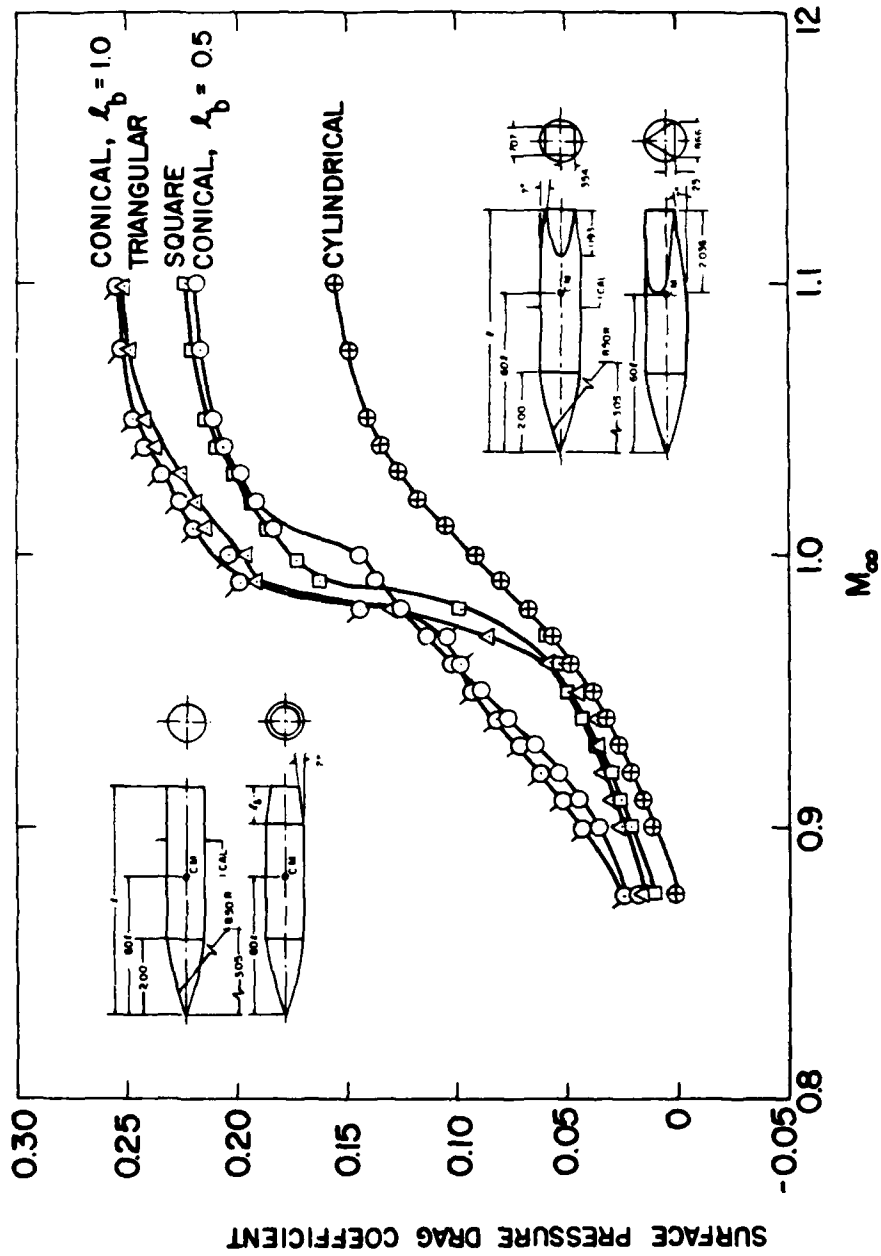


Figure 19 Effect of various boattail geometries on C_D variation with M_∞ for a 5 caliber length, fixed nose geometry projectiles.

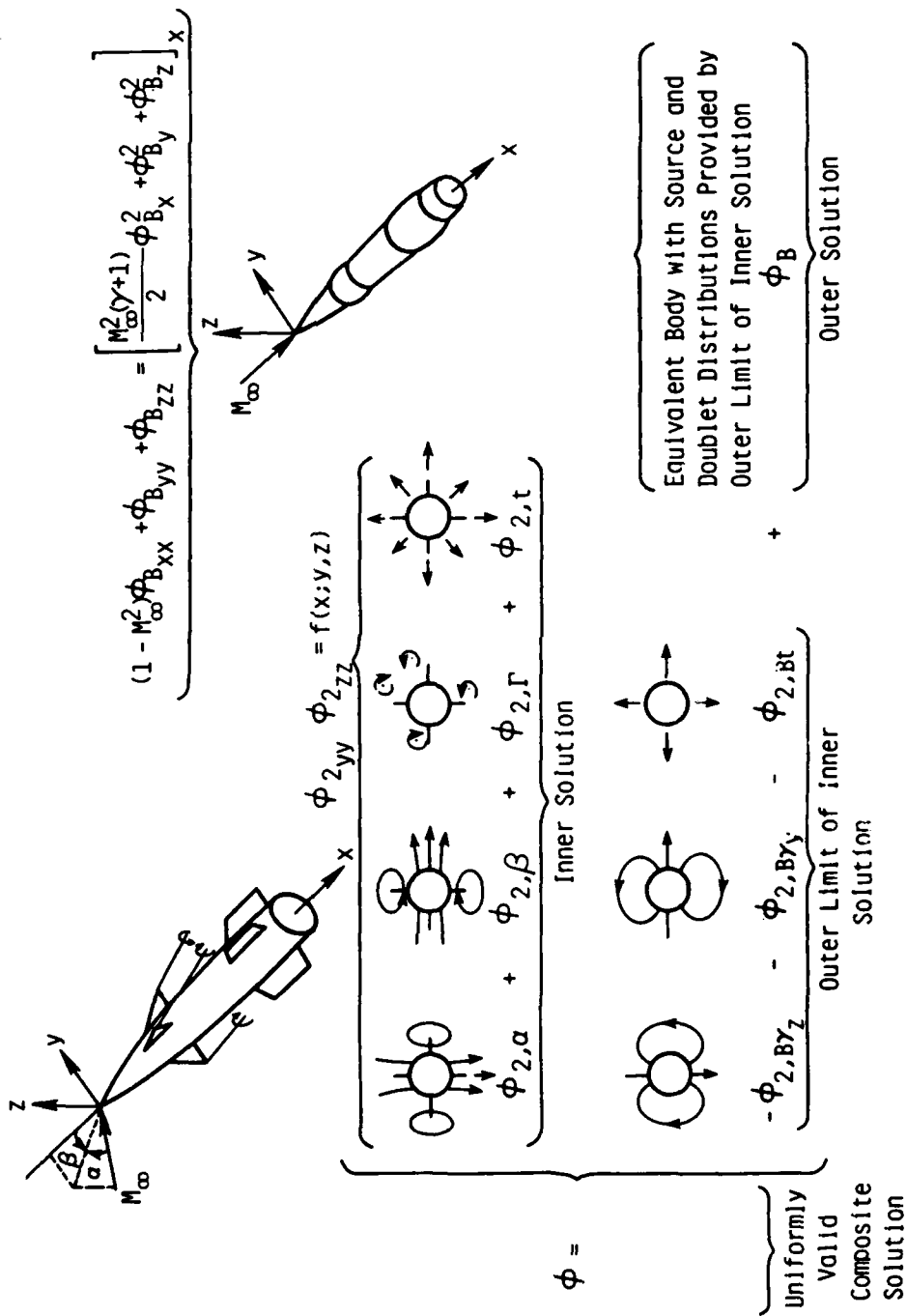


Figure 20 Application of transonic equivalence rule concepts to typical canard-cruciform tail missile configurations at high angle of attack transonic conditions.

STORE SEPARATION - A REVIEW

ARTHUR R. MADDOX

NAVAIR RESEARCH PROFESSOR

U. S. NAVAL ACADEMY

This paper reviews developments in the field of store carriage and separation. First, the Store Separation Program Plan, a long term effort carried out at NWC, China Lake, is summarized, and then corresponding efforts are reviewed from a wide variety of sources. The recommendations of the NWC study are, with some changes in emphasis, still valid in this rapidly changing technological environment, but especially important is the recommendation of accelerating efforts to apply transonic techniques.

European literature suggests a greater application of analytical techniques to this field than corresponding United States literature. There is still a strong requirement for high quality experimental data suitable for rigorous comparisons and critical correlations.

INTRODUCTION

The problem of carriage and release of stores from aircraft has been periodically reviewed, and references 1 - 4 are representative of some of these efforts. These references contain much of the historical perspective, and buried within them are many other references which repeatedly discuss differing points of view or approaches.

Several years ago the Store Separation Program Plan was initiated at Naval Weapons Center, China Lake to pragmatically evaluate the techniques being used and to generate one common well instrumented data block which could serve as a fundamental validation base for future work. This program enjoyed the enthusiastic support of nearly all the diverse facilities involved in this problem over a period of nearly six years. Unfortunately, at the completion of the effort, there was no follow-up.

Elsewhere, in this country, there is a strong urge to back off from analytical simulation of this problem to experimental efforts even though techniques to generalize experimental data for more effective use have not been broadly pursued. In some areas of the Air Force, the flow angularity method, now labeled 'grid technique', is broadly used in conjunction with experimental data on the aircraft flow field. On the other hand, Air Force funding has focused some of the best panel method techniques of the day on a purely analytical simulation of the problem, but again there appears little follow-up.

Available literature on European approaches to the problem also reveal a predilection to use the flow angularity method also but with an analytical description of the aircraft basic flow field. Panel method techniques are preferred for this flow field specification. In at least one case, however, a simplified panel technique was reported to be used for the integrated problem.

By far the most significant development related to this problem is the emergence of what appears to be effective transonic aerodynamic techniques. These are reaching the stage where they could be termed engineering solutions while, at the same time, appear able to account for the complex geometry associated with store carriage and release.

GENERAL DISCUSSION

Store Separation Program Plan

The Store Separation Program Plan was initially proposed ⁽⁵⁾ to evaluate and, where necessary, develop the methodology to deal with the problem of store carriage and separation. Three fundamental assumptions were made. First, the analytical simulation of the problem was not well developed. Second, the wind tunnel simulation, although well developed with a variety of techniques available, frequently produced misleading data with large changes in the results related to seemingly minor changes in technique. Third, the full scale flight data, also well developed in technique, sometimes differed catastrophically with the above approaches. Finally, both wind tunnel and flight data were already expensive and getting more so.

Some of the early work on this program has been described before ⁽⁶⁾, but the most significant feature was a competitive examination of a number of available analytic simulations on a common data base believed to be the best available at the time. The results of this competition was that the best correlation was produced by a six degree-of-freedom code developed by Nielsen Engineering and Research (NEAR) ⁽⁷⁾. A later correlation partially extended this effort to include an early panel technique ⁽⁸⁾. Unfortunately this work concentrated more on the correlation of the basic aircraft flow field than the loading on a store. Thus, the ability of the panel method to include more geometric detail and all the interference loading was not exercised. Comparisons of NEAR results with extensive wind tunnel and flight results ⁽⁹⁾ have shown weaknesses which, in many cases, may be due to some of the simplifications made in this code.

A large amount of experimental data on this field, particularly with the wind tunnel, was being taken at about the time this program plan was being put into effect, and a significant block of the data being taken was oriented toward this program. The outstanding work by Dix ^(10,11) has shown the sensitivity of the interference loading to a wide variety of test parameters. It would appear that the true geometric representation of the configuration is a critical factor. Even under the best of conditions, however, the wind tunnel is not an absolute predictor of hazardous trajectories ⁽¹²⁾. Unfortunately, a large quantity of wind tunnel data is not taken under the best of conditions.

Figure 1 (13) is an example of such data in which wind tunnel loading taken on a sweep of the sting in one direction differs significantly from the loading taken on a sweep in the opposite direction. It is not clear if most or

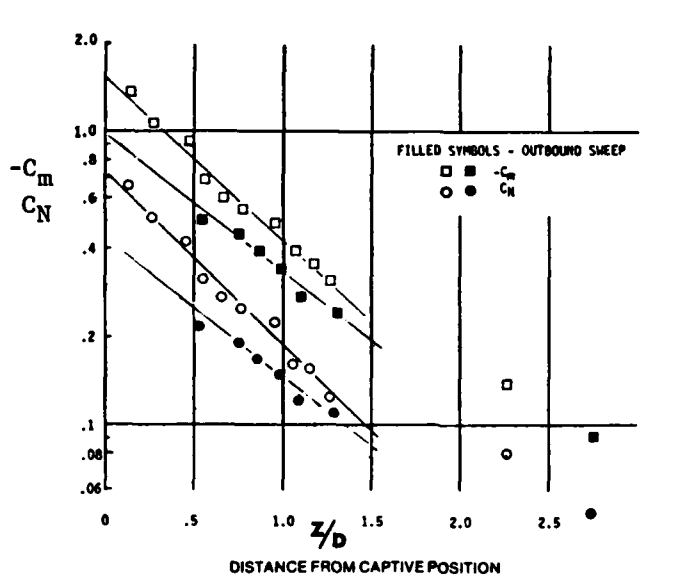


Figure 1 Store Interference Loading by a Moving Sting

all of this anomaly is due to mechanical sloppiness of the system or a result of a flow phenomenon, but such data is generally unacceptable.

The Store Separation Program Plan was a wide ranging effort encompassing a number of separate but related studies. The resulting conclusions covered a number of areas. Correlation efforts should be extended into the transonic and supersonic regimes and to other families of configurations. The theoretical efforts should be improved in certain areas, and more advanced approaches of computational aerodynamics should be explored for their usefulness on this problem. Transonic flow should receive more emphasis. Reliable full scale data should be taken on other configurations and/or mountings. This lack of good base data has been reaffirmed recently by Covert (14).

Related Developments on the National Scene

The complexity of the store carriage/separation problem has prompted a number of analytical methods to be developed. Prior to the development of the NEAR subsonic model, which makes an estimate of the mutual interference between a store and the wing, there were a number of other techniques more simplified in approach. Most of these approaches seem to have been discarded. After the NEAR approach became widely known, another of a similar approach was developed by Martin ⁽¹⁵⁾, but it is not clear if this method is in a complete form.

More recently the large scale panel techniques have been brought to bear on this problem ⁽¹⁶⁾. These are certainly able to account for all the mutual interference and even provide good results in supersonic flow. The supersonic results, however, may not be general. As expected, the costs of such added capability are high with a complex configuration and multiple stores taking of the order of one-half hour on a fast computer. Costs of this level have been considered too high by many organizations, especially when viscous effects are still excluded and the transonic range has not been covered. This has led investigators in this field to continue the search for methods more effective than the NEAR approach and less expensive than the large scale panel methods for operational analysis of store loads and trajectories.

In this country, the emphasis on alternate methods has been heavily weighted toward wide use of experimental data either directly or in some semi-empirical form. The organization of large data collections into data banks based on some form of similarity has always had a wide appeal, but this approach has no serious proponents for detailed specific trajectory analysis.

Perhaps, as a result of this emphasis on the empirical approach, a large

number of organizations in recent years have devoted a substantial effort to devise cost effective wind tunnel systems. The result has been a number of good systems coupling hardware and computer systems together which can quickly generate large quantities of specific trajectory information. Application of this specific information to full scale operations, however, has been made rather awkward by the difficulty in generalizing the data. A number of years ago Bamber (17) recognized this, and somewhat recently Spahr, Everett and Kryvoruka (18) tried out a procedure to accomplish such a generalization with some beneficial results. It would appear that a great deal of benefit would come from continued work along this line, especially if empirical approaches are to continue on a grand scale, but little has become known.

Perhaps the most widespread approach to the analysis of store loading and release is known as the "flow angularity" method (19) but often referred to now as a "grid" method. This is not to be confused with the wind tunnel technique known as the grid method in which loads on a store are taken as the store is positioned in a grid in the aircraft flow field. The result is a set of aerodynamic coefficients for the store, including all the mutual interference effects, as a function of a position in a regular array enclosing the expected trajectory. The trajectory can then be determined for any given initial condition.

In the flow angularity method, the flow field in the vicinity of the aircraft can be determined by experimental or analytical means, and by a separate operation the store loads are determined usually by examining the store section-by-section with a combination of free stream and non-uniform flow fields. Wind tunnel flow surveys are the most frequent flow field source in this country. This approach has found widespread use as part of other approaches such as by Fernandes (20), and its origin extends so far back in the literature that the source is anonymous.

This general acceptance, with good results in many cases, has come despite the fact that the interference effects generated in this manner are incomplete. The approach is fundamentally invalid in that it considers only an influence of the non-uniform stream on the store and not any mutual interference. It has certain advantages, however, such as being equally applicable at all Mach numbers for which the flow field of the basic aircraft can be defined including transonic flows. With this method, the store loading is forced to become a known function of the free stream as the store moves away from the aircraft. This frequently does not occur in other analytical approaches such as that of NEAR, and this point has been a troublesome point with some investigators.

Probably the most significant development on the national scene is the very large effort, apparently with some success, on transonic flow. In the past, the only approaches with any measure of success were those which simply pushed subsonic techniques to slightly higher Mach numbers such as Nielsen (21) or perhaps by a similar approach from the supersonic side. Stahara (22) has been developing an analysis with the transonic equivalency rule. Analysis of wing-body combinations have become common by this and by other techniques such as Yu (23) with good results in many cases. More recently, Rubbert (24) has indicated a marked increase in the capability of generating the flow field around a wing-body-pylon-nacelle combination at transonic Mach numbers. These procedures use finite differencing techniques and large scientifically oriented computing machinery; thus the computing power is a factor.

Related Developments on the International Scene

The approach to the store carriage/release problem taken by other nations is just as varied as within this country. The one general difference, however, is a seemingly greater dependence on analytical development.

In the United Kingdom, the NEAR approach is favored, and Pugh ⁽²⁵⁾ reports some extensions made in it along with reasonably good correlations. From the published reports generally available, it would appear that the United Kingdom is the only country with a coordinated effort on the overall problem of integrating stores with an aircraft. Peckham ⁽²⁶⁾ has given a summary of a number of related problems, and Haines ⁽²⁷⁾ has continued his work primarily on the drag effects.

Elsewhere Deslandes ⁽²⁸⁾, in Germany, indicates a preference for the flow angularity method except that the basic aircraft flow field is not determined experimentally. Panel methods are employed for this purpose. Available literature from French sources ⁽²⁹⁾ show an involvement with finite difference techniques as applied to transonic flow and wing-body interference effects.

One intriguing approach to the store loading problem is reported by van den Brock ⁽³⁰⁾ in which panel methods are used for the complete problem. The interesting aspect is that through a number of simplifications the effort required is said to approach that of the NEAR method. From time to time, there have been suggestions of ways the panel methods could be more economically applied to this problem, but no known literature exists of such an adaptation. Too little information exists in this reference to see which short cut may have been employed or to make a truly valid comparison.

CONCLUSIONS

Store carriage/release is a most complex problem in which a truly complete analysis is still not yet available even at great cost. As one might expect, the various approaches taken to simplify or approximate parts of the problem, particularly in the analysis of the loads, have led to disagreements on which best satisfy the needs.

It would appear, from the quantity of literature available, that the effort devoted to store carriage and release in this country has diminished over the past few years. As a result, the conclusions made as part of the Store Separation Program Plan conducted at the Naval Weapons Center a few years ago are still generally valid. Correlations between methods and experimental data should be continued to further explore the validity of techniques to avoid surprises after an analysis of a situation indicates no problem. Further requirements must also be defined. Closely related to this effort is the need for a more reliable experimental data base for such correlation to be meaningful.

Available literature suggests that European agencies make more use of purely analytical techniques than agencies in this country where a reliance on empirical data is widespread. This is occurring despite the fact that most of the analytical methods in use for air loads have been developed in this country where this science is progressing at a rapid rate. Application of these new techniques to the store load/release problem has not been aggressively pursued. Much more of this work, especially transonic, needs to be examined for its validity to this problem.

REFERENCES

1. "A Summary of NASA Data Relative to External-Store Separation Characteristics", Linwood W. McKenney and Edward C. Polhamus, NASA TN D-3582, November 1966
2. "Determination of Captive Loads and Separation Trajectories of Airborne Stores", Dale E. Knutsen, NWC TP 4328, Naval Weapons Center, June 1968
3. "Store Separation", L. H. Schindel, AGARDograph No. 202, June 1975
4. "Drag and Other Aerodynamic Effects of External Stores", Edited by Charles B. Mathews, Chapters 4 and 5, AGARD Manual AR-107, November 1977
5. "A Store Separation Program Plan", A. R. Maddox and R. L. Meeker, Aircraft/Stores Compatibility Symposium Proceedings, JTCC/ALNNO WP-12-2, Dayton, Ohio, December 1971
6. "The Problem of Separating Stores from Aircraft", Arthur R. Maddox, NWC Tech. Memorandum 3938, July 1979, Naval Weapons Center
7. "Extension of the Method for Predicting Six-Degree-of-Freedom Store Separation at Speeds up to the Critical Speed to Include a Fuselage with Non-Circular Cross Section", F. K. Goodwin, M. F. E. Dillenius and J. N. Nielsen, Nielsen Engineering and Research Inc. Report, Vol I and II, November 1974 (see also AFFDL-TR-74-130)
8. "A Comparison between the Nielsen and Woodward Programs in Predicting Flow Fields and Store Loads", R. M. Rogers, TM 2854, Naval Weapons Center, July 1976
9. "In-Flight Captive Store Loads Compared with Wind-Tunnel and Mathematical Simulations", A. R. Maddox, R. E. Dix and G. R. Mattasits, AIAA Journal of Aircraft, May 1979
10. "Simulation of Sway Braces and Mounting Gaps on Small Scale Models for Wind Tunnel Tests", R. E. Dix, Proceedings of Fourth JTCC Aircraft/Stores Compatibility Symposium, October 1977
11. "Influences of Sway Braces and Mounting Gaps on the Static Aerodynamic Loading of External Stores", R. E. Dix, AEDC-TR-77-117, Arnold Engineering Development Center, February 1978
12. "Store Separation Trajectory Analysis", A. R. Maddox, AIAA Journal of Aircraft, November 1980
13. "Store Separation - State of the Art Review", G. F. Cooper, A. R. Maddox, J. R. Marshall and E. F. McCabe, Proceedings of the Tenth Navy Symposium on Aeroballistics, July 1975
14. Paper on Store Loading, E. E. Covert, AIAA Journal of Aircraft, to be published.

15. "Drag and Other Aerodynamic Effects of External Stores", AGARD Report AR-107, Contributions by R. Deslandes, R. A. Grow, B. Hunt, F. W. Martin and J. N. Nielsen edited by C. B. Mathews, November 1977
16. "PAN AIR Applications to Weapons Carriage and Separation", A. Cenko, E. N. Tinoco, R. D. Dyer and J. DeJongh, Paper no. 80-0187, AIAA 18th Aerospace Sciences Meeting, January 1980
17. "Two Methods of Obtaining Aircraft Store Trajectories from Wind Tunnel Investigations", M. J. Bamber, David Taylor Model Basin AERO Report 970, January 1960
18. "A Multifaceted Store Separation Analysis", H. R. Spahr, R. H. Everett and J. K. Kryvoruka, AIAA 9th Aerodynamic Testing Conference, June 1976
19. "Use of the Flow Angularity Technique for Predicting Store Separation Trajectories", S. C Korn, AFATL-TR-71-140, October 1971
20. "Theoretical Prediction of Interference Loading on Aircraft Stores", F. D. Fernandes, NASA CR-112065-1, -2, -3, June 1972
21. "Predictions of Forces and Moments on External Stores at Transonic Speeds", J. N. Nielsen, NEAR Paper No. 41, April 1976
22. "Study of Transonic Flow Fields about Aircraft: Application to External Stores", S. S. Stahara, AGARD Conference Proceedings No. 285 on Subsonic/Transonic Configuration Aerodynamics, May 1980
23. "Grid Generation and Transonic Flow Calculations for Three-Dimensional Configurations", N. J. Yu, Paper Number AIAA-80-1391, AIAA 13th Fluid and Plasma Dynamics Conference, July 1980
24. Informal notes and personal communication with Dr. P. E. Rubbert of the Boeing Airplane Co., April 1981
25. "The Use and Validation of Ground-Based Techniques for the Prediction of the Trajectories of Stores Released from Aircraft at Subsonic Speeds", P. G. Pugh and J. W. Peto, Royal Aircraft Establishment Tech Memo Aero 1862, August 1980
26. "Aerodynamic Interactions of Stores and Airframes", D. H. Peckham, Royal Aircraft Establishment, AERO TM 1728, September 1977
27. "Prospects for Exploiting Favourable and Minimising Adverse Aerodynamic Interference in External Store Installations", A. B. Haines, Aircraft Research Association, Memo No. 222, April 1980
28. "Evaluation of Aircraft Interference Effects on External Stores at Subsonic and Transonic Speeds", R. Deslandes, AGARD Conference Proceedings No. 285, Subsonic/Transonic Configuration Aerodynamics, May 1980
29. "Etude par La Method des Elements Finis des Interactions Voilure-Fuselage-Nacelle D'un Avion du Type Falcon a Mach = 0,79", G. Heckmann, AGARD Conference Proceedings No. 285, Subsonic/Transonic Configuration Aerodynamics, May 1980

30. "The Analytical Prediction of the Separation Behaviour of External Stores after Release from the Carrier Aircraft Part II - Applications", G. J. van den Broek, NIAST 79/103, Council for Scientific and Industrial Research, Pretoria, South Africa, August 1979

STUDY OF FLOW FIELDS AND STORE FORCES IN CLOSE PROXIMITY TO A
TRIPLE EJECTION RACK AT TRANSONIC SPEEDS

Frederick K. Goodwin and Jack N. Nielsen
Nielsen Engineering & Research, Inc., Mountain View, California

ABSTRACT

The information presented in this paper shows what parent aircraft effects are important when determining the forces and moments acting on a store in close proximity to a triple ejection rack. The large gradients in the store forces and moments which exist near the carriage position are demonstrated. Areas are shown in which improvements to the AFFDL/Nielsen subsonic store separation computer program are required if the launch dynamics of a store released from such a configuration are to be accurately predicted.

INTRODUCTION

Recently the AFFDL/Nielsen subsonic store separation program¹ has been used to make predictions for comparisons with flight and wind-tunnel captive store loads on a MK-83 bomb on an F-4C aircraft. The bomb was mounted on the bottom station of a triple ejection rack (TER) with dummy bombs mounted on the two shoulder stations. The comparisons are presented in Reference 2 and indicate that deficiencies may exist in the TER model in the computer program. The work of Maddox, Dix, and Mattasits² describes a carefully monitored flight test program designed to provide data to compare with wind-tunnel data and mathematical predictions.

The work described in this paper had two main objectives. The first was to provide a data base which could be used to determine where deficiencies in the computer program exist. The second objective was to attempt to identify the deficiencies by making comparisons of computer program results with the data.

The test program was conducted in the 4-Foot Transonic Wind Tunnel (4T) of the Propulsion Wind Tunnel Facility (PWT) at the Arnold Engineering Development Center (AEDC). The test program was jointly sponsored by the Naval Weapons Center (NWC) and the Air Force Wright Aeronautical Laboratories (AFWAL/FIGC).

This paper will briefly describe the test program and the types of data obtained. A discussion of the experimental results follows this. The compatibility of the captive or attached loads with the grid loads is discussed. Then phenomena exhibited by the data during the parent aircraft build-up sequence are discussed. Finally, the paper presents some comparisons between the experimental data and predictions made using the computer program of Reference 1. The test program and the experimental results are discussed in

more detail in Reference 3, the final technical report on this investigation. That report also contains more comparisons between data and predictions.

This work was supported by the Naval Weapons Center, China Lake, California, under Contract N60530-79-C-0169. The Technical Coordinator was Mr. Ray E. Smith.

NOMENCLATURE

CA	axial-force coefficient, axial force/qS
CLL	rolling-moment coefficient, rolling moment/qSD
CLM	pitching-moment coefficient, pitching moment/qSD
CLN	yawing-moment coefficient, yawing moment/qSD
CN	normal-force coefficient, normal force/qS
CY	side-force coefficient, side force/qS
D	store maximum diameter, 0.7 inch
M_∞	free-stream Mach number
q	free-stream dynamic pressure
S	store frontal area, 0.385 in ²
VY/V	local sidewash velocity divided by free-stream velocity, positive to the right when viewed from the rear
VZ/V	local upwash velocity divided by free-stream velocity, positive up when viewed from the rear
X_p	distance from tip of store nose, negative aft
Z_p, Z_s	vertical distance measured from carriage position on rack, positive down
α_s	store angle of attack relative to free stream

WIND-TUNNEL TEST PROGRAM

The purpose of the test program was to provide a systematic set of data which could be used in evaluating and improving the capability of the computer program of Reference 1 to predict the aerodynamic forces and moments acting on stores carried in a TER configuration. The capability of calculating store forces and moments with the store in the carriage position is of interest as well as the capability in the detached position. For this reason force and moment tests were performed using both bracket supported and captive trajectory system (CTS) supported force models. In order to calculate analytically the forces and moments acting on a store, the aircraft induced flow field in which the store is immersed must be predicted. Flow-field survey data were taken, using a 20° half angle conical probe, to provide information on the aircraft induced flow field.

The basic details of the five-percent (1/20th) scale model of the F-4C used in the tests are shown in Figure 1. The model is geometrically similar to the full-scale aircraft except that the part aft of the engine exhausts has been removed to minimize CTS interference. This removal does not influence the results of this test program.

Details of the F-4C pylons are shown in Figure 2. For most tests only the left-wing inboard pylon was used. All testing was done under the left wing. Pylons were not installed on the right wing for any of the tests.

The triple ejector rack (TER) used in the test program is shown in Figure 3. The TER was used in conjunction with the left-wing inboard pylon. This rack model simulates sway braces and ventilating passages.

The stores which were used are shown in Figure 4. They are models of the MK-83 bomb. Figure 4(a) shows the actual bomb shape and Figure 4(b) shows a model which was modified for CTS sting support. Models with identical body shapes but without tail fins were also used. The dummy stores used on the shoulder locations of the TER were the shape shown in Figure 4(a). Both finned and unfinned models were used. Four force models were used during the captive force and moment tests. Tests were performed with both configurations shown in Figure 4 with and without tail fins.

The Mach number range used in the test program was 0.6 to 0.95. All testing was performed at a nominal Reynolds number per foot of 3.5×10^6 . The store angle of attack was varied from -4° to 16° . Since the store is oriented on the TER one degree nose down relative to the aircraft reference waterline (aircraft angle of attack is measured relative to this line), the aircraft angle of attack varied from -3° to 17° .

Eight parent aircraft configurations were used during the test program. They are listed in Table 1. The first column lists the eight numbers. These numbers will be used in the next sections of this paper. The remaining eight columns list model components which could be attached to the parent F-4C. These components are:

P_C	fuselage centerline pylon
P_I	left-wing inboard pylon
P_O	left-wing outboard pylon
T	TER attached to left-wing inboard pylon
$(S_2)_U$	unfinned dummy store attached to outboard shoulder station on TER
$(S_3)_U$	unfinned dummy store attached to inboard shoulder station on TER
$(S_2)_F$	finned dummy store attached to outboard shoulder station on TER with fins vertical and horizontal
$(S_3)_F$	finned dummy store attached to inboard shoulder station on TER with fins vertical and horizontal

Further details of the test program including lists of the specific runs made are contained in Reference 3.

RELATIONSHIP BETWEEN ATTACHED AND GRID LOADS

A significant problem in store loads is whether a sting-supported store will yield the attached store loads (forces and moments) as it approaches the attached-store position as close as possible under practical testing conditions without making contact with the rack. In fact, the nature of the interference forces on the store for small gaps between store and rack is not well understood.

Knowledge of the loads on a store in close proximity to the attached position is not extensive, but light has been shed on this subject by the tests of Dix⁴. The tests were of MK-83 bombs on a TER rack mounted on a model of an F-4C airplane and included both attached loads and loads on a sting-supported bomb. His results are presented for $\alpha_s = 0^\circ$ and do not include parent aircraft component build-up results. His data show that the captive loads cannot be obtained by extrapolating CTS data to zero Z/D in general. For some coefficients (CLM, CA, CLN), such extrapolation was better than for others (CN, CY). Large changes occurred for Z/D < 0.2 which could not be measured with the CTS system because of limitation in accuracy of positioning the store.

In this investigation a more extensive investigation was made of the problem, and the effects of angle of attack and configuration build-up were measured. Also flow-field data in the vicinity of the attached bottom store position were taken.

Stores S_{MF}, Figure 4(b), and S_{MU}, an unfinned version of this store are the ones tested both on the attached-loads balance and the CTS sting supported balance. Data for store S_{MF} in combination with configuration 3 of Table 1 (F-4C, inboard pylon, TER) are shown in Figure 5. In Figure 5(a) the normal-force coefficient is shown versus Z_p/D for five angles of attack at M_∞ = 0.6. The sting data extend down to Z_p/D = .07. There is a large change in CN in the range 0 < Z_p/D < .07 as indicated by the attached-store data which cannot be reproduced by extrapolating the sting results to zero gap. This range of Z_p/D representing only 0.05 in. model scale, 1.0 in full scale, produces surprisingly large interference forces which increase with angle of attack.

Examination of the other parts of Figure 5 for the other coefficients shows that extrapolation of the sting data to Z_p = 0 is fairly accurate. The question naturally arises whether the attached loads are accurately measured. It is our belief based on the overall consistency of the data as well as the results of Dix that the attached loads are valid.

These results are typical of those obtained for store S_{MU} and for other parent aircraft configurations.

EFFECT OF CONFIGURATION ON ATTACHED LOADS

Attached store loads (forces and moments) were measured for configurations 3, 4, 5, 6, and 8 of Table 1. The variations of loads for store S_{AF}, Figure 4(a), at M_∞ = 0.6 with angle of attack are shown in Figure 6 for the above five configurations. Figure 6(a) shows that at angles of attack between -4° and +8°, configuration 3 yields the least normal force (positive upward). Configurations 4 and 8, which only have one shoulder store, yield more normal force; and configurations 5 and 6, with two shoulder stores, yield the largest normal forces. What is of particular interest is that the addition of fins to the shoulder stores (4 vs 8 and 5 vs 6) has a small effect on normal force. Also at angles of attack above 8°, the effects of configuration differences are much less than at lower angles of attack.

The side-force variation with α_s shown in Figure 6(b) shows that the side force is relatively insensitive to configuration especially for angles of attack less than 8°. Positive side force is directed towards the fuselage from the left-wing inboard pylon.

Pitching-moment coefficients shown in Figure 6(c) are generally nose down. For angles of attack less than about 6° , the effect of configuration on the magnitude of the pitching-moment coefficient is similar to its effect on normal force. However in the range above 6° to 8° , configurations 5 and 6 have smaller pitching moments than configurations 4 and 8. Again adding fins to the shoulder stores causes negligible effect.

The yawing-moment coefficients in Figure 6(d) are slightly nonlinear with α_s from -4° to 16° and are positive. There are significant differences due to configuration changes, but the addition of fins to the shoulder store has a negligible effect.

The rolling-moment coefficients in Figure 6(e) are positive, nonlinear, and have maxima around 6° to 8° . The configuration effects are significant. The addition of the fins to the shoulder stores causes a significant effect in the higher angle range.

The same kind of data as Figure 6 for other Mach numbers show the same general qualitative effects.

EFFECT OF CONFIGURATION ON GRID LOADS

The grid loads on the bottom store as it moves downward from close proximity to the rack are influenced by angle of attack, configuration, Mach number, addition of fins to the shoulder stores, and the number of shoulder stores. Figure 7 shows the loads on store S_{MF} at $M_\infty = 0.6$ as influenced by configuration and store vertical position. Only the first 1.25 diameter of store vertical position are shown.

Examination of the normal-force results shows the least normal force for configuration 2 with a small positive increment due to addition of the TER. Addition of one shoulder store contributes positive increments about twice those due to the TER. Addition of the other shoulder store adds an even larger positive increment to the normal force. Addition of the fins to the shoulder stores adds further small positive increments in normal force. It is concluded that the addition of the shoulder stores are most important, followed by the addition of the TER, and finally the addition of the fins to the shoulder stores.

The side-force results in Figure 7(b) show that the largest effects of configuration occur at small Z_p/D . The effect of adding the second shoulder store is to almost cancel the increment due to adding the first. The effect of adding fins to the shoulder stores is again fairly small.

The pitching-moment results show the same qualitative effects as the normal-force results. The yawing-moment results show large configuration effects at small Z_p/D (on an expanded scale) and small effects at large Z_p/D . The store alone has a rolling-moment coefficient of .037 at $\alpha_s = 0^\circ$ because of fin cant. Additional rolling moments of about the same magnitude can be developed at small Z_p/D because of configurational differences. At these small values of Z_p/D , increments in CLL as large as 0.01 can be developed by the addition of fins to the shoulder stores.

COMPARISON BETWEEN EXPERIMENT AND THEORY

The basic objective of the experimental investigation was to provide data for validating the computer program of Reference 1 and to provide insight into methods for upgrading the computer program. Accordingly the comparisons between theory and experiment are directed toward these ends. In order to make sure comparisons meaningful, it is of interest to describe the main assumptions that are made in the computer program especially with respect to pylon, rack, and stores and to suggest areas where refinements in the computer program may appear necessary.

The computer program for calculating the parent aircraft flow field is based on linear theory, Laplace's equation for the flow field with the Glauert-Prandtl theory to account for compressibility. The fuselage, which can be non-circular, is modeled by using sources, doublets, and high-order solutions along the axis of the fuselage to satisfy its boundary conditions, with a vortex-lattice layout on the wing to satisfy the wing boundary conditions. The vortex-lattice system is imaged in the fuselage (assumed circular). Wing thickness is modeled by source panels. Account is taken of airflow through inlets and ducts by changing the effective cross-sectional area distribution of the body.

The pylon is modeled with regard to thickness by source panels and with regard to the normal velocity boundary condition by a vortex-lattice layout.

The rack is modeled for volume by a body of revolution.

The stores are modeled for volume by three-dimensional source distributions along their axes. No mutual interference between stores or between stores and rack is accounted for. No doublets to model store angle of attack distributions are included. The tail fins of the shoulder stores are not modeled.

The forces and moments acting on the ejected store are calculated by slender-body theory. Both upwash and sidewash distributions are taken into account. Also a loading due to buoyancy is included in the calculation. If the flow separates at some axial station, crossflow drag theory is used to calculate the loading downstream of separation. The tail fin contributions are determined using the spanwise variation of induced downwash across the tail span together with reverse-flow theorems in a method which has accuracy nearly equivalent to full linear theory.

In the ensuing comparisons, the effects of adding the pylon to the clean airplane, the effect of adding the rack to the pylon, and the effect of adding the shoulder stores to the rack will be isolated and compared with theory. These increments are all to be added to the clean airplane characteristics as a base configuration. It is therefore of interest to examine the comparison between experiment and theory for the clean airplane.

In Figure 8 the downwash and sidewash angles are shown along the $Z_p/D = 0$ location for $M_\infty = 0.6$ for various angles of attack. The store nose location is $X_p = 0$. It is noted that the experimental upwash angle is predicted fairly well up to about 8° angle of attack although it is consistently less than theory. Significantly large deviations between experiment and theory occur by the time $\alpha_s = 16^\circ$ is reached. The sidewash is predicted well up to $\alpha_s = 8^\circ$.

In Figure 9, the loads on store S_{MF} in combination with the clean airplane at $Z_p/D = 0$ are shown for the angle of attack range from 0° to 16° and compared with the predictions of the computer program. The normal force is predicted well up to about 8° , and is about half of its free-stream value for the same angle of attack. The side force is predicted well up to about 12° . The pitching moments and yawing moments are not well predicted, but they are generally less than those for the store in the free stream. The center-of-pressure position for yawing moment is in error by as much as 0.5 diameters. In the theory, the separation position on the boattail corresponding to α_s has been used. The results of Figure 8 show that the average angle of attack on the boattail is much less than α_s . Accordingly separation occurs more aft than predicted. This yields more download on the boattail and more nose-up moment.

The effects on the flow field of adding the pylon to the airplane can be determined by subtracting data for configuration 1 from that for configuration 2. In this way the effects of the pylon can be examined unmasked by configuration 1 effects. The next two figures show the pylon effects on upwash and sidewash at $M_\infty = 0.6$ for the following conditions:

<u>Figure</u>	<u>α_s</u>	<u>Z_p/D</u>
10	0	0
11	4°	0

It is clear that the pylon effect on the flow field is small and accurately predicted for the conditions shown.

It would be normally assumed that if the flow angles induced by the pylon at the store location are small, that the corresponding loads induced by the pylon on the store would be small. As an example, consider Table 2 which shows the loads on the S_{MF} store for four cases due to the addition of the pylon. Generally speaking the difference between experiment and theory is not large so that the loads were satisfactorily predicted.

The effects on the flow field of adding the rack to the airplane pylon combination are shown in Figures 12 and 13. These results for both data and theory represent configuration 3 minus configuration 2. The first thing that is clear is that the induced angles of upwash and sidewash are generally several times larger than those due to the pylon at $Z_p/D = 0$. It is also apparent that the effect of the rack attenuates much in going from $Z_p/D = 0$ to $Z_p/D = 1.0$. For instance, the induced upwash maxima fall from about -0.04 to about -0.01 in this distance. It happens that the $Z_p/D = 0$ position is about one diameter below the centerline of the rack and the $Z_p/D = 1.0$ position is about two diameters below the rack centerline. This suggests that the upwash is strongly source dominated. The effect of the rack is modeled solely by sources in the theory. However, the theoretical source effect is too weak, particularly at $Z_p/D = 0$.

Looking at the sidewash angle, the maximum sidewash exists at $Z_p/D = 0$ and attenuates greatly at $Z_p/D = 1$. The theory predicts no sidewash since the rack sources produce none directly below themselves. It is clear that

mechanisms to produce sidewash due to addition of the rack must be introduced into the computer program.

It is not to be expected that the loads on store S_{MF} due to addition of the rack to the pylon will be predicted well for $Z_p/D = 0$ since the upwash and sidewash are significant at this location, and the theory underpredicts them. It is of interest to examine the load increments due to the rack in a similar form to that for the pylons.

Examination of Table 3 immediately shows that the computer program gives no contribution to CY, CLN, and CLL due to addition of the rack. This shortcoming of the method is more important at $\alpha_s = 4^\circ$ than $\alpha_s = 0^\circ$ since the sidewash is greater at $\alpha_s = 4^\circ$. An error of about 0.2 in side-force coefficient occurs and about 0.045 in yawing-moment coefficient. There is a surprising effect on rolling-moment at $\alpha_s = 4^\circ$ and $Z_p/D = 0$, the value of CLL for configuration 3 being 0.064 and for configuration 2 being 0.025. There is a sidewash gradient between the top and bottom fins of the X arrangement which is, if anything, weaker at $Z_p/D = 0$ than at $Z_p/D = 1.0$. Since the effect does not occur at $Z_p/D = 1.0$, some other phenomenon must be producing this difference which is equivalent to about 2° of cant of all fins. The phenomenon is believed due to a trailing vortex from the rack pylon.

The effect of adding the shoulder stores will be determined by taking the difference between the results for configuration 5 and configuration 3. Any effects of the fins of the shoulder stores will not be included by this means. Also, the theory does not include the effect of shoulder store fins, and these have been shown to be small.

Figures 14 and 15 show the effects on the upwash and sidewash angles along the store axis position for $\alpha_s = 0^\circ$ and two vertical positions at $M_\infty = 0.6$. Both experiment and theory are shown. The upwash angles get to be nearly as large as -5° , while the sidewash is generally much less than 1° . The theory in some cases predicts the upwash well, but more often underpredicts it. The degree of agreement is surprising in view of the fact that only the volume effect of the two stores are modeled with no interference between them. Thus the theoretical VZ/V increment due to the shoulder stores at a fixed value of Z_p/D does not vary with α_s . The theoretical sidewash increment, VY/V , is small.

At $Z_p/D = 0$ some sidewash exists but at $Z_p/D = 1$ it is negligible for $\alpha_s = 0^\circ$. The rapid decay of this sidewash suggests that some dipole distribution is causing it. The two shoulder stores are subject to sidewashes which are not equal. Dipoles to cancel these sidewash boundary conditions will produce differential sidewash under the rack. This represents a possible source of the sidewash. Likewise doublets to cancel the downwash distribution along the shoulder stores would modify the upwash and could account in part for the differences between experiment and theory. Some account of mutual interference between shoulder stores and rack-ylon may be required to get accurate flow fields. The shoulder stores can change the rack-ylon lifting surface boundary condition, the pylon can influence the boundary conditions of the shoulder stores, and the shoulder stores can interfere with each other. These interferences can be evaluated to see which are of sufficient magnitude to influence the flow field.

It is of interest to see the magnitude of the loads on the bottom store induced by the shoulder stores. Table 4 presents the results for two angles of attack and two vertical positions. The table shows that the addition of shoulder stores has its maximum effects on CN and CLM, and has generally small effects on CY, CLN, and CLL. This result is in general accordance with the flow-field comparisons. It is noted that the changes in CN and CLM are better predicted at $Z_p/D = 1.0$ than at $Z_p/D = 0$, a fact also in agreement with the flow-field results. Some error at $Z_p/D = 0$ is due to prediction of the flow field. But even with an accurate flow-field prediction, some errors in loads will be predicted at this position. It is probable that mutual interference between all three stores, at least for volume effects, will influence the loads.

CONCLUSIONS

ATTACHED VERSUS GRID LOADS

1. The forces and moments on a store in close proximity to a TER can exhibit large changes within the first few tenths of a store diameter from the attached position.
2. It is not generally feasible using present measuring methods to extrapolate loads measured on a CTS supported model to those for the attached position.

ATTACHED LOADS

1. Adding the shoulder stores to the rack had the following effects on the attached loads of store S_{AF} at $M_\infty = 0.6$.
 - (a) The normal forces received a large positive increment due to addition to the rack of the outboard shoulder store in the low angle of attack range, and further increments of comparable magnitude by subsequent addition of inboard shoulder store. At high angles of attack, $\alpha_s > 10^\circ$, the increments became much smaller.
 - (b) The changes in side-force coefficient were small.
 - (c) There were definite changes in the pitching-moment coefficient, but these were greater than those in yawing-moment coefficient.
 - (d) Rolling-moment coefficient exhibited significant changes.

2. Adding fins to the shoulder stores under the conditions of (1) generally causes small changes in the store loads except at large angles of attack.

GRID LOADS

1. At $M_\infty = 0.6$ and at $\alpha_s = 0^\circ$ with store S_{MF} within 1 store diameter of the rack the most important things influencing the bottom store loads are in

decreasing order of importance:

- (a) Addition of shoulder stores to TER.
- (b) Addition of TER to pylon.
- (c) Addition of fins to the shoulder stores.

Changing the angle of attack to 8° does not change the foregoing conclusion.

2. The addition of fins to the shoulder stores for the ranges of M_∞ and α_s of the tests has a generally small effect, and the effect is largest at small values of Z_p/D .

COMPARISON BETWEEN EXPERIMENT AND THEORY

1. For the clean airplane, the upwash and sidewash angles near the store location at the inboard pylon are predicted adequately for preliminary design purposes to $\alpha_s = 8^\circ$ but not up to $\alpha_s = 16^\circ$.

2. For store S_{MF} in combination with the clean airplane near the attached inboard position, the normal force, side force, and rolling moment are well predicted by the computer program up to $\alpha_s = 8^\circ$. However, the pitching moment and yawing moment are not predicted well probably as a result of movement of the separation position on the boattail afterbody due to the nonuniform flow field and its resulting effects on afterbody and tail normal forces.

3. Adding the pylon to the clean airplane produced downwash and sidewash changes near the location of the attached store on the inboard pylon which were usually less than 0.5° and which were accurately predicted by the computer program.

4. The loads on store S_{MF} at $Z_p/D = 0$ and 1 due to the addition of the pylon were predicted satisfactorily. In magnitude they correspond in some cases to a change in angle of attack of the store in the free stream of 1° to 2° .

5. Adding the TER to the airplane-pylon combination caused changes in downwash angle and sidewash angle at the attached store position. They are several times greater than those due to the addition of the pylon, and the theory generally underpredicts these changes. In fact the theory predicts no sidewash changes since the rack is modeled by a body of revolutions with volume only (sources and sinks).

6. Generally the computer program predicts zero yawing-moment, side-force, and rolling-moment contributions due to addition of the rack since no sidewash is predicted. The normal-force and pitching-moment increments are fairly well predicted.

7. The upwash distribution due to adding the shoulder stores to the rack is predicted fairly well at $Z_p/D = 1.0$ but is underestimated at $Z_p/D = 0$. The use of doublets to cancel the upwash acting on the shoulder stores could be one source of upwash not included in the theory. Another source could be mutual interference between shoulder stores and rack pylon.

REFERENCES

1. Goodwin, F. K. and Dillenius, M. F. E.: Extension of the Method for Predicting Six-Degree-of-Freedom Store Separation Trajectories at Speeds Up to the Critical Speed to Include a Fuselage with Noncircular Cross Section. Vol. II - Users Manual for the Computer Program. AFFDL-TR-74-130, Vol. II, November 1974.
2. Maddox, A. R., Dix, R. E. and Mattasits, G. R.: In-Flight Measurements of Captive Loads on a Store as Compared with Wind Tunnel and Mathematical Simulation. NWC TP 6026, April 1978.
3. Goodwin, F. K. and Nielsen, J. N.: Experimental and Theoretical Study of Flow Fields and Store Forces in Close Proximity to a Triple Ejection Rack at Transonic Speeds. NWC TP 6210, June 1980.
4. Dix, R. E.: Comparison of Two Methods Used to Measure Aerodynamic Loads Acting on Captive Store Models in Wind-Tunnel Tests. AEDC-TR-76-122, September 1976.

Table 1. Parent Aircraft Configurations.

CONFIG. NO.*	P _E	P _I	P _O	T	(S ₂) _U	(S ₃) _U	(S ₂) _F	(S ₃) _F
1								
2		X						
3		X		X				
4		X		X	X			
5		X		X	X	X		
6		X		X			X	X
7	X	X	X	X			X	X
8		X		X			X	

* Configuration composed of basic F-4C model with addition of components indicated in line across table.

Table 2. Loads Due to Pylon.

$$S_{MF}; M_{\infty} = 0.6$$

(a) $\alpha_s = 0^\circ$ $Z_p/D = 0$

	Z_p/D	ΔCN	ΔCY	ΔCLM	ΔCLN	ΔCLL
Data	0.07	0.063	-.019	-.206	0.028	0.002
Theory	0	.031	-.010	-.145	.001	0

(b) $\alpha_s = 0^\circ$ $Z_p/D = 1.0$

Data	1.20	0.030	-.008	-.100	0.012	0.001
Theory	1.00	.016	-.004	-.077	.001	0

(c) $\alpha_s = 4^\circ$ $Z_p/D = 0$

Data	0.10	0.069	-.061	-.220	0.071	0
Theory	0	.028	-.048	-.138	.051	0.001

(d) $\alpha_s = 4^\circ$ $Z_p/D = 1.0$

Data	1.24	0.031	-.024	-.096	0.031	-.003
Theory	1.00	.020	-.022	-.072	.029	0

AD-A111 763

NAVY AEROBALLISTICS ADVISORY COMMITTEE
PROCEEDINGS OF THE NAVY SYMPOSIUM ON AEROBALLISTICS (12TH) HELD--ETC(U)
MAY 81

F/G 20/4

UNCLASSIFIED

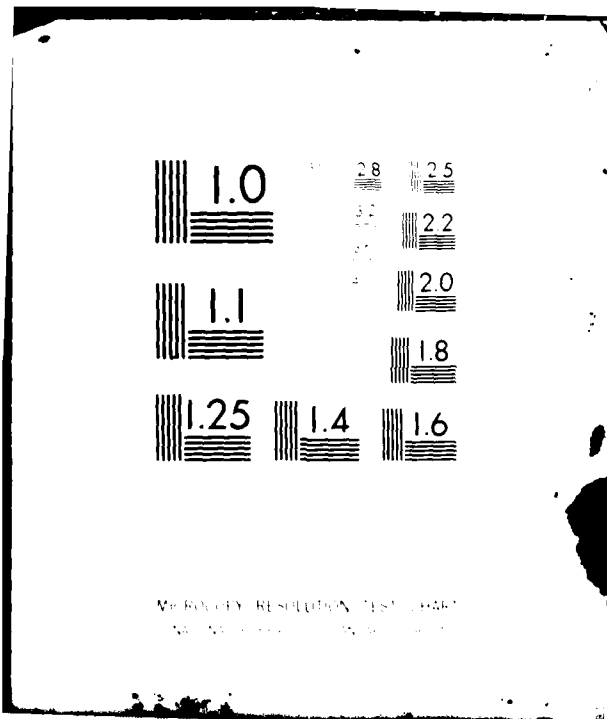
NL

4 of 5

AD-A

111 763





METRIC RESOLUTION TEST CHART
NBS 1963-A

Table 3. Loads Due to Rack.

$$S_{MF}; M_{\infty} = 0.6$$

(a) $\alpha_s = 0^\circ$ $Z_p/D = 0$

	Z_p/D	ΔCN	ΔCY	ΔCLM	ΔCLN	ΔCLL
Data	0.07	0.116	-.059	-.222	-.003	0.007
Theory	0	.051	.001	-.035	-.002	0

(b) $\alpha_s = 0^\circ$ $Z_p/D = 1.0$

Data	1.21	0.037	-.015	-.086	0.045	0.001
Theory	1.00	.024	.001	-.027	-.001	0

(c) $\alpha_s = 4^\circ$ $Z_p/D = 0$

Data	0.07	0.042	-.196	0	-.034	+.039
Theory	0	.050	+.001	0.031	-.001	0

(d) $\alpha_s = 4^\circ$ $Z_p/D = 1.0$

Data	1.23	0.019	-.043	-.063	0.040	0
Theory	1.00	.024	0	-.024	0	0

Table 4. Loads Due to Shoulder Stores.

$$S_{MF}; M_{\infty} = 0.6$$

(a) $\alpha_s = 0^\circ$ $Z_p/D = 0$

	Z_p/D	CN	CY	CLM	CLN	CLL
Data	0.07	0.456	-.018	-1.049	-.049	0.006
Theory	0	.334	.008	-.605	-0.012	0

(b) $\alpha_s = 0^\circ$ $Z_p/D = 1.0$

Data	1.2	0.201	-.008	-.452	-.021	0.003
Theory	1.0	.190	.003	-.380	-.010	0

(c) $\alpha_s = 4^\circ$ $Z_p/D = 0$

Data	0.07	0.237	-.063	-.955	-.022	0.208
Theory	0	.320	.006	-.551	-.008	-.005

(d) $\alpha_s = 4^\circ$ $Z_p/D = 1.0$

Data	1.23	0.130	0	-.389	-.070	0.013
Theory	1.0	.181	0.005	-.385	-.007	0

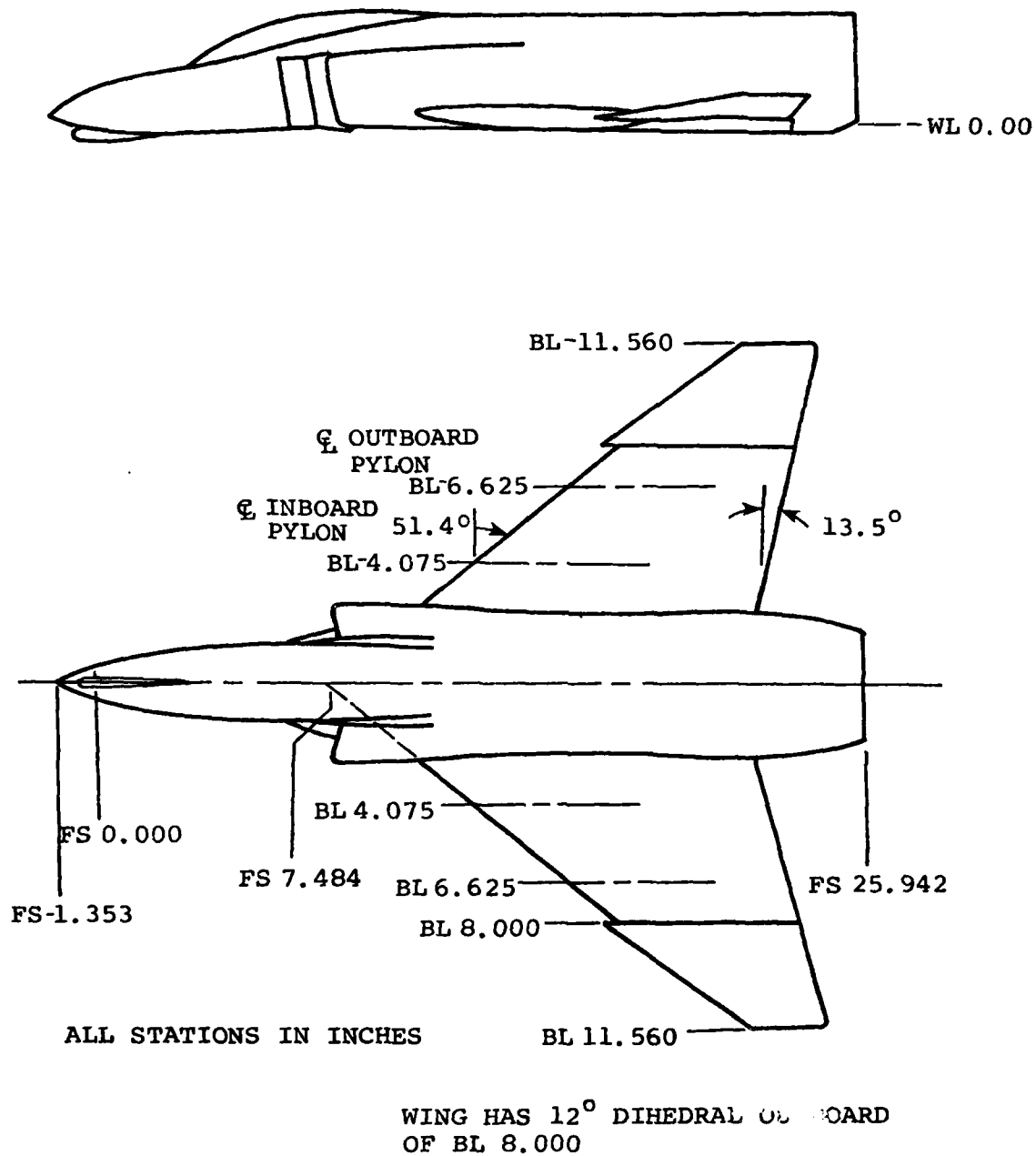
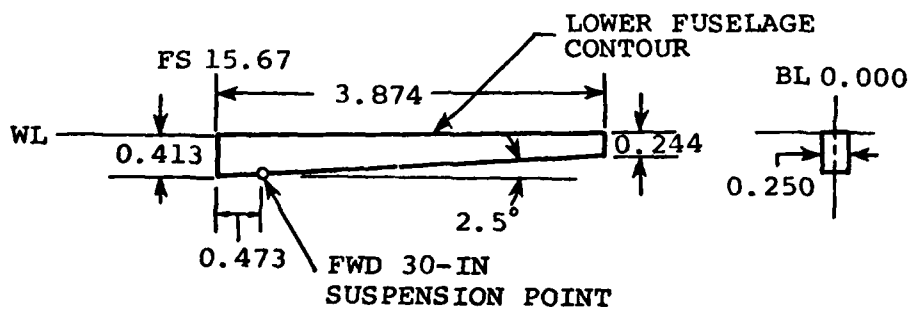
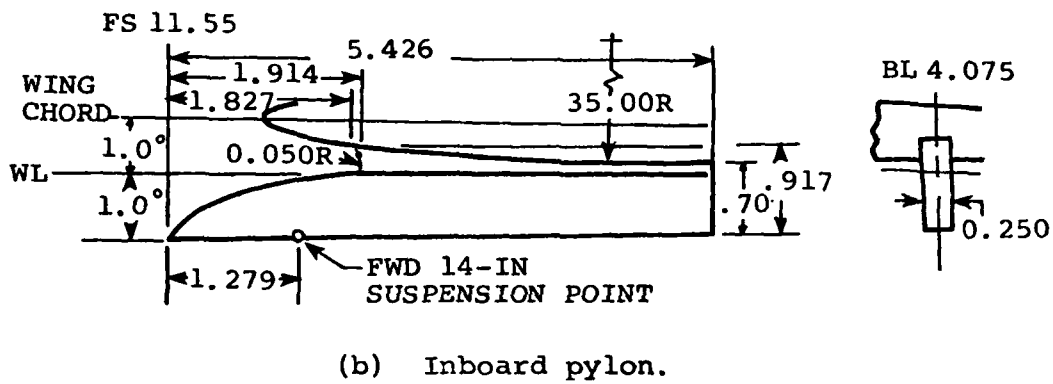
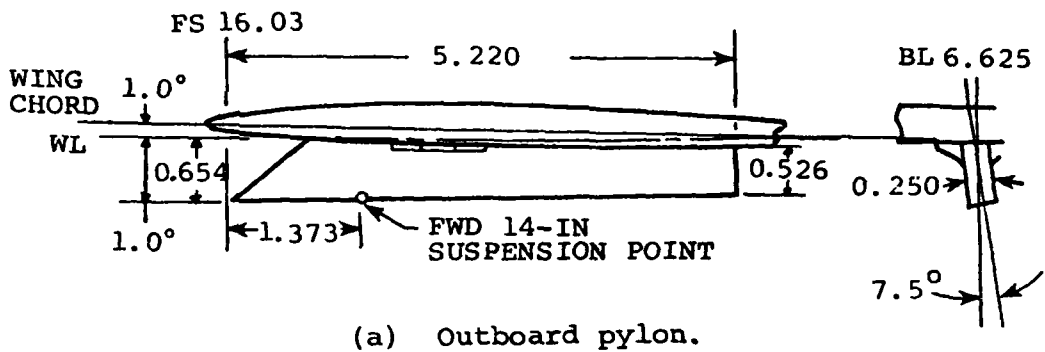
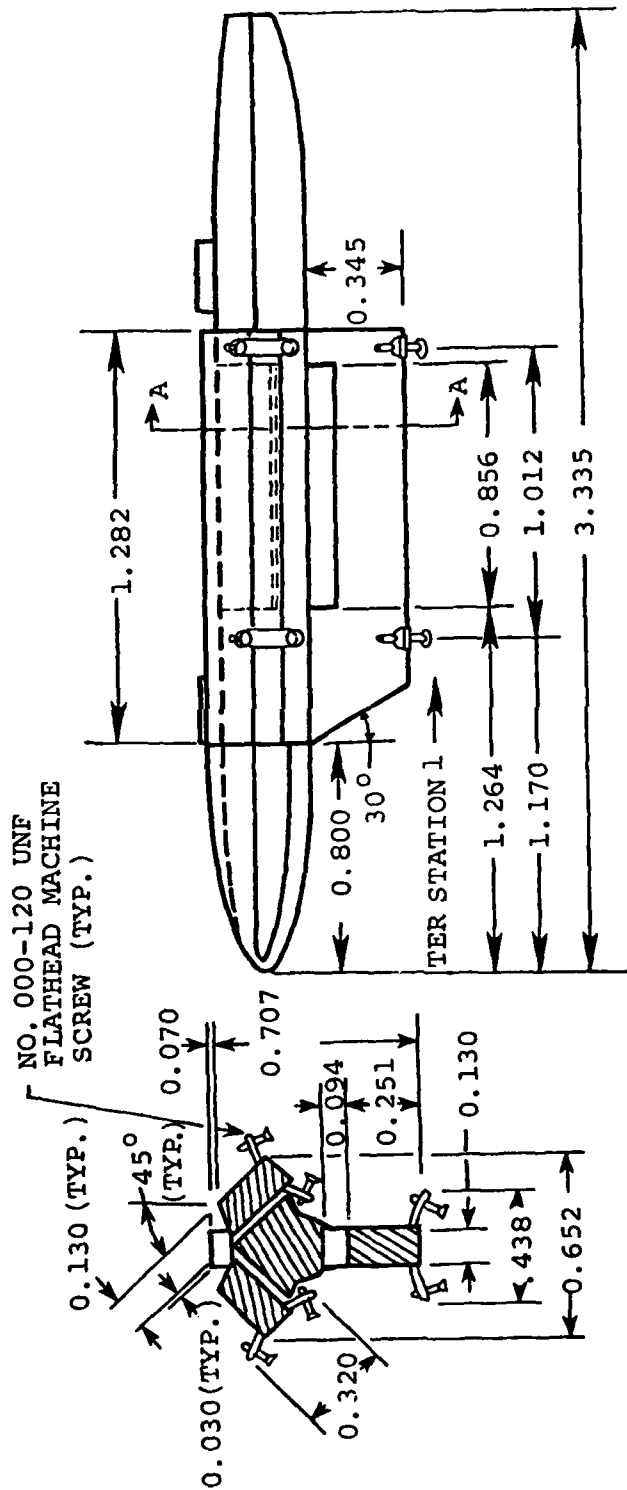


Figure 1. Five-Percent Scale Model of the F-4C Aircraft.



ALL DIMENSIONS IN INCHES

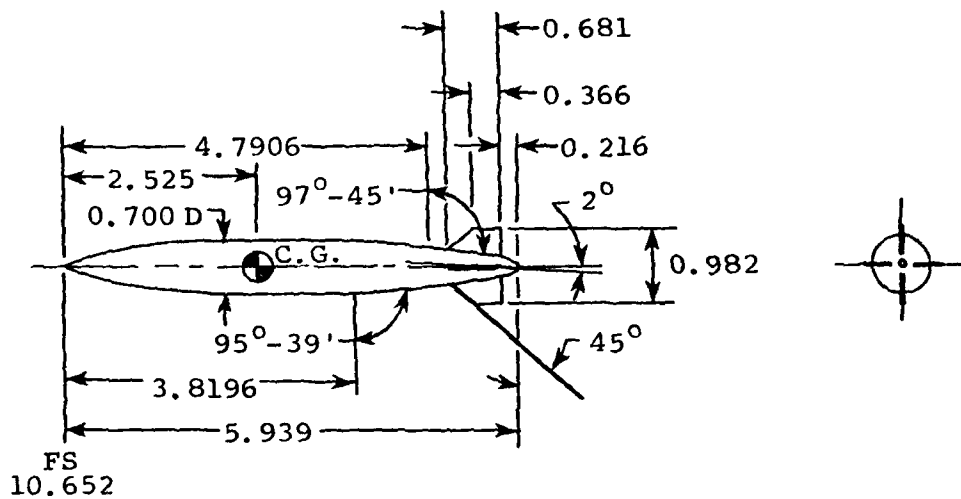
Figure 2. Details of the Models of the F-4C Pylons.



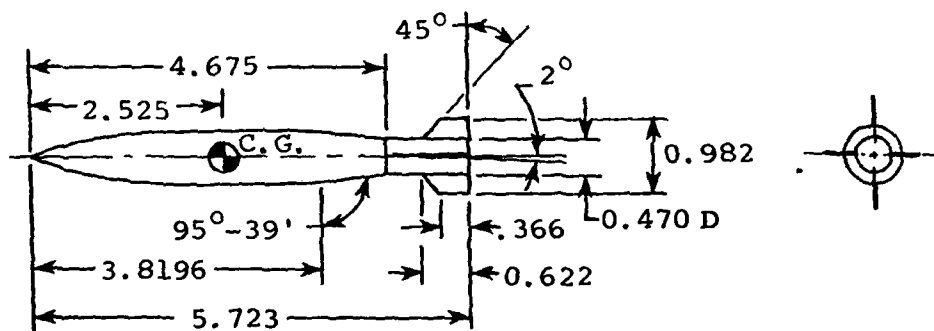
ALL DIMENSION IN INCHES

FS
11.509

Figure 3. Details of the Model of the Triple Ejector Rack.



(a) Actual configuration,
store S_{AF} .



ALL DIMENSIONS IN INCHES

(b) Configuration modified for sting support,
store S_{MF} .

Figure 4. MK-83 Bomb Models.

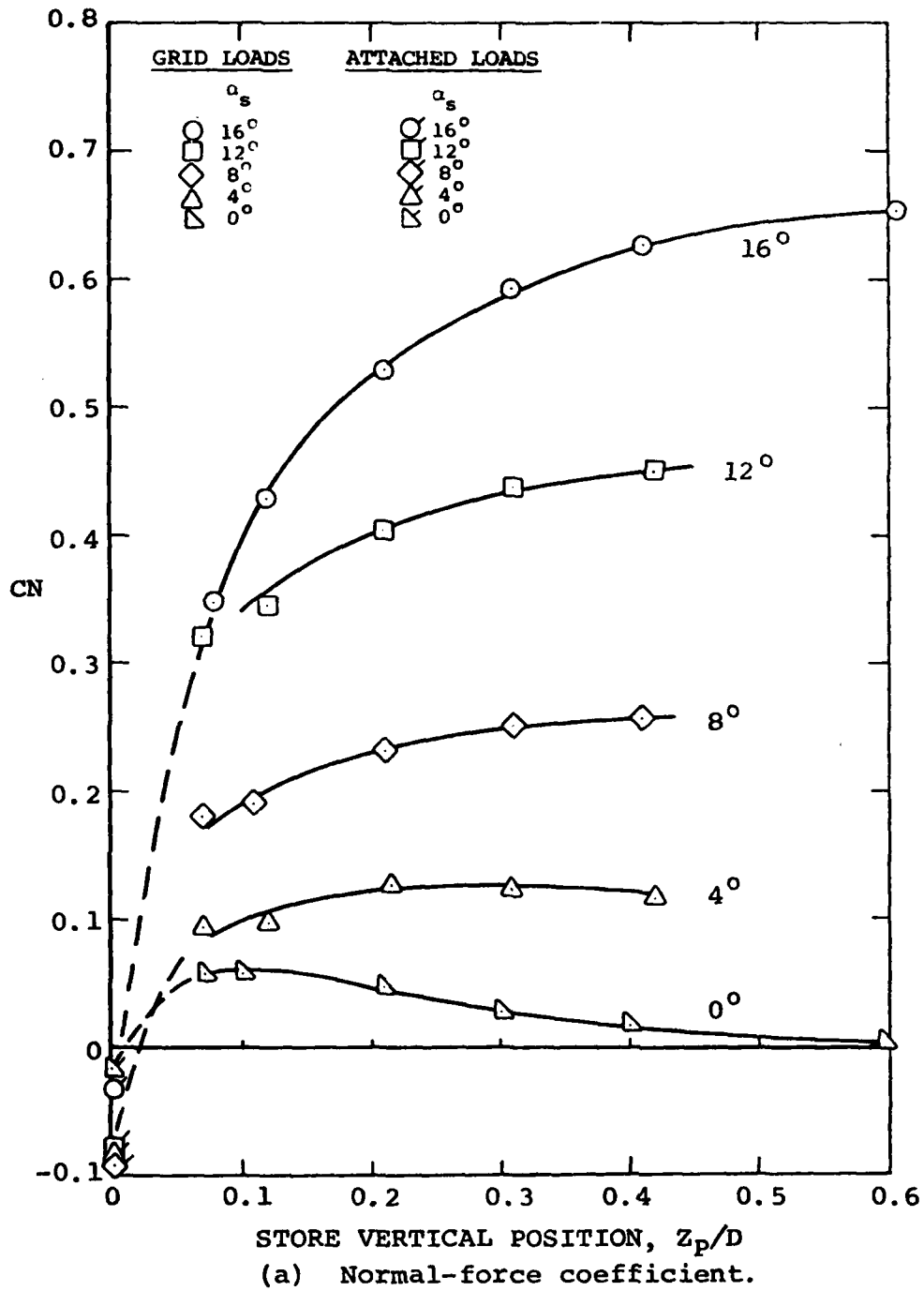
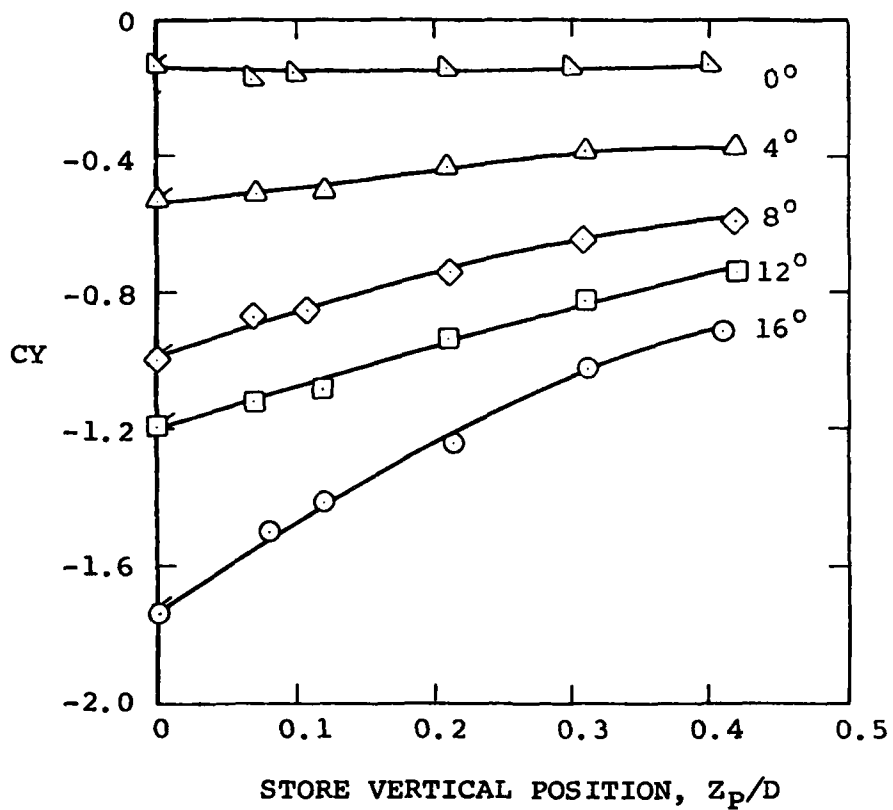
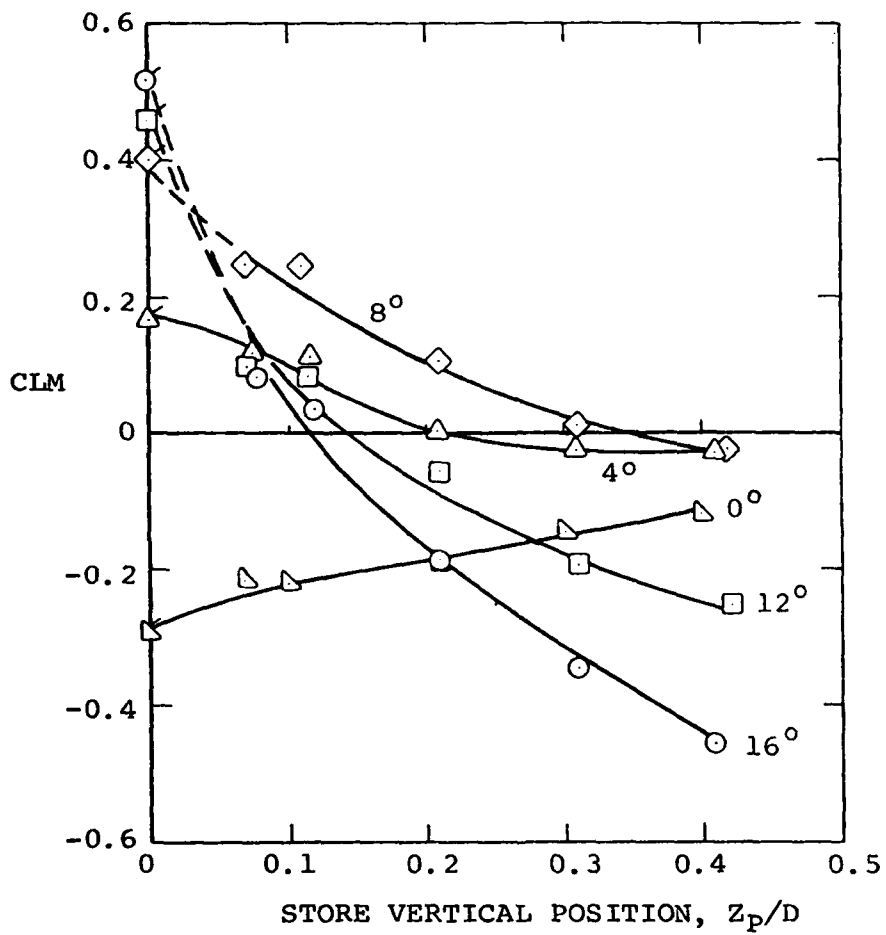


Figure 5. Comparison of Attached and Grid Loads for Store S_{MF} in Combination with Configuration 3 at $M_\infty = 0.6$.



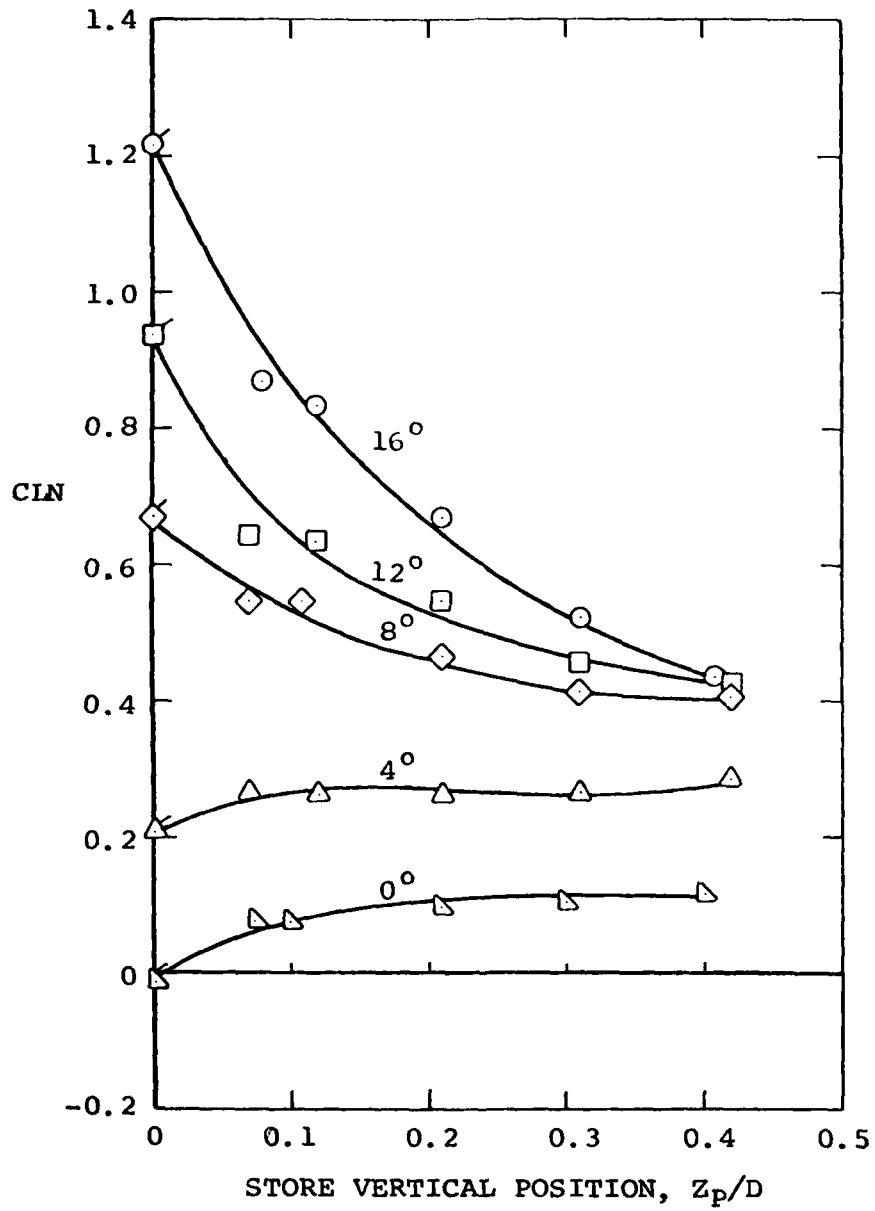
(b) Side-force coefficient.

Figure 5. Continued



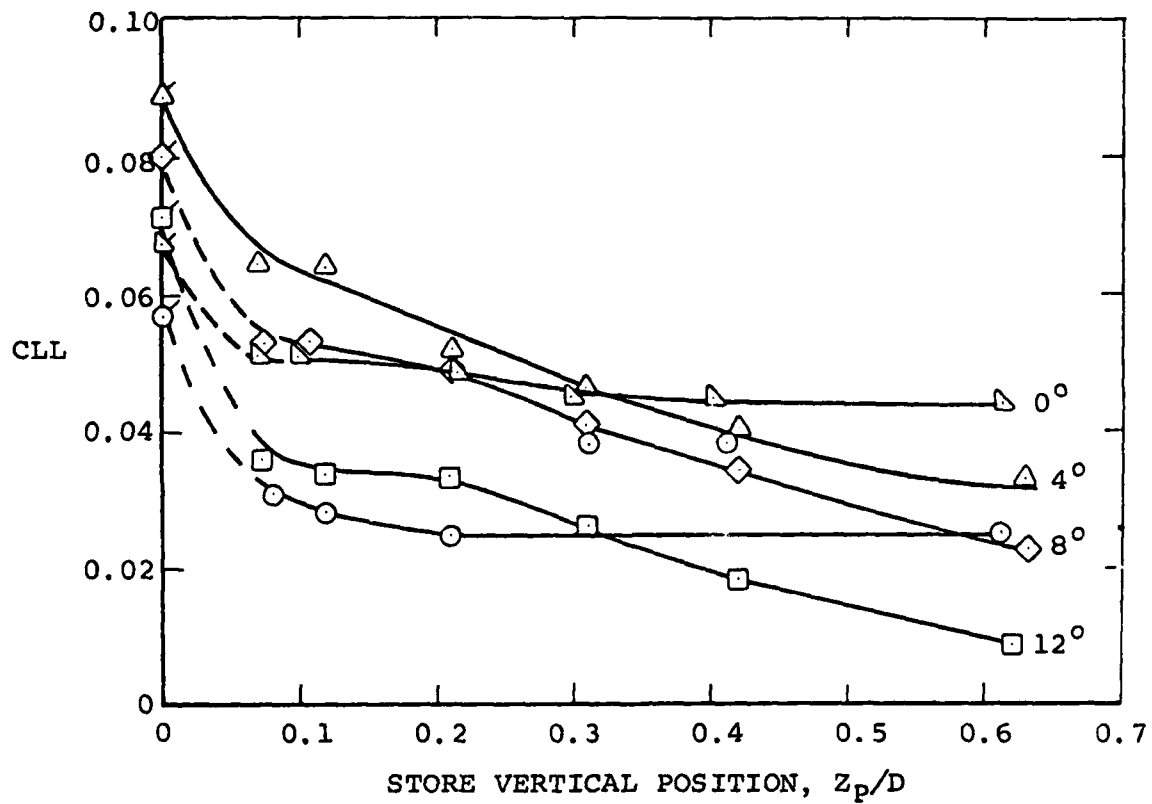
(c) Pitching-moment coefficient.

Figure 5. Continued



(d) Yawing-moment coefficient.

Figure 5. Continued



(e) Rolling-moment coefficient.

Figure 5. Concluded

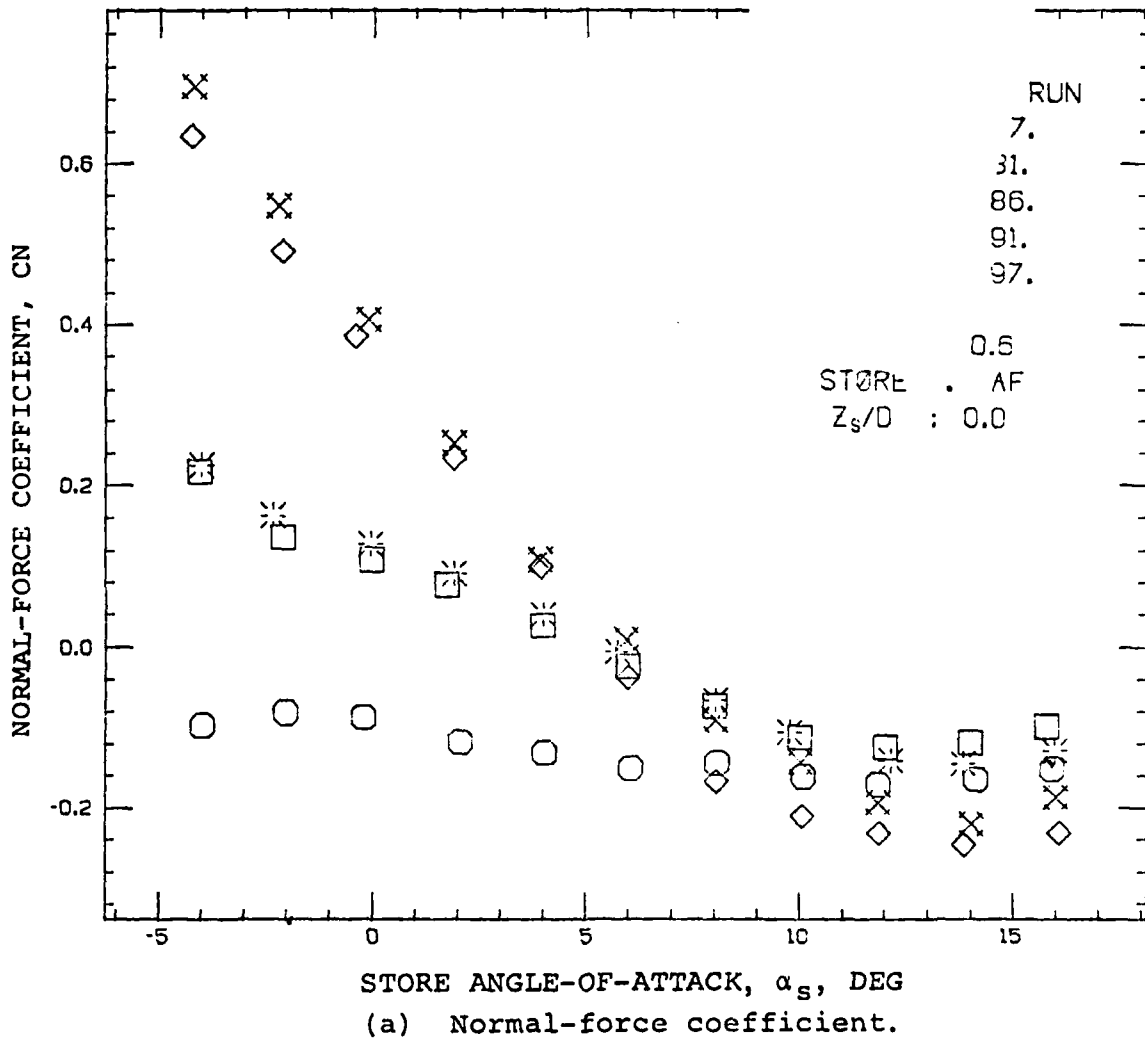


Figure 6. Effect of Airplane Configuration on Attached Loads of Bottom Store S_{AF} at $M_\infty = 0.6$.

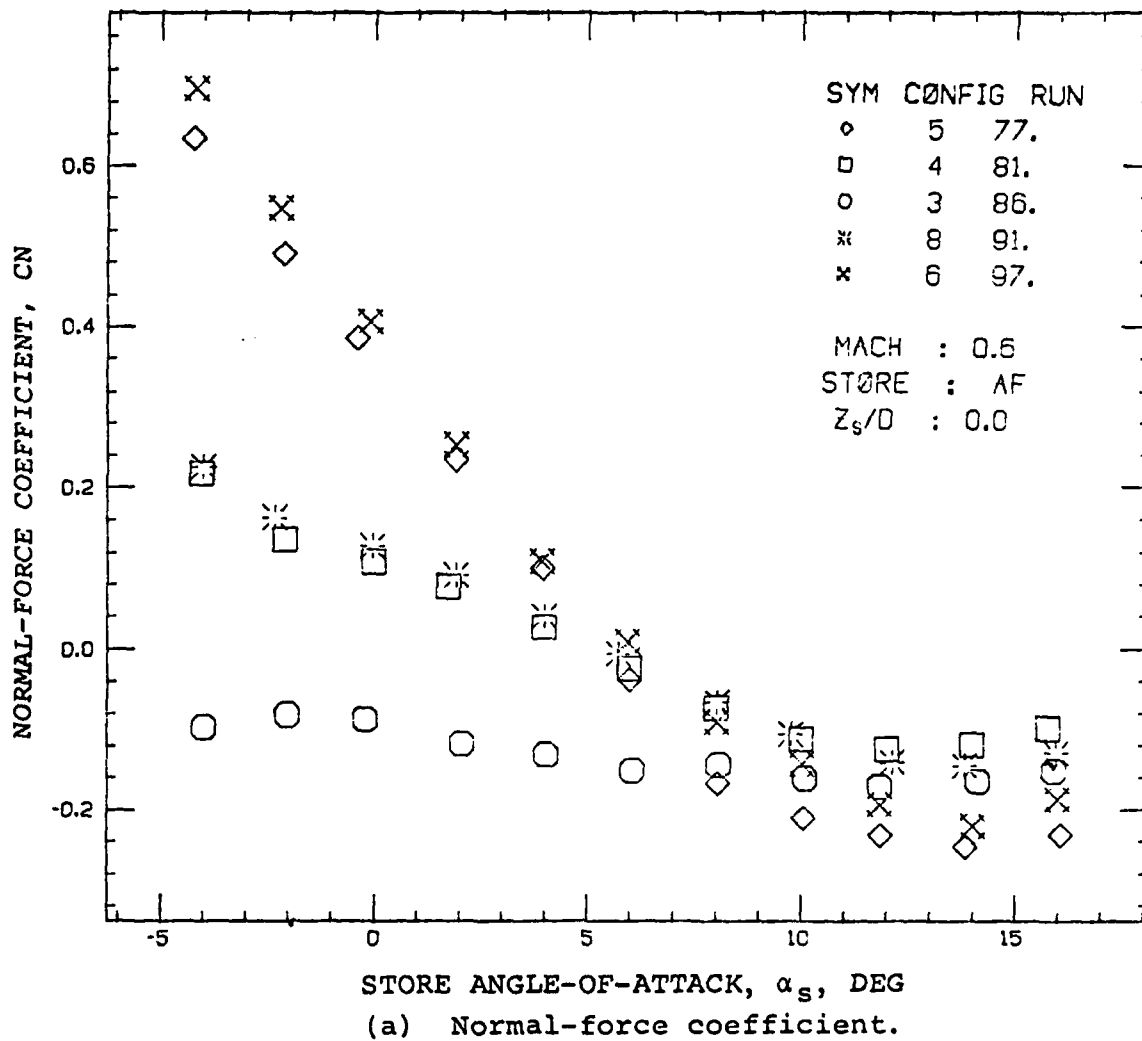
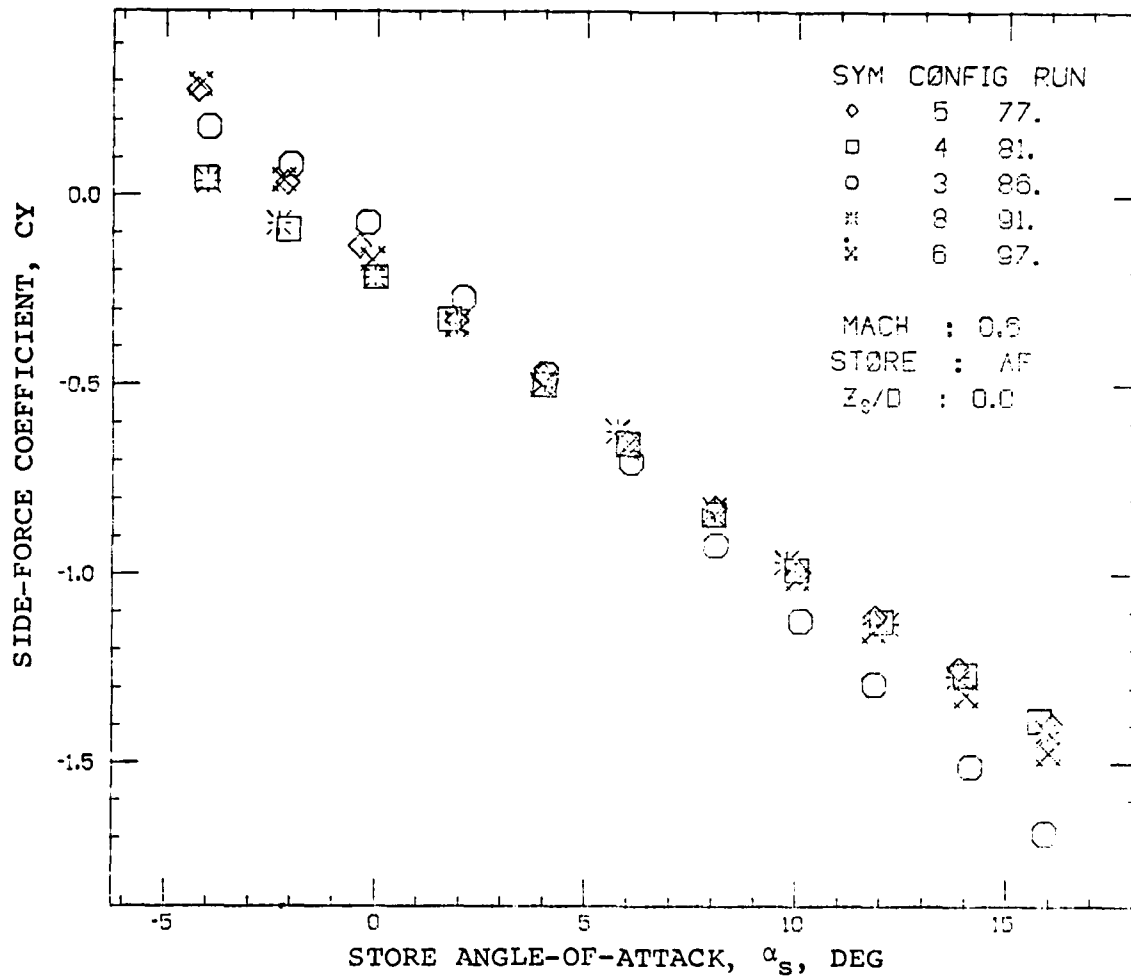
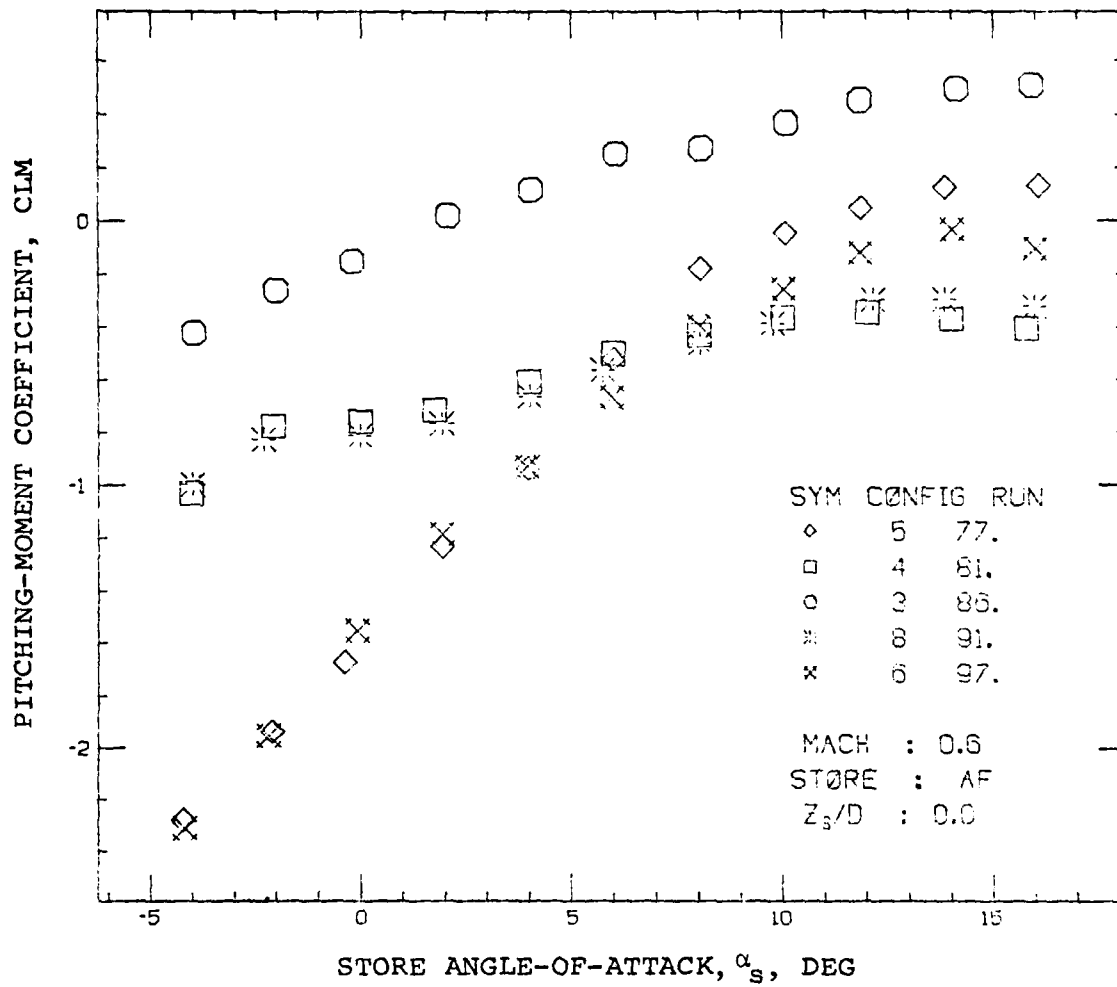


Figure 6. Effect of Airplane Configuration on Attached Loads of Bottom Store S_{AF} at M_∞ = 0.6.



(b) Side-force coefficient.

Figure 6. Continued



(c) Pitching-moment coefficient.

Figure 6. Continued

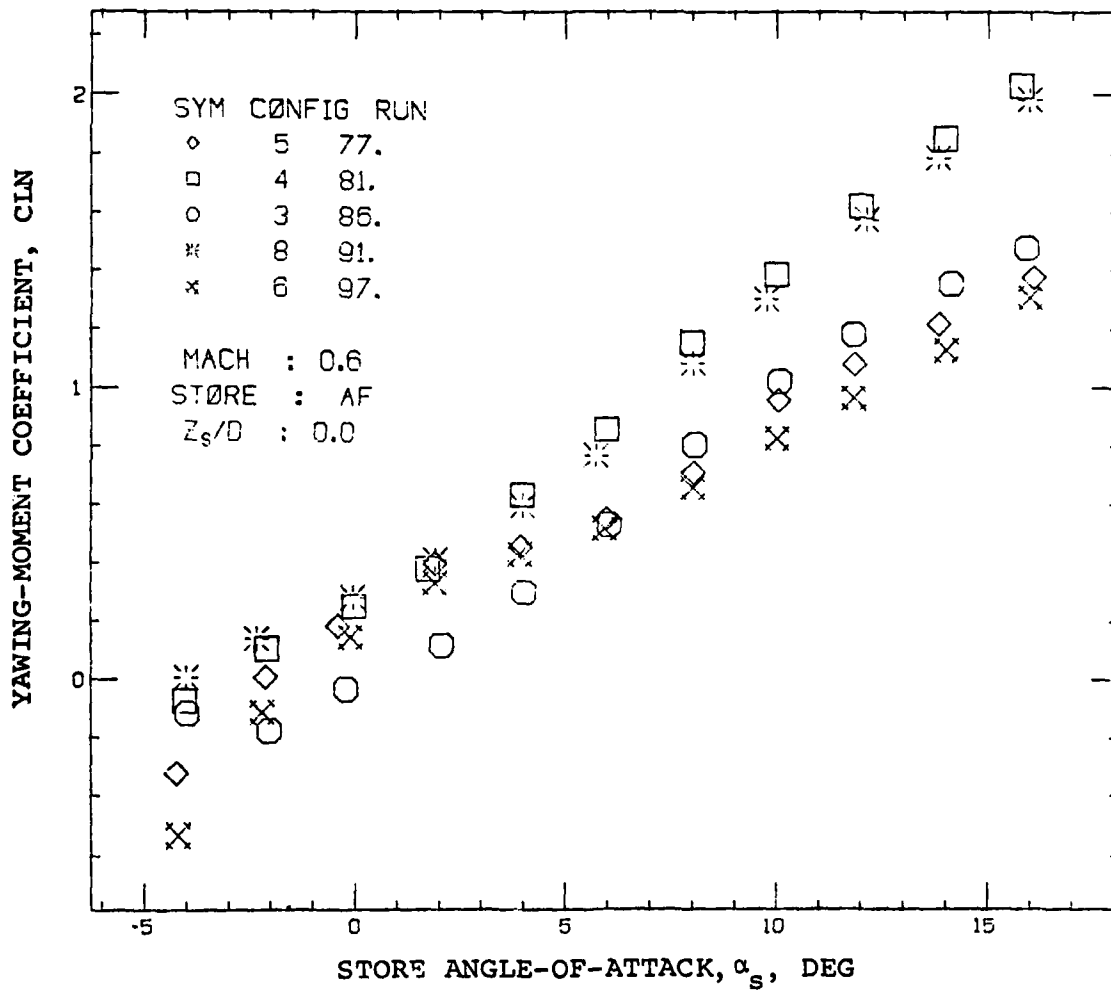
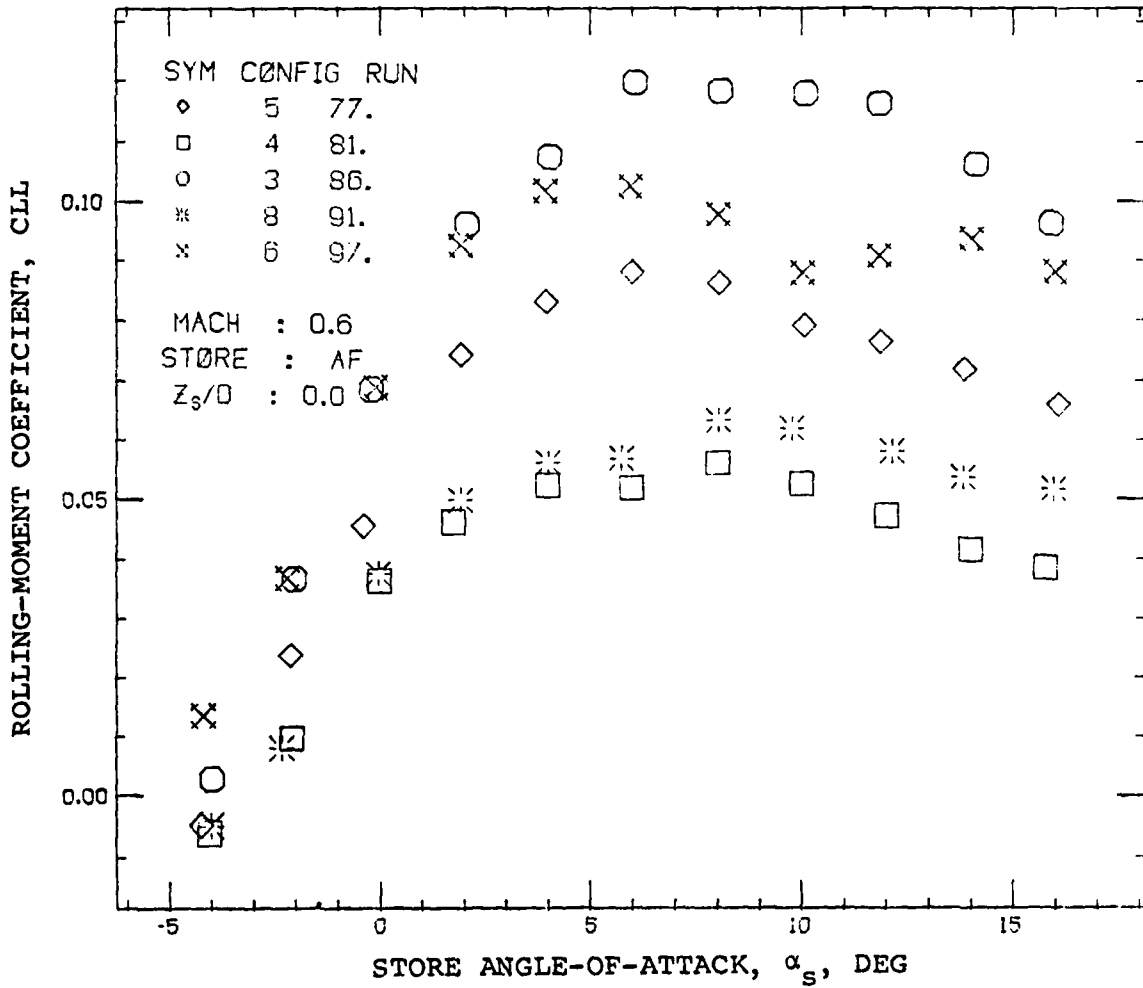


Figure 6. Continued



(e) Rolling-moment coefficient.

Figure 6. Concluded

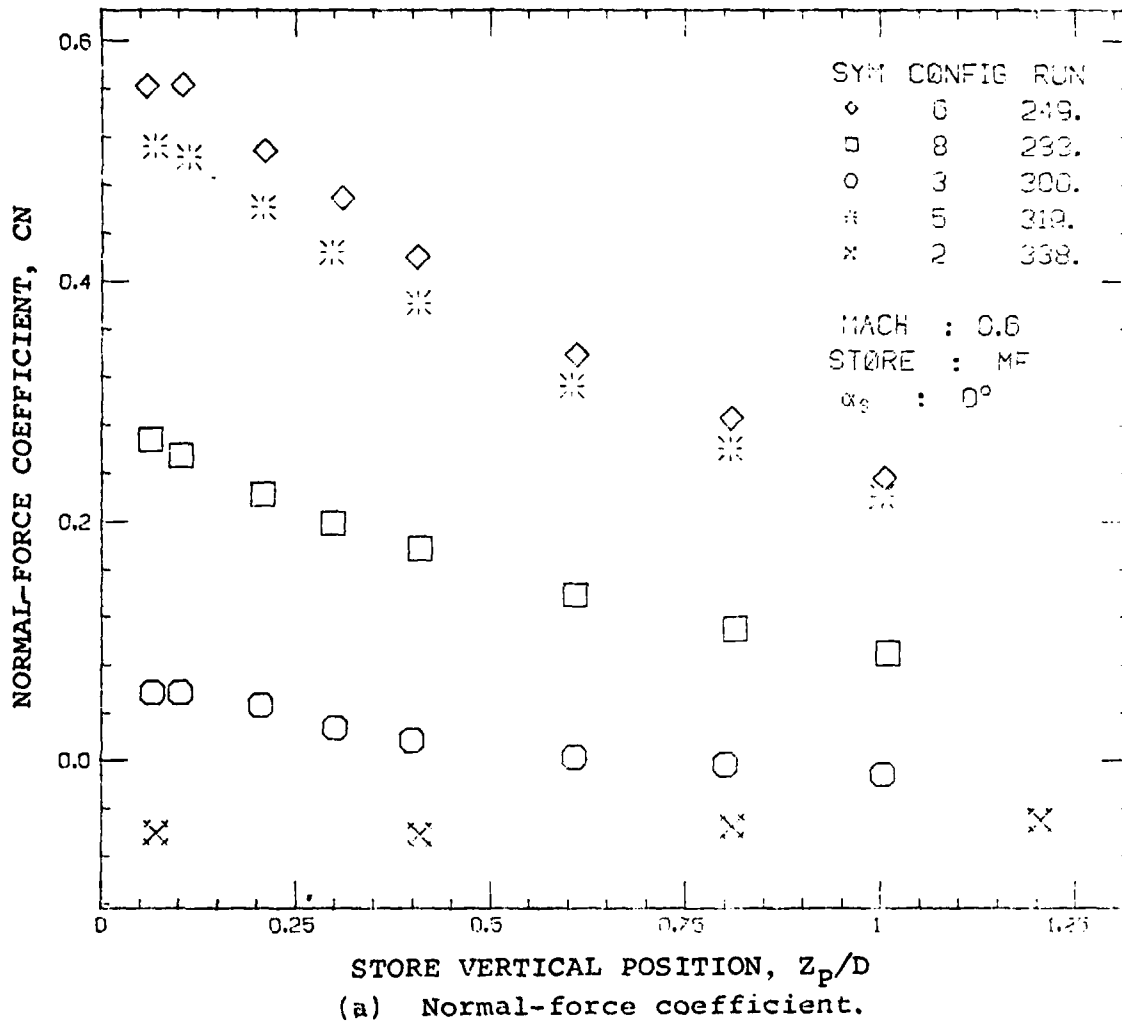


Figure 7. Grid Loads on Store S_{MF} as Influenced by Airplane Configuration; $M_\infty = 0.6$, $\alpha_s = 0^\circ$.

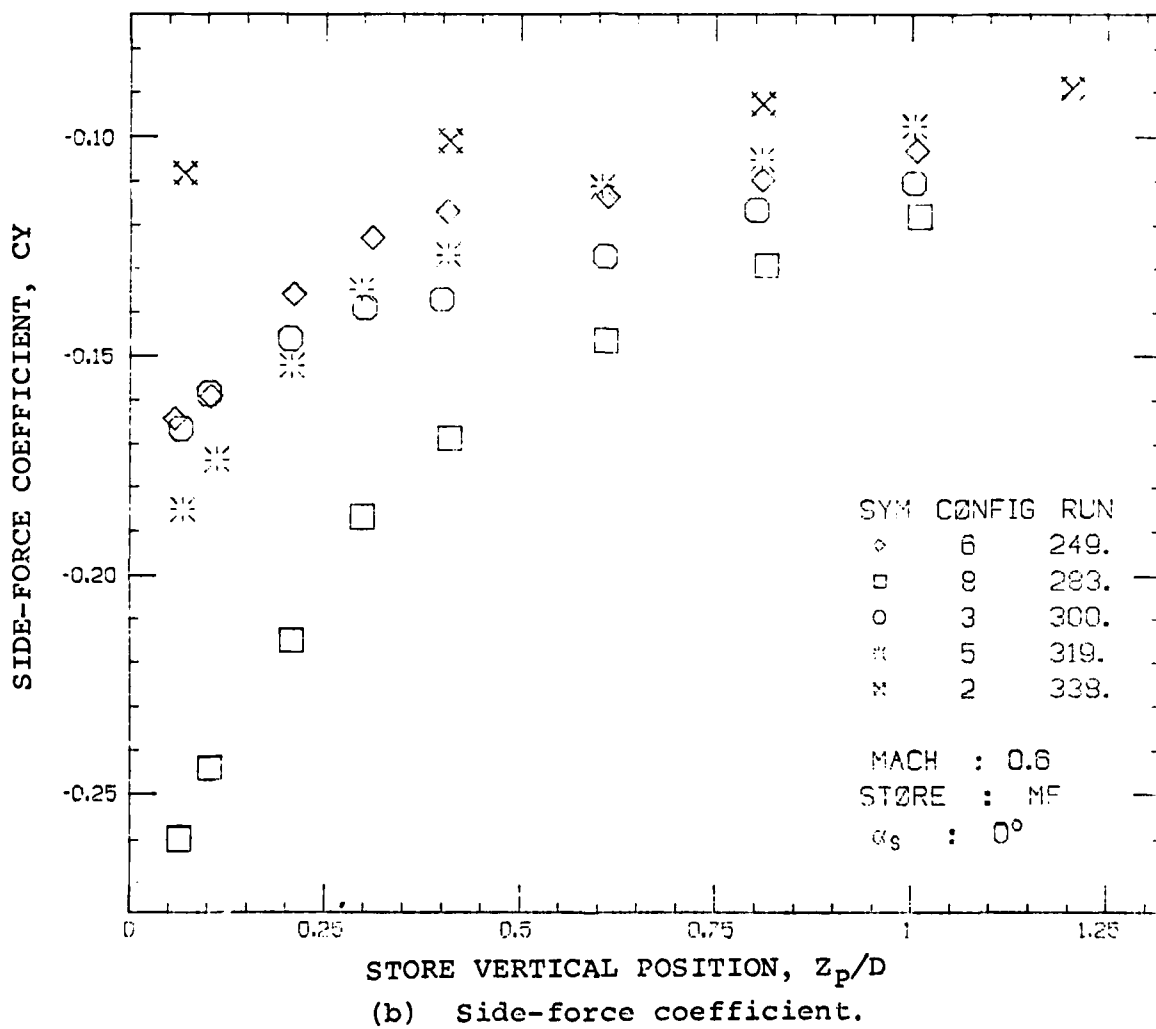
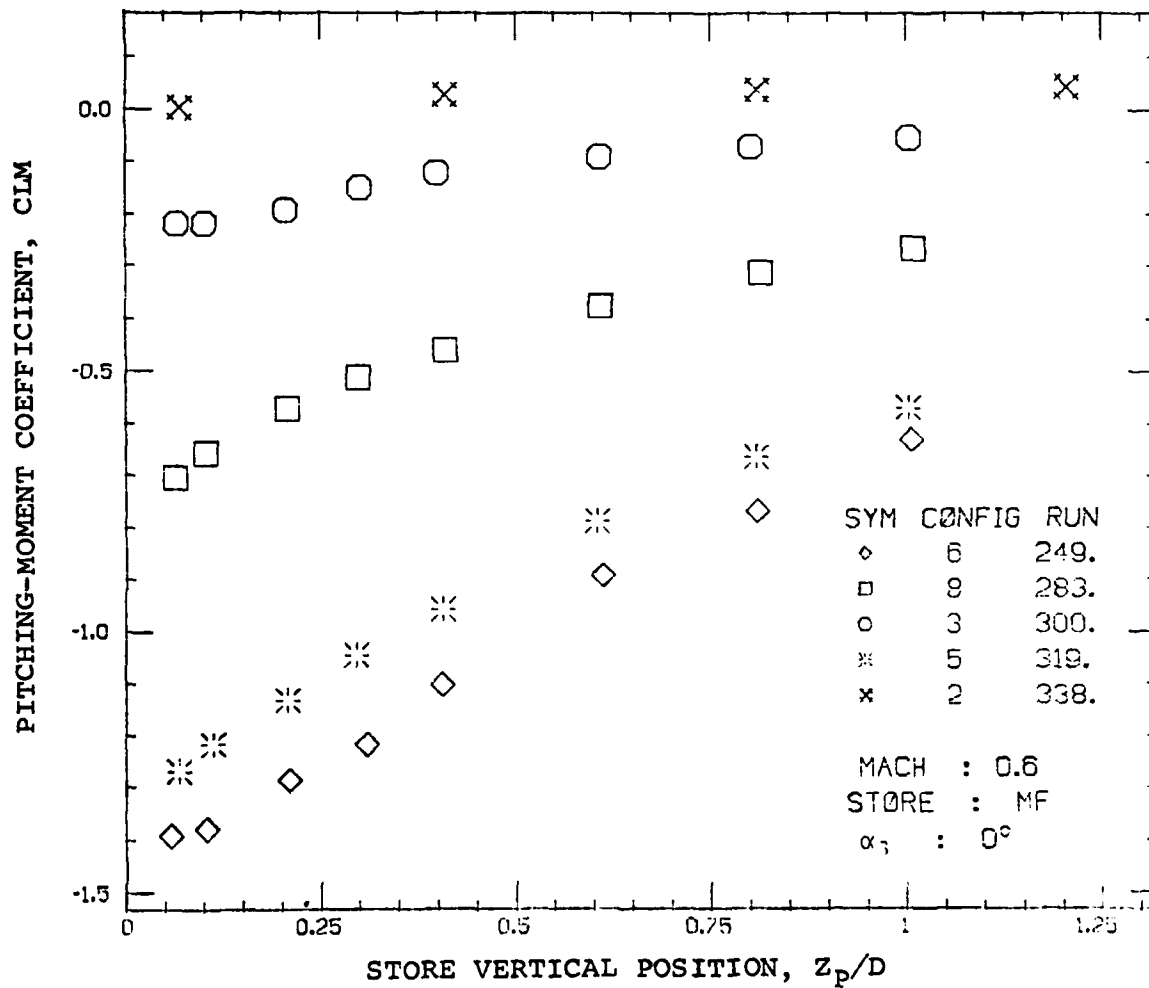
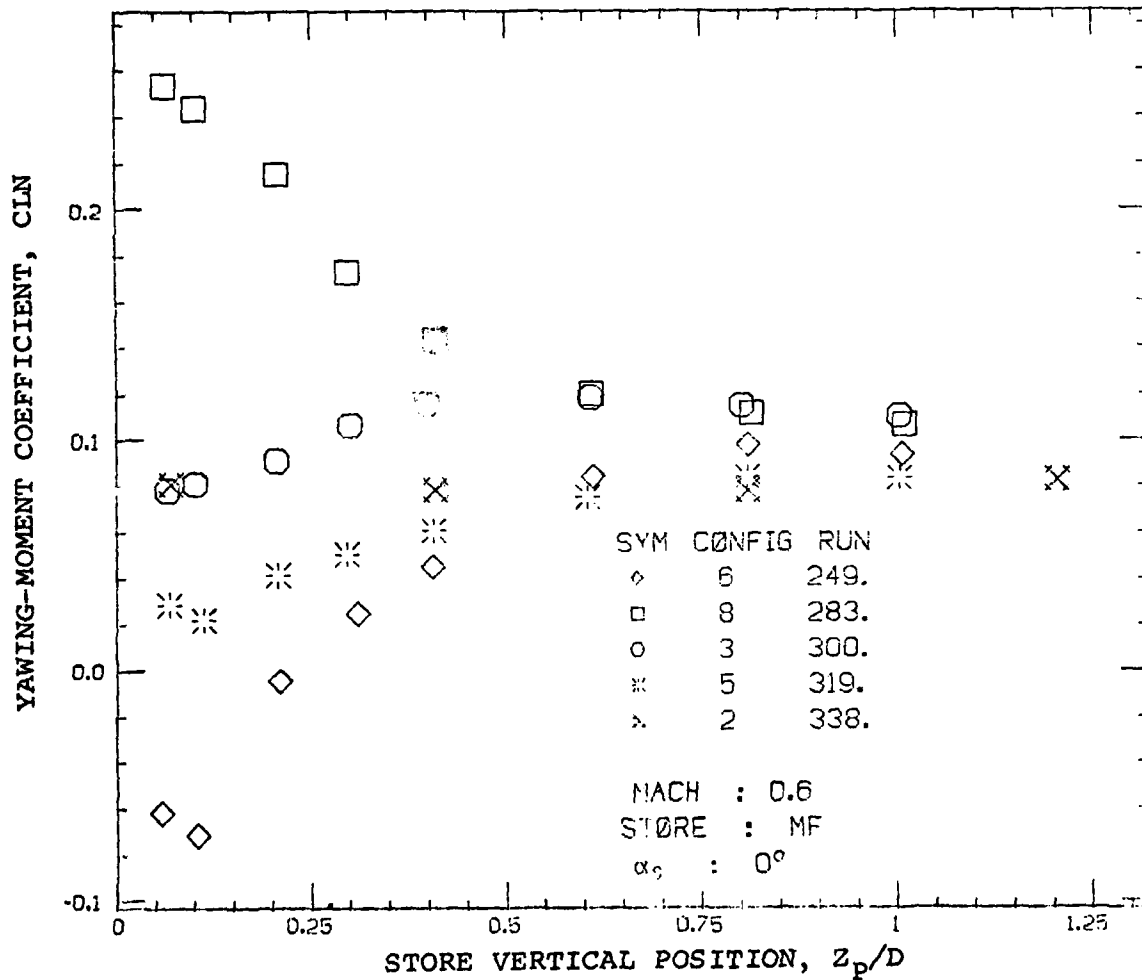


Figure 7. Continued



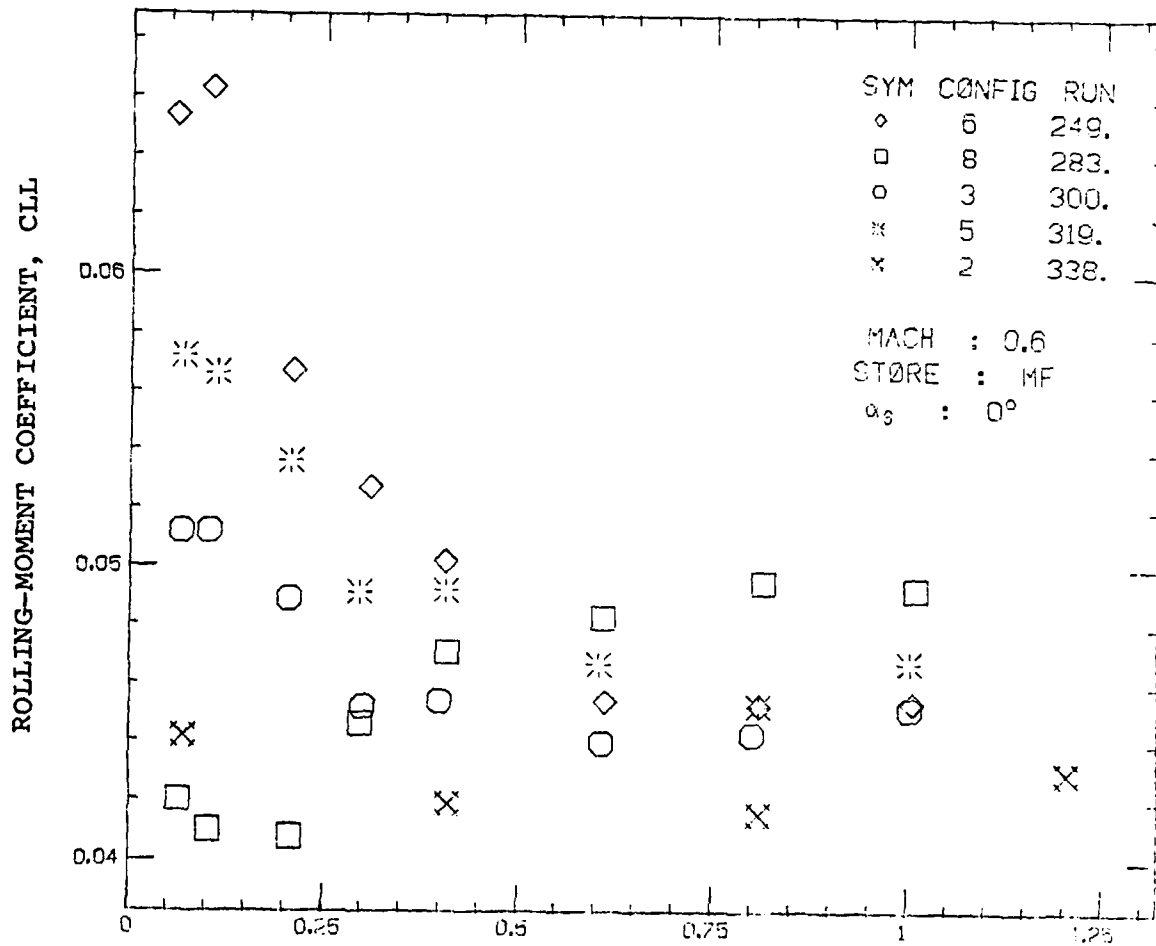
(c) Pitching-moment coefficient.

Figure 7. Continued.



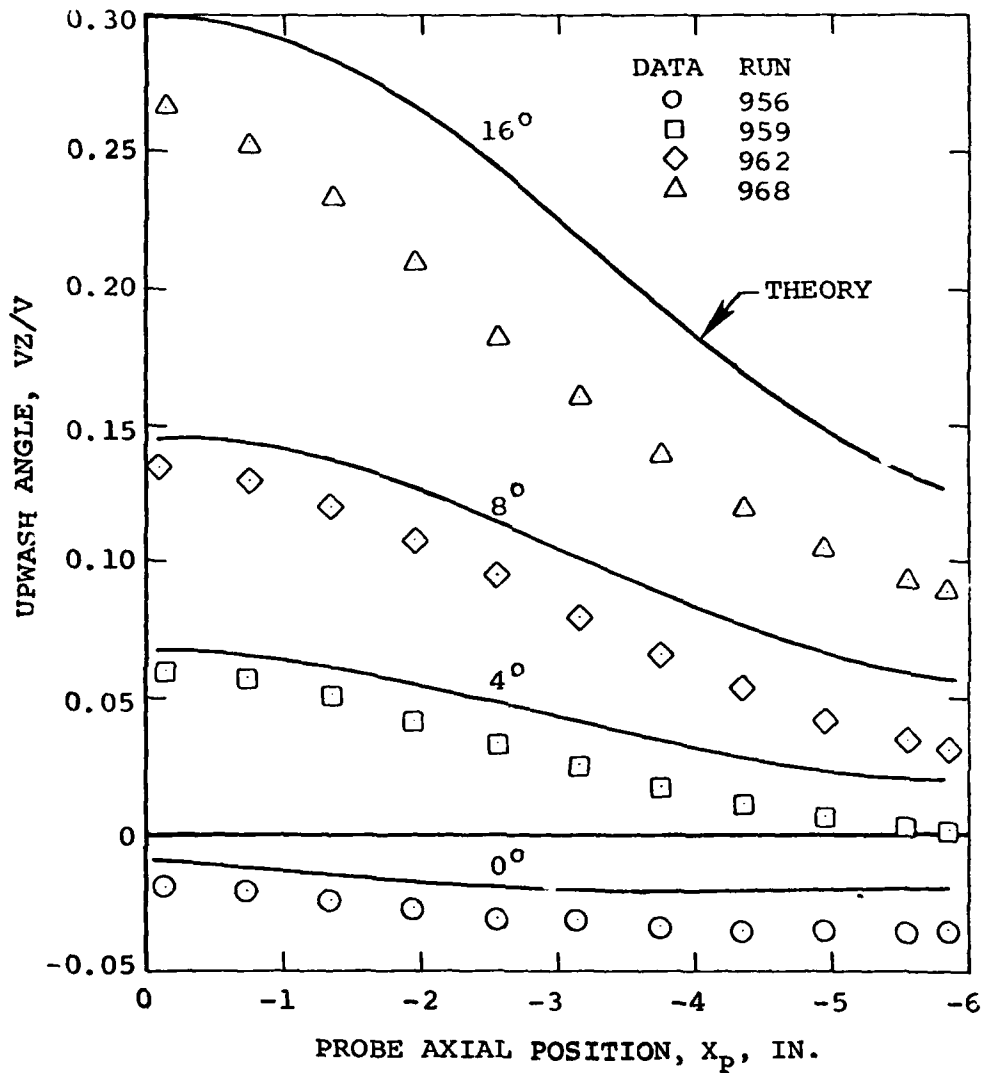
(d) Yawing-moment coefficient.

Figure 7. Continued.



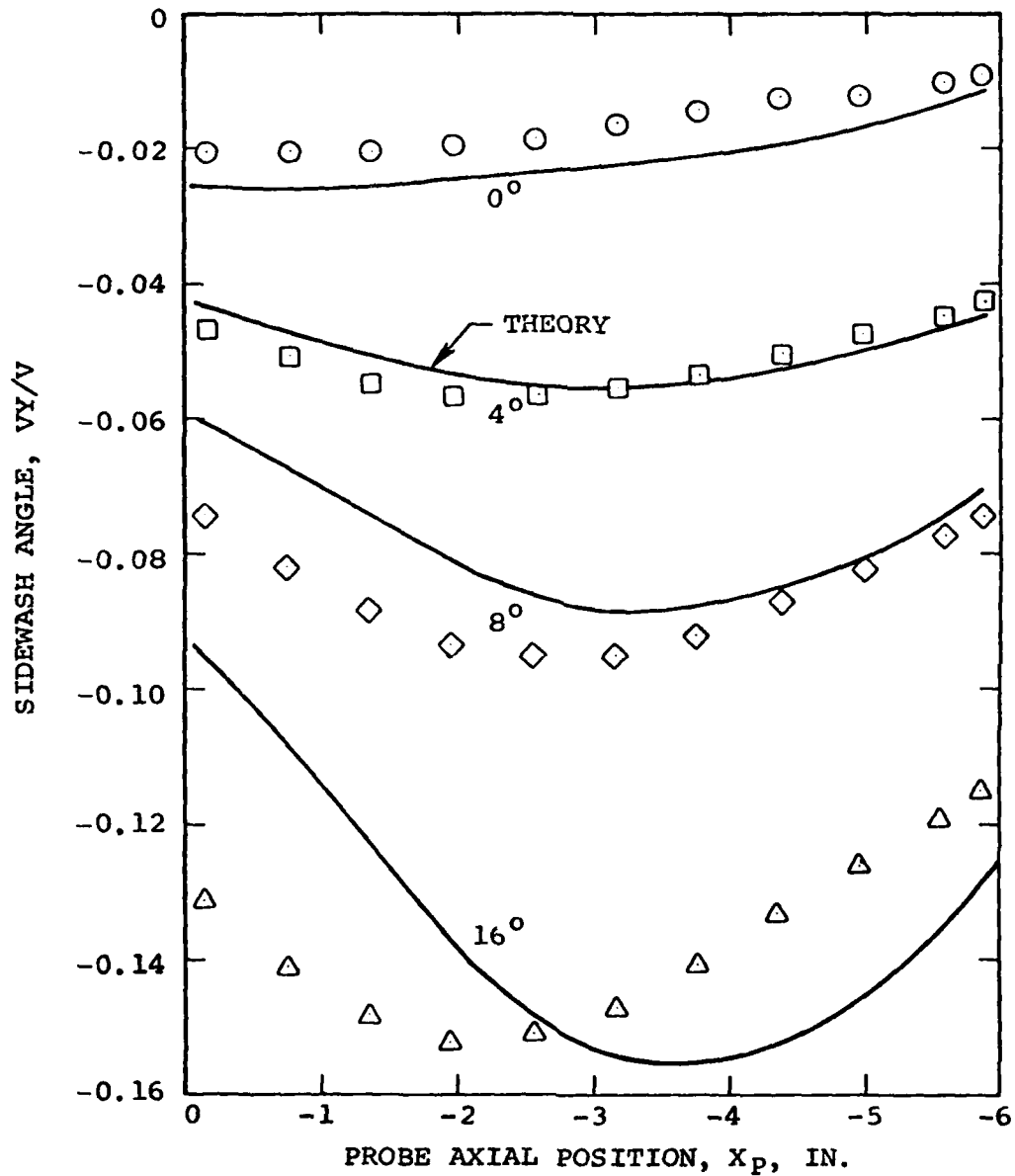
(e) Rolling-moment coefficient.

Figure 7. Concluded



(a) Upwash angle.

Figure 8. Flow Field Comparisons for Clean Airplane at $M_\infty = 0.6$ and $Z_p/D = 0$ as a Function of Angle of Attack.



(b) Sidewash angle.

Figure 8. Concluded

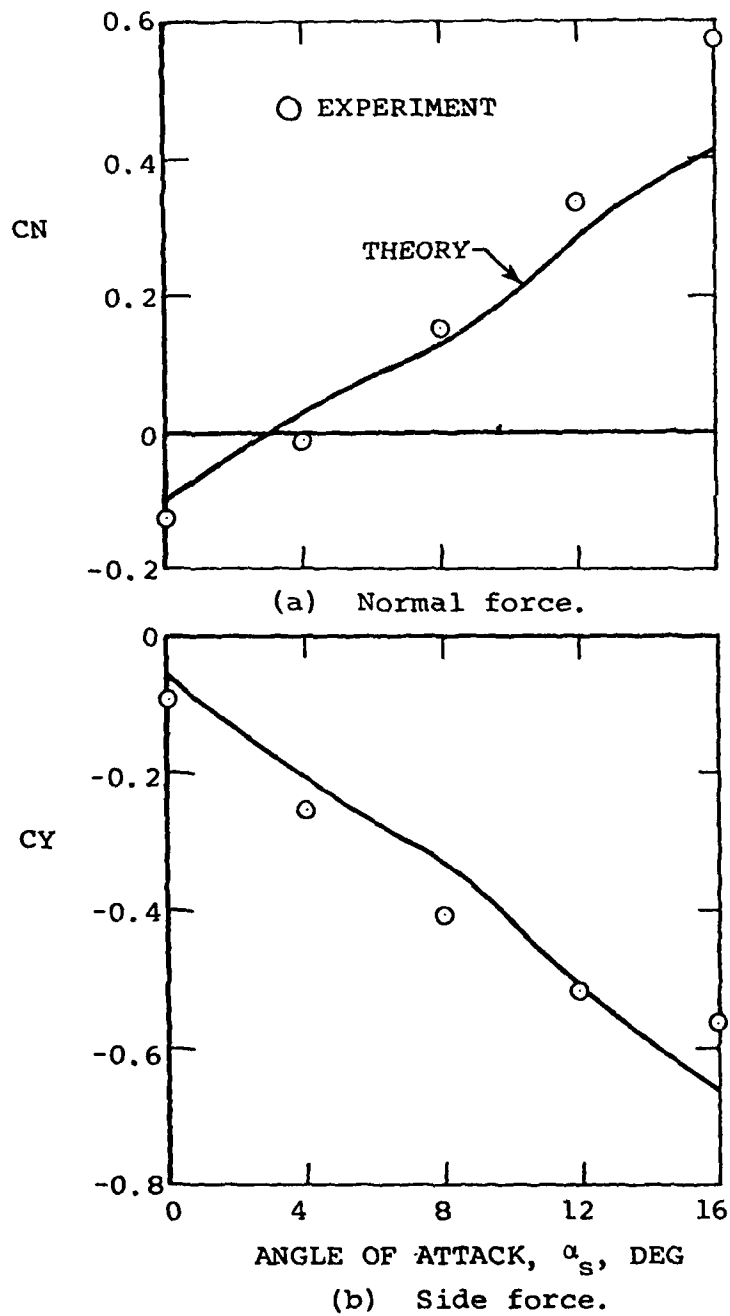
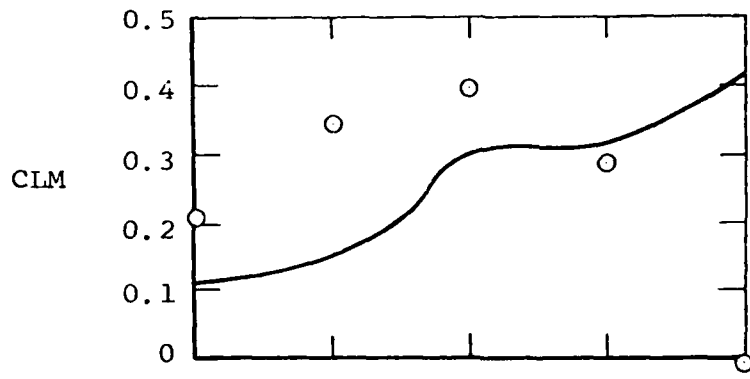
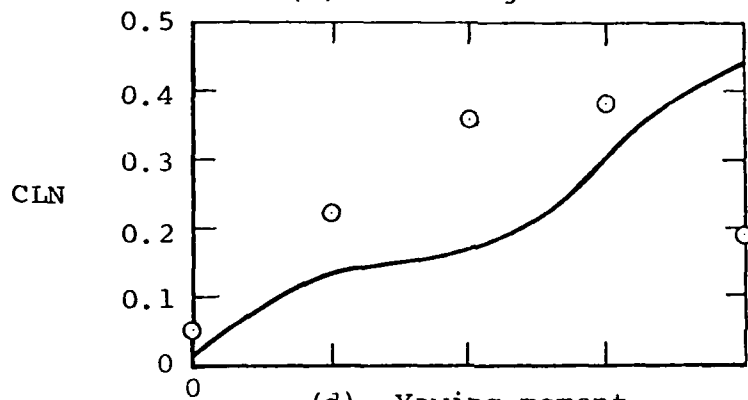


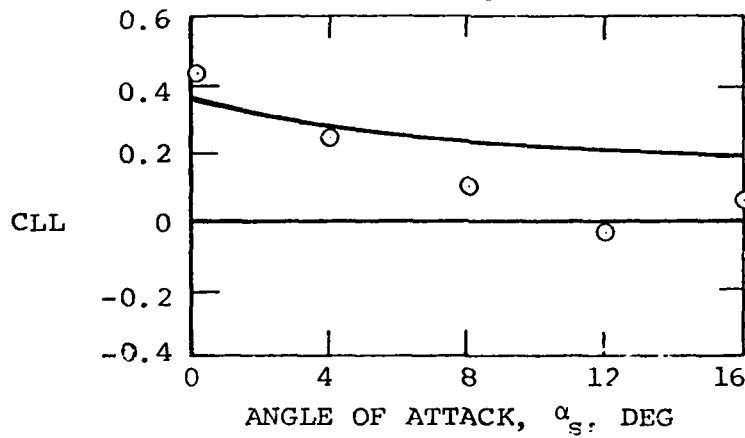
Figure 9. Loads on Store S_{MF} in Combination with Clean Airplane at $M_\infty = 0.6$, $Z_p/D = 0$.



(c) Pitching moment.

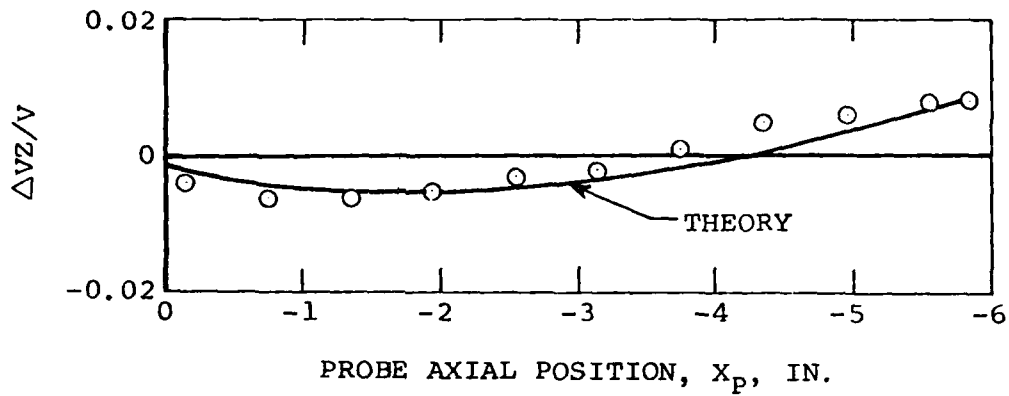


(d) Yawing moment.

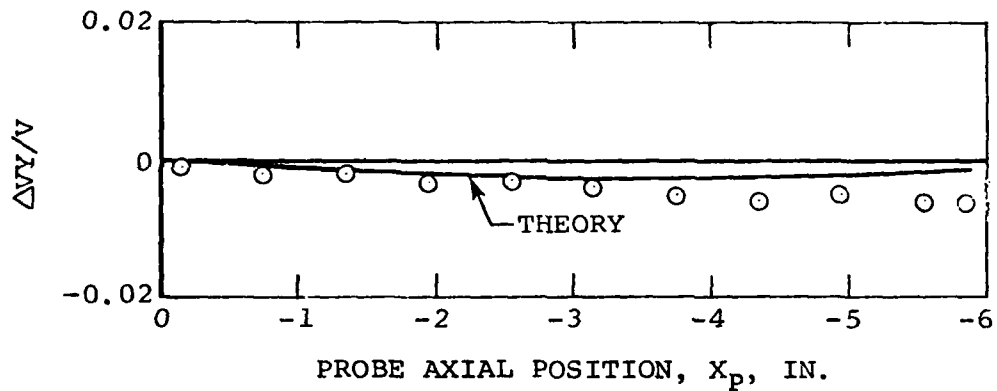


(e) Rolling moment.

Figure 9. Concluded

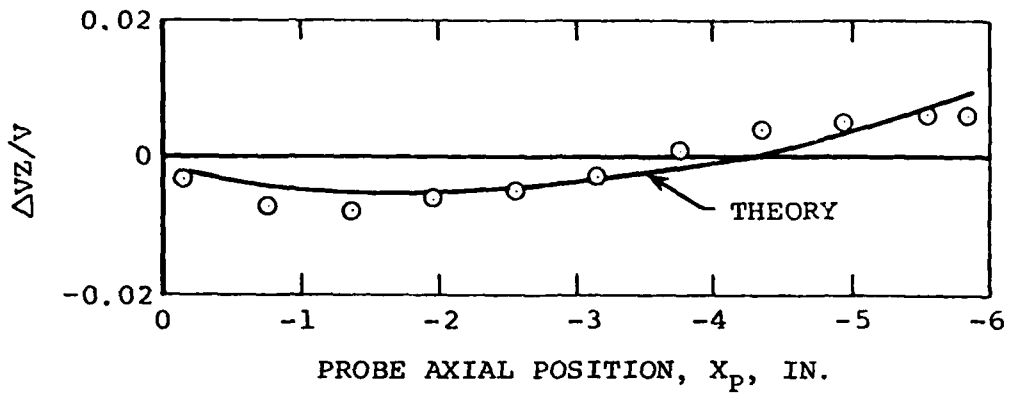


(a) Upwash angle.

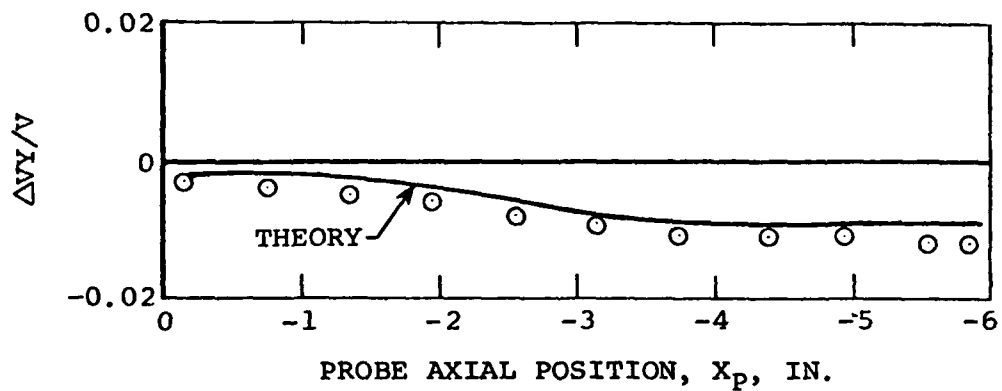


(b) Sidewash angle.

Figure 10. Effect of Adding a Pylon to the Clean Airplane on the Flow Angles Along the Centerline Position of the Bottom Store at $M_\infty = 0.6$; $\alpha_s = 0^\circ$; $Z_p/D = 0$.

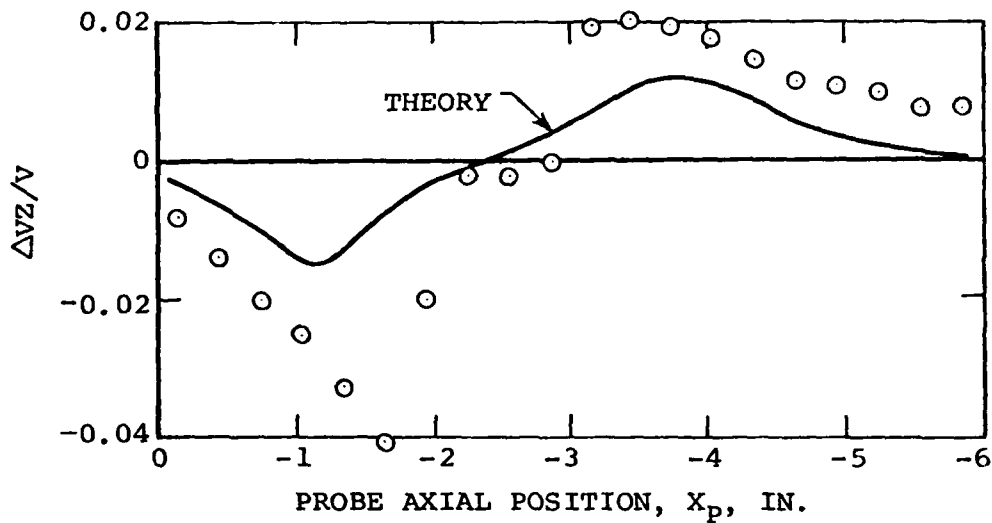


(a) Upwash angle.

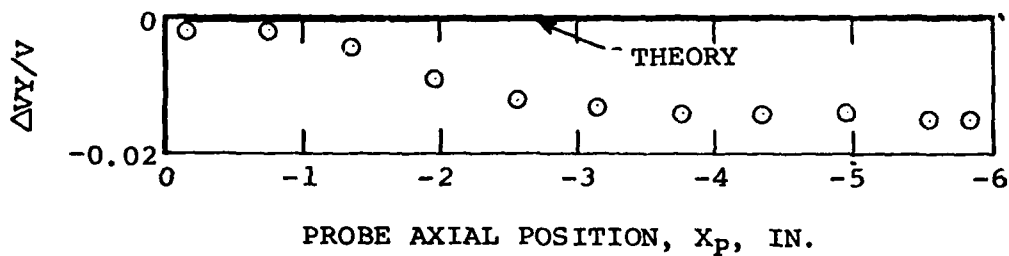


(b) Sidewash angle.

Figure 11. Effect of Adding a Pylon to the Clean Airplane on the Flow Angles Along the Centerline Position of the Bottom Store at $M_\infty = 0.6$; $\alpha_s = 4^\circ$; $Z_p/D = 0$.

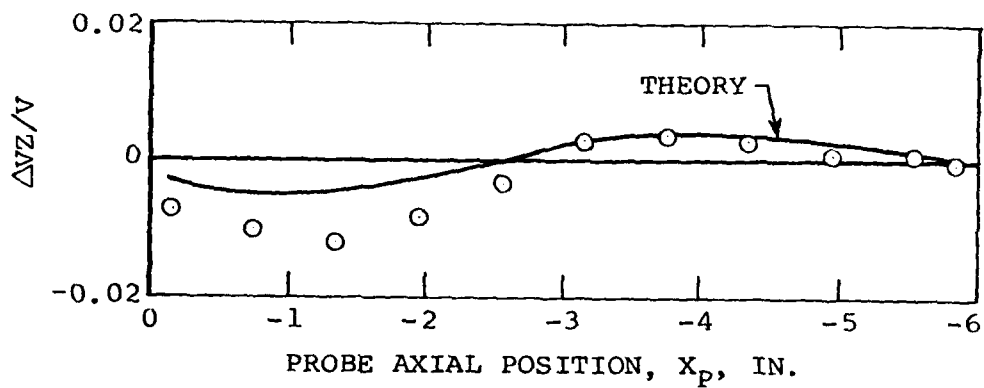


(a) Upwash angle.

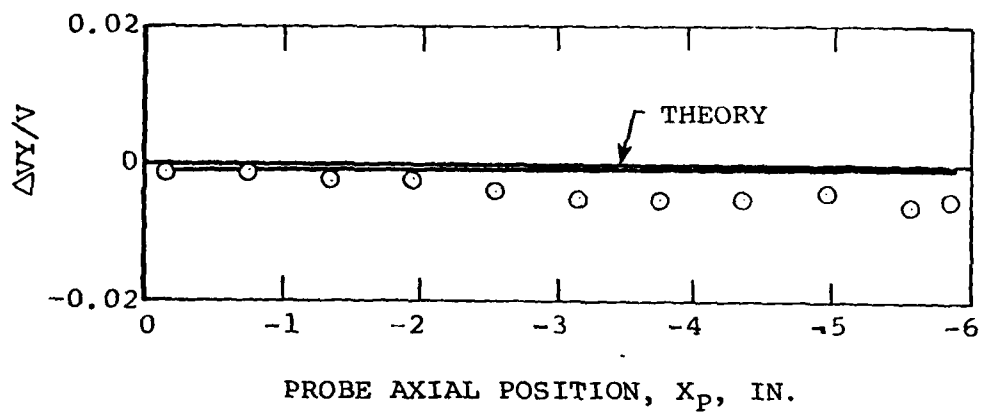


(b) Sidewash angle.

Figure 12. Effect of Adding TER to Pylon on the Flow Angles Along the Centerline Position of the Bottom Store at $M_\infty = 0.6$; $\alpha_s = 0^\circ$; $Z_p/D = 0$.

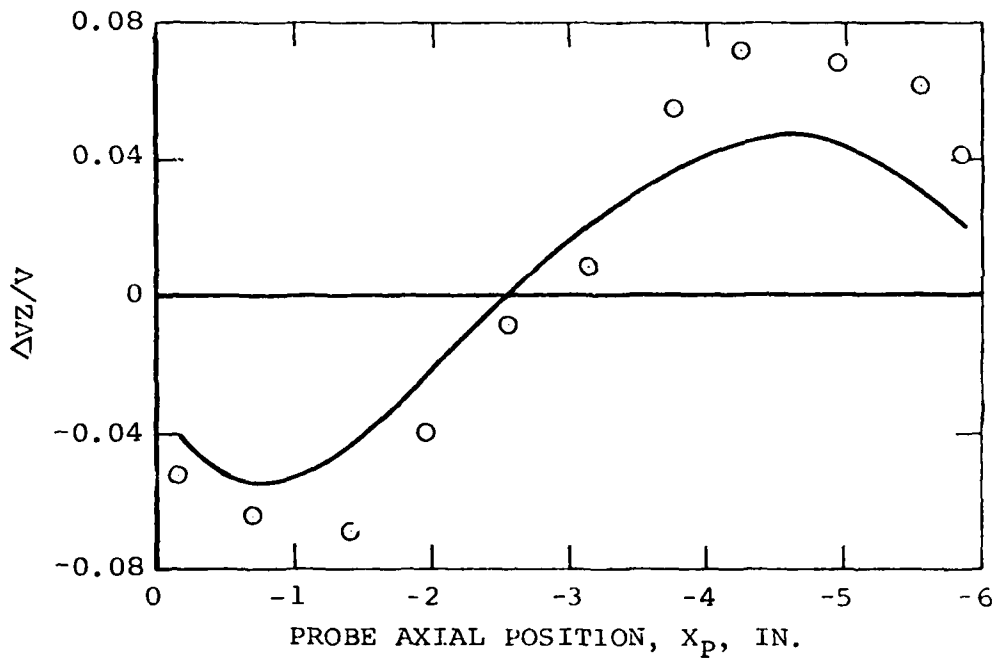


(a) Upwash angle.

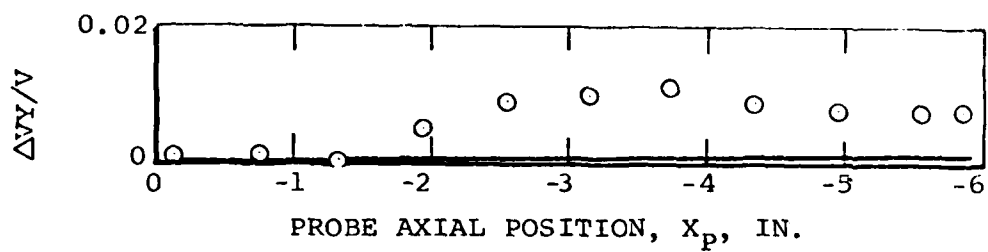


(b) Sidewash angle.

Figure 13. Effect of Adding TER to Pylon on the Flow Angles Along the Centerline Position of the Bottom Store at $M_\infty = 0.6$; $\alpha_s = 0^\circ$; $Z_p/D = 1.0$.

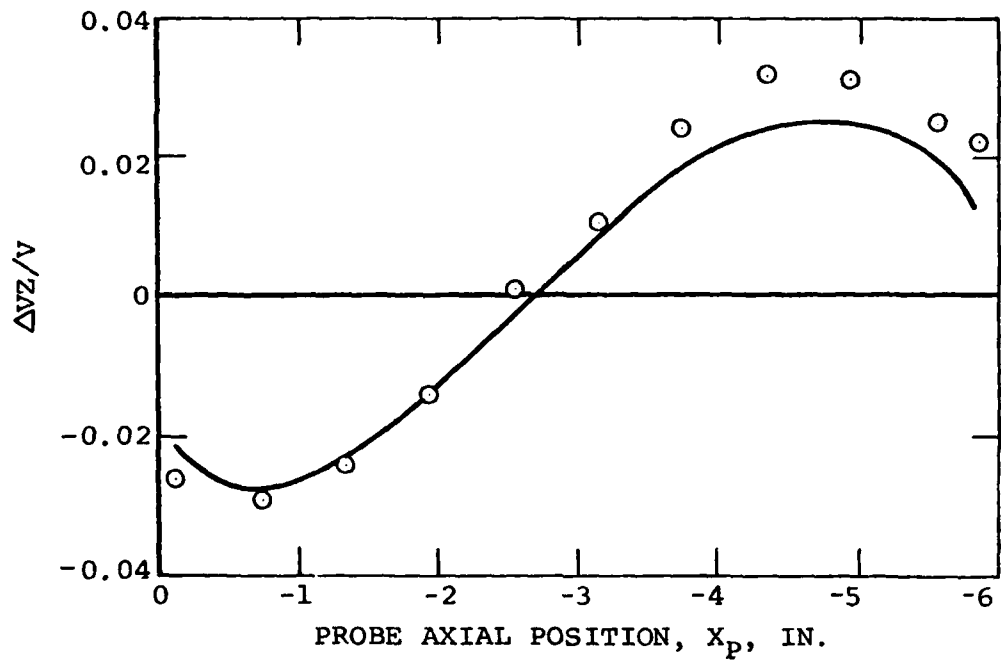


(a) Upwash angle.

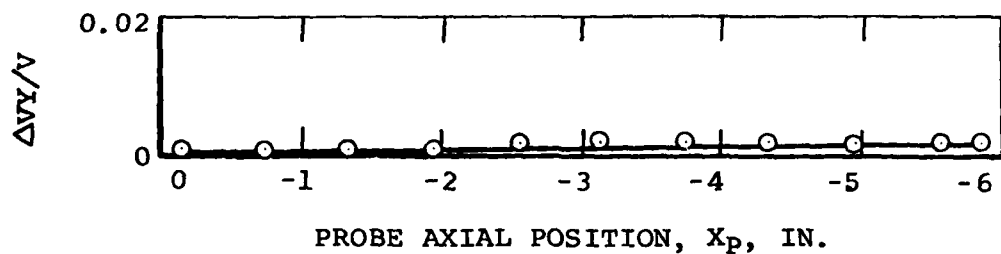


(b) Sidewash angle.

Figure 14. Effect of Adding Shoulder Stores to Configuration 3 on the Flow Angles Along the Centerline Position of the Bottom Store; $M_\infty = 0.6$, $\alpha_s = 0^\circ$, $Z_p/D = 0$.



(a) Upwash angle.



(b) Sidewash angle.

Figure 15. Effect of Adding Shoulder Stores to Configuration 3 on the Flow Angles Along the Centerline Position of the Bottom Store; $M_\infty = 0.6$, $\alpha_s = 0^\circ$, $Z_p/D = 1.0$.

RECENT EXPERIMENTAL EFFORTS IN STORE SEPARATION AT DTNSRDC

KENNETH A. PHILLIPS

DAVID W. TAYLOR NAVAL SHIP RESEARCH AND DEVELOPMENT CENTER

ABSTRACT

In the early 1960's much of the philosophy and procedures used today for captive trajectory testing was developed at the David W. Taylor Naval Ship Research and Development Center (DTNSRDC). After limited use of these procedures in the late 1960's and early 1970's, the system was inactive for several years. In the past few years, work in this area has been restarted, and several programs have been completed. The support system has been used in the captive trajectory (CTS) mode, grid mode, and pressure survey mode. Extremely good agreement has been seen for CTS data when compared with flight test results. These data have been used to guide flight test planning and to study control system acceptability. Grid data, collected on several stores, provided the means to investigate control systems and to parametrically examine other launch variables. In addition, pressure field data have been generated in support of analytical separation programs. In some cases, scale problems were encountered and have been successfully solved.

INTRODUCTION

From the time aircraft were first pressed into service as launching platforms for weapons, there have been problems with safely launching or firing those weapons. The firing of a gun through a propeller and the release of bombs so as not to damage wing struts, landing gears, or empennage are examples of early problems encountered. Generally, these problems were solved by modifying flight hardware or by some change in flight procedures. However, as the use of aircraft for this purpose increased and, more importantly, the use of external carriage increased, the seriousness of this problem became greater. In addition, the increase in flight speed as technology progressed compounded the problem by imposing greater loads on the weapons and carriage equipment.

Another important factor which added more complexity to this problem was the larger number of aircraft configurations and weapon carriage arrangements being introduced. Several wing planforms became common place. Weapons carriage at many stations on the wings and fuselage using several multiple carriage racks appeared. These various configurations produced many different types of airflow in which weapons had to be launched. The carriage and launch equipment add more variation to this problem by affecting this airflow in different ways and by providing different ejection characteristics during launch. In addition to these aircraft-related differences, the weapons presented a wide range of mass properties and aerodynamic stability characteristics. From very low density articles, such as fuel tanks, to very dense general purpose bombs, the full range of mass properties were encountered. Also, stability of the weapons during launch varies greatly from instability to very stable.

This severe environment and the greater number of different weapon configurations made it very difficult to predict with which weapon and under what conditions a problem would develop. Therefore, it became necessary to conduct extensive flight testing before a weapon was introduced to the operating forces. Since most other flight problems had been successfully solved with sub-scale models in wind tunnels, methods were developed to study weapon separation in the same fashion. These testing techniques fall into four basic categories: dynamic drop, computer/tunnel trajectory simulation, grid data survey, and flow field mapping. Although dynamic drop testing is done in the wind tunnels at DTNSRDC, this paper will concentrate on the other methods.

These methods, computer/tunnel trajectory simulation or captive trajectory method, grid data survey, and flow field mapping, use a dual support system. Much of the early work to develop the concept and the mathematics for these testing techniques was done at DTNSRDC in the late 1950's and early 1960's.^{1,2} These reports address both the use of a computer controlled captive trajectory system (CTS) and the use of grid data collected using a weapon model in the flow field of an aircraft. These pioneering efforts led to the development of a dual support system in the 7- by 10-foot transonic wind tunnel at DTNSRDC. This system was used on several test programs during the early 1960's, but was hampered by mechanical problems and the lack of computer facilities. In the late 1960's a new support system was obtained, increased computer capability was purchased, and new software was developed. With these new components several successful programs were conducted in the early 1970's. Grid data for comparison studies^{3,4} were produced with this system as well as a separation of the HARPOON from the P-3.⁵ For several years, the system was used very little with only one study reported.⁶

In the late 1970's, a commitment was made to reactivate and update the system for use in Navy programs. These efforts will be discussed in this paper to summarize the recent developments and to illustrate the capabilities of the present system. These efforts include CTS testing, grid data generation, and flow field mapping using flow angularity probes.

DESCRIPTION OF TESTING TECHNIQUES

The three testing techniques presented use the dual support system in the 7- by 10-foot transonic tunnel. An aircraft model is mounted inverted on the main support system. Either a weapon model or a flow angularity probe is mounted on an auxiliary support system, and this support system allows access to the volume beneath the aircraft model. A typical installation is shown in Figure 1. The following sections describe the procedures for using the system with the various test techniques.

CAPTIVE TRAJECTORY SYSTEM (CTS)

When using the CTS technique, the support system is on-line with a computer in a closed-loop operation. The tunnel is brought to the desired Mach number and the aircraft model set to desired attitude. The weapon or store is then manually placed in the position where the trajectory begins. This initial point can be a stowed position or another position where motion parameters are known.

From this initial point, data are read from the balance in the weapon, and aerodynamic forces are computed for full-scale conditions of the launch. In these calculations, aerodynamic forces are adjusted for scale and altitude. The forces and moments due to dynamics, ejectors, thrust, and controls are computed and added to the adjusted aerodynamic forces and moments. With these forces, the equations of motion are solved, and the motion of the store is predicted. The support system is then placed under computer control, and the store is moved by the computer to the predicted position in the flow field. In determining the location of the store in the tunnel, sting deflection and aircraft movement are accounted for. This process is continued until safe separation is demonstrated or the weapon contacts the aircraft. In addition to the Mach number and altitude conditions, the software can account for the attitude of the aircraft flight path, vertical acceleration by the aircraft, and accelerations of the aircraft along the flight path. Throughout this interactive process, the computer is continually checking tunnel conditions, balance loads, and data accuracy to ensure accurate trajectory simulations.

GRID DATA COLLECTION

To compute a trajectory using grid data, a two-step process is utilized. Force and moment data are collected from a balance in a weapon throughout a volume beneath the launch position on the aircraft. The size and location of this volume is selected to contain the expected trajectory of the store when launched. This collection of data, or grid of data, is then used as input to a six-degree-of-freedom trajectory program and interpolated as necessary. As with the CTS technique, these data are corrected to full-scale conditions, and other forces and moments are mathematically accounted for.

The collection of these data can be done with two procedures at DTNSRDC. The first is a mechanical system which sweeps the store in vertical planes taking data on a time trigger at random positions in the flow. By manually changing the attitude and starting location, an entire volume can be covered. These data will not be recorded at any prescribed location in the aircraft flow field, and if the computer program to use these data is designed for data in specified location, another step of interpolation is required. The other method employed for collecting data resolved this problem by having the computer on-line to position the model and account for deflections and aircraft attitude. In many cases, software which makes use of grid data is designed to work with data at specific points relative to the aircraft. It is, therefore, imperative to have this computer controlled acquisition system.

FLOW FIELD SURVEY

Obtaining data in a flow field survey is similar to generating a data grid. For a flow survey, an angularity probe is used in place of a store, and the flow velocity (speed and direction) at points in the aircraft flow field is recorded. This information can then be used to calculate forces and moments on a weapon in the flow or to verify or correct analytical prediction of flow parameters. Generally, these data are taken using the computer control technique, as opposed to the mechanical system, since specific locations are desirable. In addition,

the technique using the mechanical system for taking grid data records data while the support system is moving in the vertical plane. This movement has little effect on the balance readings; however, for pressure measurements, errors may result from the reaction time of the measuring system.

RESULTS OF RECENT EFFORTS

In recent years, several test programs have been completed using the dual support system in various modes. During that time, changes have been made to accommodate tunnel power restrictions and data requirements. These changes have increased data rates and added versatility to the testing capabilities. These changes were made to take advantage of the experience gained from previous testing and to minimize restrictions imposed by power limitations. The results presented were selected to illustrate these changes and to show examples of the work performed.

HARPOON MISSILE SEPARATION

An example of the use of the support system in the CTS mode is the separation study of the HARPOON missile from the A-6E aircraft. This program provided an opportunity to exercise many changes to the CTS software, and later a flight test provided data with which a correlation study was performed. In the wind tunnel study, launches from both wing stations were performed with various loadings of fuel tanks and HARPOON's on the other stations. Variations of Mach number, altitude and flight path angles were studied as well as aircraft load factor. The primary objective of the test was to provide information to aid in the planning of a flight test program. A secondary objective was to determine if the roll authority of the control system was sufficient to stabilize the missile in roll when the control system was activated. This was done by defining the rolling moment and roll rates as accurately as possible during the wind tunnel separations and comparing those values (scaled to full scale) with the estimated capabilities of the control system.

There were about 70 trajectories performed during this test with no separation problems encountered. During several trajectories, rather high roll rates were experienced, but all were determined to be within the capability of the control system. These data were instrumental in obtaining clearance for flight tests during which four launches were made with boilerplate aerodynamic test vehicles (BATV) of HARPOON. These flight tests provided data for correlation with the wind tunnel results.

The flight test plan called for two drops at a low dynamic pressure, a condition expected to produce the greatest pitching motion, and two drops at high dynamic pressure which was expected to produce the highest roll rate. Due to either data collection problems or a mismatch in launch conditions, there was only one flight for which wind tunnel data was available. This launch was from the inboard pylon with a 300-gallon tank on the outboard station at an altitude of 3,050 ft in straight, level flight at Mach 0.79. The mass properties of the BATV were similar to the design properties of the HARPOON; however, the moments of inertia were slightly low and the center of gravity was more forward making the vehicle more stable. This condition was chosen for a repeat run during the wind tunnel test giving another set of data for correlation.

Figures 2, 3, and 4 present the data for runs 25 and 45 of the CTS test and the flight test results from the BATV-4 drop. The data selected for presentation are considered to be representative of the data taken and show all significant motions during separation. In Figure 2 near perfect agreement is seen for the vertical displacement during separation. Some disagreement is seen in pitch angle; however, there are several factors that could contribute to this disagreement. Table 1 compares the inertia properties of the BATV and the properties used in the CTS test. Several characteristics would contribute to data mismatch. First the more forward c.g. location of the BATV increased stability causing a faster response to pitch disturbances and, in addition, the lower moment inertia adds to this higher response. These two effects produce a stiffer system in pitch and increase pitch rates.

The correlation of data in the yaw plane is shown in Figure 3. Generally, these data compare favorably. Agreement of the repeat runs during the wind tunnel test appears to be very good with some slight differences with flight test data in the spanwise displacement. The data for yawing motion correlate extremely well.

As mentioned, the high Mach number (high dynamic pressure) conditions were chosen because these should produce the highest roll rates for the HARPOON during separations. As can be seen in Figure 4, high roll rates and significant roll displacements were experienced. The rolling motion showed the greatest disagreement between CTS and flight test data with the flight test producing significantly higher roll rates and, therefore, higher roll angles than the windtunnel test. Although the moment of inertia of the BATV was low, that difference was not enough to account for these large differences. The flight test data show a very high roll acceleration at initiation of the launch indicating large rolling moment in the stowed position. During the wind tunnel test it was noted that very high gradients in the rolling moment near the stowed position were present. Therefore, slight differences in the spacing from the pylon at launch could account for the disagreement in these data. In addition, due to the small scale the magnitude of the rolling moment produced by the wind tunnel model was very difficult to read. Because these moments were small compared to the balance capabilities, some inaccuracy was expected.

In general, very good agreement was shown with this limited amount of data. The correlation was especially good for those motions critical to safe separation (vertical displacement, pitch, and yaw motion). The data seem to support the contention that special care needs to be taken to reproduce the conditions at launch as faithfully as possible to ensure a true representation of the launch trajectory.

SEPARATION STUDIES OF THE BQM-74C

In an effort to expand training capability at sea, the ground-launched, MQM-74 target vehicle has been modified for carriage and launch from aircraft. The air-launched configuration, BQM-74C, was designed for use on several Navy aircraft, including the A-6 and A-4, to provide the fleet with launch platforms that would be available at sea. This would minimize the need for support from land-based aircraft during practice exercises. Since this target vehicle is relatively lightweight and has a high wing loading, separation characteristics were of concern. In addition, rolling moments created by flow on both aircraft

needed to be investigated to ensure that they did not present problems for the control system. The flow around the A-6 wing stations has caused rolling moments for other stores, and the carriage position on the A-4 places the target's outboard wing in front of the swept leading edge of the aircraft wing causing rolling moments due to gradients in the upwash. Although the roll control system is active during separation, the limit of its effectiveness was an area of concern. To simulate the roll control system, the store was not allowed to roll; however, the rolling moments were recorded and these moments were compared to the control system capabilities.

The primary objective of this program was to define a safe separation envelope for the flight test program. A range of flight conditions were run to cover the Mach number/altitude region to be used for launch. Most trajectories were started from level flight with thrust on the BQM-74C and with several pitch control surface settings. The study of control surface settings provided guidelines as to what conditions allow the safest launch envelope.

This program started with a captive trajectory system study of the BQM-74C from the A-6E aircraft, using 6.25-percent scale models in the 7- by 10-foot transonic wind tunnel. Generally, the first part of any CTS program is a comparison of store model data with isolated aerodynamic data. In this test, an unexpected problem was encountered when the isolated data were examined. As can be seen in Figure 5, when data without grit is compared with predicted data, the normal force was non-linear and the agreement of pitching moment data was poor. Several possible causes for this nonagreement were examined (mechanical slippage, data system and data reduction errors) to no avail. Once data problems were ruled out, aerodynamic causes were investigated, model buildup data were taken, and the problem was narrowed to the horizontal tail surfaces. The traditional methods for boundary layer trip did not hold for such small surfaces; therefore, some experimenting was done. The solution that came from this was to apply transition grit lightly over the entire tail surface. The data obtained with this change are also shown in Figure 5. In the test program with the A-4 aircraft, a 10-percent model was used, and similar problems were encountered. The same approach again produced data that agreed with previous results.

After obtaining satisfactory isolated data, approximately 36 trajectories were run on each aircraft. The conditions for these trajectories were spread over a range of Mach numbers and altitudes to cover the entire launch envelope. The objective was to show safe separation and determine pitch control settings that provided good separation characteristics. The majority of the trajectories were run with thrust on the BQM-74C and the roll control system simulated by not allowing the store to roll. A few runs were made with no thrust and roll permitted. These runs were to simulate an emergency jettison condition or a failure of the control system.

Figure 6 presents typical data from the CTS study. These data show the effect of control deflections for a launch from the A-6 outboard wing station. The conditions for these data were the worst encountered during the test with low altitude and high dynamic pressure. As can be seen, a 3 deg deflection to give the store a nose-down pitching moment is sufficient to provide safe separation.

The other area of investigation, jettison conditions, proved to be equally successful. The concerns here were two-fold. Without an active control system, the store may roll a wing or tail surface into the pylon or with no pitch control deflection the store may fly into the aircraft. The data show that neither of these events occur. The store cleared the pylon before the roll angle was high enough to hit the aircraft, and with the high roll angles the lift vector is rotated to where the store did not exhibit any motion toward the aircraft.

The trajectory data from the test of the A-4 show equally safe separations. In the stowed position, rolling moments were higher than those on the A-6; however, since the store was not allowed to roll (control system simulation), the trajectories were not affected. These rolling moment were expected since in the stowed position the outboard wing of the BQM-74C was forward of the A-4 wing leading edge, placing that wing more into the upwash of the wing. These rolling moments decreased rapidly as the store dropped from the aircraft. As on the A-6, the jettison tests show that the rolling moments cause enough roll to prevent the development of high forces that would lift the store back toward the aircraft. However, the ejector produced enough acceleration to have the store clear the aircraft before the roll produced any collision.

PRESSURE SURVEY OF A-6

In an effort to analytically study the separation of stores from the A-6 aircraft, a mathematical model of that aircraft was developed. To verify the validity of this model, experimental data were needed for comparison, and very little wind tunnel testing relating to store separation had been done on the A-6 aircraft. Therefore, it was desirable to obtain basic flow field data for correlation with analytical predictions.

Using a flow angularity probe mounted on the support system, a grid of points were surveyed beneath each station on the left wing and centerline in the station plane at the points illustrated in Figure 7. Data were taken at these points for two Mach numbers and two angles of attack, with and without pylons. From these data, velocity perturbations were computed throughout the flow field.

Figure 8 presents a sample of these data taken at the inboard wing station with the pylon in place. As can be seen, expected trends are present in these data, and a limited amount of correlation has shown good agreement; however, additional work is needed.

FUTURE PLANS

Throughout these testing efforts, improvements have been made to the equipment and operating procedures. However, there are several additional changes that are planned which will increase utility and versatility of these test techniques.

The primary link in the improvement process will be the conversion to a new computer system. The software for CTS operation is now limited by memory capacity of the computer being used, but conversion to a new machine will eliminate this problem. This greater memory capacity will allow control systems to be added to the CTS software as well as permit improved printout and data handling. This new equipment will have graphics capability, and plans are being made to make use of this feature.

The new computer system will also allow other improvements in the operating software. By expanding the software, several optional packages will be selectable ranging from CTS operations to automated collection of isolated data on the store. With the peripheral equipment available, the handling of input constants will be streamlined to improve testing efficiency. In addition, software will be developed to improve procedures for doing sting deflections and balance check loading, shortening installation time considerably. In converting the basic CTS software for the new computer system, major improvements will be made in the operations of the computer/CTS system which will streamline the interface between the operator and the equipment. The system will be more automated such that less input from the operator is necessary; however, increased information for monitoring the operations will be made available. This will allow the system to work more efficiently and yet provide engineers with more data to judge performance during testing.

In addition to these major changes, smaller improvements are planned for the support system that will increase versatility of all the testing techniques. Changes to the mounting system for the parent model are planned which will allow easier access to various positions on the model. Relative motion due to wind tunnel air loads have caused problems in the past. Several improvements are being sought that will solve these problems.

REFERENCES

1. Bamber, M.J., "Two Methods of Obtaining Aircraft Trajectories from Wind Tunnel Investigations," AERO Report 970 (AD 233198), David Taylor Model Basin, Washington D.C. (Jan 1960).
2. Nichols, J. H. Jr., "A Method for Computing Trajectories of Store Launched from Aircraft," DTMB-R-1378 (AD-612515), David Taylor Model Basin, Washington D.C. (Nov 1964).
3. Maddox, A.R. R.E. Dix and G.R. Matasitis, "In-Flight Measurements of Captive Loads on a Store as Compared with Wind Tunnel and Mathematical Simulations," Naval Weapons Center TP 6026, China Lake, California (Apr 1978).
4. Maddox, A.R. "Store Separation Trajectory Analysis," Naval Weapons Center TP 6067, China Lake, California (Jan 1980).
5. McCabe, E.F., Jr., "HARPOON/P-3 Orion Separation Program," Presented at JTCL Aircraft/Store Compatibility Symposium, Sacramento, California (Sep 1973).
6. McCabe, E.F. Jr., and D.W. Lacey, "Aerodynamic Feasibility for Airborne Retrieval of a Remotely Piloted Vehicle," David Taylor Naval Ship Research and Development Center Report 76-0043, Bethesda, Maryland (Nov 1976).

TABLE 1 - HARPOON TEST CONDITIONS

PARAMETERS	FLIGHT TEST	WIND TUNNEL TEST
Altitude (ft)	3050	2993
Mach No.	0.79	0.80
C.G. Position (MS)	83.03	83.08
Inertia (slug-ft ²)		
X	6.4	6.9
Y	340.2	360.9
Z	342.2	360.7
Weight (lbs)	1149	1145



Figure 1 - Typical CTS Installation

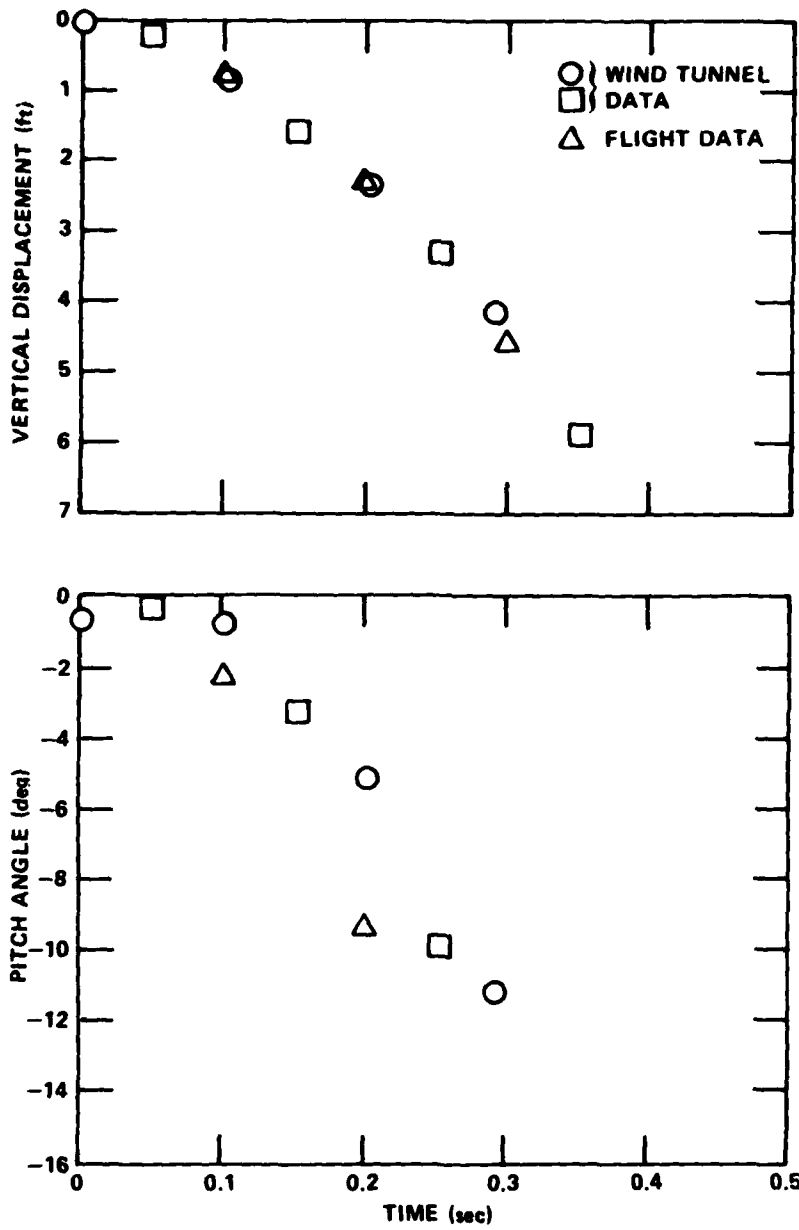


Figure 2 - Pitch Plane Motion

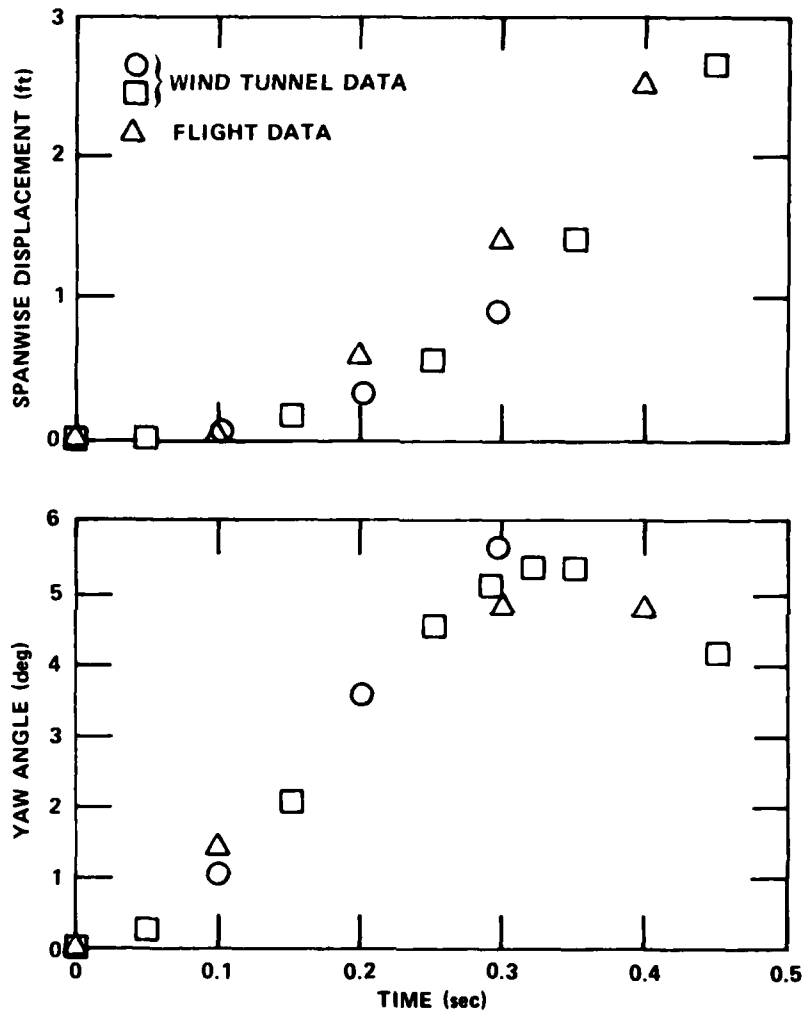


Figure 3 - Yaw Plane Motion

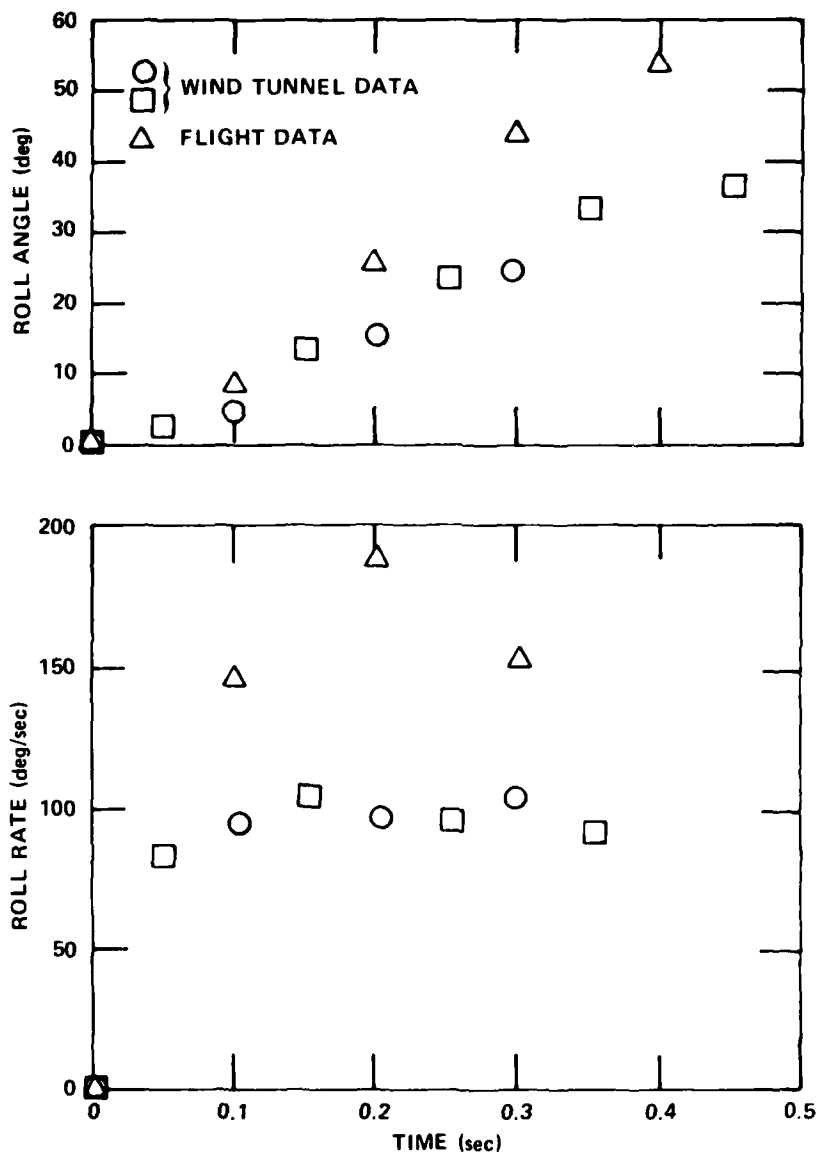


Figure 4 - Roll Motion

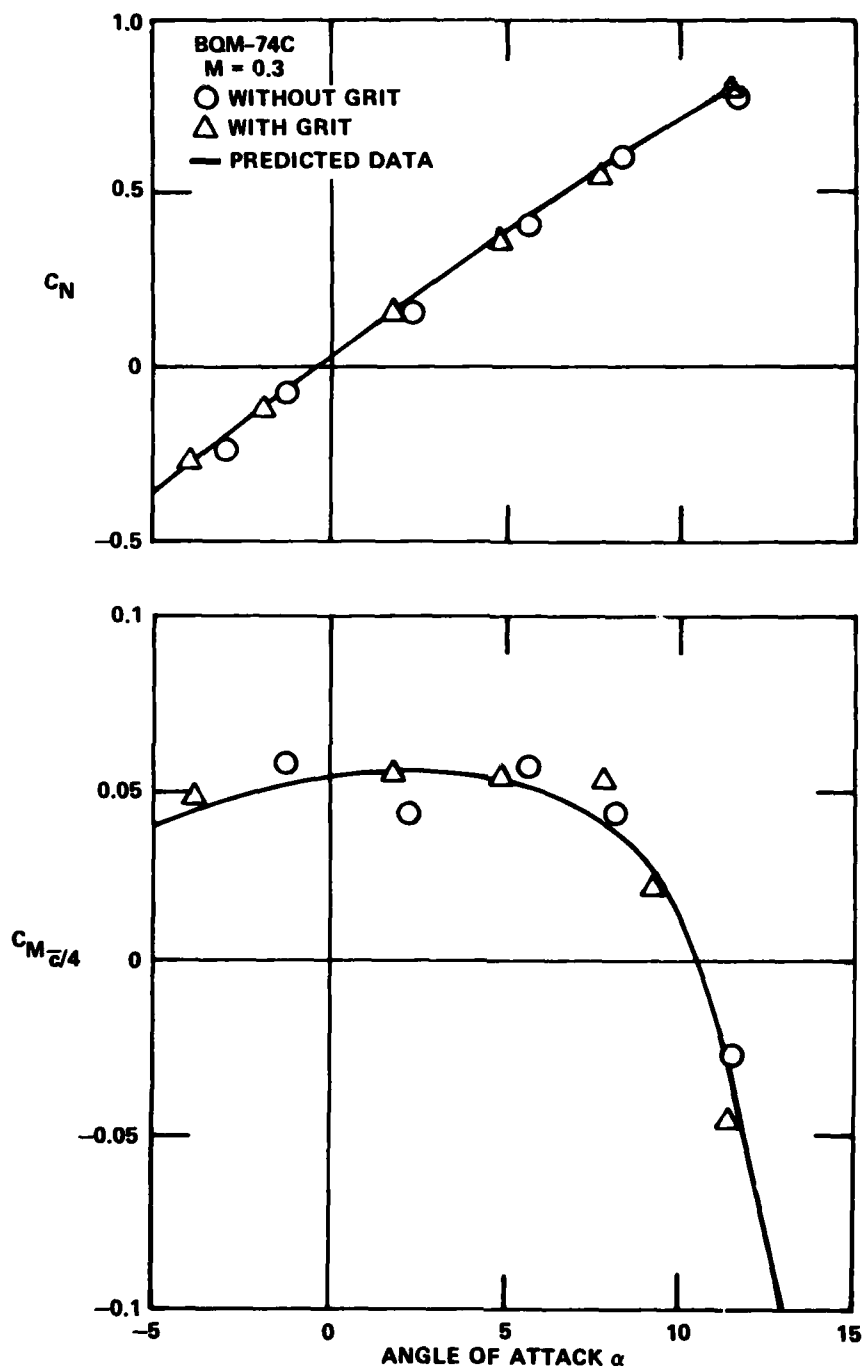


Figure 5 - Isolated Data for BQM-74C

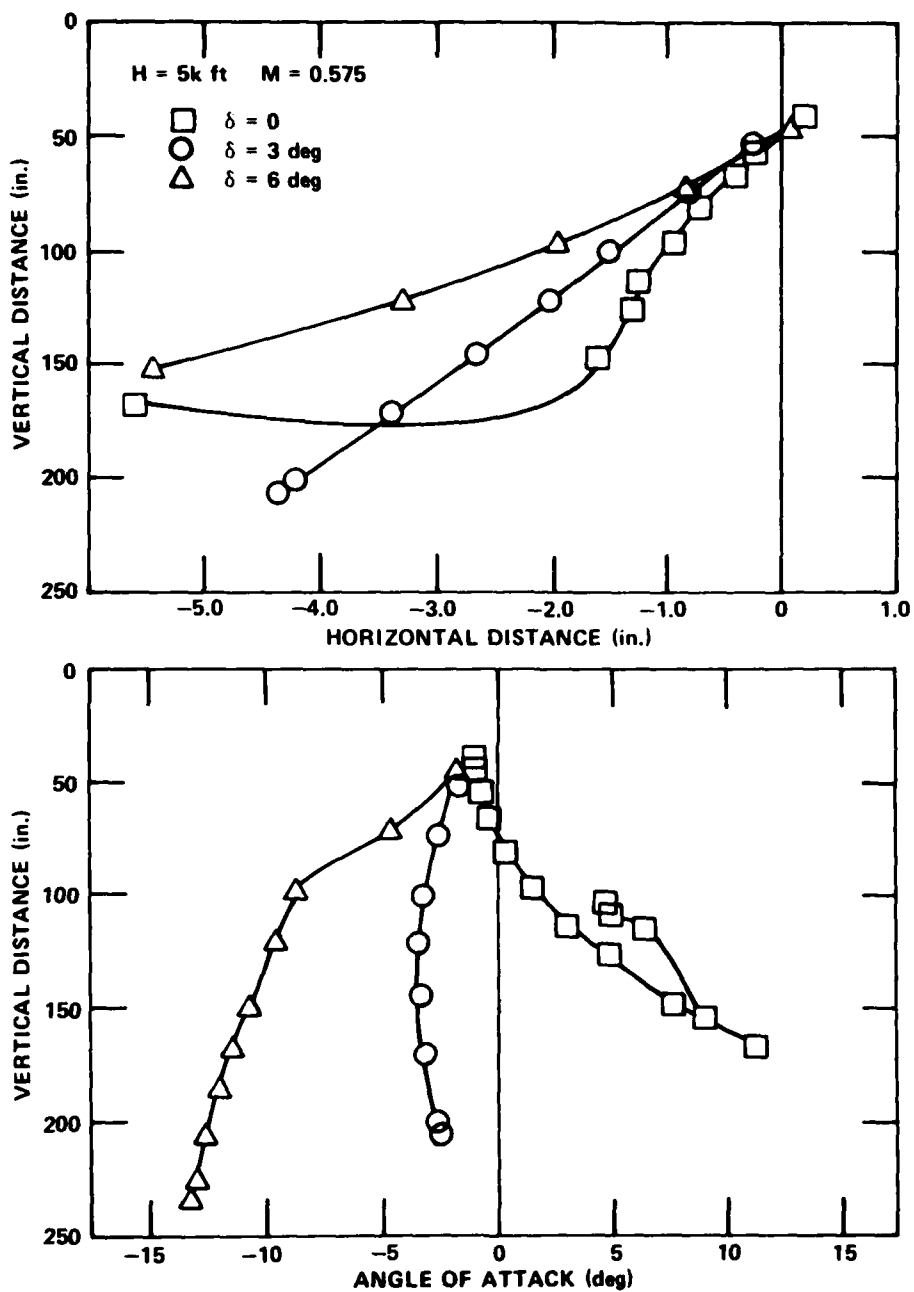
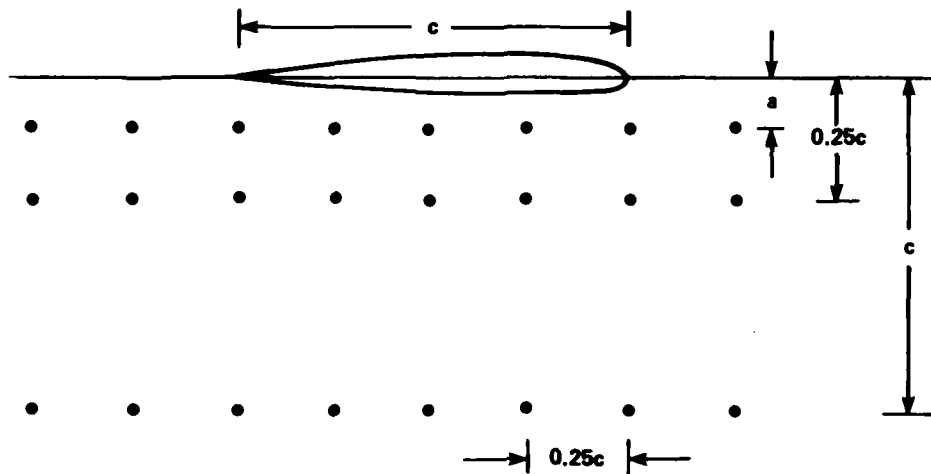


Figure 6 - Effect of Control Deflection on Separation Characteristics of BQM-74C



- c** - LOCAL CHORD LENGTH
- a** - DISTANCE FROM WING PLANE TO THE CENTERLINE OF A MK-81 ON THE PYLON

Figure 7 - Pressure Survey Grid

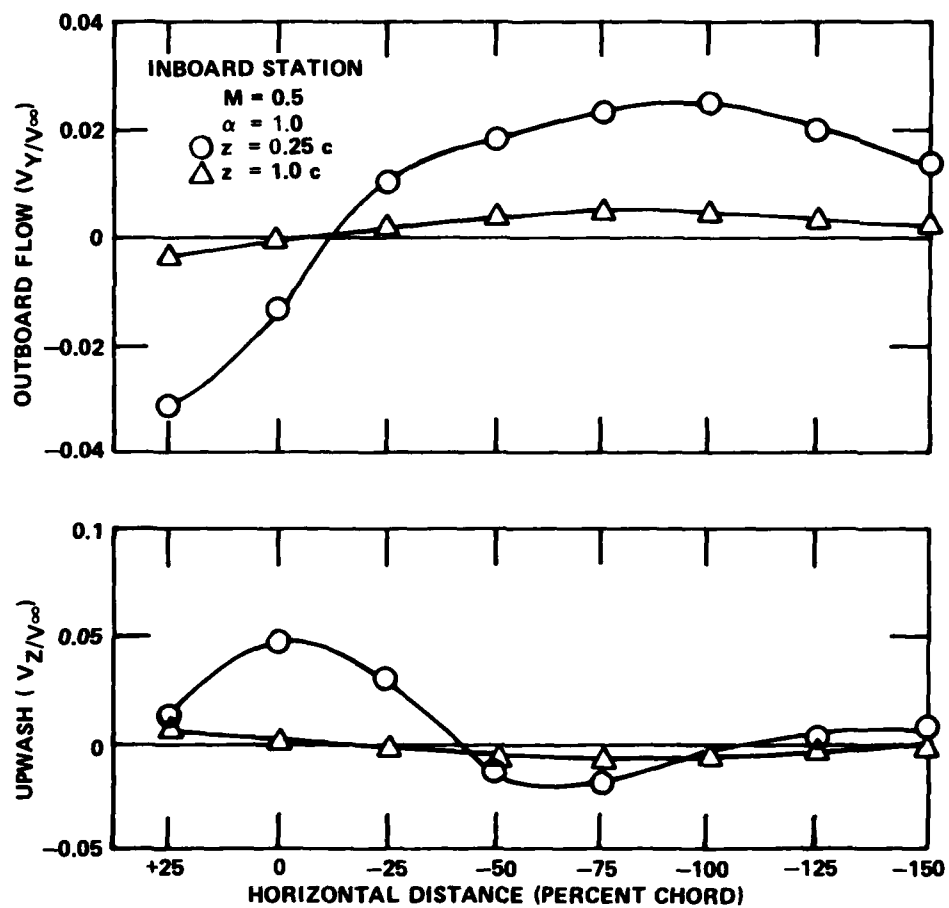


Figure 8 - Perturbation Velocity Beneath A-6 Inboard Pylon

COMPUTER PROGRAM FOR SIMULATING THE SIX-DEGREE-OF-FREEDOM MOTION OF MISSILE DEBRIS FRAGMENTS

Michael J. Hensch
Nielsen Engineering & Research, Inc., Mountain View, California

ABSTRACT

The rational modeling and empirical correlations used to build a comprehensive computer code for simulating general six-degree-of-freedom motions of missile debris fragments are described. The approach is deterministic in that a number of possible generic fragment shapes were defined, methods were selected to describe the aerodynamic loads on these shapes, and the results were incorporated in a six-degree-of-freedom trajectory program. The method chosen is simple enough to avoid large computation times and yet represents coning and tumbling conditions as well as trimmed flight.

INTRODUCTION

NAVSEA has an extensive program concerned with point defense of targets against incoming missiles. When a defensive weapon system damages an attacking missile, the trajectories of the debris fragments remain of interest, since they may hit the target or nearby areas and cause significant damage. Clearly, the possibility of such an occurrence increases with decreasing intercept distance and with increasing attacker velocity. To determine minimum intercept distances for a given level of probable damage, it is necessary to estimate the trajectories of the various portions of debris following a missile breakup. This requires calculation of the aerodynamic forces and moments over $0-180^\circ$ angle of attack range and a wide range of flight speeds, angular rates and acceleration conditions. The methods, of course, are also applicable to range safety calculations.

Under contract with NAVSEA, Nielsen Engineering & Research, Inc. (NEAR) has developed engineering methods for prediction of the aerodynamic characteristics of missile debris fragments in six-degree-of-freedom motion. The purpose of this paper is to outline those methods, to describe the resulting computer program, DEBRIS, and to give representative sample calculations.

OVERALL APPROACH

To be useful, the methodology adopted for the simulation of six-degree-of-freedom trajectories of missile fragments must encompass realistic ranges of fragment shapes, attitudes and velocities. Although a very wide range of fragment shapes is possible, this work is concerned with a set of generic shapes which, depending on conditions, could be stable, tumble or trim to a

nonzero angle of attack. Since the various shapes can tumble or trim depending on the relative locations of the fragment center of gravity and aerodynamic center of pressure, the methodology has been designed to compute the fragment aerodynamic characteristics for pitch and yaw angles up to 180° and roll angles up to 360° . Any speed is allowed except that the empirical input for the methods described was developed for the Mach range 0.8 to 3.0.

The fragment shapes for which the methods may be used are shown in Figure 1. Note that there are three basic shapes: (1) a cylindrical body alone with circular cross section and with or without pointed nose; (2) body with one set of identical fins; (3) body with two sets of fins, each set having identical fins. Each finned section may have up to four fins set at arbitrary circumferential positions on the body.

Except for aerodynamics methodology, the basic framework for the computer program was provided by the Science Applications, Inc. (SAI) code known as MAT6. The SAI program consists of a main program, a Runge-Kutta integration subroutine, a routine to perform coordinate transformations and calculate the derivatives of the equations of motion, a table look-up subroutine for computing aerodynamic forces and moments and an autopilot algorithm. A description of the methodology and a list of the program is given in Reference 1. For the purposes of this work the subroutine supplied by SAI for the computation of aerodynamic forces and moments has been replaced by a new routine, GENERIC, and its satellite routines. The new program has been named DEBRIS.

Subroutine GENERIC and its satellite routines represent the methodology derived during the present work. They compute the aerodynamic forces and moments acting on a debris fragment given the kinematic state of the fragment and the local properties of the atmosphere. Most of the computations are done by satellite routines with GENERIC acting, in effect, as a driver program for the force and moment calculations. For a typical case, GENERIC performs the following steps as it builds up the loads for a complete fragment:

- (a) Compute forces and moments acting on the fuselage or body of the debris fragment as if no fins were present.
- (b) Compute two velocity components at the area centroid of each fin in the wing section. The first component is parallel to the body axis. The second is perpendicular to the plane the fin would occupy if it were not deflected. These velocity components include the increments due to rigid body rotation about the fragment center of gravity.
- (c) Compute the "equivalent" angle of attack for each fin in the wing section.
- (d) Compute normal force and center of pressure for each wing fin. The equivalent angles of attack computed above are used to determine the fin normal forces based on a wing-alone correlation. A similar approach is used to obtain the fin centers of pressure.
- (e) Compute overall forces and moments due to wing section. The methods of Pitts, Nielsen, and Kaattari² are used to determine body carryover loads due to the presence of the wing section.

(f) Compute wing-tail interference. At this point, an estimate is made of the interference effects of the wing section on the tail section. This is done by estimating an equivalent angle of attack for each tail fin due to the trailing vortices shed by the wing section. First, an estimate of the strength and location of those vortices over the tail section is made. Then the methods of Reference 2 are used to get the overall downwash. Finally, the appropriate components of that downwash for each fin are computed.

(g) Steps (b) through (e) are repeated for the tail section.

The program is also capable of estimating thrust effects, side forces and moments due to a transverse jet, and out-of-plane side forces and moments due to asymmetric vortex shedding. To gain confidence in the computations for debris fragments, the user can compute the static forces and moments for the complete vehicle configuration (before break-up) and compare those results with available data. Complete details of the methodology are available in Reference 3.

In the rest of the paper, the procedures used for computing body-alone forces and moments, fin equivalent angle of attack, fin forces and wing-tail interference are given. The paper is concluded with example calculations and a summary.

PROCEDURES FOR BODY-ALONE METHOD

The forces and moments acting on a slender body without fins are obtained from slender body theory augmented by the crossflow theory of Allen (Reference 4, Ch. 4). The effects of rigid body rotation about the body center of gravity have been included. However, acceleration terms (i.e. terms dependent on \dot{u} , \dot{v} , \dot{w} , \dot{p} , \dot{q} , \dot{r}) have been neglected. Two physical effects are modeled:

- (1) loading due to instantaneous values of the crossflow velocities;
- (2) loading due to apparent mass effects which arise when there is a variation of crossflow velocity with axial position on the body axis (Reference 4, Ch. 10).

When crossflow velocities are high enough compared to the axial velocity, flow separation on the leeward side of the body will occur. The effects of separation on the loading of type (1) above are accounted for by including crossflow drag. It is assumed that the type (2) loading above is unaffected by separation. This is equivalent to assuming that the apparent mass for viscous flow over a cross section of the body is the same as for inviscid flow. Since the apparent mass is primarily dependent on the body cross sectional dimension normal to the crossflow and since the separated flow affects this dimension only slightly, the assumption appears to be reasonable.

The appropriate expressions for the forces and moments have been developed previously by Goodwin et al. (Reference 5, eqs. (46)-(49) and (51)-(54)) and are presented below.

$$F_z = -\pi\rho_\infty u \int_0^\ell \frac{d}{dx_s} a^2 [w - q(x_{s,m} - x_s)] dx_s$$

$$- \rho_\infty \eta c_{d_c} \int_0^\ell a V_{CF} [w - q(x_{s,m} - x_s)] dx_s \quad (1)$$

$$F_y = -\pi\rho_\infty u \int_0^\ell \frac{d}{dx_s} a^2 [v + r(x_{s,m} - x_s)] dx_s$$

$$- \rho_\infty \eta c_{d_c} \int_0^\ell a V_{CF} [v + r(x_{s,m} - x_s)] dx_s \quad (2)$$

$$M = \pi\rho_\infty u \int_0^\ell (x_{s,m} - x_s) \frac{d}{dx_s} a^2 [w - q(x_{s,m} - x_s)] dx_s$$

$$+ \rho_\infty \eta c_{d_c} \int_0^\ell (x_{s,m} - x_s) a V_{CF} [w - q(x_{s,m} - x_s)] dx_s \quad (3)$$

$$N = -\pi\rho_\infty u \int_0^\ell (x_{s,m} - x_s) \frac{d}{dx_s} a^2 [v + r(x_{s,m} - x_s)] dx_s$$

$$- \rho_\infty \eta c_{d_c} \int_0^\ell (x_{s,m} - x_s) a V_{CF} [v + r(x_{s,m} - x_s)] dx_s \quad (4)$$

where

$$V_{CF} = \sqrt{[v + r(x_{s,m} - x_s)]^2 + [w - q(x_{s,m} - x_s)]^2}$$

The coordinate system used is shown in Figure 2. It has been assumed that c_{d_c} is independent of position along the body axis. This assumption requires that the variations along the body of crossflow Mach number and Reynolds number not be significant or

$$r(x_{s,m} - x_s) \ll v$$

$$q(x_{s,m} - x_s) \ll w \quad (5)$$

These two assumptions essentially say that the increment in velocity at any point on the body due to body rotation is small compared to the translational velocity of the body. A quick check on this can be made by considering a five foot long body traveling at sonic speed, say 1,000 feet per second. If

the center of rotation is midway along the body, the rotational speed necessary for the maximum rotational velocity increment to reach $\pm 10\%$ of the flight speed is given by

$$\begin{aligned}
 q &= 0.1 \frac{w}{(x_{s,m} - x_s)} \\
 &= \frac{(0.1)(1000 \text{ ft/sec})}{2.5 \text{ ft}} \\
 &= 40 \text{ radians per second} \\
 &= 382 \text{ RPM}
 \end{aligned}$$

Clearly, it is reasonable to assume that actual rotational speeds will not exceed this value. An additional advantage is that assumption (5) allows the integration of equations (1-4) to be carried out.

Carrying out the integrations of equations (1-4) and breaking out the linear force and moment terms so that empirical data can be used instead of slender body values gives the following expressions.

$$\begin{aligned}
 F_z &= -\frac{\pi}{2} \rho_\infty |u| w a_0^2 C_{N_\alpha} - \pi \rho_\infty u q \left[a_0^2 (\ell - x_{s,m}) + a_1^2 x_{s,m} \right] \\
 &\quad - \rho_\infty \eta c_{d_c} \left\{ w \sqrt{v^2 + w^2} \cdot I_1 + \left[w \frac{(rv - qw)}{\sqrt{v^2 + w^2}} \right. \right. \\
 &\quad \left. \left. - q \sqrt{v^2 + w^2} \right] \cdot I_2 - q \frac{(rv - qw)}{\sqrt{v^2 + w^2}} \cdot I_3 \right\} \tag{6}
 \end{aligned}$$

$$\begin{aligned}
 F_y &= -\frac{\pi}{2} \rho_\infty |u| v a_0^2 C_{N_\alpha} - \pi \rho_\infty u r \left[a_0^2 (\ell - x_{s,m}) + a_1^2 x_{s,m} \right] \\
 &\quad - \rho_\infty \eta c_{d_c} \left\{ v \sqrt{v^2 + w^2} \cdot I_1 + \left[v \frac{(rv - qw)}{\sqrt{v^2 + w^2}} \right. \right. \\
 &\quad \left. \left. + r \sqrt{v^2 + w^2} \right] \cdot I_2 + r \frac{(rv - qw)}{\sqrt{v^2 + w^2}} \cdot I_3 \right\} \tag{7}
 \end{aligned}$$

$$\begin{aligned}
M = & \frac{\pi}{2} \rho_{\infty} |u| w a_0^2 (x_{s,m} - \bar{x}) C_{N_{\alpha}} - \pi \rho_{\infty} u q \left[a_0^2 (\ell - x_{s,m})^2 \right. \\
& \left. - a_1^2 x_{s,m}^2 + I_4 \right] + \rho_{\infty} \eta c_{d_c} \left\{ w \sqrt{v^2 + w^2} \cdot I_2 \right. \\
& \left. + \left[w \frac{(rv - qw)}{\sqrt{v^2 + w^2}} - q \sqrt{v^2 + w^2} \right] \cdot I_3 - q \frac{(rv - qw)}{\sqrt{v^2 + w^2}} \cdot I_5 \right\} \quad (8)
\end{aligned}$$

$$\begin{aligned}
N = & - \frac{\pi}{2} \rho_{\infty} |u| v a_0^2 (x_{s,m} - \bar{x}) C_{N_{\alpha}} - \pi \rho_{\infty} u r \left[a_0^2 (\ell - x_{s,m})^2 \right. \\
& \left. - a_1^2 x_{s,m}^2 + I_4 \right] + \rho_{\infty} \eta c_{d_c} \left\{ v \sqrt{v^2 + w^2} \cdot I_2 \right. \\
& \left. + \left[v \frac{(rv + qw)}{\sqrt{v^2 + w^2}} + r \sqrt{v^2 + w^2} \right] \cdot I_3 + r \frac{(rv - qw)}{\sqrt{v^2 + w^2}} \cdot I_5 \right\} \quad (9)
\end{aligned}$$

where

$$\begin{aligned}
I_1 &= \int_0^{\ell} a \, dx_s & I_2 &= \int_0^{\ell} a(x_{s,m} - x_s) \, dx_s \\
I_3 &= \int_0^{\ell} a(x_{s,m} - x_s)^2 \, dx_s & I_4 &= \int_0^{\ell} a^2(x_{s,m} - x_s) \, dx_s \\
I_5 &= \int_0^{\ell} a(x_{s,m} - x_s)^3 \, dx_s
\end{aligned} \quad (10)$$

a_0 = radius of the cylindrical portion of the body

$$a_1 = \begin{cases} 0, & \text{if nose is pointed} \\ a_0, & \text{if nose is flat faced} \end{cases}$$

where η , c_{d_c} , $C_{N_{\alpha}}$ and \bar{x} are to be determined from empirical correlations. To avoid unnecessary computer run time, available methods were reduced to the simplest possible forms which did not sacrifice accuracy substantially³.

EQUIVALENT ANGLE OF ATTACK FORMULATION FOR FINS

The equivalent angle-of-attack concept is described in detail in References 6 and 7. In brief, the idea is to calculate somehow an equivalent angle of attack, α_{eq} , so that

$$C_{N_i}(\alpha_c, \phi, \delta_1, \delta_2, \delta_3, \delta_4, (\Delta\alpha_{eq})_{v_i}) = C_{N_w}(\alpha_{eq,i}) \quad (11)$$

where

C_{N_i} = normal-force coefficient acting on fin i based on planform area

C_{N_w} = normal-force coefficient acting on wing alone composed of two opposing fins with same exposed planform as fin i joined at the root chords. Reference area is the planform area.

Equation (11) represents an attempt to correlate the variations of the fin normal force due to body angle of attack, body roll angle, and fin deflection through a single parameter, α_{eq} . The quantity C_{N_w} is the wing-alone normal-force coefficient. The wing alone is obtained by removing the body between two opposing fins and joining them together at their root chords. Using experimental values for C_{N_w} allows the incorporation of nonlinear effects.

Consider the side-edge view of a fin shown in Figure 3. The first step is to compute the velocity components V_{p_i} and V_{n_i} seen by the area centroid of the fin. The velocity increments due to body rotation are included. Component V_{p_i} is parallel to the body axis. Component V_{n_i} is perpendicular to the plane the fin would occupy if δ_i were zero.

Due to flow around the body in the crossflow plane, the average normal velocity seen by points on the fin is increased. This phenomenon is known as Beskin upwash⁴ and is primarily a function of the shape, angle of attack and Mach number of the body⁷.

Using slender body theory, one can show that the ratio of the normal force acting on two opposing fins in the presence of the body with no sideslip and zero fin deflection to the normal force acting on a wing alone composed of the two fins is a function of the ratio of the body diameter to the fin span only. This ratio is called K_w .

For the present work, we shall assume that the effective normal velocity seen by the area centroid of fin i is given by $K_w V_{n_i}$ when the fin is undeflected.

As a first step in the calculation of the effects of fin deflection, we assume that fin i is the only fin on the body (no fin-fin interference). Then the velocity component parallel to the fin root chord is given by

$$V'_{p_i} = V_{p_i} \cos \delta_i - K_w V_{n_i} \sin \delta_i \quad (12)$$

The velocity component perpendicular to the fin is given by

$$V'_{n_i} = K_W V_{n_i} \cos \delta_i + V_{p_i} \sin \delta_i \quad (13)$$

To include vortex effects, the increment in fin normal velocity induced by the trailing vortices from the wing section is added to V'_{n_i} to get

$$V'_{n_i} = K_W V_{n_i} \cos \delta_i + V_{p_i} \left[\sin \delta_i + \sin(\Delta\alpha_{eq})_{v_i} \right] \quad (14)$$

A method for estimating $(\Delta\alpha_{eq})_{v_i}$ is given later in the paper.

To account for fin-fin interference, a factor Λ is applied to the deflection angle of each fin as follows

$$V'_{n_i} = K_W V_{n_i} \cos \delta_i + V_{p_i} \left[\sin(\delta_i \Lambda_i) + \sin(\Delta\alpha_{eq})_{v_i} - \sum_{\substack{j=1 \\ j \neq i}}^{NFINS} \sin(\delta_j \Lambda_j) \right] \quad (15)$$

where NFINS is the number of fins attached to the body at the axial location being considered. Hence, each fin contributes to the equivalent angles of attack of all the other fins in that section. Values for Λ_j obtained from slender body theory are given in Reference 3.

The results of Equations (12) and (15) give α_{eq_i} as follows

$$\alpha_{eq_i} = \tan^{-1} \left(\frac{|V'_{n_i}|}{V_{p_i}} \right) \quad (16)$$

Then, the force on the fin is given by

$$F_{N_i} = C_{N_W}(\alpha_{eq_i}) S_{fin} Q_i V'_{n_i} / |V'_{n_i}| \quad (17)$$

where

$$Q_i = \frac{1}{2} \rho_{\infty} (V_{p_i}^2 + V_{n_i}^2) \quad (18)$$

Methodology for computing the wing-alone normal force coefficient is given in the next section.

FIN NORMAL FORCE

The wing-alone normal-force coefficient for low aspect ratio fins has been correlated in a manner similar to that used by Allen for slender bodies⁴. The equation is

$$C_{N_w} = \frac{1}{2} C_{N_\alpha} \sin 2\alpha \cos \alpha + K \sin^2 \alpha, \quad 0 \leq \alpha \leq 90^\circ \quad (19)$$

where C_{N_α} is the linear normal-force coefficient slope and K is the drag coefficient of the wing when it is normal to the flow. In general the factor K depends on aspect ratio and Mach number. In Reference 3, correlations for C_{N_α} and K are presented. Also presented are similar correlations for high aspect ratio swept planforms and correlations for longitudinal and lateral positions of the fin center of pressure.

WING-TAIL INTERFERENCE

The method used here for the computation of wing-tail interference is essentially that of Reference 2. However, since that methodology was derived for an unrolled cruciform or monoplane missile, some modification is needed to handle the more general cases encountered for this work. The approach here is to treat the missile as if it were unrolled but with the crossflow velocity equal to $\sqrt{v^2 + w^2}$ and with the wing section developing the actual normal force component which is parallel to and in the same direction as the crossflow velocity vector as seen by the body. The methods of Reference 2 are used to compute an equivalent angle of attack acting parallel to the crossflow velocity vector at the axial location of the tail fin area centroid. That angle of attack is then resolved into components normal to each of the tail fins at their actual orientations. The mathematical details are given in Reference 3.

EXAMPLE CASES

SURFACE-TO-AIR MISSILE

For the surface-to-air missile simulation, it was assumed that the rocket motor had burned out and that the guidance, ordnance and autopilot/battery sections had been separated from the missile as shown in Figure 4. The piece of debris considered was the aft fragment. The computed static margin for the fragment was found to be negative for the transonic and supersonic speed range. Hence, the fragment can be expected to tumble if the control surfaces are not deflected.

Results for the computed trajectory are given in Figure 4. Initially, the missile is in a 10° dive. At $t = t_0$, the forebody is separated. The aft fragment is assumed to be given a slight initial q by the separation event. It immediately pitches up and rapidly tumbles. The velocity of the fragment drops quickly and the aft fragment hits the ground roughly 2,000 feet short of the aiming point. It has been assumed, of course, that the fragment does not disintegrate during the high- q pitch up. It is interesting to note that the trajectory does not appear to be ballistic until $t - t_0 = 2$ seconds.

Essentially, this means that downrange travel of the fragment would probably have been underestimated by a two-dimensional computation based on an average drag coefficient.

RYAN BQM-34A TARGET

The geometrical characteristics of the BQM-34A target as given in Reference 8 are shown in Figure 5. The debris fragment to be considered is that portion of the configuration which is aft of the dashed line in the side view (nose and engine gone). Because of the methodology limitations it was necessary to model the body aft of the fragment as a circular cylinder. Three trajectories were run for the BQM aft fragment to illustrate the effect of small changes in the predicted static margin. At the time of separation, the vehicle is assumed to be in level flight at $M_\infty = 0.75$ at an altitude of 500 feet AGL. The computed results are shown in Figure 6. During trajectory #1, the damaged vehicle pitched up to about 1.7° angle of attack and maintained that attitude until impact. During trajectory #2, the vehicle quickly pitched up to 1.5° angle of attack. It continued to slowly increase the pitch attitude until the top of its trajectory at which point the angle of attack was approximately 40° . It then nosed over and fell to the ground. During trajectory #3, the vehicle slowly pitched up to roughly 1° angle of attack. At $t - t_0 = 6$ seconds (4,000 feet downrange), it no longer had sufficient speed to maintain level flight and descended until impact.

The "trimmed" flight behavior of the BQM aft fragment as shown in Figure 6 appears to be a result of the tendency of the center of pressure of the fragment to move aft as the angle of attack is increased. Hence, it is possible for there to be an angle of attack, α_0 , such that for $\alpha < \alpha_0$ the fragment is unstable. Any slight disturbance would cause the vehicle to pitch to α_0 . This phenomenon causes the particular flight behavior encountered to be very sensitive to the center-of-pressure and center-of-gravity locations if the stability of the fragment at small angle of attack is nearly neutral.

SUMMARY

A set of methods has been developed for computing the longitudinal, lateral and control aerodynamic characteristics of a wide range of missile debris fragments. The methods have been incorporated into a computer program which simulates the six-degree-of-freedom trajectories of the fragments. Sample cases presented in this paper and in Reference 3 demonstrate that ballistic, tumbling, coning and "trimmed" flight trajectories can all be predicted for reasonable cost. Typical running times range roughly from 0.5 to 5 times real time on a CYBER 175 computer depending on the complexity of the motion. While the computer program was designed to determine the lethality of a missile once it has broken up, it can also be used for range safety studies.

LIST OF SYMBOLS

a	local radius of body, feet
a_o	radius of cylindrical portion of body alone, feet
a_1	radius of body at $x_s = 0$, feet
C_{N_i}	coefficient of normal force acting on fin i; normal force/ $Q_\infty S_{ref}$
C_{N_w}	normal-force coefficient of wing alone formed by putting together two opposing fins at their root chords; normal force/ $Q_\infty S_{ref}$
C_{N_α}	derivative of normal-force coefficient with respect to angle of attack, α , at $\alpha = 0$
c_{d_c}	crossflow drag coefficient
F_{N_i}	normal force acting on fin i, lb_f
F_x, F_y, F_z	component in body-fixed coordinate system of force acting on fragment, lb_f
K	drag coefficient of a wing when it is normal to flow
K_w	ratio of normal force acting on two opposing fins in presence of body to normal force of wing alone at same angle of attack as body; no sideslip and no fin deflection
L, M, N	components in body-fixed coordinate system of moment acting on fragment, $ft \cdot lb_f$
l	length of body, feet
p, q, r	components along body-fixed coordinates of rate of rotation of body about its center of mass, radian/sec
$\dot{p}, \dot{q}, \dot{r}$	rate of change of p, q, r with respect to time, radian/sec^2
Q_i	$\frac{1}{2} \rho_\infty (V_{p_i}^2 + V_{n_i}^2)$
u, v, w	components along body-fixed coordinates of velocity of body center of mass, ft/sec
$\dot{u}, \dot{v}, \dot{w}$	rate of change of u, v, w with respect to time, ft/sec^2
V_{p_i}	velocity component parallel to body axis at fin i area centroid with no fin deflection, ft/sec
V_{n_i}	velocity component normal to fin i at fin i area centroid with no fin deflection, ft/sec

LIST OF SYMBOLS (Concluded)

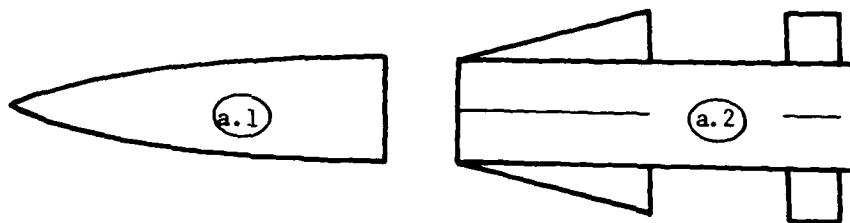
x_s	rearward distance along body axis from nose tip, ft
$x_{s,m}$	distance from nose tip of fragment to center of mass, ft
\bar{x}	axial location of center of pressure measured from nose tip of fragment, ft
α_c	angle of incidence, $\tan^{-1}(V_{CF}/u)$
α_{eq_i}	equivalent angle of attack of fin i
δ_i	deflection angle of fin i
η	parameter accounting for finite length of body, dimensionless
Λ_i	fin-fin interference factor due to deflection of fin i
$(\Delta\alpha_{eq})_{v_i}$	increment in equivalent angle of attack of tail fin i due to presence of vortices shed from wing section
ϕ	missile roll angle, $\tan^{-1}(w/v)$
ρ_∞	atmospheric density, slugs/ft ³

REFERENCES

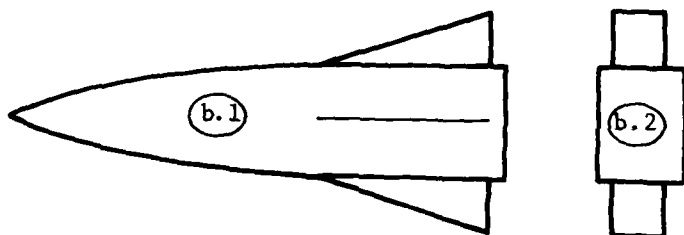
1. Anon: Baseline Six-Degree-of-Freedom Model. Science Applications, Inc. Report SAI-164-087-252, Sept. 1978.
2. Pitts, W. C., Nielsen, J. N., and Kaattari, G. E.: Lift and Center of Pressure of Wing-Body-Tail Combinations at Subsonic, Transonic, and Supersonic Speeds. NACA TR 1307, 1957.
3. Hensch, M. J.: Computer Program for Simulating the Six-Degree-of-Freedom Motion of Missile Debris Fragments, Volume I. Methods Development. Nielsen Engineering & Research, Inc., TR-220, July 1980.
4. Nielsen, J. N.: Missile Aerodynamics. McGraw Hill Book Co., 1960.
5. Goodwin, F. K., Dillenius, M. F. E., and Nielsen, J. N.: Prediction of Six-Degree-of-Freedom Store Separation Trajectories at Speeds Up to the Critical Speed. Vol. I - Theoretical Methods and Comparisons with Experiment. AFFDL-TR-72-83, Vol. I, Oct. 1974.
6. Hensch, M. J., Smith, C. A., Nielsen, J. N., and Perkins, S. C., Jr.: Calculation of Component Forces and Moments of Arbitrarily Banked Cruciform Missiles with Control Deflections. ONR-CR215-226-3, Nov. 1976.

REFERENCES (Concluded)

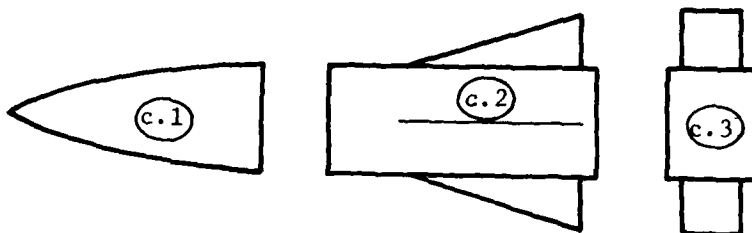
7. Nielsen, J. N., Hensch, M. J., and Smith, C. A.: A Preliminary Method for Calculating the Aerodynamic Characteristics of Cruciform Missiles to High Angles of Attack Including Effects of Roll Angle and Control Deflections. ONR-CR215-226-4F, Nov. 1977.
8. Jaseniuk, R. P.: Actual Detail Weight Report U.S. Navy Model BQM-34A Aerial Target Drone, Serial Number BQ-19626 Teledyne Ryan Model 124M. Teledyne Ryan Aeronautical Report No. TRA 12444-66, July 1976.



- (a) Nose blown off: - a.1 Noses of varying slenderness
 a.2 Cylindrical bodies with or without wings and tails



- (b) Tail blown off: - b.1 Noses with afterbodies of varying slenderness, with wing section
 b.2 Short cylindrical section with tail section



- (c) Nose and tail blown off: - c.1 Noses of varying slenderness
 c.2 Cylindrical sections of varying length, with wing section
 c.3 Cylindrical bodies with wing and tail sections

Figure 1. Possible debris fragment shapes

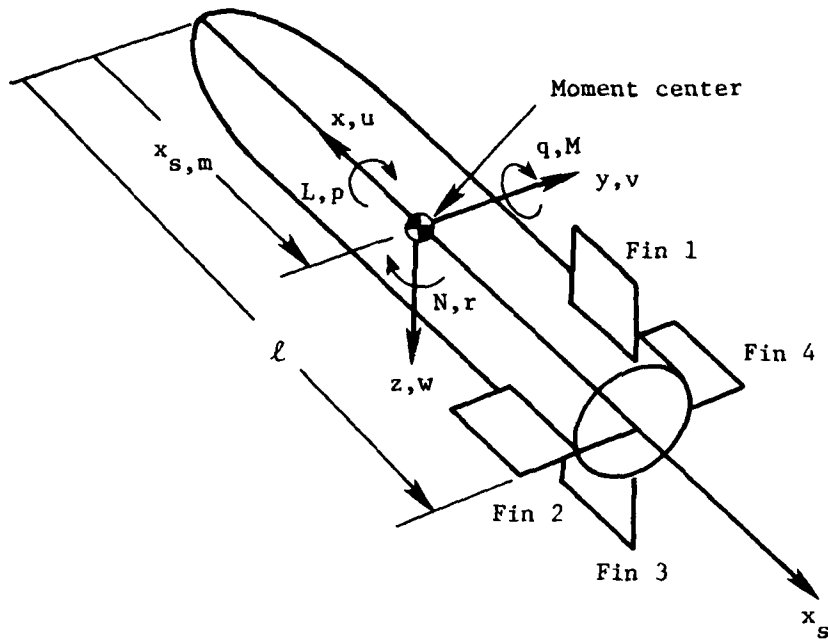


Figure 2. Coordinate system fixed in debris fragment and used in force and moment calculation

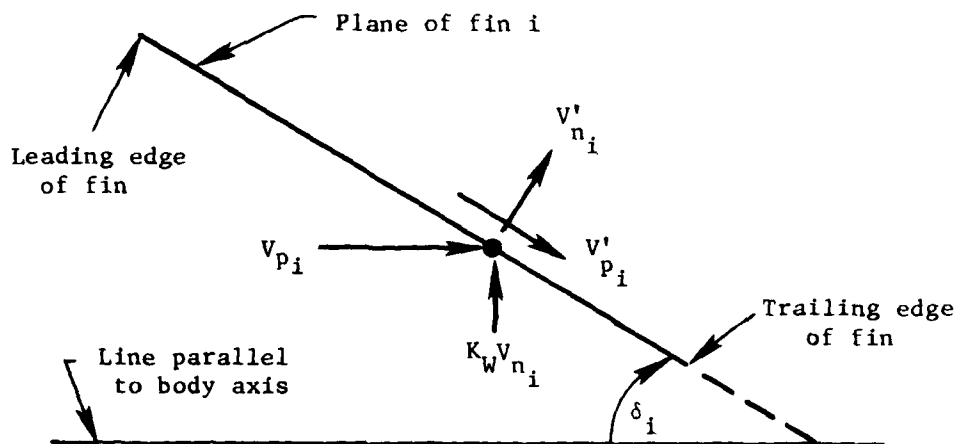


Figure 3. Side-edge view of fin i showing velocity components

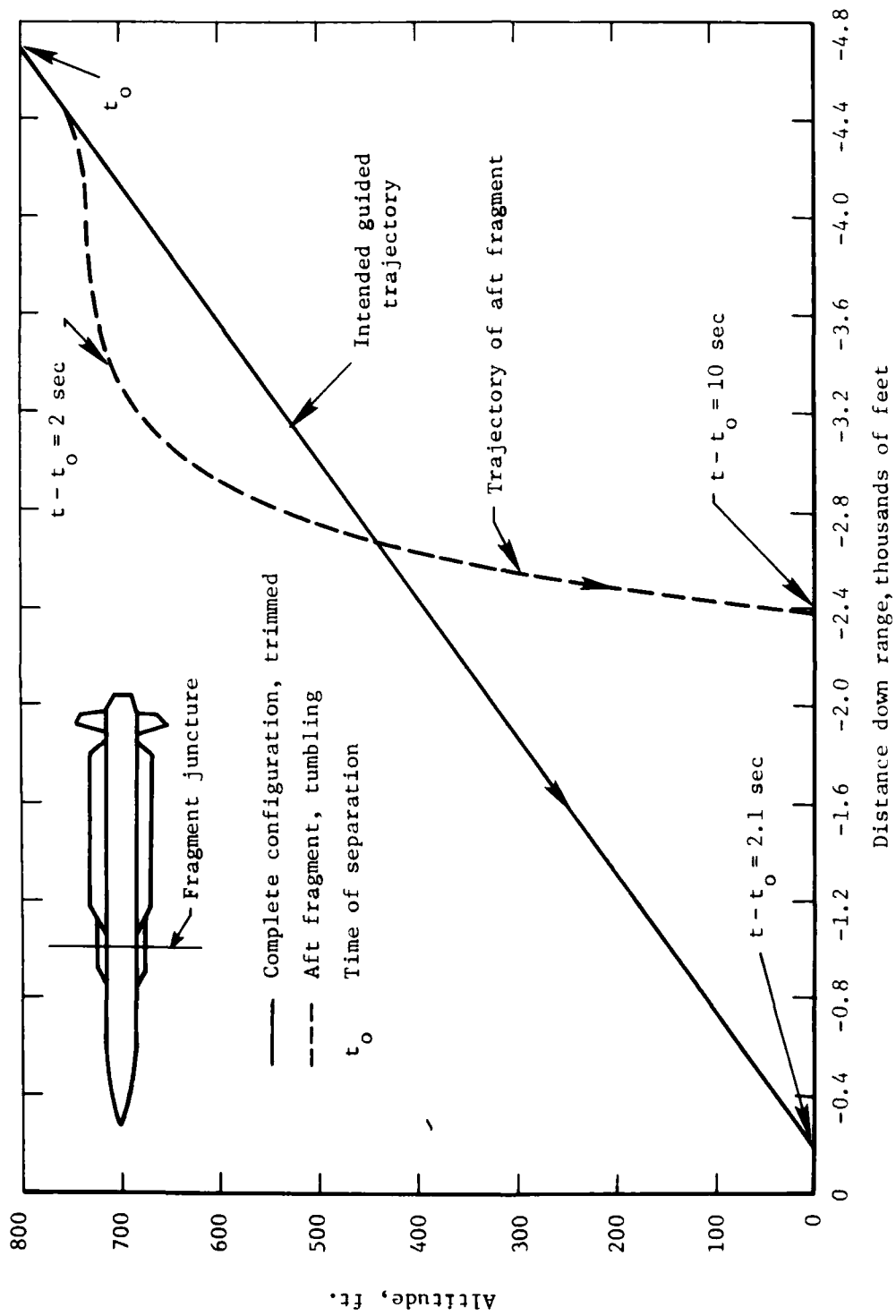


Figure 4. Simulated trajectory of surface-to-air missile

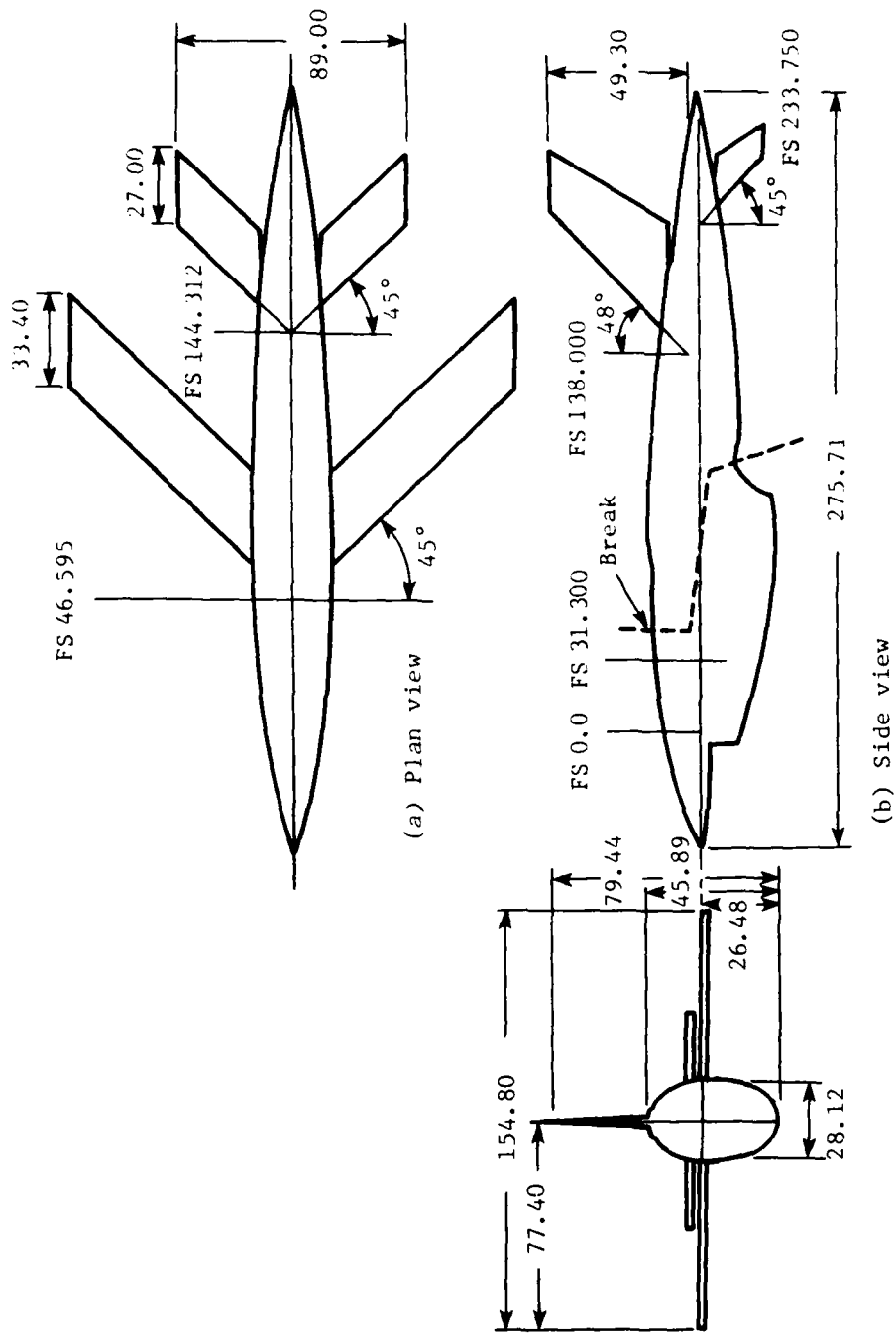


Figure 5. Dimensional data for BQM-34A target
(all dimensions and stations are in inches)

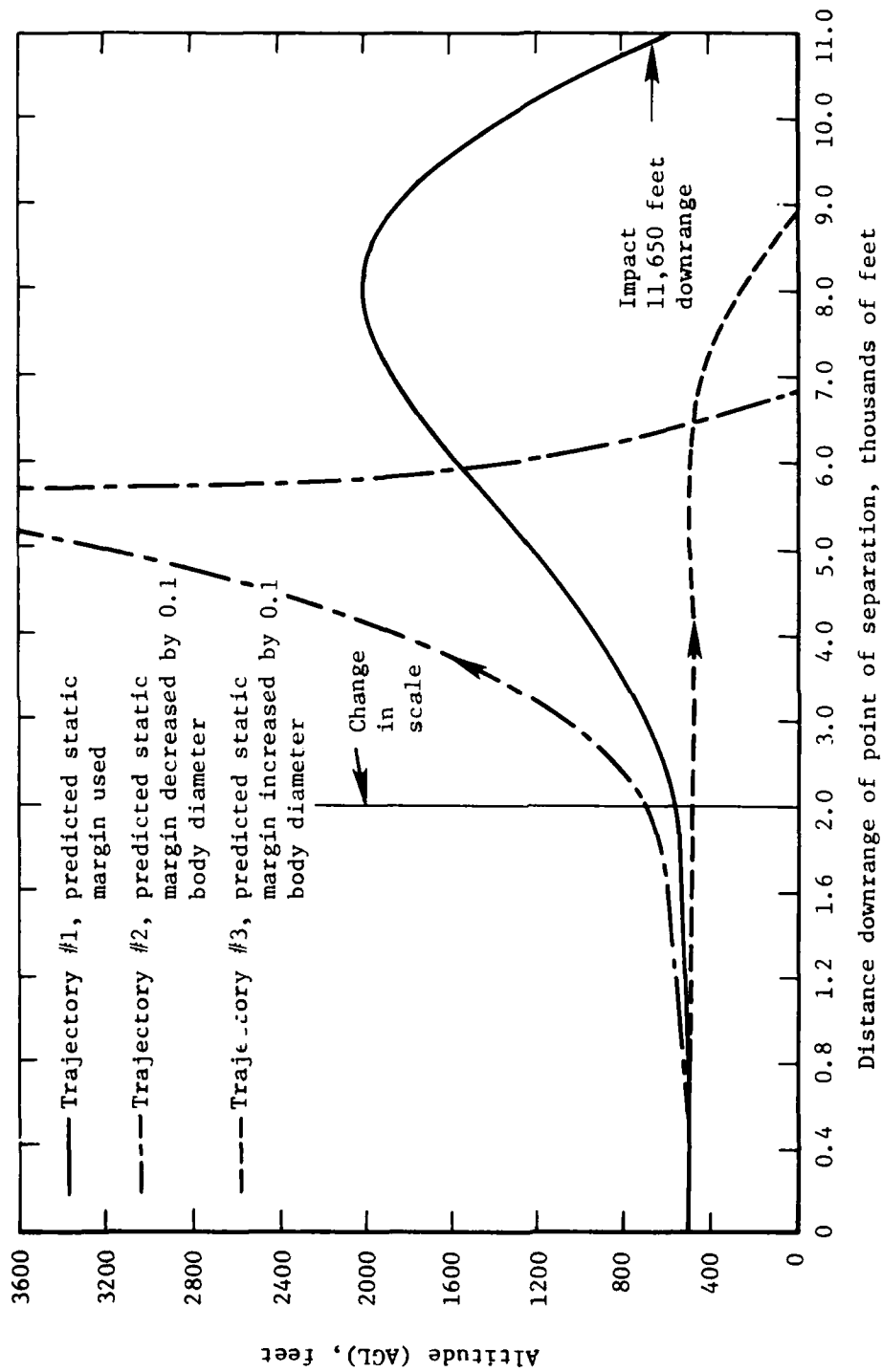


Figure 6. Simulated trajectories of BQM debris fragment

AN INFLUENCE FUNCTION METHOD FOR
PREDICTING STORE AERODYNAMIC
CHARACTERISTICS DURING WEAPON SEPARATION

R. Meyer and A. Cenko
Grumman Aerospace Corporation, Bethpage, NY

S. Yaros
NASA Langley Research Center, Hampton, VA

ABSTRACT

A method has been developed for predicting the forces and moments on a store during weapon separation based on previous wind tunnel data for another store in the same flow field. This new technique uses conventional grid survey store force and moment data and parameter identification analysis to "identify" the local angle-of-attack distribution in proximity to the parent aircraft. Predicted force and moment characteristics for other stores based on this derived angle-of-attack show excellent correlation with supersonic data. The evidence to date indicates that the method will be applicable to virtually all stores at subsonic-supersonic Mach numbers.

INTRODUCTION

Aircraft weapon system effectiveness is dependent on efficient store carriage and satisfactory weapon separation throughout the required flight envelope. Shock-wave formation accompanying supersonic/transonic flight aggravates the already difficult problem of predicting the weapon aerodynamics as it traverses the mutually interfering aircraft weapon flow field. Despite the encouraging progress in theoretical/computational techniques 1,2,3,4, the only comprehensive engineering approach at this time calls for extensive wind tunnel testing of specific aircraft-weapon combinations. Maddox, in Reference 5, notes that wind tunnel results generally show good agreement with flight data but "occasionally" will differ significantly from the full-scale result.

The cost implications of conducting an adequate wind-tunnel test program to demonstrate satisfactory weapon separation are prohibitive. The wide variety of weapon/store loadings and flight conditions that need to be evaluated cannot be accommodated. A curtailed program, accepting the risk of not uncovering some "unsafe" situations or sacrificing possible launch envelope extension to "play it safe", is inevitably the result. Past attempts to mitigate this problem by trying to generalize weapon separation data from one store to another, using isolated-store aerodynamic characteristics to account for observed differences, have proven unsatisfactory. It has long been recognized that this simple approach is unacceptable whenever the flow field angularity varies significantly over the store length, making it impossible to define an "effective α " environment.

S. Korn addresses the "effective α " limitation in Reference 6. To overcome this objection he, and others since ^{3,7}, developed the idea of distinguishing between the angle-of-attack experienced by the nose, mid-section, and tail-section of the store. Practical implementation of these concepts depended on using measured or theoretically determined parent aircraft flow field angularity data and estimating nose, mid-section, and tail-section force and moment contributions as a function of their respective local angle-of-attack. If these basic ideas are extended to their logical conclusion one is led quite naturally to consideration of an "Influence Function Method" for predicting store aerodynamic characteristics during weapon separation. The development of just such a method is described below.

TECHNICAL APPROACH

The fundamental assumption underlying the present Influence Function Method (IFM) for predicting store aerodynamic characteristics in a nonuniform flow is that the total store force and moment can be correlated with the angle-of-attack distribution along the store length. Limiting ourselves for the present to a linear correlation and a finite subdivision of the store into N elements, we see (Figure 1) that the store aerodynamic characteristics can be expressed in terms of a corresponding number of normal force (A_i) and pitching moment (B_i) influence coefficients, the zero-lift angle-of-attack (α_0), and the zero-lift pitching moment coefficient, C_{m_0} . The assumed linearity of the analytical model is not intended to suggest any restriction to linear, potential flow aerodynamics - it only implies the existence of a linear input/output relationship similar to the usual practice of approximating aircraft stability characteristics with aerodynamic derivatives obtained by sloping wind-tunnel data. Buoyancy forces are implicitly accounted for in this representation since the causative flowfield pressure gradients (Figure 2) are directly related to flowfield curvature and, hence, the angle-of-attack distribution along the store length.

Practical application of the present IFM technique depends on:

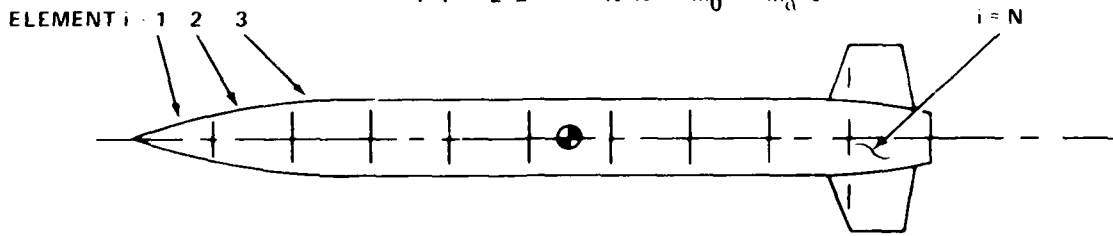
- A. Determining the A_i , B_i influence coefficients and α_0 , C_{m_0} that characterize the store aerodynamics in a nonuniform flow at the Mach number of interest
- B. Using this information and wind-tunnel-measured store force and moment data (obtained in the course of a conventional grid survey in proximity to the parent aircraft) to calculate what the angle-of-attack distribution "had to be" along the traverse to produce the observed force and moment data.
- C. Using the derived angle-of-attack and known A_i , B_i , α_0 , C_{m_0} characteristics for any "other" store to calculate the forces and moments that this "other" store would experience along the same traverse.

$$C_N = \sum_{i=1}^N A_i (\alpha - \alpha_0)_i$$

$$= A_1 \alpha_1 + A_2 \alpha_2 + \dots + A_N \alpha_N - C_{N\alpha} \alpha_0$$

$$C_m = \sum_{i=1}^N B_i (\alpha - \alpha_0)_i + C_{m_0}$$

$$= B_1 \alpha_1 + B_2 \alpha_2 + \dots + B_N \alpha_N + C_{m_0} - C_{m\alpha} \alpha_0$$

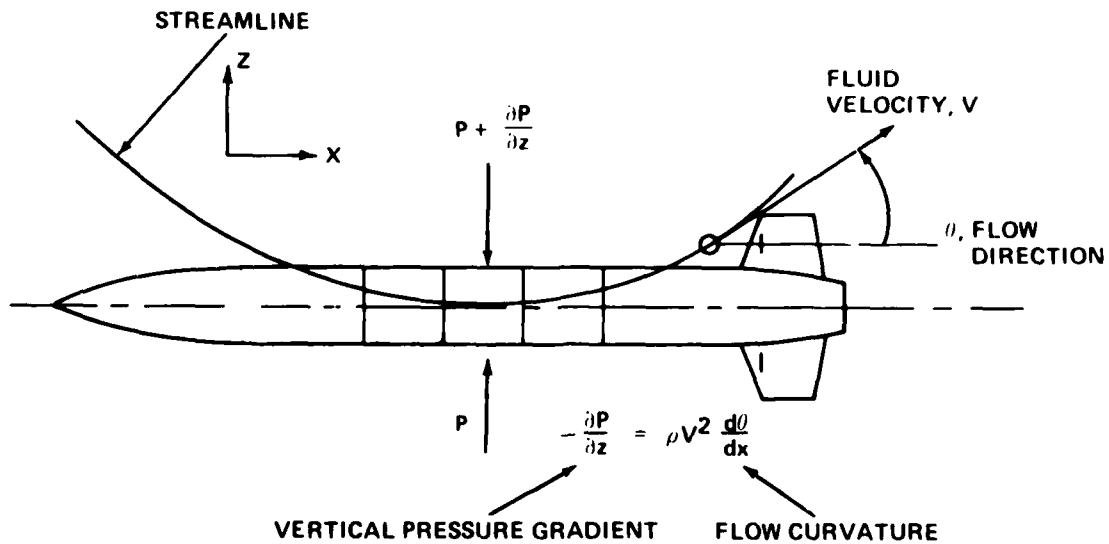


WHERE

- A_i = C_N INFLUENCE COEF FOR i TH ELEMENT
- α_i = LOCAL α AT i TH ELEMENT
- B_i = C_m INFLUENCE COEF FOR i TH ELEMENT
- $C_{N\alpha}$ ISOLATED STORE NORMAL FORCE SLOPE
- C_{m_0} ISOLATED STORE C_m ZERO LIFT PITCHING MOMENT

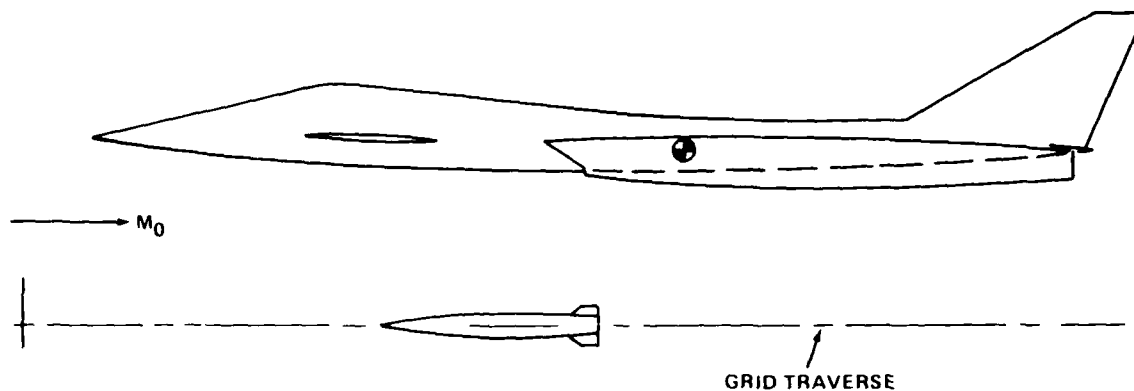
0401-001D

Fig. 1 Mathematical Model for Store Aerodynamics in a Non-Uniform Flow



0401-002D

Fig. 2 Buoyancy Forces in a Curvilinear Flowfield



IF INFLUENCE COEFFICIENTS FOR "STORE A" AND "STORE B" ARE KNOWN, THEN:

- C_m, C_N DATA FROM "STORE A" GRID TRAVERSE CAN BE USED TO CALCULATE THE α DISTRIBUTION ALONG THE TRAVERSE
- ABOVE α DISTRIBUTION & KNOWN INFLUENCE COEFFICIENTS FOR "STORE B" ALLOW CALCULATION OF "STORE B" C_m, C_N ALONG SAME TRAVERSE

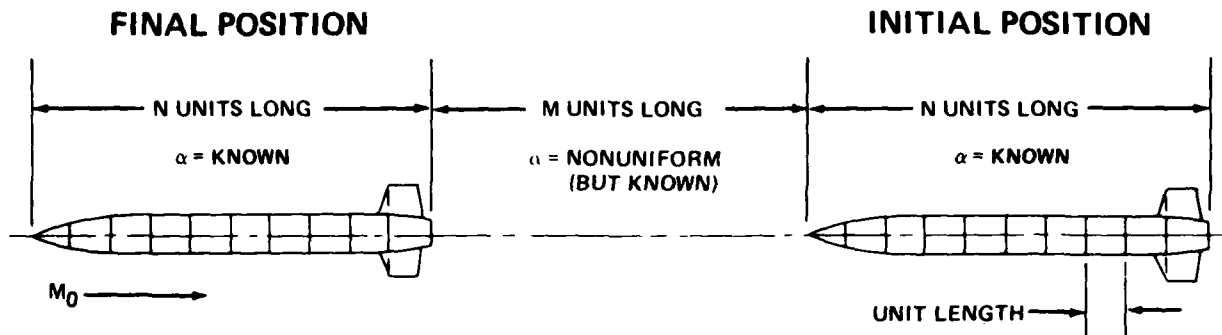
0401-003D

Fig. 3 Applying the Influence Function Method

The overall idea is summarized in Figure 3, where "Store A" designates the original store tested and "Store B" represents the store whose force and moment characteristics are to be predicted. If the foregoing A, B, C process can be successfully implemented it would mean that production grid survey force and moment data for any one store could be used to establish an experimentally derived aircraft "flowfield angularity" data bank for subsequent use in estimating the launch characteristics of other weapons without the need for additional testing. Whether such angularity data must be corrected for flowfield effects induced by the weapon itself (including proximity to the aircraft) has to be answered pragmatically. The indications are that, in most cases, one can ignore these secondary effects and still obtain satisfactory force and moment predictions to within one store diameter of the carriage position. In particularly difficult situations, or where greater accuracy is required, a theoretically determined proximity correction could be applied. The calculation of such a correction would appear to be within the capability of available methods. This subject will be revisited in the closing section of the paper after reviewing some representative data correlations.

The conceptual wind-tunnel test indicated in Figure 4 illustrates how the required store influence coefficients can be determined experimentally (Step A). The sting-mounted store to be "calibrated", i.e., whose A_i, B_i are to be determined, is traversed (downstream to upstream) through a known non-uniform calibration flowfield and the measured store balance force and moment noted. Referring to Figure 4 and assuming that force and moment data are recorded each time the store is indexed forward one store element length, we see that the $M+N$ unit long traverse defines $M+N+1$ " C_N " equations to determine the N " A_i ", $i=1$ to N , influence coefficients and α_0 . In the typical equation shown (Figure 4), the measured C_N and $\alpha_1, \alpha_2, \dots, \alpha_N$ (the calibration flow field α 's acting at each store element at that point in the traverse) are the "knowns" and the A_1, A_2, \dots, A_N , and α_0 are the unknowns to be determined.

C_N, C_M WIND TUNNEL DATA ARE RECORDED AS STORE IS INDEXED UPSTREAM FROM ITS INITIAL TO FINAL POSITION



GENERATES $1 + M + N$ C_N EQUATIONS TO DETERMINE N A_i 'S

TYPICAL EQUATION: $C_N = A_1 \alpha_1 + A_2 \alpha_2 + A_3 \alpha_3 + \dots + A_N \alpha_N - C_{N\alpha} \alpha_0$

0401-004D

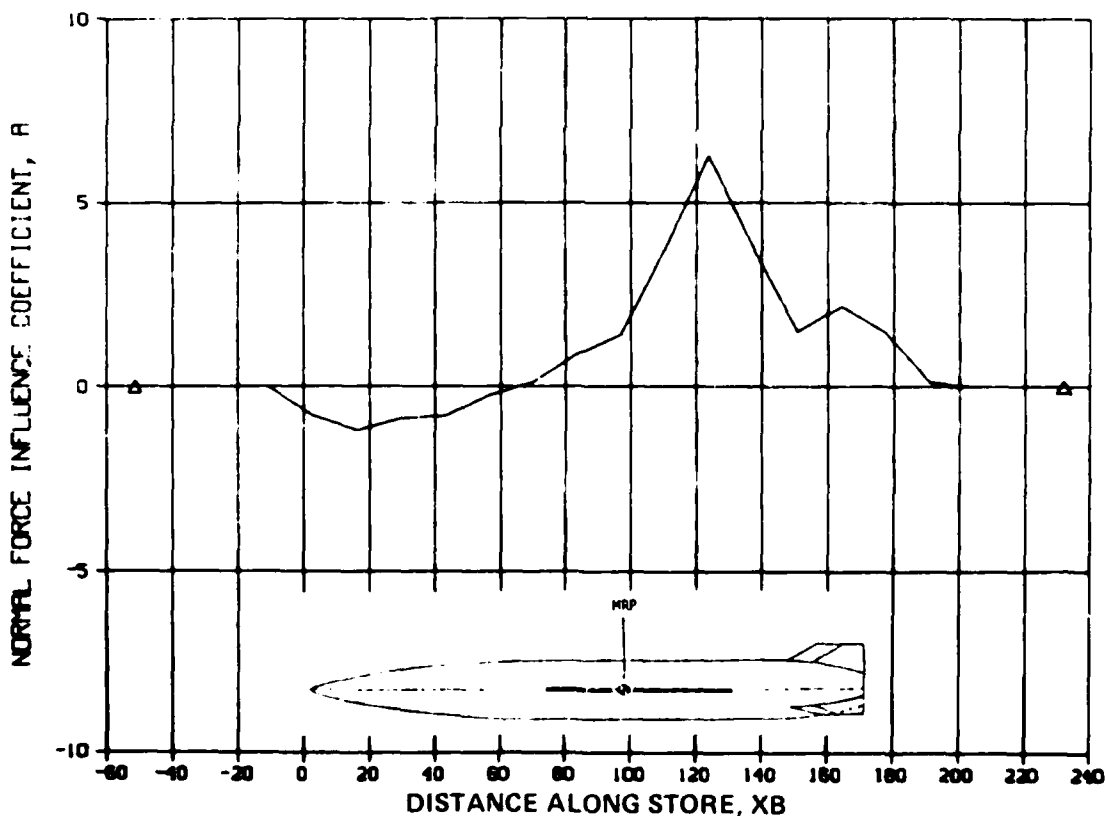
Fig. 4 Experimental Determination of Store/Weapon Influence Coefficients

The fact that this system is overdetermined, i.e., that we have more equations than unknowns, can be used to advantage as it allows us to construct a "best" estimate for the A_i 's that, on-average, best satisfies all the data. Various mathematical procedures, often referred to as parameter identification techniques, are available to construct such "optimal" estimates given a redundant set of noisy data. We have found that a simple least squares estimation technique works extremely well for the A_i and B_i determination from experimental data.

The choice of calibration flow field is only limited by the requirement that the flowfield angularity be accurately known and sufficiently nonuniform to establish a substantial angle-of-attack variation over the store length. AFWAL/Grumman supersonic wind-tunnel test experience at AEDC and the WPAFB Trisonic Gasdynamics Test Facility show that accurate store calibrations can be accomplished using a simple 2-D oblique shock flowfield generated by a flat plate at incidence. Satisfactory store calibration requires that the flowfield angularity be known to within a few tenths of a degree. This requirement virtually eliminates the use of yaw head angularity data. While this may appear to be a disadvantage, it is not, since there is no need to measure the calibration flowfield angularity - it can be predicted theoretically with sufficient accuracy if the flowfield is selected appropriately, i.e., wedge flows and a variety of axisymmetric forebody flow-fields.

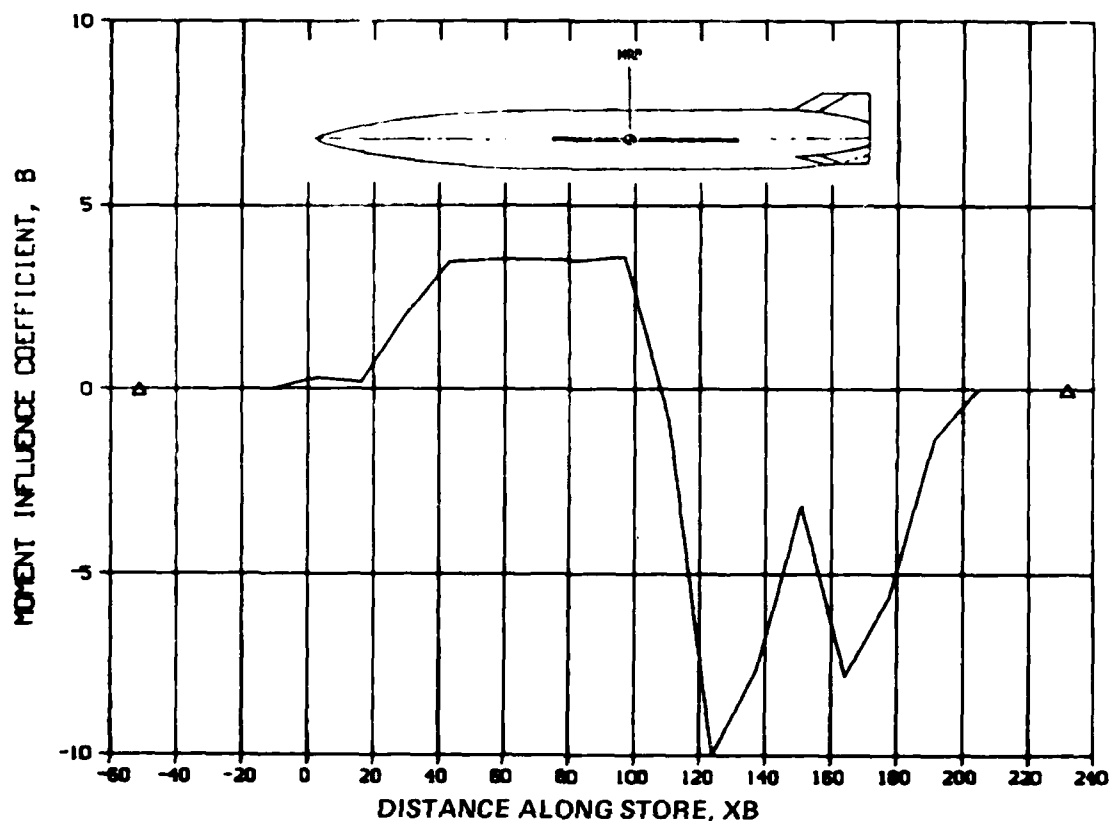
Figures 5 and 6 show the experimentally derived normal force (A_i) and pitching moment (B_i) influence coefficient distribution for a representative winged supersonic standoff weapon at $M=1.89$. In this case the store was divided into 16 elements and the respective A_i , B_i for each element determined from a least squares analysis of the C_N , C_m data taken during a store calibration through a four-degree oblique shock wave. It should be noted that the A_i distribution in Figure 5 does not represent the weapon longitudinal loading distribution - it represents the total normal force that the store would experience if a unit α were applied to the i th store element and α were zero for all other elements.

Maximum span for this delta-winged weapon occurs at missile station 132, which accounts for the large positive A_i (large positive C_N response) and large negative B_i (large negative C_m response) at that location. The negative A_i 's over the forebody are due to buoyancy effects and are real. Note the twin negative peaks in the B_i distribution (Figure 6), which coincide with the wing trailing edge station and the tail location. The intervening valley is due to the gap between the wing and tail which was sensed in the original calibration data. Mach wave inclination, wake effects and data fairing account for the non-zero A_i , B_i values noted slightly upstream and downstream of the nose and tail stations.



0401-005D

Fig. 5 Planar Wing Weapon Normal Force Influence Coefficient Distribution, $M = 1.89$



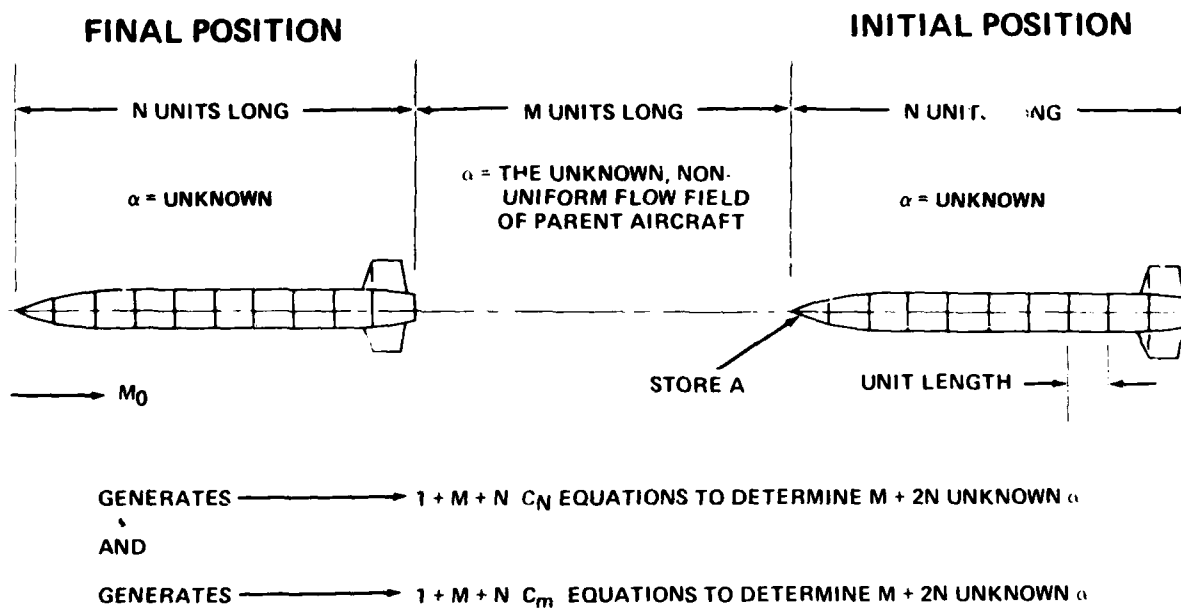
0401-0060

Fig. 6 Planar Wing Weapon Pitching Moment Influence Coefficient Distribution, $M = 1.89$

All experience and evidence to date indicate that satisfactory experimental calibrations can be accomplished within the usual data accuracy standards associated with grid survey force and moment data. This observation is directly supported by wind-tunnel data for $M = 1.5$ to 2.3 , and there is no reason to expect contrary results at subsonic speeds.

Proceeding to the next phase in the application of the IFM technique to weapon separation, we now show how conventional grid survey force and moment data, taken in proximity to the parent aircraft, can be used to calculate the angle-of-attack distribution along the same traverse (Step B). The problem is illustrated in Figure 7. The sting-mounted and previously calibrated store is assumed to traverse upstream, one store element length at a time, while the store balance data are recorded. This process generates $M+N+1$ " C_N " and a like number of " C_m " equations, or $2M+2N+2$ equations that define the $M+2N$ unknown α 's spanning the nose-to-tail extremities of this traverse. A redundant set of equations is obtained provided the store is traversed at least one store length forward.

C_N C_m WIND TUNNEL DATA ARE RECORDED AS STORE IS INDEXED UPSTREAM FROM ITS "INITIAL" TO "FINAL" POSITION DURING A GRID SURVEY



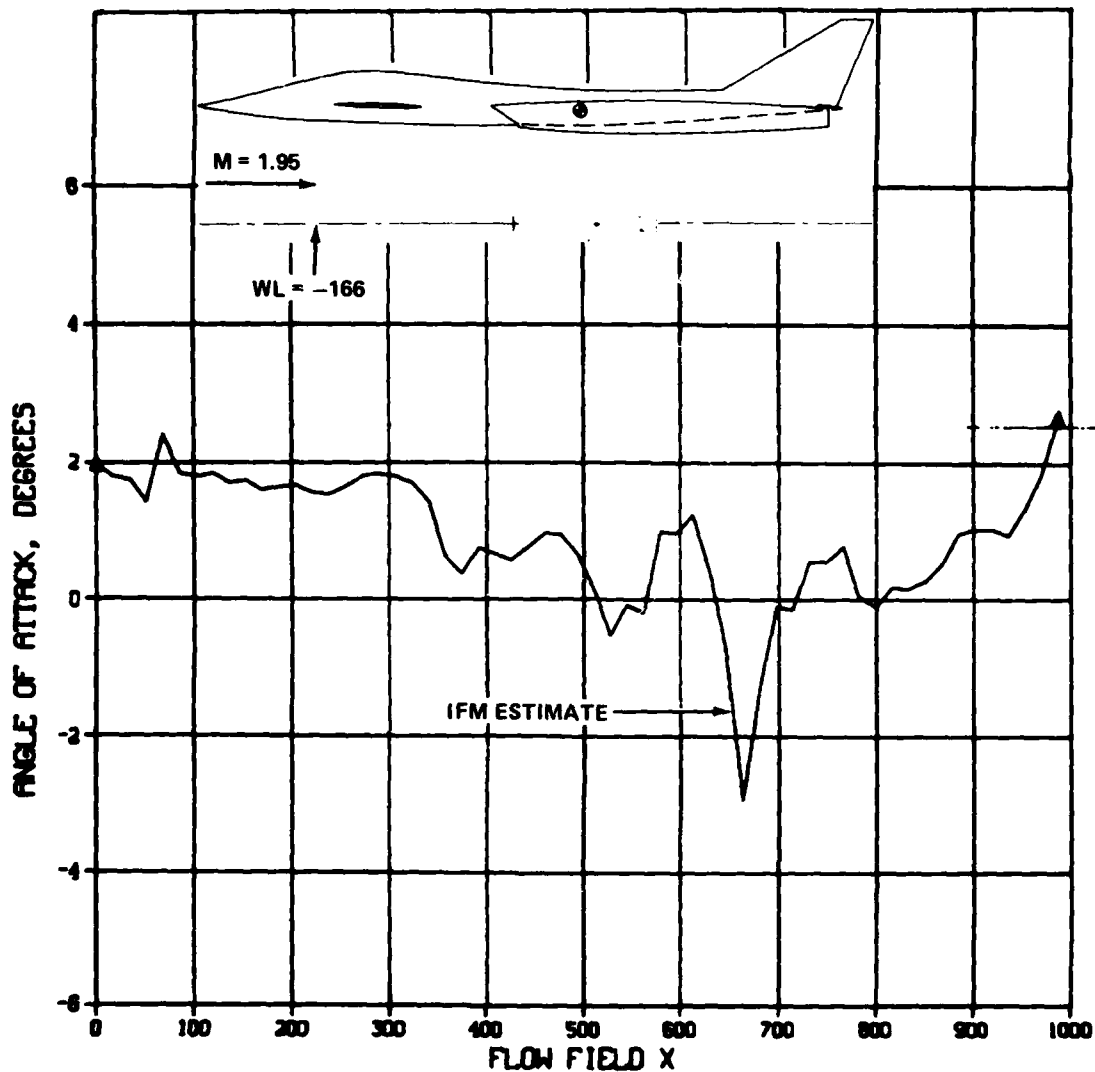
0401-007D

$$\text{TYPICAL EQUATION: } C_N = A_1 \alpha_1 + A_2 \alpha_2 + A_3 \alpha_3 + \dots + A_N \alpha_N - C_{N\alpha} \alpha_0$$

Fig. 7 Determination of Non-Uniform Flowfield Angle-of-Attack Distribution from Grid Survey Force and Moment Data

Figure 8 shows a typical least square estimate of the α distribution along a traverse in proximity to the parent aircraft. These particular results are based on conventional grid survey force and moment data taken at AEDC for a traverse location 166 inches (full scale) below the FRL of Grumman's 1/27-scale Supersonic Tactical Aircraft (STAC) wind-tunnel model. As would be expected, each of the peaks and crests in this predicted α distribution is related to some prominent configuration feature such as the nose, canard, inlet, or wing.

The final "Step C" in the IFM prediction process requires nothing more than taking the derived angle-of-attack distribution in proximity to the aircraft (as determined in Step B) and the influence coefficient data for any "other" previously calibrated store to construct a normal force/pitching moment prediction for this "other" store. Figure 9 illustrates the conceptual process. In this case, "Store B" represents the store whose force and moment characteristics along the indicated traverse are to be estimated. As indicated in the representative equations shown, C_N and C_m can be calculated by direct substitution for the known A_i , B_i , α_0 , C_{m_0} and the known α_i along the traverse.



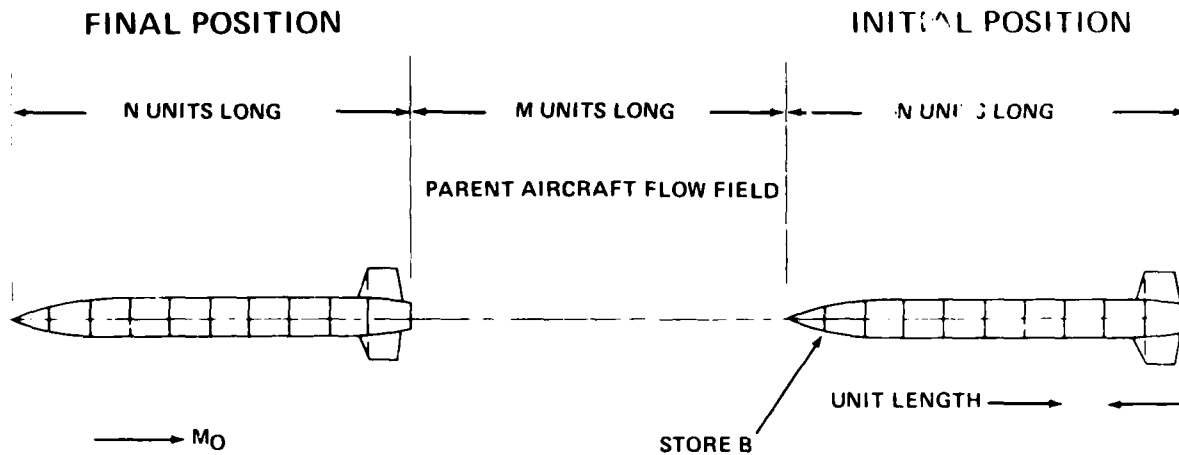
0401-008D

Fig. 8 "Estimated" Local Angle-of-Attack Distribution Along WL-166 Traverse in Proximity to Grumman STAC

In principle, the A, B, C process outlined above shows how grid survey force and moment data for one store can be used to estimate the force and moment characteristics of another store in the same flowfield. The essential requirement in this predictive process is that both stores must have been previously "calibrated" at the Mach number of interest.

In the interests of clarity we have consistently described the mechanics of the present IFM in terms of an experimental/operational approach to emphasize that the concepts can be so implemented. In many cases, however, it may prove more economical to calibrate a particular store using theoretical/computational techniques to duplicate the experimental process described herein. AFWAL/Grumman experience to date shows excellent correla-

CONCEPTUALLY, "STORE B" IS INDEXED UPSTREAM FROM ITS "INITIAL" TO "FINAL" POSITION ALONG TRAVERSE WHERE α DISTRIBUTION IS KNOWN



IF "STORE B" INFLUENCE COEFFICIENTS ARE KNOWN, THEN "STORE B" C_N , C_m CAN BE CALCULATED DIRECTLY, I.E.,

$$C_N = \sum_{i=1}^N A_i \alpha_i - C_{N\alpha} \alpha_0$$

$$C_m = \sum_{i=1}^N B_i \alpha_i + C_{m0} - C_{m\alpha} \alpha_0$$

05 0401-009D

Fig. 9 Predicting the Aerodynamic Force and Moment on a Calibrated Store

tion between the experimentally derived and theoretically calculated influence coefficients. The outlook for continued success in this area is certainly promising.

Another interesting "wrinkle" is the use of "secondary" experimental calibrations to calibrate a store without the necessity of setting up a dedicated wind-tunnel test. This involves traversing the "uncalibrated" store along a conventional grid survey traverse that has been previously surveyed by a "calibrated" store. For example, the estimated α distribution along the -166 inch waterline shown in Figure 8 (established using the calibrated planar wing weapon) and measured grid C_N , C_m data for our hypothetical "uncalibrated" store along this same traverse would suffice to calibrate that store per the earlier discussion surrounding Figure 4. Experience indicates that such secondary calibrations are very nearly as accurate as the primary calibration data obtained from dedicated testing.

EXPERIMENTAL RESULTS

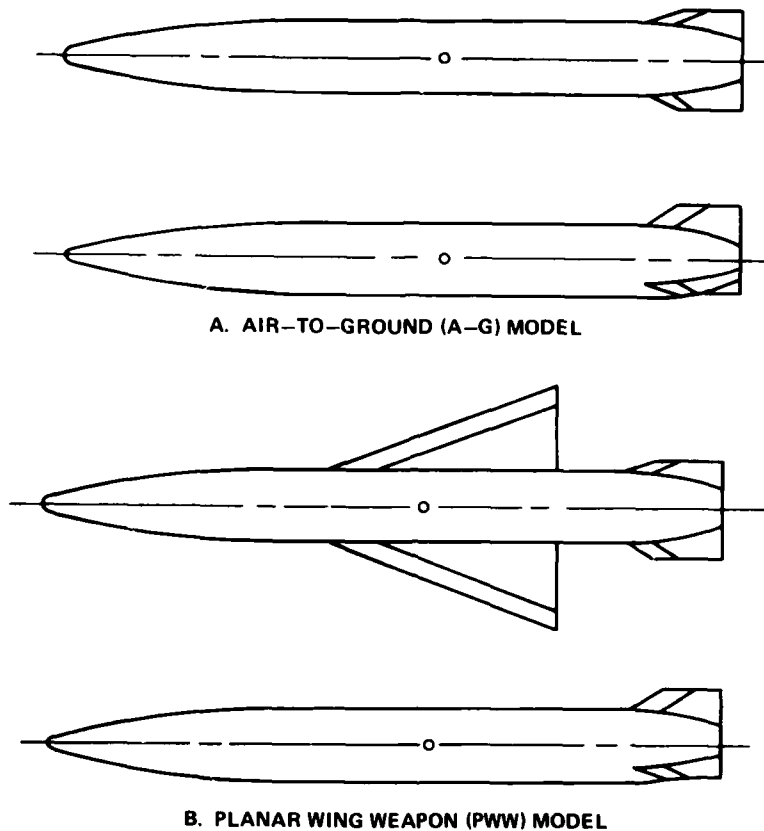
Representative IFM prediction - wind tunnel data correlations are included herein. The $M = 1.95$ data were taken in proximity to a 1/27-scale model of Grumman's STAC configuration (Figure 10). In this case, the planar wing weapon (Figure 11) grid survey data were used to estimate the air-to-ground weapon (Figure 11) data along the $WL = -166$, $BL = 0$ and $WL = -76$, $BL = 54$ traverses indicated in Figure 12. Both stores were "calibrated" in the WPAFB Trisonic Gasdynamics Test Facility using a four-degree oblique shock calibration flowfield.



0401-010D

Fig. 10 Grumman Supersonic Tactical Aircraft Configuration (STAC)

The IFM predicted C_N , C_m for the air-to-ground store show good agreement with the wind-tunnel data at $WL = -166$ (Figures 13 and 14). The theory-data discrepancy upstream of station 100 and downstream of station 800 is characteristic of IFM predictions near the "ends" of a traverse since the α 's in



0401-0110

Fig. 11 1/27-Scale Grumman Store Models

this region are not accurately defined by the least squares identification process. IFM predictions at $WL = -76$, $BL = 54$ also show good agreement with air-to-ground test data (Figures 15 and 16). In this case, the weapon traverse comes within one store diameter of the model nacelle.

The foregoing IFM predictions were based on parent aircraft flow-field angularity distributions determined from grid survey store force and moment data. None of the angularity estimates were corrected for secondary flow-field effects due to the weapon itself.

Judging from weapon/flat plate proximity data from the WPAFB Trisonic Facility at $M=1.5$ and 1.9 , it appears that the weapon-induced effect is less than 20% of the total store force and moment to within one diameter of the carriage position. In exceptional cases, or where greater prediction accuracy is required, a theoretical proximity correction could be applied. The accuracy level demanded of this correction would be modest, e.g., a 25% error in a theoretically calculated correction would result in only ~5% error in the total store force and moment estimate. The calculation of such

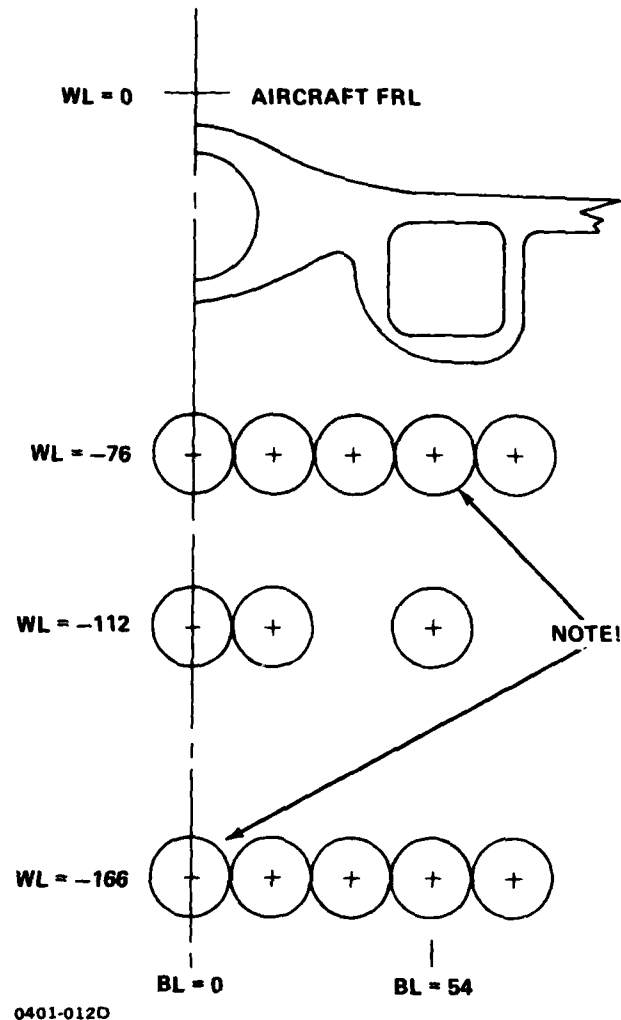
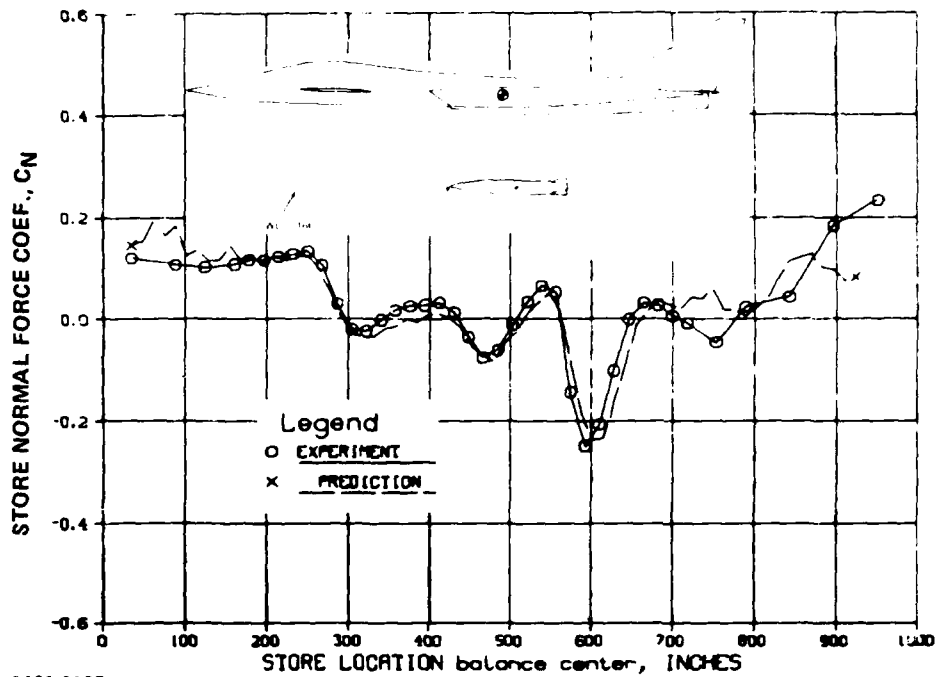


Fig. 12 Cross-Sectional View of 1/27-Scale STAC Grid Survey at AEDC

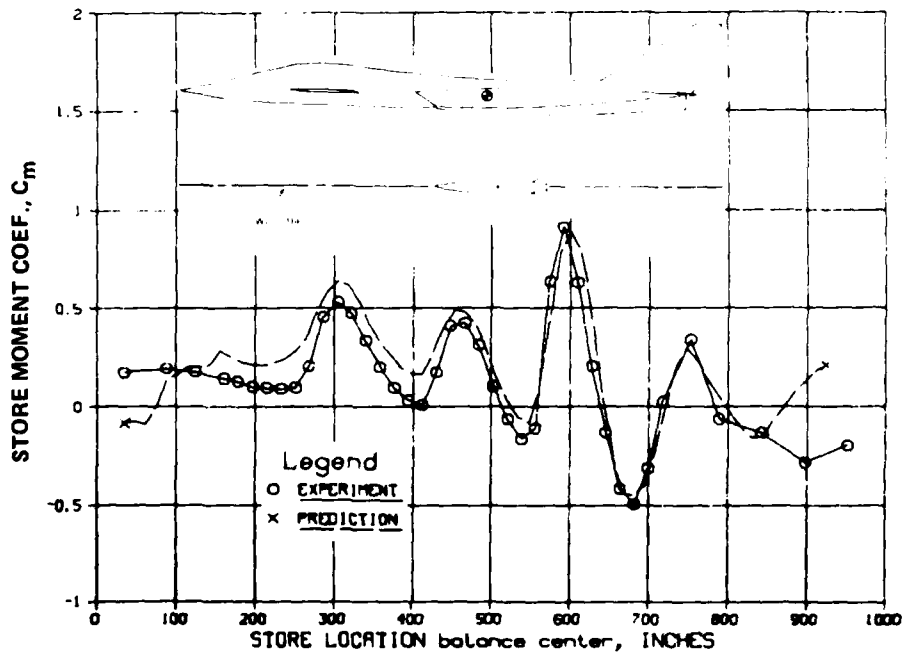
a correction is much less demanding or difficult than attempting to calculate the total aircraft flowfield since only the reflection effect need be modeled. As noted in Reference 1, the volume effect of the store nose is probably the only induced interference effect that may need to be accounted for.

The present IFM has been successfully applied to a significant number of supersonic grid survey data sets; those shown here are representative. Grumman is presently under contract to AFWAL/FIMM to finalize the IFM technique for supersonic applications, develop user oriented codes, and address specific issues related to future subsonic/transonic applications.



0401-013D

Fig. 13 Air-To Ground Weapon IFM Normal Force Prediction Compared with Wind-Tunnel Data, $M = 1.95$



0401-014D

Fig. 14 Air-to-Ground Weapon IFM Pitching Moment Prediction Compared with Wind-Tunnel Data, $M = 1.95$

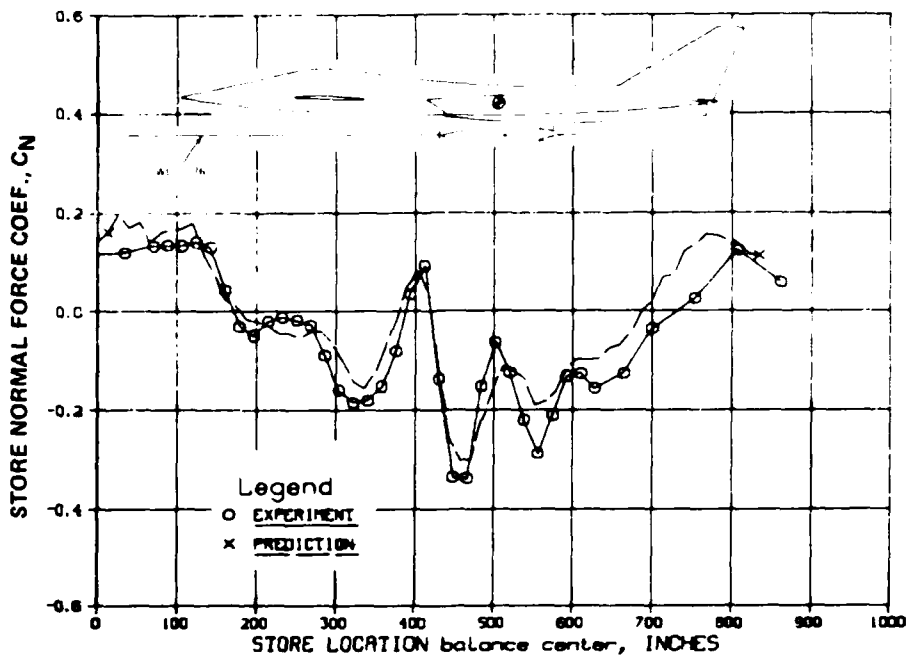


Fig. 15 Air-to-Ground Weapon IFM Normal Force Prediction Compared with Wind-Tunnel Data, $M = 1.95$

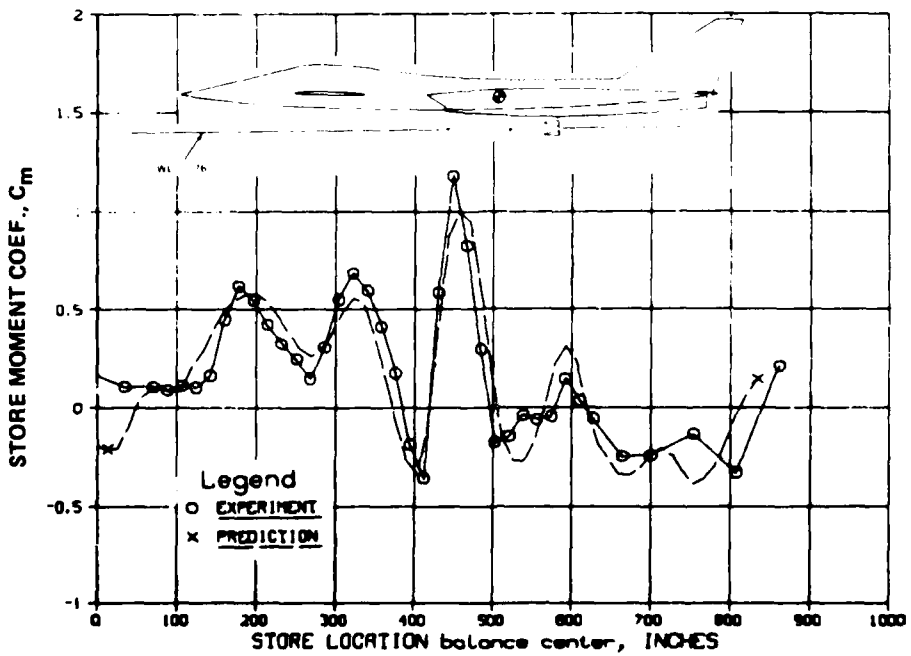


Fig. 16 Air-to-Ground Weapon IFM Pitching Moment Prediction Compared with Wind Tunnel Data, $M = 1.95$

CONCLUSION

A method has been developed for predicting the aerodynamic forces and moments acting on a store during weapon separation based on previous wind-tunnel data for another store in the same flowfield. Predicted forces and moments based on this Influence Function Method (IFM) show excellent correlation with supersonic test data. This work is currently being extended to the subsonic/transonic speed range and should provide a comprehensive and unified approach to predicting store separation aerodynamics. Continued development of this technique is expected to result in substantial improvements in the cost-effectiveness of future weapon separation test programs.

The present IFM technique can be implemented as a strictly experimental/operational technique for the wind-tunnel prediction of weapon separation characteristics. In many cases, however, it may prove advantageous to employ theoretical/computational techniques to implement selected elements of the prediction process. The best "mix" of experimental/theoretical implementation will be dictated by cost/capability considerations.

REFERENCES

1. Dillenius, M.F.E., Goodwin, F.K., and Nielsen, J.N., "Prediction of Supersonic Store Separation Characteristics," AFFDL-TR-76-41, May 1976.
2. Cenko A., Tinoco, E.N., Dyer, R.D., and DeJongh, J., "Pan Air Applications To Weapons Carriage and Separation." AIAA Journal of Aircraft, February 1981.
3. Shanker, V., Malmuth, N.D., "Computational and Simplified Analytical Treatment of Transonic Wing-Fuselage - Pylon - Store Interactions," AIAA 18th Aerospace Sciences Meeting, Paper 80-0127, Jan. 1980.
4. Stahara, S.S., "Study of Transonic Flow Fields About Aircraft: Application to External Stores," AGARD Symposium on Subsonic/Transonic Configuration Aerodynamics, Munich, Germany, 5-7 May 1980.
5. Maddox, A.R., "Store Separation Trajectory Analysis," AIAA Journal of Aircraft, Nov. 1980.
6. Korn, S.C., "Use of the Flow Angularity Technique for Predicting Store Separation Trajectories." Aircraft/Stores Compatibility Symposium Proc., 7-9 Dec '71, AFFDL.
7. Deslandes, R., "Evaluation of Aircraft Interference Effects On External Stores At Subsonic and Transonic Speeds," AGARD Symposium On Subsonic and Transonic Configuration Aerodynamics, Munich, Germany, May 1980.

SUBMISSILE AERODYNAMICS DURING DISPENSING

Thomas E. Lundy, William F. Braddock
and Lajpat R. Utreja

Lockheed-Huntsville Research & Engineering Center
Huntsville, Alabama

ABSTRACT

A combined analytical and experimental study was conducted to determine the aerodynamic interference effects of a submissile in the presence of a dispenser missile. The analytical predictions are made using NEAR codes modified for applications to missile systems. A wind tunnel test was conducted to measure the static aerodynamic coefficients of a submissile in the flow field of a dispenser missile at Mach numbers 0.8 and 1.2. The parameters observed to have the greatest effect on the interference aerodynamics are the addition of fins on the submissile, the removal of the dispenser bay covers, the dispenser angle of attack and the submissile pitch angle.

INTRODUCTION

Several missile systems are currently being developed involving the release of submissiles from a dispenser missile. The deployment of submissiles may occur over a range of Mach numbers from 0.5 to 2.0 and over a range of angles of attack from 0 to 30 deg. The initial motion of the submissile is dominated by aerodynamic interference forces which influence the trajectory that follows. The aerodynamic interference forces must be known to determine the transient loads during deployment that are critical to target lock-on. The results of a survey by Lockheed for the U. S. Army Missile Command (MICOM) showed that there are very little experimental data available for evaluating interference. Several aircraft store separation codes were identified which with modifications, can be used for multiple missiles. However, the accuracy of the codes is unknown.

In an effort to gain an understanding of the aerodynamic interference, MICOM sponsored a combined analytical and experimental study to determine the aerodynamic interference effects of a submissile in the presence of a dispenser missile. The analytical effort was directed toward identification of the applicable computer codes and the modification of selected codes for application to the missile-submissile systems. The modified Nielson Engineering and Research (NEAR) subsonic and supersonic aircraft-store separation codes were used to generate aerodynamic interference data on the submissile for various locations relative to the dispenser missile. Simultaneously, a wind tunnel test was conducted to measure the static aerodynamic coefficients of a submissile in the flow field of a dispenser missile.

Several parameters were varied to determine their effect on the interference aerodynamics of the submissile. Some test runs were specifically made for a direct comparison with the NEAR code results.

The purpose of this paper is to present the results of the wind tunnel test data analysis, and a comparison of some of the results with the NEAR code predictions. The wind tunnel results are presented for the interference forces and moments on a submissile in the presence of a dispenser with and without bay covers. The NEAR codes do not have any provision for simulating a dispenser without bay covers and thus the predicted results are for the dispenser with bays closed. For the sake of brevity the results are presented for parameters which most affect interference aerodynamics. The results for parameters not presented are available upon request.

In general, the interference effects are observed to be the largest for submissile locations closest to the dispenser. A submissile located very close to a dispenser with bays open is characterized by large negative normal force coefficients and large positive pitching moment coefficients. The parameters which affect the interference aerodynamics the most are, the addition of fins on the submissile, the removal of the dispenser bay covers, the dispenser angle of attack and the submissile pitch angle. Whereas, the fin orientation, the nose shape and the submissile yaw angle did not influence the interference aerodynamics greatly. Comparison of the wind tunnel test data and the NEAR code predictions does not show good agreement.

WIND TUNNEL TEST DESCRIPTION

The wind tunnel test was conducted in the Vought Corporation High Speed Wind tunnel. The test models were designed and fabricated by the Jet Propulsion Laboratory. The dispenser model was designed to resemble a typical Army missile. This model has three sets of bays in its forward section for storage of submissiles. Because of its position on the constricted area of the three caliber ogive nose, the forward set of bays has positions for only five submissiles of the size desired. The center and aft bay positions can each accommodate eight.

Sketches of the preliminary design indicated that a rather long sting was needed to support the submissile. Use of such a sting would have restricted the angle of attack obtainable and vertical displacement as well as inducing possible deflection problems. To shorten the sting, it was necessary to truncate the dispenser model and move it aft on its sting. The result was that the center of pressure of the truncated model was too far forward of the balance center for any available balance to withstand the loads. Although it was desired to measure the interference effects of the submissile on the dispenser missile, the decision was made to replace the dispenser balance with a solid sting.

The model tested was a 5.593 in. long, 0.932 in. diameter axisymmetrical vehicle designed to represent typical submissile type configurations and investigate certain configuration parameters. The model could be configured

with a tangent ogive nose of either 1/2 or 2 calibers. It could be tested either with or without its four aft mounted rectangular fins. The submissile model was designed to be tested in the presence of the forebody model of a dispenser missile. The dispenser had a 3.750 in. diameter cylindrical body, a 3 caliber ogive nose and three sets of submissile bays, in the nose and forward part of the body, each with several submissile storage positions. There was also a second submissile model which was the same configuration as the model to be tested, but non-metric and designed to mount to the dispenser missile using a pylon. This non-metric submissile was used to determine the effect of its wake on the metric submissile which was tested behind it. The submissile and dispenser dimensions are shown in Figures 1 and 2.

The metric submissile was designed to fit on a six-component internal balance to be able to obtain total vehicle static stability coefficients and base pressure coefficients. The Vought Flight Dynamics Simulator was used to obtain these coefficients while in the presence of the dispenser vehicle. With the non-metric submissile mounted to the dispenser missile, the metric submissile was used to obtain coefficients while in the presence of the dispenser missile and in the wake of a more forward submissile.

The models were tested in several configurations and over a range of several parameters described in the table below.

Test Parameter Ranges

α_D	Dispenser angle of attack	-5 to +5 deg
$\Delta\alpha_S$	Submissile angle of attack relative to dispenser	-10 to +10 deg
M	Mach number	0.4 to 1.4
X	Horizontal distance behind nose of dispenser to submissile center of gravity, positive for submissile moving aft of dispenser nose	1 to 5 diameters (dispenser)
Z	Vertical distance of submissile from dispenser, positive for submissile moving down (below) dispenser	1/2 to 3 diameters

DESCRIPTION OF ANALYTICAL CODES

The NEAR subsonic and supersonic computer codes were developed by Nielson Engineering and Research to predict the trajectories of external stores dropped from an aircraft. Some modifications to the NEAR codes

were necessary for application to missile systems. The first attempt to calculate aerodynamic forces on a submissile in the flow field of a carrier missile, using the NEAR codes, was made by reducing the wing size, modeling the dispenser missile as the fuselage and the submissile as the store. In the subsonic case the reduced wing was placed far behind the fuselage. In the supersonic case the reduced wing was placed at the tail end of the fuselage. The program would not run if the wing was placed farther aft.

In order to further improve the efficiency of the codes, modifications were made to the codes to eliminate completely the input and calculations related to the dispenser missile wing. Basically, the store data were converted to fuselage coordinate system, which in the original program were given relative to the wing. Also, the flowfield computations were allowed to bypass the subroutines involving the wing influence. The modified NEAR codes were exercised for the Army models tested in the wind tunnel. It was observed that the submissile aerodynamics obtained using the two techniques: (1) reduction of the wing to a small size and its placement far away from the fuselage, and (2) elimination of the wing, were identical. A substantial reduction in the execution time was, however, achieved by eliminating the wing. Comparable execution times for six selected lateral positions for the subsonic case using the two techniques were 14.21 and 0.583 sec, respectively. The execution time for seven consecutive cases for the supersonic case was 1.099 sec compared to 6.46 sec for the reduced wing case.

An option was added to the NEAR code to facilitate the generation of parametric data base. The original version moved the store along a trajectory determined by the forces experienced. The option allows the submissile to follow a predetermined path for which the aerodynamics can be calculated. The option currently allows a single parameter to be varied in even increments. Either position (X, Y, Z) or attitude (θ , ψ , ϕ) can be varied, the increment and the maximum value of the parameter.

The results were obtained in terms of the incremental normal force and pitching moment coefficients. The parameters varied were the geometric placement of the submissile relative to the dispenser missile (X location, Z location, and relative attitude), and the freestream Mach number.

DESCRIPTION OF RESULTS

The results are presented in terms of the interference pitch plane coefficients plotted as a function of submissile geometric location relative to the dispenser missile. These results are presented for two Mach numbers. The effect of the parameters varied on the submissile interference aerodynamics will be discussed in the following paragraphs.

RADIAL SEPARATION

Typical results for a submissile traversing a vertical trajectory are shown in Figure 3 for a submissile deployed from a dispenser with bays closed and open. The closed bay results for Mach number = 0.8 do not

show appreciable interference effects in the values of the normal force, the pitching moment, and the axial force coefficients. However, the removal of bay covers significantly alters the submissile aerodynamics. The interference effects with bays open are largest for a submissile location closest to the dispenser. Typical largest values of the normal force and the pitching moment coefficient are -0.65 and 1.4, respectively. The axial force coefficient has a minimum value of 0.09 at this location. The interference aerodynamic coefficients are observed to approach their freestream values at about three diameters below the dispenser. The supersonic results with bays open are similar to the subsonic case showing a large negative normal force coefficient and a large positive pitching moment coefficient when closest to the dispenser. The submissile axial force coefficient increased from 0.2 when closest to the dispenser to about 0.4 at three diameters below the dispenser. It is noted that the data were a function of the submissile location in the wind tunnel and affects the interference plots at larger separation distances.

LONGITUDINAL SEPARATION

The results of the longitudinal sweep of a submissile for three vertical locations below the dispenser are presented in Figure 4. The interference effects are observed to be largest at submissile locations under the nose portion of the dispenser. Mach = 0.8 results show no appreciable variation in the interference values after the submissile has traversed about three diameters behind the dispenser nose. The results at a supersonic Mach number of 1.2 show that both the normal force and the pitching moment drop down to zero at about five diameters behind the dispenser nose.

FIN ORIENTATION

The addition of fins have a significant effect on the interference aerodynamics of a submissile. However, the fin orientation does not influence the magnitude of the interference effect greatly. Figure 5 shows the aerodynamics data for a finless submissile and submissiles with three fin orientations. The results have been plotted for submissiles traversing a vertical trajectory from the center bay of the dispenser. Compared with finless submissiles the finned submissiles have a larger negative normal force and a larger positive pitching moment when closest to the dispenser. The finned submissiles have larger axial force compared to the finless submissile, however, the interference increment is similar for the two cases.

WAKE EFFECT

A submissile deployed from a dispenser in the wake of another submissile is in the interference flow field of both the dispenser and the submissile. Plots in Figure 6 depict the aerodynamic coefficient variation of a submissile traversing a vertical trajectory starting from the center bay of the dispenser. The front submissile is located at two diameters below a longitudinal location simulating a forward bay of the dispenser. The pitch plane aerodynamic coefficients are observed to oscillate about their nominal values as the submissile traverses through the wake of the forward submissile.

DISPENSER ANGLE OF ATTACK

The dispenser angle of attack greatly influences the aerodynamics of the dispensing submissile. Typical results for a submissile deployed from a forward bay of the dispenser at 0 and ± 5 deg angle of attack are shown in Figure 7. Note that the submissile angle of attack relative to the freestream is the same as the dispenser in each case. At a subsonic Mach number of 0.8 the interference effects are found to be greatest for a dispenser angle of attack of 5 deg. An estimate of the magnitudes of the maximum incremental normal force and pitching moment coefficients are -1.0 and 1.0, respectively. There is no significant effect, however, on the value of the submissile normal force coefficient for the case of dispenser at -5 deg angle of attack. The axial force coefficients did not vary much from their interference free values except when closest to the dispenser. Similar general trends are obtained for a supersonic Mach number of 1.2 with the exception of axial force reduction close to the dispenser. The value of this interference did not vary with dispenser angle of attack.

SUBMISSILE PITCH

Positive submissile pitch produces positive normal forces and negative pitching moments. Typical results for a submissile at 0 and ± 10 deg pitch angle (and dispenser at zero) are presented in Figure 8. Both at $M = 0.8$ and at $M = 1.2$, the interference effects are largest at zero degree pitch angle. At $M = 0.8$ the interference normal force coefficients and the pitching moment do not vary appreciably from their freestream values. For the supersonic Mach number of 1.2, the interference effects are observed up to about two diameters below the dispenser.

COMPARISON OF WIND TUNNEL RESULTS AND NEAR CODE PREDICTIONS

The submissile aerodynamic interference data obtained in the wind tunnel have been compared to the analytical predictions developed with the NEAR codes. The subsonic results at a Mach number of 0.8 for a submissile without fins are presented in Figures 9 and 10. Figure 9 shows the effect of lateral separation of a submissile from the dispenser placed parallel to the free stream. The normal force coefficient obtained in the wind tunnel is of opposite sign compared to the NEAR code predictions. The wind tunnel normal force data for this configuration is not typical of the general trends which show negative normal force for a submissile closest to the dispenser. The pitching moment data, however, are in reasonable agreement. The effect of dispenser angle of attack is also shown in Figure 9. The predicted normal force is significantly different from the measured data for submissile locations up to one diameter below the dispenser. The pitching moment magnitude, however, is in disagreement even at larger distances from the dispenser. The persistent interference beyond three diameters in the experimental data shown in Figure 9 is possibly due to the wind tunnel flow angularity. The variation of the interference normal force and the pitching moment coefficient for the submissile at an angle of attack with respect to the dispenser is shown in Figure 10. The results are for a submissile located one diameter below the dispenser.

The interference effects of a submissile for a supersonic Mach number of 1.2 are presented in Figures 11 through 16. Reasonable agreement observed for a submissile without fins at a longitudinal location simulating a forward bay, traversing laterally apart in a fixed trajectory. These results are shown in Figure 11. However, at a different longitudinal location simulating a center bay, comparison is not good as shown in Figure 12. The effect of the dispenser angle of attack on the submissile aerodynamics is shown in Figure 13. Both the predicted and the experimental results follow similar trends. The effect of submissile fins in the dispenser interference flow field has not been predicted accurately. This is observed in Figure 14 which depicts longitudinal sweeps of a submissile with fins at a fixed lateral location. Incremental normal force and pitching moment variation with angle of attack agree reasonably well with experimental data (see Figure 15).

The modified NEAR codes are used to determine the submissile interference aerodynamics in the presence of regular shaped dispenser geometries. They cannot, in their present form, determine the flow field around a dispenser with its bays open. This is one of the biggest limitations on the use of the NEAR codes for practical situations of submissile being deployed from a dispenser with bays open. Therefore, the experimental data for the dispenser with open bays can be compared with only the results of the dispenser with closed bays predicted by the NEAR codes. Typical results are shown in Figure 16 for a submissile traversing a longitudinal trajectory at a fixed vertical location. Note that the comparison shown is for different nose shapes, but the effect of the nose shape on the interference normal force and the pitching moment coefficients is insignificant as observed in the submissile aerodynamics wind tunnel test data analysis. The disagreement between the wind tunnel data and the NEAR code prediction is primarily because the NEAR codes cannot determine the flow field around an open bay dispenser.

CONCLUSIONS

The following conclusions are drawn from an analysis of the wind tunnel test conducted to determine the aerodynamic interference effects of a submissile in the flow field of a dispenser:

In general, the interference effects are observed to be largest when the submissile is located closest to the dispenser. This is characterized by large negative normal force coefficients and large positive pitching moment coefficients. The axial force coefficient however decreases to its lowest value for these locations. The interference effects are reduced considerably by covering the dispenser bays. This reduction is pronounced at $M = 0.8$ for which the normal force and pitching moment coefficients do not differ appreciably from their freestream values.

In a longitudinal sweep, the submissile experiences considerable aerodynamic interference when it is under the nose portion of the dispenser. For a Mach number of 1.2 the interference effects reduce to zero at approximately seven diameters behind the nose of the dispenser.

The finned submissile experiences greater interference effects compared to a finless submissile. However, interference aerodynamics of the finned submissile is observed to be independent of the fin orientation.

The aerodynamics of a submissile is altered when deployed in the presence of another submissile. The effect is more pronounced as a submissile traverses through the wake of the forward missile.

The submissile interference aerodynamics are at positive dispenser angles of attack and are larger than zero or negative dispenser angle of attack.

The submissile attitude relative to the dispenser affects the submissile aerodynamics considerably. For positive pitch angles the submissile develops a positive normal force and a negative pitching moment, and vice versa for negative submissile pitch angles. Interference effects are more pronounced at zero attitude when the submissile is parallel to the dispenser missile.

A complete evaluation of the NEAR codes has not been made at the present time. However, some general conclusions are drawn based on the limited comparisons. The disagreements in the NEAR code prediction and experimental results are observed both in the subsonic and the supersonic cases. In the subsonic flow, the difference is due to the underprediction of bouyancy contribution to the normal force in the NEAR code. In the supersonic case, however, no definite reason can be given regarding the difference in agreements of interference forces at two longitudinal locations under the dispenser. No comparison is made of trajectories for which the submissile traversed through the shock wave off the dispenser nose.

For a case of submissile with fins, it was observed that the approach taken in the NEAR codes does not simulate the fin contribution correctly. Finally, the NEAR codes in their present form cannot simulate a dispenser missile with open bays and, therefore, the resulting submissile interference aerodynamics cannot be predicted.

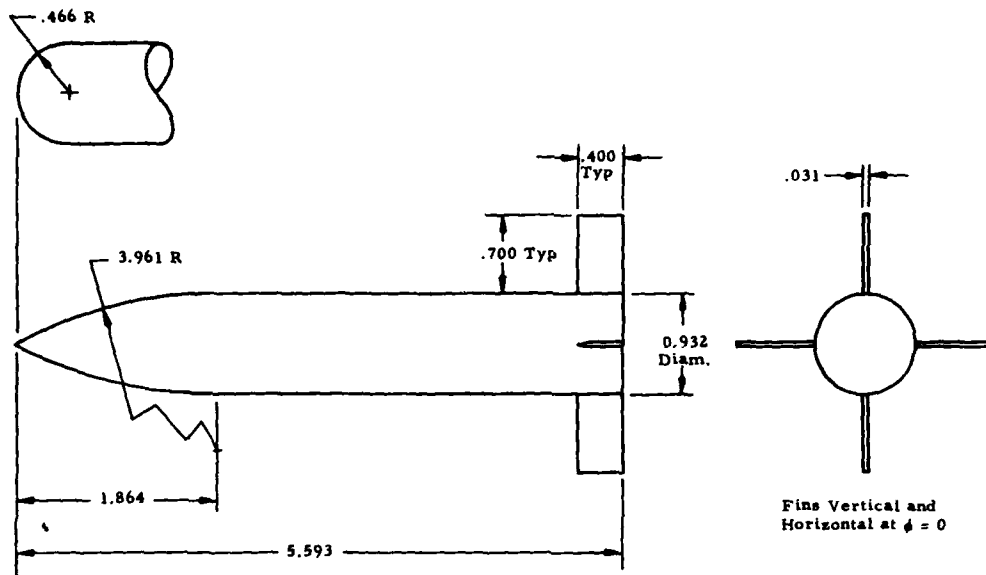


Figure 1. Submissile Design

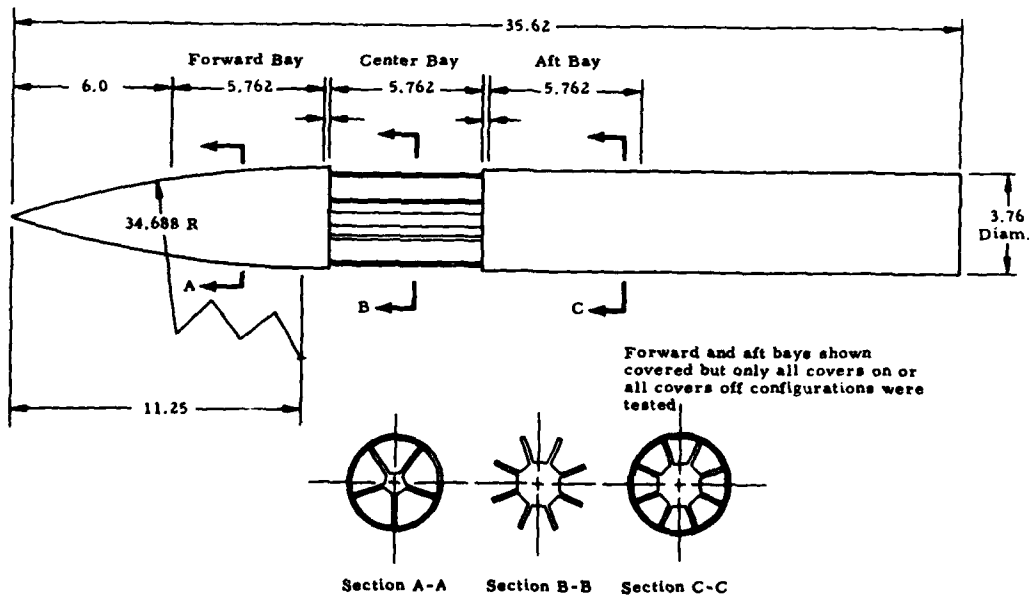


Figure 2. Dispenser Missile Design

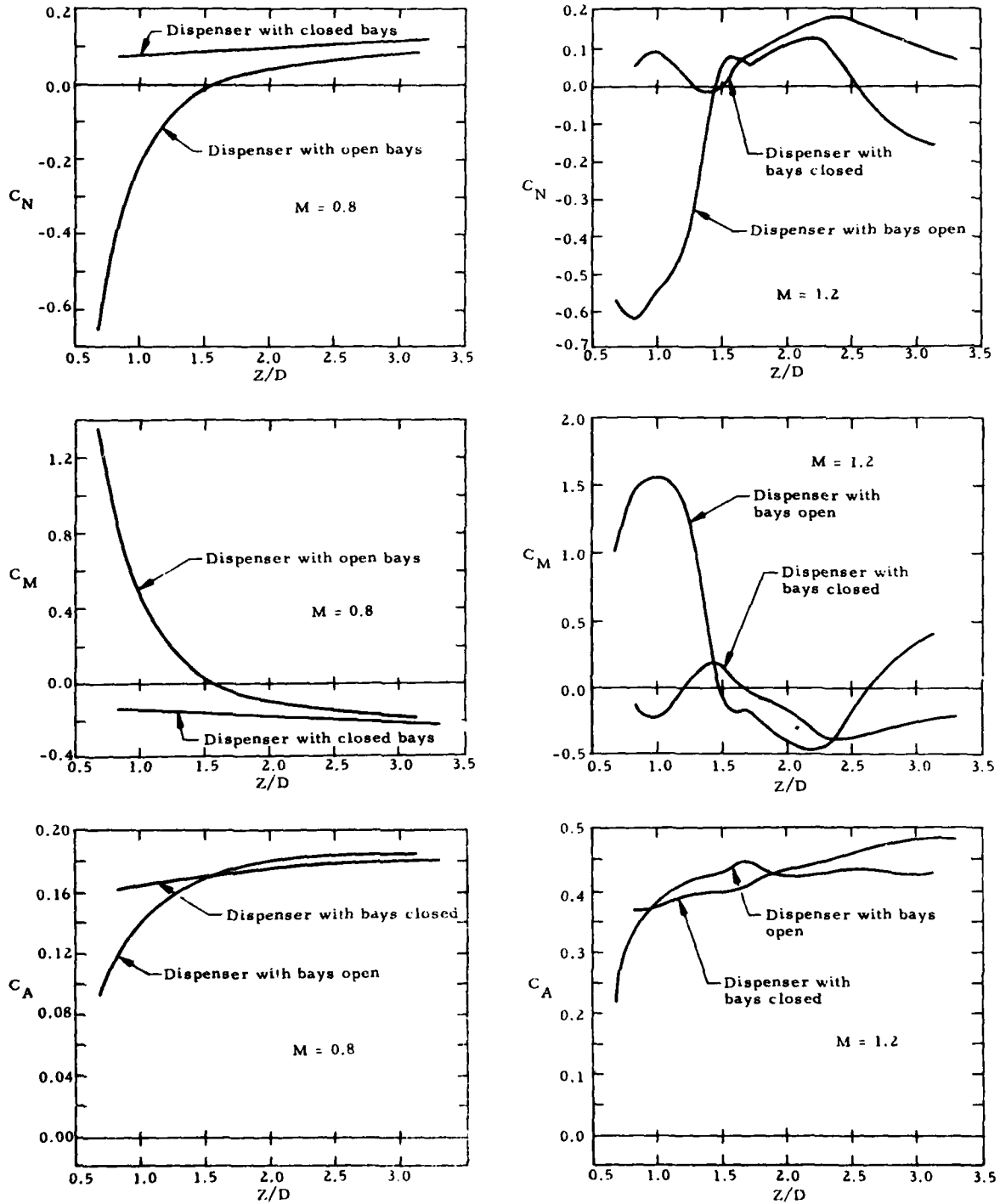


Figure 3. Submissile Aerodynamics as a Function of Submissile Vertical Position ($X/D = 4.0$, $\alpha_D = 0$ deg, $\Delta\alpha_S = 0$ deg)

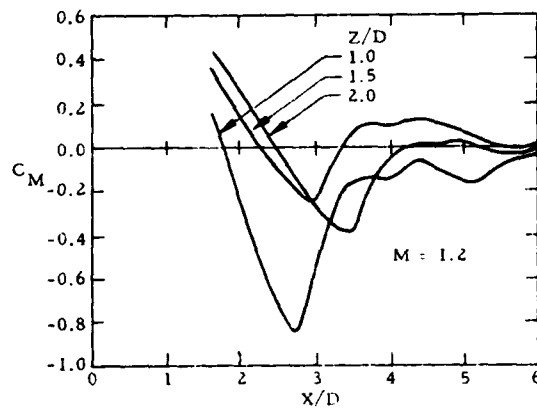
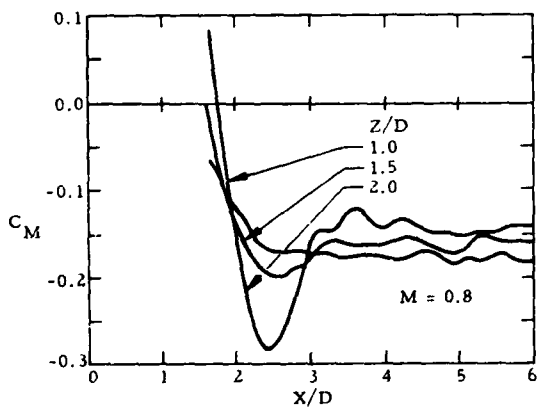
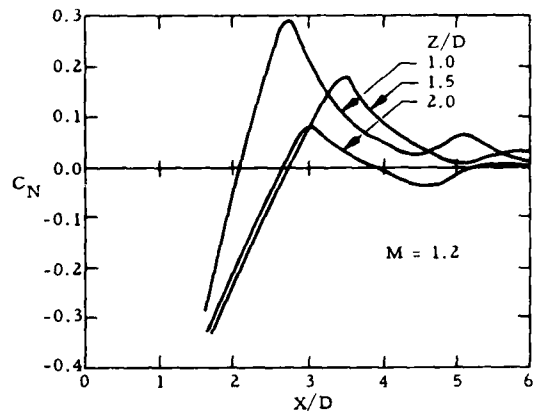
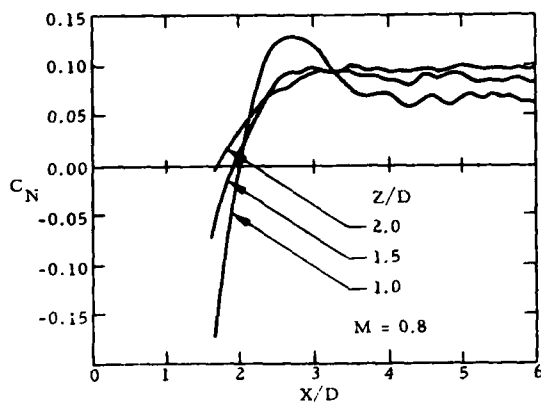


Figure 4. Submissile Aerodynamics as a Function of Submissile Longitudinal Position ($\alpha_D = 0$ deg, $\Delta\alpha_S = 0$ deg)

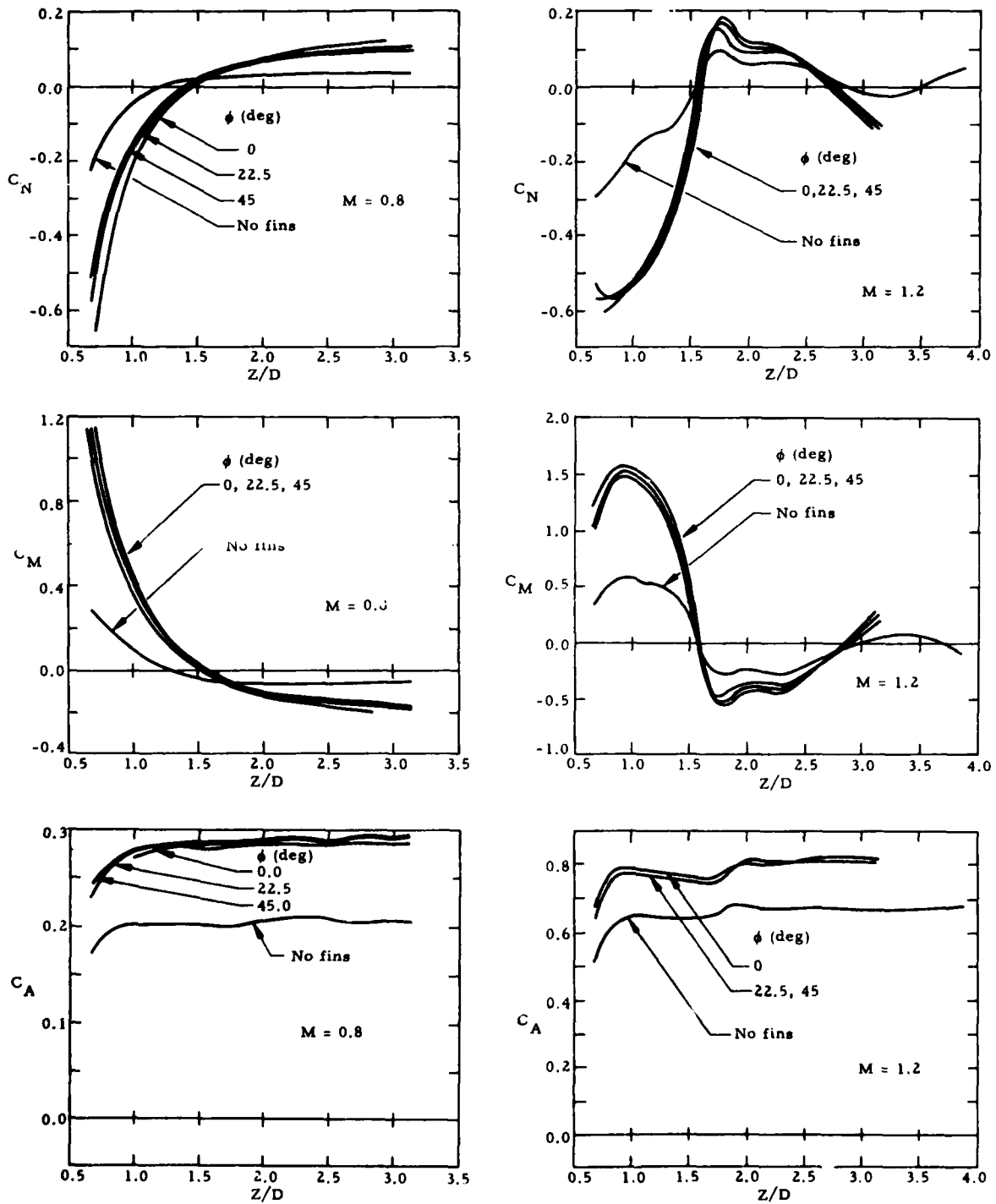
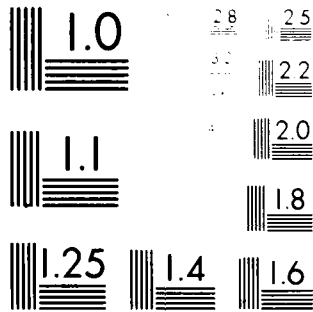


Figure 5. Effect of Fin Orientation on Submissile Aerodynamics
 $(X/D = 4.0, \alpha_D = 0 \text{ deg}, \Delta\alpha_S = 0 \text{ deg})$



MIRACLY RESOLUTION TEST CHART
NATIONAL BUREAU OF STANDARDS-1963-A

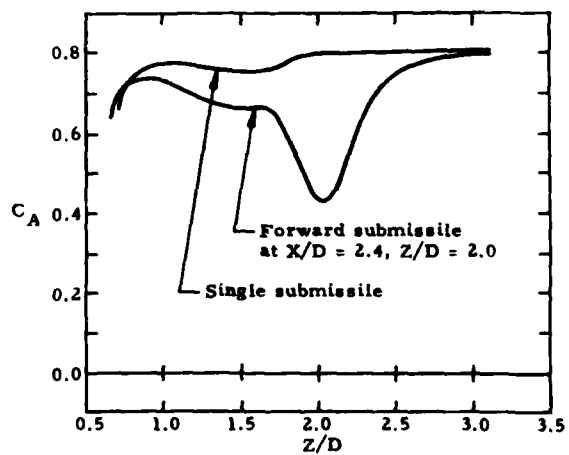
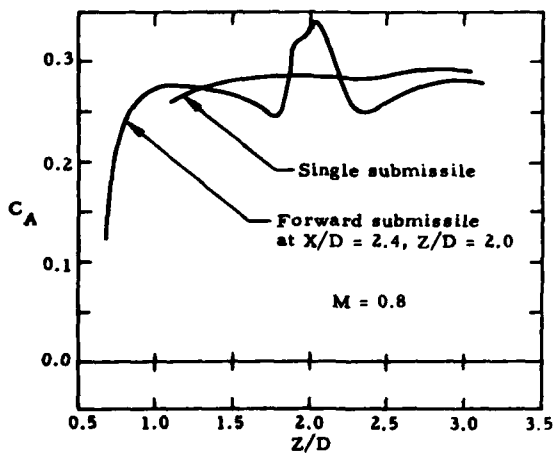
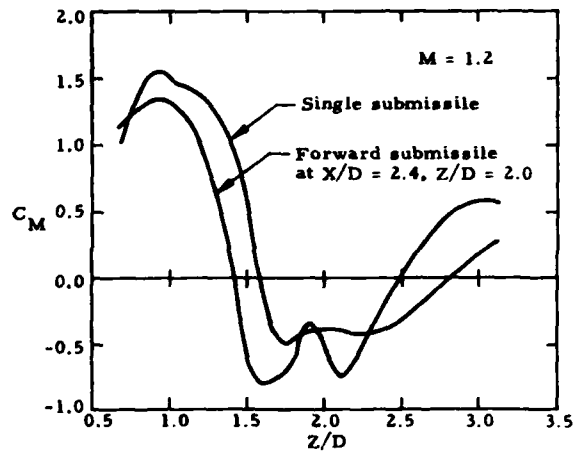
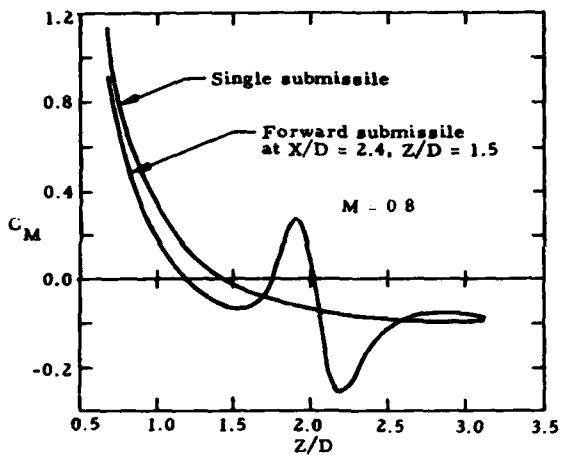
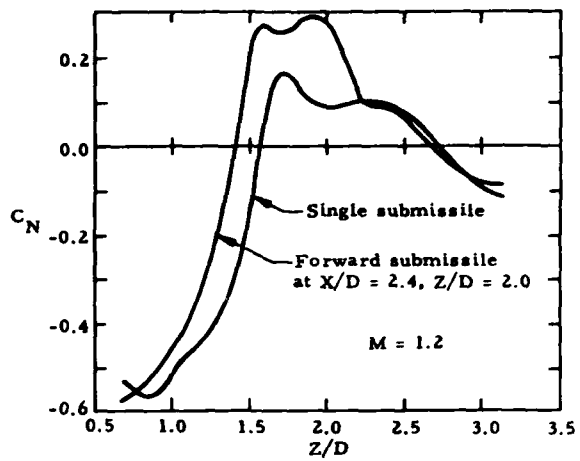
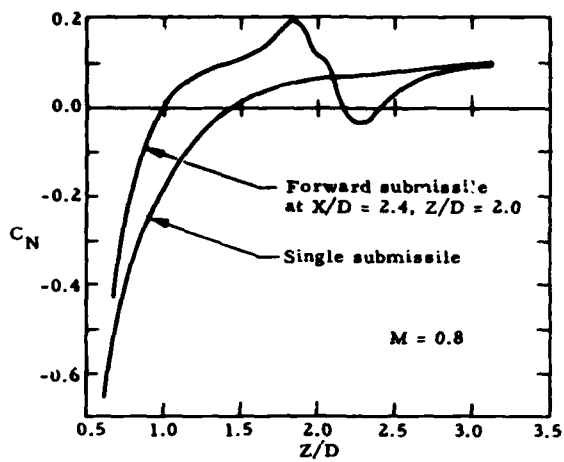


Figure 6. Submissile Interference Aerodynamics in the Wake of Another Submissile ($X/D = 4.0$, $\alpha_D = 0$ deg, $\Delta\alpha_S = 0$ deg)

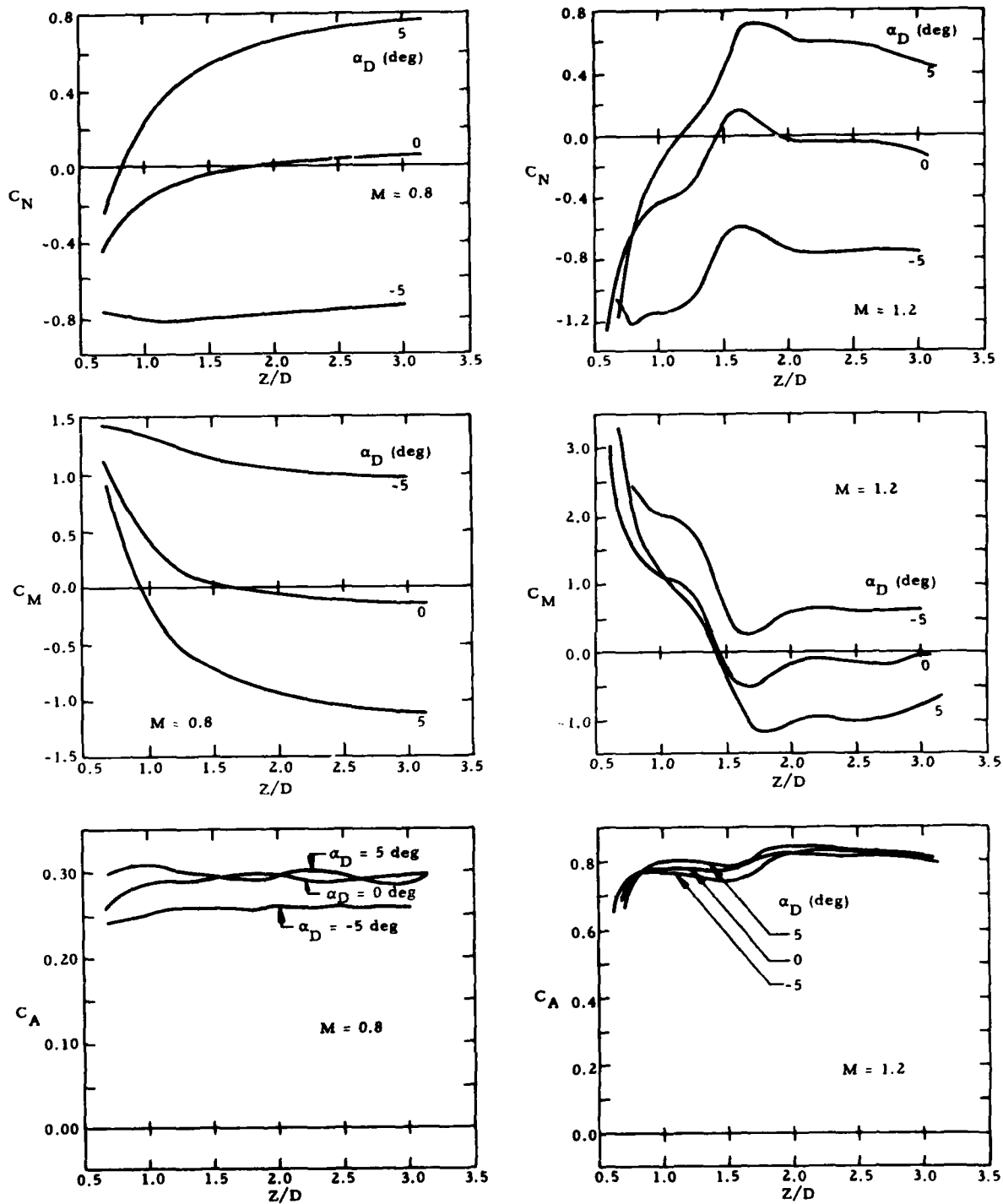


Figure 7. Effect of Dispenser Angle of Attack on Submissile Aerodynamics ($X/D = 2.4$, $\alpha_D = 0$ deg, $\Delta\alpha_S = 0$ deg)

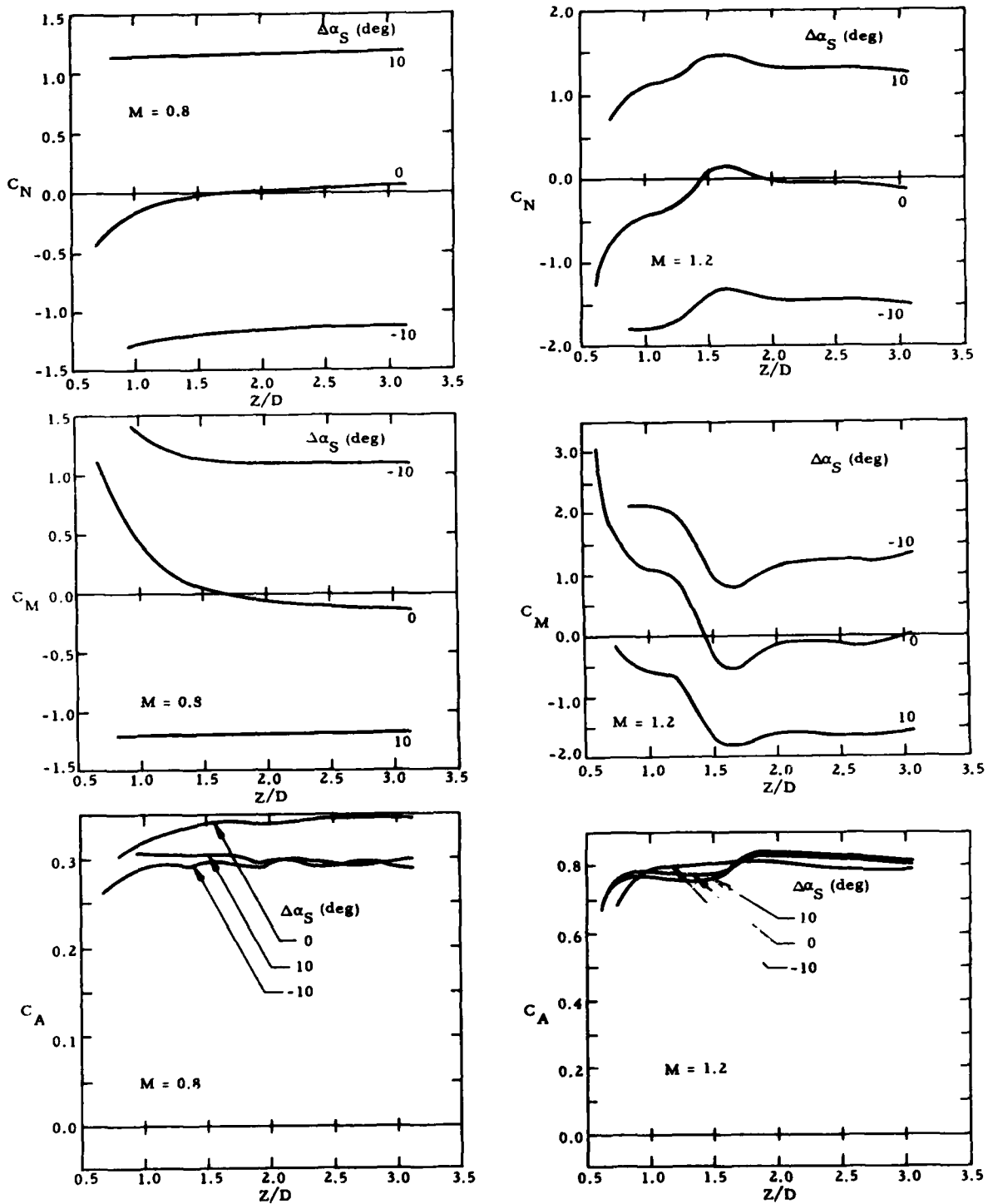


Figure 8. Effect of Submissile Pitch on Submissile Aerodynamics ($X/D = 4.0$, $\alpha_D = 0$ deg)

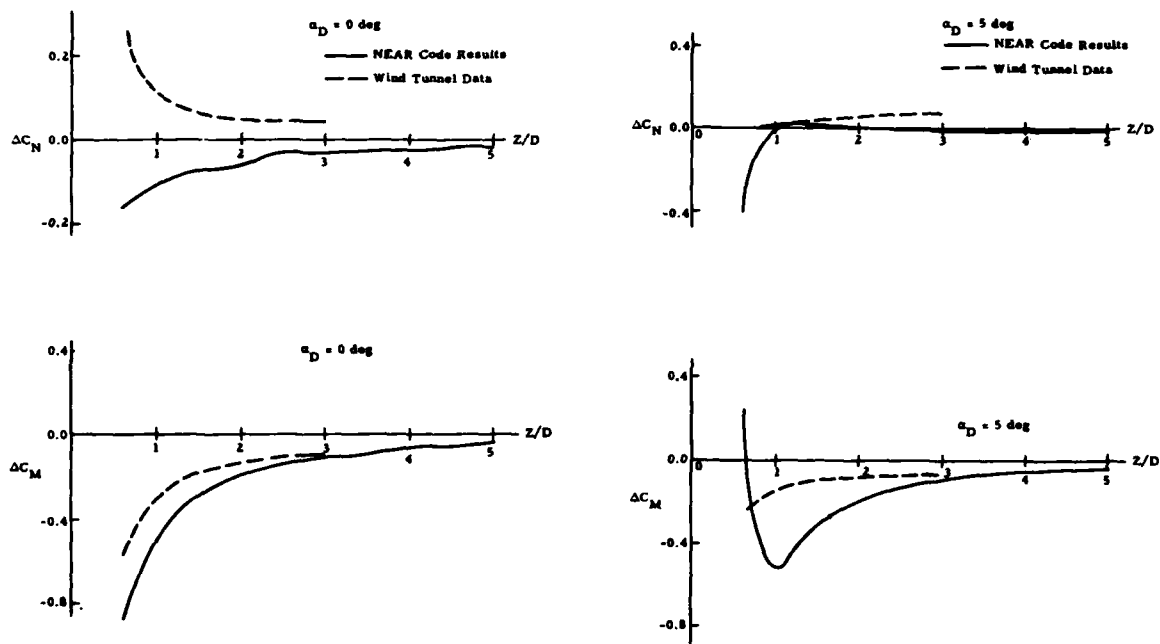


Figure 9. Comparison of Submissile Interference Aerodynamics as a Function of Submissile Vertical Displacement ($M = 0.8, \Delta\alpha_S = 0$ deg)

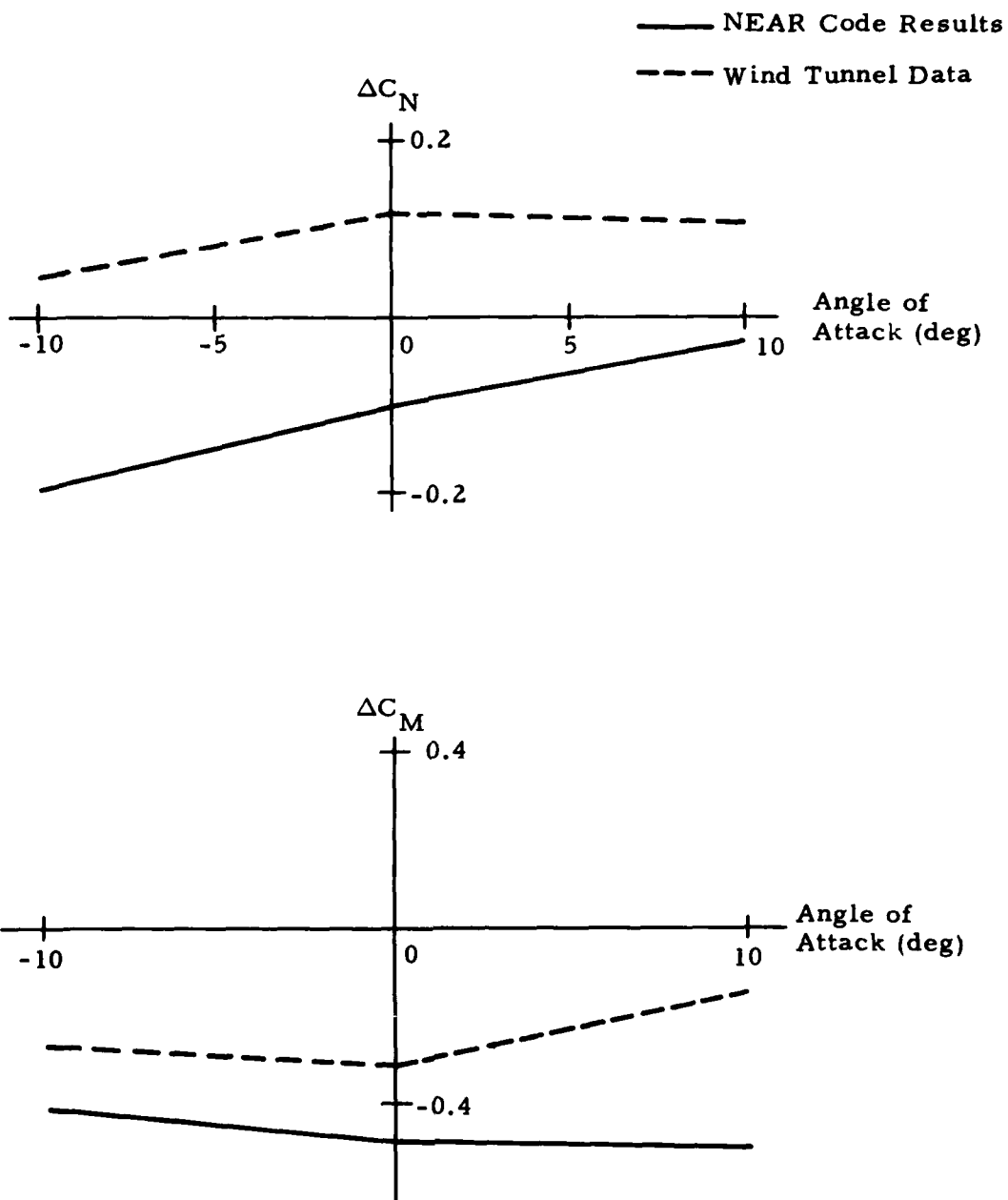


Figure 10. Comparison of Submissile Interference Aerodynamics as a Function of Submissile Angle of Attack Relative to Dispenser ($M = 0.8$, $X/D = 2.4$, $Z/D = 1.0$, $\alpha_D = 0$ deg)

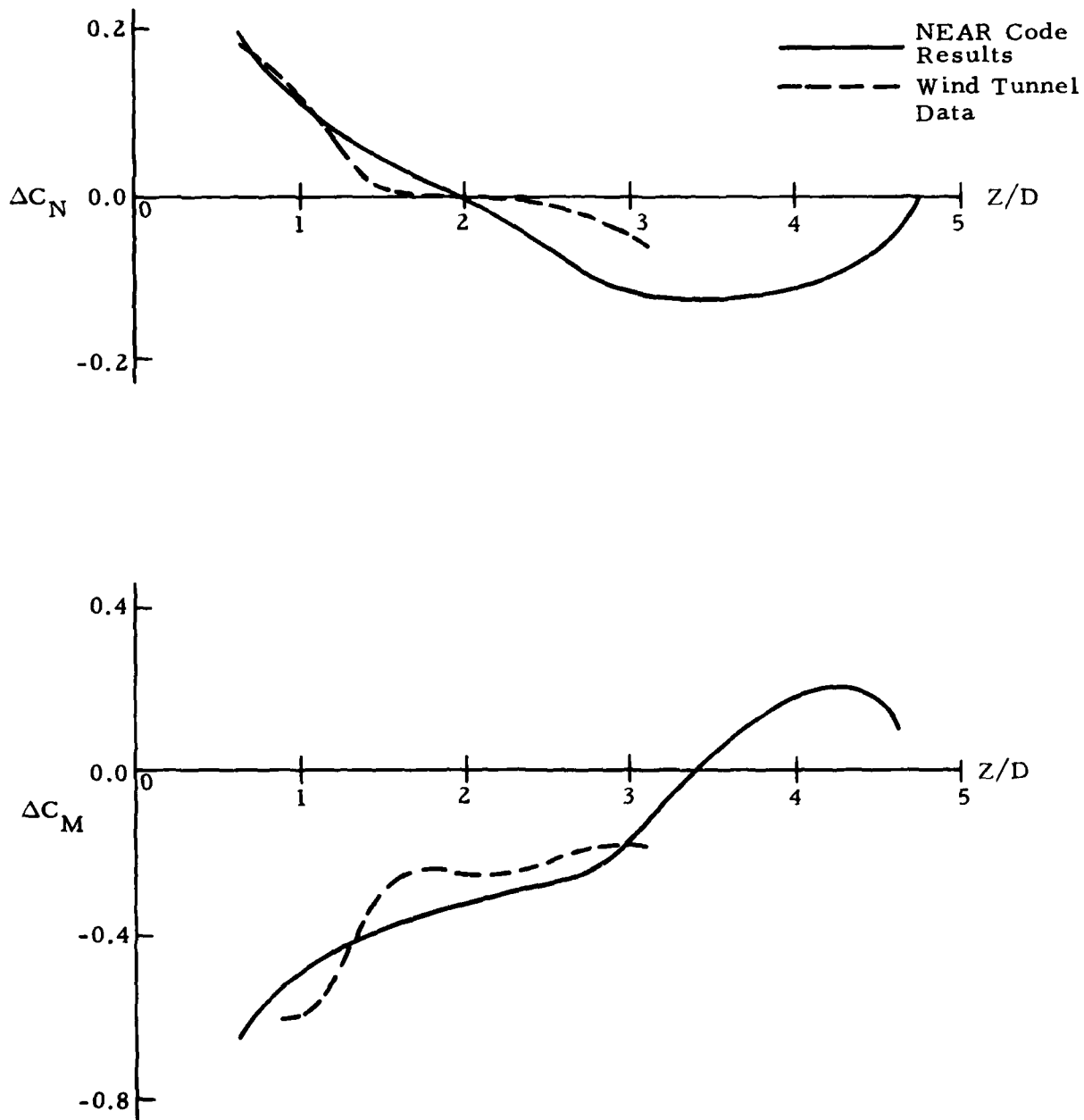


Figure 11. Comparison of Submissile Interference Aerodynamics as a Function of Submissile Vertical Displacement ($M = 1.2$, $X/D = 2.4$, $\alpha_D = 0$ deg, $\Delta\alpha_S = 0$ deg)

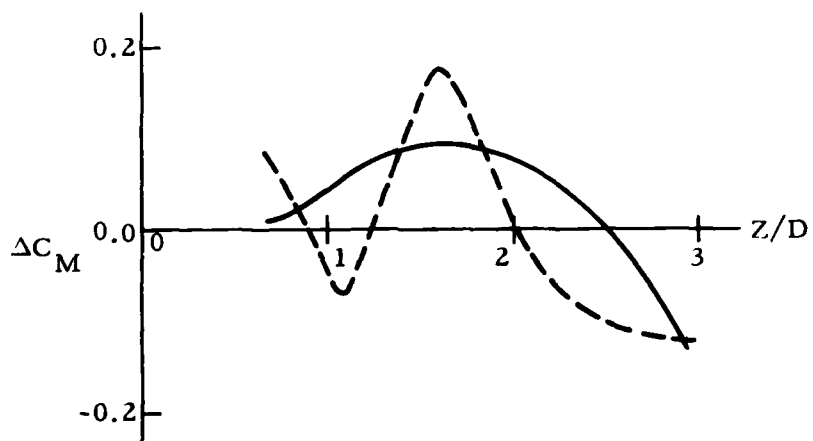
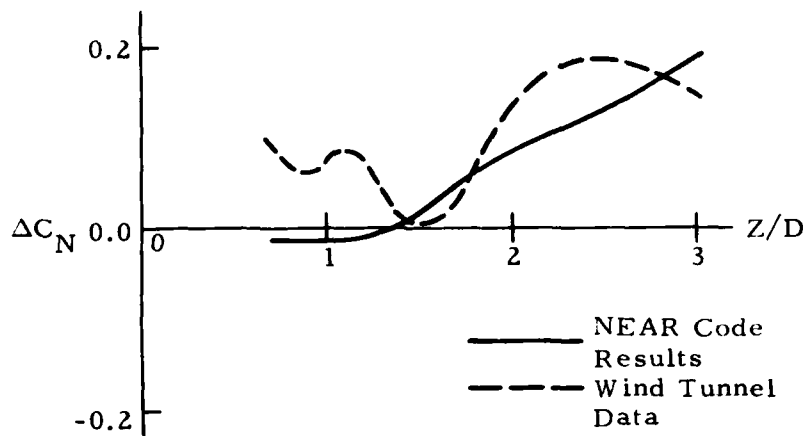


Figure 12. Comparison of Submissile Interference Aerodynamics as a Function of Submissile Vertical Displacement ($M = 1.2$, $X/D = 4.0$, $\alpha_D = 0$ deg, $\Delta\alpha_S = 0$ deg)

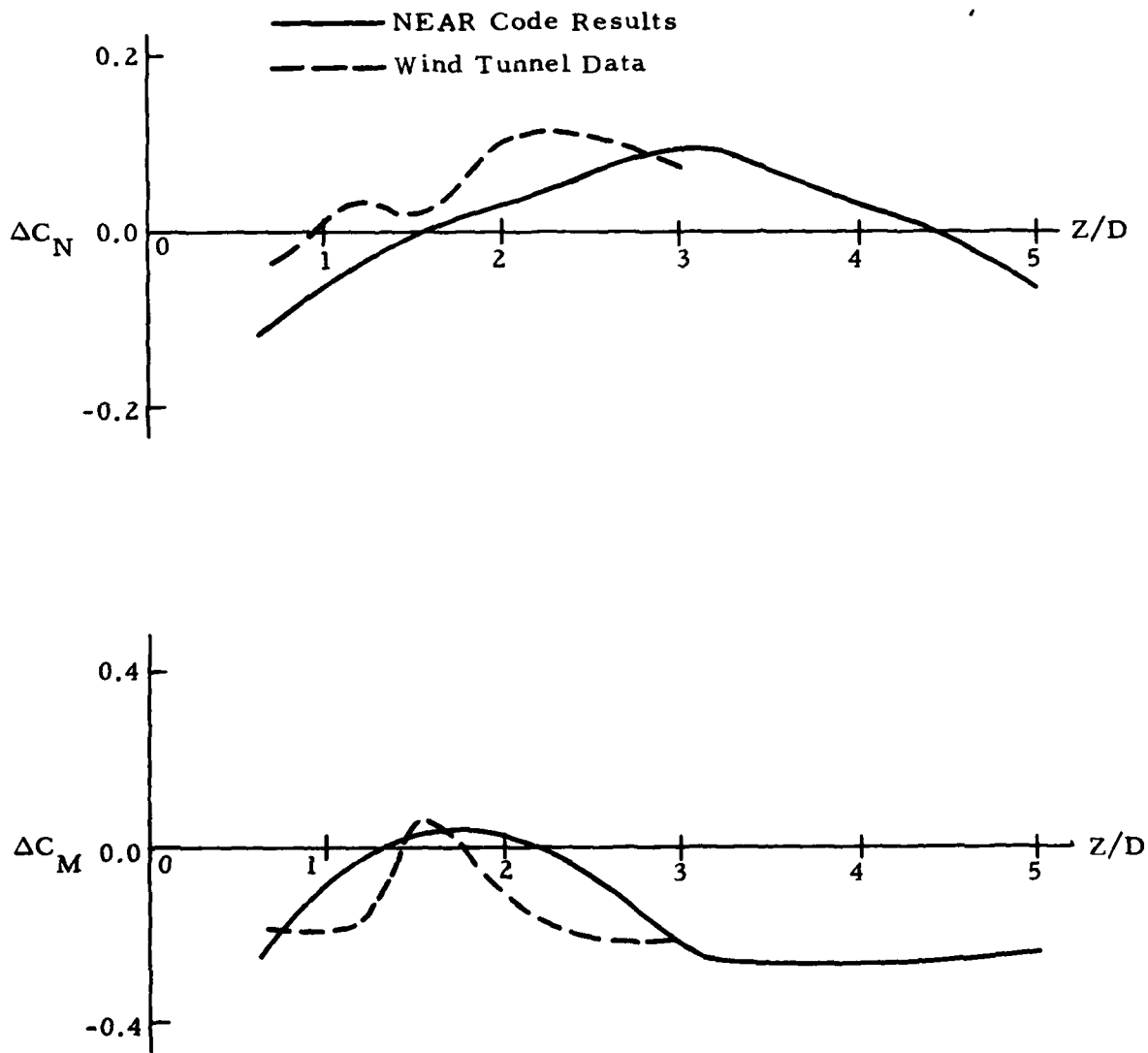


Figure 13. Comparison of Submissile Interference Aerodynamics as a Function of Submissile Vertical Displacement ($M = 1.2$, $X/D = 4.0$, $\alpha_D = 5$ deg, $\Delta\alpha_S = 0$ deg)

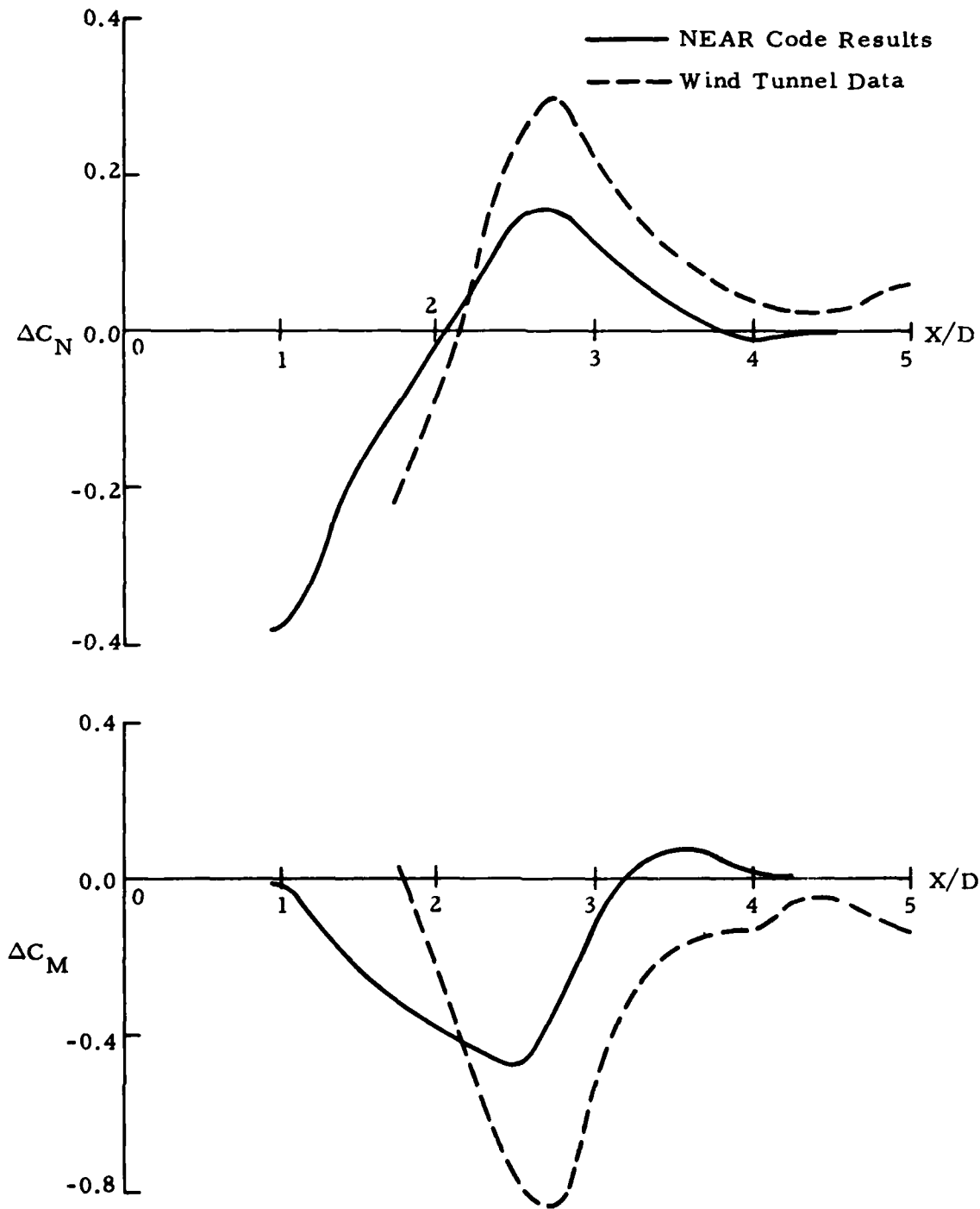


Figure 14. Comparison of Submissile Interference Aerodynamics as a Function of Submissile Longitudinal Displacement ($M = 1.2$, $Z/D = 1.0$, $\alpha_D = 0$ deg, $\Delta\alpha_S = 0$ deg)

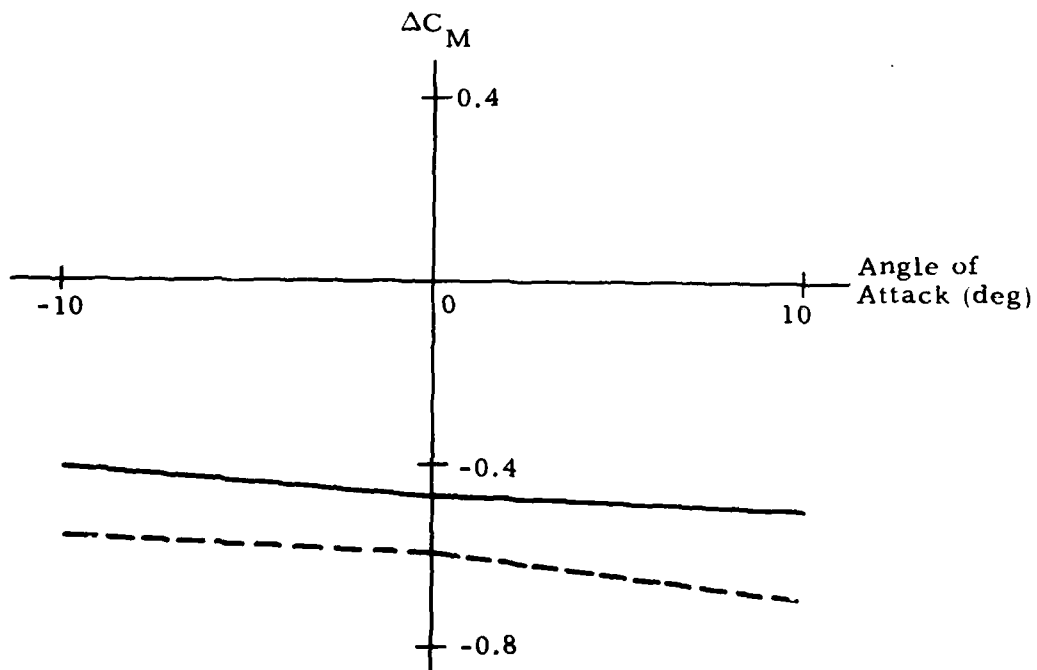
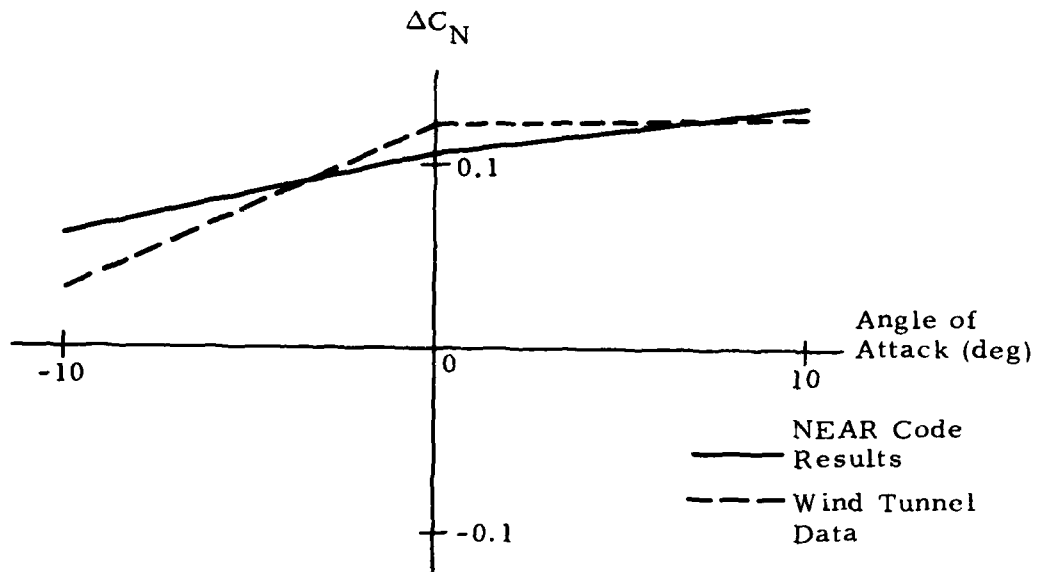


Figure 15. Comparison of Submissile Interference Aerodynamics as a Function of Submissile Angle of Attack Relative to Dispenser ($M = 1.2$, $X/D = 2.4$, $Z/D = 1.0$, $\alpha_D = 0$ deg)

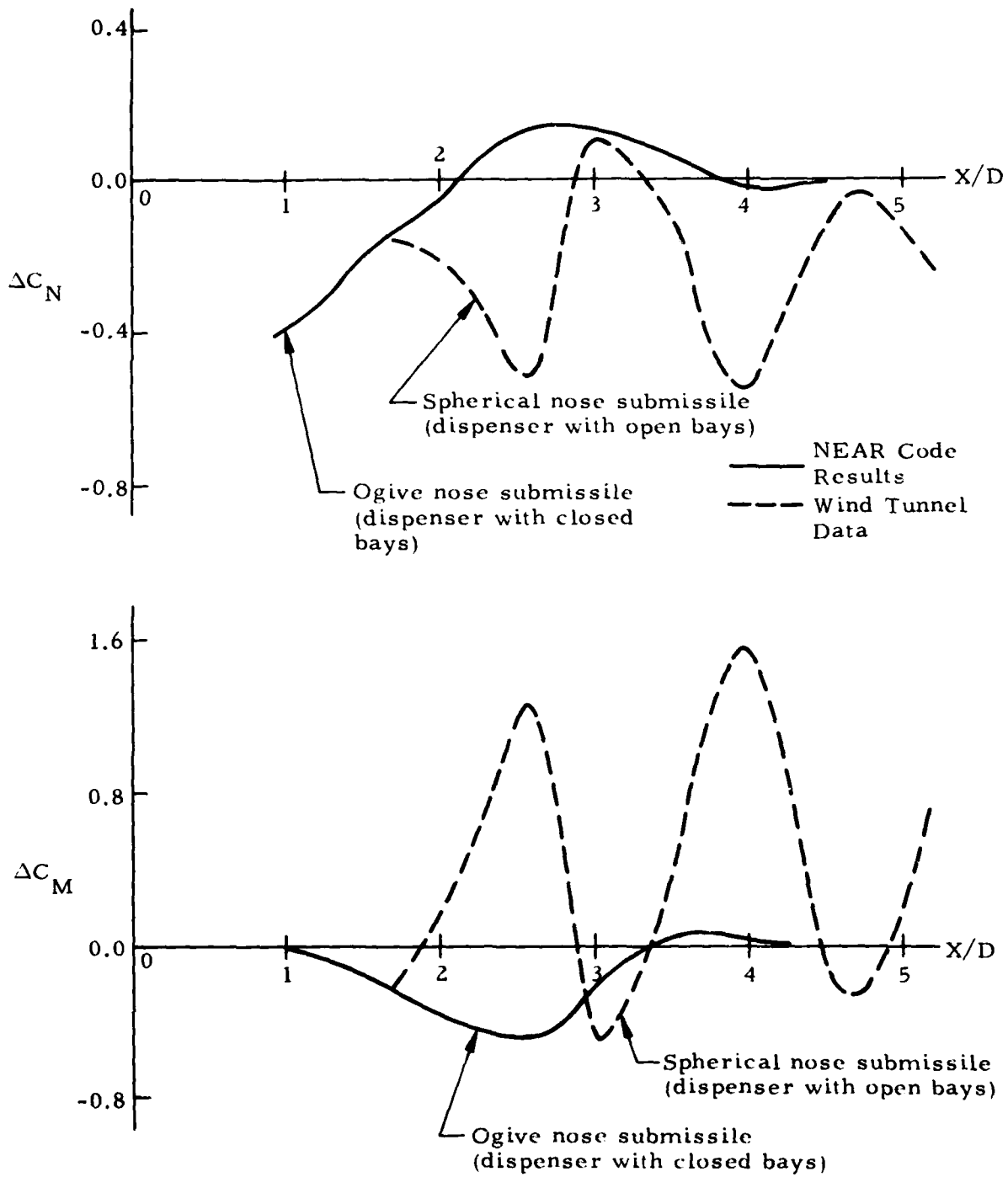


Figure 16. Comparison of Submissile Interference Aerodynamics Depicting NEAR Code Limitations ($M = 1.2$, $Z/D = 1$, $\alpha_D = 0$ deg, $\Delta\alpha_S = 0$ deg, Submissile with Fins)

GUN LAUNCH DYNAMICS OF THE NAVY 5-INCH GUIDED PROJECTILE

George Fotieo

Martin Marietta Aerospace
Orlando, Florida

ABSTRACT

The design and qualification of the Navy 5-inch guided projectile components and structure were accomplished by a combination of analytical and experimental techniques. Gun launch accelerations approach 8000 g and produce the peak structural loads. The rapid pressure decay on the projectile base at muzzle exit drives the shock loading of internal components. An analytical model was used to calculate structural loads and to define the shock environment for components. The structure and components were qualified by testing them in canisters fired from 8-inch guns, and also in the laboratory using shock machines and a pendulum impact facility.

The Navy 5" Guided Projectile (GP) is a gun launched, fin stabilized, terminally guided projectile. It uses interchangeable semiactive laser and infrared guidance units. The infrared system is a point defense weapon capable of intercepting high speed air targets. The semiactive laser system is designed to attack illuminated moving and stationary surface targets.

The GP, shown in Figure 1, consists of a guidance head, control section, warhead, motor, and stabilizing fins. An obturator is located at the aft end of the motor; it decouples the GP from the spin induced by the rifling of the gun, and also prevents high pressure gases from propagating forward. The rocket motor is a low thrust propulsion unit, used to obtain increased range for the GP. Both guidance systems achieve required terminal accuracy by canard control surfaces and a gyro-stabilized seeker.

The pressures acting on the base of the GP during gun launch are shown in Figure 2. The peak gun launch pressure is 43,000 psi, which results in a rigid body acceleration of approximately 8000 g. At muzzle exit the pressure is nominally 7500 psi. For a worn gun, the muzzle exit pressure can be as high as 9500 psi. In both cases, the rate of decay of the base pressure has been determined to be very rapid, falling exponentially to 100 psi in approximately 500 microseconds. As will be discussed later, this rapid pressure decay at muzzle exit is the driver for the set forward (tension) loads of the GP primary structure; it also is the principal contributor to the shock loading of internal components.

PRECEDING PAGE BLANK-NOT FILMED

Design requirements for the GP primary structure have been determined from the following conditions:

- set back
- balloting
- angular acceleration
- set forward

The set back (compression) loads are directly related to the peak base pressure. They are of relatively long duration when compared to the period of the GP structural modes. Consequently, they can be considered to be the equivalent of static loads.

The balloting loads are lateral loads that result from lateral impacting of the GP structure against the bore of the gun during launch. These loads are difficult to define accurately but they have been found to be small when compared to other gun loads.

The angular acceleration which results from the rifling in the bore is 60,000 radians/sec². Again, this condition produces relatively small loads. However, it is important in defining right hand or left hand requirements for threaded joints and preload nuts in order to prevent loss of preload during gun launch.

The maximum set forward loads occur at muzzle exit and their magnitude is strongly influenced by the rate of decay of the base pressure. As noted earlier the rate of decay is very rapid and results in strong excitation of the GP structural modes. The set forward design loads were calculated by means of a dynamic response analysis of the GP to the gun launch pressure time history. The model used in the analysis included structural modes up to 10 KHz and damping 2 percent of critical.

The same model was used to calculate the input shock environment for internally mounted components. A typical acceleration response of the GP structure to the gun launch pressure pulse is shown in Figure 3. The oscillatory response shown at muzzle exit is composed primarily of the response of the first two longitudinal modes of the GP. These modes have frequencies of 1350 Hz and 2200 Hz. The higher modes contribute very little to the overall dynamic response.

The shock spectra calculated from the acceleration response time history are shown in Figure 4. Two types of spectra are shown. The maxi-max spectra, which are almost always the maximum positive spectra, represent set back loadings. The maximum negative spectra shown represent set forward loadings. These spectra are useful for the design of components which are more critical for set forward loading than they are for set back loading. The negative spectra are also useful in defining the preload required for component assemblies to prevent unloading which would result in impacting of the component elements.

Two test methods have been developed to qualify components for the gun launch shock environment. The first method involves testing on a standard shock machine using a shock amplifier system. A lightweight and a heavy weight amplifier have been used. The lightweight amplifier is shown in Figure 5. These amplifiers have the capability of producing half sine pulses ranging from 5 Kg and 400 microseconds duration to 30 Kg and 120 microseconds duration.

The second test method involves testing in a full up GP structure which is impacted at the rear by a 34 pound hammer swung on the end of a 14 foot pendulum (Figure 6). This test method is particularly attractive since the GP structure is able to provide a shock transient which has the correct frequency content. Another advantage of the pendulum shock test is that the effect of structural joints opening and impacting on closing, as would occur at muzzle exit, are included in the test. This test method also qualifies the GP primary structure for the design set forward loads when the peak set forward g loadings are achieved. Pendulum shock test results have also been used to verify the accuracy of the analytical model.

Qualification of structure and components for set back loading is accomplished by installing these systems in canisters which are fired out of 8 inch guns and parachute recovered. Smaller structures and components are being qualified by testing in a small, high g centrifuge normally used to test microelectronic parts.

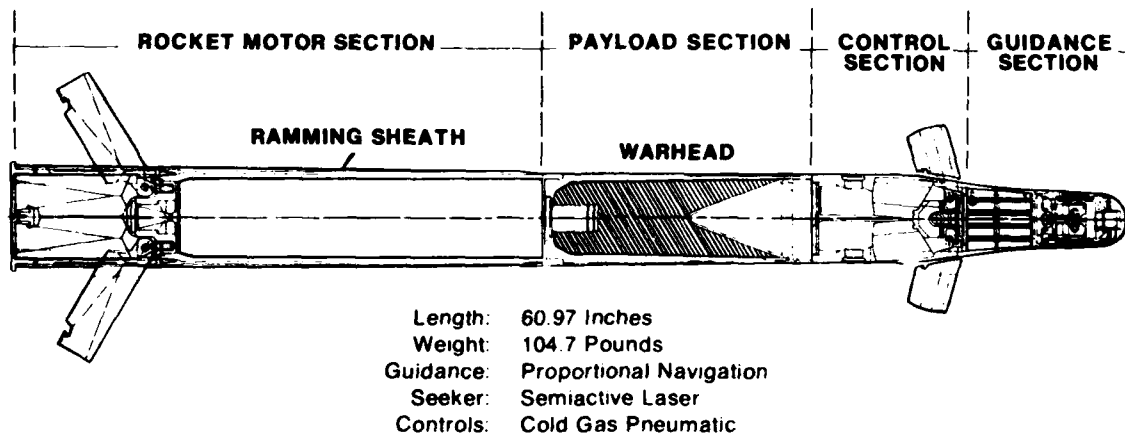


Figure 1. Navy 5-Inch Guided Projectile

Figure 2. 5-Inch GP Base Pressure

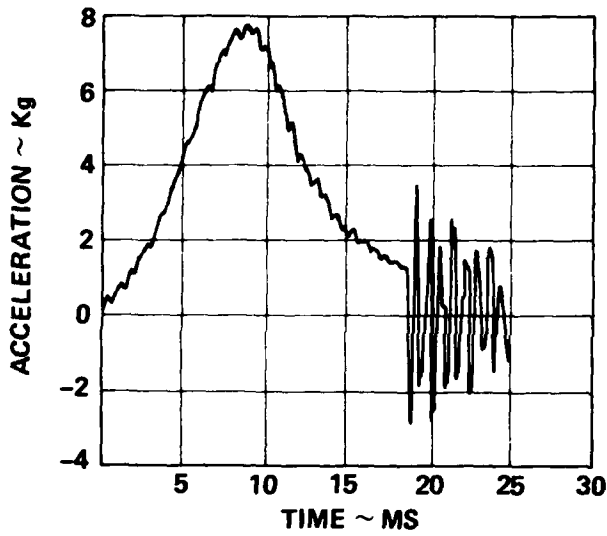
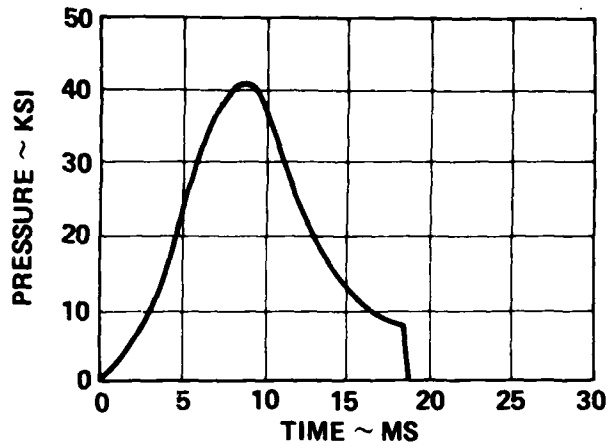
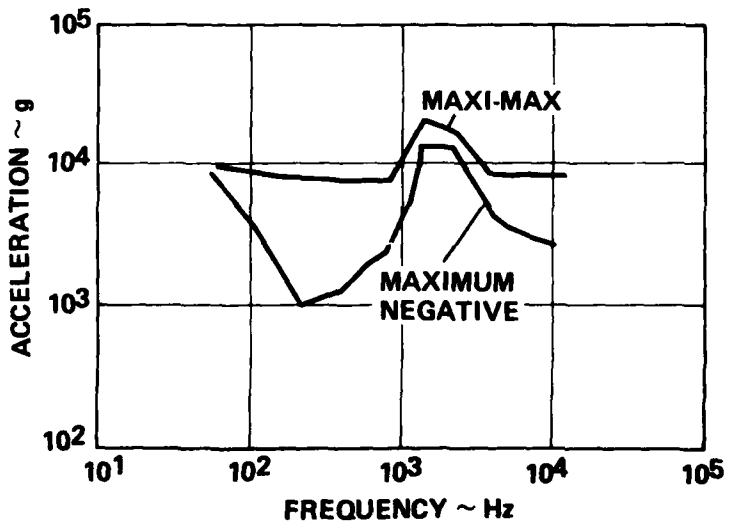


Figure 3. GP Response to Gun Launch Pressure Pulse

Figure 4. Shock Spectra



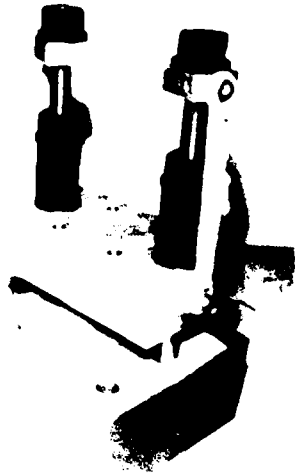


Figure 5. Lightweight Amplifier

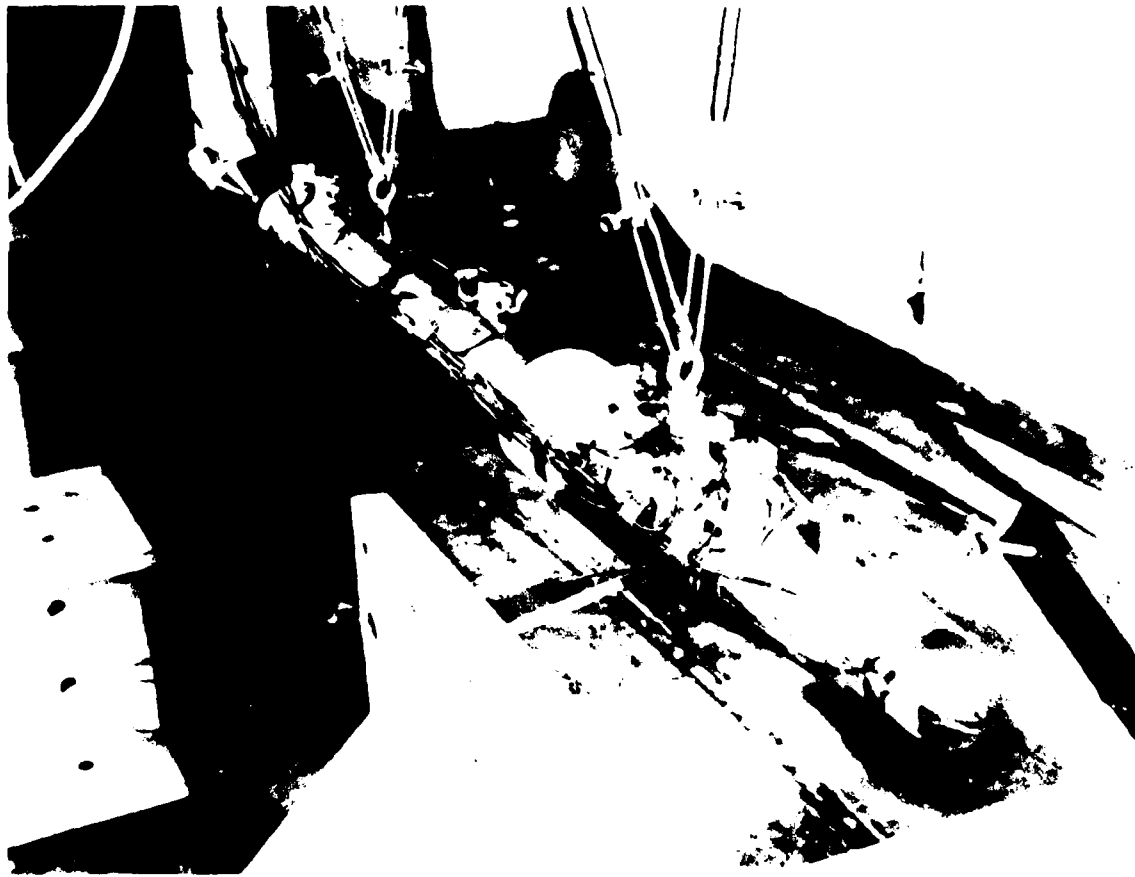


Figure 6. Pendulum Impact Test

DYNAMICS OF SUBSONIC TRACER PROJECTILES

Jaime H. Cuadros
General Dynamics, Pomona Division
Pomona, California

Gerald L. Winchenbach
Air Force Armament Laboratory
Eglin AFB, Florida

Billy F. Lucas
Air Force Armament Laboratory
Eglin AFB, Florida

ABSTRACT

An evaluation of four tracer rounds at subsonic Mach numbers has been conducted. This evaluation indicated that three of the four subsonic tracer rounds possessed large dispersion characteristics. The fourth round, the 7.62 mm NATO round, has acceptable dispersion characteristics; however, even this round demonstrated a dynamic instability at the subsonic Mach numbers. It was found that this instability can be characterized by a growing precessional vector and it is present with or without the tracer ignited. Data indicated that the instability is tolerable when the tracer is ignited because of its small effect on the dispersion of the round.

INTRODUCTION

The VIPER antiarmor weapon system is being developed by the General Dynamics Pomona Division for the U.S. Army, MIRADCOM, Redstone Arsenal, Huntsville, AL. The tactical rocket is a tube launched, shoulder fired, 2.75 inch diameter rocket containing a shaped charge warhead. For training purposes a system was proposed whereby the troops could gain experience in estimating target speed, range, etc., at one thousandth the operational cost of the tactical round. This training system consists of a standard small caliber tracer round which would duplicate as near as possible the trajectory of the tactical rocket at subsonic Mach numbers.

There were four tracer rounds which appeared to be the most likely candidates for the training application. These four candidates were the .45 Cal ACP, the .30 Cal Carbine, the 5.56 mm, and the 7.62 mm NATO round. A search of the literature for subsonic flight characteristics of the subject rounds showed either incomplete data or no data available. The data that existed were obtained primarily at higher Mach numbers (Refs 1 and 2). In order to generate computer trajectory simulations for the candidate rounds, subsonic aerodynamic data (primarily drag) were required to best match the trajectory of the tactical rocket. Also, concern existed about the dispersion of the four candidate rounds at extended ranges of up to 500 meters.

TEST DESCRIPTION

The aerodynamic tests were conducted at the Aeroballistic Research Facility (ARF) and the dispersion tests were conducted at the Ballistic Experimentation Facility (BEF). Both of the facilities are managed and operated by the Air Force Armament Laboratory and are located at Eglin AFB Florida. The ARF is an enclosed, atmospheric, instrumented, concrete structure used to examine the exterior ballistics of various free-flight munitions. The range has 131 locations as instrumentation sites. Each location has a physical separation of 1.5 meters and presently 50 of the sites are used to house fully instrumented orthogonal shadowgraph stations. The nominal operating temperature of the range is 22° Celsius. For a complete description of the ARF see Reference 3. The BEF is an outdoor range located on Test Area A22 and consists of concrete gun pads, large open area, and projectile impact revetments along with limited instrumentation.

The aerodynamic data were obtained using classical data reduction procedures, see References 4 and 5, and six degree of freedom numerical integration data reduction techniques as outlined in References 6 and 7. The numerical integration technique determines the aerodynamic coefficients and derivatives directly from the fitted motions; thereby, eliminating the rotating vectors analogy inherent in the classical data reduction procedure.

All the drag data obtained during the Phase I firing in the ARF were obtained using a simplified distance time analysis. The distance data were not obtained by computing the projectiles position as measured from the shadowgraph film as is the normal procedure. These distance data were obtained by measuring the distance between infrared (IR) light screens and the associated times were those corresponding to the IR screen sensor pulses. This initial approach to the test program was dictated by the fact that many rounds were to be fired in a short period of time and that initially only the total average drag coefficients were of concern. For a complete description of the tests and all the results obtained see Reference 8.

TEST RESULTS

The 5.56MM projectiles were test fired at the ARF to establish the CD coefficient at various Mach numbers for input to the computer simulation. Figure 1 is the CD profile from these tests and Figure 2 is a shadowgraph of the 5.56MM bullet at the 200 m. station showing the angle of attack developed by this range.

The .45 cal projectiles were similarly tested in the ARF. Due to the age of the cartridges the tracer failed to ignite in about 50% of the firings. When the tracer did not ignite the flight was more erratic. Outdoor firings were also conducted at the BEF where the trajectory was shown to be unsatisfactory (a growing spiral after about 300 meters). The same results were encountered with the .30 cal carbine projectile. Figure 3 is the CD profile for the .45 caliber tracer bullet. No CD profile is available for the .30 cal carbine tracer bullet as it was too unstable to be fired in the ARF.

The firings of the 7.62MM M-62 tracer at the BEF did not show the instability displayed by the other rounds. The 7.62MM bullet became the preferred bullet for the Viper tracer trainer. Sufficient firings were then conducted at the ARF to develop the data required. Figure 4 is a typical velocity versus range data collection for the 7.62MM projectile. The scatter is caused by the interaction of the tracer light with the IR screens. Figure 5 is the CD profile for the 7.62MM, M-62 tracer bullet.

As mentioned before, when the tracer failed to ignite, the 7.62MM rounds experienced an obvious and severe motion amplitude growth. It should be noted that only a small percentage of the tracers failed to ignite properly. However, since the cause of this motion growth phenomenon was unknown and the result severe, it seemed prudent to fire ten additional 7.62MM rounds in the ARF (Phase II) and extract all the aerodynamic coefficients and derivatives in order to investigate this phenomenon. These ten 7.62MM M-62 rounds were fired from a .30 cal carbine barrel (1 turn in 10 inches) using a standard .30 cal carbine case loaded with 4.8 grains of Unique® propellant. The tracer was not permitted to ignite on five of the rounds by applying a thin coat of Silastic 140 RTV Adhesive/Sealant® to the base of the rounds. The other five rounds were fired without any modification and the tracer ignited normally.

A summary of the classical Linear Theory results for the five 7.62MM rounds with the tracer ignited are shown in Table 1. A typical angular motion pattern for one of these rounds is shown in Figure 6. As can be seen from Table 1, the magnitude of the nutational vector (K10) is much smaller than the magnitude of the precessional vector (K20). Also, the damping rate of the precessional vector (L2) is positive for all rounds except for the round experiencing the smallest angles of attack. However, the typical motion pattern shown in Figure 6 indicates that the nutational vector is obviously damped (negative value of L1). For this condition, where the nutational vector is small and decreasing and the precessional vector is large and increasing, the angular motion pattern tends to become an ever increasing circle. For the rounds where the tracer is ignited this undamped precessional vector develops into angles of attack of about 10 degrees during the measured portion of the flight.

A summary of the classical Linear Theory results for the five 7.62MM rounds for which the tracer did not ignite is shown in Table 2. A typical motion pattern for one of these rounds is shown in Figure 7. All the comments made previously concerning the rounds where the tracer ignited hold for these "tracer off" rounds as well except for one significant difference. This difference is that the damping rate of the precessional vector (see L2 in Table 2) is much larger (still positive) than previously indicated in Table 1. This large positive value for L2 causes the aforementioned circular motion pattern to develop much faster and culminates in larger angles of attack.

Since the angular motions for both "tracer on" and "tracer off" rounds are characterized by the precessional vector and its downrange growth coupled with the nutational vector, predictions of the total angle of attack as a function of distance can be accurately made by ignoring the nutational vector and considering the precessional vector only. This prediction has been accomplished and is shown in Figure 8. The curves shown in Figure 8 were computed with the following relation

$$K_p = (K20)d^{(L2)X}$$

where

K20 = Initial amplitude of the precessional vector (assumed to be 5.73 degrees)

L2 = Average of the precessional damping rates as shown in Table 1 and Table 2

X = Downrange distance

The curves shown in Figure 8 show that the typical "tracer off" rounds reach a total angle of attack of 90 degrees prior to traveling 1640 ft (500M). It is not believed that the rounds actually tumble end over end but most likely remain in a "flat spin" condition. The curve in Figure 8 showing a typical "tracer on" round also indicates that the motion is growing; however, the maximum angle of attack expected at 500 meters is about 20 degrees. The outdoor firings indicate that this angle of attack (20 degrees) does not severely affect the dispersion of the rounds at 500 meters.

It is not known why the burning tracer has the effect of decreasing the dynamic instability of the 7.62MM rounds at subsonic Mach numbers, it is suspected that a jet damping effect could be acting or perhaps a wind vane effect caused by the tracer plume.

CONCLUSIONS

In summary the following conclusions can be made.

1. The 7.62MM tracer round is dynamically unstable at subsonic Mach numbers, with or without the tracer ignited.
2. The dynamic instability is decreased when the tracer is ignited.
3. The angular motion of the round with or without the tracer ignited, can be characterized by a growing precessional vector.
4. The dynamic instability for the "tracer on" rounds is acceptable because of its small effect on the dispersion.
5. The .30 cal carbine, .45 cal ACP and the 5.56 MM tracer rounds have very poor low velocity stability characteristics and therefore are not suitable for the Viper tracer trainer application.

REFERENCES

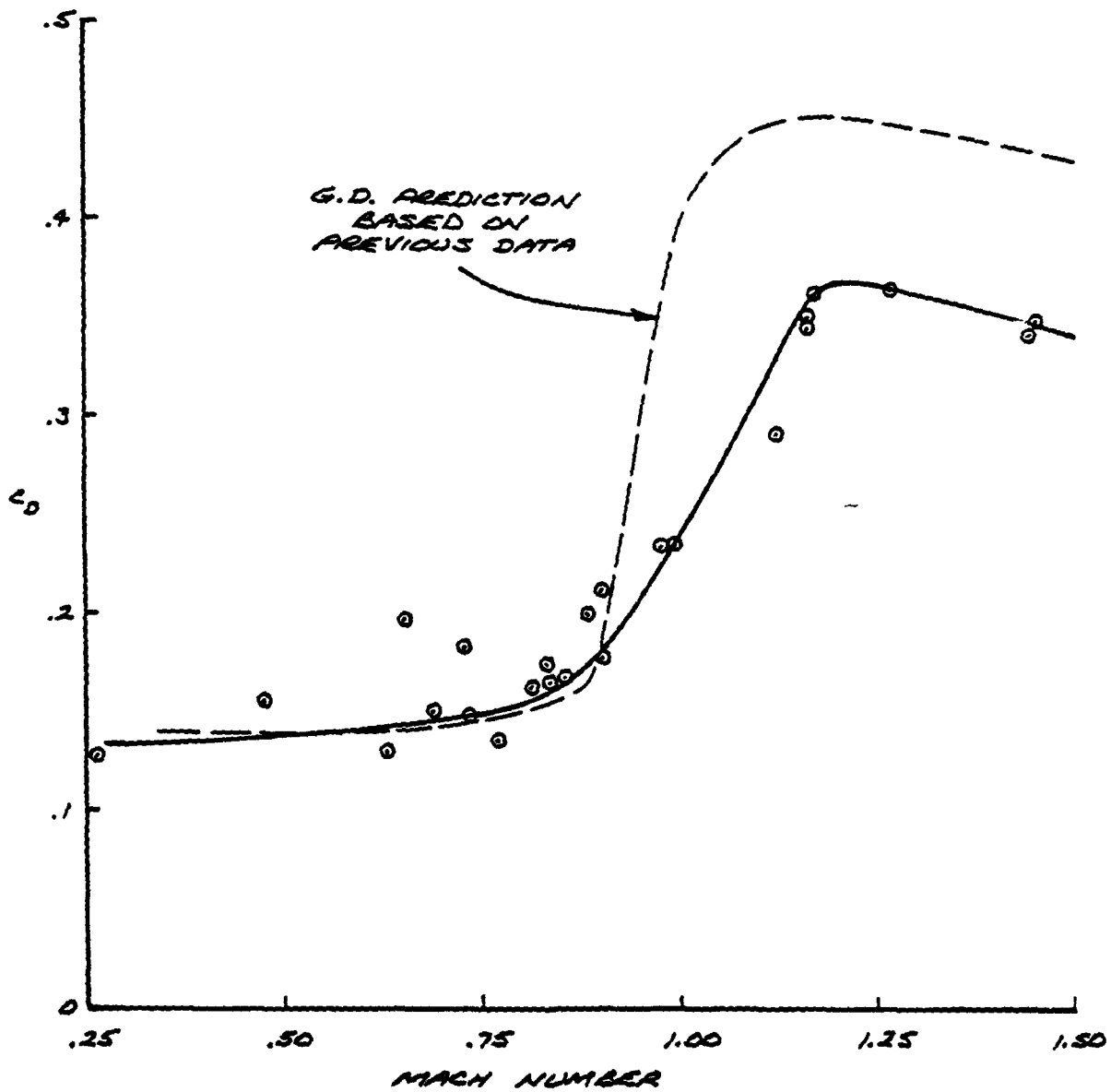
1. Piddington, Maynard J., "Aerodynamic Characteristics of the 7.62MM NATO Ammunition M-59, M-80, M-61, M-62", BRL Memorandum Report No. 1833, March 1967.
2. Braun, Walter F., "Aerodynamic Data For Small Arms Projectiles", BRL Report No. 1630, January 1973.
3. Winchenbach, G. L., Galanos, D. G., Kleist, Judith Sullivan and Lucas, Billy F., "Description and Capabilities of the Aeroballistic Research Facility", AFATL-TR-78-41, February 1978.
4. Murphy, C.H., "Data Reduction For the Free-Flight Spark Ranges", BRL Report No. 900, February 1964.
5. Murphy, C.H., "Free-Flight Motion of Symmetric Missiles", BRL Report No. 1216, July 1963.
6. Whyte, Robert H. and Hathaway, Wayne H., "Aeroballistic Range Data Reduction Technique Utilizing Numerical Integration", AFATL-TR-74-41, February 1974.
7. Whyte, Robert H. Winchenbach, G.L. and Hathaway, Wayne H., "Analysis of Free Flight Trajectory Data for a Complex Asymmetric Missile Configuration at Subsonic Mach Numbers", Paper presented at the Atmospheric Flight Mechanics Conference, AIAA, August 6, 7, 8 1979, Boulder, Colorado.
8. Cuadros, J. H., "Summary Report Viper Tracer Trainer Development", General Dynamics Pomona Division TM 6-348-97.4-4, July 1979.

Table 1. Linear Theory Results for Five 7.62MM Rounds with "Tracer ON"

Shot No.	Mach	DBSQ DEG2	K10 DEG	K20 DEG	L1 1/M	L2 1/M	W10 Deg/M	W20 Deg/M	WD1 Deg/M	WD2 Deg/M
S79060732	.840	73.7	1.57	6.52	-.00656	.00680	142.347	21.511	0.00000	.00893
S79060733	.816	42.7	.60	5.71	-.00656	.00328	145.368	22.943	0.00000	-.03737
S79060735	.801	5.3	.49	3.00	-.00656	-.00316	145.508	23.214	0.00000	-.00995
S79060838	.811	74.7	.35	8.29	-.00656	.00112	143.812	22.195	0.00000	-.00768
S79061142	.770	76.2	.87	6.06	-.00656	.00417	141.831	21.743	0.00000	-.01111

Table 2. Linear Theory Results for Five 7.62MM Rounds With "Tracer OFF"

Shot No.	Mach	DBSQ DEG2	K10 DEG	K20 DEG	L1 1/M	L2 1/M	W10 Deg/M	W20 Deg/M	WD1 Deg/M	WD2 Deg/M
S79060731	.693	113.4	.05	5.40	-.00656	.00838	147.146	20.201	0.00000	-.01833
S79060837	.810	156.0	1.00	5.54	-.00656	.01048	145.341	21.914	0.00000	-.04266
S79061139	.746	148.0	1.03	6.86	-.00656	.00563	143.769	21.299	0.00000	-.02187
S79061140	.733	308.8	.72	5.47	-.00656	.01034	145.341	22.272	0.00000	-.04927
S79061141	.749	141.7	.11	5.77	-.00656	.00718	141.207	19.781	0.00000	-.02185

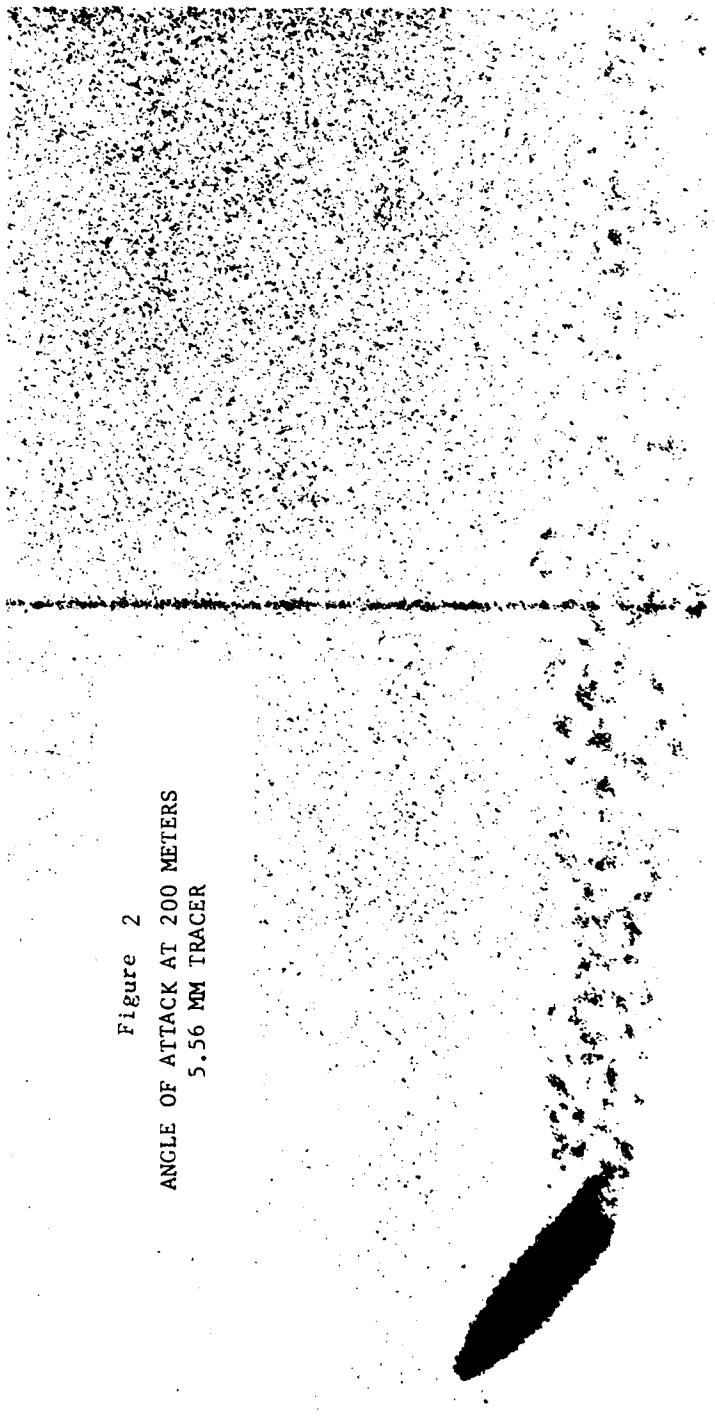


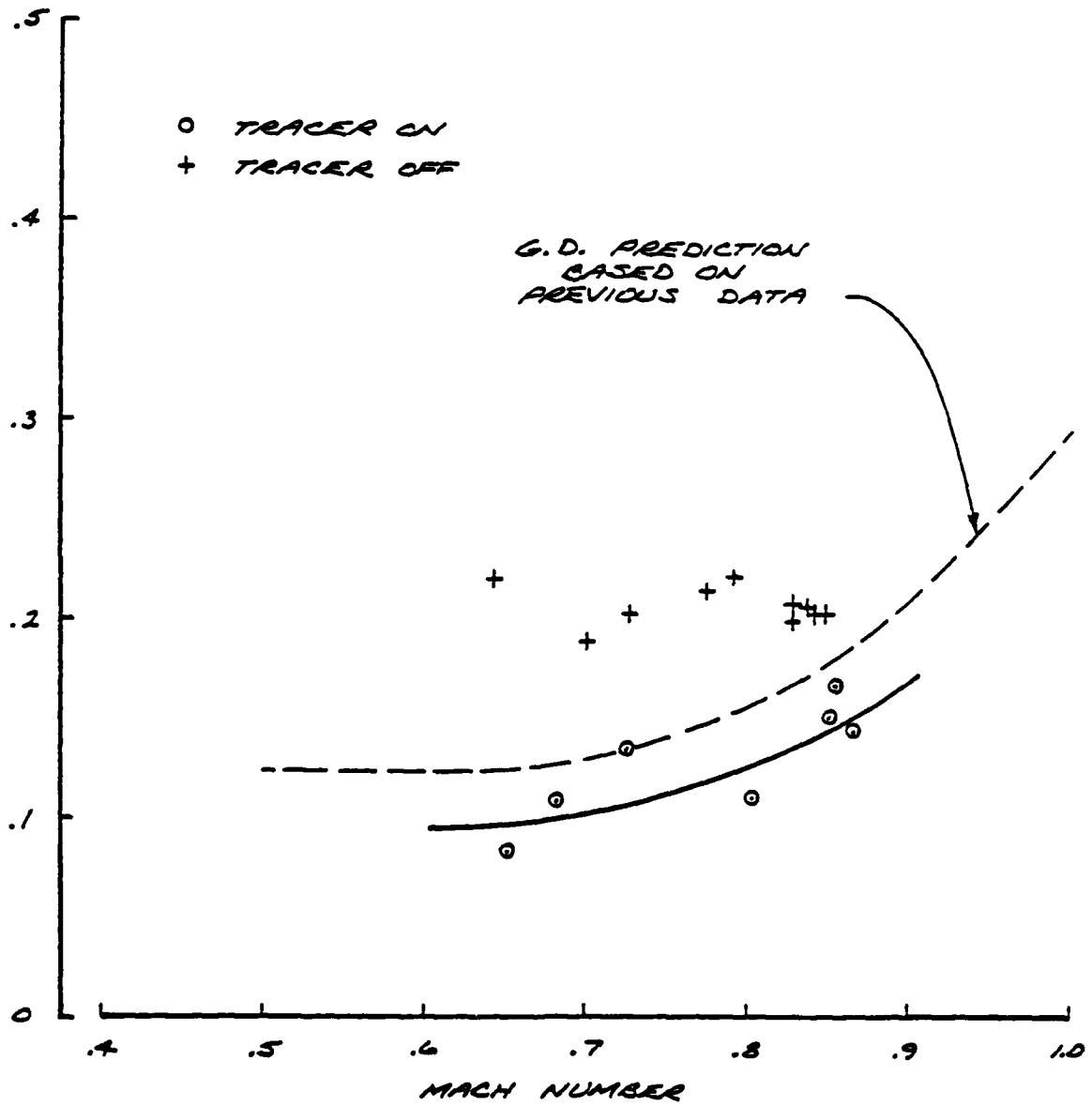
5.56 TRACER ROUNDS

Figure 1

C_D VS Mach No. 5.56 mm Tracer Bullet

Figure 2
ANGLE OF ATTACK AT 200 METERS
5.56 MM TRACER





0.45 CAL
 TRACER ROUNDS

Figure 3

C_D VS Mach No. .45 Caliber Tracer Bullet

60 SMALL CALIBER DRAG TEST

TEST SHOT # 149

7.60 TRACER

4.8 GR UNIQUE

.30 CARB CASE

$$C_D = 0.169$$

MID RANGE MACH NO.

$$= 0.729$$

INITIAL VELOCITY = 872.1

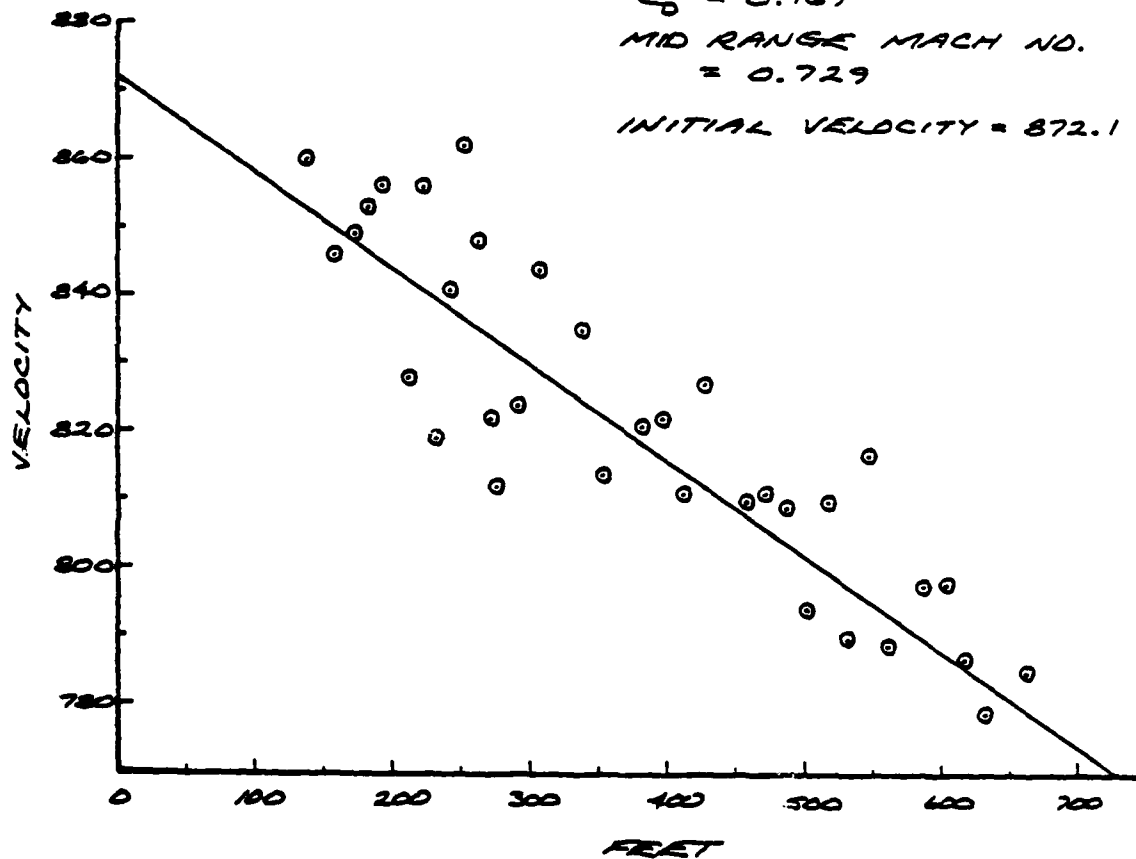
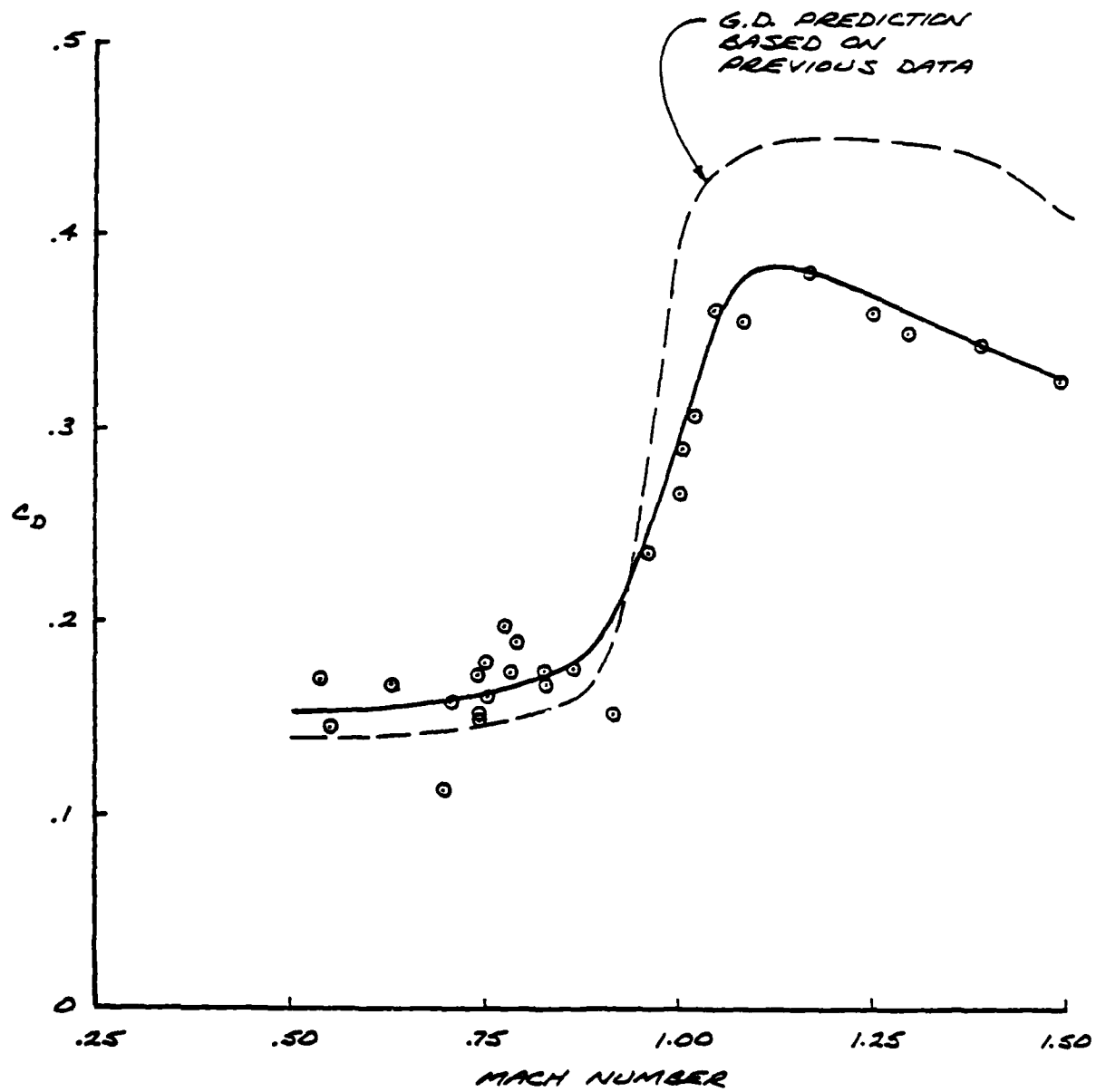


Figure 4

Typical Velocity VS Range Plot to a 7.62 mm Tracer Bullet Test

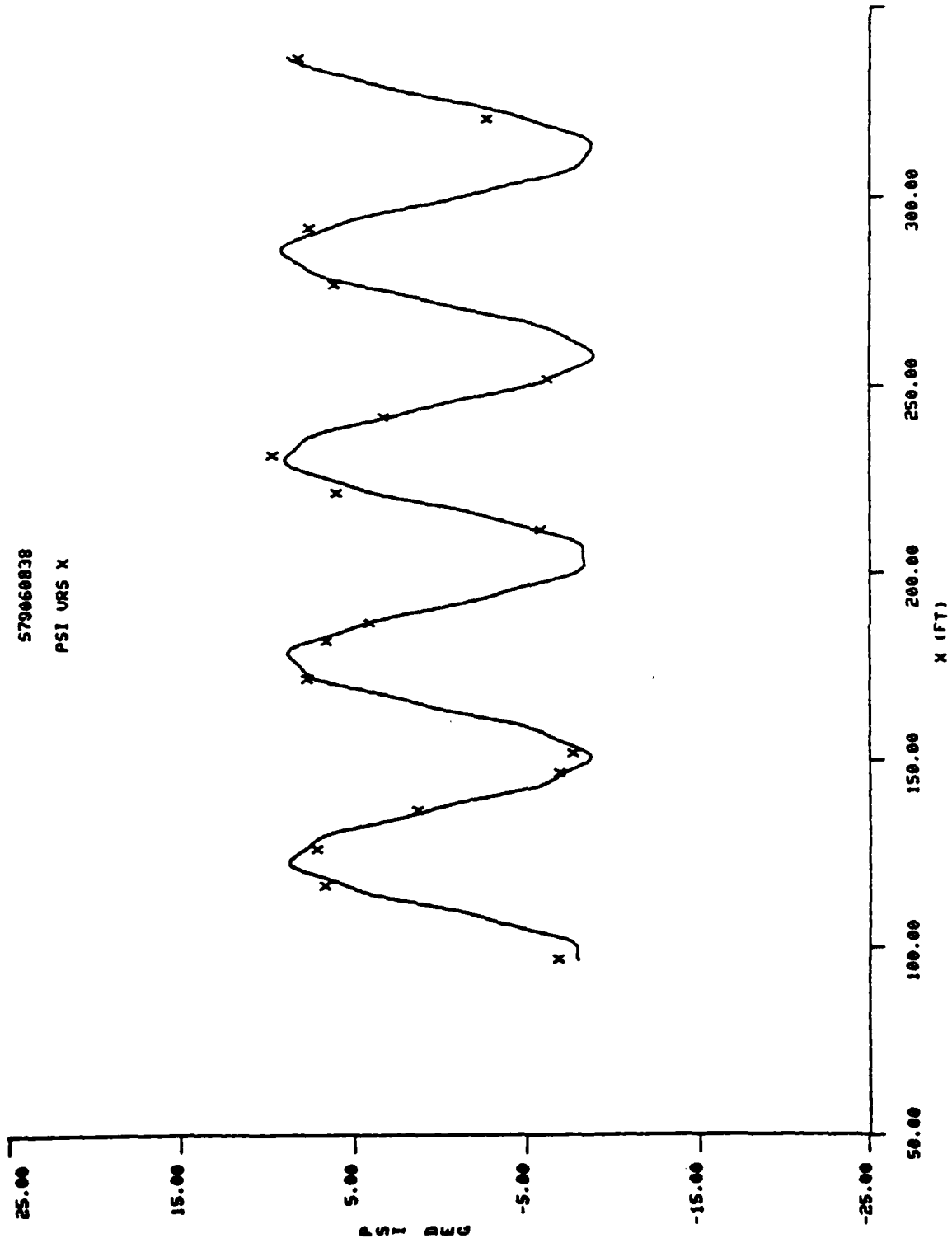


7.62 TRACER ROUNDS

Figure 5

C_D VS Mach No. 7.62 mm Tracer Bullet

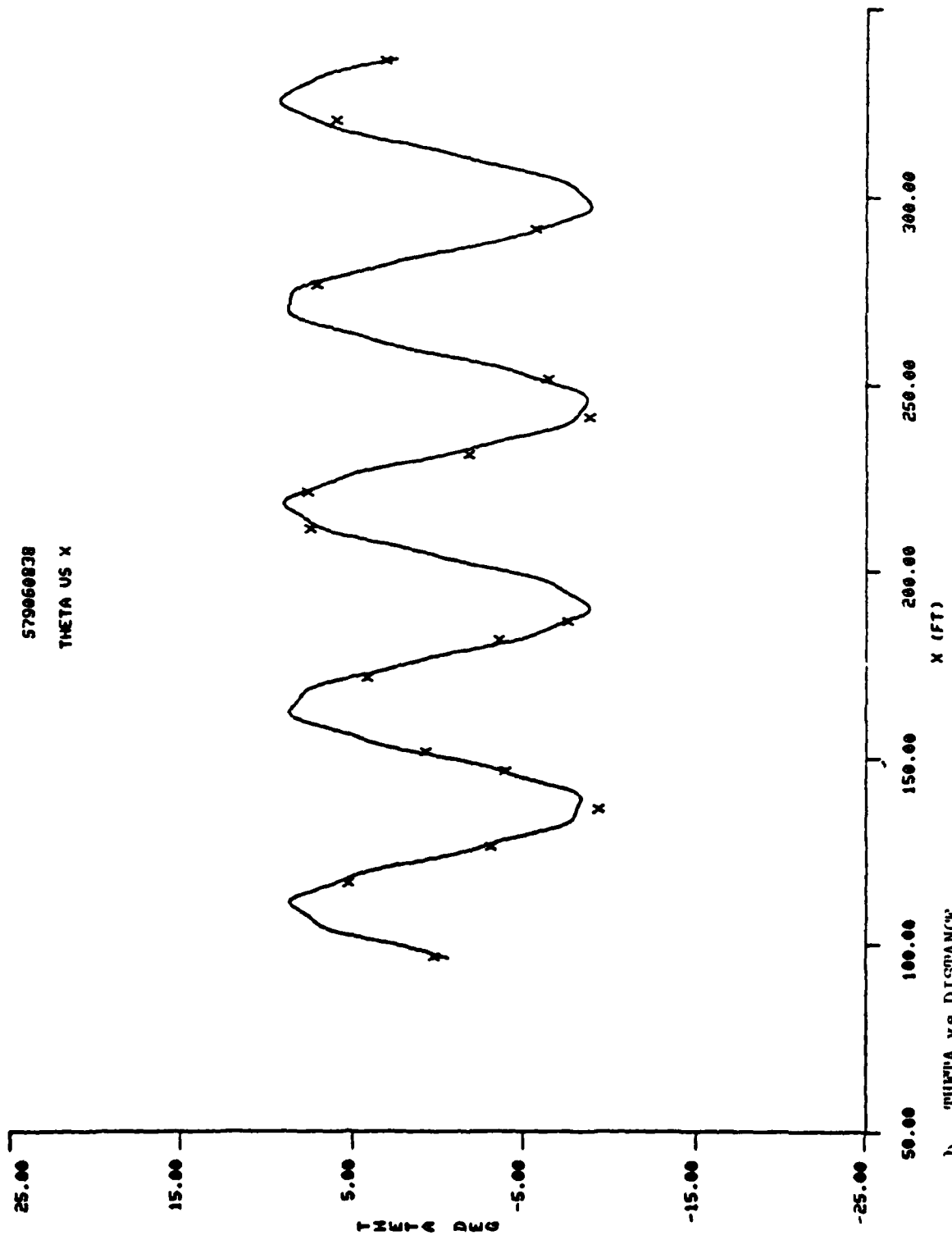
579060838
PSI URS X



a. PSI vs DISTANCE

FIG 6. TYPICAL MOTION PATTERN FOR "TRACER ON" ROUNDS

579060838
THETA US X



b. THETA vs DISTANCE

FIG 6 (CONTINUED)

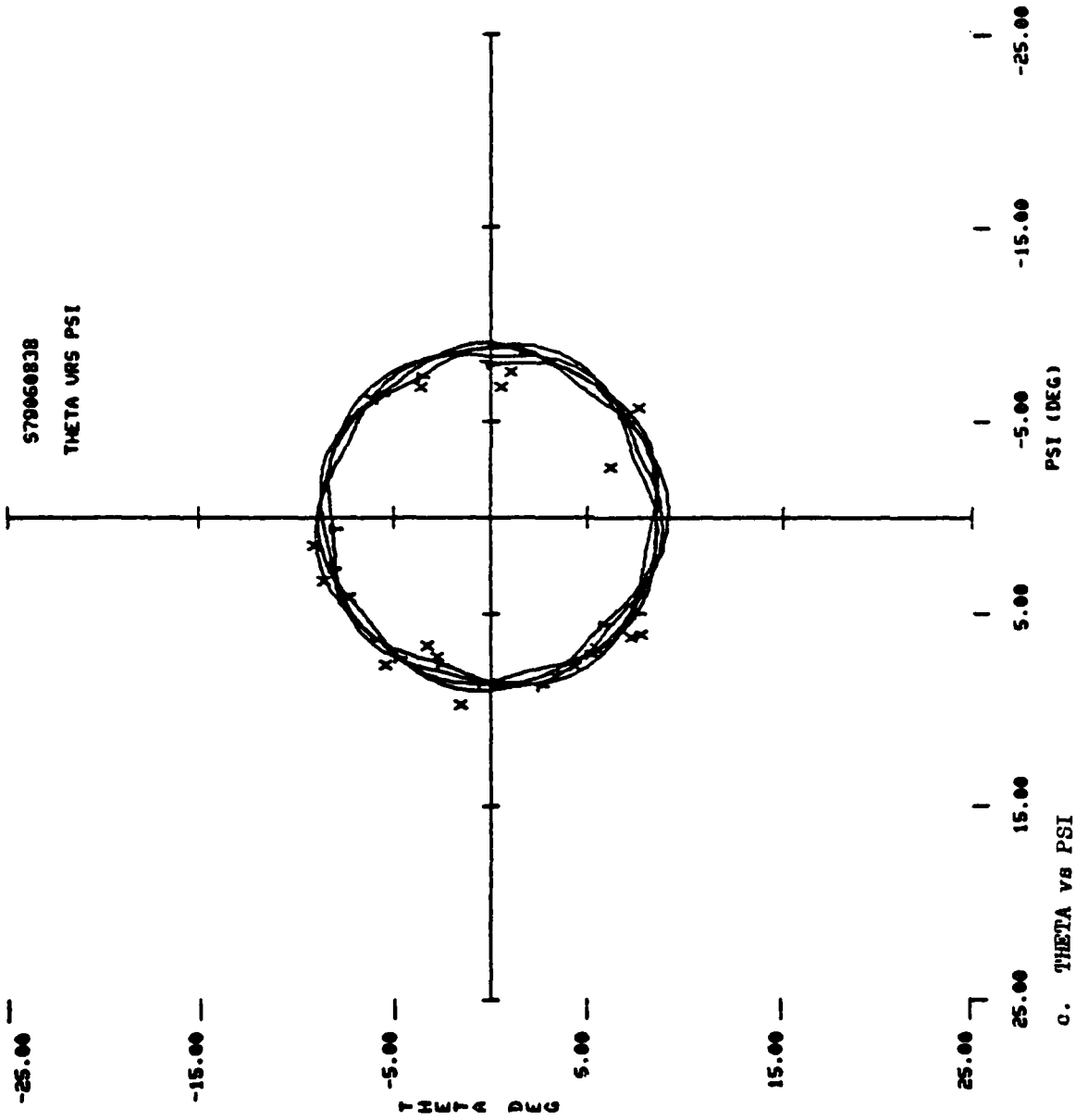
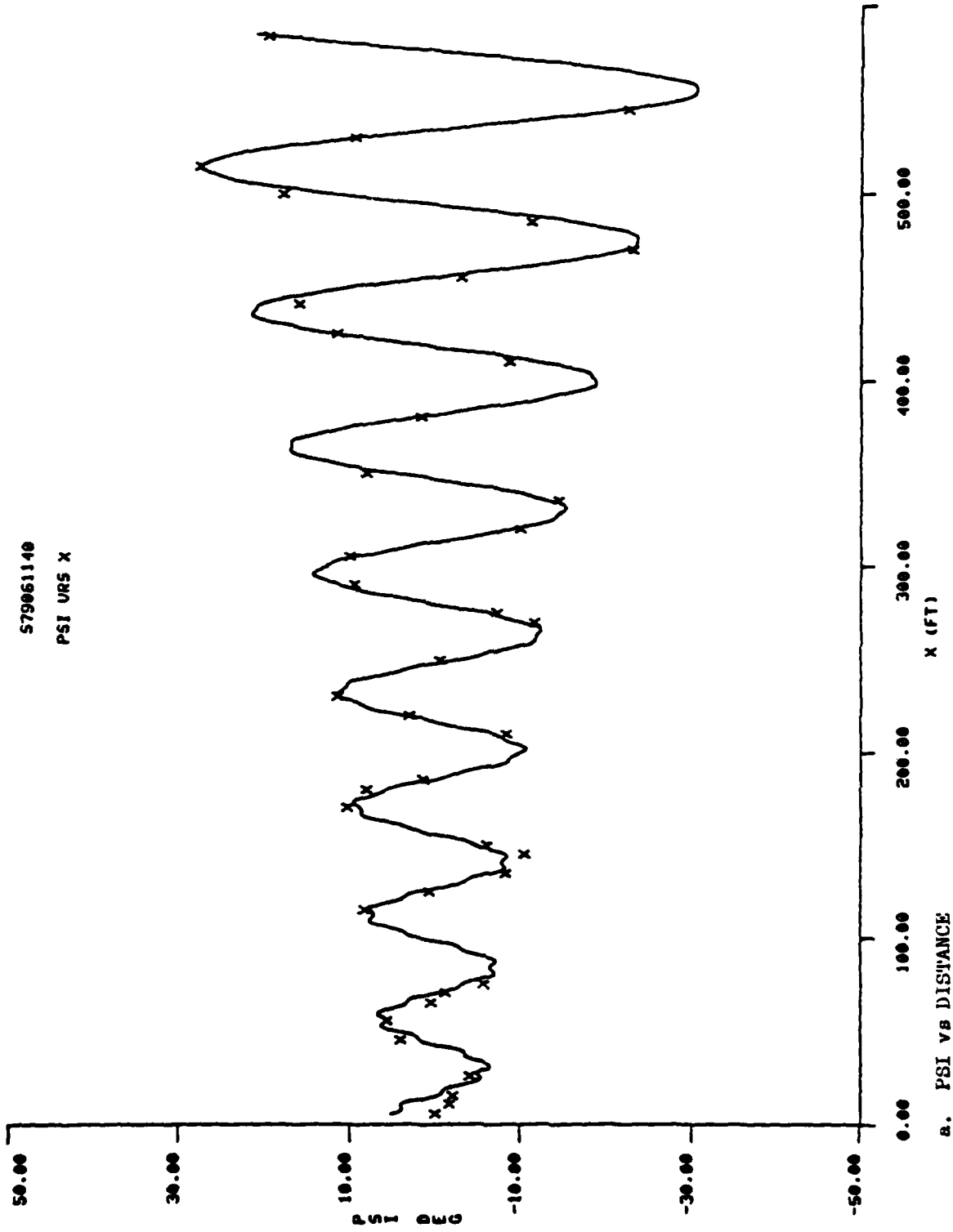


FIG 6 (CONCLUDED)

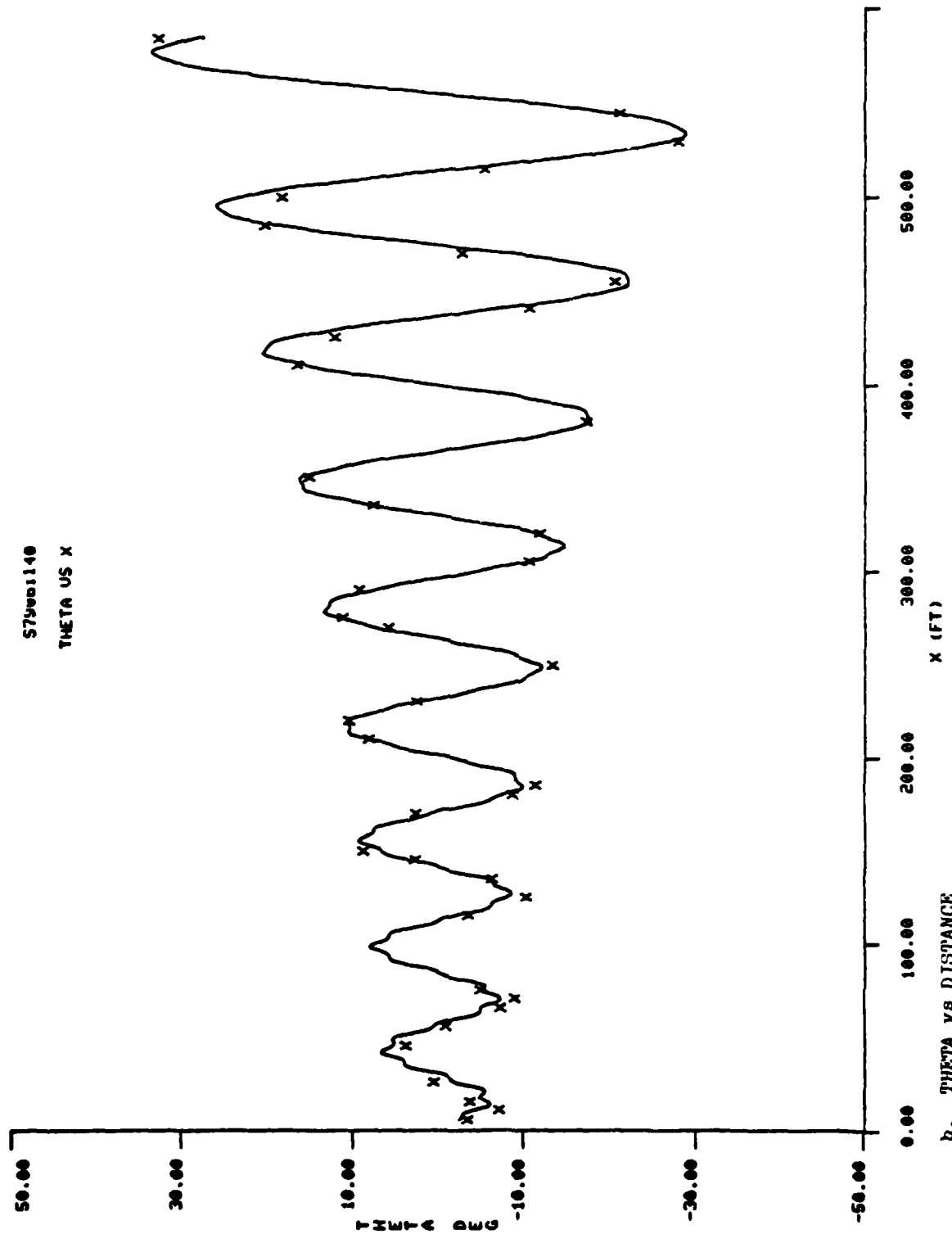
579861140
PSI URS X



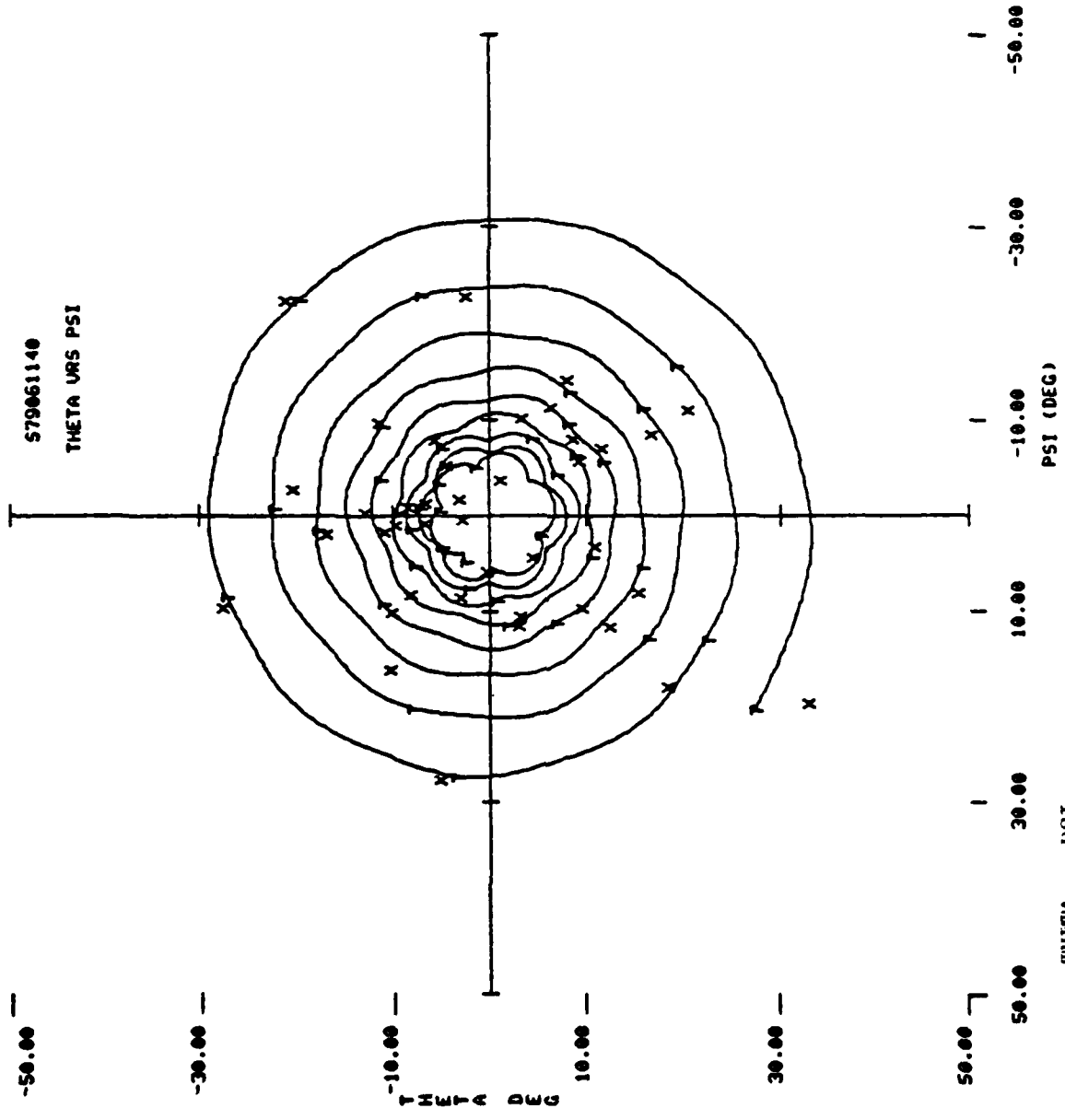
a. PSI vs DISTANCE

FIG 7. TYPICAL MOTION PATTERN FOR "TRACER OFF" ROUNDS

S79001140
THETA US X

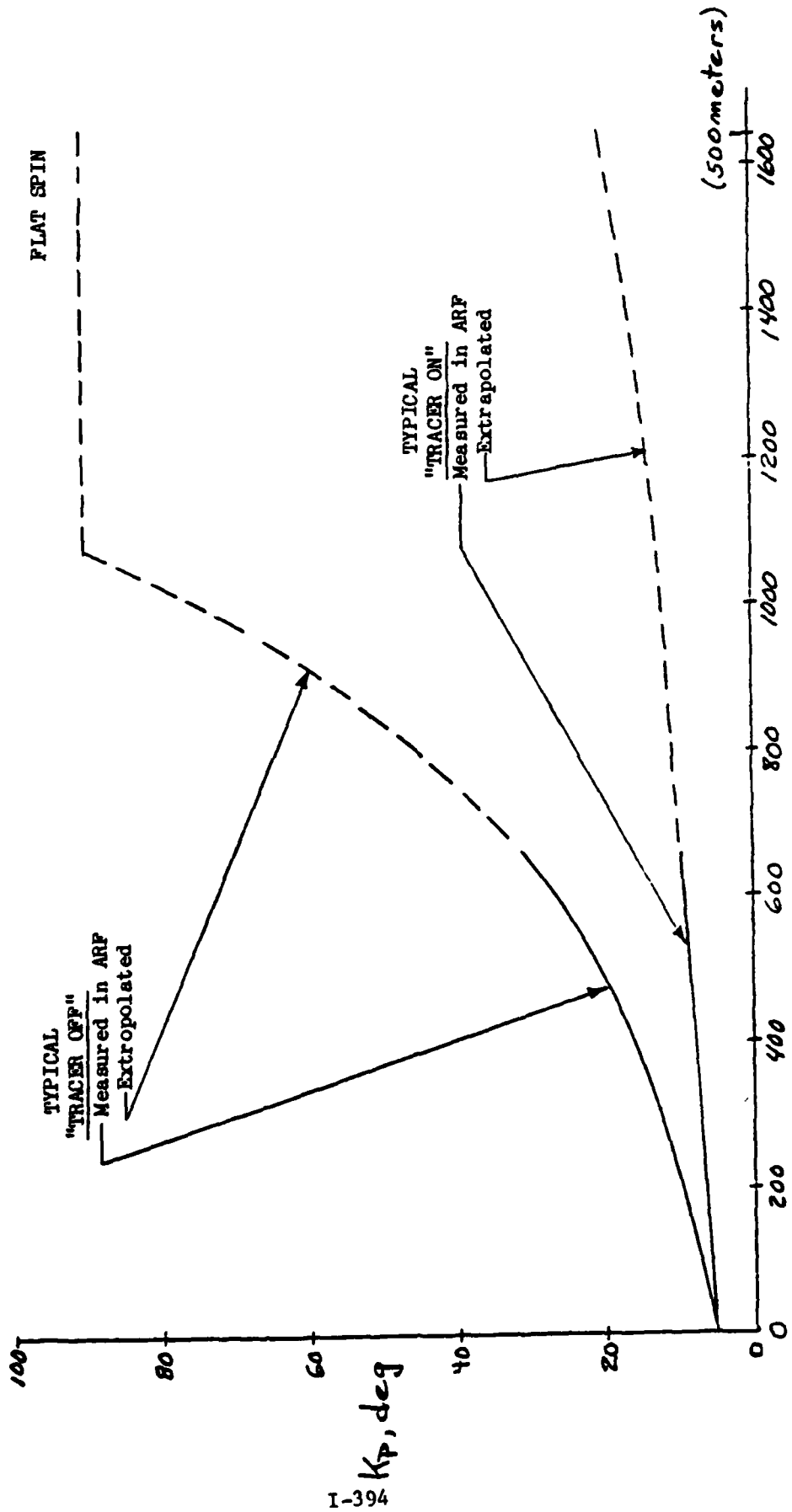


b. THETA vs DISTANCE
FIG 7 (CONTINUED)



c. THETA vs PSI

FIG 7 (CONCLUDED)



Downrange Distance, ft

FIG 8. TYPICAL MOTION GROWTH OF RECESSIONAL VECTOR

THRUST AUGMENTATION FOR TOMAHAWK CRUISE MISSILE

B.F. North and In-Kun Kim
General Dynamics Convair Division, San Diego, California

ABSTRACT

A multiple orifice canister baseplate was designed for the Tomahawk Cruise Missile to achieve required thrust augmentation characteristics during surface ship and ground launches. This new baseplate will replace the present single orifice baseplate which was analytically determined unsatisfactory under extreme launch conditions. Scaled model tests using room temperature air were conducted and flight test data were utilized to predict the discharge characteristics of new baseplates under the real launch conditions. These discharge characteristics were used in a computer program simulating a Tomahawk launch to predict the launch dynamics and thrust augmentation characteristics. The improved thrust augmentation with the new baseplate will assure a successful Tomahawk missile launch for the full range of ground or ship launch conditions.

INTRODUCTION

Extension of the Tomahawk Cruise Missile missions to include surface ship and ground launch capability has required special launch considerations. The initial Tomahawk missile and its booster were designed for an underwater boost phase which required an initially low thrust during underwater travel followed by rapid increasing thrust after broach. To allow use of the booster without redesign for ship and ground launch capability, a technique to augment initial booster thrust was developed. Thrust augmentation is achieved by restricting the flow of booster exhaust gas with the baseplate of the launch canister. The resultant pressure build up in the canister provides additional force to accelerate the missile to a required launch velocity.

The thrust augmentation and resulting missile motion, however, have to meet various requirements to be satisfactory. Those requirements are imposed by the structural limit of the canister, the guidance package acceleration restrictions and considerations for successful flight after the launch. Furthermore, a particular design should be applicable for a wide range of launch conditions defined by combinations of launch parameters. The significant parameters are: booster grade and grain temperature, friction drag, canister pressurization, missile weight, launch angle and cover installation.

Various single orifice baseplates have been flight tested with a final selection of 4.9 in diameter. Even though General Dynamics has successfully launched several Tomahawk missiles with this baseplate, we have predicted for some time that a single orifice baseplate cannot satisfy all the launch requirements under extreme launch conditions. This prediction was based on our computer simulation of Tomahawk launches which predicts thrust augmentation and launch dynamics during a canister launch.

An important input for the computer simulation is the discharge coefficient of the orifice(s) at the baseplate. For a single orifice plate, it was well established from flight test correction. For other orifice configurations, they were not known. Scaled model tests were conducted to determine the discharge coefficients with various baseplate orifice configurations. The results from these model tests and the discharge coefficient during a flight test (with single orifice) were used to predict the discharge coefficient. The predicted discharge coefficients were in turn used in a computer program to simulate a Tomahawk launch. A new baseplate orifice configuration was selected based on the thrust augmentation and launch dynamics information derived from this simulation.

DESIGN CRITERIA

The goal of this design study was to find a baseplate orifice configuration which generates a satisfactory thrust augmentation under any platform launch conditions. A launch condition is defined by combination of launch parameters whose extremes are given in Table 1.

TABLE 1

<u>Parameters</u>	<u>Extremes</u>
Booster Grade & Grain Temperature:	110°F, +2 σ to -20°F, -2 σ
Missile Weight:	3000 lb _m to 3500 lb _m
Launch Angle:	34° to 90°
Cover:*	GDC or MMC + GDC
Friction Drag:	200 lb _f to 2000 lb _f
Canister Pressure:	3 psig to 7 psig

- * GDC refers to a General Dynamics Convair designed fly-through cover which is installed on the Tomahawk launch canister. MMC refers to a Martin Marietta Corporation designed fly-through cover which is installed in their Vertical Launch Systems (VLS) canister. When Tomahawk launches from the VLS it must penetrate both covers.

A combination of minimum parameter values and maximum booster constitutes a favorable launch condition while those from the upper limits and minimum booster result in an unfavorable launch condition.

The thrust augmentation and resulting missile motion must meet several requirements to be considered satisfactory. These requirements are shown in Table 2.

TABLE 2

Maximum Baseplate Pressure (psig)	120
Maximum Acceleration (g)	11
Minimum Exit Velocity (ft/sec)	85
Maximum Time in Canister (sec)	0.8

The first two requirements provide an upper limit of the thrust augmentation usually under a favorable launch condition while the next two requirements constitute a lower limit which are applicable to an unfavorable launch condition.

The thrust augmentation problem with a single orifice baseplate arises when the missile displacement (x) is small. Figure 1 shows the exhaust plume-baseplate relationship. The booster exhaust plume vs orifice configuration at a small x is such that a large portion of the exhaust gas escapes through the orifice unrestricted. After this initial stage ($x > 1.5$ ft), the thrust augmentation is predictable and adequate. Reducing the orifice size will improve the thrust during the initial stage but this will result in excess baseplate pressure, and also an acceleration which exceeds the limits. The desirable thrust augmentation characteristic is an immediate pressure build up during the initial stage, as would be expected of a small orifice baseplate followed by constant or slightly decreasing pressure as the launch continues.

COMPUTER SIMULATION OF A TOMAHAWK LAUNCH

A computer program has been developed in house by the author which simulates the Tomahawk launch dynamics. This program has its base on Newton's 1st Law ($F = ma$) and considers all the relevant parameters involved during a launch. The forces considered are:

- Booster Thrust
- Forces to Break Cover(s)
- Force Due To Compression of Gas Between Cover and Missile
- Drag Forces Due to Seal and Cover(s)
- Force Due to Thrust Augmentation Pressure

The input variables are:

- Missile Weight
- Launch Angle
- Atmospheric Pressure
- Canister Pressurization
- Cover Specification
- Discharge Coefficient of the Baseplate Orifice
- Booster Discharge Mass Flow and Thrust

The discharge coefficient of the baseplate orifice is an important parameter that controls the thrust augmentation performance. An accurate discharge coefficient is vital for a reliable simulation of the Tomahawk launch. The discharge coefficient of a baseplate during a Tomahawk launch is a complex parameter which depends on the baseplate-booster nozzle distance, exhaust plume geometry and orifice configuration and must be determined experimentally.

This program has provided successful pre-launch predictions for many previous Tomahawk launches with a single orifice baseplate. An accurate prediction has been vital for the canister and baseplate design and the performance of a new baseplate will be predicted with this computer simulation once the discharge coefficient is known.

PROCEDURE OF STUDY

After careful examination of the present problems with a single orifice baseplate it was concluded that a multiple orifice baseplate, when orifices are properly distributed, may possibly generate the desired thrust augmentation during the launch. The discharge coefficient of this baseplate must be determined experimentally. The present design study was to be accomplished in three steps.

- a. Model tests with room temperature air
- b. Estimation of the discharge coefficient during a Tomahawk launch with new baseplate
- c. Computer simulation

The model tests were conducted with a 0.344 scale model baseplate and room temperature air. See Figure 2 for schematics of test procedures. Internal studies (Reference 1) conducted previously indicated that the shape of a hot gas plume is considerably different from a cold air plume. The difference in plume shape certainly will affect the discharge characteristics at the baseplate orifice(s) and the hot gas discharge coefficient must be estimated from cold air-model test results and hot gas-flight test results.

Several candidate baseplate orifice configurations were examined before two basic configurations were selected for the model test. These orifice configurations are shown in Figure 3. The preliminary phase of the study determined a superior basic orifice configuration (Configuration I or Configuration II). In the final phase of the study, the orifice distribution was systematically changed within the basic configuration selected to determine an optimum orifice distribution.

MODEL TEST (PRELIMINARY PHASE)

The model test was composed of scale tests and static simulation tests. The scale tests were conducted to find the discharge coefficient of the baseplate orifice when flow was from a large plenum. The results of these tests represent the discharge performance of the baseplate when the missile displacement is large. The discharge coefficient is calculated from:

$$\dot{m} = C_D A_{\text{orifice}} \sqrt{\frac{2k}{k-1} g_c P_1 \rho_1 \left[\left(\frac{P_2}{P_1} \right)^{2/k} - \left(\frac{P_2}{P_1} \right)^{\frac{k+1}{k}} \right]}$$

for $P_2/P_1 > 0.528$

and

$$\dot{m} = C_D A_{\text{orifice}} P_1 \sqrt{\frac{k}{RT} g_c \left(\frac{2}{k+1} \right)^{\frac{k+1}{k-1}}} \quad \text{for } P_2/P_1 < 0.528$$

where

$$R = \text{gas constant} \left(\frac{\text{ft} \times \text{lb}_f}{\text{lb}_m \times ^\circ R} \right)$$

$$A_{\text{orifice}} = \text{total area of the orifice (ft}^2\text{)}$$

$$k = \text{adiabatic exponent (dimensionless)} = 1.4$$

P_1 and P_2 are baseplate pressure and ambient pressure (lb_f/ft^2 abs), respectively

C_D is a discharge coefficient

$$g = \text{gravitational conversion constant (lb}_m\text{-ft/lb}_f\text{-sec}^2\text{)} = 32.174$$

ρ_1 and T_1 are density (lb_m/ft^3) and temperature (R) of air in the baseplate cavity, respectively

Figure 4 shows the discharge coefficient of three baseplates as a function of plenum pressure. Two things are notable. First, the discharge of air through Configuration II baseplate is most efficient while the discharge is most inefficient for Configuration O. This difference between different configurations is substantial and will affect the thrust augmentation accordingly. Second, the magnitude of the discharge coefficient seems to indicate that the orifices perform more or less like a short pipe, rather than a sharp-edged plate. The discharge coefficient of a sharp-edged plate is much smaller ($C_D = 0.6 \sim 0.7$).

The general shape of the discharge coefficient plots seems to agree with previously reported sharp-edged single orifice discharge coefficient (see Reference 2). The discharge coefficients measured with multiple orifices are reported by Kolodzie, Jr. et al (Reference 3). Their discharge coefficients and the present test results showed excellent agreement for similar pitch-to-hole diameter ratio and plate thickness to hole diameter ratio.

The importance of the scale test is twofold. First, these test results indicated reliability of the present measurements. Second, the discharge coefficients at high pressure provide the asymptotic values for the test results in the static simulation test. The distance between the baseplate and nozzle tested in the static simulation test covers up to 8 in. This test result with Configuration O is especially essential since the discharge coefficient from the static simulation test doesn't converge fully in the test range. The variation of C_D with the baseplate pressure is not as significant as it may look because the baseplate pressure reaches the maximum pressure (75 ~ 110 psig) in a fraction of second (~ .1 sec) and within the pressure range, the variation of C_D was $\pm 1.5\%$.

Static simulation tests were conducted with a simulated nozzle in place. The static simulation test measured the mass flow rate as a function of nozzle baseplate distance and of baseplate pressure. Discharge coefficients are calculated by the same equations used for scale test. The baseplate pressure (P_1) is not the only parameter that drives the discharge as seen from the discharge coefficient which is larger than unity for small X. This is due to the definition used to determine the discharge coefficient. Because of the convergent-divergent nozzle used, there is a supersonic core with a pressure distribution across the orifice which, if accurately measured, would provide an integrated value which would result in a discharge coefficient < 1 . The test results are shown in Figure 5.

ESTIMATION OF TOMAHAWK DISCHARGE COEFFICIENT

The present test results are obtained from scale model - cold air tests. The thrust augmentation of candidate baseplates may be properly compared only when the discharge coefficients during a Tomahawk launch with these baseplates are known. The present section describes a scheme predicting the Tomahawk discharge coefficient from available information.

Figure 6 shows the discharge coefficient during the T-16:2 launch in addition to the test results previously shown in Figure 4. The discharge coefficient of Configuration O is compared with that from Figure 5. The important features revealed from this comparison are:

- a. The peak discharge coefficient during the Tomahawk launch is approximately 50% of that of cold air. This indicates that the hot-gas plume is larger than the cold air plume.
- b. The discharge coefficient of Tomahawk launch varies gradually around the peak C_D . This may indicate that the plume boundary of hot gas is not as sharp as that of cold air.
- c. It takes twice as much distance for the hot gas discharge coefficient to drop to that of cold air.

These comparative features were used to predict the discharge coefficient of Tomahawk launch with new baseplates which are shown in dotted lines in Figure 6. The accuracy of these C_D predictions, especially that of Configuration I, may be questioned. Slightly different predictions were made and resulting thrust augmentations were compared to find possible error in this prediction. Small variation of C_D at small R ($R < 0.15$) did not change thrust augmentation significantly. For large R , the discharge coefficient of hot gas is expected to be the same as that of cold air and it is this C_D that affects the thrust augmentation most. The hot gas discharge coefficient of Configuration II was predicted to be almost identical to or slightly lower than the cold air test result.

COMPUTER SIMULATION

The predicted Tomahawk discharge coefficients of new baseplates were used in the computer program to predict the thrust augmentation during the Tomahawk launches with new baseplates. Figure 7 shows the predicted baseplate pressures along with the T16:2 data. Some of the important characteristics are summarized in Table 3.

TABLE 3

	<u>Configuration I</u>	<u>Configuration II</u>
Minimum Baseplate Pressure (psig)	95	126
Maximum Acceleration (g)	9.23	12.5
Exit Velocity (ft/sec)	98.2	98.7
Time in the Canister (sec)	.42	.39

This comparison clearly indicated that Configuration I generates more desirable thrust augmentation. The thrust augmentation characteristics of Configuration I meet all the requirements previously given in Table 2 whereas the baseplate pressure and acceleration are too high with Configuration II. The launch parameter used for this prediction represents only an average condition. With extreme launch parameters, the baseplate pressure and acceleration will be even higher. Furthermore, the thrust augmentation characteristic of Configuration I may be easily changed by varying the orifice size at the center. With Configuration II, this is not possible.

Based on the results of this simulation, Configuration I was selected as the basic configuration (a small hole in the center and peripheral holes) for the final baseplate. The orifice sizes would be optimized in the final phase of the study to make sure the thrust augmentation with the optimized baseplate meet all the requirements under the extreme launch conditions.

FINAL PHASE

Early into the present study, the computer predicted thrust augmentation characteristics of all the available launch cases were compared to determine two extreme launch cases, one most favorable and one most unfavorable. This comparison found that BGM-109B launch with a high performance booster is most favorable and BGM-109G with a low performance booster is most unfavorable. The launch parameters of two extreme cases are given as follows:

TABLE 4

<u>Parameters</u>	<u>BGM-109B</u>	<u>BGM-109G</u>
Missile Weight (lb)	3078	3310
Launch Angle (deg)	34	56
Booster	110°F, +2 J	-20°F, -2J
Friction Drag (lb)	200	2000
Cover	MMC	GDC
Canister pressure (psig)	3	7

Using the estimated Tomahawk discharge coefficient of Configuration I (see Figure 6), the thrust augmentation of the two extreme cases was predicted. The baseplate pressures from this prediction are shown in Figure 8 and the important augmentation characteristics are shown in Table 5.

TABLE 5

<u>Parameters</u>	<u>BGM-109B</u>	<u>BGM-109G</u>
Maximum Baseplate Pressure (psig)	108	78
Maximum Acceleration (g)	12.1	6.9
Exit Velocity (ft/sec)	112.0	83.8
Time in Canister (sec)	.39	.51

The thrust augmentation characteristics of the two extreme cases revealed that the acceleration (12.1 g) is too high for the most favorable case and the exit velocity (83.8 ft/sec) is not quite enough for the most unfavorable case. It was known that a change of orifice configuration cannot reduce acceleration for one case and increase the exit velocity for the other simultaneously. A decision was made to reduce the maximum acceleration of the BGM-109B launch by enlarging the center hole. This will reduce the exit velocity of BGM-109G which already was low. However, a separate study indicated that this low exit velocity may be increased to the required velocity by reducing the friction drag (2000 lb_f) used for this case. A baseplate with 8% larger center hole but the same overall open area was selected to examine the effect of the center hole to overall exhaust performance and thus the thrust augmentation. This baseplate is called Configuration I-1 and shown in Figure 9.

Also examined during this phase of the study was Configuration I-2 which has five orifices. Configuration I-2 baseplate has an identical center hole as Configuration I-1 but has four peripheral holes. This configuration was examined to obtain a data basis for the five-hole configuration or a possible three-hole configuration. A baseplate configuration with less peripheral holes is considered necessary because of space restrictions for baseplate orifices. This new configuration is shown in Figure 9 also.

The exhaust performance of Configuration I-1 and Configuration I-2 are shown in Figure 10 along with that of Configuration I. Configuration I-1 shows considerably higher discharge coefficient for small X/D than Configuration I but Configuration I-2 shows very little difference. The discharge coefficients of the two new baseplates were virtually identical to that of Configuration I for large X/D (X/D > .36). The discharge performance of Configuration I-2 seems to indicate that the thrust augmentation of five-hole or three-hole configurations may

be similar to the seven-hole configuration if the size of the center orifice is kept unchanged and overall open area is maintained.

The thrust augmentation of Configuration I-1 is predicted in Figure 11 and the important augmentation characteristics during two extreme launches are given in Table 6.

TABLE 6

<u>Parameters</u>	<u>BGM-109B</u>	<u>BGM-109G</u>
Maximum Baseplate Pressure (psig)	99.1	70.1
Maximum Acceleration (g)	11.1	6.18
Exit Velocity (ft/sec)	111.3	81.7
Time in the Canister (sec)	.41	.54

The thrust augmentation characteristics in Table 6 indicate that Configuration I-1 is satisfactory except for the exit velocity of the BGM-109G launch. This exit velocity may be increased to a required velocity (85 ft/sec) if the friction drag (2000 lb) is reduced to approximately 500 lb, which may be possible in the final canister redesign.

CONCLUSIONS AND RECOMMENDATIONS

The present study showed that a multiple orifice baseplate, when orifices are properly distributed, can greatly improve the thrust augmentation characteristics over those of a single orifice baseplate. However, this study also showed that the selected baseplate orifice configuration will marginally meet the requirements under the extreme launch conditions. The margin of safety was smaller than desired.

A baseplate configuration I-4 (Figure 9) is recommended as the new baseplate configuration and the corresponding full scale baseplate is shown in Figure 12.

REFERENCES

1. Shih, P.K., "Computer Programs PLUME, Preheat and LTUBE," General Dynamics report DN- 626, 1977.
2. Lea, F.C., Hydraulics, 6th edition, P.87, Edward Arnold and Co., 1938.
3. Kolodzie, Jr., P.A. and M. VanWinkle, "Discharge Coefficients Through Perforated Plates," AIChE Journal, Vol. 3, No. 3, 1959.

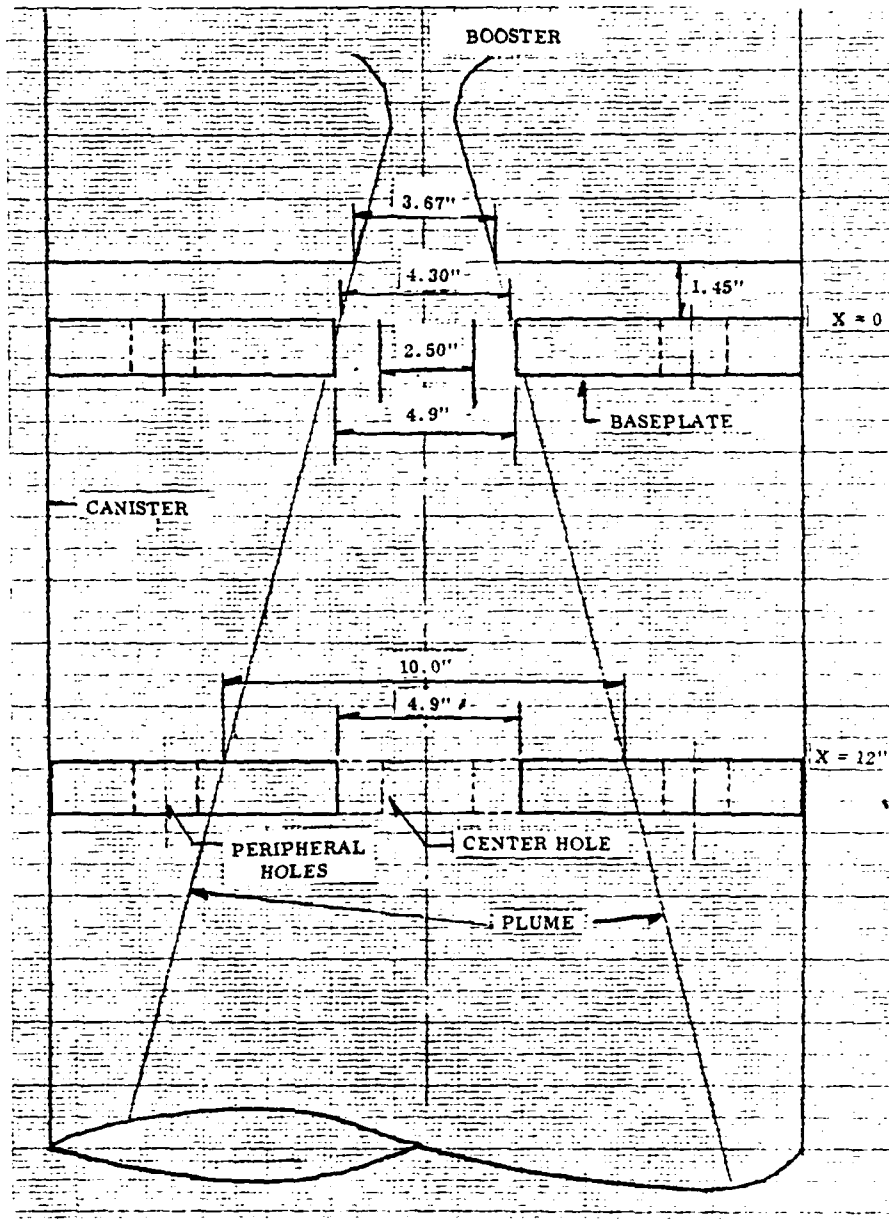


FIGURE 1. PLUME VS. BASEPLATE EXHAUST

CANISTER REDESIGN STUDY

1. SCALE TEST
TO OBTAIN DISCHARGE COEFFICIENT OF VARIOUS
BASEPLATE EXHAUST CONFIGURATIONS

2. STATIC SIMULATION TEST TO EXAMINE:
a) P_1 VS. TIME FOR $L_1 = .52$ IN.
b) P_1 AS A FUNCTION OF L_1
c) DISCHARGE COEFFICIENT VS. L_1

3. DYNAMIC TEST TO OBTAIN:
a) X VS. TIME
b) P_1 VS. TIME
c) ACCELERATION VS. TIME AND DISTANCE
TO SIZE EXHAUST OPENING AREA FOR
SELECTED PATTERN

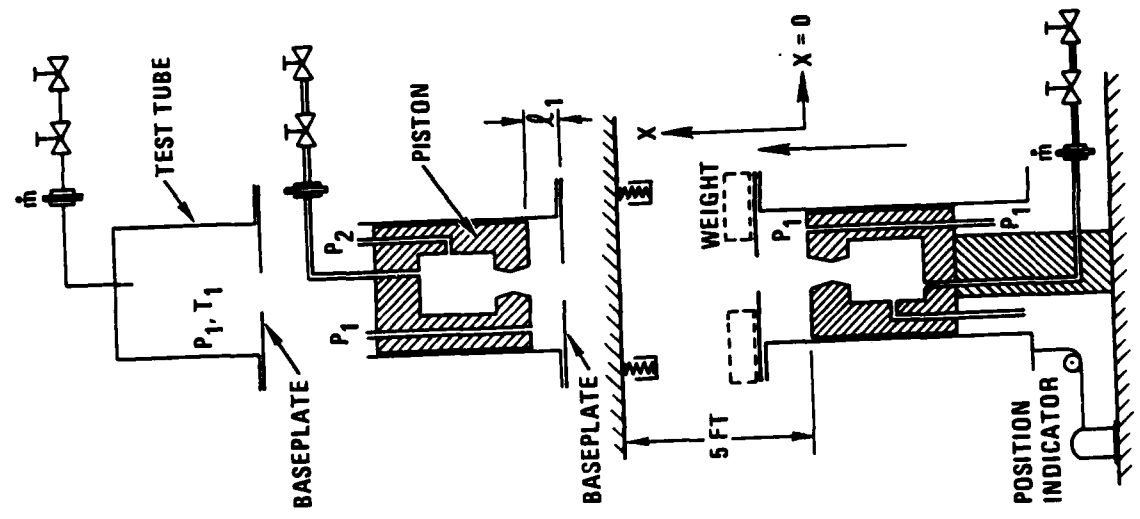


FIGURE 2. TEST PLAN (.3442 SCALE MODEL)

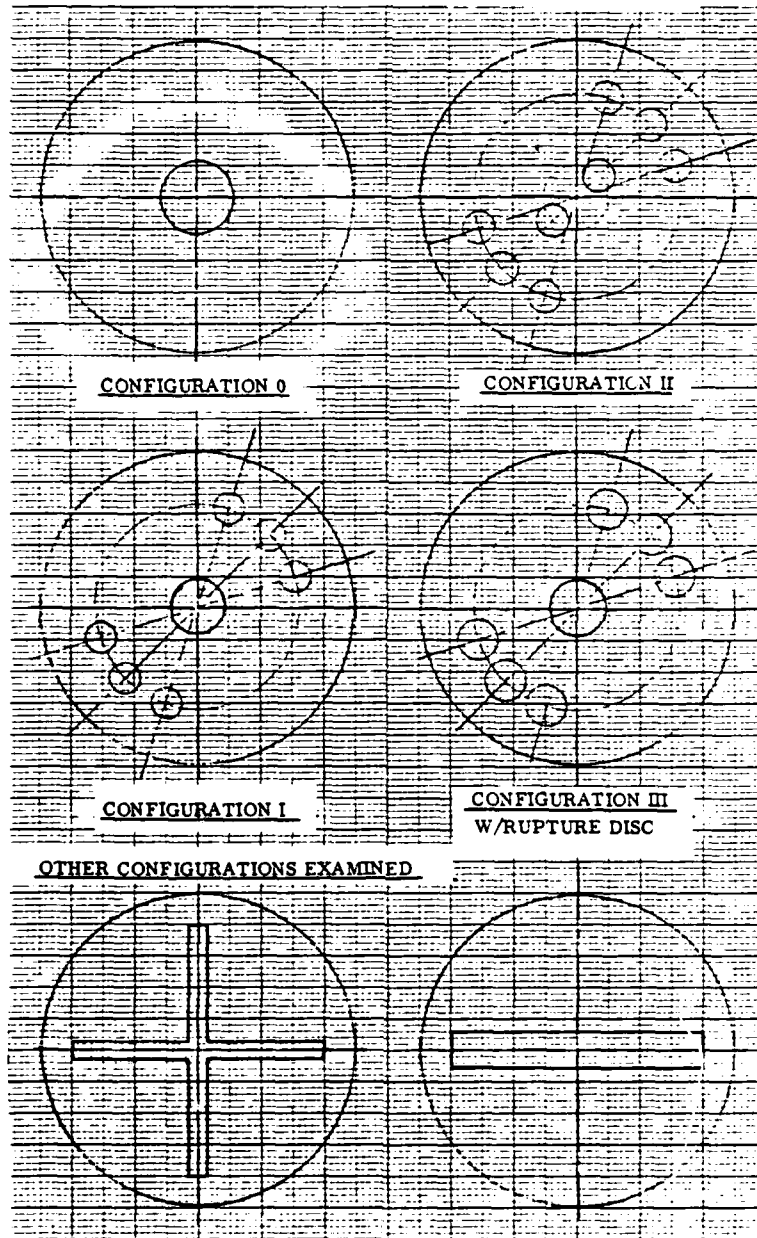


FIGURE 3. CANDIDATE BASEPLATE EXHAUST CONFIGURATION

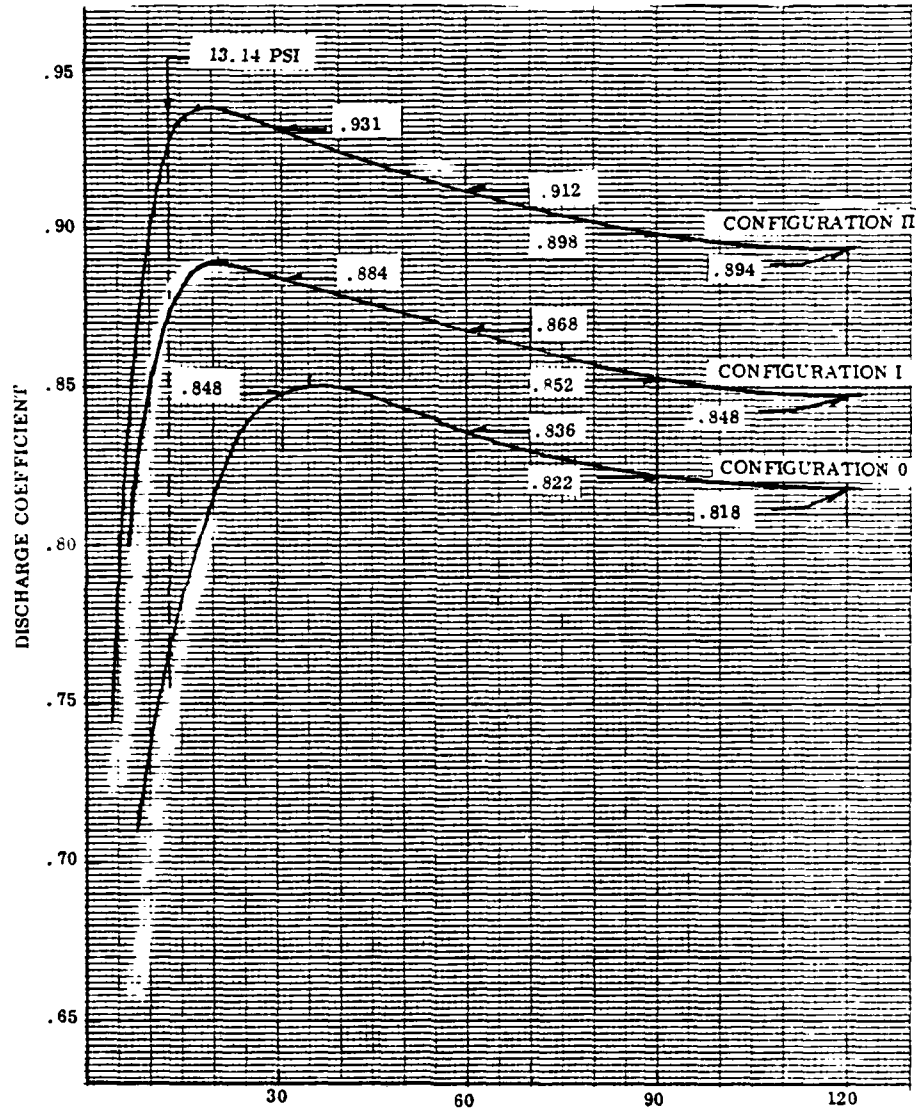


FIGURE 4. PLENUM PRESSURE (PSIG)

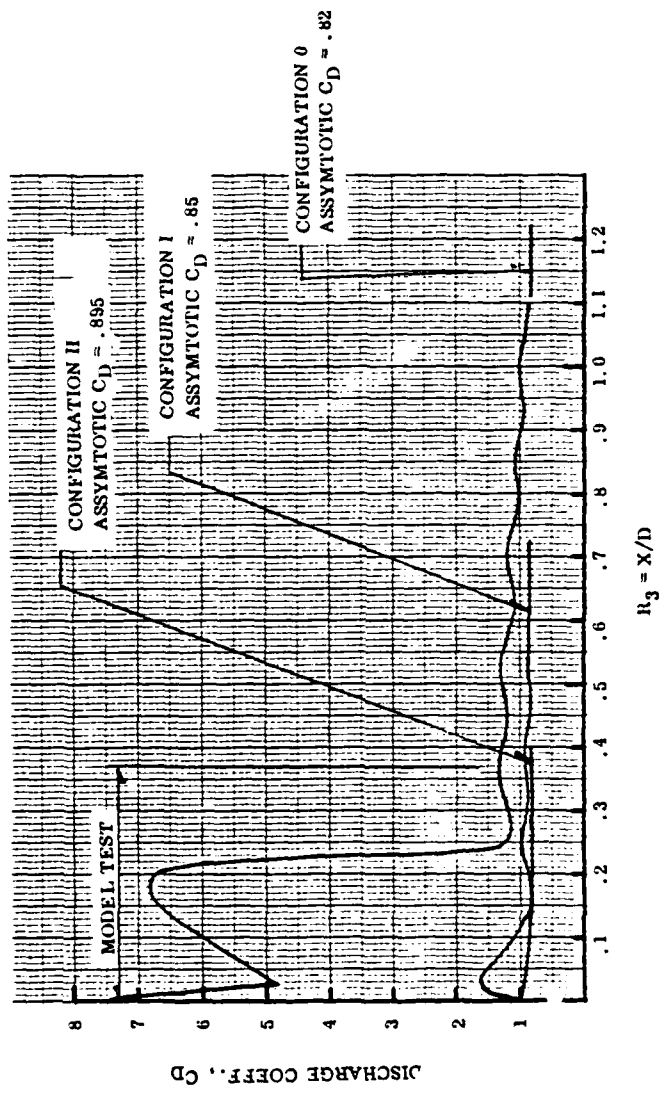


FIGURE 5. DISCHARGE COEFFICIENT FROM STATIC SIMULATION TEST

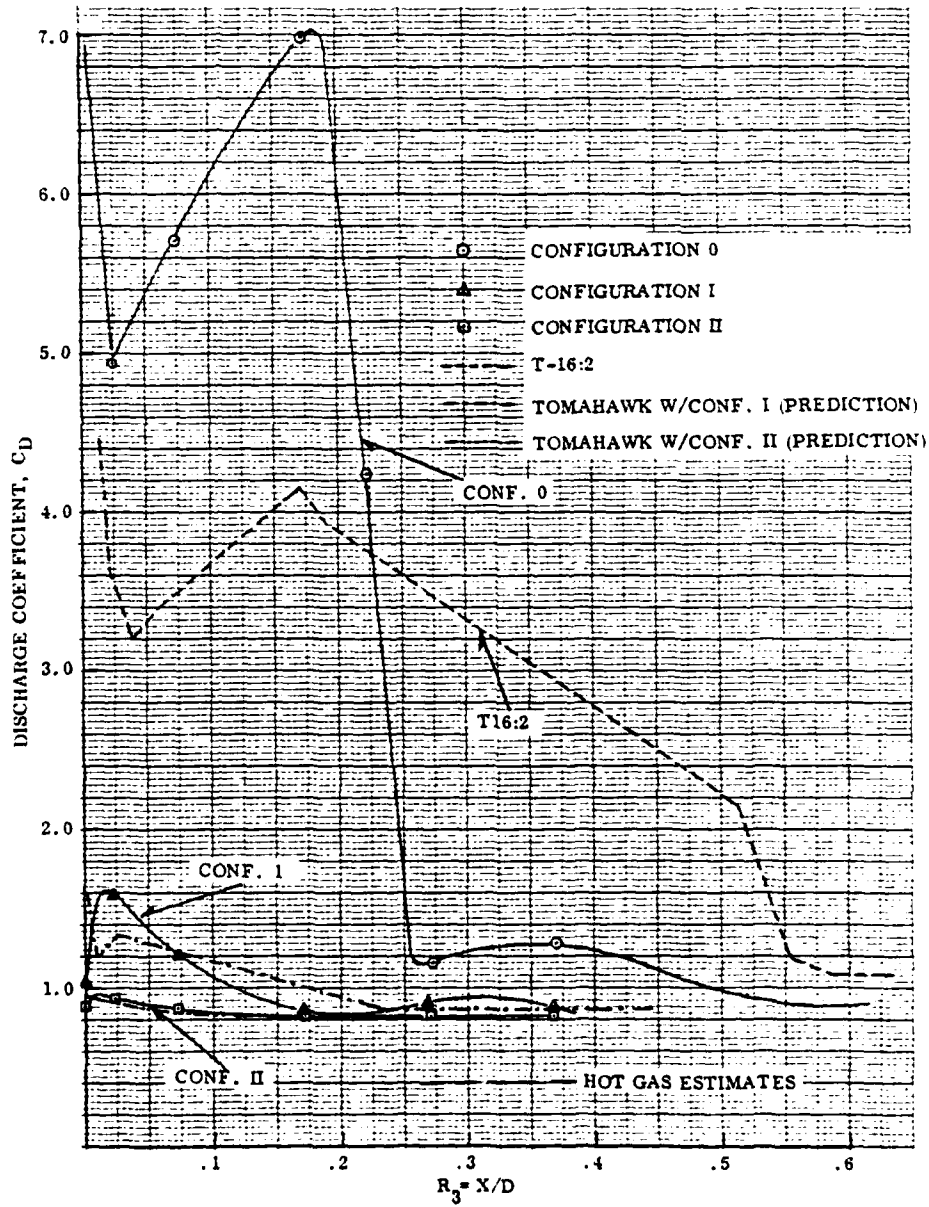


FIGURE 6. DISCHARGE COEFFICIENT, TEST VS PREDICTION

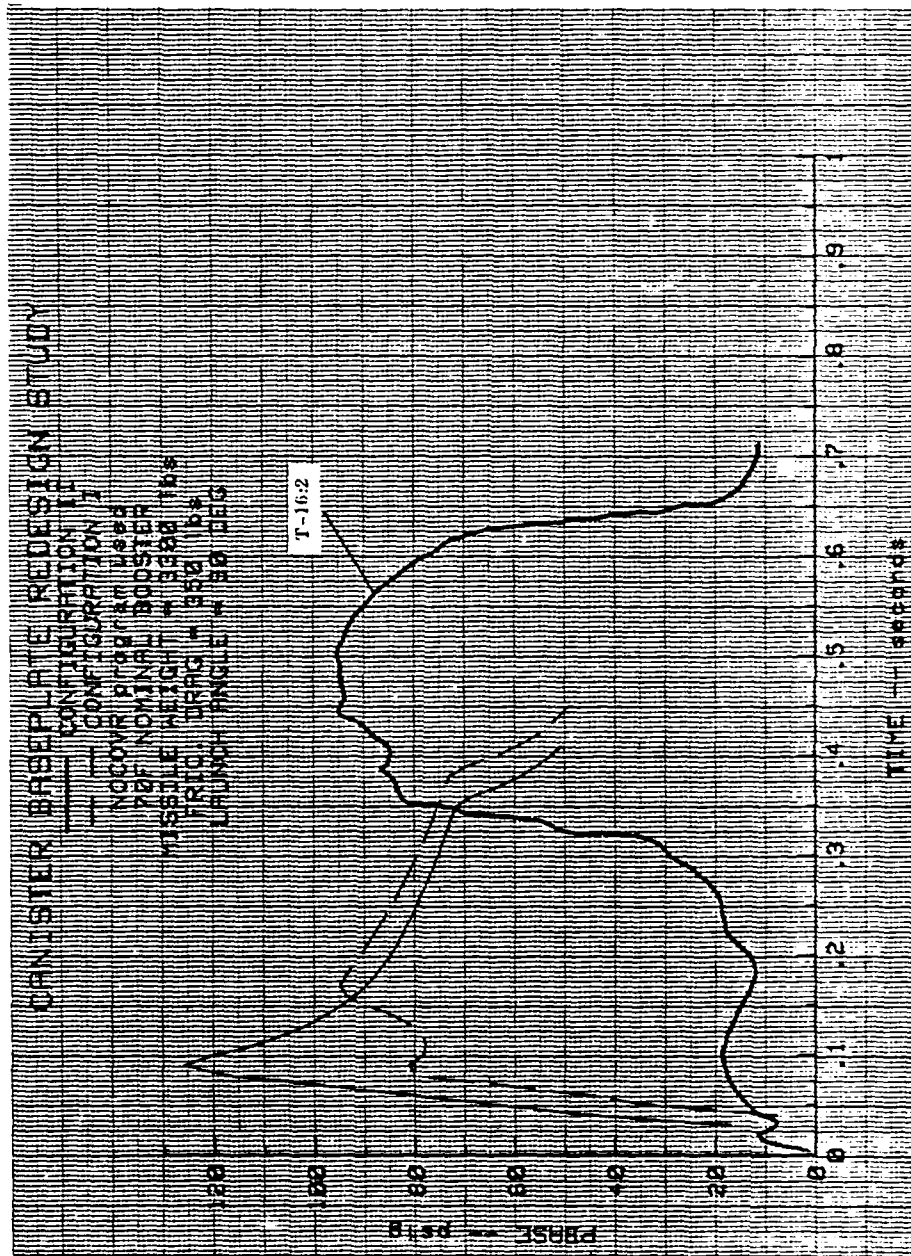


FIGURE 7. COMPUTER PREDICTED BASEPLATE PRESSURE AND FLIGHT TEST DATA

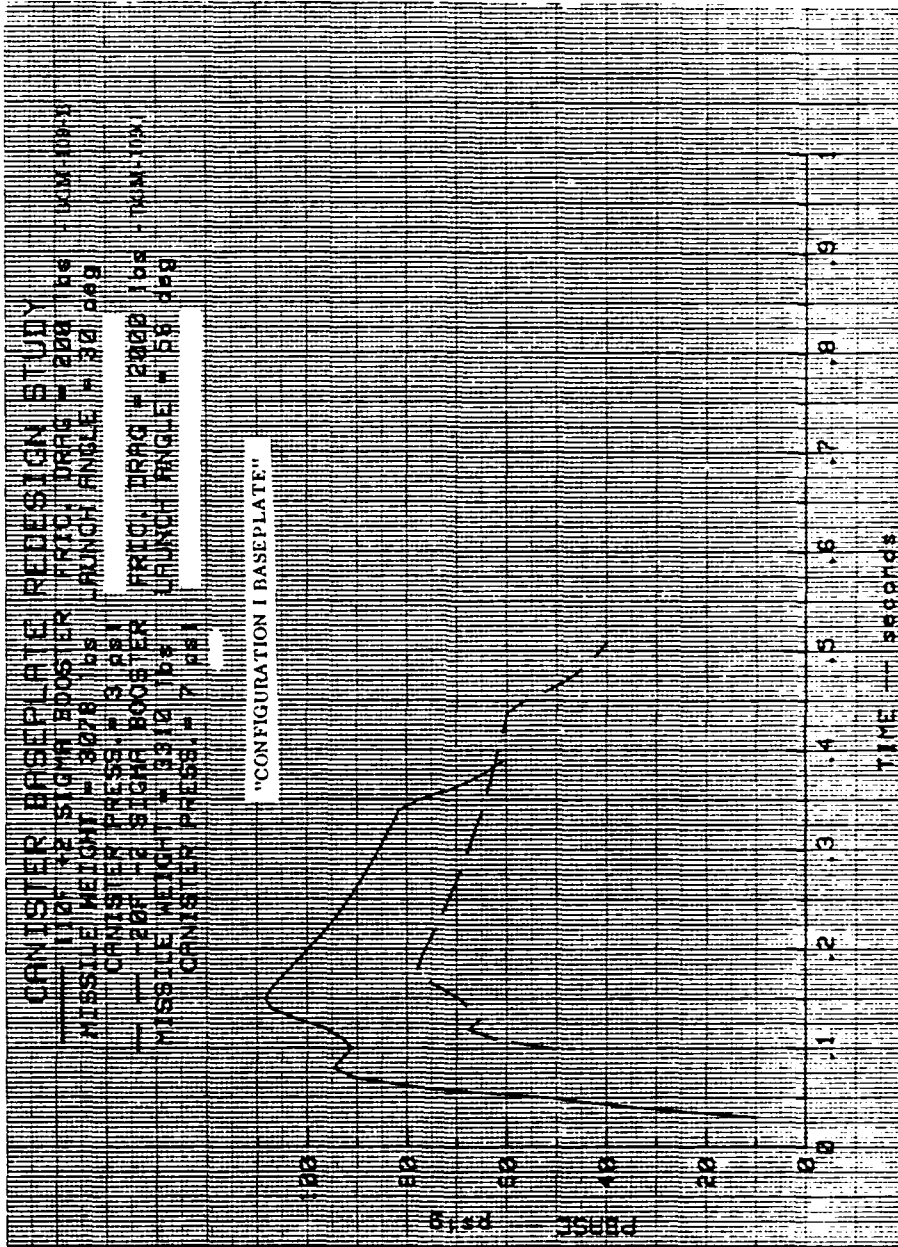


FIGURE 8. COMPUTER PREDICTED BASEPLATE PRESSURE FOR EXTREME CASES

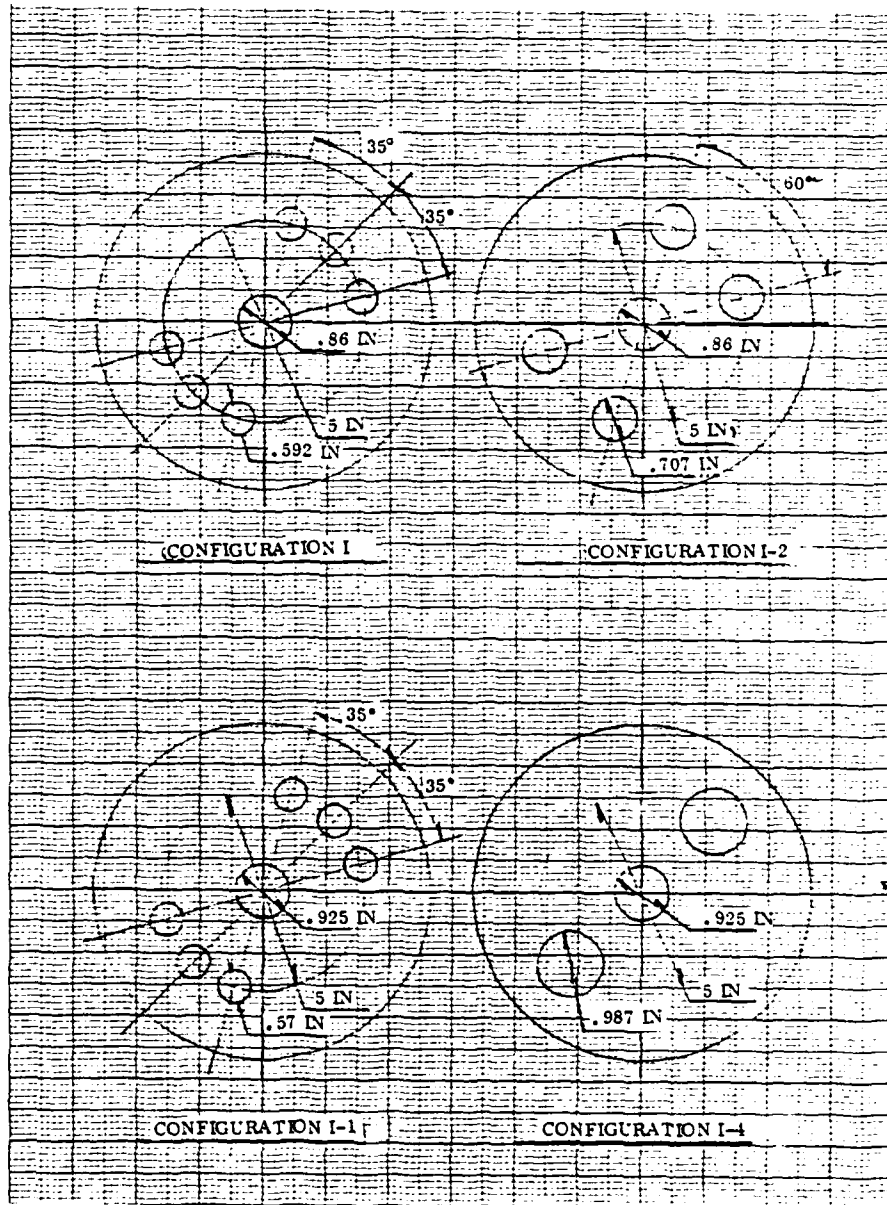


FIGURE 9. BASEPLATES TESTED DURING FINAL PHASE

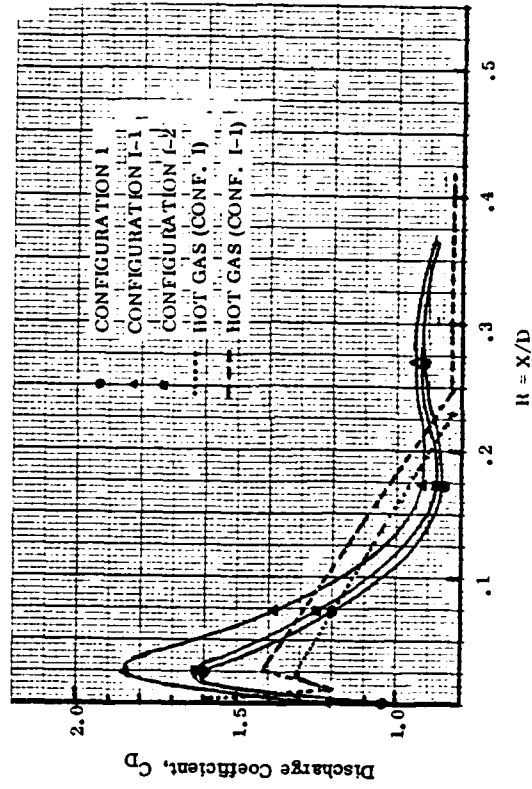


FIGURE 10. DISCHARGE COEFFICIENT FROM STATIC SIMULATION TESTS - FINAL PHASE

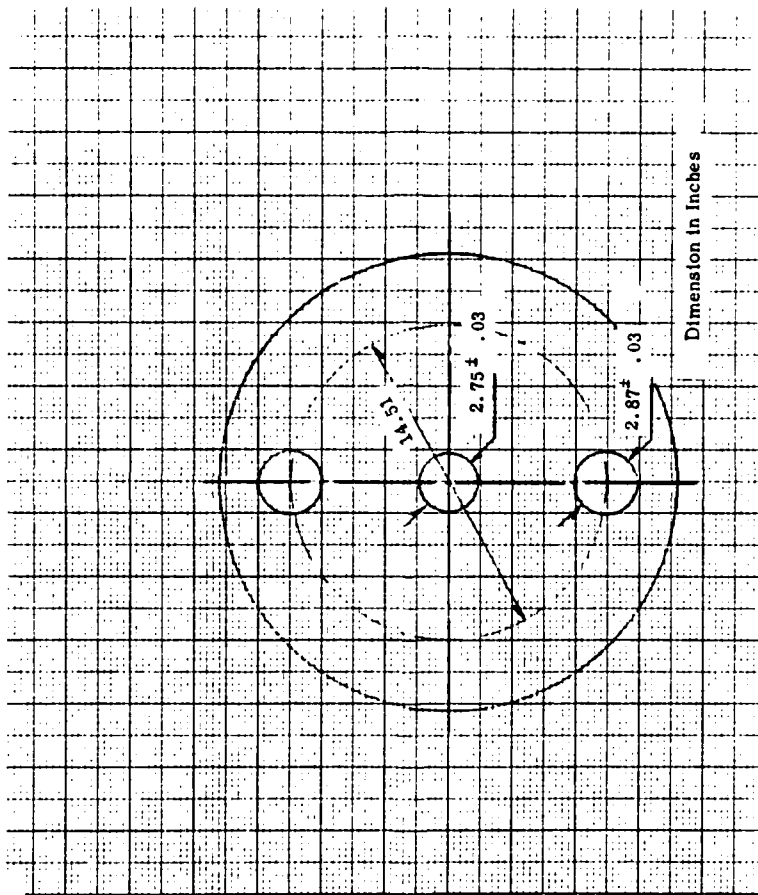


FIGURE 12. RECOMMENDED BASEPLATE ORIFICE CONFIGURATION

DRAG CHARACTERISTICS AND SUITABILITY
OF THREE-FOOT LONG PARACHUTE DECELERATORS

Carl T. Calianno
Naval Air Development Center
Warminster, Pennsylvania 18974

ABSTRACT

Air drop and wind tunnel tests were conducted to verify the stability of sonobuoys with decelerators limited to a total length of three feet. This limitation was established for safety reasons. The existing decelerator systems are configured to a length of 5 to 12 feet, with cross-type canopies varying in area from 1.5 to 3.5 square feet. Sonobuoys are blunt nose right circular cylinders, 4-7/8 inches in diameter, 36 inches long ranging in weight from 12 to 39 pounds. Testing established that suitable stability could be achieved using a three-foot long decelerator. Drag coefficient, opening load, high altitude air descent time and stability data were also determined for three-foot long decelerators.

INTRODUCTION

Sonobuoys are expendable electro-acoustic sensors which are air deployed from Navy fixed and rotary wing aircraft. The air deployed body is blunt nosed, cylindrically shaped 4-7/8 inches in diameter 36 inches long ranging in weight from 12 to 39 pounds. The center of gravity varies randomly between 13 to 18 inches from the end opposite the decelerator. A Ballistic Coefficient (B), a ratio of weight to effective drag area ratio of 18 ± 1.0 pounds per square foot is specified for sonobuoys weighing between 34 to 39 pounds and 12.3 ± 1.0 for all other weights.

The launch angle of the sonobuoy relative to the airstream varies between fixed and rotary wing aircraft. The fixed wing orientation is down and aft 45° from the horizontal. Rotary wing launches are either vertical straight down or horizontal 90° from the direction of flight.

After launch a decelerator system is deployed which must sufficiently stabilize the sonobuoy prior to water impact. The stability must be adequate enough so that the electro-acoustic and hydromechanical systems function normally after water impact.

Currently the decelerator systems utilize cross-type parachutes which have canopy areas varying between 1.5 and 3.5 square feet. The length to width ratio of the canopy is 3 to 1. The uninflated length of the decelerator system, i.e., the length of the fully extended uninflated decelerator from the attachment point on the buoy to the tip of the uninflated canopy vary from 5 to 12 feet with no relation to area. Due to a safety of flight requirement, a maximum three-foot limitation was placed on the uninflated decelerator total length.

A program of wind tunnel and air drop testing was conducted to verify if the performance and configuration requirements could be met. The effect of close coupling the parachute to the store is of particular interest. Decelerator systems up to 12 feet in length and a variety of canopy areas were tested for comparison.

WIND TUNNEL TESTING

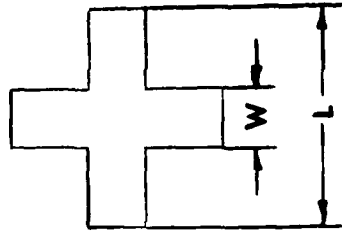
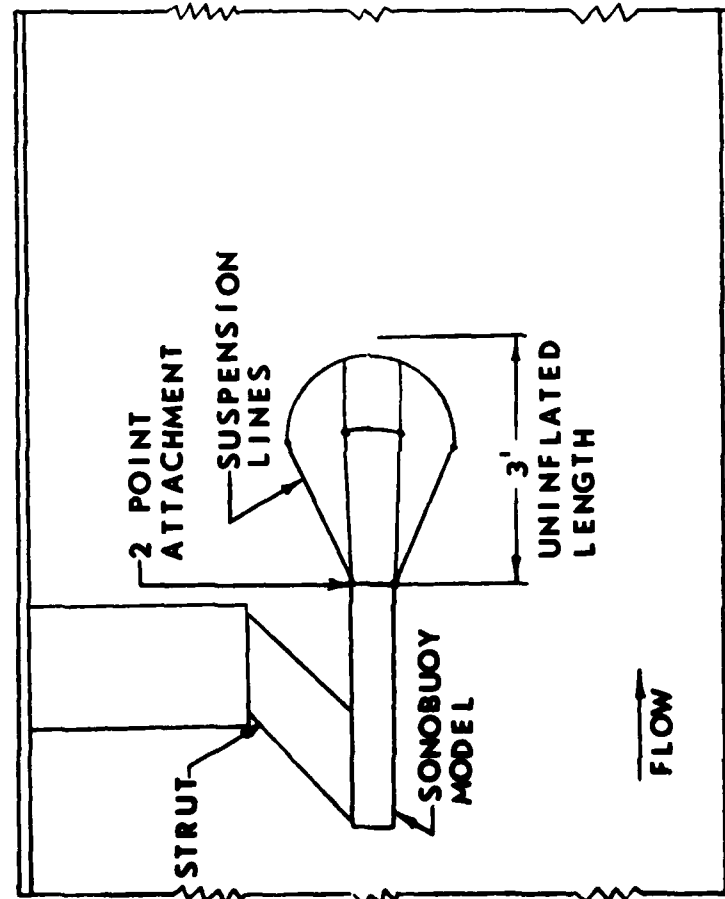
A test program was conducted at the National Aeronautics and Space Administration (NASA), Lewis Research Center's 10 foot x 10 foot wind tunnel to evaluate decelerator characteristics as a function of total system length. The wind tunnel test model set-up is shown in Figure 1. A full scale model of the sonobuoy was placed in the wind tunnel parallel to the direction of flow. It is fixed to the ceiling by a strut. The parachute is stowed in the aft end of the model and is deployed on command. A captivated windflap is released into the airstream when a dynamic pressure of 150 pounds per square foot, the wind tunnel maximum, is reached. The windflap deploys the parachute from its stowage location in the model initiating parachute inflation. The tunnel drive is shut down and a braking system is activated to slow the tunnel.

A load cell is used in the model to measure parachute loading only. The initial one second of load cell data is displayed on a high speed visicorder to evaluate opening loading. Load cell data and tunnel conditions are recorded as the tunnel decelerates for further evaluation.

The decelerators tested had canopies made of lightweight nylon material predominantly 2.25 ounce/square yard. Ten percent of the canopies had 1.1 ounce/square yard material. The chutes were packed in a deployment bag and a line first deployment method was used. Some basic cross-chute configuration details are shown in Figure 1. To achieve higher effective drag area ($C_D S_O$) the number of suspension lines was varied from 2 to 3 per parachute panel and evaluated. The total quantity of runs made in the wind tunnel was approximately 100 including a combination of decelerator lengths and canopy area.

Since the total decelerator length requirement is a unique design constraint a more conventional design parameter, suspension line length/canopy effective diameter (L_g/D_O), is introduced at this time and will be included in the data.

Examples of recorded opening load data are shown in Figures 2 and 3 for system total lengths equal to three feet and greater than three feet respectively. These curves represent some of the more severe loading measured. There appeared to be no clear cut trend between snatch load and opening load factor, based as average load, related to length. About 5 percent of the snatch loads observed were 2 to 3 times the average load and appeared not to be related to decelerator length. The other snatch loads were less than the average load measured. The opening load factor varied between 1.3 and 1.5 and it also appeared to be independent of length. Although line first deployments were used in every test it seems that these systems are sensitive to packing technique, which may account for some of the high snatch loading. The opening load factor measured should



S_0 = CANOPY SURFACE AREA

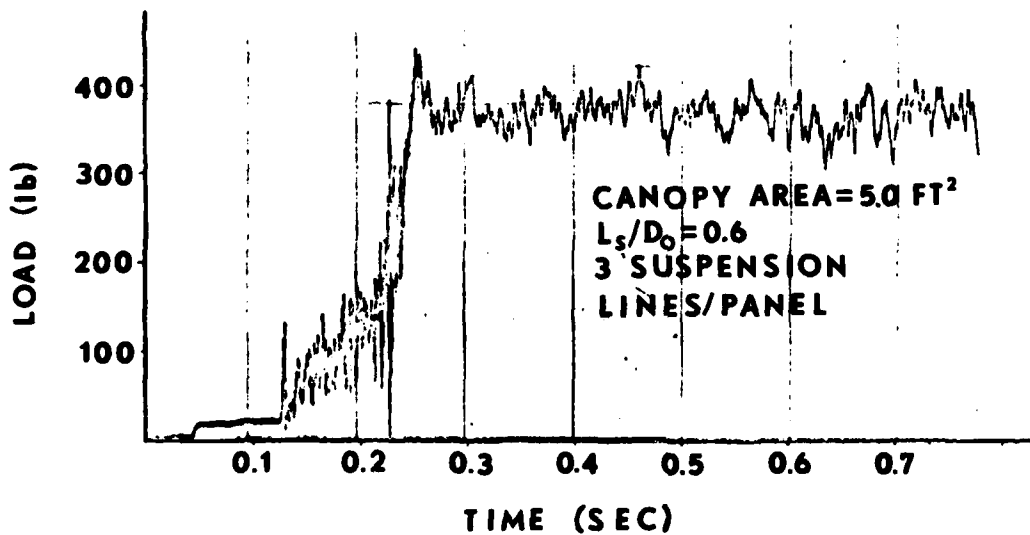
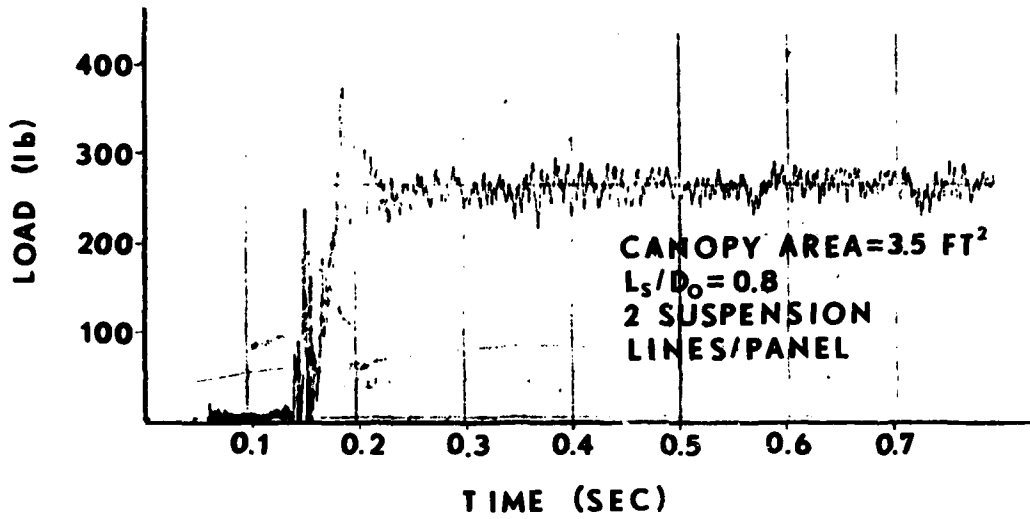
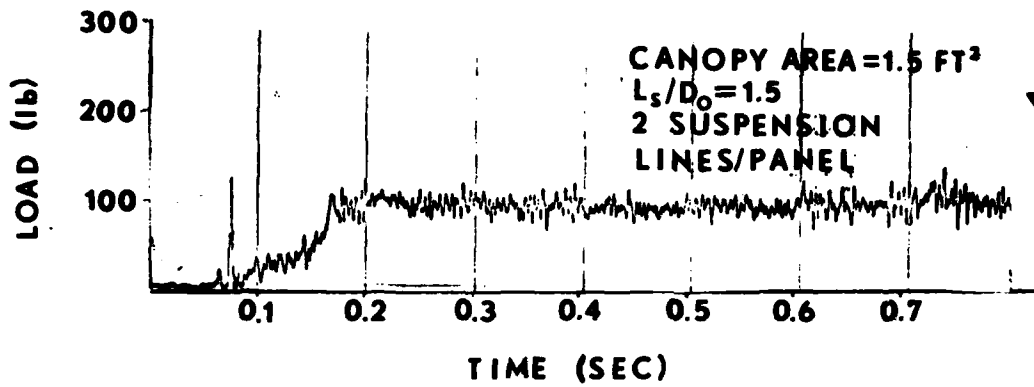
$$S_0 = 2LW - W^2$$

D_0 = EFFECTIVE DIAMETER

$$D_0 = \sqrt{\frac{4 S_0}{\pi}}$$

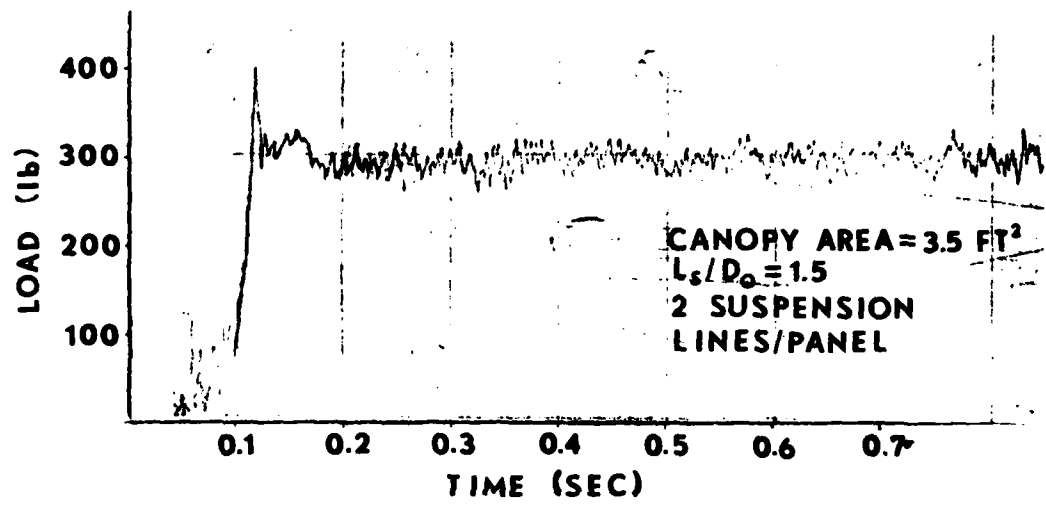
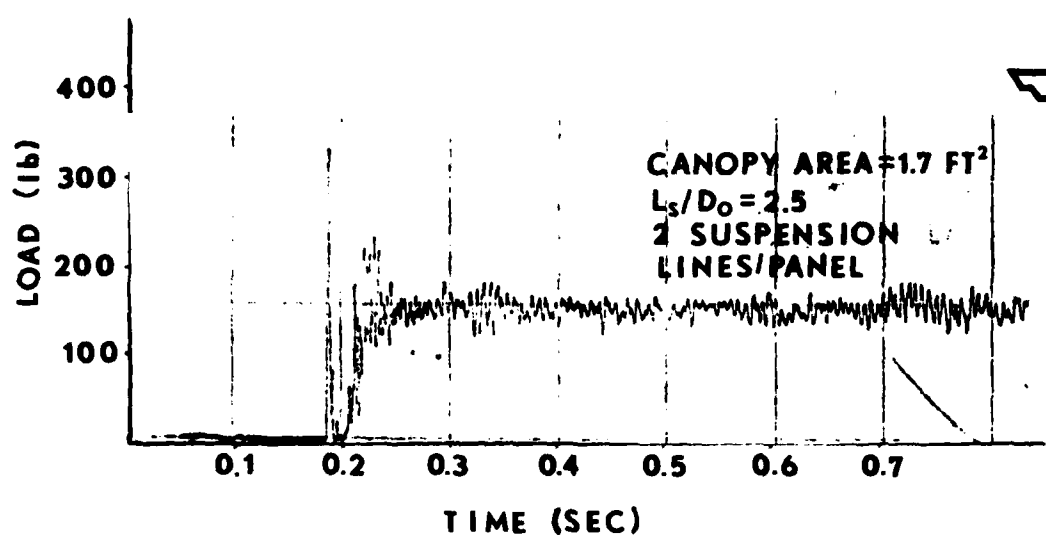
WIND TUNNEL ARRANGEMENT

FIGURE 1



DECELERATOR INFLATION EVENT
 SYSTEM LENGTH = 3 FEET

FIGURE 2



DECELERATOR INFLATION EVENT
SYSTEM LENGTH > 3 FEET

FIGURE 3

influence design practices if these types of chutes are used.

Drag Coefficient (C_d) data was then computed based on drag measured at Equilibrium Velocity (V_e) for the specified Ballistic Coefficient. Figure 4 shows the relationship between cross chute C_d and L_s/D_o , area and number of suspension lines. Figure 5, which applies to the three-foot maximum decelerator length requirement, shows how C_d varies as a function of decelerator area and number of suspension lines per panel. The L_s/D_o relationship is also shown to comply with popular design practices. It was noted after reviewing all data that the weight of the material has no appreciable effect on C_d ; therefore it was not included in Figures 4 and 5.

HIGH ALTITUDE TESTING

A series of high altitude air drop tests from 25,000 feet was conducted at NASA Wallops Flight Center to determine how air descent time is related to the sonobuoy weight to effective drag area ratio. A variety of buoy weights and weight to effective drag area ratios were tested. The altitude of the drop aircraft and the altitude/time history of the buoy air descent was determined by radar. Ten samples of each configuration was tested and the average time for that sample was used for C_d computation.

A drag coefficient was computed based on air descent time, altitude, decelerator size and sonobuoy weight by varying the drag coefficient in a computer program until the average time measured was achieved. Figure 6 shows a comparison of the C_d computed based on air descent time and the C_d measured in the wind tunnel for the same configuration. All systems met the three-foot maximum length decelerator requirement.

This data shows that for a given sonobuoy weight, as the ballistic coefficient is reduced, the sonobuoy is more stable. This is shown by the air descent time which compares more favorably with a predicted time based on wind tunnel measured drag coefficient.

LOW ALTITUDE TEST

A series of air drop tests were conducted at the Naval Air Development Center Field Station, Key West, Florida. The purpose was to determine if the sonobuoy could be adequately stabilized prior to water impact when launched from low altitude. The launch points used are shown on Table I.

TABLE I

LOW ALTITUDE TEST POINTS

Altitude (Feet)	Airspeed (KIAS)
1,500	300
500	350
200	300
150	200

CROSS CHUTE C_D vs L_s/D_o

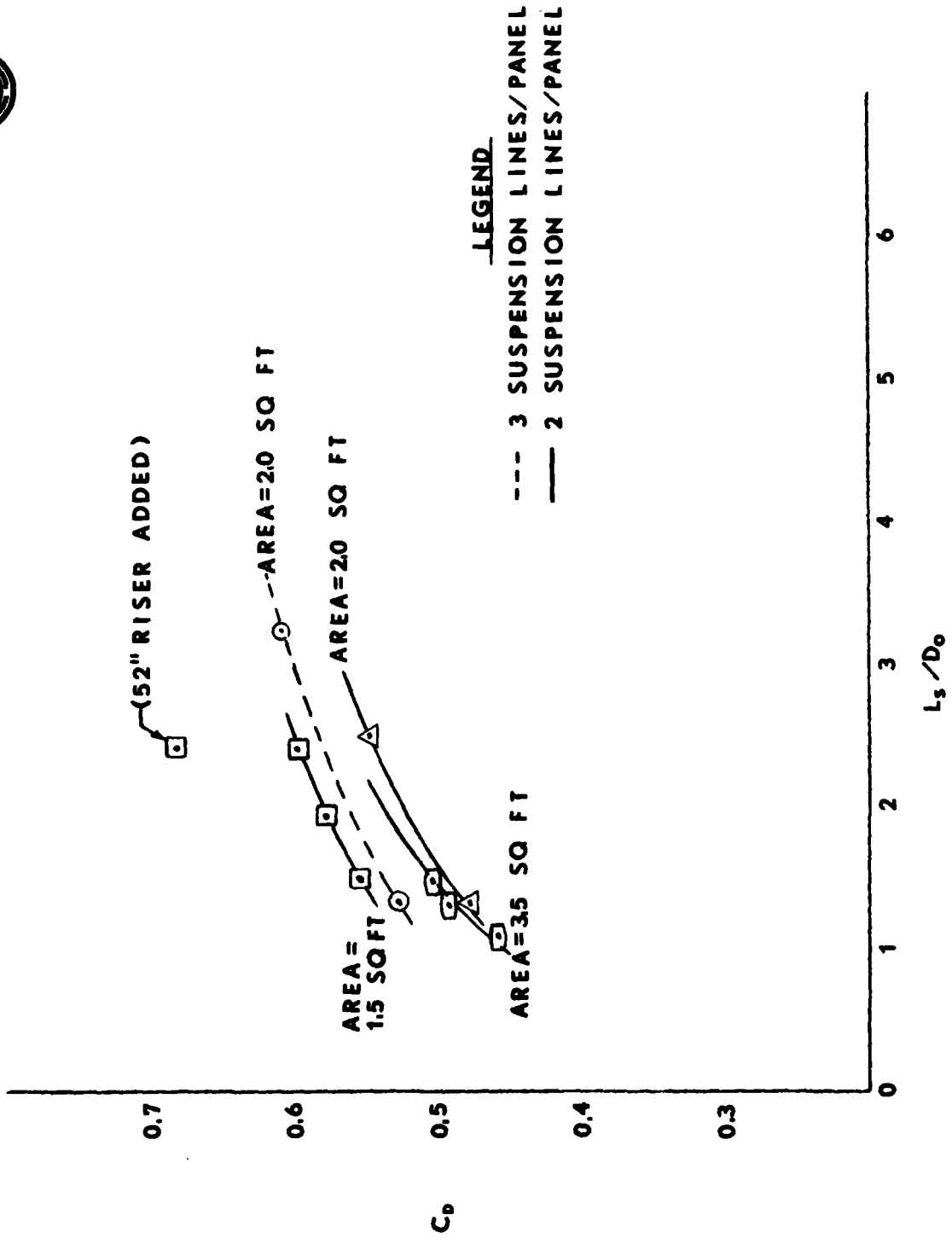


FIGURE 4

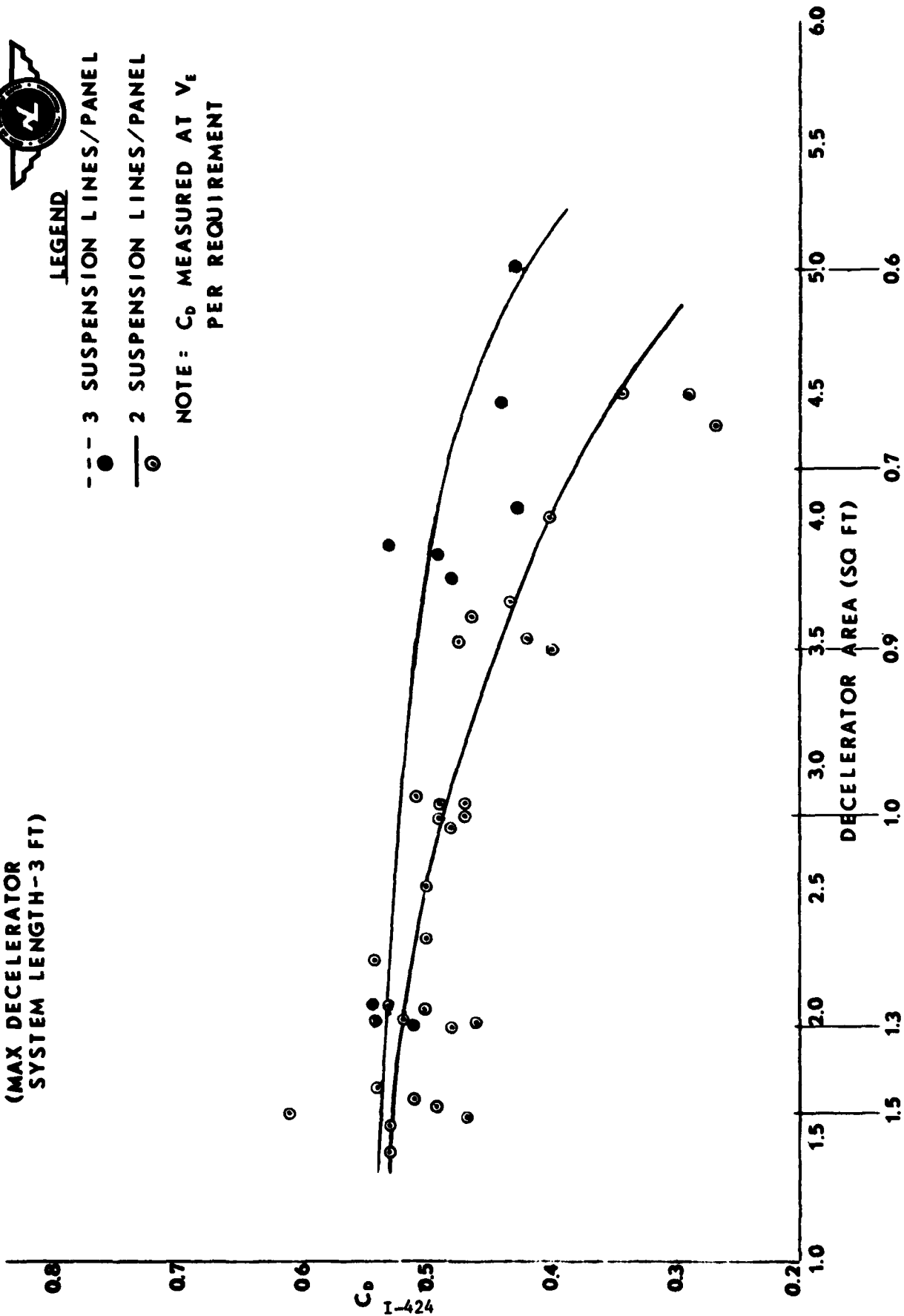
CROSS CHUTE C_D VS AREA CHARACTERISTIC
(MAX DECELERATOR
SYSTEM LENGTH-3 FT)



LEGEND

- 3 SUSPENSION LINES/PANEL
- 2 SUSPENSION LINES/PANEL

NOTE: C_D MEASURED AT V_E
PER REQUIREMENT

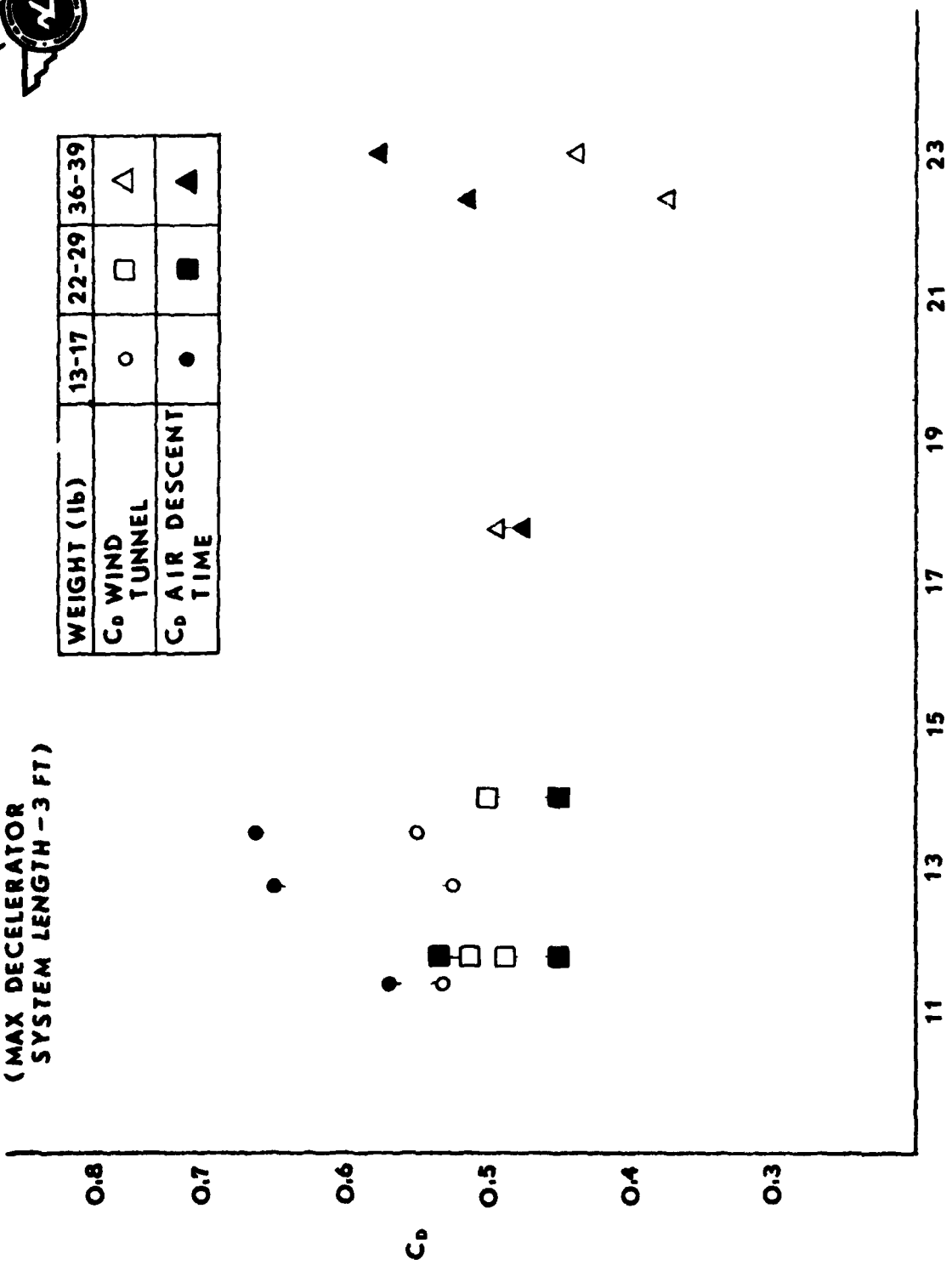


L_s/D_0
FIGURE 5



CROSS CHUTE C_D vs β
 (MAX DECELERATOR
 SYSTEM LENGTH - 3 FT)

WEIGHT (lb)	13-17	22-29	36-39
C_D WIND TUNNEL	○	□	△
C_D AIR DESCENT TIME	●	■	▲



I-425

FIGURE 6

The time for store stabilization is minimal at the lower test altitudes. The stability at water entry must be adequate enough so the sonobuoy internal components could function after impact. Sonobuoys ranging in weight from 14 to 39 pounds were dropped from each launch point. The sample size in all cases was five.

The results of the tests showed that decelerators sized within the established constraints could provide sufficient stability. The shallowest water entry angle that the buoys were exposed to was 35° relative to the water surface. The stability was such that the sonobuoy body oscillations about the trajectory angle varied by no more than $\pm 5^{\circ}$. The sonobuoy in-water functioning was not affected.

CONCLUSION

Blunt nose stores ranging in weight from 12 to 39 pounds can be adequately stabilized with a cross-type parachute sized to the ballistic coefficient and total length requirements outlined above. Useful decelerator design information is compiled herein which would have a variety of applications.

DATE
FILMED
-8